M. Chraibi · M. Boltes
A. Schadschneider · A. Seyfried
Editors

TRAFFIC AND GRANULAR FLOW '13

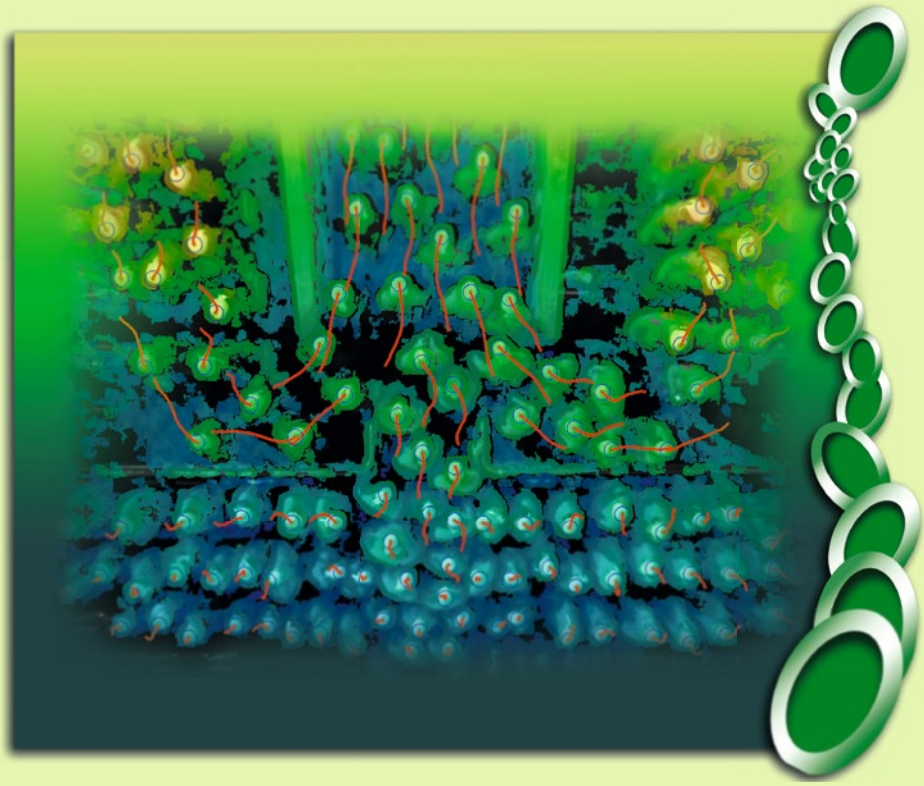

Springer

Traffic and Granular Flow ’13

Mohcine Chraibi • Maik Boltes •
Andreas Schadschneider • Armin Seyfried
Editors

Traffic and Granular Flow ’13

Springer

Editors
Mohcine Chraibi
Maik Boltes
Armin Seyfried
Jülich Supercomputing Centre
Forschungszentrum Jülich
Jülich
Germany

Andreas Schadschneider
Institut für Theoretische Physik
Universität zu Köln
Köln
Germany

ISBN 978-3-319-10628-1 ISBN 978-3-319-10629-8 (eBook)
DOI 10.1007/978-3-319-10629-8
Springer Cham Heidelberg New York Dordrecht London

Library of Congress Control Number: 2014957202

Mathematics Subject Classification (2010): 00B20, 60G99, 68U20, 70K99, 82C22, 82C31, 82D99, 91F99

Printed on acid-free paper

Springer is part of Springer Science+Business Media (www.springer.com)

Foreword

For its tenth edition, the international conference "Traffic and Granular Flow" (TGF) returned to the location of the very first meeting held in 1995. From 25 to 27 September, 2013, 105 international researchers came again together at the Forschungszentrum Jülich.

The purpose of the TGF'13 is bringing together international researchers from different fields ranging from physics to computer science and engineering to stimulate the transfer between basic and applied research and to discuss the latest developments in traffic-related systems.

In 1995 the TGF was probably the first conference with this objective. The workshop was attended by about 130 participants from 14 countries. My colleagues – D. E. Wolf and M. Schreckenberg – and I conceived the workshop to facilitate new ideas by considering the similarities of traffic and granular flow. To develop a unified view of flow instabilities like traffic jams or clogging of a hopper by powder was a purpose of the international workshop. Traffic as well as Granular Flow have both intriguing conceptual analogies. Traffic jams can be described by the same equations as density waves in granular pipe flow, and efficient simulation tools like cellular automata have been developed along similar lines in both fields, just to name two examples.

I am pleased to see that after so many years the field of traffic and granular flow is still progressing and that numerous problems could be solved by new facilities. Nevertheless, we are facing plenty of new challenges in these research fields. In 2013 the international conference covers a broader range of topics related to driven particles and transport systems. Besides the classical topics of granular flow and highway traffic, its scope includes data transport (Internet traffic), pedestrian and evacuation dynamics, collective motions in biological systems (swarm behaviour, molecular motors, social insects, etc.), complex networks and their dynamics (transportation network, Internet, epidemics, social networks, etc.) and intelligent traffic systems.

Supercomputing is one of the instruments in traffic and granular research, and Forschungszentrum Jülich, as one of the largest national centre for supercomputing and part of PRACE, is proud to play an important role in security research. In

the Jülich Supercomputing Centre, a division focuses on models of self-driven systems with applications in civil security and traffic planning. Experiments are performed and methods of data capturing are refined to support the developments of reliable models usable for security-related applications.In combination with high performance computing, we are able to tackle challenges in the simulation of large systems using high fidelity models.

I would like to thank the entire Organizing Committee and the Scientific Committee of the conference for their intensive and excellent work.

Jülich, Germany Achim Bachem
September 2013

Preface

In its tenth edition, "Traffic and Granular Flow" returned to the location of the very first conference held in 1995 at Forschungszentrum Jülich in Germany. The conference took place from 25 to 27 September 2013 and was organized in cooperation with the Institute for Theoretical Physics, University of Cologne, and the Jülich Supercomputing Centre of the Forschungszentrum Jülich.

Originally initiated to disseminate new ideas by considering the similarities of traffic and granular flow, TGF'13 covered a broad range of topics related to driven particle and transport systems. Besides granular flow and highway traffic, its scope includes data transport, pedestrian and evacuation dynamics, intercellular transport, swarm behaviour and collective dynamics of other biological systems.

One hundred five international researchers from different fields ranging from physics to computer science and engineering came together to discuss the state of the art developments. The stimulating atmosphere has facilitated many discussions and several new cooperations have been initiated.

A special thank goes to all colleagues who helped behind the scenes in the organization of the conference, especially Erik Andresen, Matthias Craesmeyer, Christian Eilhardt, Kevin Drzycimski, Stefan Holl, Ulrich Kemloh, Gregor Lämmel, Wolfgang Mehner, Daniel Salden, Bernhard Steffen, Antoine Tordeux and Jun Zhang.

The organizers gratefully acknowledge the financial support from the German Federal Ministry of Education and Research (BMBF) within the program Research for Civil Security, grant number 13N12045.

The conference series will continue and the next conference will be held in Delft (the Netherlands) in 2015.

Jülich, Germany — Mohcine Chraibi
Jülich, Germany — Maik Boltes
Köln, Germany — Andreas Schadschneider
Jülich, Germany — Armin Seyfried

Contents

Contributors

Vincent Aguiléra Paris-Est University LVMT, Marne-la-Vallée, France

Fernando Alonso-Marroquín School of Civil Engineering, The University of Sydney, Sydney, NSW, Australia

Igor Anufriev St. Petersburg State Polytechnical University, St. Petersburg, Russia

Cecile Appert-Rolland Laboratory of Theoretical Physics, Batiment 210, CNRS UMR 8627, University Paris-Sud, Orsay Cedex, France

B. van Arem Faculty of Civil Engineering and Geosciences, Department of Transport and Planning, Delft University of Technology, Delft, The Netherlands

Chikashi Arita Theoretische Physik, Universität des Saarlandes, Saarbrücken, Germany

Johanna Bamberger Bismarckgymnasium, Karlsruhe, Germany

Stefania Bandini Department of Informatics, Systems and Communications, Complex Systems and Artificial Intelligence Research Center, University of Milano-Bicocca, Milano, Italy

Marc Barthelemy Institut de Physique Théorique, CEA, CNRS-URA 2306, Gif-sur-Yvette, France

Somayyeh Belbasi University of Zanjan, Zanjan, Iran

Johannes Brügmann Fakultät für Physik, Universität Duisburg-Essen, Duisburg, Germany

Martins Brics Institute of Physics, Rostock University, Rostock, Germany

Marek Bukáček Faculty of Nuclear Sciences and Physical Engineering, Czech Technical University in Prague, Prague, Czech Republic

Jonathan Busch School of Civil Engineering, The University of Sydney, Sydney, NSW, Australia

Alexander P. Buslaev MADI, MTUCI, Moscow, Russia

Antonia Chechina Keldysh Institute of Applied Mathematics RAS, Moscow, Russia

Tao Chen Institute of Public Safety Research, Tsinghua University, Beijing, China

T. Chmura Nottingham University, Nottingham, UK

Keechoo Choi Department of Transportation Engineering, TOD-based Sustainable Urban Transportation Center, Ajou University, Suwon, Korea

Natalia Churbanova Keldysh Institute of Applied Mathematics RAS, Moscow, Russia

Luca Ciandrini DIMNP UMR 5235 CNRS, and Laboratoire Charles Coulomb UMR 5221 CNRS, Université Montpellier II, Montpellier Cedex, France

Julien Cividini Laboratoire de Physique Théorique d'Orsay, Bâtiment 210, Université Paris-Sud 11, Orsay Cedex, France

G. Costeseque Université Paris-Est/Ecole des Ponts ParisTech/CERMICS, Marne la Vall ee Cedex 2, France

Université Paris-Est/IFSTTAR/GRETTIA, Marne-la-Vallée Cedex 2, France

Matthias Craesmeyer Institut für Theoretische Physik, Universität zu Köln, Köln, Germany

Luca Crociani Department of Informatics, Systems and Communications, Complex Systems and Artificial Intelligence Research Center, University of Milano-Bicocca, Milano, Italy

Winnie Daamen Faculty of Civil Engineering and Geosciences, Department of Transport and Planning, Delft University of Technology and NS Stations, Netherlands Railways, Delft, The Netherlands

Felix Dietrich Munich University of Applied Sciences, München, Germany

Technische Universität München, Garching bei München, Germany

Ning Ding Center for Intelligent and Networked Systems, Tsinghua University, Beijing, China

Li-Yun Dong Institute of Applied Mathematics and Mechanics, Shanghai University, Shanghai, China

Dorine C. Duives Delft University of Technology, Delft, The Netherlands

Christian Eilhardt University of Cologne, Institute of Theoretical Physics, Köln, Germany

Takahiro Ezaki Department of Aeronautics and Astronautics, School of Engineering, The University of Tokyo, Tokyo, Japan

Japan Society for the Promotion of Science, Tokyo, Japan

M. Ebrahim Foulaadvand University of Zanjan, Zanjan, Iran

M. Fukui Nakanihon Automotive College, Sakahogi, Japan

Marion Gödel Munich University of Applied Science, Munich, Germany

Yuan Gao Center for Intelligent and Networked Systems, Tsinghua University, Beijing, China

Michael Gauß Fernstudienzentrum – Karlsruhe Institute of Technology (KIT), Karlsruhe, Germany

Anna-Lena Geßler Bismarckgymnasium, Karlsruhe, Germany

Ralph Germ Technische Universität Dresden, Dresden, Germany

Bernat Goñi Ros Faculty of Civil Engineering and Geosciences, Department of Transport and Planning, Delft University of Technology, Delft, The Netherlands

Andrea Gorrini Information Society Ph.D. Program, Department of Sociology and Social Research, University of Milano-Bicocca, Milano, Italy

David Greenwood Faculty of Engineering, University of Bristol, Bristol, UK

Samer H. Hamdar Department of Civil and Environmental Engineering Academic Center, School of Engineering and Applied Science, The George Washington University, NW Washington, DC, USA

Peter Heitzelmann Bismarckgymnasium, Karlsruhe, Germany

P. Hemmerle Daimler AG, HPC: 059-X832, Sindelfingen, Germany

Gerhard Hermanns University of Duisburg-Essen, Duisburg, Germany

B. Herz Universitat Pompeu Fabra, Barcelona, Spain

Jeroen van den Heuvel Faculty of Civil Engineering and Geosciences, Department of Transport and Planning, Delft University of Technology and NS Stations, Netherlands Railways, Delft, The Netherlands

Poul G. Hjorth Department of Applied Mathematics and Computer Science, Technical University of Denmark, Kongens Lyngby, Denmark

Ingmar Hofsäß PTV Group, Karlsruhe, Germany

Serge P. Hoogendoorn Faculty of Civil Engineering and Geosciences, Department of Transport and Planning, Delft University of Technology and NS Stations, Netherlands Railways, Delft, The Netherlands

Pavel Hrabák Faculty of Nuclear Sciences and Physical Engineering, Czech Technical University in Prague, Prague, Czech Republic

Tsumugi Ishida Department of Complex Systems Science, Nagoya University, Nagoya, Japan

Mayuko Iwamoto Graduate School of Advanced Mathematical Sciences, Meiji University, Tokyo, Japan

Anders Johansson Faculty of Engineering, University of Bristol, Bristol, UK

David de Jong Delft University of Technology, Delft, The Netherlands

Roxana Josens Instituto de Fisiología, Biología Molecular y Neurociencias, FCEN – UBA, Pabellon II, Ciudad Universitaria, de Buenos Aires, Argentina

Gerta Köster Munich University of Applied Sciences, München, Germany

Rene Kahlmeyer Bismarckgymnasium, Karlsruhe, Germany

Jevgenijs Kaupužs Institute of Mathematical Sciences and Information Technologies, University of Liepaja, Liepaja, Latvia

Institute of Mathematics and Computer Science, University of Latvia, Riga, Latvia

Boris S. Kerner Physik von Transport und Verkehr, Universität Duisburg-Essen, Duisburg, Germany

Arne Kesting TomTom Development Germany GmbH, Berlin, Germany

M. Kikuchi Cybermedia Center, Osaka University, Toyonaka, Japan

Ekaterina Kirik Institute of Computational Modelling SB RAS, Akademgorodok, Krasnoyarsk, Russia

Sarah Klein Universität des Saarlandes, Saarbrücken, Germany; Laboratory of Theoretical Physics, Batiment 210, University Paris-Sud, Orsay Cedex, France

Victor L. Knoop Faculty of Civil Engineering and Geosciences, Department of Transport and Planning, Delft University of Technology, Delft, The Netherlands

Florian Knorr Fakultät für Physik, Universität Duisburg-Essen, Duisburg, Germany

Micha Koller IT-Designers GmbH, Esslingen am Neckar, Germany

Sara Korn Bismarckgymnasium, Karlsruhe, Germany

Valery V. Kozlov Steklov Mathematical Institute, Russian Academy of Sciences, Moscow, Russia

Milan Krbálek Faculty of Nuclear Sciences and Physical Engineering, Czech Technical University in Prague, Prague, Czech Republic

Tobias Kretz PTV Group, Karlsruhe, Germany

I.N. Kulkov University of Duisburg-Essen, Duisburg, Germany

Bharat Kunwar University of Bristol, Bristol, UK

Valentina Kurtc St. Petersburg State Polytechnical University, St. Petersburg, Russia

Sylvain Lassarre IFSTTAR GRETTIA, Marne-la-Vallée, France

Jean-Patrick Lebacque Université Paris-Est/IFSTTAR/GRETTIA, Champs sur Marne, Marne la Vall ee Cedex 2, France

Karsten Lehmann PTV Group, Karlsruhe, Germany

Zhi-Yang Lin Institute of Applied Mathematics and Mechanics, Shanghai University, Shanghai, China

Hans van Lint Delft University of Technology, Delft, The Netherlands,

Siuming Lo Department of Civil and Architectural Engineering, City University of Hong Kong, Tat Chee Avenue, Kowloon, Hong Kong SAR

Celia Lozano Facultad de Ciencias, Departamento de Física, Universidad de Navarra, Navarra, Spain

Xue Hao Lu Jing Ye High School, Shanghai, China

Robert Lubaś Department of Applied Computer Science, AGH University of Science and Technology, Kraków, Poland

Peter B. Luh Department of Electrical and Computer Engineering, University of Connecticut, Storrs, CT, USA

Wei Lv State Key Laboratory of Fire Science, University of Science and Technology of China, Hefei, China

Alma R. Méndez Department of Applied Mathematics and Systems, Universidad Autónoma Metropolitana (Cuajimalpa), Alvaro Obregón, México

Jian Ma National United Engineering Laboratory of Integrated and Intelligent Transportation, School of Transportation and Logistics, Southwest Jiaotong University, Chengdu, PR China

Reinhard Mahnke Institute of Physics, Rostock University, Rostock, Germany

Xu Mai State Key Laboratory of Fire Science, University of Science and Technology of China, Hefei, PR China

Andrey Malyshev Institute of Computational Modelling SB RAS, Akademgorodok, Krasnoyarsk, Russia

Christian Marschler Department of Applied Mathematics and Computer Science, Technical University of Denmark, Kongens Lyngby, Denmark

Takashi Matsuoka Graduate School of Advanced Mathematical Sciences, Meiji University, Tokyo, Japan

Dinesh Mohan Transportation Research and Injury Prevention Programme, Indian Institute of Technology New Delhi, New Delhi, India

J.D. Muñoz Universidad Nacional de Colombia, Bogotá, D.C., Cundinamarca, Colombia

Marcin Mycek Department of Applied Computer Science, AGH University of Science and Technology, Kraków, Poland

A. Nakayama Faculty of Science and Technology, Meijo University, Nagoya, Japan

Ryosuke Nishi National Institute of Informatics, Tokyo, Japan

JST, ERATO, Kawarabayashi Large Graph Project, Tokyo, Japan

Katsuhiro Nishinari Research Center for Advanced Science and Technology, The University of Tokyo, Tokyo, Japan

Kazumichi Ohtsuka Research Center for Advanced Science and Technology, The University of Tokyo, Tokyo, Japan

L.E. Olmos Universidad Nacional de Colombia, Bogotá, D.C., Cundinamarca, Colombia

Gaurav Pandey Transportation Research and Injury Prevention Programme, Department of Civil Engineering, Indian Institute of Technology New Delhi, New Delhi, India

Daniel R. Parisi Instituto Tecnológico de Buenos Aires, de Buenos Aires, Argentina

Saira Saleem Pathan Fraunhofer Institute for Factory Operation and Automation, Magdeburg, Germany

T. Pitz Rhine-Waal University of Applied Sciences, Kleve, Germany

Egor Popel Siberian Federal University, Krasnoyarsk Krai, Russia

Jakub Porzycki Department of Applied Computer Science, AGH University of Science and Technology, Kraków, Poland

Lingqiao Qin Department of Civil and Environmental Engineering Academic Center, School of Engineering and Applied Science, The George Washington University, NW Washington, DC, USA

Álvaro Ramírez-Gómez Escuela Técnica Superior de Ingeniería y Diseño Industrial, Universidad Politécnica de Madrid, Madrid, Spain

K. Ramchandra Rao Department of Civil Engineering, Indian Institute of Technology New Delhi, New Delhi, India

Hubert Rehborn Daimler AG, HPC: 059-X832, Stuttgart, Germany

Shahreena Rhasbudin Shah Faculty of Civil Engineering and Geosciences, Delft University of Technology, Delft, The Netherlands

Klaus Richter Fraunhofer Institute for Factory Operation and Automation, Magdeburg, Germany

Michel Roussignol Paris-Est University LAMA, Marne-la-Vallée, France

Zeinab Sadjadi Department of Theoretical Physics, Saarland University, Saarbrücken, Germany

Qi Hao Sang Jing Ye High School, Shanghai, China

Ludger Santen Department of Theoretical Physics, Saarland University, Saarbrücken, Germany

Andreas Schadschneider Institut für Theoretische Physik, Universität zu Köln, Köln, Germany

W.J. Schakel Faculty of Civil Engineering and Geosciences, Department of Transport and Planning, Delft University of Technology, Delft, The Netherlands

Michael Schreckenberg Fakultät für Physik, Universität Duisburg-Essen, Duisburg, Germany

M. Reza Shaebani Department of Theoretical Physics, Saarland University, Saarbrücken, Germany

Shrikant Sharma Buro Happold, Bath, UK

A. Shibata Computing Research Center, High Energy Accelerator Research Organization (KEK) & Graduate University for Advanced Studies (Sokendai), Tsukuba, Japan

Kenichiro Shimura Research Center for Advanced Science and Technology, The University of Tokyo, Tokyo, Japan

Jan Sieber College of Engineering, Mathematics and Physical Sciences, University of Exeter, Exeter, UK

Isabella von Sivers Munich University of Applied Sciences, München, Germany

Weiguo Song State Key Laboratory of Fire Science, University of Science and Technology of China, Hefei, PR China

Jens Starke Department of Applied Mathematics and Computer Science, Technical University of Denmark, Kongens Lyngby, Denmark

Yūki Sugiyama Department of Complex Systems Science, Nagoya University, Nagoya, Japan

Kohta Suzuno Graduate School of Advanced Mathematical Sciences, Meiji University, Tokyo, Japan

Shin-ichi Tadaki Department of Information Science, Saga University, Saga, Japan

Yohei Taniguchi Department of Advanced Interdisciplinary Studies (AIS), Graduate School of Engineering, The University of Tokyo, Tokyo, Japan

Alexander G. Tatashev MTUCI, MADI, Moscow, Russia

Akiyasu Tomoeda Meiji Institute for Advanced Study of Mathematical Sciences, Meiji University, Tokyo, Japan

CREST, Japan Science and Technology Agency, Tokyo, Japan

Antoine Tordeux Paris-Est University LVMT, Marne-la-Vallée, France

Marina Trapeznikova Keldysh Institute of Applied Mathematics RAS, Moscow, Russia

Martin Treiber Technische Universität Dresden, Dresden, Germany

Daishin Ueyama Graduate School of Advanced Mathematical Sciences, Meiji University, Tokyo, Japan

R.M. Velasco Department of Physics, Universidad Autónoma Metropolitana (Iztapalapa), Iztapalapa, México

Giuseppe Vizzari Department of Informatics, Systems and Communications, Complex Systems and Artificial Intelligence Research Center, University of Milano-Bicocca, Milano, Italy

Aral Voskamp Faculty of Civil Engineering and Geosciences, Department of Transport and Planning, Delft University of Technology and NS Stations, Netherlands Railways, Delft, The Netherlands

Hai L. Vu Delft University of Technology, Delft, The Netherlands,

Jarosław Wąs Department of Applied Computer Science, AGH University of Science and Technology, Kraków, Poland

Femke L.M. van Wageningen-Kessels Delft University of Technology, Delft, The Netherlands

Zhi Jie Wang Jing Ye High School, Shanghai, China

Hans Weber Department of Physics, Luleå University of Technology, Luleå, Sweden

Xiaoge Wei State Key Laboratory of Fire Science, University of Science and Technology of China, Hefei, China

S.C. Wong Department of Civil Engineering, The University of Hong Kong, Pokfulam, Hong Kong

Daichi Yanagisawa College of Science, Ibaraki University, Bunkyo, Mito, Ibaraki, Japan

Marina V. Yashina MTUCI, MADI, Moscow, Russia

T. Yosida Nakanihon Automotive College, Sakahogi, Japan

Guan Zong Yuan Jing Ye High School, Shanghai, China

S. Yukawa Department of Earth and Space Science, Osaka University, Toyonaka, Japan

Thomas Zaksek Fakultät für Physik, Universität Duisburg-Essen, Duisburg, Germany

Hui Zhang Institute of Public Safety Research, Tsinghua University, Beijing, China

Peng Zhang Institute of Applied Mathematics and Mechanics, Shanghai University, Shanghai, China

Part I
Pedestrian Traffic and Evacuation Dynamics

Modeling of Pedestrians

Cecile Appert-Rolland

Abstract Different families of models first developed for fluid mechanics have been extended to road, pedestrian, or intracellular transport. These models allow to describe the systems at different scales and to account for different aspects of dynamics. In this paper, we focus on pedestrians and illustrate the various families of models by giving an example of each type. We discuss the specificities of crowds compared to other transport systems.

1 Introduction

What is the common point between fluids, cars, pedestrians or molecular motors? Though they are quite different and evolve in systems of very different sizes, they all result into flows, and they all obey simple conservation laws. As a result, the families of models that have been developed in the past to describe fluids at different scales have also been adapted to describe highway traffic [1], crowds [2] or axonal transport [3, 4] (Table 1).

Let us consider first macroscopic models: At large scales, individuals are not visible anymore, and the state of the system can be characterized by locally averaged density and velocity. For fluids, Navier-Stokes equations express the conservation of mass and of momentum.

For road traffic, mass conservation is still relevant, and provides a first equation relating density and velocity. However, as vehicles are in contact with the road, momentum is not conserved. A second relation must be provided to close the equations. The simplest way is to give the (possibly data-based) fundamental diagram, relating the flow of vehicles and the density. The resulting model is a so-called first order model, a prominent example being the LWR model [14, 15]. The more sophisticated second-order models [16, 17] express the fact that the adjustment of flow to density may not be instantaneous but rather takes place within a certain

C. Appert-Rolland (✉)
Laboratory of Theoretical Physics, CNRS UMR 8627, University of Paris-Sud, 91405 Orsay Cedex, France
e-mail: Cecile.Appert-Rolland@th.u-psud.fr

M. Chraibi et al. (eds.), *Traffic and Granular Flow '13*,
DOI 10.1007/978-3-319-10629-8_1

Table 1 Correspondence of model families, for four different physical systems: fluids, road traffic, pedestrian traffic and intracellular traffic. We mention a few models (with their reference) as prominent and/or historical examples of a given model type. The scale at which the system is described increases as one goes down in the table

Fluids	Road traffic	Pedestrians	Molecular motors
Molecular dynamics [5, 6] m **a** = $\sum$ **f**	Car-following [7–9] a(ΔV, Δx)	Ped-following	Molecular dynamics m **a** = $\sum$ **f**
Kinetic theory P(v,x,t)	Kinetic theory P(v,x,t)	Kinetic theory P(v,x,t,ξ)	
Cellular automata *FHP Model* [10]	Cellular automata *Nagel-Schreckenberg model* [11]	Cellular automata *Floor Field model* [12]	Cellular automata *Langmuir kinetics* [13]
Continuous PDEs Conservation of mass and momentum *Navier-Stokes Eqs*	Continuous PDEs Conservation of mass + fundamental diagram $j(\rho)$ *LWR Model* [14, 15]	Continuous PDEs Conservation of mass and ...	Continuous PDEs Open system: balance of fluxes

relaxation time. The second relation between density and velocity is then a second partial differential equation.

For pedestrians also, the mass conservation equation must be completed to provide a closed set of equations. However, the complexity is increased by the fact that pedestrians, first, walk in a two-dimensional space, and, second, do not necessarily all go in the same direction.

Within cells, intracellular transport also involves some "walkers", i.e. some molecules equipped with some kind of legs that perform stepping along some cylindrical tracks called microtubules. In contrast with human pedestrians, these so-called molecular motors do not only walk along microtubules, they can also detach from the microtubules, diffuse around, and attach again. Thus, if one considers the density of motors on the microtubule, even mass conservation is not realized any more. The equations that determine the evolution of density and velocity must then rather express some balance of fluxes between different regions of the system.

In the same way as various macroscopic models can be proposed for all these systems, there are some equivalents of molecular dynamics or of cellular automata approaches that have been developed for road, pedestrian or intracellular traffic.

In most cases, for a given physical system, different types of models have been proposed independently to account for the behavior of the system at different scales, leading to large families of models. In some cases however, it is possible to relate the models at the different scales and to understand how the macroscopic behavior can emerge from the individual dynamics.

In this paper, we shall focus on pedestrian modeling, and give an example for each family of models. Part of this work (Sects. 2, 3, and part of 4) was performed in the frame of the interdisciplinary PEDIGREE project [18]. The teams involved are presented in Table 2.

Table 2 The PEDIGREE Project involved four French teams listed below

Laboratory	IMT	INRIA	CRCA	LPT
Team leader	P. Degond	J. Pettré	G. Theraulaz	C. Appert-Rolland
Participants	J. Fehrenbach	S. Donikian	O. Chabiron	J. Cividini
	J. Hua	S. Lemercier	E. Guillot	A. Jelić
	S. Motsch		M. Moreau	
	J. Narski		M. Moussaïd	

The work of Sect. 5 was performed as part of the master and PhD of Julien Cividini, in collaboration with H. Hilhorst.

2 Ped-Following Model

Fluids can be described at the level of molecules, by taking into account all the interaction potentials between atoms in a more or less refined way, as is done in molecular dynamics simulations [5,6]. When vehicles or pedestrians are considered, two main difficulties arise. First the interaction potential is not know – actually the interaction cannot in general be written as deriving from a potential. Second, the interaction is in general highly non-isotropic, and does not depend only on the position but also on the velocity and on the target direction of each individual.

In road traffic, cars naturally follow lanes. This features greatly simplifies the problem. Each car has a single well-defined predecessor on its lane. Apart from lane changes, a car driver can only adjust its speed. He will do so depending on the conditions in front (distance, velocity, acceleration of the predecessor). Actually several cars ahead could be taken into account (and indeed some empirical studies [19] have shown that a driver may take into account several of its leaders). But still, there is a clear hierarchy among the leaders, given by their order in the lane.

In pedestrian traffic, individuals evolve in a two-dimensional space, and may interact with several pedestrians at the same time, without a clear hierarchy. Besides, the combination of interactions is in general not a simple sum of one-by-one interactions. However, there are situations where the flow is organized in such a way that it is quasi one dimensional.

For example in corridors, all pedestrians mostly go in the same direction. Even if two opposite flows are considered, it is known that some lanes are formed spontaneously, and within each lane the flow is again quasi one dimensional and one directional.

The way pedestrians follow each other is even more clear when pedestrians walk in a line. Such a configuration can be met for example in very narrow corridors. It has been realized in several experiments [20–22], in order to study how pedestrians react when they can only adjust their speed. One may then wonder how the acceleration of a pedestrian is related to the distance, velocity, acceleration of

its predecessor, and how the behavior of a pedestrian differs from the one of a car. However, in order to evaluate the following behavior of a pedestrian, one needs to be able to track at the same time, and on long enough time windows, the trajectory of both the pedestrian under consideration and its predecessor.

Such an experiment has been realized in the frame of the PEDIGREE project [18]. Pedestrians were asked to walk as a line, i.e. to follow each other without passing [23]. Their trajectory was circular, in order to avoid boundary effects. The motion of all pedestrians was tracked with a high precision motion capture device (VICON) [24]. As a result, the trajectories of all pedestrians were obtained for the whole duration of the experiment (from 1 to 3 min).

Various combinations of the dynamic coordinates of the predecessor have been tested against the acceleration a of the follower. It turned out that the best correlation was obtained [23, 25] for the relation

$$a(t) = C \frac{\Delta v(t-\tau)}{[\Delta x(t)]^{\gamma}} \tag{1}$$

where v is the velocity of the predecessor, and Δx the distance between the predecessor and its follower.

One important difference with car traffic is the time delay τ introduced in the velocity: While the follower is able to evaluate quite instantaneously the position of his predecessor, he needs some time delay τ to evaluate his velocity.

Another difference with car traffic is the ability of pedestrians to flow even at very large local densities [26]. In the aforementioned experiment, the velocity was still of the order of 1 or 2 dm/s at local densities as high as 3 ped/m. This can be achieved thanks to the ability of pedestrians to keep walking even at very low densities: they can reduce the amplitude of their steps almost to zero while still keeping a stepping pace almost constant [27].

In contrast to cars, pedestrians can also take advantage of any space left by the predecessor, synchronizing partially their steps as was observed in previous experiments [20]. Surprisingly, this synchronization effect is also observed for pedestrians walking at a larger distance [27], probably as a result of the tendency of pedestrians to synchronize with external rhythmic stimuli [22].

Here we have presented a model for one-dimensional pedestrian flows. In general, pedestrians move in a two-dimensional space, and various agent based models have been proposed which we shall not review here.

3 One-Dimensional Bi-directional Macroscopic Model for Crowds

At the other extreme, when seen from a distance, crowds can be described as continuous fluids. As mentioned in the introduction, one important difference with fluids is that pedestrians have a target – which may not be the same for all of them.

A simple configuration is met in corridors: the flow is quasi one-dimensional, but pedestrians can walk in both directions. There is thus a need to distinguish two densities $\rho_\pm$ of pedestrians, one for each walking direction. Each density obeys a conservation law:

$$\partial_t \rho_+ + \partial_x(\rho_+ u_+) = 0,$$
$$\partial_t \rho_- + \partial_x(\rho_- u_-) = 0,$$

where $u_\pm$ is the locally averaged velocity of pedestrians going in the $\pm$ direction.

Two other relations are needed to determine the four unknown densities and velocities. This is achieved by writing two other differential equations for the momentum [28, 29]

$$\partial_t(\rho_+ u_+) + \partial_x(\rho_+ u_+ u_+) = -\rho_+ \left(\frac{d}{dt}\right)_+ [p(\rho_+, \rho_-)],$$
$$\partial_t(\rho_- u_-) + \partial_x(\rho_- u_- u_-) = \rho_- \left(\frac{d}{dt}\right)_- [p(\rho_-, \rho_+)],$$

in which, by analogy to the pressure in fluid mechanics, the interactions between pedestrians are described by a term $p(\rho_\pm, \rho_\mp)$. There is however a major difference with fluid mechanics: following [17], the derivative

$$(d/dt)_\pm = \partial_t + u_\pm \partial_x \tag{2}$$

is taken in the referential of the walking pedestrians, and not in the fixed frame as for fluids. Indeed, pedestrians react to their perception of the surrounding density as they see it while walking.

The term $p(\rho_\pm, \rho_\mp)$ is actually not a pressure as in fluid mechanics, but rather a velocity offset between the achieved velocity $u_\pm$, and another quantity $w_\pm$ which, as it is conserved along each pedestrian trajectory, can be interpreted as the desired velocity that the pedestrian would have if he was alone. In other words,

$$u_+ = w_+ - p(\rho_+, \rho_-)$$
$$-u_- = w_- - p(\rho_-, \rho_+)$$

where $w_\pm$ are Riemann invariants

$$\partial_t w_+ + u_+ \partial_x w_+ = 0$$
$$\partial_t w_- + u_- \partial_x w_- = 0$$

conserved along the trajectories of $\pm$ pedestrians. The function $p(\rho_\pm, \rho_\mp)$ can be determined from experimental measurements.

One difficulty coming from the fact that pedestrians do not necessarily have the same target site is that they may converge towards the same region, leading in the simulations to density divergences. A special treatment is thus required in order to limit the density to physical values. The solution retained in [28, 29] was to let $p(\rho_{\pm}, \rho_{\mp})$ diverge when the density approaches its upper limit value.

4 Kinetic Models

In kinetic models, instead of describing explicitly the presence of a particle (molecule, vehicle or pedestrian) at a given location with a given velocity, one deals with the corresponding probability.

For example, in [30], with G. Schehr and H. Hilhorst, we have considered the case of a bidirectional two-lane road. Cars had different desired velocities, but the overtaking can occur only if there is enough space on the other lane (see Fig. 1). Assuming translation invariance of the probability distributions along the road, the problem results in finding the distribution of effective velocities as a function of the distribution of desired velocities. The solution of this problem requires to evaluate the overtaking probability. To do so, we assume that the probability to find a sufficient empty interval in the other lane at a given time and given place is equal to the average probability (mean-field assumption). Under these assumptions, we find that a symmetry breaking can occur between the lanes. This model developed for road traffic could be seen as a first attempt to model pedestrians in a corridor when lanes are formed, i.e. at high enough densities. However, this organization into lanes will not be as stable as in road traffic.

To account more completely for pedestrian flows, one has to consider the full joint probability distribution $f(\mathbf{v}, \mathbf{x}, t, \boldsymbol{\xi})$ of finding in position $\mathbf{x}$ at time t a pedestrian with velocity $\mathbf{v}$ and target site located in ξ. It is out of scope yet to find universal equations for this distribution. However, one may try to derive those from microscopic models. Two such derivations have been proposed by P. Degond et al. in [31] and [32], starting from agent based models in which pedestrians modify their direction (and possibly velocity modulus) in order to avoid possible collisions in the near future, while still trying to keep as close as possible to their target direction. Some mean-field approximations have to be done to go from the

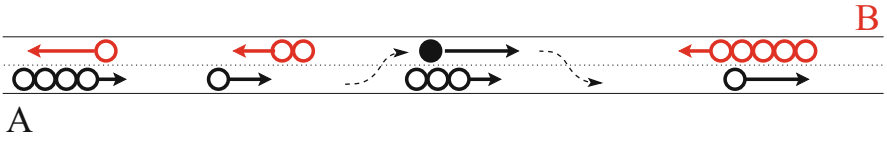

Fig. 1 Kinetic model for a bidirectional two-lane road. The vehicles (*red* and *black circles*) have different desired velocities, leading to platoon formation. Overtaking can take place only if there is enough free space on the other lane (From [30])

microscopic discrete models to the kinetic ones. The smoothing due to these mean-field expressions has to be balanced by the introduction of some appropriate noise in the equations for the probability distribution f.

Once they have been obtained, these kinetic models can themselves be taken as a starting point to derive macroscopic models [31, 32] in two dimensions.

5 Cellular Automata

To complete our comparison between pedestrian and fluid models, we shall now consider cellular automata models. For fluids, the story started in 1986, with the FHP model [10], in which pointlike particles were hopping onto a hexagonal lattice, and undergoing collisions at the nodes of the lattice. Providing that these collisions conserve mass and momentum but still mix enough the particle distributions, and that the lattice has enough symmetries, the resulting lattice gas was found to obey equations very close to Navier-Stokes equations [33]. Hence direct simulations of this lattice gas were providing solutions of the (almost) Navier-Stokes equations – a breakthrough given the difficulty to solve the latter.

A similar approach was proposed in 1992 for road traffic by Nagel and Schreckenberg [11]. Of course in this case there is no momentum conservation anymore, but rather some rules expressing the increase of velocity up to some maximal velocity, under the constraint of collision avoidance.

For pedestrians, interactions can be quite long ranged and one has to combine interactions taking place in any direction. It is thus a priori quite complex to develop a cellular automaton based on interactions between neighboring cells. A solution inspired from ants was provided by the use of some effective pheromones, which mediate the interactions between pedestrians [12, 34, 35].

Apart from the geometry of the lattice and the evolution rules, a cellular automaton is also defined by the sequence under which lattice sites are updated. Processes in continuous time, with independent events occurring with given rates, are well described by random sequential updates, in which a site is chosen at random and updated at each micro-time step. However this update leads to large fluctuations (the same site can be chosen twice in a row while another one will be ignored for a long time). Thus, for traffic applications, more regular updates are preferred. In particular the parallel update in which all the sites are updated in parallel at discrete time steps ensures a certain regularity in the flow. It introduces a time scale (the aforementioned time step) which can be interpreted as the reaction time of individuals.

Parallel update is widely used in road traffic modeling. It is also employed for pedestrians [36, 37], but requires to be complemented by extra rules. Indeed, in two-dimensional flows, two pedestrians may chose the same target site, resulting in a conflict that has to be solved by ad-hoc rules. Though these conflicts may be given a physical meaning in terms of friction [37], some other updates which do not require these extra rules have been proposed.

The random shuffle update [38–41] ensures that each site will be updated exactly once per time step, but in an order that is randomly chosen at each time step. This update has indeed been used in early cellular automata simulations of pedestrian evacuations [41, 42].[1]

The frozen shuffle update [43, 44] associates to each pedestrian a fixed phase τ, i.e. a real number between 0 and 1, and updates pedestrians once per time step in the order of increasing phases. This update allows to have higher fluxes than parallel update, reproducing the tendency of pedestrians to flow even at high densities. Besides, the phase τ can be given a physical meaning. It can represent the phase in the stepping cycle. It allows also to some extend to map the cellular automaton dynamics onto a continuous time/continuous space dynamics [44].

Cellular automata simulations can be useful to simulate large systems [41]. They can also help to understand some pattern formation [45], for example lane formation in counterflows [12, 46], or diagonal patterns at the crossing of two perpendicular flows [47, 48].

Conclusion

In this paper we have reviewed a few models for pedestrians proposed in the past years, to illustrate the various families of models that span over the different physical systems considered at the TGF conference.

For completeness, we must mention that at even larger scales than considered in this paper, models for road or pedestrian traffic must be supplemented with route choice models, as in [49].

Acknowledgements The PEDIGREE project has been supported by the French 'Agence Nationale pour la Recherche (ANR)' (contract number ANR-08-SYSC-015-01, from 2008 to 2011).

Subsequent data analysis was partially supported by the 'RTRA Triangle de la physique' (Project 2011-033T).

References

1. D. Chowdhury, L. Santen, A. Schadschneider, Statistical physics of vehicular traffic and some related systems. Phys. Rep. **329**, 199 (2000)
2. T. Vicsek, A. Zafeiris, Collective motion. Phys. Rep. **517**(3–4), 71–140 (2012)
3. T. Chou, K. Mallick. R.K.P. Zia, Non-equilibrium statistical mechanics: from a paradigmatic model to biological transport. Rep. Prog. Phys. **74**, 116601 (2011)

[1] Note that in some communities, *random shuffle update* is called *random sequential update*, as done in [42]. We shall stick to the denomination used in physics, for which *random sequential update* rather refers to an update close to continuous time.

4. C. Appert-Rolland, M. Ebbinghaus, L. Santen, Intracellular transport driven by cytoskeletal motors: general mechanisms and defects. Phys. Rep. (submitted)
5. B. Alder, T.E. Wainwright, Studies in molecular dynamics. I. General method. J. Chem. Phys. **31**, 459 (1959)
6. A. Rahman, Correlations in the motion of atoms in liquid argon. Phys. Rev. **136**, A405–A411 (1964)
7. L. Pipes, An operational analysis of traffic dynamics. J. Appl. Phys. **24**, 274–281 (1953)
8. R. Chandler, R. Herman, E. Montroll, Traffic dynamics: studies in car following. Oper. Res. **6**, 165–184 (1958)
9. D. Gazis, R. Herman, R. Potts, Car following theory of steady state traffic flow. Oper. Res. **7**, 499–505 (1959)
10. U. Frisch, B. Hasslacher, Y. Pomeau, Lattice-gas automata for the Navier-Stokes equation. Phys. Rev. Lett. **56**, 1505–1508 (1986)
11. K. Nagel, M. Schreckenberg, A cellular automaton model for freeway traffic. J. Phys. I **2**, 2221–2229 (1992)
12. C. Burstedde, K. Klauck, A. Schadschneider, J. Zittartz, Simulation of pedestrian dynamics using a 2-dimensional cellular automaton. Physica A **295**, 507–525 (2001)
13. A. Parmeggiani, T. Franosch, E. Frey, Totally asymmetric simple exclusion process with Langmuir kinetics. Phys. Rev. E **70**, 046101 (2004)
14. M. Lighthill, G. Whitham, On kinematic waves. II. A theory of traffic flow on long crowded roads. Proc. R. Soc. Lond. Ser. A, Math. Phys. Sci. A **229**, 317–345 (1955)
15. P. Richards, Shock waves on the highway. Oper. Res. **4**, 42–51 (1956)
16. H. Payne, Models of freeway traffic and control, in *Mathematical Model of Public Systems*. Simulation Councils Proceedings Series, La Jolla, vol. 1 (1971), pp. 51–60
17. M.R.A. Aw, Resurrection of "second order" models of traffic flow and numerical simulation. SIAM J. Appl. Math. **60**, 916–938 (2000)
18. PEDIGREE project: website http://www.math.univ-toulouse.fr/pedigree (2009–2011)
19. S. Hoogendoorn, S. Ossen, M. Schreuder, Empirics of multianticipative car-following behavior. Transp. Res. Rec. **1965**, 112–120 (2006)
20. A. Seyfried, B. Steffen, W. Klingsch, M. Boltes, The fundamental diagram of pedestrian movement revisited. J. Stat. Mech. **2005**, P10002 (2005)
21. U. Chattaraj, A. Seyfried, P. Chakroborty, Comparison of pedestrian fundamental diagram across cultures. Adv. Complex Syst. **12**, 393–405 (2009)
22. D. Yanagisawa, A. Tomoeda, K. Nishinari, Improvement of pedestrian flow by slow rhythm. Phys. Rev. E **85**, 016111 (2012)
23. S. Lemercier, A. Jelic, R. Kulpa, J. Hua, J. Fehrenbach, P. Degond, C. Appert-Rolland, S. Donikian, J. Pettré, Realistic following behaviors for crowd simulation. Comput. Graph. Forum **31**, 489–498 (2012)
24. Experiments were organized and realized by the PEDIGREE partnership at University Rennes 1, with the help of the laboratory M2S from Rennes 2
25. C. Appert-Rolland, A. Jelic, P. Degond, J. Fehrenbach, J. Hua, A. Crétual, R. Kulpa, A. Marin, A.-H. Olivier, S. Lemercier, J. Pettré, Experimental study of the following dynamics of pedestrians, in *Pedestrian and Evacuation Dynamics 2012*, ed. by U. Weidmann, U. Kirsch, M. Schreckenberg (Springer, Heidelberg, 2014), pp. 305–316
26. A. Jelić, C. Appert-Rolland, S. Lemercier, J. Pettré, Properties of pedestrians walking in line – fundamental diagrams. Phys. Rev. E **85**, 036111 (2012)
27. A. Jelić, C. Appert-Rolland, S. Lemercier, J. Pettré, Properties of pedestrians walking in line. ii. Stepping behavior. Phys. Rev. E **86**, 046111 (2012)
28. C. Appert-Rolland, P. Degond, S. Motsch, Two-way multi-lane traffic model for pedestrians in corridors. Netw. Heterog. Media **6**, 351–381 (2011)
29. C. Appert-Rolland, P. Degond, S. Motsch, A macroscopic model for bidirectional pedestrian flow, in *Pedestrian and Evacuation Dynamics 2012*, ed. by U. Weidmann, U. Kirsch, M. Schreckenberg (Springer, Heidelberg, 2014), pp. 575–584

30. C. Appert-Rolland, H. Hilhorst, G. Schehr, Spontaneous symmetry breaking in a two-lane model for bidirectional overtaking traffic. J. Stat. Mech. **2010**, P08024 (2010)
31. P. Degond, C. Appert-Rolland, M. Moussaid, J. Pettré, G. Theraulaz, A hierarchy of heuristic-based models of crowd dynamics. J. Stat. Phys. **152**, 1033–1068 (2013)
32. P. Degond, C. Appert-Rolland, J. Pettré, G. Theraulaz, Vision-based macroscopic pedestrian models. Kinet. Relat. Models **6**, 809–839 (2013)
33. J.-F. Gouyet, C. Appert, Stochastic and hydrodynamic lattice gas models: mean-field kinetic approaches. Int. J. Bifurcat. Chaos **12**, 227–259 (2002)
34. A. Schadschneider, A. Kirchner, K. Nishinari, From ant trails to pedestrian dynamics. Appl. Bionics Biomech. **1**, 11–19 (2003)
35. K. Nishinari, K. Sugawara, T. Kazama, A. Schadschneider, D. Chowdhury, Modelling of self-driven particles: foraging ants and pedestrians. Physica A **372**, 132–141 (2006)
36. A. Kirchner, H. Klüpfel, K. Nishinari, A. Schadschneider, M. Schreckenberg, Simulation of competitive egress behaviour: comparison with aircraft evacuation data. Physica A **324**, 689–697 (2003)
37. A. Kirchner, K. Nishinari, A. Schadschneider, Friction effects and clogging in a cellular automaton model for pedestrian dynamics. Phys. Rev. E **67**, 056122 (2003)
38. M. Wölki, A. Schadschneider, M. Schreckenberg, Asymmetric exclusion processes with shuffled dynamics. J. Phys. A-Math. Gen. **39**, 33–44 (2006)
39. M. Wölki, M. Schadschneider, M. Schreckenberg, Fundamental diagram of a one-dimensional cellular automaton model for pedestrian flow – the ASEP with shuffled update, in *Pedestrian and Evacuation Dynamics 2005*, ed. by N. Waldau, P. Gattermann, H. Knoflacher, M. Schreckenberg (Springer, Berlin, 2007), p. 423
40. D.A. Smith, R.E. Wilson, Dynamical pair approximation for cellular automata with shuffle update. J. Phys. A: Math. Theor. **40**(11), 2651–2664 (2007)
41. H. Klüpfel, The simulation of crowds at very large events, in *Traffic and Granular Flow'05*, ed. by A. Schadschneider, T. Poschel, R. Kuhne, M. Schreckenberg, D. Wolf (Springer, Berlin/Heidelberg, 2007), pp. 341–346
42. H. Klüpfel, T. Meyer-König, J. Wahle, M. Schreckenberg, Microscopic simulation of evacuation processes on passenger ships, in *Proceedings of the 4th International Conference on Cellular Automata for Research and Industry (ACRI00)*, Karlsruhe, ed. by S. Bandini, T. Worsch (Springer, 2000), pp. 63–71
43. C. Appert-Rolland, J. Cividini, H. Hilhorst, Frozen shuffle update for an asymmetric exclusion process on a ring. J. Stat. Mech. **2011**, P07009 (2011)
44. C. Appert-Rolland, J. Cividini, H. Hilhorst, Frozen shuffle update for a deterministic totally asymmetric simple exclusion process with open boundaries. J. Stat. Mech. **2011**, P10013 (2011)
45. S.P. Hoogendoorn, W. Daamen, Self-organization in Pedestrian Flow, in *Traffic and Granular Flow '03*, ed. by S.P. Hoogendoorn, S. Luding, P.H.L. Bovy, M. Schreckenberg, D.E. Wolf. (Springer-Verlag Berlin, Heidelberg, 2005), pp. 373–382
46. C. Burstedde, A. Kirchner, K. Klauck, A. Schadschneider, J. Zittartz, Cellular automaton approach to pedestrian dynamics – applications, in *Pedestrian and Evacuation Dynamics*, ed. by M. Schreckenberg, S.D. Sharma (Springer-Verlag Berlin, Heidelberg, 2001), p. 87
47. J. Cividini, C. Appert-Rolland, H. Hilhorst, Diagonal patterns and chevron effect in intersecting traffic flows. Europhys. Lett. **102**, 20002 (2013)
48. J. Cividini, Generic instability at the crossing of pedestrian flows, in *Traffic and Granular Flow '13*, ed. by M. Chraibi, M. Boltes, A. Schadschneider, A. Seyfried (Springer, Cham, 2014)
49. S.P. Hoogendoorn, P.H.L. Bovy, Pedestrian route-choice and activity scheduling theory and models. Transp. Res. Part B: Methodol. **38**, 169–190 (2004)

Generic Instability at the Crossing of Pedestrian Flows

Julien Cividini

Abstract Diagonal stripe formation is a well-known phenomenon in the pedestrian traffic community. Here we define a minimal model of intersecting traffic flows. It consists in an $M \times M$ space-discretized intersection on which two types of particles propagate towards east ($\mathscr{E}$) and north ($\mathscr{N}$), studied in the low density regime. It will also be shown that the behaviour of this model can be reproduced by a system of mean field equations. Using periodic boundary conditions the diagonal striped pattern is explained by an instability of the mean-field equations, supporting both the correspondence between equations and particle model and the generality of this pattern formation. With open boundary conditions, translational symmetry is broken. One then observes an asymmetry between the organization of the two types of particles, leading to tilted diagonals whose angle of inclination slightly differs from 45° both for the particle system and the equations. Even though the chevron effect does not appear in the linear stability analysis of the mean-field equations it can be understood in terms of effective interactions between particles, which enable us to isolate a macroscopic nonlinear propagation mode which accounts for it. The possibility to observe this last chevron effect on real pedestrians is then quickly discussed.

1 Introduction

Numerical models of pedestrians are expected to reproduce experimentally observed phenomena, at least in some simple cases. Depending on the application, these phenomena may include pattern formation, non-monotonic variation of evacuation times, queuing behaviour, ... In this work we address the opposite issue. Instead of designing a model reproducing all these phenomena we try to isolate the simplest possible ingredients necessary to exhibit a given feature, here stripe formation at the intersection of two perpendicular flows. This will lead us to explain this pattern, but also to dig out a much more subtle effect.

J. Cividini (✉)
Laboratoire de Physique Théorique d'Orsay, Bâtiment 210, Université Paris-Sud 11, 91405 Orsay Cedex, France
e-mail: julien.cividini@th.u-psud.fr

M. Chraibi et al. (eds.), *Traffic and Granular Flow '13*,
DOI 10.1007/978-3-319-10629-8_2

Stripe formation at the intersection of perpendicular flows is a well-known generic phenomenon in the pedestrian dynamics community. For now it has mainly been observed in pedestrian simulations [1, 2] but is also known to happen in experiments [3].

In this work we first design a minimal model containing the main ingredients ensuring that stripe formation will be observed. The definition of the model and its relation to previous literature will be discussed in Sect. 2. Striped pattern formation will then be explained in Sect. 3 by considering this model with periodic boundary conditions (PBC). Open boundary conditions (OBC) will be studied in Sect. 4 where a smaller 'chevron effect' will be observed, measured and explained. And the final section presents the Conclusion and perspectives.

2 The Model

A *lane* is modeled as a one-dimensional lattice of $M + L$ sites, which we may label from 1 to $M + L$ for clarity. Pedestrians are modeled by particles that may occupy these sites. They are however constrained by the *exclusion principle*, i.e. there cannot be more than one particle on a given site. Particles are allowed to stochastically enter the lane on site 1 at an average frequency determined by the parameter $\alpha \in [0; 1]$, to hop form site i to $i + 1$ and to hop outside of the lattice from site $M + L$. These two actions are taken to be deterministic, i.e. if a particle hops with probability 1 if the hop is allowed by the exclusion principle. If a particle attempts to hop on an already occupied site the hop is discarded and the particle is *blocked*.

A *street* of width M is then modeled as a set of M parallel non-interacting identical lanes. The intersection of two perpendicular identical streets leaves us with an $M \times M$ *intersection square* effectively populated by two types of particles. The $\mathscr{E}$ particles ($\mathscr{N}$) enter the intersection from the west (south) and exit it towards east (north). A scheme is drawn in Fig. 1.

In the scope of modeling pedestrians we choose very regular update schemes. In particular we restrict ourselves to update schemes in which each pedestrian attempts to move exactly once per time step. More precisely we study *alternating parallel update*, in which all the particles of a given type move at the same time and alternate with the other type, and *frozen shuffle update*, in which every particle $\mathscr{P}$ is given a fixed phase $\tau_{\mathscr{P}} \in [0; 1]$ at its creation and is updated at times $\in \mathbb{N} + \tau_{\mathscr{P}}$.

With these update schemes the deterministic hopping implies that the motion of the particles in the 'entrance corridors' of size L is simply a translation, so that the value of L turns out to be unimportant. We therefore end up with a very simple two-parameter model. For a fixed M a jamming transition occurs when α increases, which was studied in detail in Refs. [4,5]. Here we keep the entrance rate low enough to ensure that the system stays in free flow, $\alpha \lesssim 0.1$ for $M \sim 100$. In this regime α is practically equal to the average density ρ of the system.

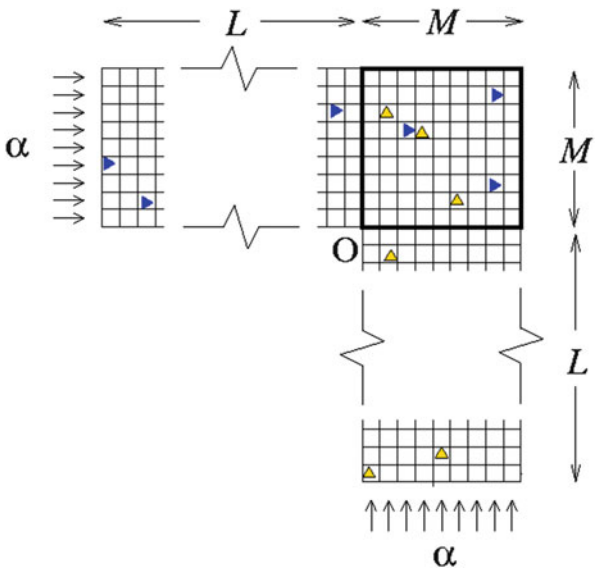

Fig. 1 Scheme of the open system. The *bold line* surrounds the $M \times M$ intersection square. $\mathscr{E}$ particles are represented by *blue right-pointing triangles* and $\mathscr{N}$ particles by *orange up-pointing triangles*. Particles of type $\mathscr{E}$ ($\mathscr{N}$) are enabled to enter the system with entrance probability α at the beginning of the western (southern) entrance lane

One might think that values of M of the order of 100 are completely unrealistic. We however argue that the relevant parameter here is the number of collisions in which a pedestrian is involved when he goes through the whole intersection. This number is on average $\rho M \sim 0.1 \times 100 \sim 10$ for typical values of the parameters of the model, which is comparable to what one would expect to have in a typical experiment.

Similar models have already been studied mainly in the road traffic literature. The Biham-Middleton-Levine (BML) model has been introduced in Ref. [6]. The BML model is a PBC version of the model described above in which the sites represent intersections in a Manhattan-like city and the particles represent cars. In this context the authors observe the striped pattern but do not attempt to explain it. The BML model has been studied by Ding et al. [7] with a 'randomized' version of the update scheme. The behaviour of the system then changes as they do not observe any pattern formation.

3 Pattern Formation in PBC

We begin with studying the case of a periodic crossing, i.e. particles going out of the intersection at its east (north) boundary immediately enter it again at the west (south) boundary. This problem is simpler than the OBC case because it has translational invariance.

The stationary state of a typical realization of the system is shown in Fig. 2. After a transient regime particles are observed to segregate into diagonal alignments.

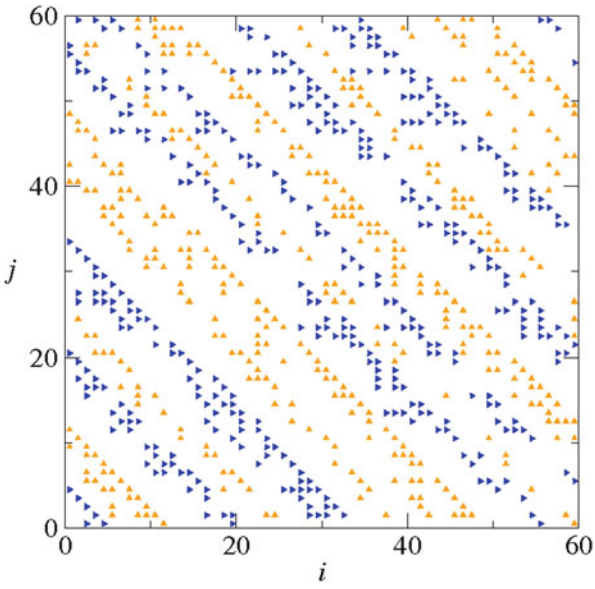

Fig. 2 Stationary state of a typical realization of the particle model with PBC for $M = 60$ and particle density $\rho = 0.1$. Particles of the same type are aligned along diagonals parallel to the $(1, -1)$ direction that have a width of some sites (Taken from Ref. [8])

The pattern propagates towards the $(1, 1)$ direction. The angle of the diagonals with respect to the vertical axis is exactly 45°, as imposed by the symmetry with respect to direction $(1, 1)$ at every point of the system.

This pattern can be understood by writing *mean-field* equations for the particle densities. Defining $\rho_t^{\mathscr{E},\mathscr{N}}(\mathbf{r})$ as an average probability that site $\mathbf{r}$ is occupied by an $\mathscr{E}$ (a $\mathscr{N}$) particle at time t, we can write the phenomenological equations

$$\begin{aligned}\rho_{t+1}^{\mathscr{E}}(\mathbf{r}) &= [1 - \rho_t^{\mathscr{N}}(\mathbf{r})]\rho_t^{\mathscr{E}}(\mathbf{r} - \mathbf{e}_x) + \rho_t^{\mathscr{N}}(\mathbf{r} + \mathbf{e}_x)\rho_t^{\mathscr{E}}(\mathbf{r}),\\ \rho_{t+1}^{\mathscr{N}}(\mathbf{r}) &= [1 - \rho_t^{\mathscr{E}}(\mathbf{r})]\rho_t^{\mathscr{N}}(\mathbf{r} - \mathbf{e}_y) + \rho_t^{\mathscr{E}}(\mathbf{r} + \mathbf{e}_y)\rho_t^{\mathscr{N}}(\mathbf{r}).\end{aligned} \tag{1}$$

The first of Eqs. 1 simply means that an $\mathscr{E}$ particle will hop forward if there is no $\mathscr{N}$ particle on its target site and will not move otherwise, the second equation is the symmetrical.

A constant uniform density profile $\rho_t^{\mathscr{E}}(\mathbf{r}) = \rho_t^{\mathscr{N}}(\mathbf{r}) = \overline{\rho}$ solves Eqs. 1. A linear stability analysis can therefore be performed around this solution. More precisely, we set $\rho_t^{\mathscr{E},\mathscr{N}}(\mathbf{r}) = \overline{\rho} + \delta\rho_t^{\mathscr{E},\mathscr{N}}(\mathbf{r})$ with $|\delta\rho^{\mathscr{E},\mathscr{N}}| \ll 1$, allowing us to keep only the linear terms in the mean-field equations. Taking the Fourier transform we find that the homogeneous solution is unstable, with a maximal instability for the wave-vector parallel to the $(1, 1)$ direction with a wavelength

$$\lambda_{\mathbf{max}} = \frac{\sqrt{2}\pi}{\arccos\left(\frac{1-2\overline{\rho}}{2-2\overline{\rho}}\right)} = 3\sqrt{2} + O(\overline{\rho}), \tag{2}$$

which explains the observed pattern.

The explanation of the pattern coming from the equations justifies the postulated equations a posteriori. It also gives an indication about the generality of the observed pattern, as the equations are expected to represent a mean-field theory for a broad class of regular enough motion rules or update schemes. We now turn on to OBC, in which case the subtle chevron effect will be studied, making the correspondence between particle model and equations even more robust.

4 Chevron Effect and Effective Interactions

The same kind of simulations can be performed with open boundary conditions, i.e. with the entrance corridors drawn in Fig. 1. A typical snapshot of the system in the stationary state is shown in Fig. 3.

Some differences with the PBC case appear. There is a penetration zone of characteristic size $\xi(\alpha)$ near the boundaries in which the particles seem disorganized. Outside of this penetration zone particles still segregate into alignments of a given type, however the intersection is not homogeneous. Instead it can roughly be divided into two triangles separated by a small transition zone along the main diagonal. In the upper (lower) triangle the $\mathscr{N}$ particles ($\mathscr{E}$) are organized in very compact nearly diagonal alignments whereas the $\mathscr{E}$ particles ($\mathscr{N}$) fill largely randomly the rest of the space, as shown in Fig. 4. The angle of the organized alignments can be accurately measured and proved to be equal to $45° \pm \Delta\theta_0$ everywhere inside of the upper (lower) triangle. The stripes therefore have the shape of chevrons and give its name to the *chevron effect*.

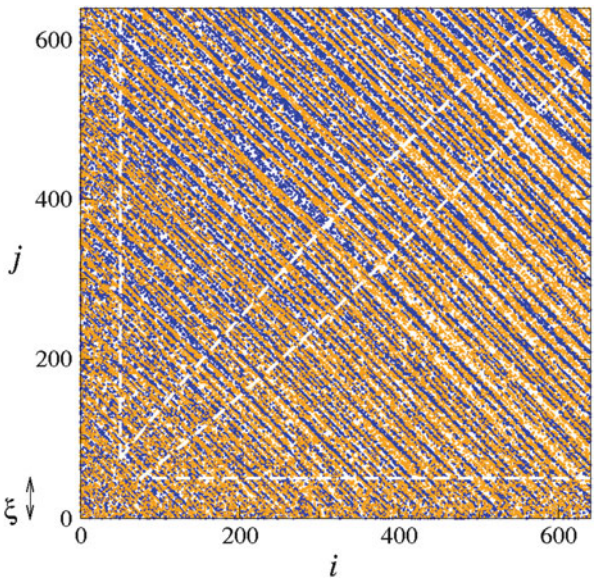

Fig. 3 Snapshot of the stationary state of the intersection square with open boundary conditions, for $M = 640$ and $\alpha = 0.09$ and with frozen shuffle update. The *white dashed lines* delimit the upper and lower triangles. Near the entrance boundaries is a disordered penetration zone of width ξ, and a transition zone along the main diagonal has been excluded from the triangles. The difference of color between the two triangles is a good clue to detect the asymmetry (Taken from Ref. [8])

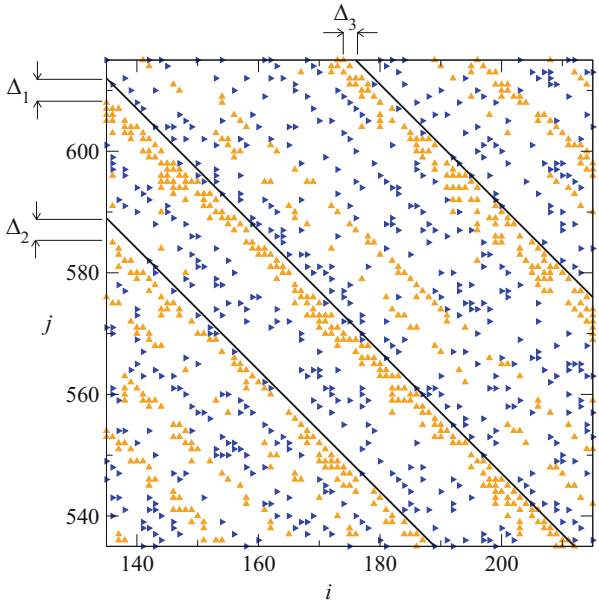

Fig. 4 Zoom on a region of Fig. 3, located in the *upper triangle*. The $\mathscr{N}$ particles are compacted into dense stripes whereas the $\mathscr{E}$ particles fill the remaining space in a more random fashion. The angle between the alignments of $\mathscr{N}$ particles and the vertical axis is slightly more than 45°. This has been highlighted by drawing *solid black lines* at an angle of 45° (Taken from Ref. [8])

A natural attempt to explain this pattern would be to perform an other linear stability analysis on the mean-field equations with adapted boundary conditions. Such an analysis has been performed and no trace of the chevron effect has been found. A numerical resolution of the nonlinear mean-field equations however shows the same chevron effect as in the particle system, which constitutes a confirmation of the robustness of this effect and of the close connection between equations and particle model.

An explanation of this effect can be formulated as follows. Consider a single $\mathscr{E}$ particle hopping on an infinite lattice. The sites of this lattice are taken to be filled randomly by particles of type $\mathscr{N}$ with density $\rho^{\mathscr{N}}$, and all the particles move according to e.g. frozen shuffle or alternating parallel update. It is now possible to construct the set of sites which are necessarily empty (the *wake*) due to the $\mathscr{E}$ particle blocking the $\mathscr{N}$ particles that could have hopped on these sites, for any given time step and initial configuration (see Fig. 5). An other $\mathscr{E}'$ particle can then be dropped somewhere on this wake and its escape rate from the wake can be computed by means of rate equations.

The calculation performed in Ref. [9] shows that $\mathscr{E}'$ is stabilized by the wake of the first one, the most striking effect being that $\mathscr{E}'$ cannot escape the wake from the back. In the case of alternating parallel update this effect is even stronger, as it can

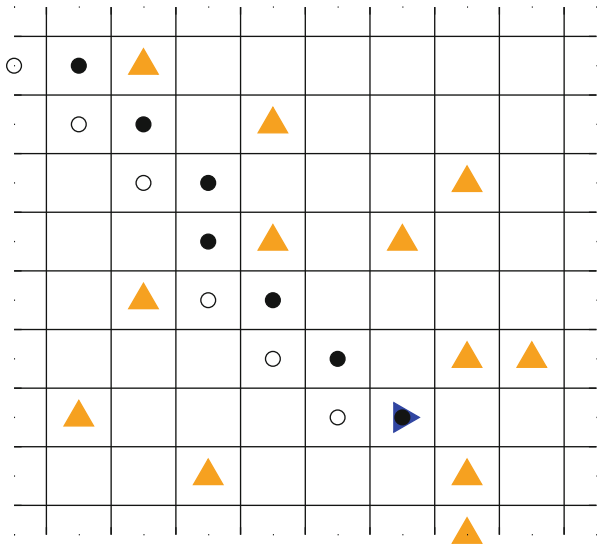

Fig. 5 Wake of a single $\mathscr{E}$ particle in an infinite lattice randomly occupied by $\mathscr{N}$ particles. The set of *dotted sites* can easily be constructed for any initial condition. A second $\mathscr{E}'$ particle can then be added on one of these *dotted sites* and its escape rate can be computed exactly

be shown that $\mathscr{E}'$ cannot escape the set of black dotted sites shown in Fig. 5. More $\mathscr{E}$ particles can then be added, and the state in which all the black-dotted sites are occupied by an $\mathscr{E}$ particle is a macroscopic stable propagation mode. The deviation of the angle of the wake from 45° is on average $\frac{\rho^{\mathscr{N}}}{2}$, which is in total agreement with the measurements for alternating parallel update.

The chevron effect is therefore a purely nonlinear effect that has been explained by isolating a particular propagation mode. The construction of this mode shows that the chevron effect stems from the asymmetry in the organization of the two types of particles, which is itself caused by the difference in the number of collisions undertaken by both types of particles at a given location of the intersection.

Conclusion and Perspectives

In this work we have formulated a simple generic model for intersecting traffic flows, having in mind the application to pedestrians. The ingredients necessary for a system to exhibit diagonal stripe formation, which had already been observed in experiments and simulations of pedestrians, have been isolated and indeed lead to a diagonal pattern when studied with periodic boundaries. This pattern formation has then been ex-pained by a linear stability analysis of mean-field equations. With open boundaries the *chevron*

(continued)

effect appears, the angle of the alignment is different in the two triangular regions separated by the main diagonal. This fully nonlinear effect has been shown to arise from the asymmetry in the organization of the two particle types, and is understood by resulting from a particular propagation mode.

Eventually, this model raises some applied as well as fundamental issues. It is questionable whether this chevron effect can be observed in experiments, as it is observed for large intersections and very regular motion. We however already argued in Sect. 2 that the important parameter here is the number of collisions ρM, a statement which seems to be supported by the mechanism of the chevron effect itself. As the density is actually much larger in experiments than in the model, the chevron effect might also be more pronounced.

A natural perspective for this model would be to extend it to incorporate lane changes, turns ... It is currently not known whether the studied patterns would survive these changes, and their survival would probably depend on their precise implementation. It is also of more fundamental interest to ask if the chevron effect can really be sustained in the $M \to \infty$ limit. We performed simulations up to $M = 2{,}900$ which seem to support this assertion, however only an analytical proof would be satisfying.

Acknowledgements I thank C. Appert-Rolland and H.J. Hilhorst for their collaboration in this work.

References

1. S. Hoogendoorn, P.H. Bovy, Simulation of pedestrian flows by optimal control and differential games. Optim. Control Appl. Methods **24**, 153–172 (2003)
2. K. Yamamoto, M. Okada, Continuum model of crossing pedestrian flows and swarm control based on temporal/spatial frequency, in *2011 IEEE International Conference on Robotics and Automation*, Shanghai, 2011, pp. 3352–3357
3. S.P. Hoogendoorn, W. Daamen, Self-organization in walker experiments, in *Traffic and Granular Flow '03*, ed. by S. Hoogendoorn, S. Luding, P. Bovy et al. (Springer, Berlin/New York, 2005), pp. 121–132
4. S.-I. Tadaki, Two-dimensional cellular automaton model of traffic flow with open boundaries. Phys. Rev. E **54**, 2409–2413 (1996)
5. H. Hilhorst, C. Appert-Rolland, A multi-lane TASEP model for crossing pedestrian traffic flows. J. Stat. Mech. **2012**, P06009 (2012)
6. O. Biham, A. Middleton, D. Levine, Self-organization and a dynamic transition in traffic-flow models. Phys. Rev. A **46**, R6124–R6127 (1992)
7. Z.-J. Ding, R. Jiang, B.-H. Wang, Traffic flow in the Biham-Middleton-Levine model with random update rule. Phys. Rev. E **83**, 047101 (2011)
8. J. Cividini, C. Appert-Rolland, H.J. Hilhorst, Diagonal patterns and chevron effect in intersecting traffic flows. Europhys. Lett. **102**, 20002 (2013)
9. J. Cividini, C. Appert-Rolland, Wake-mediated interaction between driven particles crossing a perpendicular flow. J. Stat. Mech. **2013**, P07015 (2013)

Crowd Flow Modeling of Athletes in Mass Sports Events: A Macroscopic Approach

Martin Treiber

Abstract We propose a macroscopic model in form of a dispersion-transport equation for non-congested flow of the athletes which is coupled to a kinematic-wave model for congested flow. The model takes into account the performance (i.e., free-flow speed distributions) of the athletes in the different starting groups. The model is calibrated and validated on data of the German *Rennsteig Half Marathon 2012* and the Swedish *Vasaloppet 2012* cross-country ski race. Simulations of the model allow the event managers to improve the organization by determining the optimum number of starting groups, the maximum size of each group, whether a wave start with a certain starting delay between the groups is necessary, or what will be the effects of changing the course. We apply the model to simulate a planned course change for the Rennsteig Half Marathon 2013, and determine whether critical congestions are likely to occur.

1 Introduction

Mass-sport events for runners, cross-country skiers, or other athletes, are increasingly popular. Prominent examples include the New York Marathon, the Vasaloppet cross-country ski race in Sweden, and the nightly inline-skating events taking place in nearly every major European city. Due to their popularity (the number of participants is typically in the thousands, sometimes in the ten thousands), "traffic jams" occur regularly (Fig. 1). They are not only a hassle for the athletes (since the time is ticking) but also pose organisational or even safety threats, e.g., because a spillback from a jam threatens to overload a critical bridge. Nevertheless, scientific investigations of the athletes' crowd flow dynamics [1] are virtually nonexisting.

The crowd dynamics can be described by two-dimensional active-particle systems [2]. Unlike the situation in general pedestrian traffic, the flow is unidirectional since all athletes share the same destination (the finishing line). This means, the

M. Treiber (✉)
Technische Universität Dresden, D-01062 Dresden, Germany
e-mail: treiber@vwi.tu-dresden.de

M. Chraibi et al. (eds.), *Traffic and Granular Flow '13*,
DOI 10.1007/978-3-319-10629-8_3

Fig. 1 Jams at the Swedish Vasaloppet cross-country race 2012 (*left*) and at the Rennsteig Marathon 2012 (*right*)

dynamics is equivalent to that of mixed unidirectional vehicular traffic flow which may be lane-based, as in cross-country ski races in the classic style [3], or not, as in skating and running events but also in mixed vehicular traffic flow in many developing countries [4]. The uni-directionality allows to simplify the mathematical description to a macroscopic, one-dimensional model for the motion along the longitudinal (arc-length) coordinate.

In this contribution, we formulate a macroscopic dispersion-transport model for free flow which is coupled to a kinematic-wave model for congested flow. We calibrate and validate the model by data of the Rennsteig 2012 Half Marathon and the Vasaloppet 2012 and apply it to simulate the effects of a planned course change for the next Rennsteig Half Marathon 2013 to avoid the overloading of a critical bridge.

In the next section, we develop the macroscopic model and show its workings on data of past running and ski events. In Sect. 3, we apply it to simulate organisational changes for the Rennsteig Half Marathon 2013. Finally, Sect. 4 gives a discussion.

2 The Macroscopic Model

Our proposed macroscopic model has two components for free and congested traffic, respectively. Since, in free traffic, individual performance differences translate into different speeds, we formulate the free-traffic part as a multi-class model. In contrast, "everybody is treated equal" in congested traffic, so a simple single-class kinematic-wave model is sufficient. During the simulation, the free-traffic part provides the spatio-temporally changing traffic demand (athletes per second). A congestion arises as soon as the local demand exceeds the local capacity. The resulting moving upstream boundary of the jam is subsequently described by standard shock-wave kinematics.

Fig. 2 Two possible starting schemes. (**a**) Mass start (Rennsteig Marathon 2012); (**b**) wave start (Jizerska Padesatka 50 km, 2012)

2.1 Free Traffic Flow

In most bigger mass sports events, the athletes are classified according to performance into starting groups. All groups start either simultaneously ("mass start", Fig. 2a), or sequentially with fixed delays between the groups which, then, are also called waves ("wave start", Fig. 2b).

Generally, each athlete wears an individual RFID chip recording the starting and finishing time, and also split times when passing refreshment stations along the course. The information of the starting groups is highly useful since the speed distribution within each group is much narrower than that for the complete field. Thus, by considering each group individually, the model makes more precise predictions.

Figure 3 shows the distributions of the final times of the German Rennsteig Half Marathon and the time for a section of the Vasaloppet 2012 where no major jams are observed. We fitted the data of each group by Gaussians parameterized, for reasons of robustness, by the median and the inter-quartile gap instead of the arithmetic mean and standard deviation. We infer that, in the absence of major disturbances, the speed distribution within each group is nearly Gaussian. Significant deviations are only observed (i) for the small elite groups due to platooning, (ii) for the low-speed tails. (Generally, the low-speed tails are fatter compared to Gaussians. However, at the Vasaloppet, the slowest athletes are taken out of the race thus reversing this effect.)

Using the normal kinematic relation $T = L/v$ for the time T that athletes of group k take to cover the distance L at speed v, we obtain by elementary probability theory following relation between the density functions $f_k^v(v)$ of the speed and the (non-Gaussian) density function $f_k^T(T|L)$ of the needed time,

$$f_k^T(T|L) = \frac{L}{T^2} f_k^v\left(\frac{L}{T}\right). \tag{1}$$

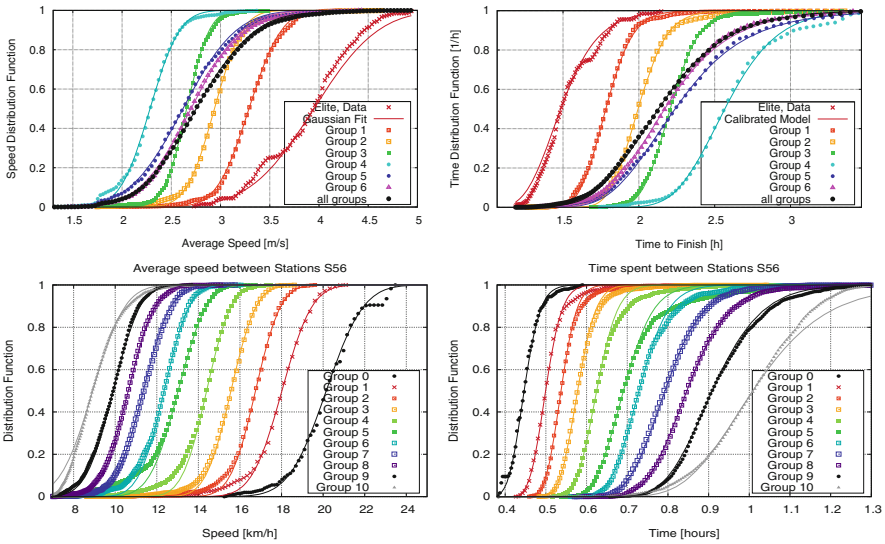

Fig. 3 Distribution of the average speeds (*left*) and times (*right*) of the different starting groups at the Rennsteig Half Marathon 2012 (whole race, *top*) and at the Vasaloppet 2012 (a 9 km section between the stations 5 and 6, *bottom*). *Symbols*: data; *curves*: model

Finally, we assume that the relative performance of an athlete persists throughout the race. In other words, in free traffic, a fast runner remains fast and a slow athlete slow. This means, the flow dynamics obeys a dispersion rather than a diffusion equation. Specifically, we assume constant speed distributions on flat terrain and identical relative speed changes for inhomogeneities such as uphill or downhill gradients. In the following, we will assume a flat terrain, for notational simplicity.

Denoting the number of athletes in each group by n_k and assuming a wave start where group k starts a time delay τ_k after the starting gun goes off (indicating the start of the first and elite waves), the free-traffic demands $Q_{\text{free}}(x,t)$ and densities $\rho_{\text{free}}(x,t)$ read

$$Q_{\text{free}}(x,t) = \sum_k Q_k(x, t-\tau_k), \quad Q_k(x,t) = n_k\, f_k^T(t|x), \tag{2}$$

$$\rho_{\text{free}}(x,t) = \sum_k \rho_k(x, t-\tau_k), \quad \rho_k(x,t) = \frac{t}{x}\, Q_k(x,t), \tag{3}$$

where Q_k and ρ_k are set to zero for time arguments $t - \tau_k \le 0$. Figure 4 shows, for the Rennsteig race, that the model prediction for the total traffic demand $Q_{\text{free}}(x,t)$ at the finish line fits well with the data (possibly, the small deviation at the peak is due to congestions). Thus, we are now able to estimate the free-flow traffic demand upstream of a congestion at any location and at any time during the race. Moreover,

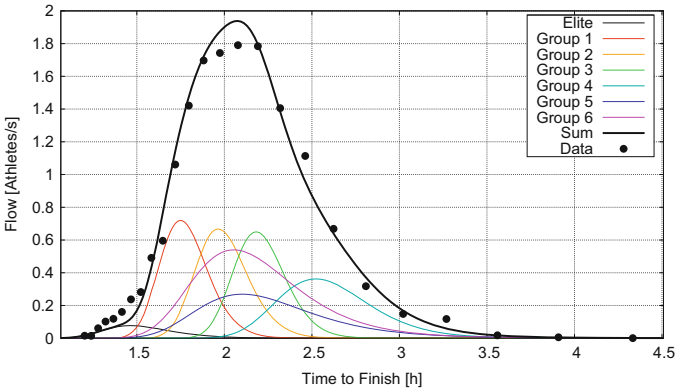

Fig. 4 Partial flows $Q_k(x,t)$ of the different starting groups of the Rennsteig race (mass start) at the finish at 21.1 km (*colored curves*) and total flow according to (2) (*thick curve*) compared with the actual flow (*data points*)

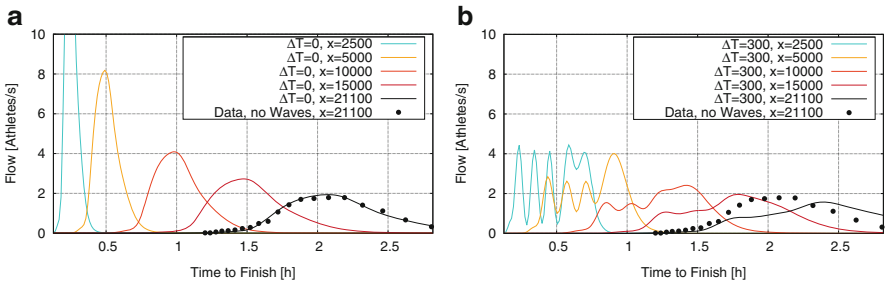

Fig. 5 Simulated effect of a wave start on the local flow of athletes (all starting groups) at different locations from $x = 2{,}500$ m to the finish. (**a**) Reference (mass start), (**b**) delay of 5 min

we now can anticipate the consequences of organisational changes such as realizing a wave start rather than a mass start (Fig. 5).

2.2 *Kinematic-Wave Model for Congested Crowds*

We propose a quasi-onedimensional Lighthill-Whitham-Richards model with a triangular fundamental diagram. In terms of the local capacity $C(x)$ (maximum number of athletes per second that can pass a cross section at location x), the free-flow speed V_0, and the maximum local one-dimensional density (athletes per meter) $\rho_{\max}(x)$, the fundamental diagram can be expressed by [1]

$$Q_e(\rho) = \max\left[V_0\rho, \frac{C(\rho_{\max}-\rho)}{\rho_{\max} - C/V_0}\right]. \tag{4}$$

Notice that the observed capacity C increases weakly with the maximum speed V_0 such that V_0 essentially cancels out in the congested branch of (4). A traffic breakdown arises if, at any location or time, the free-flow demand $Q_{\text{free}}(x,t)$ exceeds the local capacity C_B at a bottleneck $x = x_B$ (where the capacity is at a local minimum). The resulting congested traffic region has a one-dimensional density

$$\rho_{\text{cong}}(x) = \rho_{\max}(x)\left(1 - \frac{C_B}{C(x)}\right) + \frac{C_B}{V_0}. \tag{5}$$

The congestion has a stationary downstream front at the bottleneck location x_B while the upstream front $x_{\text{up}}(t)$ is moving according to the shock-wave formula

$$\frac{\mathrm{d}x_{\text{up}}}{\mathrm{d}t} = \frac{C_B - Q_{\text{free}}(x_{\text{up}},t)}{\rho_{\text{cong}}(x_{\text{up}}) - \rho_{\text{free}}(x_{\text{up}},t)}. \tag{6}$$

The congestion dissolves as soon as $x_{\text{up}}(t)$ crosses x_B in the downstream direction. Finally, the outflow downstream of the congested region has a constant flow $Q_{\text{free}}^{\text{down}}(x,t) = C_B$ equal to the bottleneck capacity.

Both the local capacities and maximum densities are proportional to the local width $w(x)$ of the course:

$$C(x) = J_{\max} w(x), \quad \rho_{\max}(x) = \rho_{\max}^{\text{2d}} w(x). \tag{7}$$

The maximum flow density (specific capacity) $J_{\max}$ and the maximum 2d density $\rho_{\max}^{\text{2d}}$ are model parameters depending on the kind of race and on the local conditions (e.g., gradients). From past congestions, we can estimate $\rho_{\max}^{\text{2d}} = 2\,\text{m}^{-2}$ and $J_{\max} = 1.5\,\text{m}^{-1}\text{s}^{-1}$ for running competitions on level terrain (which is comparable to normal unidirectional pedestrian flows), and $\rho_{\max}^{\text{2d}} = 0.7\,\text{m}^{-2}$, $J_{\max} = 0.6\,\text{m}^{-1}\text{s}^{-1}$ for level-terrain cross-country ski events.

3 Simulating Scenarios for a Marathon Event

At the 2012 Rennsteig Half Marathon, there were six starting groups. The last group contained significantly more participants. For 2013, the managers plan eight groups of equal size $n_k \leq 850$, with the first five groups sorted to performance, and the last three groups available for the runners for which no previous performance are known or who registered too late. Based on the 2012 data, we set the average speeds to $v_1 = 3.5\,\text{m/s}$, $v_2 = 3.1\,\text{m/s}$, $v_3 = 2.7\,\text{m/s}$, $v_4 = 2.4\,\text{m/s}$, $v_5 = 2.1\,\text{m/s}$, and $v_6 = v_7 = v_8 = 2.7\,\text{m/s}$. All speed variances are assumed to be $\sigma_v^2 = 0.15\,\text{m}^2/\text{s}^2$.

Due to external constraints, the course of the 2013 Marathon must be changed. There are several options:

- Scenario 1: Mass start. The 5 m wide starting section has a capacity of 7 athletes/s. The first bottleneck at $x = 1{,}000$ m is a 7 % uphill gradient section of 4.5 m width. At $x = 2{,}200$ m, the athletes encounter a 3.5 m wide downhill section. The critical bottlenecks, however, consist of a bridge at $x = 3{,}000$ m (level, 3 m wide), and, 100 m afterwards, a steep uphill gradient (11 %) where the course has a width of 3.5 m.
- Scenario 1a: As Scenario 1, but wave start with a delay of 300 s per wave
- Scenario 1b: As Scenario 1a, but the capacity of the starting section has been reduced to 5.5 athletes/s.
- Scenario 2: The course is reorganized such that the 7 % gradient is at $x = 1{,}400$ m, the downhill bottleneck at $x = 2{,}700$ m, and the bridge with the subsequent steep uphill section at $x = 5{,}700$ and 5,800 m, respectively.

Based on past experience, the maximum 2d density is set to $\rho^{2d}_{max} = 2\,m^{-2}$ and the specific capacities to $J_{max} = 1.5\,m^{-1}s^{-1}$ for level sections (including the bridge), and 1.2 , 1.0 , and $1.3\,m^{-1}s^{-1}$ for the 7, 11 %, and the downhill gradients, respectively. Figure 6 displays the resulting fundamental diagrams for the bridge (capacity $C = 4.5\,s^{-1}$) and the subsequent uphill section ($C = 3.5\,s^{-1}$)

While some congestions are unavoidable, we must require that there is no significant congestion on the 60 m long bridge itself because this may result in dangerous overloading.

Figure 7 shows the main results: With a mass start (Fig. 7a), massive jams will form at and upstream of all the bottlenecks, including a spillback to the bridge, so this is no option. Adopting a wave start (Fig. 7b) reduces the congestion at the first bottleneck to a tolerable level. Furthermore, jams are no longer expected at the downhill bottleneck while the bridge itself has even capacity to spare. However, the

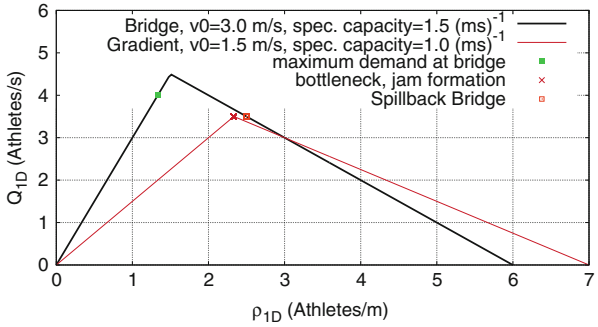

Fig. 6 Fundamental diagram for different situations of the simulation of the Rennsteig Half Marathon 2013 (see the main text for details)

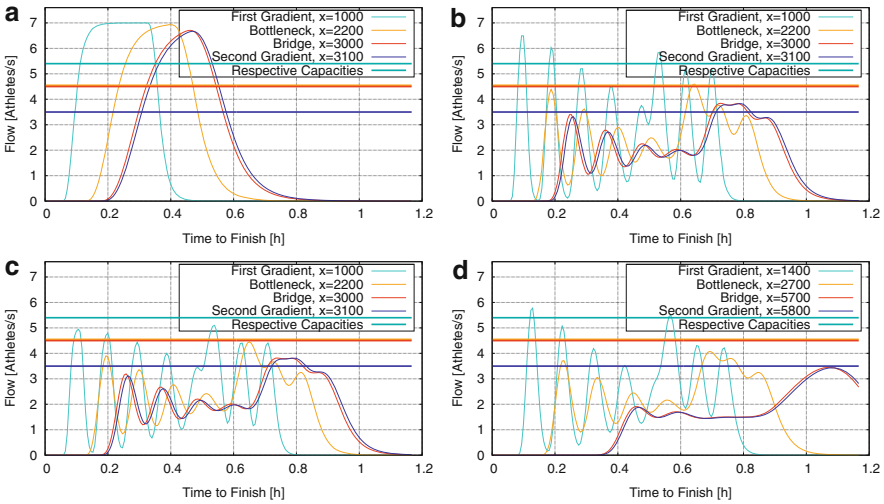

Fig. 7 Two simulated scenarios for the Rennsteiglauf Half Marathon 2013. The *horizontal lines* give the capacities of the various bottlenecks of the course, and the curves of the same color the predicted demands at these positions

demand exceeds the capacity of the steep uphill section leading to a supply-demand mismatch of up to about 150 athletes (the area between the blue curve and the blue capacity line of Fig. 7b). This corresponds to a jam of about 150 m, i.e., there is a spillback with a density of 2.5 athletes/m (cf. Fig. 6) onto the bridge. Reducing the initial capacity of the starting field to 5.5 athletes/s (Fig. 7c) does not help much in this situation. Only a rearrangement of the course with the bridge section located further away from the start yields a significant improvement with the only (minor) jam expected at the uncritical first bottleneck.

4 Discussion

We have proposed a macroscopic dispersion-transport model that allows managers of mass-sports events to assess the implications of changing the course, or the spatio-temporal organization of the start, without prior experiments. As a general rule, critical bottlenecks should be moved as far away from the start as possible. If the situation remains critical, a wave start and/or a restriction of the number of participants will be necessary.

References

1. M. Treiber, A. Kesting, *Traffic Flow Dynamics: Data, Models and Simulation* (Springer, Heidelberg/New York, 2013)
2. D. Helbing, Traffic and related self-driven many-particle systems. Rev. Mod. Phys. **73**, 1067 (2001)
3. M. Treiber, R. Germ, A. Kesting, From drivers to athletes – modeling and simulating cross-country skiing marathons, in *Traffic and Granular Flow '13*, ed. by M. Chraibi, M. Boltes, A. Schadschneider (Springer, *Traffic Flow Dynamics: Data, Models and Simulation*, 2014)
4. V. Arasan, R. Koshy, Methodology for modeling highly heterogeneous traffic flow. J. Transp. Eng. **131**(7), 544 (2005)

Pedestrian Evacuation Optimization Dynamic Programming in Continuous Space and Time

Serge P. Hoogendoorn, Winnie Daamen, Dorine C. Duives, and Femke L.M. van Wageningen-Kessels

Abstract This paper deals with the optimal allocation of routes, destination, and departure times to members of a crowd, for instance in case of an evacuation or another hazardous situation in which the people need to leave the area as quickly as possible. The generic approach minimizes the evacuation times, considering the demand dependent waiting times at bottlenecks within the considered infrastructure. We present the mathematical optimization problem for both the optimal instructions, and the continuum model describing the pedestrian flow dynamics. The key contribution of the approach is that it solves the evacuation problem considering the entire solution space in a continuous manner (i.e. both the time dimension and the routing), implying that for each location and for each time instant the optimal path towards the most favorable exit is calculated, taking into consideration the traffic flow operations along the routes. The approach is generic in the sense that different network loading models can be used, and that a variety of components can be added to the optimization objective without loss of generality. Next to presenting the framework and the mathematical model, we propose an iterative numerical solver to compute the optimal instructions. We demonstrate the abilities and opportunities of this optimization framework with two case studies.

1 Introduction

As evacuation procedures are becoming an established part of large-scale event risk assessment plans, event organizers are increasingly challenged to proof that their plans are in order and visitors can efficiently leave the premises in case of an emergency. Over the years numerous evacuation models have been proposed to assist in this endeavor. A good overview of these models is given by e.g. [1]. All proposed evacuation prediction models are capable of computing an effective evacuation. However, these models cannot predict the most effective one achievable. In contrast to the accumulation of literature treating pedestrian evacuation behavior

S.P. Hoogendoorn (✉) • W. Daamen • D.C. Duives • F.L.M. van Wageningen-Kessels
Delft University of Technology, Stevinweg 1, Delft, The Netherlands
e-mail: s.p.hoogendoorn@tudelft.nl; w.daamen@tudelft.nl; d.c.duives@tudelft.nl; f.l.m.vanWageningen-Kessels@tudelft.nl

M. Chraibi et al. (eds.), *Traffic and Granular Flow '13*,
DOI 10.1007/978-3-319-10629-8_4

and pedestrian evacuation models, there have only been limited attempts to optimize pedestrian evacuation behavior. Amongst these, to the authors' knowledge none of them provide efficient ways to optimize optimal evacuation instructions, for both small and large scenarios.

In this paper, we introduce a mathematical optimization framework that computes optimal instructions efficiently. Furthermore, we propose an iterative numerical solver to compute the optimal instructions. Departure times, destinations and routes of individual members of a crowd are considered in the evacuation instructions. The approach minimizes the evacuation times, considering the demand dependent waiting times at bottlenecks within the considered infrastructure. This optimization framework, which is continuous in time and space, is generic with respect to the macroscopic pedestrian flow model that is also presented in this paper.

2 Mathematical Preliminaries

Let us define the infrastructure from which the people need to evacuate. The area is defined by $\Omega \subset \mathbb{R}$. Within this area, there are M obstacles that cannot be penetrated. These are defined by areas $B_m \subset \Omega$ for $m = 1, \ldots, M$. Finally, we define J exit areas $D_j \subset \Omega$, which represent the safe havens in area Ω. For the sake of simplicity, we assume a one-level area.

We will look for the optimal path $\mathbf{x}^*_{[t,T)}$ starting at time instant t from any location $\mathbf{x}(t) \in \Omega$. These paths are defined as follows:

$$\mathbf{x}_{[t,T)} = \{\boldsymbol{\xi}(s) \in \Omega | t \leq s \leq T, \boldsymbol{\xi}(s) \notin B_m\} \tag{1}$$

Here, t denotes the departure time, and T denotes the terminal time when the evacuee either reaches one of the safe havens or when the evacuation is otherwise ended (i.e. total simulation time has elapsed).

Since we assume that the paths are differentiable, we could analogously describe the path in terms of the *velocity path*:

$$\mathbf{v}_{[t,T)} = \{\mathbf{v}(s) \in \Gamma(s, \boldsymbol{\xi}(s)) | t \leq s \leq T\} \tag{2}$$

where $\boldsymbol{\xi}(s) = \boldsymbol{\xi}(t) + \int_t^s \mathbf{v}(\tau) d\tau$ and where $\Gamma(s, \boldsymbol{\xi})$ denotes the set of velocities that yield admissible paths at time s and location $\boldsymbol{\xi}$.

For each path $\mathbf{x}_{[t,T)}$, or equivalently, the velocity path $\mathbf{v}_{[t,T)}$, we define the path costs $J(t, \mathbf{x}(t) | \mathbf{v}_{[t,T)})$ as follows:

$$J(t, \mathbf{x}(t) | \mathbf{v}_{[t,T)}) = \int_t^T L(s, \mathbf{x}(s), \mathbf{v}(s)) ds + \phi(T, \mathbf{x}(T)) \tag{3}$$

subject to $\frac{d}{dt}\mathbf{x} = \mathbf{v}$. In this expression, the function $L(t, \mathbf{x}, \mathbf{v})$ denotes the so-called running cost, which is the cost added to the total cost during the infinitesimal period $[s, s + dt)$. The running cost is a function of the time s, the location $\mathbf{x}(s)$ and the velocity $\mathbf{v}(s)$. This cost can reflect different factors, such as the travel time or cost incurred because the evacuee is too close to a hazard (fire, smoke). When we only consider travel times, we can choose $L = 1$. The function $\phi(T, \mathbf{x}(T))$ expresses the cost incurred being at a certain location $\mathbf{x}(T)$ at time instant T, which in turn denotes the terminal time, which is either the end of the evacuation period (denoted by $T = t_1$) or the time an evacuee arrives at one of the safe havens. In the former case, we would set the cost of not being at one of the safe havens at the end of the evacuation to a high value.

In the remainder, we present a network loading model that is continuous in time and space in detail. This model describes the dynamics of the densities $\rho(t, \mathbf{x})$ representing the mean number of pedestrians (per unit area) at time instant t and location x, in relation to the flows and the velocities. To determine the walking speed, we assume dependence on the densities according to the well know relation:

$$v^e(t, \mathbf{x}) = V(\rho(t, \mathbf{x})) \tag{4}$$

which in fact denotes the fundamental relation for pedestrian flows. The direction is determined by the prevailing route choice.

3 Modeling Framework

The aim of the framework is to evacuate as many people as possible within the allotted time period $[t_0, t_1)$, taking into consideration the limited supply available due to the infrastructure and possible queues due to these supply limitations, and the physical capabilities of the evacuees.

To this end, we determine the *optimal cost function* $W(t, \mathbf{x})$ with $t_0 \leq t \leq t_1$ and $\mathbf{x} \in \Omega$ that describes the minimal costs (e.g. time) to get to one of the safe havens D_j for $j = 1, \ldots, J$. That is:

$$W(t, \mathbf{x}) = \min_{\mathbf{v}_{[t,T)}} J(t, \mathbf{x} | \mathbf{v}_{[t,T)}) \tag{5}$$

subject to $\frac{d}{dt}\mathbf{x} = \mathbf{v}$ and $\mathbf{v}(s) \in \Gamma(s, \mathbf{x}(s))$. Note that $\Gamma(s, \mathbf{x}(s))$ can be used to describe the influence of obstacles present, as well as physical limitations of the evacuee (including limitations in the speed due to other evacuees present).

If the minimum costs are known, determining the optimal path can be achieved easily by determining the directions in which the costs decrease the quickest [4], i.e.:

$$\mathbf{v}^*(t, \mathbf{x}) = \nabla W(t, \mathbf{x}) \tag{6}$$

Note that by necessity, we have $|\mathbf{v}^*(t, \mathbf{x})| \leq \min(w, \mathbf{v}^e(t, \mathbf{x}))$.

The pedestrian flows are expressed as continuum flows through the infrastructure, and are modeled by means of simple conservation equations, yielding the densities $\rho(t, \mathbf{x})$ (and speeds and flows) as functions of time and space. This is explained in detail in the next section.

The objective of the evacuation problem is to find the optimal cost function $\tilde{W}(t, \mathbf{x})$ (and thus the optimal paths) that minimizes the evacuation costs of the evacuees, given the evacuation flows (and thus densities $\tilde{\rho}(t, \mathbf{x})$). That means that we would need to solve a dynamic assignment problem in continuous time and space until we achieve consistency between the optimal evacuation routes (and staging, i.e. departure times) and the resulting flows.

4 Network Loading by First-Order Pedestrian Flow Modeling

In this paper, a macroscopic approach is taken where flow is described in terms of the dynamics of pedestrian densities $\rho(t, \mathbf{x})$ in time and space. The proposed model is similar to the well known kinematic wave model [5] for vehicular traffic, with the exception that next to the fundamental diagram, also the flow direction needs to be considered.

The dynamic network loading model used here is described by a simple conservation of pedestrians equation. That is, assuming that the velocity $v(t, x)$ is known, the flow propagation satisfies:

$$\frac{\partial \rho}{\partial t} + \frac{\partial (\rho \cdot \mathbf{v})}{\partial x} = \frac{\partial \rho}{\partial t} + \frac{\partial \mathbf{q}}{\partial x} = r - s \tag{7}$$

subject to initial conditions $\rho(t_0, \mathbf{x}) = \rho_0(\mathbf{x})$ for all $\mathbf{x} \in \Omega$. Here $r = r(t, \mathbf{x})$ denotes a source term where evacuees flow into the area Ω; $s = s(t, \mathbf{x})$ denotes a sink term, where evacuees leave the area Ω (i.e. at the safe destinations D_j).

In the proposed framework, the (optimal) direction of the flow is determined at the path choice level. This yields a unitary vector $\boldsymbol{\gamma}^*(t, \mathbf{x})$ that points into the optimal walking direction. This vector is defined by:

$$\boldsymbol{\gamma}^*(t, \mathbf{x}) = \frac{\nabla W(t, \mathbf{x})}{||\nabla W(t, \mathbf{x})||} \tag{8}$$

That is, the unitary vector points into the steepest descent direction of the minimum cost function $W(t, \mathbf{x})$.

For the (absolute) speed $||\mathbf{v}||$ we assume that the flow behaves according to the fundamental relation between density and speed, i.e. $||\mathbf{v}(t, \mathbf{x})|| = V(\rho(t, \mathbf{x}))$. Alternatively, we use the flow-density relation, which then results in:

$$\mathbf{q}(t, \mathbf{x}) = ,^*(t, \mathbf{x}) \cdot Q(\rho(t, \mathbf{x})) \tag{9}$$

Note that for the sake of simplicity, we assume that the absolute flow is only a function of the density. We will use a simple linear speed-density function, i.e.: $V(\rho) = v^0 \cdot (1 - \rho/\rho_{jam}) = 1.34 \cdot (1 - \rho/5.4)$.

Note that with the presence of obstacles $B_m \in \Omega$, we need to respect that no evacuees can flow into the obstacles. This means that the velocities satisfy:

$$\mathbf{v}(t, \mathbf{x}) \cdot \mathbf{n}_m(t, \mathbf{x}) \geq 0 \tag{10}$$

where $\mathbf{n}_m(t, \mathbf{x})$ denotes the outward pointing normal vector of the boundary of obstacle B_m.

The mathematical properties of the flow model proposed here will not be investigated further. However, many of the approaches used for the kinematic wave model can also be applied to 2D (e.g. method of characteristics). To keep matters simple, we have opted for a simple approach: the Lax-Friedrich scheme [3].

5 Optimal Dynamic Routing in Continuous Time and Space with Exogenous Speeds

For the path choice modeling in continuous time and space, we will use the approach first described in [4]. The key to this approach is that instead of explicitly determining the optimal paths, we will determine the optimal direction (and speed) at each location and at each time instant towards the (nearest) destination D_j.

As we have seen in the above, the optimal velocity $\mathbf{v}^*(t, \mathbf{x})$ of an evacuee moving in a two-dimensional area Ω is a function of the minimum actual cost $W(t, \mathbf{x})$ towards a safe haven. Note that these optimal velocities describe not only the path choice, but also the destination choice as well as the evacuation staging (departure times).

The minimum actual cost $W(t, \mathbf{x})$ can be determined by solving the so-called *Hamilton-Jacobi-Bellman* (HJB) equation (see [2] and [4]):

$$-\frac{\partial}{\partial t} W(t, \mathbf{x}) = H(t, x, \nabla W) \tag{11}$$

with terminal conditions reflecting the penalty of not arriving at the safe haven before the end time t_1: $W(t_1, \mathbf{x}) = \infty$ and boundary conditions describing the cost or preference of arriving at a specific destination D_j: $W(t, \mathbf{x}) = d_j$ for $\mathbf{x} \in D_j$ and $t \leq t_1$.

The so-called Hamilton function H is defined by:

$$H(t, \mathbf{x}, \nabla W) = \min_{v \in \Gamma(t, \mathbf{x})} [L(t, \mathbf{x}, \mathbf{v}) + \mathbf{v} \cdot \nabla W] \tag{12}$$

Here, $\Gamma(t, \mathbf{x})$ denotes the set of admissible velocities. This includes the admissible directions as well as the possible walking speeds, which are influenced by both infrastructure and flow conditions (i.e. density); L denotes the so-called running costs, which describes the cost incurred over a short time interval $[t, t + dt)$, given the time t, the location $\mathbf{x}$ and the velocity $\mathbf{v}$. Note that in [4], we discuss existence and uniqueness of solutions to the HJB equation.

It is important to note that in this contribution, we consider a dynamic problem, in the sense that the densities, speeds, and thus the optimal route choice will change over time (and space) during the simulation period. As such, static approximations of the optimal route choice problem (see [4]) are not applicable.

Let us briefly look at the problem specification for the evacuation problem. First of all, we define the cost. For now, we will assume that evacuees will aim to minimize their evacuation times. This implies $L = 1$. This leaves us with the specification of the admissible velocities. We assume that these velocities are determined by two factors. First of all, the obstacles restrict the walking directions.[1] Equation (10) describes how the admissible set $\Gamma(t, \mathbf{x})$ is shaped by the obstacles. Second of all, the traffic conditions determine the possible speeds. Given the local density $\rho(t, \mathbf{x})$, the choice of velocities is limited by the fundamental diagram as follows:

$$||\mathbf{v}(t, \mathbf{x})|| \leq V(\rho(t, \mathbf{x})) \tag{13}$$

For the sake of simplicity, we will use a finite difference approach to numerically solve the HJB equation. We will use the same mesh as used in the pedestrian flow model described in the previous section. In [4], details are given.

6 Optimal Evacuation by Dynamic Assignment in Time and Space

Let us briefly describe the different steps in the approach proposed in this paper, consisting of the following five steps:

1. *Initialization.* We first set the iteration index at zero, i.e. $k = 0$. We determine the initial density profile $\rho(t_0, \mathbf{x}) = \rho_0(\mathbf{x})$ for all $\mathbf{x} \in \Omega$. Having not yet computed the optimal paths, we set $\rho^{(0)}(t, \mathbf{x}) = \rho_0(\mathbf{x})$ for all $\mathbf{x} \in \Omega$ and $t \in [t_0, t_1]$. Based on these densities, and the geometry of the obstacles, we determine the admissible velocities $\Gamma^{(1)}(t, \mathbf{x})$.

[1] Note that the high running costs of being close to obstacles will automatically steer the evacuees away from the obstacles which may make adding restrictions on the admissible velocities unnecessary.

2. *Optimal path calculation*. Given the set of admissible velocities, we solve Eq. (11). Based on the optimal cost $W^{(k)}(t, \mathbf{x})$ that is determined, we compute the optimal velocities (direction and speeds) for iteration k. The optimal directions $\gamma_*^k(t, \mathbf{x})$ are used in the next step.
3. *Flow propagation*. The optimal direction $\gamma_*^k(t, \mathbf{x})$ is fixed while the densities $\rho^{(k)}(t, \mathbf{x})$ are determined by solving Eq. (7) using the numerical scheme presented in this paper.
4. *Update average densities*. The densities computed in the previous step are used to redetermine the optimal paths (step 2). However, using the densities directly will cause oscillating behavior hampering convergence of the scheme. This is why we introduce an exponentially smoothed density $\bar{\rho}^{(k)}(t, \mathbf{x}) = (1 - \alpha)\bar{\rho}^{(k-1)}(t, \mathbf{x}) + \alpha\rho^{(k)}(t, \mathbf{x})$ for some value of $0 \leq \alpha \leq 1$. The smoothed densities are used to determine the set of admissible velocities $\Gamma^{(k)}(t, \mathbf{x})$ that are used in step 2.
5. *Check for convergence and continue.* We check if the optimal cost function has not changed much over the last iteration, i.e. $\max_{t,\mathbf{x}} |W^{(k)}(t, \mathbf{x}) - W^{(k-1)}(t, \mathbf{x})| \leq \epsilon$. If not, we go to step 2 for the next iteration step.

7 Case Study

To show the (numerical) characteristics of the approach and the solutions that result from its application, we will consider the evacuation route computations for a simple maze. Figure 1 illustrates this case. The evacuees are initially on the left-hand-side (black area) with a density of $2.5\,\mathrm{P/m^2}$. The safe area is located on the right of the 50 m by 50 m area. The figure shows the walls and the doors the evacuees need to use in order to reach the safe area. There are six doors in total. The doors have different widths (door 1 and 2 are wide (2.5 m); door 3–6 are narrow doors (1.25 m)). Clearly, there are multiple routes available.

The figure shows the results of the initial evacuation route computation (i.e. iteration 1, assuming zero density, that is free speeds anywhere, anytime) for $t = 0$. For this situation, the area was discretized using cells of 0.25 m by 0.25 m, while using a time step op 0.1 s (both for the route choice computation and flow propagation). We simulated a period of 250 s. The colors indicate the minimum cost (or in this case, time) to reach the safe area on the right. The optimal route that the evacuees take from any location is determined by the steepest descent path (i.e. perpendicular to the iso-cost curves). For the free flow conditions situation, this will for instance mean that when reaching door 2, evacuees are best off choosing door 4. Note that since zero density is assumed for the entire simulation period, the optimal routes are equal for all time instances.

When applying the flow model using these free flow optimal routes, queueing occurs at different locations in the network. Since the evacuees will not react to the reduced speeds caused by the high densities, these queues will persist during a large part of the simulation (actually, some evacuees will still be left at the end of the

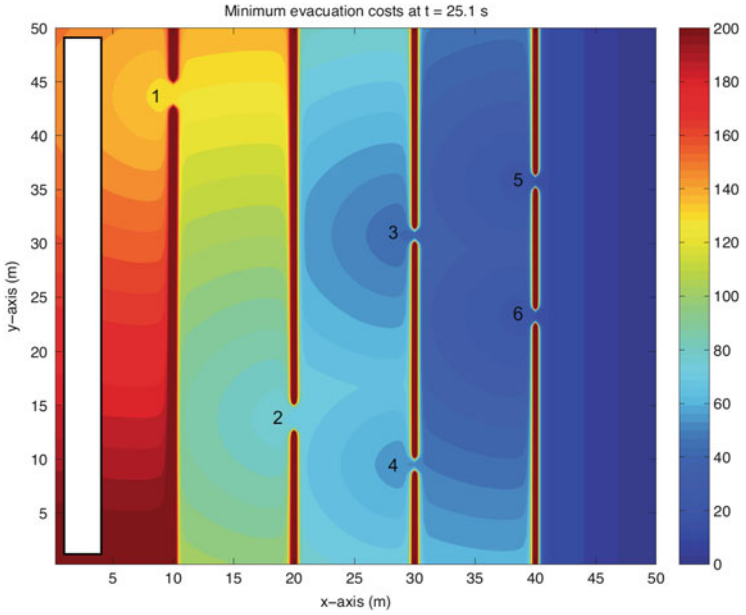

Fig. 1 Minimum cost of getting to the exit on the right in case of unhindered walking

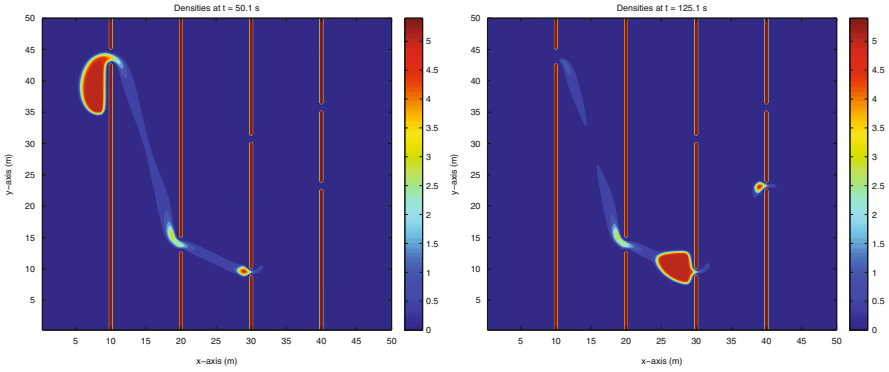

Fig. 2 Evacuee assignment using optimal free flow routing

simulation). Figure 2 shows the results for two time steps (after 25 s and after 125 s). Maximum (jam) densities ($5.4\,\mathrm{P/m^2}$) are observed at various locations, yielding low speeds and hence a slow evacuation. Furthermore, we clearly see that in this case, the capacities of the – especially wide – doors are not fully used (evacuees have the tendency to curl around the doors). Also, available capacity from other doors is not used either: doors 3 and 5 are not used, while queuing occurs at door 4 and (to a lesser extent) door 6. In this end, this results in an incomplete evacuation of the 300 (or so) evacuees, about 140 of which are not able to get our of the area within the

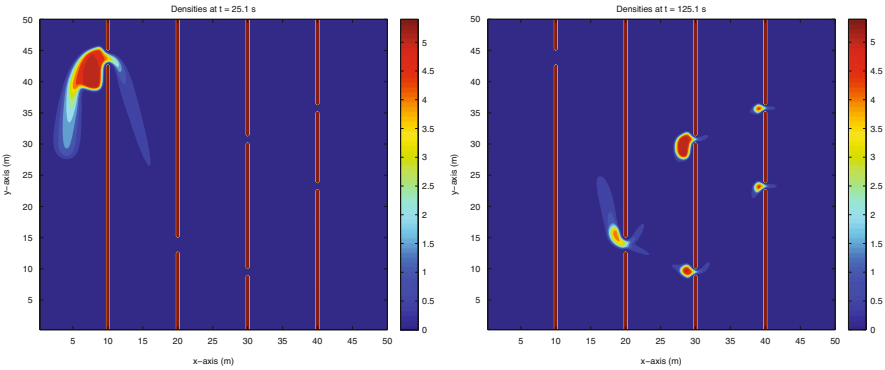

Fig. 3 Evacuee assignment for two time stamps

250 s simulation period. It is important to note that this is obviously an intermediate result (result from the initial iteration) that does not reflect any realistic (or optimal) situation. It does illustrate, however, that taking into consideration the congestion in finding the optimal evacuation routes is very important.

Let us see how applying the procedure proposed in this paper would yield a better evacuation strategy. To this end, we have applied the proposed iterative optimization scheme (with $\alpha = 0.05$) using a maximum number of iterations of 30. Figure 3 shows the results at two different time stamps (50 and 125 s). The two graphs clearly show the dynamic nature of the evacuation scheme. First of all, for $t = 25$ s, we see that the wide doors are utilized more effectively (flow spans the entire width of the doors). Second of all, we see that after some time, doors 3 and 5 are used as well (see snapshot at $t = 125$ s. In fact, it turns out that in the end, the available capacity of all doors is used fully.

These favorable properties of the evacuation scheme allows clearing the area well within the 250 s period. In fact, for this iteration the total evacuation time was 235 s, showing that the approach leads to large improvements compared to the free flow scheme.

Conclusions

This contribution describes a novel, generic approach to determine optimal evacuation instructions. The paper focuses on the theory, showing that optimization of the pedestrian decision behavior consisting of exit, departure, and route choice can indeed yield substantial improvements in evacuation times compared to for instance shortest distance paths. The workings of this optimization framework have been shown for two case studies: one in which the optimal route choice has been illustrated, while the second case study demonstrates the optimal destination choice. Unlike previous

(continued)

attempts to optimize evacuations, this approach covers optimal allocation of routes, destination, and departure times, including pedestrian behavior in the form of the well-known speed-density relation, and a first-order continuum pedestrian flow model, comparable to the LWR model for vehicular traffic. As the pedestrians dynamics are described by a macroscopic pedestrian flow model, the approach is applicable to larger infrastructures, or other large-scale applications (many pedestrians present). Despite that several practical and theoretical issues still need to be tackled, we believe that the approach put forward here has clear potential in terms of providing a strong theoretical basis for evacuation plan design. The cases presented in this paper clearly reveal this potential.

Acknowledgements The research presented in this paper has been sponsored by the Dutch Foundation of Scientific Research MaGW−NWO and is part of the VICI subsidy Modeling and Management of Traffic and Transportation in case of Exceptional Events as well as the Aspasia subsidy Understanding emergent crowd behaviour: from individual behaviour dynamics to macroscopic phenomena.

References

1. C.J.E. Castle, P.A. Longley, Building evacuation in emergencies: a review and interpretation of software for simulating pedestrian egress, in *Geospatial Technologies and Homeland Security*, vol. 94, ed. by D. Sui (Springer, Dordrecht, 2008), pp. 209–228
2. W.H. Fleming, H.M. Soner, *Controlled Markov Processes and Viscosity Solutions*. Applications of Mathematics, vol. 25 (Springer, New York, 1993)
3. C. Hirsch, *Numerical Computation of Internal and External Flows* (Wiley, Chichester, 1995)
4. S.P. Hoogendoorn, P.H.L. Bovy, Pedestrian route-choice and activity scheduling theory and models. Transp. Res. Part B: Methodol. **38**(2), 169–190 (2004)
5. M.J. Lighthill, G.B. Whitham, On kinematic waves. II: a theory of traffic flow on long crowded roads. Proc. R. Soc. **229A**(4), 317–345 (1955)

Generalized Macroscopic Fundamental Diagram for Pedestrian Flows

Winnie Daamen, Victor L. Knoop, and Serge P. Hoogendoorn

Abstract It has been shown that a relation exists between the number of pedestrians in an area and the average flow in that area (production); this is called the Macroscopic Fundamental Diagram (MFD). Using this relation, we can express the average production of a network as a function of the average density (or accumulation) of the network. One of the assumptions under which a proper shape of the MFD is found, is that the congestion is spread homogeneously over the network. In vehicular traffic, it is shown that when this assumption is relaxed, the spatial variation of density within the network leads to a decreased production. This paper shows to which extent a function of accumulation and an aggregated variable of the spatial spread can predict the performance of a pedestrian traffic flow.

1 Introduction

Traffic congestion is not only a local problem: due to route choice behaviour it spreads out over the network. To increase insights into network dynamics and how to characterise these dynamics, the concept of the Macroscopic Fundamental Diagram (MFD) has been re-introduced [1]. One of the assumptions under which a proper shape of the MFD is found, is that the congestion is spread homogeneously over the network [1]. Knoop and Hoogendoorn [3] show the effect of inhomogeneity by deriving the so-called *generalised macroscopic fundamental diagram* (GMFD).

Hoogendoorn et al. [2] have shown that a similar relation exists between the number of pedestrians in an area and the average flow in that area (production). However, the effects of spatial inhomogeneity of the density has not been considered. In the paper at hand we show to which extent a function of the number of pedestrians and an aggregated variable of the spatial spread can predict the performance of a large scale pedestrian traffic flow. Similar to vehicular traffic, we found that a larger spatial variation in density leads to higher flows in the network (at the same density).

W. Daamen (✉) • V.L. Knoop • S.P. Hoogendoorn
Delft University of Technology, Stevinweg 1, Delft, The Netherlands
e-mail: w.daamen@tudelft.nl; v.l.knoop@tudelft.nl; s.p.hoogendoorn@tudelft.nl

M. Chraibi et al. (eds.), *Traffic and Granular Flow '13*,
DOI 10.1007/978-3-319-10629-8_5

Next to providing insights into network pedestrian traffic dynamics, MFDs can be important for (on-line) applications such as pedestrian traffic control. Busy pedestrian facilities (e.g., metro and train stations, airports and shopping centres) need to be monitored for safety and operational performance. The use of pedestrian counting devices combined with a reliable MFD could provide a good estimator for the traffic state in real time applications.

The paper starts with an experimental design (Sect. 2), then shows the resulting MFDs (Sect. 3) and ends with conclusions.

2 Experimental Design

In the experimental design we introduce the simulation set-up and data used to derive the Generalized Macroscopic Fundamental Diagram for pedestrians for a specific network layout. Section 2.1 gives an overview of the corresponding layout, while Sect. 2.2 shows the traffic demand for the two data sets. Section 2.3 shows how the characteristics of the MFD (flow and density) are calculated.

2.1 Layout

In order to control the data and to identify the effects of different flow patterns on the shape of the MFD we have chosen to model both one-directional traffic and crossing traffic flows. Figure 1a, b show an overview of these two layouts, where the red pedestrians walk from left to right and the blue pedestrians walk from top to bottom. The area measures 10×10 m, while the exits have a width of 1 m. In order to create congestion upstream of the exits, the entrances have a width of 6 m. To make sure that the capacity of the exit is correct, we have added a short corridor downstream of the exit, having the same width. However, the observations are made only for the central area.

2.2 Traffic Demand

Traffic demand is increased in a stepwise way, until a largest flow of 1.65 P/s is generated. This demand is maintained during 30 s, to let congestion set in, after which demand is gradually decreased. This way, both the effects of congestion onset and its resolution are included in the GMFD. For the crossing flow scenario, the crossing flow (from top to bottom)is much smaller than the main flow (from left to right). The main flow in this scenario is 2 P/s, while the crossing flow is equal to 0.5 P/s. An overview of these demand profiles is shown in Fig. 2. The total duration of the simulation is 900 s.

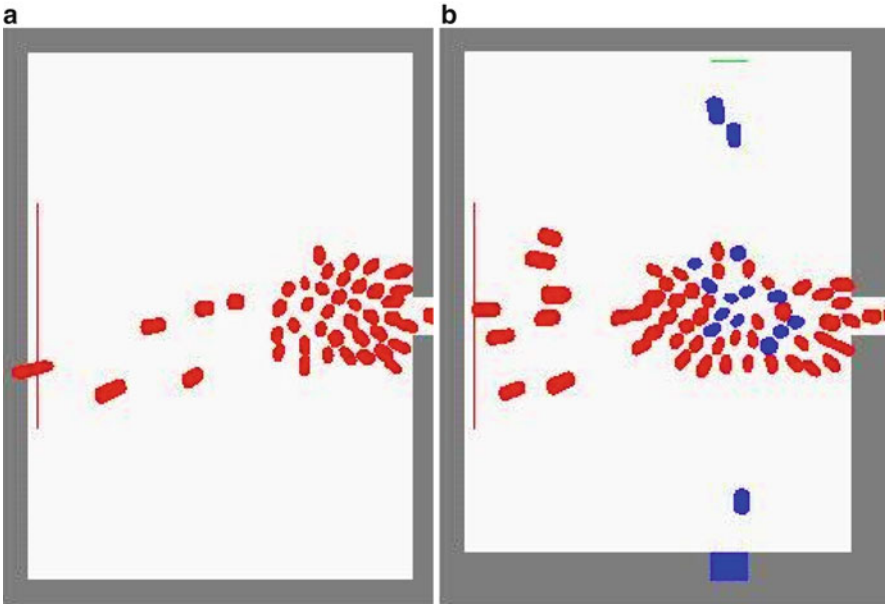

Fig. 1 Layout for the two data sets. (**a**) One directional. (**b**) Crossing flows

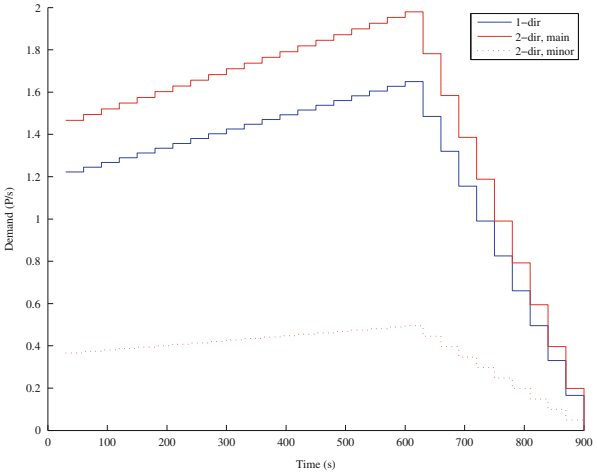

Fig. 2 Traffic demand over time in both scenarios

2.3 MFD Characteristics

To visualise the effect of spatial variation in the density on the density and the flow, both density and flow need to be calculated. As the application of the GMFD is to

see whether sufficient space is available to cope with the existent pedestrian flows and how efficiently this space is used, we include the empty areas in the density calculation. The local or individual density k_i is equal to the inverse of the empty space around an individual pedestrian A_i

$$k_i = \frac{1}{A_i} \tag{1}$$

Then, we calculate the so-called space mean density, where all local densities k_i are weighed:

$$k(t) = \frac{1}{\frac{\sum_i 1/k_i}{N}} = \frac{N}{\sum_i 1/k_i} = \frac{N}{\sum_i A_i} = \frac{N}{A} \tag{2}$$

where A is the area of the whole surface. Note that by this weighting of individual pedestrian's individual space we obtain a consistent equation for the density, expressed as the number of pedestrians divided over the area in space.

The speed for each individual pedestrian is calculated directly from the trajectory data:

$$v_i = \sqrt{v_{xi}^2 + v_{yi}^2} \tag{3}$$

Here, we take the absolute speed, as we want to discard the walking direction. To calculate the flow, we use the previously calculated density and speed:

$$q(t) = \frac{\sum_i k_i \cdot v_i}{n} \tag{4}$$

3 Generalized Network Fundamental Diagrams

First, we show the resulting densities (accumulation) of the simulation runs for both scenarios in Fig. 3. It can be seen that in both scenarios the accumulation slightly increases, although a lot of variation in the accumulation is visible as well. We can see a rather short period in which the accumulation is relatively constant, after which the density decreases further.

The resulting Generalized Network Fundamental Diagrams are shown in Fig. 4a, b. The axes show the density and the density variation respectively, while the color of each dot indicates the corresponding flow (high flows in green, low flows in red). As we can see in both configurations, when the density increases, also the

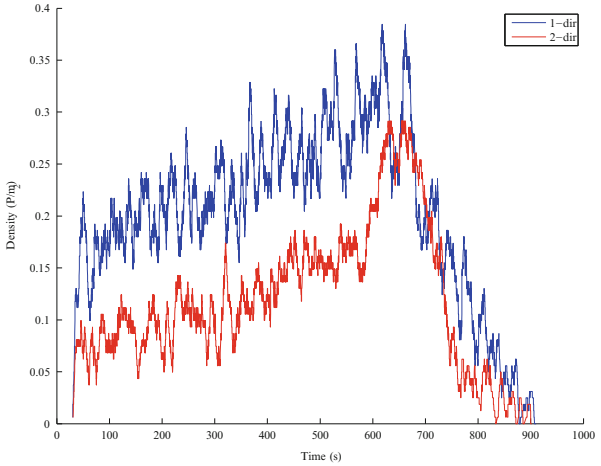

Fig. 3 Accumulation of both scenarios over time

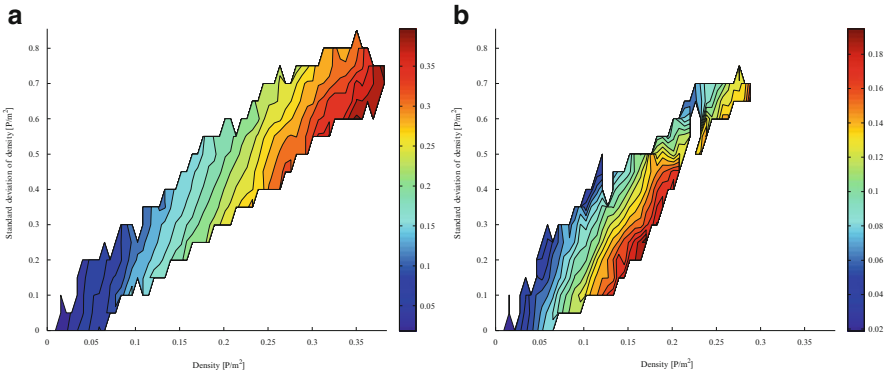

Fig. 4 Generalized macroscopic fundamental diagram. (**a**) One directional. (**b**) Crossing flows

standard deviation of the density increases. This can be expected, as the reason of the density increase is the onset of congestion, which causes high densities and low speeds just upstream of the exit, while the remaining part of the area remains almost empty. In the latter areas the pedestrians can walk with their free speeds. For a given density, it can be seen that flow increases with an increase in density variation. A smaller spatial variation of density implies less variation in conditions (being the experienced densities), and thus on average lower flows. For crossing flows, the spatial variation in density is even larger. In this case, the crossing flow, even though it is only small, is hindered by the congestion in the main flow, leading to a lower speed than would be expected according to volumes. The hinder caused by the crossing pedestrians causes disturbances in the queue, leading to a longer, and also more spatially distributed queue. The tendency of larger flows corresponding

to a larger spatial distribution of the density also holds for this crossing scenario. As the spatial distribution is larger, this tendency is even better visible in the crossing flow scenario.

Conclusions
In this paper we have shown the Macroscopic Fundamental Diagrams also exist in pedestrian traffic. When the assumption of homogeneously distributed congestion over the area is dropped, the spatial variation in density appears to affect the MFD: a lower spatial variation implies lower flows, and higher variation implies higher flows. The exact shape of the MFD and the influence of the spatial variation in the density depends on the flow pattern (one-directional versus crossing flows). A reliable MFD combined with the use of pedestrian counting devices could provide a good estimator for the traffic state in real time applications.

Acknowledgements The research presented in this paper has been sponsored by the Dutch Foundation of Scientific Research MaGW-NWO and is part of the Aspasia subsidy Understanding emergent crowd behaviour: from individual behaviour dynamics to macroscopic phenomena, and the VENI subsidy Space to Change Lane and the VICI subsidy Modeling and Management of Traffic and Transportation in case of Exceptional Events.

References

1. C.F. Daganzo, Urban gridlock: macroscopic modeling and mitigation approaches. Transp. Res. Part B: Methodol. **41**(1), 49–62 (2007)
2. S.P. Hoogendoorn, M.C. Campanella, W. Daamen, Fundamental diagrams for pedestrian networks, in *Pedestrian and Evacuation Dynamics* (Springer, New York, 2011), pp. 255–264
3. V.L. Knoop, S.P. Hoogendoorn, Empirics of a generalised macroscopic fundamental diagram for urban freeways. Transp. Res. Rec. 2391, 133–141 (2013)

Pedestrian Route Choice by Iterated Equilibrium Search

Tobias Kretz, Karsten Lehmann, and Ingmar Hofsäß

Abstract In vehicular traffic planning it is a long standing problem how to assign demand such on the available model of a road network that an equilibrium with regard to travel time or generalized costs is realized. For pedestrian traffic this question can be asked as well. However, as the infrastructure of pedestrian dynamics is not a network (a graph), but two-dimensional, there is in principle an infinitely large set of routes. As a consequence none of the iterating assignment methods developed for road traffic can be applied for pedestrians. In this contribution a method to overcome this problem is briefly summarized and applied with an example geometry which as a result is enhanced with routes with intermediate destination areas of certain shape. The enhanced geometry is used in some exemplary assignment calculations.

1 Introduction

For pedestrians (and vehicles alike) it holds that in general travel times along a route increase with increasing demand. This is because walking speeds are lower when density is higher and because higher demand implies larger queues in front of bottlenecks and therefore higher (enforced) dwell times. Obviously when there is more than one route available which connects the same origin and destination it can make sense – with regard to the objective of minimizing travel times – that a fraction of the pedestrians walks along these alternative routes. The process to calculate these fractions such that either all routes have the same travel time (user equilibrium) or the average of travel times is minimal (system optimum) is called (dynamic) assignment.

For vehicular traffic research on assignment methods has a history of more than a half century [2,3,5,17,21] and applying these methods is an established and major aspect of traffic planning.

Concerning pedestrians we have to go one step back and ask: what is a route? Or better: what distinguishes two different routes? It does not make sense to say –

T. Kretz (✉) • K. Lehmann • I. Hofsäß
PTV Group, D-76131 Karlsruhe, Germany
e-mail: Tobias.Kretz@ptvgroup.com

M. Chraibi et al. (eds.), *Traffic and Granular Flow '13*,
DOI 10.1007/978-3-319-10629-8_6

with regard to assignment methods – that two pedestrians have been walking two different routes, if their paths are the same everywhere except for a few millimeters. Instead we require that two paths only then belong to two different routes, if they cannot be transformed continuously one into the other without moving a path during the transformation over an obstacle of a given minimum extent. Recently we have proposed such a method [14–16] and will apply and demonstrate it with an example geometry and in combination with a simple assignment method in the remainder of this contribution.

Before we do so, one has to ask first for the motivation or better for the benefit. The benefit of a method to find a set of relevant and mutually sufficiently distinct routes in a pedestrian walking geometry probably is evident to every expert in the field. However, is there a benefit to compute a user equilibrium for pedestrian dynamics? After all there is not such a eminent day-by-day commuting traffic as it is in vehicular traffic and day-by-day experience is *the* argument which explains why in road traffic there should be an equilibrium. Yet there are comparable situations in pedestrian traffic. Public transport commuters meet daily in large numbers in large stations. Their day-by-day experience may suggest them to use a route which may be longer or more arduous but saves them time; compare for example in this book [19] where the average travel times of commuters on an escalator and those walking stairs (not parallel to the escalators) are astonishingly similar. A fire safety engineer can have a totally different motivation to compute a user equilibrium: s/he may not assume that the user equilibrium emerges spontaneously from the system if every occupant decides on his or her own which route to take. But knowing that the user equilibrium usually also is an efficient distribution on the available routes with relatively small delay and travel times the fire safety engineer might want to take the results from the assignment calculation as basis for the escape plan, i.e. as answer to the question where an escape route sign has to point into one direction and where into another one.

At the end of this introduction we would like to point the reader to another contribution in this book which approaches the pedestrian assignment with a different method [20].

2 Example Application

Figure 1 shows a walking geometry where pedestrians have to pass two times through one of two differently wide doors. Figure 2 shows the same geometry enhanced by routes and their intermediate destinations which have been calculated automatically with the method introduced in [15].

For this work operationally pedestrians are simulated using PTV Viswalk [1, 4, 13] which itself utilizes a combination of the circular specification and the elliptical specification II of the Social Force Model [7]. The pedestrians are approaching the intermediate destination with the direction of the desired velocity set into the direction of the spatially shortest path to the next intermediate destination area. This

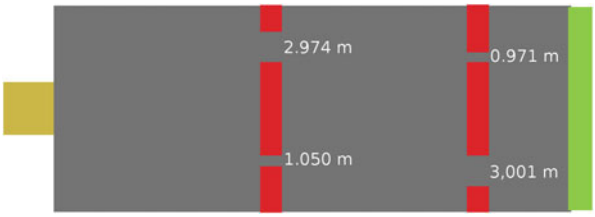

Fig. 1 Walking geometry. Pedestrians are set with a given rate and spatially equally distributed into the simulation on the *yellow area* to the left, have to pass through the bottlenecks formed by the *red obstacles* and arrive on the *green area* on the right side

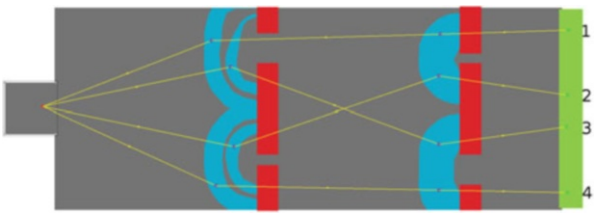

Fig. 2 Walking geometry enhanced with automatically computed routes (*yellow*) and their intermediate destinations (*blue*). Note the numbers by which the routes will be identified in the text

implies that pedestrians will arrive at an intermediate destination usually walking orthogonally to the boundary of its area. Any deviation from this must be due to forces between pedestrians. As the upstream borders of all intermediate destinations are computed such that each point on that border has the same distance to the closest point on the next downstream intermediate destination this implies that pedestrians will not at all make a turn when they have reached an intermediate destination area and then proceed to the next one.

On the tactical level the distribution of the pedestrians on the four routes is done iteratively by he assignment method. In each iteration step one simulation is carried out. In the first iteration step 25 % of the pedestrians are sent on each of the routes. For each pedestrian the travel time is measured from the point where the pedestrian leaves the origin area to the moment when he reaches the destination area. From the average travel times on each of the routes the route choice ratios for the next iteration step are computed according to the following equation.

It is easy to see that an equilibrium distribution on the four available routes must depend on the total pedestrian volume set into the simulation (demand volume). We have done the iterated assignment with eleven different demand volumes: 0.5, 1.0, 1.5, 2.0, 2.5, 3.0, 3.5, 4.0, 4.5, 5.0, and 6.0 pedestrians per second. These numbers cover the whole range from total demand being below the capacity of the more narrow doors and total demand exceeding global capacity. For each demand volume the assignment procedure was carried out five times with different seed values for the random number generator.

As termination condition was chosen that the largest and the smallest average travel time must not differ by more than 0.5 s. This is a relatively strict condition given the variation of walking speeds (default for men and women of an age of 30–50 years as required by the International Maritime Organization [6]). For this example study it was chosen this way to guarantee to see the dynamics of the assignment process unfold to the end. This comes at the danger of running into oscillations of a cycle length of two to four or five iteration steps toward the end of the assignment process when equilibrium is in principle reached, but the stochastic fluctuations are large enough that the termination condition is always missed by a small amount. In such a case we chose that iteration as result which came closest to the termination condition.

In the assignment process in each iteration step (a step is one simulation run) the travel times of all pedestrians who arrived at the destination area between $t = 300$ and $t = 600$ s after the beginning of the simulation were recorded. At the end of the simulation the average travel time on each route was calculated. Then for the next iteration step the route choice probability for the route with the smallest average travel time t_{min} was increased and the route choice probability for the route with the largest average travel time t_{max} was decreased by the same amount. This probability shift Δp was calculated as

$$\Delta p = \alpha \left(\frac{t_{max} - t_{min}}{t_{max} + t_{min}} \right)^{\delta} \tag{1}$$

where α is a general sensitivity factor which was chosen to be $\alpha = 0.1$ in all computations and δ is a dynamic adaptation factor which usually was $\delta = 1$, but was decreased when the routes with the longest and the smallest travel time were identical in subsequent iterations and which was increased when they exchanged roles in subsequent iterations.

Figure 3 shows for a demand of three persons per second how route choice ratios and average travel times on each of the four routes evolve in the iteration process.

As described above we have carried out five assignment processes with different random numbers. It is of course interesting to compare how different assignment

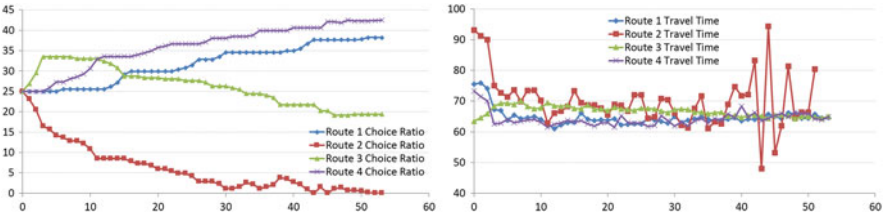

Fig. 3 Route choice ratios (*left*, in percent) and travel times (*right*, in seconds) for all four routes in the course of iterations if demand is 3 pedestrians per second. The travel time for route 2 becomes unstable when its route choice ratio is small (below 5 %) as then only few pedestrians (20 or even less) walk along route 2 and thus the average travel time is based only on few values

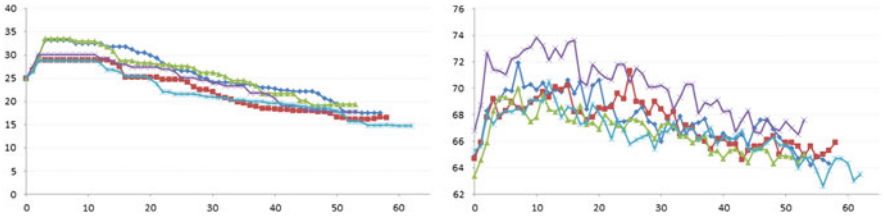

Fig. 4 Route choice ratios (*left*, in percent) and travel times (*right*, in seconds) for route 3 if demand is 3 pedestrians per second for all five iteration processes in comparison. While a general trend appears similar in all five processes there are differences which at least partly have their cause in the wide distribution of desired walking speeds of the pedestrians

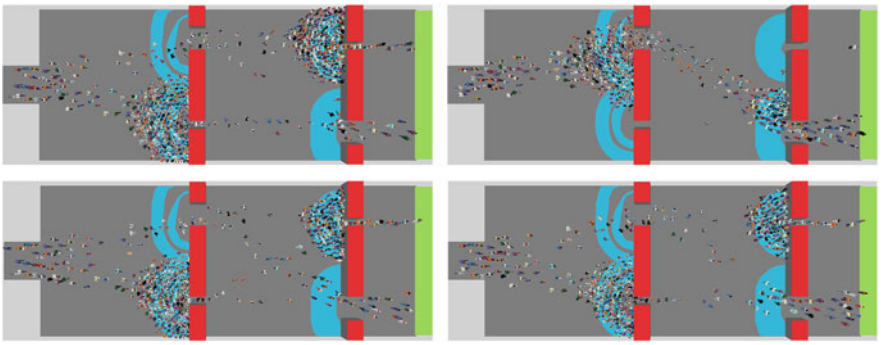

Fig. 5 Situation after 450 simulation seconds with a demand of 3 pedestrians per second: *upper left*: if pedestrians walk 50:50 the two shortest routes; *upper right*: if all pedestrians walk the route with highest capacity; *lower left*: if all routes are used equally; *lower right*: according to the result of the assignment process (39.4 : 0 : 17.2 : 43.4)

processes evolve. For the sake of clarity we do not force travel times and route choice ratios of all routes into a diagram, but compare in Fig. 4 the route choice ratios and travel times of the five different assignment processes only for route 3.

Figure 5 shows a comparison of the situation after 450 simulation seconds as it occurs when different route choice ratios are chosen. One can get the impression – and this is correct – that pedestrians could be assigned more efficiently. The reason for this is that in our – so far rather simple assignment method – only pedestrians who arrive within the relevant time interval at the destination can contribute. In the discussion we will elaborate on how the calculation of route choice ratios could be improved.

Having looked to the details if demand is set to 3 pedestrians per second we will furthermore present the results of all demand volume variants we have considered. For this larger set of result data due to space limitations we have to restrict ourselves to choice ratios and travel times when equilibrium is reached or the assignment process has terminated otherwise.

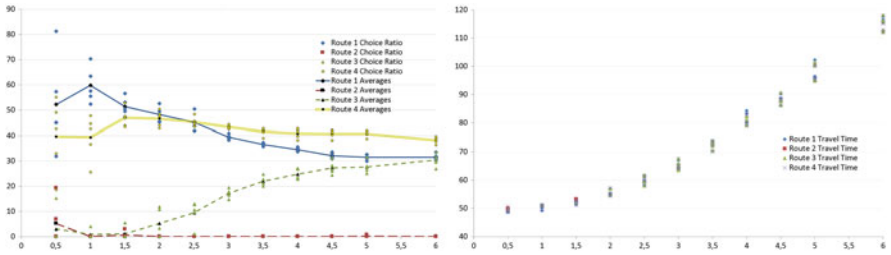

Fig. 6 Route choice ratios (*left*, in percent) and travel times (*right*, in seconds) vs. demand as they result from the assignment process. It can be seen how route 3 which leads through the two wider doors with increasing demand gains volume and thus leads to a more efficient walking behavior. It can also be seen how the travel times for a particular demand volume for all routes and all assignment processes all have a similar value compared to the overall dynamics of travel times with increasing demand. For small demand route 1 has a higher load than route 4 although both mainly differ in the sequence of bottleneck widths (route 1: wide, narrow; route 4: narrow, wide). Even the narrow door has a capacity to easily accommodate the demand (about half of the total demand) of the cases with 0.5 or 1 pedestrians per second total demand. Why then is there a difference between the two route choice ratios? The reason is that along route 4 in periods of above average demand pedestrians have to align in less time to pass through the narrow bottleneck. If pedestrians don't manage to do so some of them have a time delay and that is sufficient to trigger the observed differences

Figure 6 shows the route choice ratios and the travel times as they result from the assignment processes.

Summary, Conclusions, and Outlook

This study gave an example of how a recently proposed method to compute and model routing alternatives for pedestrians in simulations can be applied. The computation of routing alternatives is formulated such that the proposed alternatives are sufficiently different which means more precisely that the routes are separated by at least one obstacle (or non-walkable ground) of a certain, configurable minimum size. Pedestrians follow the routes by heading sequentially from intermediate destination to intermediate destination. Hereby they can prefer to walk into the direction of the shortest path – which is the usual strategy in a model of operational pedestrian dynamics [18] – nevertheless as a consequence of the intermediate destinations globally they can walk arbitrary detours. The intermediate destinations are geometrically shaped such that no artificial sharp turns or artificial bottlenecks are introduced locally into the motion. In other words: if the intermediate destinations are not marked specifically an observer could not guess their presence from observing local pedestrian behavior.

(continued)

The routes which result from this method can easily be used for an assignment computation to find the user equilibrium with regard to travel times (Wardrop's principle: "No traveler can improve his or her travel time by choosing a different route."). This was done in this contribution with a rather simple geometry which nevertheless allowed to see exemplified how the method of route and intermediate destination computation works.

Furthermore the method to compute from simulation results (travel times) the route choice ratios for the next iteration step was rather simple. It only relied on the simulation results of the very last iteration step. One can imagine that oscillations in the results could be reduced if a longer history of simulation results is considered. Second, the method ignores the current travel times of pedestrians who are still in the simulation when the relevant time interval ends. It is, however, a difference, if at that time all pedestrians who are still on their way have a current travel time below the one which has been measured as average for a particular route or if there are individuals who have had long delays and thus travel times well above that average. This is related to a third issue: we have considered all pedestrians who have arrived within a certain time interval. One could also try to consider pedestrians who depart within a certain time interval. This is more difficult as there is no guaranteed maximum simulation time, but after all the route decision occurs when a pedestrian departs, so naturally it makes sense to aggregate based on time intervals of departure.

Independent of the details of the assignment method it would be interesting to compare in future studies the results as well as the performance (mainly concerning computation time) of the proposed iterative method with one-shot methods where it is tried to achieve a good – i.e. travel time-based near user equilibrium – within one single simulation run [8–12].

References

1. PTV AG, PTV Vissim 5.40 – User Manual. PTV Group, Haid-und-Neu-Str. 15, D-76131 Karlsruhe, 2012. Version 5.40-08
2. H. Bar-Gera, Origin-based algorithm for the traffic assignment problem. Transp. Sci. **36**(4), 398–417 (2002)
3. M. Beckmann, C.B. McGuire, C.B. Winsten, Studies in the economics of transportation. Technical report, Yale University Press, 1956
4. M. Fellendorf, P. Vortisch, Microscopic traffic flow simulator vissim, in *Fundamentals of Traffic Simulation* (Springer, New York, 2010), pp. 63–93
5. G. Gentile, K. Noekel, Linear user cost equilibrium: the new algorithm for traffic assignment in visum, in *Proceedings of European Transport Conference 2009*, Leiden, 2009
6. International Maritime Organization, Msc circ 1238. Technical report, IMO, 2007
7. A. Johansson, D. Helbing, P.K. Shukla, Specification of the social force pedestrian model by evolutionary adjustment to video tracking data. Adv. Complex Syst. **10**(4), 271–288 (2007)

8. A.U. Kemloh Wagoum, A. Seyfried, S. Holl, Modeling the dynamic route choice of pedestrians to assess the criticality of building evacuation. Adv. Complex Syst. **15**(07), 1250029 (2012)
9. T. Kretz, The use of dynamic distance potential fields for pedestrian flow around corners, in *First International Conference on Evacuation Modeling and Management*, TU Delft, 2009
10. T. Kretz, The effect of integrating travel time, in *Pedestrian and Evacuation Dynamics 2012*, ed. by U. Weidmann, U. Kirsch, M. Schreckenberg (Springer International Publishing, 2014, in press), pp. 1013–1027
11. T. Kretz, A. Große, S. Hengst, L. Kautzsch, A. Pohlmann, P. Vortisch, Quickest paths in simulations of pedestrians. Adv. Complex Syst. **14**, 733–759 (2011)
12. T. Kretz, S. Hengst, V. Roca, A. Pérez Arias, S. Friedberger, U.D. Hanebeck, Calibrating dynamic pedestrian route choice with an extended range telepresence system, in *2011 IEEE International Conference on Computer Vision Workshops: First IEEE Workshop on Modeling, Simulation and Visual Analysis of Large Crowds*, Barcelona, 6–13 Nov 2011, pp. 166-172
13. T. Kretz, S. Hengst, P. Vortisch, Pedestrian flow at bottlenecks – validation and calibration of VISSIM's social force model of pedestrian traffic and its empirical foundations, in *International Symposium of Transport Simulation 2008 (ISTS08)*, Monash University, Gold Coast, ed. by M. Sarvi (2008), page electronic publication
14. T. Kretz, K. Lehmann, T. Friderich, Selected applications of a dynamic assignment method for microscopic simulation of pedestrians, in *European Transport Conference 2013*, Frankfurt, 2013, page online
15. T. Kretz, K. Lehmann, I. Hofsäß, User equilibrium route assignment for microscopic pedestrian simulation. Adv. Complex Syst. **17**(2), 1450070 (2014)
16. T. Kretz, K. Lehmann, I. Hofsäß, A. Leonhardt, Dynamic assignment in microsimulations of pedestrians, in *93rd Annual Meeting of the Transportation Research Board*, Washington DC, 2014, page on CD
17. L.J. LeBlanc, E.K. Morlok, W.P. Pierskalla, An efficient approach to solving the road network equilibrium traffic assignment problem. Transp. Res. **9**(5), 309–318 (1975)
18. A. Schadschneider, H. Klüpfel, T. Kretz, C. Rogsch, A. Seyfried, Fundamentals of pedestrian and evacuation dynamics, in *Multi-Agent Systems for Traffic and Transportation Engineering*, ed. by A. Bazzan, F. Klügl (Information Science Reference, Hershey, 2009), pp. 124–154. ISBN:978-1-60566-226-8
19. J. van den Heuvel, A. Voskamp, W. Daamen, S.P. Hoogendoorn, Using bluetooth to estimate the impact of congestion on pedestrian route choice in train stations, in *Traffic and Granular Flow 2013*, ed. by M. Chraibi, M. Boltes, A. Schadschneider, A. Seyfried (Springer, Cham, 2014)
20. F.L.M. van Wageningen-Kessels, W. Daamen, S.P. Hoogendoorn, Pedestrian evacuation optimization – dynamic programming in continuous space and time, in *Traffic and Granular Flow 2013*, ed. by M. Boltes, M. Chraibi, A. Schadschneider, A. Seyfried, M. Schreckenberg (Springer, Cham, 2014)
21. J.G. Wardrop, Road paper. some theoretical aspects of road traffic research. ICE Proc.: Eng. Div. **1**, 325–362 (1952)

How Navigation According to a Distance Function Improves Pedestrian Motion in ODE-Based Models

Felix Dietrich and Gerta Köster

Abstract We present a new ODE-based model for pedestrian motion where a superposition of gradients of distance functions directly changes the direction of the velocity vector: the Gradient Navigation Model (GNM). The approach differs fundamentally from force based models where the accelerative term is affected by forces and in turn changes the velocity. In the GNM, model induced oscillations are avoided completely since no actual forces are present. The use of fast and accurate high order numerical integrators is possible through smooth derivatives in the equations of motion. As a consequence, almost no overlapping of pedestrians occurs. Empirically known phenomena are well reproduced. The parameter calibration is performed by theoretical arguments based on empirically validated assumptions rather than numerical tests. The Gradient Navigation Model is compared quantitatively and qualitatively to Helbing's Social Force Model.

1 Introduction

Many microscopic models for pedestrian dynamics are based on systems of ordinary differential equations (ODE) [1, 2, 4, 9]. The trajectories of the pedestrians in two-dimensional space are solutions to these systems. Most of the ODE models describe acceleration based on Newtonian mechanics: forces change acceleration, which is integrated to velocity, which is then again integrated to position. Inertia is a natural consequence of this way of modeling. This causes phenomena natural to molecular dynamics, such as oscillations around critical points and overlapping of particles. Although they are natural to particle physics these phenomena are not desired in pedestrian models. Pedestrians do not oscillate around targets or repeatedly bump

F. Dietrich (✉)
Munich University of Applied Sciences, Lothstr. 64, 80335 München, Germany

Technische Universität München, Boltzmannstr. 3, 85747 Garching bei München, Germany
e-mail: felix.dietrich@tum.de

G. Köster
Munich University of Applied Sciences, Lothstr. 64, 80335 München, Germany
e-mail: gerta.koester@hm.edu

M. Chraibi et al. (eds.), *Traffic and Granular Flow '13*,
DOI 10.1007/978-3-319-10629-8_7

into others. There have been attempts to mitigate the problems associated with inertia in force based models [1]. We introduce the Gradient Navigation Model [2], an attempt to get rid of many of the problems of force based models. We use a different approach than Newtonian mechanics to model motion, where no inertia in the classical sense is present. The model is then compared quantitatively and qualitatively to Helbing's Social Force Model [5].

This paper is structured as follows. Section 2 briefly introduces the new Gradient Navigation Model [2] and, as representative for force based models, the Social Force Model [4]. Section 3 compares the two models: The first part focuses on microscopic artifacts caused by inertia in force based models. In the second part, we briefly analyze the computational efficiency of the models.

2 Models

The Social Force Model [4, 5] explains pedestrian motion similar to particle motion in molecular dynamics. A system of ODEs (Eq. 1) describes both the velocity $\dot{x}$ and acceleration vectors $\dot{w}$ at each point in time. Acceleration is changed by a superposition of forces F. These forces represent individual decisions, such as not to stand too close to other pedestrians or to move in the direction of the shortest path towards the target.

$$\begin{aligned} \dot{x}_i &= w_i\, g(\|w_i\|, v_i^{max}) =: v_i \\ \dot{w}_i &= F \end{aligned} \tag{1}$$

The function g sets the limits of the speed $\|w\|$ between 0 and a maximal velocity v_i^{max} (which is higher than the desired velocity v_i^{des}). $F = F_t + F_r$ is a combination of the attractive force F_t to the target and a repulsive force F_r acting on a given pedestrian i from other pedestrians j and obstacles B with

$$F_t = \frac{1}{\tau}(v_i^{des} e_i - v), \tag{2}$$

$$F_r = -(\sum_{j \neq i} \nabla V(\|x_i - x_j\|) + \sum_{B} \nabla U(\|x_i - x_B\|)). \tag{3}$$

V is an anisotropic potential field surrounding the other pedestrians j. It is elongated in their respective direction of motion. U is a potential field emanating from obstacles B. The direction of pedestrian i to a vertex of a polygonal path that leads to the target is called e_i. For formal definitions of V, U and e_i, we refer to [4].

The Gradient Navigation Model from [2] is based on three main assumptions: Firstly, we assume that physical interactions between pedestrians (pushing each other) are negligible. Pedestrians try to avoid physical contact, even in quite dense crowds. This is the most important assumption of the model. It enables us to neglect

the effects of Newtonian physics and instead directly steer the individuals into their desired navigational direction N. Note that this assumption is mostly used in discrete event models [11, 12]. Here, we use it in an ODE setting. Secondly, similar to the Social Force Model, we assume that pedestrians want to reach their targets in as little time as possible – based on their information about the environment. This assumption allows to use a floor field σ to steer pedestrians to their targets. See [3] for a detailed discussion about using such a floor field in a pedestrian context. Thirdly, we assume that pedestrians alter their speed as a reaction to other pedestrians and obstacles, after a certain reaction time. This is based on empirical research by [8]. Assumption three postulates a reaction time, which we introduce by a scalar, multiplicative relaxation term w. With these three assumptions, we can formulate the system of differential equations in the Gradient Navigation Model for a given pedestrian i:

$$\begin{aligned} \dot{x}_i &= w_i N_i \\ \dot{w}_i &= \tfrac{1}{\tau}(v_i^{des}(\rho(x_i))\|N_i\| - w_i) \end{aligned} \tag{4}$$

In this system τ is a relaxation constant and $v_i^{des}(\rho(x_i))$ is the desired velocity of the given pedestrian dependent at the local crowd density $\rho(x_i)$. In this paper, we simplify $v(\rho(x_i)) = v_i$ constant and drawn from a normal distribution $N(1.34, 0.26)$.The desired direction of motion N_i in the Gradient Navigation Model is composed similar to the force F in the SFM. However, the desired direction towards the target $N_{i,\sigma}$ is computed from the gradient of a floor field σ (see Fig. 1a):

$$N_{i,\sigma} = -\nabla\sigma(x_i) \tag{5}$$

The induced direction starting from pedestrian i away from close pedestrians j and obstacles B is called $N_{i,P}$ (see Fig. 1b):

$$N_{i,P} = -(\sum_{j \neq i} \nabla P_j + \sum_{B} \nabla P_B) \tag{6}$$

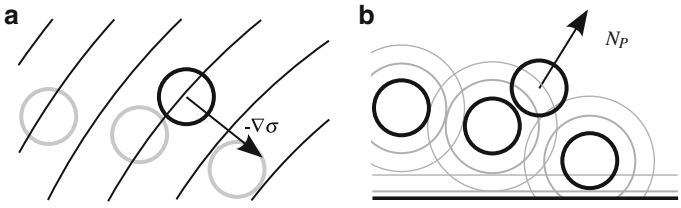

Fig. 1 Floor field and dynamic gradients in the Gradient Navigation Model. (**a**) The desired direction towards the target $N_\sigma = -\nabla\sigma$, where σ is a floor field emanating from the target area of the given pedestrian. (**b**) The induced direction N_P away from close pedestrians j and obstacles B. Three other pedestrians as well as an obstacle are shown here. The *gray circles* and *lines* represent decreasing strength of repulsion imposed by N_P

The gradients ∇P_j and ∇P_B point towards the pedestrian j and obstacle B. Their norms are equal to a function h that is monotonically decreasing with increasing distance r to pedestrian i. We chose

$$h(r; R, p) = \begin{cases} p \; exp\frac{1}{(r/R)^2-1} & |r/R| < 1 \\ 0 & otherwise \end{cases} \tag{7}$$

which is a smooth function on compact support. This choice has the major advantage that the derivatives in the ODE system stay smooth even if we stop the computation of nearest neighbors and obstacles for $r > R$. Smoothness of the floor field σ can be achieved using mollification techniques described in [2]. The two direction vectors N_σ and N_P are combined into N by clamping their length between zero and one with a smooth function $g : \mathbb{R}^2 \to \mathbb{R}^2$:

$$N = g(g(N_\sigma) + g(N_P)) \tag{8}$$

Parameter calibration in the GNM is performed using both empirically determined values and a new analytical calibration method developed in [2]. The method uses plausibility arguments to construct a scenario with one pedestrian enclosed by four others and a wall. The pedestrian in the center is assumed to have velocity zero. Together with empirically measured values, this fixes the remaining free parameters. No numerical calibration is needed.

3 Comparison

The equations of motion in the GNM and SFM differ in the treatment of velocity: the velocity $\dot{x}$ is changed indirectly in the Social Force Model (Eq. 1) and changed directly in the Gradient Navigation Model (Eq. 4). Furthermore, the navigational direction in the (original, 1995) Social Force Model is towards vertices of a polygon (the 'shortest path'), whereas the Gradient Navigation Model uses a floor field similar to cellular automata and the Optimal Steps Model [11]. Calibration of the Social Force Model has been performed in numerous ways in the past. Johansson et al. [6] for example use evolutionary adjustment to video tracking data. In contrast to this, the Gradient Navigation Model is calibrated using plausibility arguments in a simple scenario and the analytical method from [2].

In the following, we present three scenarios where the difference between the two models becomes apparent. The first one is composed of a wall, one target and one pedestrian trying to reach that target. The subject is starting so close to the wall that one would assume he or she would first move away from it and then towards the target. Figure 2 shows simulation results with the two models. On the left, the pedestrians motion is governed by the Social Force Model. The pedestrian circles around the target. This is because of inertia: the pedestrians velocity vector does not

Fig. 2 On the *left*, the pedestrians motion is governed by the Social Force Model. The pedestrian circles around the target (*cross*). This is because of inertia: the pedestrians velocity vector does not point directly to the target. In contrast, the Gradient Navigation Model directly changes the pedestrians velocity direction (*right figure*)

Fig. 3 The scenario shown contains one moving pedestrian (*left*), one stationary pedestrian (non-moving, in the *center*) and one target (*cross*, to the *right*). It is one-dimensional, so that the moving pedestrian cannot move around the stationary one but must stop

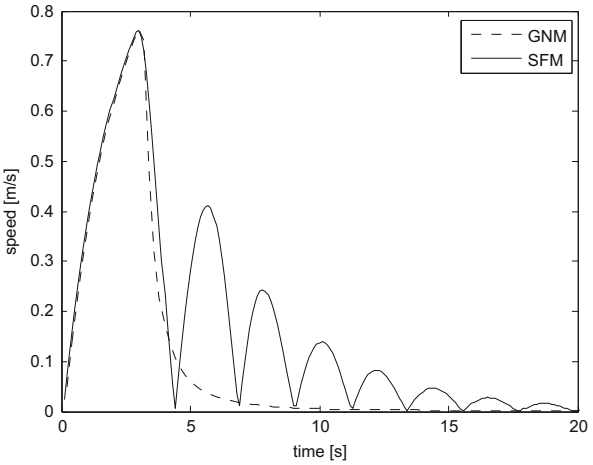

Fig. 4 Result of the scenario shown in Fig. 3 with both models. In the SFM, the moving pedestrian bounces back from the stationary one due to inertia. The GNM produces a similar acceleration spike as the SFM at first, but then rapidly slows the moving pedestrian down to a halt

point directly to the target, only the acceleration vector does. In contrast to that, on the right, the Gradient Navigation Model directly changes the pedestrians velocity. This leads to the pedestrian stepping away from the wall and then moving parallel to it, until the path to the target is in line of sight.

In the second scenario (see Fig. 3), a pedestrian moves towards a target on the right and is blocked by a stationary pedestrian. In this scenario, the moving pedestrian cannot move around the stationary one but must stop. Both models are used to compute the speed of the moving pedestrian over time. The result is shown in Fig. 4. With the SFM, the moving pedestrian passes the stable point and moves slightly into the stationary pedestrian. He/she is then repulsed and moves back

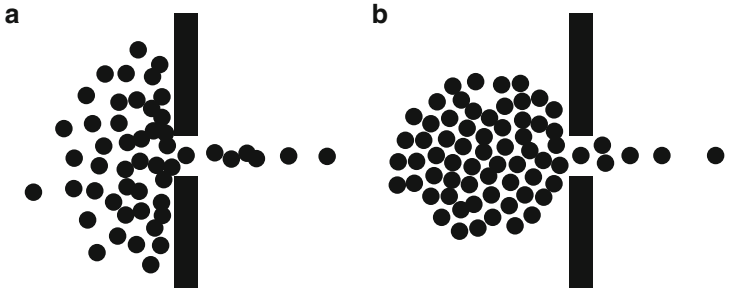

Fig. 5 Different congestion shapes produced by SFM and GNM during evacuation of a room. (**a**) Evacuation of a room modeled with the SFM. Pedestrians clog in front of the bottleneck and get pushed into the corners of the room. Many torsos overlap. (**b**) Evacuation of a room modeled with the GNM. Pedestrians wait in front of the bottleneck and do not move into the corners. Torsos rarely overlap

towards the stable point, again passing it. This produces the graph of the speed as shown by Fig. 4, where the oscillation are visible. Note that three of the parameters (including relaxation τ as well as range and strength of the interaction forces) of the Social Force Model can be changed so that it resembles a damped harmonic oscillator. This removes the oscillations, but also restricts the parameter values to unreasonable intervals. Moreover, the relaxation τ is not a free parameter of the model and must be determined by experiment. With the GNM, no oscillations occur regardless of the value of τ. In the first acceleration phase, the speed produced by the GNM is equal to the result of the SFM because the same value of the relaxation constant τ was chosen. As the pedestrian comes close to the stable point, it decelerates and never passes it. No oscillations occur.

The third scenario shows the results of the two models in a simulation of an evacuation of a room (Fig. 5). With the SFM, pedestrians clog in front of the bottleneck and get pushed into the corners of the room. Many torsos overlap. With the GNM, Pedestrians wait in front of the bottleneck and do not move into the corners. Torsos rarely overlap. The difference of the results of the two models can be explained by the different assumptions they are built on. In the SFM, pedestrians are assumed to behave similar to particles. Accordingly, they are attracted by targets and get repulsed by other pedestrians. This causes overlapping. Long ranged repulsive forces cause the arc shaped congestion. In the GNM, pedestrians are assumed to stop in high density situations. Overlapping is avoided by this. The bounded support for the interaction function h (Eq. 7) between pedestrians in combination with the movement on a floor field causes the cone shaped congestion in front of the bottleneck.

The last part of the comparison focuses on computational efficiency when the equations of motion (Eqs. 1 and 4) are solved numerically. In the original SFM, the derivatives are not smoothly dependent on their arguments. This makes efficient use of accurate integration schemes like Runge-Kutta impossible [7]. In contrast to that, the derivatives in the GNM are smooth by design. Figure 6 shows the increase in

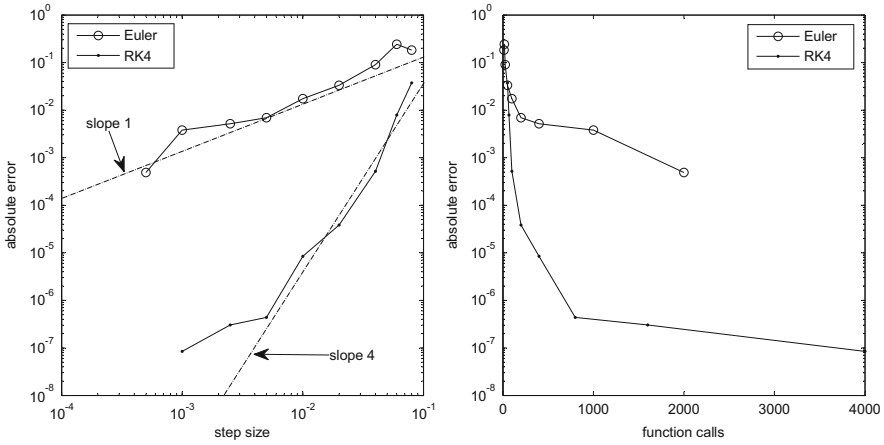

Fig. 6 Absolute errors of different numerical integrators for differing step sizes and function calls to the Gradient Navigation Model. Both the Runge Kutta 4 and the explicit Euler method are applied to solve the equations of motion. In the *left figure*, *straight lines* with slope 1 and 4 were added to emphasize the differing rates of convergence. The *right figure* clearly shows that even when using only a small number of function calls, the Runge-Kutta method can successfully be applied to achieve an accuracy two to four orders of magnitude higher than Euler's method

accuracy when using the Runge-Kutta (fourth order) instead of the explicit Euler method. The figure on the right shows that even using only a small number of function calls (calls to the right hand side of the model), the Runge-Kutta method can successfully achieve an accuracy two to four orders of magnitude higher than Euler's method. Note that step size controlling methods like Dormand-Prince-45 [10] schemes could also be applied. This would automatically use small step sizes only when needed, further increasing computation speed for a fixed accuracy.

Conclusion

We introduced a new model of pedestrian motion, the Gradient Navigation Model, and compared it to the Social Force Model. The latter is based on Newtonian mechanics, where forces affect acceleration and therefore inertia affects motion. In contrast to this, the GNM is inspired by movement in cellular automata, where the velocity vector is adjusted instantaneously to match the desired walking direction. Two scenarios showed that force based models suffer from drawbacks due to inertia, which are resolved in the GNM. Firstly, circular trajectories around a target occurred when a pedestrians was repulsed by a wall close to the target. Secondly, a moving pedestrian bounced back and forth when trying to stop close to another pedestrian. Our brief analysis reveals the difficulties of force based models regarding numerical

(continued)

integration. Many force based approaches do not take smoothness of the derivatives into account, decreasing computational efficiency as numerical integrators of high order cannot be used to speed up the numerical solution. Our approach to these difficulties is the Gradient Navigation Model, where pedestrians are not subject to inertia. This avoids any oscillatory behaviour close to targets, obstacles or other pedestrians. As the equations of motion are smooth by design, high order accurate integration methods can be used. In the future, we will make use of the possibility of fast and accurate solutions to study influences of small perturbations on the macroscopic behavior of pedestrian flows.

Acknowledgements This work was partially funded by the German Ministry of Research through the project MEPKA (Grant No. 17PNT028). Support from the TopMath Graduate Center of TUM Graduate School at Technische Universität München, Germany and from the TopMath Program at the Elite Network of Bavaria is gratefully acknowledged.

References

1. M. Chraibi, U. Kemloh, A. Schadschneider, A. Seyfried, Force-based models of pedestrian dynamics. Netw. Heterog. Media **6**(3), 425–442 (2011)
2. F. Dietrich, G. Köster, Gradient navigation model for pedestrian dynamics. Phys. Rev. E **89**, 062801 (2014)
3. D. Hartmann, J. Mille, A. Pfaffinger, C. Royer, Dynamic medium scale navigation using dynamic floor fields, in *Proceedings of the 6th International Conference on Pedestrian and Evacuation Dynamics*, Zürich, 2012
4. D. Helbing, P. Molnár, Social Force Model for pedestrian dynamics. Phys. Rev. E **51**(5), 4282–4286 (1995)
5. D. Helbing, I. Farkas, T. Vicsek, Simulating dynamical features of escape panic. Nature **407**, 487–490 (2000)
6. A. Johansson, D. Helbing, P. Shukla, Specification of the social force pedestrian model by evolutionary adjustment to video tracking data. Adv. Complex Syst. **10**, 271–288 (2007)
7. G. Köster, F. Treml, M. Gödel, Avoiding numerical pitfalls in social force models. Phys. Rev. E **87**(6), 063305 (2013)
8. M. Moussaïd, D. Helbing, S. Garnier, A. Johansson, M. Combe, G. Theraulaz, Experimental study of the behavioural mechanisms underlying self-organization in human crowds. Proc. R. Soc. B: Biol. Sci. **276**, 2755–2762 (2009)
9. M. Moussaïd, D. Helbing, G. Theraulaz, How simple rules determine pedestrian behavior and crowd disasters. Proc. Natl. Acad. Sci. **108**(17), 6884–6888 (2011)
10. P.J. Prince, J.R. Dormand, New Runge-Kutta algorithms for numerical simulation in dynamical astronomy. Celest. Mech. Dyn. Astron. **18**(10), 223–232 (1978)
11. M.J. Seitz, G. Köster, Natural discretization of pedestrian movement in continuous space. Phys. Rev. E **86**, 046108 (2012)
12. K. Yamamoto, S. Kokubo, K. Nishinari, Simulation for pedestrian dynamics by real-coded cellular automata (RCA). Phys. A: Stat. Mech. Appl. **379**(2), 654–660 (2007)

Implementation Issues of Force Based Pedestrian Motion Models

Gerta Köster and Marion Gödel

Abstract Forced based models in the form of ordinary differential equations (ODE), such as the social force model, are among the best known approaches to simulating pedestrian flow. They adopt the idea that the Newtonian laws of motion mostly carry over to pedestrian motion so that human trajectories can be computed by solving a set of ODEs for velocity and acceleration. The models are widely spread in science and application. Nevertheless, oscillations, collisions, and instabilities occur even for small step sizes. We identify some mathematical properties at the root of the problem: The right hand side of the differential equation may be non-differentiable and discontinuous at target locations. This produces undesirable behavior in the solution and severe loss of accuracy in efficient numerical schemes. Using the social force model as an example, we propose a very simple mollification so that the dynamic properties of the original many-body system are conserved. This elegantly and cost-efficiently resolves several of the issues concerning stability and numerical resolution. On the other hand, we show that it is insufficient to remove the typical but undesirable circular movement of pedestrians moving towards a target.

1 Introduction

There are many approaches to modeling pedestrian dynamics [3, 11, 12, 14]. Among them social force models are well established [5, 6]. Their proximity to equations derived from Newton's laws of motion allows direct application of standard numerical methods, such as Euler's method, to solve the equations. Nonetheless, scientists and tool users continue to run into trouble when implementing or employing the model [1, 2]. While the physical properties of the model that do not match human behavior, such as inertia, have been discussed to some extent [1] very little attention has yet been paid to the mathematical properties and the resulting effects on the stability of the supposed exact solution and numerical solution attempts.

G. Köster (✉) • M. Gödel
Munich University of Applied Science, Lothstr. 64, 80335 Munich, Germany
e-mail: gerta.koester@hm.edu

M. Chraibi et al. (eds.), *Traffic and Granular Flow '13*,
DOI 10.1007/978-3-319-10629-8_8

In this work we point out some properties of the right hand side especially concerning target locations that lead to oscillations in the solution and loss of accuracy in the numerical approximation. This background analysis is described in Sect. 2. In Sect. 3 we propose to mollify the right hand side so that the difficulties regarding the target locations disappear, while the desired properties of the original model are conserved. We also demonstrate the success of our idea by comparing numerical solutions of both models in a very simple simulation scenario and a more complex bottleneck scenario taken from [8]. At the same time our examples show that, while better mollification and consequently better numerical treatment of force based models improves computational speed, it remains insufficient to get rid of one very undesirable effect: Virtual pedestrians circle around a target before they reach it.

2 Problem Analysis

This work is built upon the original equations of the social force model as they were presented in [6] and in Molnár's dissertation [9]. We look at vectors $x, v \in \mathbb{R}^{2\times m}$ that denote the location and velocity of pedestrians $1, \ldots, m$ in two dimensional Euclidean space. Vertical movement is neglected. To make sure that the speed of an individual j does not exceed an acceptable upper limit $v_{max,j}$ we need the auxiliary velocity w in the mathematical formulation. Following [6] we set $v_{max,j} = 1.3\, v_{0,j}$ where $v_{0,j}$ is each pedestrian's individual free-flow velocity. Hence pedestrians can accelerate but will not sprint. For the jth pedestrian we have

$$\dot{x}_j = v_j(w_j) := \begin{cases} w_j & \text{if } \|w_j\| < v_{max,j}. \\ \frac{v_{0,j}}{\|w_j\|} w_j & \text{otherwise.} \end{cases} \tag{1}$$

The following set of equations for x and w forms the actual social force model:

$$\begin{aligned} \dot{x} &= v(w) \\ \dot{w} &= F(x,w) = F_{target}(x,w) + F_{ped}(x,w) + F_{ob}(x,w). \end{aligned} \tag{2}$$

F_{target}, F_{ped}, and F_{ob} stand for forces acting on each pedestrian from the attracting target(s), repelling fellow pedestrians and repelling obstacles. Forces are assumed to obey a superposition principle. Since there are usually several interacting pedestrians and several obstacles F_{ped} and F_{ob} are sums of force terms $F_{ped,i,j}$ and $F_{ob,k}$. We are aware that most simulation tools based on the social force model (SFM) use variations of the base model. But these variations still have the essential properties of the original and hence will experience similar difficulties. In particular, the acceleration $\dot{w}$ is a vector valued function. The direction of movement depends on the acceleration in a deeply physical way that cannot be easily matched with human walking behavior. Most of our observations are best presented when the system is reduced to the bare essentials. Hence we will assume one target, one or two

pedestrians depending on the scenario, and no obstacle – all unless otherwise stated. The resulting mathematical claims can easily be carried over to more complex situations.

There are two kinds of difficulties with the original SFM: Artificial behavior of the pedestrians and problems stemming from computation. Some of the former are the result from physical phenomena, such as inertia, which is caused by the emphasis on acceleration in the model. They are typical for Newtonian systems but, we think, untypical for human beings [1, 3]. Computation is either slow with tiny step sizes Δt or the spatial resolution is low which leads to collisions. We will look into the reasons why faster solvers than the explicit Euler scheme so far have not produced better results. We start with the seemingly trivial situation of one pedestrian moving towards one target in a space free of obstacles. We may drop the index for the pedestrian and force type and neglect that the velocity is bounded. Without loss of generality we set the target location to $(0, 0)$. So we get the simplified equations:

$$(\dot{x}_1, \dot{x}_2) = (v_1, v_2) \tag{3}$$

$$(\dot{v}_1, \dot{v}_2) = F((x_1, x_2), (v_1, v_2)) \quad \text{with force } F \text{ given by}$$

$$F(x, v) = \frac{1}{\tau}\left(-\frac{x}{\|x\|}v_0 - v\right). \tag{4}$$

The free-flow velocity v_0 is the presumed walking velocity of an individual across an open space. The influence of the reaction time τ modeled by pre-factor $\frac{1}{\tau}$ is not relevant for our investigations at the moment and τ is set to 0.5 s as suggested in [6] throughout the paper.

We turn our attention to a straight forward analysis of the mathematical properties of the system: Unit vectors $-x/\|x\|$ point in the direction of the target for all locations $x \neq (0, 0)$. However, the function F, that stands for the acceleration vector, has a singularity at the target $x = (0, 0)$. The right hand side displays a jump. See Fig. 1. This has two undesirable consequences: Loss of smoothness and

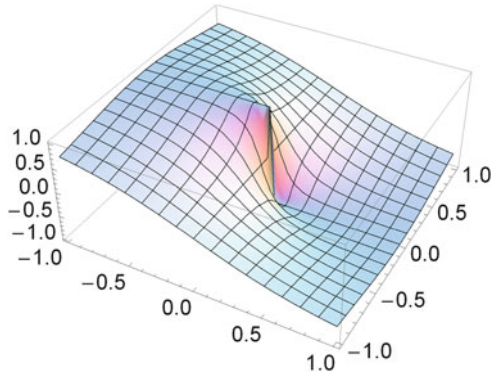

Fig. 1 Unit vector $-\frac{x_1}{\|x\|}$ that points in the direction of the target

loss of accuracy. The first means that a solution can only exist in a weak sense. More important for the practical user is the loss of accuracy, in fact of convergence, of numerical schemes near discontinuities. Higher order schemes than Euler must fail, because the right hand side of the SFM is discontinuous. Thus the solution is not smooth and even Euler's method must blow up when it hits a target. Wild oscillations and even collisions in the numerical approximation of the supposed true trajectories are observed in practical simulations.

Applying a k-step numerical scheme on a differential equation $\dot{y} = \mathscr{F}(y)$ means to discretize the equation in time. In the case of Euler's method the result simply is $y_n = y_{n-1} + \Delta t \mathscr{F}(y_{n-1})$ where y_n is the solution one step ahead in time from y_{n-1} and Δt is the step size in time. We construct a 'pathological' example using the Euler scheme: With $(x, v) = ((0.5, 0), (-1, 0))$ as starting point, the second iteration lands exactly on the target $x = (0, 0)$ leading to division by zero and abortion of the simulation run.

In the two-dimensional example in Fig. 2 the trajectories of the corresponding difference equation show a stable orbit at nearly full speed around the target. Obviously, the pedestrian will never get close to the target.

The situation improves, when the step size is reduced, but the underlying problem remains: Even with a consistent numerical scheme, such as Euler's method, there is no guarantee that the solution of the difference equation has the same properties as the – supposed – solution of the differential equation, unless an number of restricting conditions on the smoothness of the right hand side are satisfied. In the case of the social force model with its discontinuity in the right hand side at the target point we fail to meet these conditions.

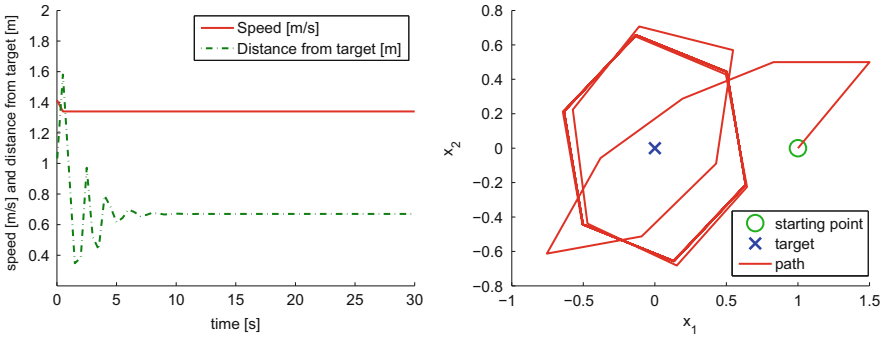

Fig. 2 Euler's scheme to solve the SFM develops a stable orbit around the target. With step size in time $\Delta t = 0.5\,\mathrm{s}$ and free-flow velocity $1.34\,\frac{\mathrm{m}}{\mathrm{s}}$ the person remains about 0.67 m off target and keeps moving at full speed

3 Mollification and Performance Comparison

We propose to mollify the classic social force model (2) for the target locations. Again we look at the simplified formulation of the social force model with a single pedestrian and only one target as in Eq. (3). The cause for the stability and convergence issues close to the target is the loss of continuity at the target point. Hence we replace the directional vector $-\frac{x}{\|x\|}$ by

$$-\frac{x}{\sqrt{x_1^2 + x_2^2 + \epsilon^2}} \text{ with } \epsilon > 0. \tag{5}$$

Clearly, the mollified version of the model is continuous and infinitely often differentiable at the target. Mollification is a standard technique in applied mathematics employed in various fields, e.g. in robotics with equations very similar to (3) [10,13]. Theory guarantees a unique solution for each initial value. Also, the target point with zero speed is a globally asymptotically stable steady state solution [7]. In other words, the pedestrian moves towards the target while steadily decreasing the speed. This behavior is desirable in itself, but it also leads to a much better numerical performance. At a safe distance from the target, the solutions of the SFM and the mollified social force model (MSFM) cannot be distinguished.

Numerical schemes to solve differential equations require, in order to work properly, a level of smoothness in the solution of the equation that matches the order of the scheme. If this is not the case, accuracy is usually lost. The right hand side of the social force equation is the first derivative of the solution. It is not differentiable in several places and discontinuous at the target. Hence the solution of the social force equations cannot be smooth. It is at best continuous and any solution is a solution in the weak sense only. We must expect severe loss of accuracy in any of the non-smooth locations. This is best demonstrated by computing the order of convergence of the numerical schemes when approaching critical locations. We select the popular, if slow converging, explicit Euler scheme and the highly efficient fifth order Runge-Kutta scheme that is the fifth order part of the default solver ode45 in Matlab, the Dormand-Prince scheme [4].

In the following scenario a single person moves towards a target where force F has its singularity in the original social force model. The initial velocity is set to $v_{\text{start}} = (0, 0)$. We look at the absolute values of the solution components (x_1, x_2) and (w_1, w_2) and observe, as expected, that the oscillations in the mollified model version are significantly attenuated. See Fig. 3. Since oscillations do not match human behavior, this outcome seems highly desirable independently of numerical effects. On the other hand, this example shows that the underlying problem cannot be resolved by mollification. The virtual pedestrians still circle around the target.

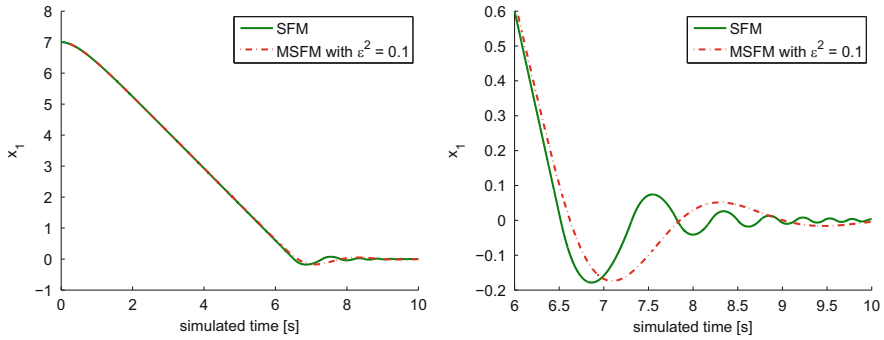

Fig. 3 Component wise comparison of a pedestrian's trajectory for the SFM and the MSFM. Scenario: A single person moves from position $(7, 4)$ to the target at $(0, 0)$ starting with a speed of $0\,\frac{\mathrm{m}}{\mathrm{s}}$. The desired velocity of the person is set to $1.34\,\frac{\mathrm{m}}{\mathrm{s}}$. Relaxation time $\tau = 0.5\,\mathrm{s}$. Mollification parameter $\epsilon^2 = 0.1$. *Right*: Focus on time $t > 6\,\mathrm{s}$ where the solution trajectory starts to go back and forth through the target

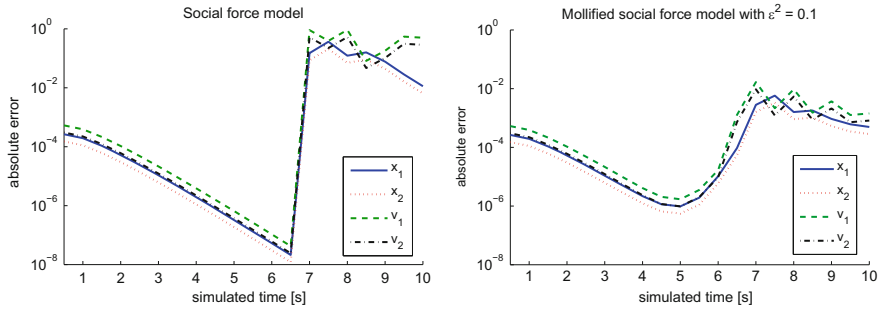

Fig. 4 Runge-Kutta scheme with step size $\Delta t = 2^{-1}\,\mathrm{s} = 0.5\,\mathrm{s}$

We look at the global truncation error of the numerical solution at time t. It is given by the difference between the numerical solution $y_{\Delta t}(t)$ and the exact solution $y(t)$.

$$err(t) = y(t) - y_{\Delta t}(t) \tag{6}$$

We use the step sizes $\Delta t = 2^{-1}\,\mathrm{s} = 0.5\,\mathrm{s}$ for the fifth order Runge-Kutta scheme and $\Delta t = 2^{-10}\,\mathrm{s} = 9.77 \cdot 10^{-4}\,\mathrm{s}$ for the Euler scheme to get approximately the same absolute error for both methods at a safe distance from the target. Each numerical solution is compared to a much finer approximation computed with the same scheme and $\Delta t = 2^{-15}\,\mathrm{s} = 3.05 \cdot 10^{-5}\,\mathrm{s}$. Then we increase the simulated time t thus approaching the target until $t_{end} = 10\,\mathrm{s}$. In Fig. 4 we compare the absolute error of the social force model to its mollified version with $\epsilon^2 = 0.1$ as the pedestrian is getting closer to the target. For the original social force model, there is a pronounced jump in the error at about $t = 6.5\,\mathrm{s}$ when the solution trajectory (x_1, x_2) starts to

circle around the target. Both methods experience a dramatic loss of accuracy, but the loss is much worse for the Runge-Kutta scheme which does not tolerate the loss of differentiability. This clearly illustrates that singularities at (intermediate) targets make the use of high performing schemes pointless. For the mollified model, on the other hand, no jump occurs. The error still increases for both numerical solutions, as must be expected when the true trajectories turn around narrow corners, but this time the error stays comparable. This means that the Runge-Kutta scheme can operate with a much larger step size to achieve the same resolution as the Euler scheme.

Computing the numerical solution at $t_{end} = 10\,\mathrm{s}$ took 1.16 s with Euler's method, but only 0.01 s with the fifth order Runge-Kutta scheme, that is, the Runge-Kutta method was *116 times faster*. The advantage becomes even more pronounced with longer time periods and more pedestrians or, when step size control is used to restrict the use of small step sizes to the areas with fast changes in the solution.

Finally, we compare the performance for a typical benchmark example inspired by [8]. N virtual persons are placed in a room of length 20 m and width 7 m. At one end of the room is a centrally placed door of width 1 m that leads to a corridor of the same width. An intermediate target is placed in the middle of the door. The final target is at a safe distance to the right outside the corridor. Hand-over from the intermediate target to the final target takes place when a person is no more than 0.4 m away from the door and the final target is in the direct line of sight (neglecting other pedestrians that may block the view). All pedestrians are identical, that is, they have the same free-flow velocity. This is unrealistic, leading to total symmetry, but it is deliberate because it helps to demonstrate the effects of insufficient resolution.

We use the explicit Euler scheme for the SFM and the fifth order Runge-Kutta scheme for the mollified SFM. In both cases we set $\Delta t = 0.1$ s so that an acceptable resolution of 0.01 m may be expected for Euler's method as long as we stay away from locations with discontinuities of the right hand side or its derivatives [7]. When the pedestrians get close to the target Euler's method fails for the classic SFM. The Runge-Kutta scheme applied on the mollified model without the discontinuity at the target encounters no more difficulties. Compare Fig. 5.

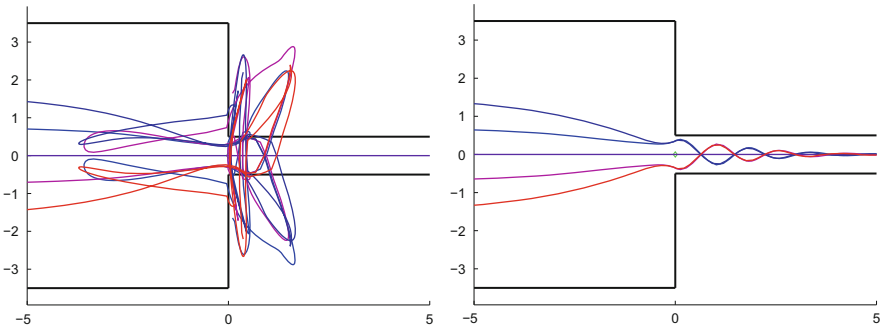

Fig. 5 Virtual pedestrians move from left to right through a bottleneck. Numerical solution of the social force equations with step size $\Delta t = 0.1$ s. *Left*: Euler's method, *Right*: fifth order Runge-Kutta method

Conclusion
In this paper we showed how to remove discontinuities of force based models at targets using mollification techniques. We demonstrated for the case of the SFM that the solution of the mollified model is almost identical to the solution of the classic model, when the pedestrians are at a safe distance from the target. That is, we have stayed faithful to the original modeling idea preserving not only the desired dynamic properties of the model, but also undesirable properties. In fact we showed in our examples, that although mollification and improved numerical treatment considerably, and usefully, speed up computation, they do not remove undesirable solution aspects. In particular the circular trajectories of the virtual pedestrians who are moving in on a target remain. This artifact is due to the emphasis on acceleration in force based models that we believe is not natural for human behavior. To achieve more natural navigation, we may have to drop Newtonian mechanics and, at the same time, find a formulation that ensures smoothness of the solution. A way to do this is to introduce a direct navigational function to compute $\dot{x}$ as in [3].

Acknowledgements This work was funded by the German Federal Ministry of Education and Research through the project MEPKA on mathematical characteristics of pedestrian stream models (grant number 17PNT028).

References

1. M. Chraibi, U. Kemloh, A. Schadschneider, A. Seyfried, Force-based models of pedestrian dynamics. Netw. Heterog. Media **6**(3), 425–442 (2011)
2. M. Chraibi, A. Seyfried, A. Schadschneider, Generalized centrifugal-force model for pedestrian dynamics. Phys. Rev. E **82**(4), 046111 (2010)
3. F. Dietrich, An ODE-based model for pedestrian motion and navigation, Bachelor's thesis, Technische Universität München, 2013
4. J.R. Dormand, P.J. Prince, A family of embedded runge-kutta formulae. J. Comput. Appl. Math. **6**(1), 19–26 (1980)
5. D. Helbing, I. Farkas, T. Vicsek, Simulating dynamical features of escape panic. Nature **407**, 487–490 (2000)
6. D. Helbing P. Molnár, Social force model for pedestrian dynamics. Phys. Rev. E **51**(5), 4282–4286 (1995)
7. G. Köster, F. Treml, M. Gödel, Avoiding numerical pitfalls in social force models. Phys. Rev. E **87**(6), 063305 (2013)
8. J. Liddle, A. Seyfried, B. Steffen, W. Klingsch, T. Rupprecht, A. Winkens, M. Boltes, Microscopic insights into pedestrian motion through a bottleneck, resolving spatial and temporal variations (2011). arXiv 1105.1532v1
9. P. Molnár, *Modellierung und Simulation der Dynamik von Fußgängerströmen*, PhD thesis, Universität Stuttgart, 1996

10. P. Molnár, J. Starke, Control of distributed autonomous robotic systems using principles of pattern formation in nature and pedestrian behavior. IEEE Trans. Syst. Man Cybern. Part B: Cybern. **31**(3), 433–436 (2001)
11. M.J. Seitz, G. Köster, Natural discretization of pedestrian movement in continuous space. Phys. Rev. E **86**, 046108 (2012)
12. A. Smith, C. James, R. Jones, P. Langston, E. Lester, J. Drury, Modelling contra-flow in crowd dynamics dem simulation. Saf. Sci. **47**(3), 395–404 (2009)
13. J. Starke, C. Ellsaesser, T. Fukuda, Self-organized control in cooperative robots using a pattern formation principle. Phys. Lett. A **375**, 2094–2098 (2011)
14. X. Zheng, T. Zhong, M. Liu, Modeling crowd evacuation of a building based on seven methodological approaches. Build. Environ. **44**(3), 437–445 (2009)

Using Bluetooth to Estimate the Impact of Congestion on Pedestrian Route Choice at Train Stations

Jeroen van den Heuvel, Aral Voskamp, Winnie Daamen, and Serge P. Hoogendoorn

Abstract At train stations escalators and stairs are common bottlenecks, typically just after train arrivals which cause a peak in pedestrian traffic from platform to station hall. Large stations typically have multiple sets of escalators and stairs, and therefore offer a route choice for passengers. In previous research the impact of waiting time and type of vertical infrastructure on pedestrian route choice behaviour have been identified, and to a limited extent quantified. This paper presents the results of a study of route choice behavior at congested stairs and escalators at Utrecht Central Station in The Netherlands. For data collection, Bluetooth scanunits have been used to measure route choice and waiting time at stairs and escalators. Several route choice models have been estimated to describe the probability of choosing a congested escalator route over alternative uncongested stairway routes. It is found that the preference of escalators over stairways is statistically significant for pedestrian route choice. Moreover, waiting time due to congestion upstream of escalators has a measurable impact on pedestrian route choice. These insights are valuable when improving design and operations of train stations.

1 Introduction

Pedestrian flows and bottlenecks are a growing challenge for station operations and design. Not only peak crowds at special events or significant train service disruptions, but also regular day-to-day operations have a significant impact on the level of service of pedestrian flows: on passenger experience, retail earnings and public transport service quality.

At many train stations the operator faces the challenge of handling growing pedestrian volumes, often concentrated in peak hours, and in a relatively small (semi-)indoor space. The severest bottlenecks tend to occur at escalators and stairs

J. van den Heuvel (✉) • A. Voskamp • W. Daamen • S.P. Hoogendoorn
Faculty of Civil Engineering and Geosciences, Department of Transport and Planning, Delft University of Technology, NS Stations, Netherlands Railways, Delft, Netherlands
e-mail: j.p.a.vandenheuvel@tudelft.nl

M. Chraibi et al. (eds.), *Traffic and Granular Flow '13*,
DOI 10.1007/978-3-319-10629-8_9

– the main vertical infrastructure (VI) – at the large train stations. This is due to long double-deck trains which carry up to over 1,000 passengers, and simultaneous train arrivals at the platform. At VI-bottlenecks, pedestrians are confronted with a choice: to wait up to minutes in situations with extreme congestion, or to select an alternative underused route to leave the platform. From the perspective of capacity usage and investments, route choice behaviour raises the question how an optimal VI-configuration should look like, and how this configuration is used in practice. With more insight into the route choice behaviour of pedestrians at bottlenecks, station operations and design can be improved. The best stations offer superior safety (no risks), maximum functionality (shorter walking times) and a good experience (seamless and comfortable trip).

This paper describes the study of pedestrian route choice behaviour at congested VI at Utrecht Central Station, performed by NS Stations and Delft University of Technology. The aim was to determine the influence of congestion at route choice behaviour of passengers who just arrived by train. For data collection, SMART Station has been used. This is a pedestrian flow measurement concept using multiple technologies amongst which Bluetooth. Its availability at Utrecht Central station offered the unique opportunity to collect data during several months.

Previous research has shown that travel time and distance are determining factors for route choice [1], also for pedestrians [6]. Type of infrastructure and congestion are important factors [1]. Various studies point at a preference for escalators over stairways, in particular for the upward direction. This is a result of a desire to minimize effort in walking [5, 11]. Similar to previous research [2, 3], we have observed pedestrians using the VI in upward direction. Fundamentally different is the configuration of available route alternatives. In existing studies, passenger had a clear choice of the VI to use, since all alternatives were simultaneously in sight after exiting the train [2, 3]. In our case however, the alternative VI is located behind the first and most obvious VI. Therefore, the route alternative is not visible from the queueing location at the primary route. In this situation, adjustments in route choice due to congestion are assumed to be less intuitive. This study contributes to the knowledge about route choice at this type of VI-configuration, which is common at train stations due to limited available platform width.

The second contribution is the data collection methodology. Data availability is a key challenge in any attempt to quantitatively describe pedestrian route choice behaviour [8]. In contrast with previous studies [1–3, 6], data are collected by automatically tracking of pedestrians using Bluetooth sensor technology. Although this technique has been used in several studies [7, 9], to our knowledge it is the first time results are published for a train station case. In doing so, we show that these data can be used for route choice research.

In the next Sect. 2 the case and data collection are described. Section 3 contains the study results, and Sect. 4 describes the model estimation. The final section concludes the paper.

2 Case Description

Utrecht Central Station is the main hub in the railway network of the Netherlands with approximately 170,000 origin and destination train passengers per day, and 60,000 transfers. Its fourteen platform tracks are used intensively by train services to and from multiple directions. All platforms are linked to the station hall either by an escalator-stairs combination, or a pair of stairs. Platform 18/19 is the only two-section platform, which is consistently used by train services that start and end at Utrecht. Route choices on this platform are observed, to allow isolation of individual trains for both VI combinations in the data. To get to the station hall from the northern section, arriving passengers generally use the escalator, which is the route first in sight. Behind the escalator an alternative route is available via the stairs. To get to the station hall from the southern section, passengers can choose from a pair of stairways. Severe congestion at the bottleneck routes occurs frequently at both platform sections shortly after train arrivals (Fig. 1).

For our analysis, the case of route choice at congested VI has been conceptualized as shown in Fig. 2. The pedestrian network – including VI – determines infrastructure capacity supply, the pedestrian flow generators (train arrivals) determine capacity demand. Queuing occurs when demand exceeds supply, and results in waiting for pedestrians upstream of the bottleneck. This has an impact on pedestrian route choice, since some passengers start to use the alternative routes, depending on destination inside or outside the station, the relative (dis)utility of the congested primary and uncongested alternative routes, including VI type. This choice is the outcome of a decision making process which itself is unknown.

To determine the impact of congestion at VI on route choice behaviour, measurements have to generate two types of data. Firstly, the degree of queuing at the platform immediately upstream of the VI and the development of congestion in time. Secondly, data about actual routes is required. By bringing together congestion and route choice, the impact of queuing (independent variable) on route choice (dependent variable) can be determined. By doing this for both escalators and stairway configurations, the effect of the VI type on route choice becomes visible. Since the VI alternatives are at different locations inside the station and route choices also can depend on the passengers' destinations, the measurement setup also has to generate destination data (control variable).

For the route choice measurements (Fig. 1), eight Bluetooth scanunits have been installed at and around platform 18/19. These sensors detect the MAC-addresses of the mobile devices of pedestrians which have Bluetooth enabled. By matching the collected MAC-addresses, moment(s) of detection and location of scanunits, the actual routes of individual pedestrians can be reconstructed. The time difference between the scans of the same MAC-address gives the route time of the individual pedestrians in the sample.The degree of congestion is determined by subtracting actual route times from the Bluetooth measurements from measured free flow times.

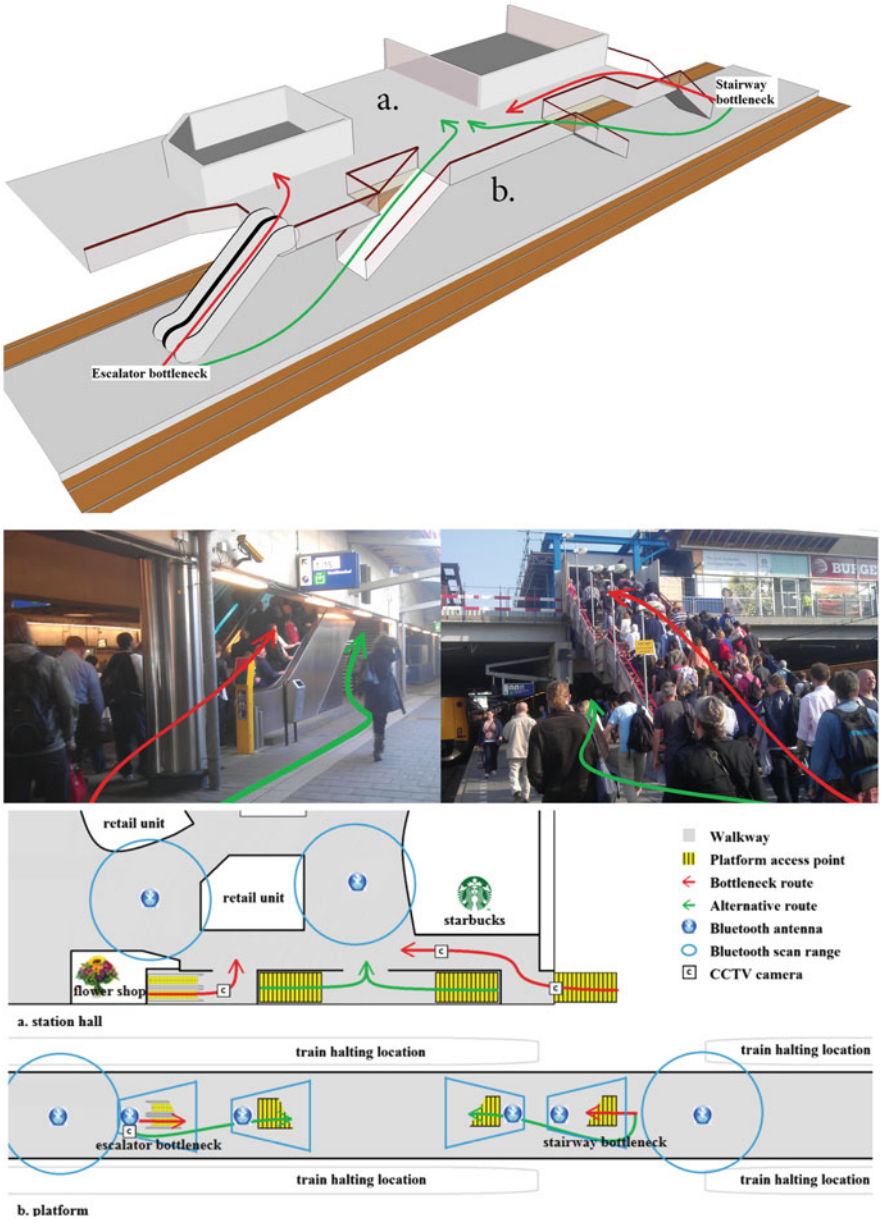

Fig. 1 Case description and sensor configuration

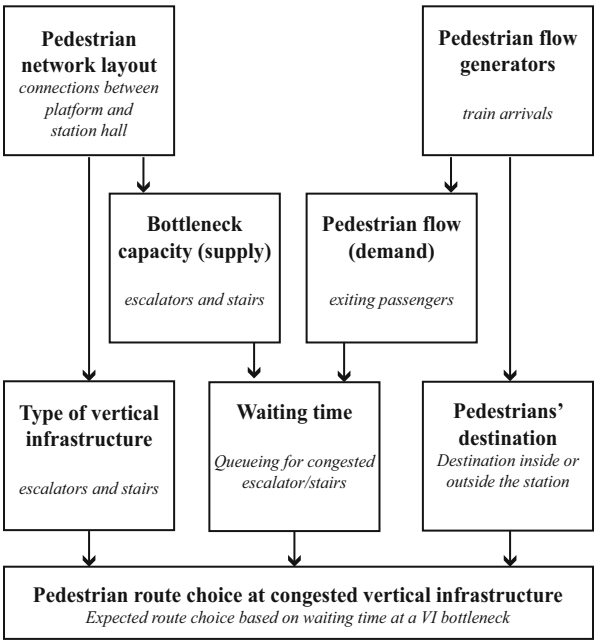

Fig. 2 Conceptualization of route choice at congested vertical infrastructure in train stations

Four specific issues arise when using Bluetooth tracking in public areas, such as train stations:

1. Similar to [7] and [9], the collected dataset contains a sample of pedestrians because a subset of the total population has a Bluetooth-enabled mobile device. For valid results and a representative sample, a minimum sample size is set, which balances the sample size of passengers per train arrival, and the sample size of train arrivals in the dataset.
2. The collected dataset contains unintended recording of pedestrian movement outside the research area, which causes noise in the dataset. To overcome this issue, each scanunit has been carefully calibrated. See [10] for a description.
3. Pedestrians may wait on their route for other reasons than congestion (i.e. waiting for others). This issue is coped with by combining the last scan of the scanunit at the bottleneck and the first scan of the scanunit downstream of the bottleneck.
4. The privacy of users of public areas is an important issue. For this research several technical measures and procedures have been implemented to guarantee the privacy of all station users at all times. See [10] for a description.

Data have been collected from the 28th of March to the 11th of May 2012. Weekend days and (public) holidays have been filtered out as they are considered as not representative due to either very high or very low congestion situations. Also, incomplete data have been excluded from analysis. The resulting dataset

contains data of the 19th of April, 1–4 May and 7 May 2012, in total 3,920 detected pedestrian movements from platform to the station hall.

3 Route Choice Behaviour at Bottlenecks

Table 1 (combined with Fig. 1) shows the use of the four alternative routes towards the exit at Starbucks for both the stairway bottleneck and the escalator bottleneck. It is clear that the preference of each route diminishes when it is located further away. This holds for both types of bottlenecks. As stated before, the distance between the bottleneck route and the first alternative is similar (for both the stairway bottleneck and the escalator bottleneck), but the choice for the bottleneck route is much larger in case of the escalator than in case of a stairway (82 % versus 66 % respectively). Although the use of the second and third alternative is limited for both bottlenecks (<7 %), the third alternative attracts most passengers in case of the stairway bottleneck, while for the escalator bottleneck the second alternative is chosen more frequently. In the latter case both alternatives are stairways and the second alternative provides simply the shortest walking distance. For the stairway bottleneck, although the second alternative has a shorter walking distance, the third alternative is an escalator. This confirms that comfort appears to be preferred over a longer walking distance.

The preference for the escalator alternative might be caused by the comfort or by the difference in congestion (waiting times) in front of the escalator or stairway respectively. From the data it has been derived that the average waiting time (during congestion) in front of the stairway equals 6.1 s, while this is 12.6 s in front of the escalator bottleneck. Observed route choices (Table 1) show that the escalator is chosen more often than the stairway alternative. This again implies a higher preference for the escalator, which is confirmed by existing research.

To assess the influence of congestion on route choice, data was required to determine whether or not congestion occurred on either the bottleneck route or the alternative route (Table 2). Therefore, time intervals in which congestion occurred have been manually observed and registered using footage from CCTV at the VI. Using this data, routes chosen while there was no congestion, have been separated from routes chosen when there was congestion. This shows that the relative usage of the alternative route is much larger when congestion occurred at the bottleneck

Table 1 Route usage

Route	Bottleneck route	1st alternative	2nd alternative	3rd alternative	Total
Stairway bottleneck	1,117 (66 %)	473 (28 %)	35 (2.1 %)	73 (4.3 %)	1,698
Escalator bottleneck	465 (82 %)	72 (13 %)	25 (4.4 %)	2 (0.4 %)	564
Total	1,582	545	60	75	2,262

Table 2 Congestion classification

	No congestion observed	Congestion observed	Total
Bottleneck route	120	471	591
Alternative route	27	214	241
Total	147	685	832
Relative usage of alternative route	18.3 %	31.2 %	

route. A chi-square test with Yates continuity correction [4] confirmed the difference to be statistically significant ($\chi^2 = 6.63$).

4 Route Choice Model Estimation

Next, a number of route choice models has been estimated, each with the different variables that could be measured by the scanunit configuration. A subset of the previous dataset has been generated by a strict application of a minimum sample size of 5 Bluetooth detections per train. At the location with largest congestion (escalator), passenger route choices have been analysed in more detail by estimating route choice models. To not only include congestion (or waiting time) but also walking distance, we have looked at the total route including the VI, and the destination in the station hall. The parameters in the choice estimation are waiting time at the escalator, route length and route time, in various combinations.

In Table 3 U_{stairs} and U_{esc} indicate the route utility via the stairs and via the escalator respectively. ASC_{stairs} is the alternative specific constant (ASC), reflecting the specific preference for the stairs route. t_{wait} represents waiting time at the escalator, averaged per train arrival. t_{route} and s_{route} represent travel time and length of the total route alternative respectively. Finally, $\beta_{time,stairs}$ and $\beta_{time,esc}$ are alternative specific parameters for the travel time, while all other refer to the estimated parameters, i.e. the value that passengers attribute to the corresponding variable.

From Table 3, it appears that only waiting time is significant. The corresponding value for β_{wait} – -0.0549 – implies that 1 s of waiting time at the escalator bottleneck reduces escalator route utility by 2.3 %, compared to the alternative route utility (stairs). At a waiting time of 44 s at the escalator bottleneck, the utilities of both routes are equal.

The value for β_{wait} is independent of other variables added to the utility functions, as done in models 2 and 3. This shows the insignificance of these variables compared to the waiting time. Moreover, model quality – expressed by $\bar{\rho}^2$ – does not increase when more variables are added. Including length or time variables of the total route results in model parameter values close to zero with very large standard errors. Only in model 4, adding an alternative specific parameter for total travel time changes the values for the alternative specific constant and the total travel time. However, the model quality decreases and both $\beta_{time,stairs}$ and $\beta_{time,esc}$ have a (non-significant)

Table 3 Model estimation results (* = statistically significant)

	Utility functions	Model reliability	Parameters	Parameter estimate	Robust standard error	Robust t-test value
1	$U_{stairs} = ASC_{stairs}$ $U_{esc} = \beta_{wait} * t_{wait}$	$\bar{\rho}^2 = 0.389$	ASC_{stairs}	−2.43*	0.262	−9.30
			β_{wait}	−0.0549*	0.0142	−3.88
2	$U_{stairs} = ASC_{stairs} + \beta_{distance} * s_{route}$ $U_{esc} = \beta_{wait} * t_{wait} + \beta_{distance} * s_{route}$	$\bar{\rho}^2 = 0.384$	ASC_{stairs}	−2.43*	0.262	−9.30
			β_{wait}	−0.0549*	0.0142	−3.88
			$\beta_{distance}$	3.12e−14	18.4	0.00
3	$U_{stairs} = ASC_{stairs} + \beta_{time} * t_{route}$ $U_{esc} = \beta_{wait} * t_{wait} + \beta_{time} * t_{route}$	$\bar{\rho}^2 = 0.384$	ASC_{stairs}	−2.43*	0.262	−9.30
			β_{wait}	−0.0549*	0.0142	−3.88
			β_{time}	1.13e−13	8.86	0.00
4	$U_{stairs} = ASC_{stairs} + \beta_{time,stairs} * t_{route}$ $U_{esc} = \beta_{wait} * t_{wait} + \beta_{time,esc} * t_{route}$	$\bar{\rho}^2 = 0.384$	ASC_{stairs}	−2.35*	0.784	−3.00
			β_{wait}	−0.0566*	0.0217	−2.61
			$\beta_{time,esc}$	0.000938	1.80e308	0.00
			$\beta_{time,stairs}$	−0.000938	1.80e308	−0.00

value close to 0. Overall, this leads to the conclusion that these attributes do not seem to have an effect on route choice behaviour. This could be due to the small difference in route length. For more complex networks, it is expected that route times will have a significant effect [3]. Following the model with the best estimation results, i.e. the route choice model with waiting time, the probability of choosing the escalator route P_{esc} is described by $\frac{1}{1+e^{U_{stairs}-U_{esc}}} = \frac{1}{1+e^{-2.43+0.0549t_{wait}}}$

Conclusions

Previous research has shown that the type of VI and congestion are important determining factors for pedestrian route choice. In this study the impact of these factors has been quantified for a train station case. Data has been used from a grid of Bluetooth scanunits around platform 18/19 at Utrecht Central Station in The Netherlands. Our case consisted of an escalator-stairways pair and a pair of stairways which both were situated behind each other at the platform where passengers exit their train. We have found a Bluetooth ratio of approximately 7–11 %, which is consistent with other studies.

The case of Utrecht Central Station has confirmed a higher preference for escalators against stairways, which has been found in other research. Moreover, passengers tend to adjust their route when congestion occurs at the primary route, which was the first route in sight. Although in our study the alternative routes were not visible from the queueing location at the primary congested route, a significant number of passengers still chose for other, uncongested routes.

We have estimated several route choice models using four route attributes: waiting time due to congestion, VI type, route length and route time. In the model estimates, only waiting time at the congested bottleneck was found to be statistically significant. Our model shows that approximately 15 % of the pedestrians is expected to chose an alternative route when the waiting time at the bottleneck is 15 s. A waiting time of 45 s results in 50 % of the pedestrians to be expected to chose an alternative route. In the situation without congestion, over 90 % is expected to chose the primary route. These insights are valuable for optimizing VI settings (operations) and configuration (design) at train stations.

Further research is required, because of two major limitations of this study. Firstly, the impact of walking distance of each alternative route (from platform to station exit) on route choice due to congestion at VI. Our study area was relatively small due to limited availability of scanunits. Therefore, the impact of the destination of passengers could not be tested. Secondly, although we have found no indications, the use of Bluetooth for measuring pedestrian routes could result in a sampling bias due to selection, since data of only a subset of pedestrian routes has been collected. The subset composition is unknown due to privacy limitations.

References

1. P.H.L. Bovy, E. Stern, *Route Choice. Wayfinding in Transport Networks*. Number 9 in Studies in Operational Regional Science (Kluwer Academic, Dordrecht/Boston/London, 1990)
2. C.Y. Cheung, W.H.K. Lam, Pedestrian route choices between escalator and stairway in MTR stations. J. Transp. Eng. **124**(3), 277–285 (1998)
3. W. Daamen, P.H.L. Bovy, S.P. Hoogendoorn, A. van de Reijt, Passenger route choice concerning level changes in railway stations, in *Transportation Research Board-84th Annual Meeting*, Washington, D.C. (Transportation Research Board, 2005)
4. A. Field, *Discovering Statistics with SPSS* (Sage, London/Thousand Oaks/New Delhi, 2005)
5. J.J. Fruin, *Pedestrian Planning and Design* (Elevator World, Mobile, 1987)
6. M.R. Hill, Spatial structure and decision-making aspects of pedestrian route selection through an urban environment, Ph.D. thesis, The University of Nebraska – Lincoln, 1982
7. E. ONeill, V. Kostakos, T. Kindberg, A. Penn, D.S. Fraser, T. Jones, *Instrumenting the City: Developing Methods for Observing and Understanding the Digital Cityscape* (Springer, Berlin/Heidelberg, 2006)
8. H.J.P. Timmermans, *Pedestrian Behavior: Models, Data Collection and Applications* (Emerald Group, Bingley, 2009)
9. M. Versichele, T. Neutens, M. Delafontaine, N. Van de Weghe, The use of bluetooth for analysing spatiotemporal dynamics of human movement at mass events: a case study of the ghent festivities. Appl. Geogr. **32**(2), 208–220 (2012)
10. A. Voskamp, Measuring the influence of congested bottlenecks on route choice behavior of pedestrians at utrecht centraal, Master's thesis, Delft University of Technology, 2012
11. U. Weidmann, *Transporttechnik der Fußgänger*. Institut für Verkehrsplanung, Transporttechnik, Strassen-und Eisenbahnbau (IVT, Zürich , 1993)

Empirical Investigation on Pedestrian Crowd Dynamics and Grouping

Andrea Gorrini, Stefania Bandini, and Giuseppe Vizzari

Abstract The definition and implementation of pedestrian simulation models requires empirical evidences, acquired by means of experiments and on-field observations, for sake of model calibration and validation. This paper describes an observation carried out in a urban commercial-touristic walkway (Vittorio Emanuele II Gallery, Milan, in collaboration with the Municipality of Milano). Although the analysis considered traditional metrics for describing pedestrian flow, such as the level of service, the main aim of this work was to quantify and characterize the presence, impact and behavior of groups in the observed population. In particular, we had confirmatory results on the frequency of groups in the observed situation, but we also achieved innovative results on trajectories and walking speeds: the walking path of individuals was 4 % longer than the average path of groups, but the average walking speed of group members was 37 % lower than the one of single pedestrians. Finally, a metric for characterizing group dispersion was defined and applied to the observed scenario: relatively large groups (size three and four) occupy more space in their movement when compared to couples. The achieved results represent useful empirical data for the calibration and validation of models for the simulation of pedestrians and crowd dynamics, but also for the development of automated techniques for data collection and analysis employing computer vision techniques.

1 Introduction

The modeling and simulation of pedestrian crowd dynamics is an innovative and complex field of study that requires interdisciplinary efforts (e.g., computer

A. Gorrini
Information Society Ph.D. Program, Department of Sociology and Social Research, University of Milano-Bicocca, Via Bicocca degli Arcimboldi 8, 20126 Milano, Italy
e-mail: a.gorrini@campus.unimib.it

S. Bandini • G. Vizzari (✉)
Department of Informatics, Systems and Communications, Complex Systems and Artificial Intelligence Research Center, University of Milano-Bicocca, Viale Sarca 336, 20126 Milano, Italy
e-mail: bandini@disco.unimib.it; vizzari@disco.unimib.it

M. Chraibi et al. (eds.), *Traffic and Granular Flow '13*,
DOI 10.1007/978-3-319-10629-8_10

science, traffic engineering, applied mathematics, social science, urban planning). Computer-based simulations allow to properly assess, plan and design mass gathering and transit spaces (e.g., large stadium, railway station), offering optimized architectural solutions to ensure the spatial efficiency of potentially crowded facilities in terms of services, comfort and safety.

In order to finalize pedestrian crowd simulations into decisions and operational steps it is necessary to validate computational models facing empirical evidences about human locomotion behavior, on both individual and aggregate level of investigations. Data collection activities imply two main methods of analysis: acquisition by means of on-field observations and controlled experimental investigations in laboratory setting. This is aimed at defining descriptive sets of metrics and parameters for characterizing the phenomenon and support the validation of computational models, both in terms of expressiveness and efficiency [1].

The early interest in studying crowd dynamics started in the late nineteenth century, thanks to the pioneering work of the French psychologist Gustave Le Bon [11]. Since then, the definition of the phenomenon is still controversial, due to the lack of standard guidances for data collection, ethical-practical restrictions (e.g. safety of individuals involved, costs of experiments) and the variability among size and typology of the phenomenon. In this respect, this work is based on the unobtrusive observation of pedestrian circulation dynamics in a urban crowded scenario. We proposed to analytically investigate the phenomenon focusing on the general framework of proxemics (i.e. human spatial behavior) [9], thanks to its ability to model the social relationships among people and groups as they interact in the environment. In this schema, we focused on:

- *Proxemics*: a type of nonverbal communication that conveys information about the nature of participants' relationship by means of the dynamic regulation of interpersonal distances [9]. In motion situations, proxemics is essentially based on the needs to avoid collision with oncoming pedestrians and to maintain spatial cohesion among group members;
- *Grouping*: defined as two or more people who interact to achieve a shared goal [15], groups are the basic interacting elements that compose a crowd (e.g., relatives, friends). Depending on the level of density in the environment, the proxemic behavior of walking groups spontaneously produces typical spatial layouts[1]: line abreast, V-like, river-like pattern [3, 13];
- *Density*: the level of density in the environment significantly impact pedestrian circulation dynamics. Due to the lower degree of freedom for spatial positioning, critical situations of high density are characterized indeed by competitive

[1] According to [3, 13], in situations of low density groups walk side by side forming a line abreast pattern. As the density increases, groups walk with a V-like pattern with the middle individual positioned slightly behind in comparison to the lateral individuals. In situations of high density, the group spatial distribution leads to a river-like pattern. Groups with more than three individuals split themselves into singles, dyads and triads, or to form other shapes, like rhombus, spherical and ellipsoidal.

interactions among pedestrians, continuous and sudden detouring maneuvers [7] and crowding [2].

In the context of early observations [5, 14, 17] and experiments [4, 8], the proposed methodological approach can be synthetically represented as a "virtuous cycle" composed of different practices for data collection: in vivo observation of pedestrian circulation dynamics in urban crowded scenarios, in vitro experimental investigation of human locomotion-spatial behavior in laboratory setting. This is aimed at validating pedestrian crowd simulations, by checking if the computational models are able to generate outcomes that are similar to the ones produced by the target. Then, in silico simulations can be used as virtual settings, considering the possibility to investigate those situations that are difficult to be directly observed (i.e. *what-if scenarios*).

In this respect, the results achieved by means of the presented case study are currently applied towards the improvement and validation of MAKKSim [16], an agent-based [6] pedestrian crowd simulation platform developed by the Complex Systems and Artificial Intelligence research center. This is aimed at improving the definition of the behavioral specifications of each agent, in relation to their interpretation of the other elements in the system (e.g., agents, groups, objects, obstacles).

This work is organized as follow: the urban scenario chosen for the observation of pedestrian circulation dynamics is described in Sect. 2. The results achieved are presented in Sect. 3, with reference to: (i) level of density and service, (ii) pedestrian flow composition in terms of groups and their proxemic spatial layouts, (iii) trajectories and walking speed of both singles and groups, (iv) spatial dispersion among group members while walking. The paper ends with final remarks about the impact of proxemics, grouping and density on pedestrian crowd dynamics, and the application of results to the validation of the computational model of MAKKSim (Sect. 4).

2 Scenario Analysis

The Vittorio Emanuele II gallery is a popular commercial-touristic walkway situated in the Milan city center (Italy). It represents an optimal scenario for the observation of pedestrian crowd dynamics thanks to the large amount of people that pass through the gallery during the weekend for shopping, entertainment and visiting touristic-historical attractions (see Fig. 1). The observation was performed on the 24th of November 2012 (on Saturday afternoon, from 2:50 to 4:08 pm).

The equipment for video footages was positioned on a balcony that surrounds the inside volume of the gallery from about 10 m in height. This allowed to limit video images distortion and trajectories occlusion, and to not influence subjects' behavior (i.e. *Hawthorne effect*).

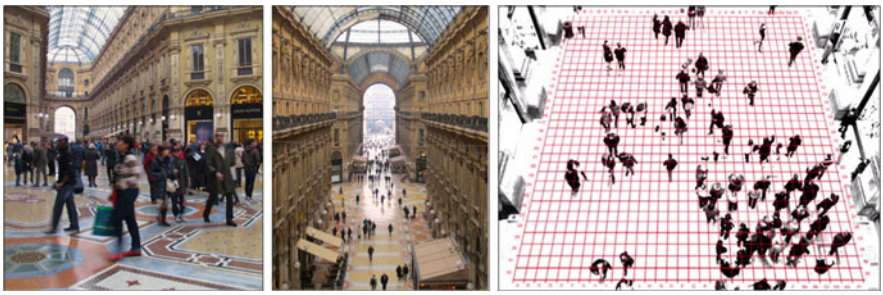

Fig. 1 As illustrated from the left to the right side: an overview of the pedestrian circulation dynamics at the Vittorio Emanuele II gallery (Milan, Italy), the aerial of the walkway, the superimposed alphanumeric grid used for data analysis

A squared portion of the walkway was considered for data analysis (12.8 m wide, 12.8 m long). The inner space of the selected area were discretized in cells by superimposing a grid on the video images (see Fig. 1). In particular, the grid was designed by using *Adobe Photoshop CS5* as composed of No. 1024 squared cells (0.4 m wide, 0.4 m long). Then, it was transformed according to the perspective of the video images and set up with an alphanumeric code on the sides. Eventually, the grid with a transparent background was superimposed to a black-white version of the video images. Data analysis was manually performed by using *VLC media player*, thanks to the possibility to playback the video frame by frame.

3 Results

3.1 Level of Density and Service

According to the Highway Capacity Manual [12], the level of density in the observed scenario was estimated by counting the number of people (No. 7773) walking through a certain unit of space (12.8 m) in a certain unit of time (from 2:50 pm to 4:08 pm). The average flow rate (7.78 pedestrian/min/m) belonged to a level of service (LOS) B [7], that is associated to irregular flows in low-medium density conditions. The observed cyclical presence of high and low peak levels is related to public transport services (i.e. subway station) from which periodic arrivals of pedestrians were detectable (see Fig. 2).

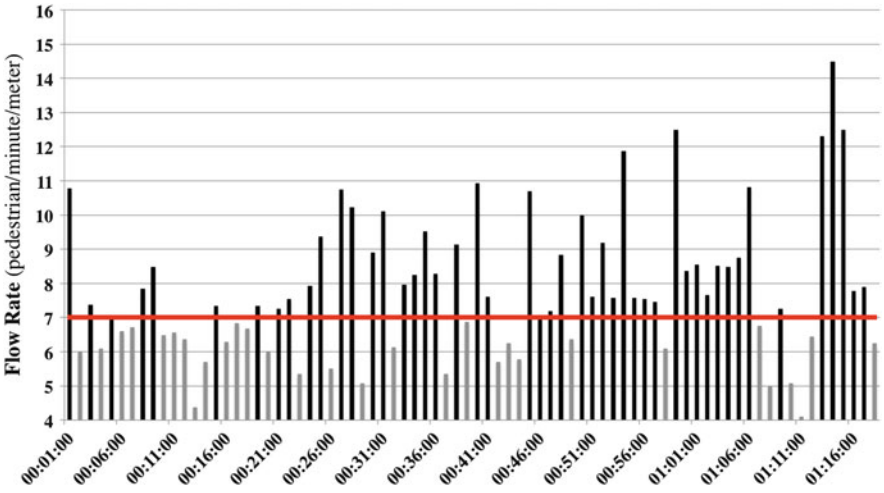

Fig. 2 The time distribution of the flow rate observed at the Vittorio Emanuele II gallery: LOS A (*grey colored*) and LOS B (*black colored*). The minute 00:01:00 reported in the X-axis refers to the starting time of the survey

3.2 Flow Composition and Group Spatial Arrangement

According to [3], the identification of groups in the stream of passersby was assessed on the basis of verbal and nonverbal communication among members (e.g., visual contact, body orientation, gesticulation, spatial cohesion). To more thoroughly evaluate all these indicators the coder was asked to rewind the video and take the necessary time to tell situations of simple local similar movements by different pedestrians from actual group situations.

A subset of 15 min was extracted sampling the video 1 min every 5: No. 1645 pedestrians were manually counted. Results showed that 16 % of the observed pedestrians walked alone, while 84 % walked in groups, as composed of 44 % of couples, 17 % triples and 23 % four members groups. The observed large structured groups, such as touristic committees, were analyzed considering sub-groups.

Results about group proxemics spatial arrangement showed that: 94 % of couples walked with a line abreast pattern, while 6 % walked with a river-like pattern; 31 % of triples were characterized by line abreast pattern, 10 % by river-like pattern and 59 % by V-like pattern. Ten percent of groups of four members were characterized by line-abreast pattern, 4 % by river-like pattern, 10 % by V-like pattern, 10 % triads followed by a single person, 6 % single individual followed by a triad, 8 % rhombus-like pattern, 32 % of the groups split into two dyads.

3.3 Walking Path and Speed

A sample of No. 122 people (30 singles, 15 couples, 10 triples and 8 groups of four members) was considered in relation to the minutes characterized by LOS B. Data analysis consisted of measuring the trajectories of each pedestrian and the needed time to pass through the monitored portion of gallery delimited by the grid[2] (pedestrians who stopped or slowed to take pictures or shopping were not taken into account).

Two tailed t-test analyses were used to identify differences among the average walking path of singles (13.96 m, sd 1.11), couples (13.39 m, sd 0.38), triples (13.34 m, sd 0.27) and groups of four members (13.16 m, sd 0.46) (as illustrated in Fig. 3). Results showed a significant difference (p value < 0.05) between the walking path of singles and couples, singles and triples, singles and groups of four members. In conclusion, results showed that the path of singles was 4 % longer than the path of group members (see Fig. 3).

About walking speed, two tailed t-test analyses were used to identify differences among singles (1.22 m/s, sd 1.16), couples (0.92 m/s, sd 0.18), triples (0.73 m/s, sd 0.10) and groups of four members (0.65 m/s, sd 0.04). Results (see Fig. 4) showed a significant difference (p value < 0.01) in walking speed between singles and couples, singles and triples, singles and groups of four members, couples and triples and triples and groups of four members (p value < 0.05). In conclusion, results showed that group members walked 37 % slower in average than the single pedestrians.

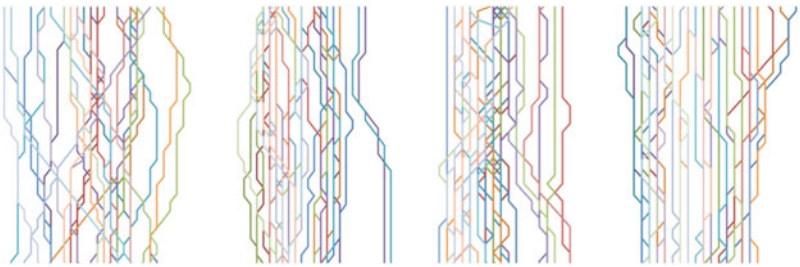

Fig. 3 As illustrated from the left to the right side, the observed trajectories of singles, couples, triples and groups of four members

[2]We considered the cell occupied by the feet of each pedestrian as its own actual position. Every straight step was measured as the segment between the center of two cells (0.4 m long path). Any oblique step cell by cell was measured as the diagonal between the two cells (0.56 m long path). The starting and final steps (i.e. entering and exiting the grid) were measured from the half of the cell (0.2 m long path).

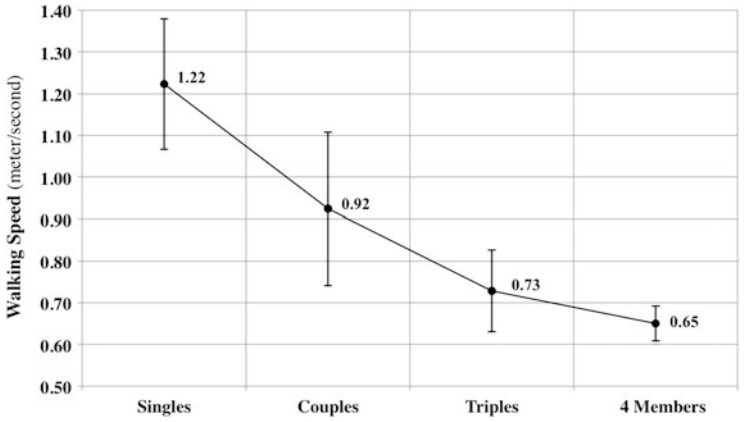

Fig. 4 The average walking speed (m/s) of single pedestrians, couples, triples and groups of four members (with standard deviation)

3.4 Group Proxemic Dispersion

The spatial dispersion of walking groups was estimated as the mean of the distances between each member and the geometrical centre of the group (i.e. *centroid*). The trajectories of the sampled pedestrians were further analyzed, considering the positions of each member within the alphanumeric grid every 40 frames (starting from the co-presence of the all members in the monitored area of the walkway delimited by the grid).

Two tailed t-test analyses were used to identify differences in spatial dispersion among couples (0.35 m, sd 0.14), triples (0.53 m, sd 0.17) and groups of four members (0.67 m, sd 0.12). Results showed a significant difference in spatial dispersion between couples and triples (p value < 0.05), couples and groups of four members (p value < 0.01). In conclusion, results showed that couples walked 41 % less disperse than triples and groups of four members.

4 Final Remarks

This paper presented the data acquired by means of the unobtrusive observation of pedestrian circulation dynamics in a urban crowded scenarios (Vittorio Emanuele II gallery, Milan, Italy).

Results demonstrated that it is crucial to consider the impact of grouping on pedestrian crowd dynamics, considering the massive presence of groups within the observed pedestrian flows (84 %). Single pedestrians walked faster than groups, often adjusting their path (generally longer than the one of group members) in order to maintain their velocity. The number of members of a group has a negative

impact on both speed and spatial cohesion, due to the higher probability of groups to disperse in case of oncoming pedestrians and the need to regroup in order to preserve the possibility to communicate.

The achieved results represent an useful contribution for the understanding of pedestrian crowd dynamics, once again in situations characterized by low-medium density. Further empirical investigations would be necessary to actually compare results in situation of high density, considering also the opportunity to employ more sophisticated and at least partly automated technologies for data analysis [10].

In conclusion, according to the proposed methodological approach, the achieved results represent an extremely interesting and significant body of empirical evidences finally aimed at supporting the improvement of the pedestrian crowd simulation platform MAKKSim. At this stage, results are currently been applied to calibrate and validate the capability of the agents to behave according to specific proxemic rules based on the needs to maintain group cohesion among members and to preserve a certain distance from other pedestrians, which belong to a different group.

Acknowledgements The survey was carried out thanks to the authorization of the Milano's Municipality and complying the Italian legislation about the privacy of the people recorded within the pedestrian flows without their consent.

References

1. S. Bandini, A. Gorrini, G. Vizzari, Towards an integrated approach to crowd analysis and crowd synthesis: a case study and first results. Pattern Recognit. Lett. (2013). http://dx.doi.org/10.1016/j.patrec.2013.10.003
2. A. Baum, P. Paulus, Crowding, in *Handbook of Environmental Psychology*, vol. 1, ed. by D. Stokols, I. Altman (Wiley, New York, 1987), pp. 533–570
3. M. Costa, Interpersonal distances in group walking. J. Nonverbal Behav. **34**(1), 15–26 (2010)
4. W. Daamen, S. Hoogendoorn, Controlled experiments to derive walking behaviour. Eur. J. Transp. Infrastruct. Res. **3**(1), 39–59 (2003)
5. M.L. Federici, A. Gorrini, L. Manenti, G. Vizzari, Data collection for modeling and simulation: case study at the university of milan-bicocca, in *Cellular Automata* (Springer, New York, 2012), pp. 699–708
6. J. Ferber, *Multi-Agent Systems: An Introduction to Distributed Artificial Intelligence*, vol. 1 (Addison-Wesley, Harlow, 1999)
7. J.J. Fruin, *Pedestrian Planning and Design* (Metropolitan Association of Urban Designers and Environmental Planners, New York, 1971)
8. A. Gorrini, S. Bandini, M. Sarvi, C. Dias, N. Shiwakoti, An empirical study of crowd and pedestrian dynamics: the impact of different angle paths and grouping, in *Transportation Research Board, 92nd Annual Meeting*, Washington, D.C., 2013, p. 42
9. E. Hall, *The Hidden Dimension* (Doubleday, Garden City, 1966)
10. J.C.S. Jacques Junior, S.R. Musse, C.R. Jung, Crowd analysis using computer vision techniques. IEEE Signal Process. Mag. **27**(5), 66–77 (2010)
11. G. Le Bon, *The Crowd: A Study of the Popular Mind* (Macmillan, London, 1897)
12. J.S. Milazzo II, N.M. Rouphail, J.E. Hummer, D.P. Allen, Quality of service for interrupted-flow pedestrian facilities in highway capacity manual 2000. Transp. Res. Rec.: J. Transp. Res. Board **1678**(1), 25–31 (1999)

13. M. Moussaïd, N. Perozo, S. Garnier, D. Helbing, G. Theraulaz, The walking behaviour of pedestrian social groups and its impact on crowd dynamics. PloS one **5**(4), e10047 (2010)
14. M. Schultz, C. Schulz, H. Fricke, Passenger dynamics at airport terminal environment, in *Pedestrian and Evacuation Dynamics 2008*, ed. by W.W.F. Klingsch, C. Rogsch, A. Schadschneider, M. Schreckenberg (Springer, Berlin/Heidelberg, 2010), pp. 381–396
15. J. Turner, Towards a cognitive redefinition of the social group. Curr. Psychol. Cogn. **1**, 93–118 (1981)
16. G. Vizzari, L. Manenti, L. Crociani, Adaptive pedestrian behaviour for the preservation of group cohesion. Complex Adapt. Syst. Model. **1**(7), 1–19 (2013)
17. A. Willis, N. Gjersoe, C. Havard, J. Kerridge, R. Kukla, Human movement behaviour in urban spaces: implications for the design and modelling of effective pedestrian environments. Environ. Plan. B Plan. Des. **31**(6), 805–828 (2004)

Experimental Analysis of Two-Dimensional Pedestrian Flow in Front of the Bottleneck

Marek Bukáček, Pavel Hrabák, and Milan Krbálek

Abstract This contribution presents an experimental study of two-dimensional pedestrian flow with the aim to capture the pedestrian behaviour within the cluster formed in front of the bottleneck. Two experiments of passing through a room with one entrance and one exit were arranged according to phase transition study in Ezaki and Yanagisawa (Metastability in pedestrian evacuation. In: Cellular automata, ed. by G. Sirakoulis, S. Bandini. LNCS, vol 7495. Springer, Berlin/Heidelberg, pp 776–784, 2012), the inflow rate was regulated to obtain different walking modes. By means of automatic image processing, pedestrians' paths are extracted from camera recordings to get actual velocity and local density. Macroscopic information is extracted by means of a virtual detector and leaving times of pedestrians. The pedestrian's behaviour is evaluated by means of density and velocity. Different approaches of measurement are compared using several fundamental diagrams. Two phases of crowd behaviour have been recognized and the phase transition is described.

1 Introduction

One of the main impacts of pedestrian behavior's study is the ability to optimize the infrastructure. Using some intervention, the capacity of a given zone (building, public area, transportation hub, etc.) can be increased, i.e. more people can pass this zone with higher velocity and lower number of conflicts [8, 12].

Many studies deal with certain aspects of pedestrian motion [2, 10, 14, 15, 17, 19]. Specific simulation tools are often supported by experimental data analyses [5, 6, 9, 18].

This article focuses on the description of the system as a whole. In particular we focus on the transition from the free to the congestion phase. This study is compared with the actual states of individual pedestrians in the system as explained below.

M. Bukáček (✉) • P. Hrabák • M. Krbálek
Faculty of Nuclear Sciences and Physical Engineering, Czech Technical University in Prague, Prague, Czech Republic
e-mail: bukacma2@fjfi.cvut.cz; pavel.hrabak@fjfi.cvut.cz; milan.krbalek@fjfi.cvut.cz

M. Chraibi et al. (eds.), *Traffic and Granular Flow '13*,
DOI 10.1007/978-3-319-10629-8_11

The density in the simplest form represents the number of pedestrians in fixed area (referred to as ρ_A) [13]. As mentioned in [16], this quantity can be understood locally as well. More precisely, the density ρ_α in the neighborhood of pedestrian α corresponds to inverse value of his space consumption, i.e., the area of his Voronoi cell.

The flow is defined as the number of persons, who crossed a given intersection during one time unit. The flow through a given area (e.g. detector area) can be evaluated from the number of pedestrians N_t^+, who entered into the monitored area A during $\langle t, t + \Delta t \rangle$, i.e., $J_A(t) = \frac{N_t^+}{\Delta t}$. The specific flow is related to uniform corridor width, therefore $J_A^s(t) = \frac{J_A(t)}{d}$, where d represents the width a of given corridor.

Using hydrodynamic approach, the density, velocity, and flow can be related by formula

$$J(\rho) = \rho v(\rho). \tag{1}$$

Both, the relations $v = v(\rho)$ or $J = J(\rho)$, are referred to as fundamental diagrams (FD) [12] and are used to illustrate the essential behaviour of the system.

In this article, we distinguish two variants of FD:

- Area FD – The system is observed through a defined area to extract the dependence $J_A(t) = J_A(t, \rho_A)$. Data cumulation over a long interval T allows to observe pedestrian behavior under different conditions, e.q., the density limits, which characterize the phase transition.
- Individual FD – For each pedestrian α the dependence $v_\alpha(t) = v_\alpha(t, \rho_\alpha)$ is evaluated. By observing pedestrians under different conditions, one can identify the conditions preceding the decrease of velocity.

Considering a room with one entrance and one exit, the following observations can be made. With low inflow, pedestrians can exit freely and move with maximal velocity. By increasing the inflow rate, the number of pedestrians in the room increases. Therefore, a cluster is created in front of the exit, which means that a pedestrian is forced to slow down and integrate into the cluster before leaving the room.

The motion of a chosen pedestrian α can be classified according to his/her velocity and local density into three states:

- Free state – the pedestrian does not react to other pedestrians and moves with his desired velocity v_α^0. This state is characterize by low density ρ_α and high velocity v_α.
- Synchronized state – the pedestrian motion is highly synchronized with pedestrians in his surrounding due to high density. This state is characterize by high density ρ_α and low velocity v_α.
- Transition state – The transition between free and synchronized state is characterized by low density ρ_α and low velocity v_α due to the anticipation or long reaction time, respectively.

Analogously, the phase of the entire system can be classified:

- Free phase – no cluster is formed in front of the exit, therefore the majority of pedestrians in the system is in free state.
- Congested phase – a stable cluster in front of the exit is formed, which leads to permanent significant ratio of pedestrians in the synchronized state.
- Metastable phase – unstable clusters arise and disappear, the ratio of pedestrians in the synchronized state changes in time from low to significant.

2 Experiment

To detect the above mentioned phases and to analyze transitions among them, a simple experiment has been designed – a group of pedestrians passed through the room with one entrance and one exit, see Fig. 1. The data samples were obtained by automatic processing of video recordings from two experiments, which differed by the size of the room.

To realize a passing-through arrangement, an experimental room was built inside the study hall of FNSPE, see the plan in Fig. 1. The walls 2 m high were made of wooden construction covered by paper. Two snapshots in Fig. 2 visualize the design and progress of the experiment.

Two cameras were used to monitor the experiment. The main camera, which covered the whole room, was fixed on the ceiling 4.5 m above the floor. The rear camera monitoring the egress of pedestrians was placed next to the exit, 2.5 m above the floor.

To control the inflow into the room, which is the crucial parameter determining the phase of the system, simple signaling device has been used. On green signal, a group of pedestrian were forced to enter the room. This green signal was altered by randomly long intervals of red light, the intervals τ were generated from trimmed normal distribution: $\mathrm{VAR}(\tau) = 1\,\mathrm{s}^2$, $\mathrm{E}(\tau) \in [1.2,\ 1.8]\,\mathrm{s}$.

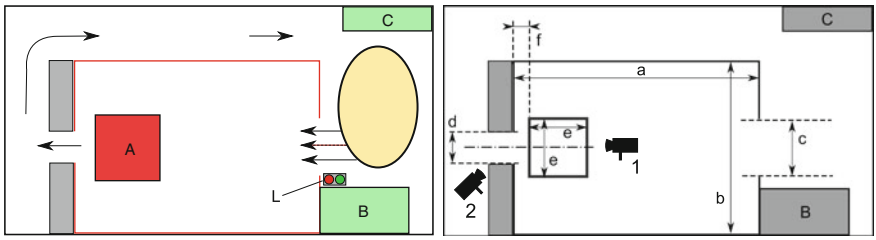

Fig. 1 *Left*: the schematic view of the experiments (area *A* represents virtual detector, *B* technical background, *C* coffee corner, *L* refers to traffic lights). *Right*: Room geometry and position of the cameras. Exp. 1: $a = 10\,\mathrm{m}$, $b = 6\,\mathrm{m}$, Exp. 2: $a = 6\,\mathrm{m}$, $b = 3.5\,\mathrm{m}$. Both: $c = 2\,\mathrm{m}$, $d = 0.6\,\mathrm{m}$, $e = 2\,\mathrm{m}$, $f = 0.5\,\mathrm{m}$

Fig. 2 Illustrating shots from the experiments

Since the pedestrians were not able to enter the room in headway shorter than 0.5 s, the inflow was controlled by the number of entering pedestrians as well. As can be seen from Table 1, this method enables the control of inflow parameter, which appears to be crucial parameter determining the free of the congestion phase, as observed by means of model simulations in [3, 4, 9].

Nine rounds with different settings were performed in the first experiment, 11 in the second one. Each of them lasted from 2 to 10 min. The conditions on the input has been changed after each round, the inflow slowly raised from low values (free flow) until the state with strong congestion (for details, see Table 1).

3 Data Processing

Pedestrians were marked by red paper hats with white rim, unlike [11]. The principle of contrast color [7] was used to detect pedestrians on each frame and their positions were recorded. Due to the width of the recorded area, the fish eye deformation influenced the data. This deformation was partially suppressed by sinus transformation (see [1] for more details).

Coordinates were assigned to one path of a given pedestrian (ref. α) with respect to the distance to coordinates on the previous frame. Therefore the trajectory of a pedestrian was reconstructed: $x_\alpha(t) = [x_\alpha^{(1)}, x_\alpha^{(2)}](t)$, where the time is understand to be discrete: $t \in \{t_0 + n\Delta t\}$, $\Delta t = 1/59$ s.

As mentioned in the introduction, the local density was derived from each frame and the local velocity was extracted from paths using central differences

$$v_\alpha^x(t) = \frac{x_\alpha(t + k\Delta t) - x_\alpha(t - k\Delta t)}{2k\Delta t}, \tag{2}$$

where $k = 5$ was used to reach sufficient smooth trajectories. Thus, the trajectory data were obtained in the form $(x_\alpha, \rho_\alpha, v_\alpha)(t)$.

Table 1 The table describes each rounds of the experiment, following qualities are evaluated: duration of a round, number of pedestrians at input and mean input period evaluated from time series generated by traffic lights. The value "MIN" referred to the round without lights, participants were asked to enter as fast as possible. The inflow is evaluated from the period and number at input

Round	Duration (min:s)	Input	Period (s)	Inflow (ped/s) (s)	Observation
1	10:50	2	1.78	1.12	Free flow, occasional delay at the exit
2	10:04	2	1.68	1.19	Free flow, occasional delay at the exit
3	8:29	2	1.59	1.26	Free flow, occasional delay at the exit
4	6:36	2	1.43	1.40	Metastable state
5	7:16	3	1.85	1.62	Cluster formation with constant size
6	6:05	3	1.69	1.78	Congestion
7	5:24	3	1.72	1.74	Congestion
8	2:55	3	1.66	1.81	Congestion
9	2:05	3	1.57	1.91	Congestion
1	6:40	2	1.60	1.25	Flow, occasional delay at the exit
2	7:47	2	1.61	1.24	Free flow, occasional delay at the exit
3	5:06	2	1.50	1.33	Free flow, occasional delay at the exit
4	4:15	2	1.37	1.46	Metastable state
5	1:52	2	MIN	± 2	Congestion
6	1:31	2	MIN	± 2	Congestion
7	8:07	3	1.76	1.70	Cluster formation with constant size
8	4:31	3	1.70	1.76	Metastable state
9	2:34	3	1.56	1.92	Cluster formation with constant size
10	3:23	3	1.55	1.94	Cluster formation with constant size
11	3:13	3	MIN	± 3	Congestion

The macroscopic approach was implemented by monitoring the "detector" area A, a virtual square 2×2 m placed in front of the exit, see Fig. 1. In this area, the density ρ_A and flow J_A were evaluated. The mean value of velocity in this area (referred to as v_A) was calculated by means of the weighted average of pedestrians' velocity inside the area. The weight of a pedestrian depends on the overlapping area of the detector and his voronoi cell. These detector-area-data are of the form $(\rho_A, J_A, v_A)(t)$.

The crossectional data $J_{out}(t)$ were processed semi-automatically from the rear camera. The leaving times were determined, the outflow can be calculated using leaving times t_α headways

$$J_{out}(t) = \frac{n_T(t)}{T}, \qquad n_T(t) = \#\left\{t_\alpha \in \left\langle t - \frac{T}{2}, t + \frac{T}{2}\right)\right\}, \tag{3}$$

where # denotes the number of set elements.

4 Results

Measured quantities can be visualized by many ways. As the first report, we show the microscopic approach. Basic review of the velocity and density is provided by their histograms – Fig. 3. As visible, two local maxima of velovity appear: the high peak at value 0.5 m/s corresponds to the synchronized state, while the wide peak at value 1.8 m/s corresponds to free motion.

Individual modes of motion are clearly described by the three-dimensional fundamental diagram (Fig. 4), regardless to their frequency of occurrence. This frequency is displayed on the z coordinate.

As mentioned above, two main states were observed. Free flow occurs until the density reaches 0.3 ped/m^2. In this mode, the participants walked within a velocity range 1.5–2.5 m/s. Conversely, when density exceeded 0.5 ped/m^2, the congested state appeared. In this state, the velocity fluctuates between 0 and 0.7 m/s. The highest observed density was 3 ped/m^2. The metastable state appeared when the density occurred in the interval 0.3–0.5 ped/m^2.

These critical values of density are significantly lower than in [19]. Such a different behavior is probably caused by two dimensional nature of the investigated movement. Pedestrians slow down due to the anticipation of side conflicts.

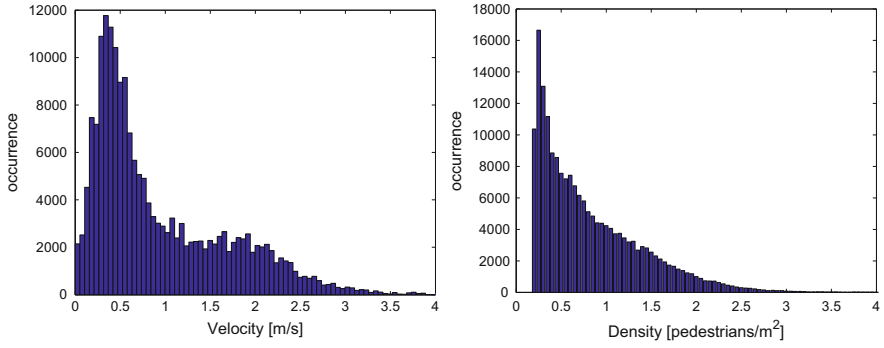

Fig. 3 Histograms of velocity and density generated from pedestrians' path data

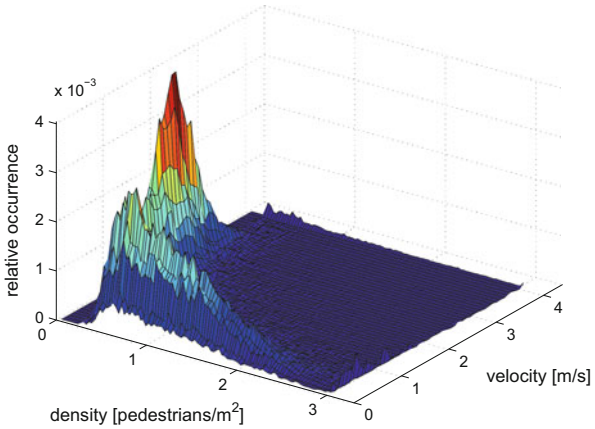

Fig. 4 The three dimensional fundamental diagram $v(\rho)$ generated from pedestrians' path data

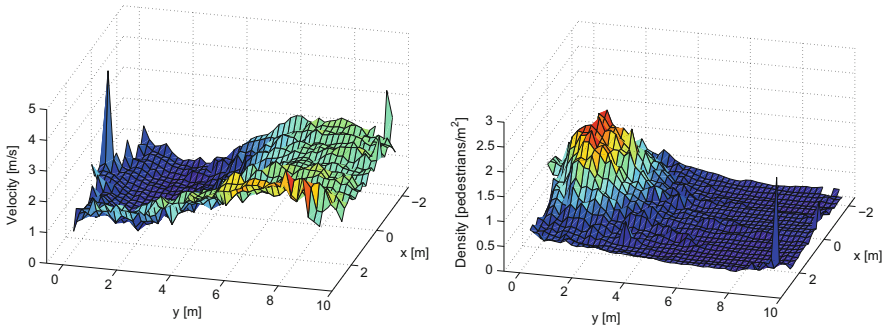

Fig. 5 The distribution of velocity and density evaluated from pedestrians' path data

The phase transition can be monitored by observing the distribution of velocity and density in the room (Fig. 5). One can see that the distance between maximal velocity and high density, which represents the process of transition from free motion to the congested state, reaches 3 m.

The pedestrian behaviour in front of the exit has been analyzed by FD $J^s(\rho)$ (in Fig. 6). The outflow, detector and pedestrian data have been compared.

The outflow data are measured just at the door, on contrary, the detector is placed in front of the door. The width of crossection, which is crossed by pedestrians, is 2 m. Due to the conservation law, the absolute flow must be conserved at all crossections which are used by all pedestrians. Therefore the specific flow at the door is much higher than the specific flow in the detector.

However, the trends of area and outflow data in FD are similar, this curves differs only in scaling. The flow linearly increases until the density reaches 0.3

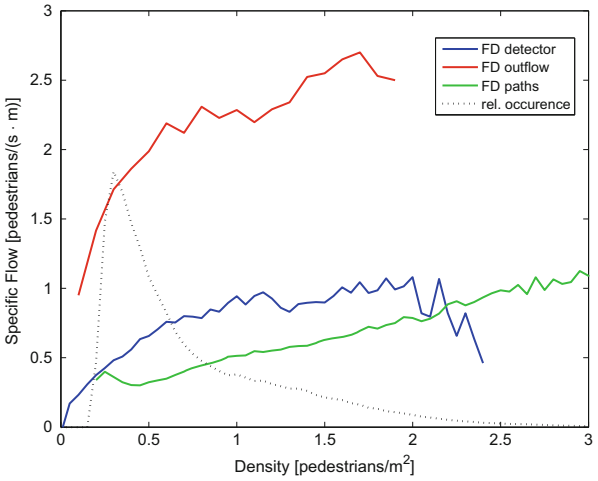

Fig. 6 Comparison of FD $J(\rho)$ evaluated from detector data (*blue*), outflow data (*red*) and pedestrians' path data (*green*). *Dotted line* illustrates the frequency of density's occurrence

(resp. 0.4) ped/m^2. This linear part characterizes the free flow state. Then, the flow continues to increase slowly and at the density 0.8 (resp. 0.9) ped/m^2, the flow is stabilized, the cluster is formed. The maximal flow occurs at the density of 1.7 ped/m^2, where the second increase comes. At the densities larger than 2 ped/m^2, a fast decrease occurs.

Using hydrodynamic relation (1), the FD $J(\rho)$ can be derived also from the pedestrians' data. Surprisingly the trend is quite different. The pedestrians' velocity decreases rapidly when the density reaches 0.3 ped/m^2 and then it fluctuates around a constant value (see Fig. 4). Thus the flow falls first and then increases linearly.

To conclude, the 3D FD generated by pedestrians' data clearly describes the phase of the system or the state of a pedestrian. But to provide the $J(\rho)$ FD, area based methods produce more relevant information.

All observation of the phase transition illustrates, that pedestrians change their velocity in advance, the slowdown process starts around 3 m in front of the obstacle.

From Table 1 it is clear that the assumption that phase transition is determined by the inflow parameter is correct. The cluster formation in front of the bottleneck is very sensitive to this parameter. The transition has been observed while the inflow is between 1.4 and 1.7 ped/s respectively between 1.7 and 1.9 ped/s depending on the size of the room.

Acknowledgements This work was supported by the grant SGS12/197/OHK4/3T/14 and the research program MSM 6840770039.

References

1. H. Bakstein, M. Havlena et al., Omnidirectional sensors and their calibration for the dirac project, Research Reports on CMP 10, Czech Technical University in Prague, 2006
2. M. Boltes, J. Zhang, A. Seyfried, B. Steffen, T-junction, Experiments, trajectory collection, and analysis, in *ICCV Proceedings*, Barcelona, 2011, pp. 158–165
3. T. Ezaki et al., Simulation of space acquision process of pedestrians using proxemic floor field model. Phys. A **391**, 291–299 (2012)
4. T. Ezaki, D. Yanagisawa, Metastability in pedestrian evacuation, in *Cellular Automata*, ed. by G. Sirakoulis, S. Bandini. LNCS, vol. 7495 (Springer, Berlin/Heidelberg, 2012), pp. 776–784
5. M.L. Federici et al., Data collection for modeling and simulation: case study at the University of Milan-Bicocca, in *Cellular Automata*, ed. by G. Sirakoulis, S. Bandini. LNCS, vol. 7495 (Springer, Berlin/Heidelberg, 2012), pp. 699–708
6. I.G. Georgoudas, G.Ch. Sirakoulis, I.Th. Andreadis, An anticipative crowd management system preventing clogging in exits during pedestrian evacuation processes. IEEE Syst. J. 2010 **5**, 129–141 (2011)
7. R.C. Gonzales, R.E. Woods, *Digital Image Processing* (Prentice Hall, Upper Saddle River, NJ, 2001)
8. D. Helbing, I. Farkas, T. Vicsek, Simulating dynamical features of escape panic. Nature **407**, 487–490 (2000)
9. P. Hrabak, M. Bukacek, M. Krbalek, Cellular model of room evacuation based on occupancy and movement prediction. , in *Cellular Automata*, ed. by G. Sirakoulis, S. Bandini. LNCS, vol. 7495 (Springer, Berlin/Heidelberg, 2012), pp. 709–718 (2012)
10. A. Jelic, C. Appert-Rolland et al., Properties of pedestrians walking in line – fundamental diagrams. Phys. Rev. E **85**(3), 057302 (2012)
11. M. Plaue, M. Chen et al., Trajectory extraction and density analysis of intersecting pedestrian flows from video recordings, in *Photogrammetric Image Analysis*, ed. by U. Stilla et al. LNCS, vol. 6952 (Springer, Heidelberg/New York, 2011), pp. 285–296
12. A. Schadschneider, A. Seyfried, Empirical results for pedestrian dynamics and their implication for cellular automata models, in *Pedestrian Behavior: Models, Data Collection and Applications* (Emerald Group, Bingley, 2009)
13. A. Schadschneider, D. Chowdhury, K. Nishinari, *Stochastic Transport in Complex Systems* (Elsevier, Amsterdam/Oxford, 2010)
14. A. Seyfried, M. Boltes et al., Enhanced empirical data for the fundamental diagram and the flow through bottlenecks. Pedestr. Evacuation Dyn. **2008**, 145–156 (2010)
15. A. Seyfried, A. Portz, A. Schadschneider, Phase coexistence in congested states of pedestrian dynamics, in *Cellular Automata*, ed. by S. Bandini et al. LNCS, vol. 6350 (Springer, Berlin, 2010), pp. 496–505
16. B. Steffen, A. Seyfried, Methods for measuring pedestrian density, flow, speed and direction with minimal scatter. Phys. A **389**(9), 1902–1910 (2010)
17. J. Was, Experiments on evacuation dynamics for different classes of situations. Pedestr. Evacuation Dyn. **2008**, 225–232 (2010)
18. J. Was, W. Mysliwiec, R. Lubas, Towards realistic modeling of crowd compressibility. Pedestr. Evacuation Dyn. **2010**, 527–534 (2011)
19. J. Zhang, W. Klingsch, A. Seyfried, High precision analysis of unidirectional pedestrian flow within the hermes project, in *The Fifth Performance-based Fire Protection and Fire Protection Engineering Seminars* arXiv:1207.5929 (2010)

Simulation of Crowd-Quakes with Heterogeneous Contact Model

Jian Ma, Weiguo Song, and Siuming Lo

Abstract Serious pedestrian trampling in crowd disasters such as the Love Parade happened almost every year all over the world. Many people lost their lives, even more were injured in these disasters. It was found that these hazardous sequence usually happened after a special crowd movement pattern, i.e., crowd turbulent flow, which was believed to be result of earthquake like "pressure release" in the crowds. In the present study, we show video recording analysis results which indicated that there were different kinds of contacts among pedestrians. These contacts mode may be the origin of the pressure release. Thus, based on the discovered contacts mode, we further built heterogeneous contact model for massive crowd. Numerical simulation results of the model can qualitatively describe the statistical properties of pedestrian movement behavior in crowd quakes.

1 Introduction

During the past few decades, pedestrian crowds occur more and more frequently. Many people were injured or even die in these crowd induced disasters. It was noticed that when located in densely packed crowds, a pedestrian can hardly move thus can only sway around his initial position or be pushed away some distance. This special phenomenon has been reported in 1990s by Fruin [1] in his discussion on pedestrian safety engineering. The very similar crowd movement pattern was

J. Ma (✉)
National United Engineering Laboratory of Integrated and Intelligent Transportation, School of Transportation and Logistics, Southwest Jiaotong University, 610031 Chengdu, PR China
e-mail: majian@mail.ustc.edu.cn

W. Song
State Key Laboratory of Fire Science, University of Science and Technology of China, 230026 Hefei, PR China
e-mail: wgsong@ustc.edu.cn

S. Lo
Department of Architecture and Civil Engineering, City University of Hong Kong, Tat Chee Avenue, Kowloon, Hong Kong SAR
e-mail: bcsmli@cityu.edu.hk

M. Chraibi et al. (eds.), *Traffic and Granular Flow '13*,
DOI 10.1007/978-3-319-10629-8_12

recently quantified and entitled as stop-and-go wave and pedestrian turbulent flow [2]. These two kinds of pedestrian flow are rather dangerous because pedestrian in crowds might fall down and get tramped due to suddenly velocity change induced "pressure release." For this reason, this kind of disaster is usually called trampling disaster or human stampede. However, epidemiologic surveillance shows that the risk posed from pedestrian fallen only counts for a small partial of the injuries and death [3], much more victims suffered suffocation due to the pedestrian contacts induced intense crowd pressures.

To facilitate our understanding of this kind of disasters, both numerical and empirical studies have been performed. Based on the occupancies feature in densely packed pedestrian crowds, it was usually assumed that people can be treated as fluid in numerical simulations [4]. Thus nonlinear features such as shock waves could be explored. It should be noticed that pedestrian contact forces, information flow in crowds could barely be quantified at that time, so they can hardly be formulized in these fluid models. Fortunately, with the development of modern video surveillance equipment, the whole process of the crowd disaster can now be detailed. As a result, empirical studies can now focus on the development process of the disaster [5] and use not only eye witness report, post disaster survey but also video recordings [6], cell phone information, RFID-based trajectories and so on. With these abundant information, more interesting crowd movement pattern, turbulent pedestrian movement has been reported in religious pilgrimage 2006 [2] and in Love Parade 2010 crowd disaster [7]. Numerical simulation with contact force considered can also display turbulent features under the circumstance of bottleneck pedestrian merging flow [8]. However, it is still puzzling why turbulent feature emerges in almost frozen crowds.

In the present study, we explore turbulent flow pattern in pedestrian crowds by firstly detailing some of the pedestrian trajectory features in Love Parade disaster. Holding these discussion, we build heterogeneous contact model in the following section and further explore the dynamics of the model by performing simulation analysis. The last section comes to our conclusions.

2 Model Formulation

The Love Parade 2010 happened in Germany caused the death of 21 people from suffocation and at least 510 more were injured. Although the reason for this disaster seems quite complex, the cause of injuries is believed to be pedestrian contacts. It was found from video surveillance recordings that pedestrian density on the ramp reaches as high as 11 people per square meter. Under this densely crowded situation, pedestrians lean against each other thus can barely move. After a critical moment, in this almost frozen crowds, a special earthquake like pedestrian movement pattern was found, i.e., crowd-quakes [7].

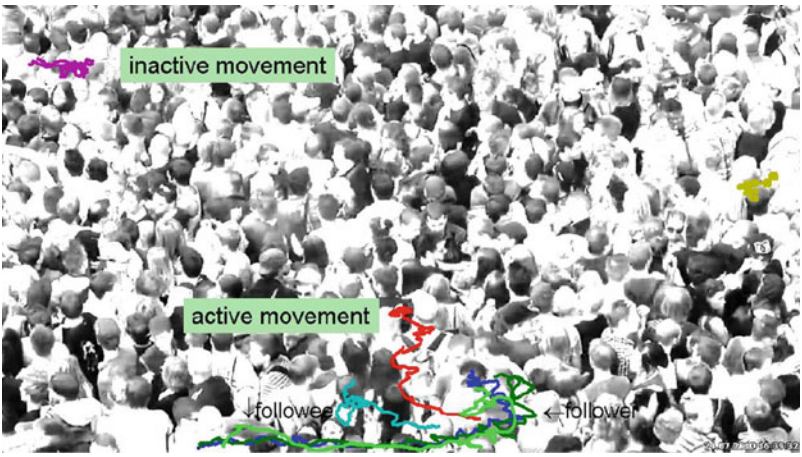

Fig. 1 Snapshot of the densely packed pedestrian crowds in Love Parade 2010 disaster

When we take a closer look at the trajectories as extracted in Ref. [7], it can be found that, as shown in Fig. 1, there were two distinct kinds of trajectories. The first ones show that the pedestrians can only sway near their initial locations, the other ones however can move a relatively longer distance. For those who can make long distance movement, we look back at the video recordings and found that these people move in a lane, as the one formed in pedestrian counter flow [9]. In the formed lane, the one in front try his best to push his way forward while the ones in the rear would follow the leader's movement, as shown in Fig. 1. Thus, we distinguish these two kinds of people as followee and follower.

Further analyzing the velocity evolution process of those who was swaying around and those who was making long distance travel, we can find from Fig. 2 that their velocities vary a lot. The former velocity was relatively larger, while the later velocity is almost zero. It should be noticed that the value of the later velocity is not absolutely zero but a little value varying from time to time, as indicated by the inset of Fig. 2. For the reason that the pedestrian density of the captured scenario is relatively high, we can deduce that the small velocity is resulted from body contacts with those who made long distance travel. For the convenient of illustration, we thus distinguish these pedestrians as inactive and active pedestrian. Active pedestrian wants to make active move to escape the crowded situation, while the inactive pedestrian wants to keep still but was pushed away from time to time.

To formulize a crowd model, it can be summarized from the above discussion that, firstly, there are active and inactive pedestrians in the crowds; secondly, active pedestrian wants to move with a high speed while inactive with low speed; thirdly, active pedestrian will follow those other active but not the inactive pedestrians' movement; fourthly, there will be body contact force as long as two

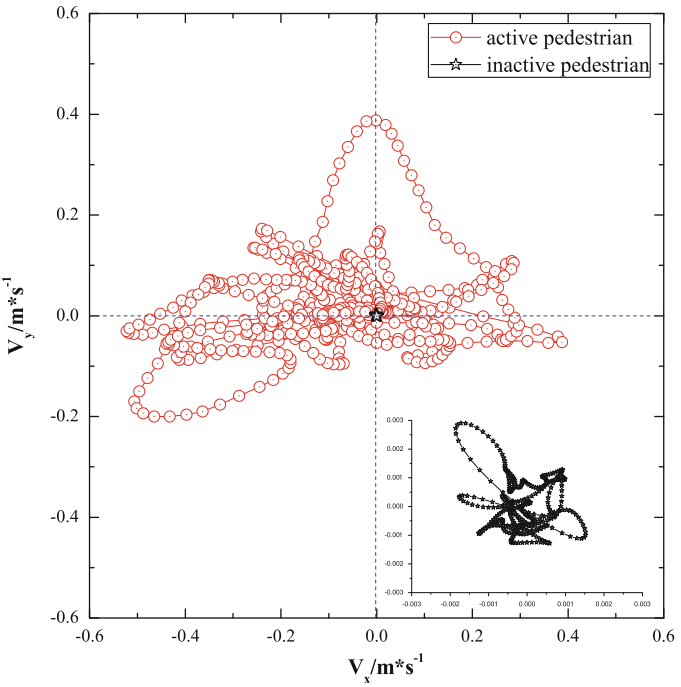

Fig. 2 Velocity evolution of active and inactive pedestrians in the crowds

pedestrian contacts each other, no matter they are active or not. Holding these basic assumptions, the model could be formulized as follows,

$$\vec{F}_i = \vec{F}_s + \vec{F}_\alpha + \vec{F}_r + \varepsilon$$

$$\vec{F}_s = k_1(v_0 - v_i)\vec{v}_i$$

$$\vec{F}_r = \begin{cases} k_2(1 - \frac{r_{ij}}{2r_0})^2 \vec{r}_{ij}, \text{if} r_i + r_j > r_{ij} > 0 \\ 0, \text{otherwise} \end{cases}$$

$$\vec{F}_\alpha = \alpha \frac{\sum_{j=1}^{N_j} \vec{v}_j}{\left| \sum_{j=1}^{N_j} \vec{v}_j \right|}$$

where $\overrightarrow{F_i}$ represents the forces exerted on pedestrian i, as shown in Fig. 3; $\overrightarrow{F_s}$ means self-driven force to travel with an expected speed v_0, and k_1 means the relaxation time whose value is chosen to be 0.5 in the present study; $\overrightarrow{F_r}$ is a repulsive force quantifying body contact force, whose value is zero when two pedestrians are far away and is none zero value when there is body contact. Here k_2 is a factor reflecting the willing to avoid body contacts in crowds; $\overrightarrow{F_a}$ stands for the active pedestrians following behavior as discussed in the former section. It should be noticed that only nearby active pedestrians were taken into consideration. Those who are too far away

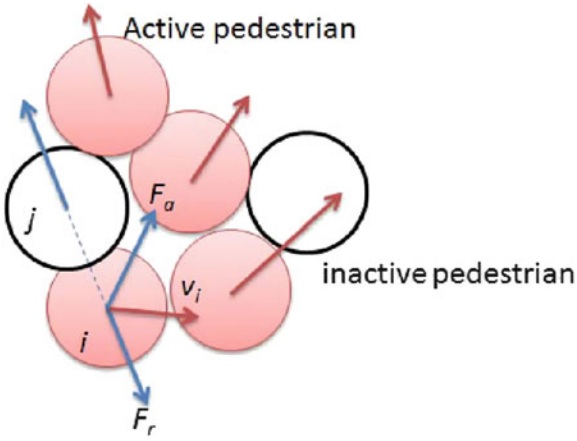

Fig. 3 Scheme of forces in the proposed heterogeneous contact model

barely affect pedestrian i's decision due to limited information transfer in crowds. Here, α represents following strength, whose value could be in between 0 and 1. It should be noted that σ is a small random number to quantify the force fluctuation.

3 Simulation Results

In this section, numerical simulations were performed with the proposed model. A 6m by 6m square with periodical boundary condition was established to accommodate 300 people. Thus the pedestrian density in this situation is higher than 8 per square meter. In this crowds, there were 21 active pedestrian whose expected speed $v_0 = 0.2$ m/s and the strength of following other active pedestrians' movement was set to be $\alpha = 0.9$. The active walkers were randomly distributed in the crowds at the beginning of the simulation. k_1 was set as 20 to quantify a strong willing to avoid body contact with others. ϵ has a mean value of zero and a standard deviation of 1 in this study. The simulation lasted 1,000 s, and only the last 500 s were used to investigate the dynamics of the model to get rid of the influence of initial condition.

In Fig. 4a we show snapshots of the simulation process. As can be found, at the beginning of the simulation, the active pedestrians were randomly located in the crowds. For the reason that they had the tendency of following other active pedestrians' movement, after a short while, the active pedestrian began to move as clusters. In each cluster, pedestrians have similar direction of movement. It is noticed that the clusters were not stable, old clusters would disassemble and form new clusters later. During this process, active pedestrian moved a relatively long distance, while other inactive ones only moved when they were pushed by others. We further explore the velocity evolution feature, as shown in Fig. 4b. Comparing Fig. 4b with Fig. 2b, we can find similar features of movement for both active and inactive pedestrian. In Fig. 4b, the active pedestrian moved almost along the

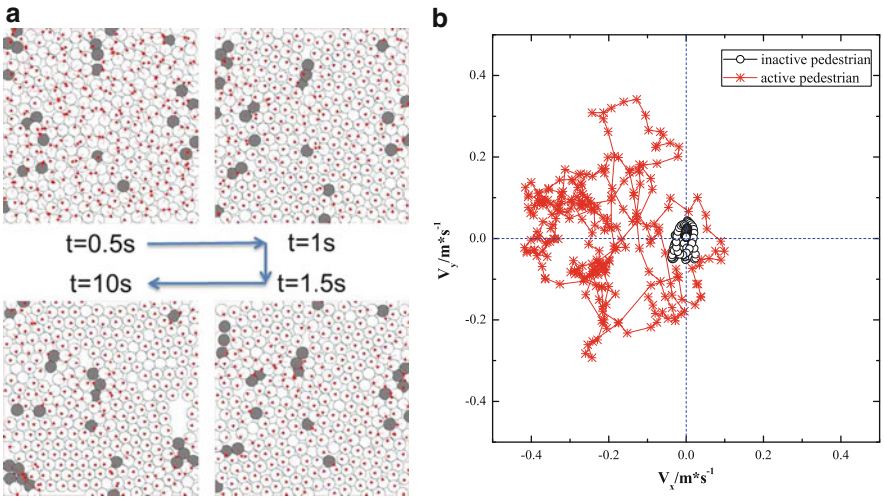

Fig. 4 Simulated heterogeneous contact model outputs (**a**) and the velocity evolution of active and inactive pedestrians in the proposed model (**b**)

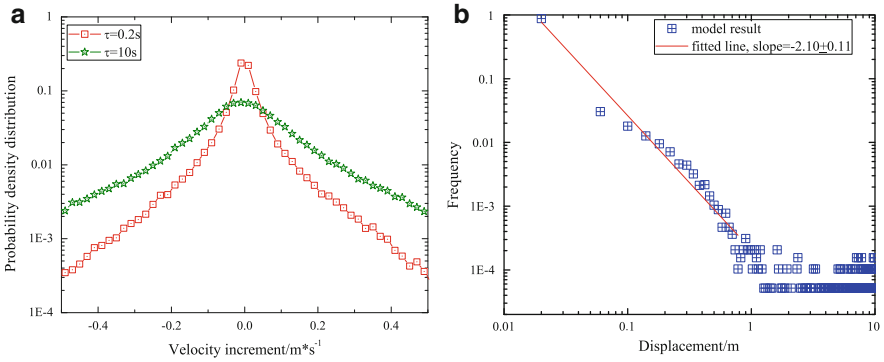

Fig. 5 Pedestrian velocity increment (**a**) and displacement distribution (**b**)

y-direction. Due to the movement of the active pedestrians, inactive pedestrian were pushed away from their initial locations, and as a result, their movement direction is also along the y-direction.

To further explore the flow pattern, we firstly define velocity increment as velocity change in a short time gap τ. Results of the velocity increment distribution was plotted in Fig. 5. As can be found from Fig. 5a, when $\tau = 0.2$ s, the probability density curve presents a sharply peaked shape. With the increase of τ, the curve shape becomes a Gaussian-like distribution. This indicates that the crowd displays typical turbulence features. Secondly, we quantify the displacement features. Displacement means location changes between two subsequent stops. It was noticed that pedestrians in the crowd actually kept a nonzero speed, thus a speed lower than

0.04 m/s was treated as a stop. We plotted displacement frequency distribution in Fig. 5b. From this figure we can see most of time, pedestrian can only make a small step forward, long distance travel appear with much lower probability. This may result from the fact that active pedestrian could travel a long distance while inactive pedestrian moved only when they were pushed away from their initial locations. The displacement distribution also follows a power law distribution, which also indicates the flow pattern seems like fluid turbulent.

Although we can find turbulent features from pedestrian movement pattern, however, from the velocity of each pedestrian, as shown in Fig. 4a, we can hardly find micro turbulent flow structures including vertex, sink or origin. Thus we reconstruct the overall flow field on the basis of each pedestrian's velocity and show in Fig. 6 the snapshot of the simulation and the corresponding streamlines. It is easy for us to find that, the flow filed shows typical vertex structure on the right part of the crowds. On the bottom-left part of the crowds, we can find origin structure. Comparing the corresponding pedestrian distribution we can deduce that the origin structure is a result of the pedestrian cluster which move mainly upward. The upward moving pedestrian cluster leaves a pedestrian gap behind and meanwhile they pushes inactive pedestrians aside, so these inactive pedestrian rushes to the gap, which makes it seems the pedestrians are origin from that location. At this very location, the velocity varies a lot, which may induce pedestrian fallen.

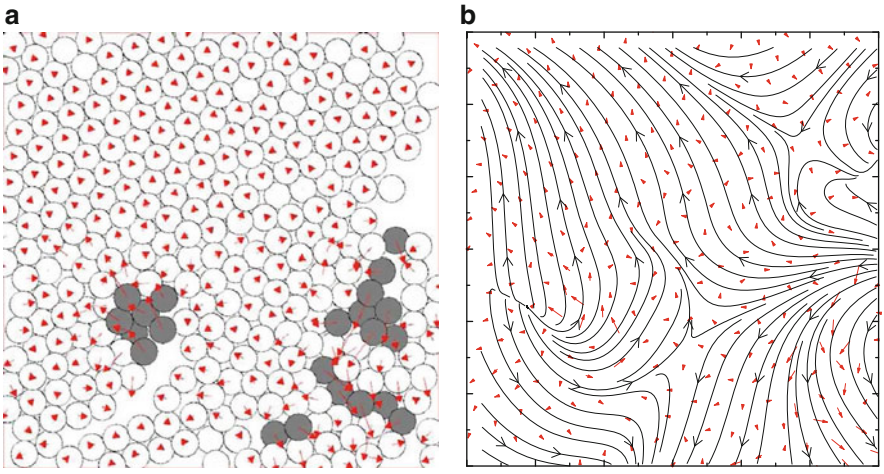

Fig. 6 Velocity field (**a**) and its corresponding streamline (**b**) of the simulated densely packed pedestrian crowds

Conclusions

In the present paper, we further analyzed the trajectories of pedestrian crowds in Love Parade 2010. Results indicated that there were two different kinds of pedestrians in the crowds, i.e., active and inactive ones. Active pedestrian moved with a relatively high speed while inactive pedestrian wanted to remain standing still. It was also noticed that active pedestrian moved in lanes in densely packed crowds, that is say, they had the tendency to follow other active pedestrians movement.

With these facts considered, a heterogeneous contact model was built. The model distinguished two kinds of pedestrian, and took into account not only body contact avoidance tendency but also active pedestrian's following behavior. Based on the proposed model, we performed numerical simulations, results of which indicate that the densely packed pedestrian crowds displays sharply peaked velocity increment probability distribution, power law displacement distribution, i.e., earthquake like movement pattern. The overall flow filed shows typical vertex and origin structures, indicating the crowds show turbulent flow pattern.

Acknowledgements The authors acknowledge the supports by grants from the China National Natural Science Foundation (Nos. 71103148, 51178445, 71473207), the Fundamental Research Funds for the Central Universities (2682014CX103), and the Research Grant Council, Government of the Hong Kong Administrative Region, China No. CityU119011.

References

1. J. Fruin, The causes and prevention of crowd disasters, in *Engineering for Crowd Safety*, ed. by S. RA, J.F. Dickie (Elsevier, New York, 1993), pp. 99–108
2. D. Helbing, A. Johansson, H.Z. Al-Abideen, Dynamics of crowd disasters: an empirical study. Phys. Rev. E **75**(4), 046109 (2007)
3. K.M. Ngai, W.Y. Lee, A. Madan, S. Sanyal, N. Roy, F.M. Burkle Jr., E.B. Hsu, Comparing two epidemiologic surveillance methods to assess underestimation of human stampedes in India. PLoS Curr. **5** (2013)
4. R.L. Hughes, The flow of human crowds. Ann. Rev. Fluid Mech. **35**, 169–182 (2003)
5. D. Helbing, P. Mukerji, Crowd disasters as systemic failures: analysis of the love parade disaster. EPJ Data Sci. **1**(1), 7 (2012)
6. B. Krausz, C. Bauckhage, Loveparade 2010: automatic video analysis of a crowd disaster. Comput. Vis. Image Underst. **116**(3), 307–319 (2012)
7. J. Ma, W.G. Song, S.M. Lo, Z.M. Fang, New insights into turbulent pedestrian movement pattern in crowd-quakes. J. Stat. Mech. **2013**(02), P02028 (2013)
8. W. Yu, A. Johansson, Modeling crowd turbulence by many-particle simulations. Phys. Rev. E **76**(4), 046105 (2007)
9. J. Ma, W. Song, J. Zhang, S. Lo, G. Liao, k-Nearest-Neighbor interaction induced self-organized pedestrian counter flow. Physica A **389**, 2101–2117 (2010)

New Definition and Analysis of Spatial-Headway in Two-Dimensional Pedestrian Flow

Xu Mai, Weiguo Song, and Jian Ma

Abstract In recent years researchers have paid attention to the dependency between required length and velocity, which is rather important for modeling pedestrian movement. Some researchers have observed that the velocity of individuals is related to the spatial headway by a linear relation. The other people have found in experiment that there is phase transitions in the following behavior through a larger range of velocities. However, most relations are derived from one-dimensional experiments such as single-file movement, while the study of spatial-headway in two-dimensional pedestrian flow is relatively rare. Here we conducted an experiment suitable for a new insight into the two-dimensional headway.

In this study, two-dimensional experiments are carried out to study pedestrian movement behaviors in a circular passageway. The full pedestrians' trajectories are extracted through an automatic image processing method of high accuracy based on mean-shift algorithm. Here we redefine the spatial-headway in two-dimensional following behavior, which is elaborated in detail later. The results show that the two-dimensional spatial-headway is distinctively different from that obtained in single-file movement. The velocity in every ligature is also extracted to get the relationship between velocity component and distance in different angles. Results of the more crowded situation show that the pedestrians turn into three steady lanes and the spatial-headway also keeps in a stable state. The findings may be useful for model calibration.

X. Mai (✉) • W. Song
State Key Laboratory of Fire Science, University of Science and Technology of China, 230026 Hefei, PR China
e-mail: ogcjm@mail.ustc.edu.cn; wgsong@ustc.edu.cn

J. Ma
National United Engineering Laboratory of Integrated and Intelligent Transportation, School of Transportation and Logistics, Southwest Jioatong University, 610031 Chengdu, PR China
e-mail: majian@mail.ustc.edu.cn

M. Chraibi et al. (eds.), *Traffic and Granular Flow '13*,
DOI 10.1007/978-3-319-10629-8_13

1 Introduction

The behavior of pedestrian streams, especially in crowded situation, draws extensive attention for a wide range of improvement in modeling and facility design. There are many interesting dynamic characteristics in pedestrian crowds, such as spontaneous collective phenomena [1, 2] and so on. A great many models [3–5] have been proposed to describe the dynamics of pedestrians, which reproduce the behavior of real crowds well, but somewhat circumscribed. So reliable experimental database is compulsive, which is rather important for validation of simulation. In the past few decades a great many one-dimensional experiments have already been carried out [6–8]. However, until now the experimental database is insufficient particularly in case of two-dimensional pedestrian flow. Also collecting the trajectories of each pedestrian precisely and promptly is very critical [9]. Two-dimensional pedestrian flows may present longitudinal interactions as well as lateral ones at the same time in a circular passage [10], and under certain conditions the emerge of new organizations allows the group to solve overcrowding efficiently without factitious control [11,12]. Such functional patterns of motion have been identified many times in the past, such as the alternating flows at a bottleneck, the formation of trails, or the walking configuration of social groups, which are considered as examples of collective intelligence. One of the most known examples is the lane formation in both unidirectional and bidirectional flows [13].

In this paper several experiments were performed and the new results are presented, which are based on the trajectories obtained through our newly developed tracking approach. Besides the discussion on basic elements as velocity, density, we also gain insights into the spatial-headway in two-dimensional situation.

2 Experimental Setup

The experiments were performed in an opening area in West Campus of USTC in September 2011. A total of 38 participants, 17 males and 21 females, took part in this experiment. These participants are all students and are between 22 and 25 years old and between 157 and 181 cm tall, averaging 23 years old and 168 cm tall. The participants were divided into different groups to wear red or yellow caps and are told to walk without panic during the evacuation as if they were walking alone at school. All of them were naive about the purpose of the experiment. Experiments were conducted in an approximate ring corridor with a small rectangle encircled by a bigger one. The size of the inner rectangle is fixed to 1.2×1.4 m but the outer one is set to 5.2×4.4 m and 4.2×3.4 m respectively, as shown in Fig. 1. All trials were made with 38 participants, corresponding to a global density of 1.70 and 2.75 $\mathrm{p/m^2}$ for the two scenes respectively. The typical duration of each trial was not measured by time but the process the whole group finished five laps in the circle.

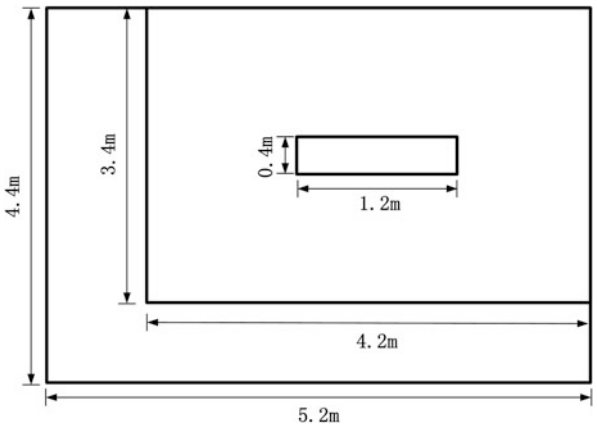

Fig. 1 Precise description of the scene

All experiments were recorded by two cameras located on the roof of a four-floor building with a viewing direction almost perpendicular to the ground. The cameras have a resolution of $1{,}920 \times 1{,}080$ pixels and a frame rate of 25 fps. Manual procedures for collecting empirical data are very time-consuming and usually cannot provide sufficient accuracy in space and time. In this study accurate pedestrian trajectories were automatically extracted from video recordings by our self-developed approach using the method of mean-shift [14, 15] by detection of the caps the participants wear. The perspective distortion effect caused by different heights of the participants could be ignored because the camera is mounted vertically above the scene so that the distortion is negligible. Nevertheless the horizontal direction should be calibrated because the camera is approximately 7 m away from the top edge of the scene. Consequently, we adopted four known points to adjust the distortion using direct linear transformation [16].

3 Measurement and Methods

3.1 Trajectories

Pedestrian characteristics including flow, density, velocity and individual distances at any time and position can be calculated through trajectories. All the results in this study are obtained by analyzing pedestrian trajectories from video recordings of the experiments. Therefore we have extracted all pedestrians positions (x coordinate and y coordinate in video recordings) at each frame and then plot them in time series to get the trajectories precisely.

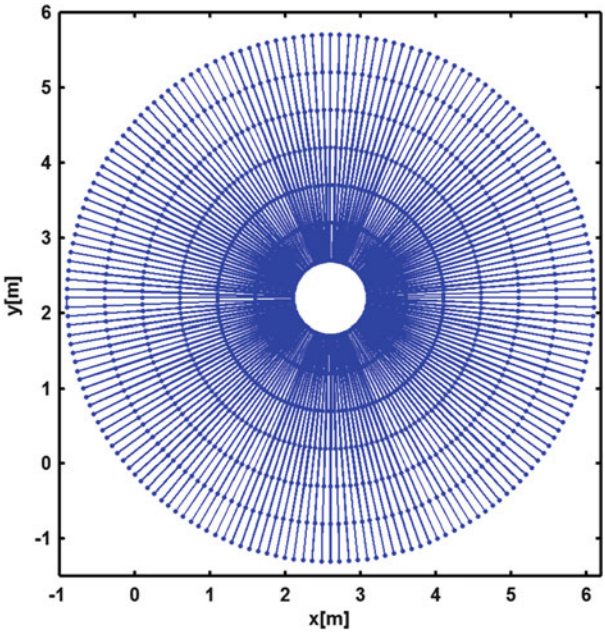

Fig. 2 Illustration of the density definition in this method

3.2 Density and Velocity

In this study we want to see the space occupancy situation as well as the illustration of the spontaneous emergence of density (velocity) gaps and density (velocity) peaks that propagate in the observation area so a method different from the traditional one is proposed [17]. The local density $\rho(\theta, t)$ at time t and in direction θ is defined as the average value of the local density $\rho(\mathbf{x}, t)$, for all points $\mathbf{x}$ of the corridor located along the direction θ (here we pick seven points along the line radiated from the origin every 2°, that is 180 lines in total, as shown in Fig. 2). The local density is defined as $\rho(\mathbf{x}, t) = \sum_j f(d_{jx})$, where d_{jx} is the distance between the center of mass of pedestrian j and his location $\mathbf{x}$, and $f(d)$ here is a Gaussian-based weight function $f(d) = \frac{1}{\pi R} exp(-d^2/R^2)$ with $R = 1$, which is a weight parameter.

3.3 Spatial-Headway

Here we redefine the spatial-headway in two-dimensional following behavior: a reference direction is proposed between the positions of the targeted pedestrian in the present frame and the next one. Based on the reference direction we draw a same

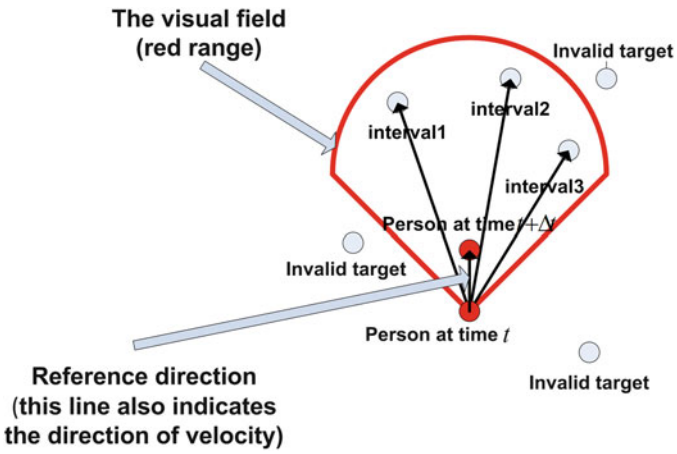

Fig. 3 Spatial-headway definition for a pedestrian in crowd

angle on both sides for example 45° as well as a visual range, 1 m as an example, and then we have a vivid visual field as shown in Fig. 3. If there are other participants right in the visual field we think that they meet the requirements thus one targeted pedestrian may correspond to more than one spatial-headway according to our rule and others are recognized as invalid ones.

4 Result and Discussion

In this paper we mainly focus on the second scenario sized 4.2×3.4 m with all the participants going unidirectional.

4.1 Intuitional Result

There are three obvious lanes formed as shown in Fig. 4 and the velocity in a certain frame is also demonstrated in Fig. 5. As we can find in the experiment, after people started to go, they spontaneously walked into three separated lanes in a very short time to avoid redundant contact with others beside them to keep them the most comfortable state. If someone wants to surpass other pedestrians, he has to push a hard way out to accomplish the action. Moreover there are more than half of the participants are females who do not like to hustle and surpass. The distribution of velocity indicated that the pedestrians in outer ring have a bigger speed with more space while the inner people maintained a relatively lower speed in a constrained situation (Fig. 6).

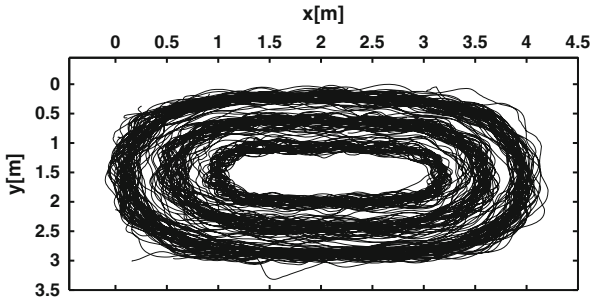

Fig. 4 Trajectories in scene 2

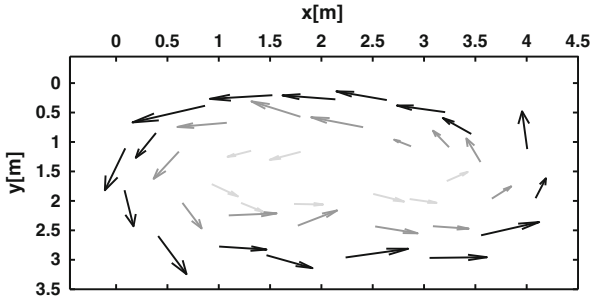

Fig. 5 Velocity in one frame in scene 2

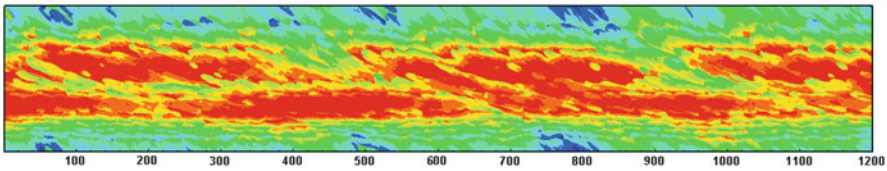

Fig. 6 Local density in time line

4.2 Density and Velocity

For the reason that density fluctuation is important, thus we further investigate timely density fluctuations in the experimental corridor, where highly crowded zones and almost empty zones can be observed at the same moment of time in different areas of the corridor as well as that of velocity. So here we adopted the method in Ref. [17], representing the local density value for all times t and in all directions theta, as shown in Figs. 7 and 8. We can see very clearly that when people gathered in the left and right part in the observation area it would generate a density gap, which is in agreement with the spatial setting. Generally speaking, people have

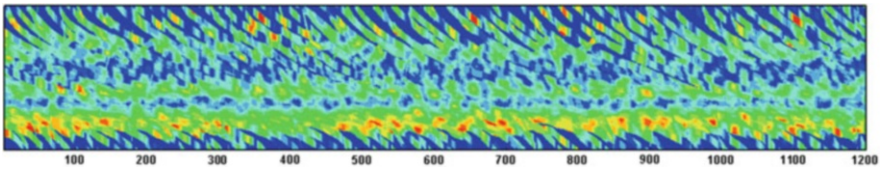

Fig. 7 Radial speed in time line

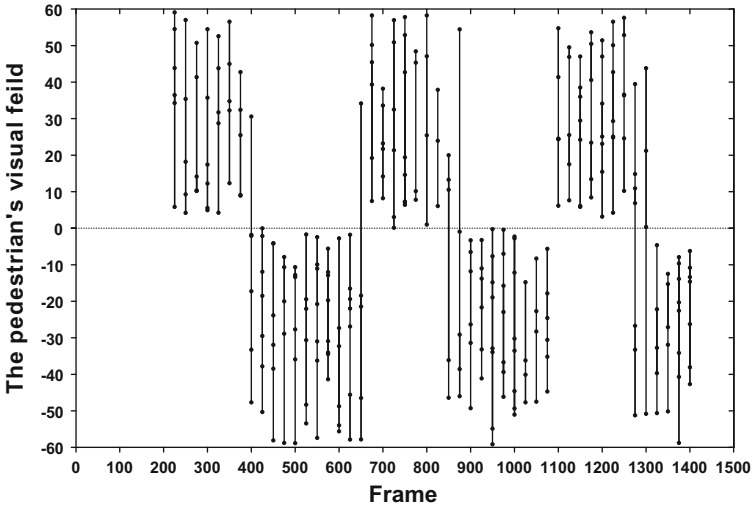

Fig. 8 Full time sketch of obstacles in front of a pedestrian

a relaxed walk in the horizontal direction while most of them should have a struggle in the thinner tunnel in the vertical direction. The place and time where the largest values of velocity occurs coincide with the emergence of high value in density.

4.3 Spatial-Headway

The spatial-headway in two-dimensional situation is not like that in single-file movement which is shown to be in a linear rule. It is not appropriate to integrate the intervals to reach the goal that one pedestrian corresponds to one interval. Full time sketch of obstacles in front of a pedestrian is presented here in Fig. 8. It is very interesting that the obstacles switched in the visual field left and right in turn. This phenomenon indicated a orientation preference while pedestrians are walking.

Conclusion and Perspectives

The trajectories of the pedestrians show us a very intense trend to formation of lanes during the whole process. From the radial speed and local density we can see more clearly how they affect each other in each frame and each degree. Nonetheless the spatial-headway in this research is limited, people choose to walk right after who are in front of them and do not want to surpass so the intervals keeps stable. More experiments containing a larger range of density and different shapes in geometry are needed for a more detailed analysis of two-dimensional spatial-headway.

Acknowledgements This study is supported by the The National Natural Science Foundation of China(51178445) and The Fundamental Research Funds for the Central Universities(WK2320000014).

References

1. M. Moussaid, S. Garnier, G. Theraulaz, D. Helbing, Collective information processing and pattern formation in swarms, flocks, and crowds. Top. Cogn. Sci. **1**, 469–497 (2009)
2. A. Schadschneider, A. Kirchner, K. Nishinari, CA approach to collective phenomena in pedestrian dynamics, in *Cellular Automata* (Springer, New York, 2002), pp. 239–248
3. P.G. Gipps, B. Marksj, A micro-simulation model for pedestrian flows. Math. Comput. Simul. **27**, 95–105 (1985)
4. A. Schadschneider, M. Schreckenberg, Cellular automation models and traffic flow. J. Phys. A: Math. Gen. **26**, L679 (1993)
5. D. Helbing, P. Molnar, Social force model for pedestrian dynamics. Phys. Rev. E **51** 4282 (1995)
6. A. Seyfried, B. Steffen, W. Klingsch, M. Boltes, The fundamental diagram of pedestrian movement revisited. J. Stat. Mech.: Theory Exp. **2005**, P10002 (2005)
7. F. Navin, R. Wheeler, Pedestrian flow characteristics. Traffic Eng. Inst. Traffic Eng. **39**, 30-33 (1969)
8. A. Polus, J.L. Schofer, A. Ushpiz, Pedestrian flow and level of service. J. Transp. Eng. **109**, 46–56 (1983)
9. S. Lemercier, M. Moreau, M. Moussad, G. Theraulaz, S. Donikian, J. Pettr, Reconstructing motion capture data for human crowd study, in *Motion in Games* (Springer, New York, 2011), pp. 365–376
10. M. Rex, H. Lwen, Lane formation in oppositely charged colloids driven by an electric field: chaining and two-dimensional crystallization. Phys. Rev. E **75**, 051402 (2007)
11. D. Helbing, L. Buzna, A. Johansson, T. Werner, Self-organized pedestrian crowd dynamics: experiments, simulations, and design solutions. Transp. Sci. **39**, 1–24 (2005)
12. D. Helbing, P. Molnar, Self-organization phenomena in pedestrian crowds (1998). arXiv preprint cond-mat/9806152
13. J. Zhang, W. Klingsch, A. Schadschneider, A. Seyfried, Ordering in bidirectional pedestrian flows and its influence on the fundamental diagram. J. Stat. Mech.: Theory Exp. **2012**, P02002 (2012)
14. D. Comaniciu, P Meer, Mean shift mode seeking and clustering. Proc. IEEE Trans. Pattern Anal. Mach. Intell. **17**, 790–799 (2002)

15. X. Liu, W.G. Song, J. Zhang, Extraction and quantitative analysis of microscopic evacuation characteristics based on digital image processing. Physica A **388**, 2717–2726 (2009)
16. R. Hartley, A. Zisserman, *Multiple View Geometry in Computer Vision* (Cambridge University Press, Cambridge, 2000)
17. M. Moussaid, E.G. Guillot, M. Moreau, J. Fehrenbach, O. Chabiron, S. Lemercier, J. Pettre, C. Appert-Rolland, P. Degond, G. Theraulaz, Traffic instabilities in self-organized pedestrian crowds. PLoS Comput. Biol. **8**, e1002442 (2012)

On the Validation of a Discrete-Continuous Model with Bottleneck Flow and Computational Artifacts

Ekaterina Kirik, Andrey Malyshev, and Egor Popel

Abstract A connection of a width of a bottleneck and unidirectional virtual people flow by the discrete-continuous pedestrian movement model (Kirik et al. Fundamental diagram as a model input direct movement equation of pedestrian dynamics. In: Proceedings of the international conference pedestrian and evacuation dynamics'2012, Zurich. Springer, 2014) is investigated. Specific and full flow rates versus bottleneck width are presented. Computational artifacts that are pronounced while simulation in front of bottleneck are discussed.

1 Introduction

Bottlenecks on pedestrian facilities gives the most considerable contribution to the upper limit of capacity of an evacuation way. Up to now literature on pedestrian dynamics does not give one quantitative answer on bottleneck questions. Qualitative descriptions have common points. Many authors investigated bottleneck flows in experimental environments ([12, 13], web resource http://ped-net.org). There were observed capacity of the bottleneck versus width, trajectories of pedestrians passing the bottleneck, and corresponding self-organization phenomenon. Flow rate have qualitatively the same behavior, it goes up with the bottleneck width increasing. The specific flow rate is given almost independently on the bottleneck width.

In this paper we consider dynamics of the SigmaEva module in bottlenecks. This module realizes stochastic discrete-continuous model SIgMA.DC [7, 8]. The discrete-continuous approach is a novel contribution to mathematical modeling of pedestrian dynamics. This model is of individual type; people (particles) move in a continuous space (in this sense model is continuous), but number of directions where particles may move is limited, in this sense model is discrete.

E. Kirik (✉) • A. Malyshev
Institute of Computational Modelling SB RAS, Akademgorodok, 50/44, 660036 Krasnoyarsk, Russia
e-mail: kirik@icm.krasn.ru; amal@icm.krasn.ru

E. Popel
Siberian Federal University, Krasnoyarsk, Russia
e-mail: evpopel@gmail.com

M. Chraibi et al. (eds.), *Traffic and Granular Flow '13*,
DOI 10.1007/978-3-319-10629-8_14

We investigated flow rate versus different widths of the bottleneck.

In the next section the main concept of the model is presented. Section 3 contains description of the case study and results obtained. We conclude with a summary.

2 Description of the Model

2.1 Space and Initial Conditions

A continuous modeling space $\Omega \in R^2$ and an infrastructure (obstacles) are known.[1] People (particles) may move in a free space. To orient in the space particles use the static floor field S [11]. Let the nearest exit is assumed as a target point.

Shape of each particle is disk with diameter $d_i, i = \overline{1, N}$, N – number of particles, $x_i(0) = (x_i^1(0), x_i^2(0))$, $i = \overline{1, N}$ – initial positions of particles which are coordinates of disks' centers (it is supposed that they are coordinates of body's mass center projection). Each particle is assigned with the free movement speed[2] v_i^0, square of projection. It is supposed that while moving people do not exceed maximal speed (free movement speed), and persons control velocity according to local density.

Each time step t each particle i may move in one of predetermined directions $\mathbf{e}_i^d(t) \in \{\mathbf{e}^\alpha(t), \alpha = \overline{1, q}\}$, q – number of directions, model parameter (here a set of directions uniformly distributed around the circle is considered). Particles that cross target line leave the modeling space.

2.2 Preliminary Calculations

To model directed movement a "map" that stores the information on the shortest distance to the nearest exit is used. The unit of this distance is meters, [m]. Such map is saved in static floor field S. Idea of field S imported from floor field (FF) CA model [11] that provides pedestrians with information about ways to exits. This field increases radially from the exit and it is zero in the exit(s) line(s) [5, 6]. It is independent of time and presence of the particles. To calculate field S modeling space Ω is covered by a discrete orthogonal grid with cell 10–40 cm in size, and, Dijkstra's algorithm with 16-nodes pattern is used, for instance. Distance to the exit from arbitrary point is given by bidirectional interpolation among nearest nodes.

[1] Here and below under "obstacle" we mean only walls, furniture. People are never called "obstacle". There is unified coordinate system, and all data are given in this system.

[2] We assume that free movement speed is random normal distributed value with some mathematical expectation and dispersion [3, 4].

2.3 Movement Equation

A movement equation for an individual is derived from a finite-difference expression of velocity. This expression allows to present new position of the particle as a function of a previous position and local particle's velocity. Thus for each time t coordinates of each particle i are given by the following formula:

$$\mathbf{x}_i(t) = \mathbf{x}_i(t - \Delta t) + v_i(t)\mathbf{e}_i(t)\Delta t,\ i = \overline{1, N}, \tag{1}$$

where $\mathbf{x}_i(t - \Delta t)$ – coordinate in previous time moment; $v_i(t)$, [m/s] – the particle's current speed; $\mathbf{e}_i(t)$ unit direction vector, Δt, [s] – length of time step that is 0.25 s.

Unknown values in (1) for each time step for each particle are speed $v_i(t)$ and direction $\mathbf{e}_i(t)$. In this model we omit to describe forces that act on person, to solve differential equations and, as a result, to get velocity vector $\mathbf{v}_i(t)$. We propose to get speed from experimental data (fundamental diagram), for example [3,4]. In this case in contrast with force-based models [1,2] we have an opportunity to divide task of finding velocity vector to two parts. At first direction is determined; then, speed is calculated according to local density in the direction.

2.4 Choosing Movement Direction

In this discrete-continuous model we took inspiration from our previously presented stochastic CA FF model [5, 6]. All predetermined directions for each particle each time step are assigned with some probabilities to move, and direction is chosen according to probability distribution obtained.

Probabilities in the model are not static and vary dynamically and issued from the following facts. Pedestrians keep themselves at a certain distance from other people and obstacles. The tighter the people flow and the more in a hurry a pedestrian, the smaller this distance. During movement, people follow at least two strategies: the shortest path and the shortest time.

Thus personal probabilities to move in each direction each time step have contributions: (a) the main driven force (given by destination point), (b) interaction with other pedestrians, (c) interaction with an infrastructure (non movable obstacles). The highest probability[3] is given to direction that has most preferable conditions for movement considering other particles and obstacles and strategy of the people movement (the shortest path and/or the shortest time).

[3]Mainly with value >0.9.

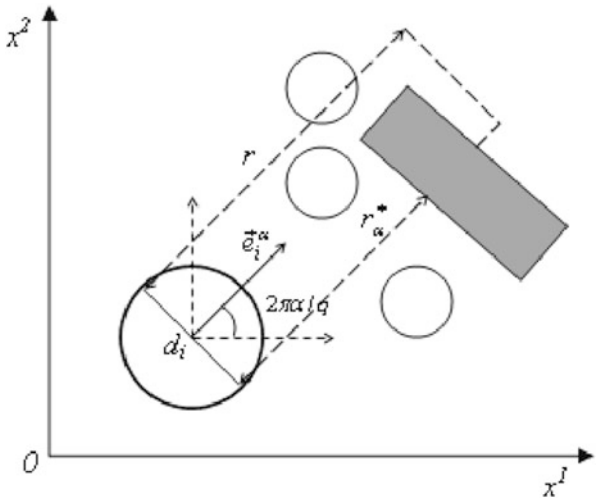

Fig. 1 Visibility area of particle i in direction α

Let particle i has current coordinate $\mathbf{x}_i(t-\Delta t)$. The probability to move from this position in direction $\mathbf{e}^{\alpha}(t) = \left(\cos\frac{2\pi}{q}\alpha, \sin\frac{2\pi}{q}\alpha\right)$, $\alpha = \overline{1,q}$ is the following:

$$p_{\alpha}^{i}(t) = \frac{\hat{p}_{\alpha}^{i}}{Norm} = \frac{exp\left(-k_W^i(1-\frac{r_{\alpha}^*}{r})\right) exp\left(-k_P^i F(r_{\alpha}^*)\right) exp\left(k_S^i \Delta S_{\alpha}\right)}{Norm} W\left(r_{\alpha}^* - \frac{d_i}{2}\right), \tag{2}$$

where $Norm = \sum_{\alpha=1}^{q} \hat{p}_{\alpha}^{i}$.

Visibility radius r ($r \geqslant \max\{\frac{d_i}{2}\}$), [m], is model parameter representing the maximum distance at which people and obstacles influence on the probability in the given direction. Obstacles can reduce visibility radius r to value r_{α}^* (see Fig. 1). People density $F(r_{\alpha}^*)$ is estimated in the visibility area, see [8]. Function $1(\cdot)$ is Heaviside unit step function. There are model parameters: $k_S^i > 0$ – field S-sensitive parameter; $k_W^i > 0$ – wall-sensitive parameter; $k_P^i > 0$ – density-sensitive parameter. More information on parameters one can find in [5,6,8].

$\Delta S_{\alpha} = S(t-\Delta t) - S_{\alpha}$, where $S(t-\Delta t)$ – static floor field in the coordinate $\mathbf{x}_i(t-\Delta t)$, S_{α} – static floor field in the coordinate $\mathbf{x} = \mathbf{x}_i(t-\Delta t) + 0,1\mathbf{e}_i^{\alpha(t)}$. With ΔS_{α} moving to the target point is controlled. Function $W\left(r_{\alpha}^* - \frac{d_i}{2}\right)$ controls approaching to obstacles. If $Norm = 0$ than particle does not leave present position. If $Norm \neq 0$ than required direction $\mathbf{e}_i(t)$ is considered as discrete random value with distribution that is given by transition probabilities obtained. Exact direction $\mathbf{e}_i(t) = \mathbf{e}_i^{\hat{\alpha}}(t) = \left(\cos\frac{2\pi}{q}\hat{\alpha}, \sin\frac{2\pi}{q}\hat{\alpha}\right)$, $\alpha = \overline{1,q}$ is determined in accordance with standard procedure for discrete random values.

As in cellular automata models here parallel update is used. Decision rules to choose direction $\mathbf{e}_i^{\hat{\alpha}}(t)$, and final conflict resolution procedure are presented in [7,8].

2.5 Speed Calculation

Person's speed is density dependent [3,4,9,12]. We assume that only conditions in front of the person influence on speed. It is motivated by a front line effect (that is well pronounced while flow moves in open boundary conditions) in a dense people mass when front line people move with free movement velocity while middle part is waiting a free space available for movement. As a result it leads to a diffusion of the flow. If not to take into account such effect simulation will be slower then real process. Thus only density $F_i(\hat{\alpha})$ in direction chosen $\mathbf{e}_i(t) = \mathbf{e}_i^{\hat{\alpha}}(t)$ is required to determine speed. According [3,4] current speed is

$$v_i(t) = v_i^{\hat{\alpha}}(t) = \begin{cases} v_i^0 \left(1 - a_l \ln \frac{F_i(\hat{\alpha})}{F^0}\right), & F_i(\hat{\alpha}) > F^0; \\ v_i^0, & F_i(\hat{\alpha}) \le F^0. \end{cases} \tag{3}$$

where F^0 – limit people density until which free people movement is possible (density does not influence on speed of people movement); a_l – factor of people adaptation to current density while moving on different way types ($a_1 = 0.295$ is for horizontal way; $a_2 = 0.4$, for down stairs; $a_3 = 0.305$, for upstairs).

Numerical procedures that is used to estimate local density is presented in [8]. Area where density is determined is reduced by direction chosen and visibility area that is presented in Fig. 1.

3 Numerical Experiments

The model presented was realised in computer program module SigmaEva. Simulations were performed by this module.

3.1 Experimental Setup

To investigate flow rate through the bottleneck there was used a geometry in Fig. 2 presented. This geometry was adopted from [13].

Simulation was done for three values of free movement speed v^0. In each case speed was given as a normal distributed random value with $Ev_i^0 = 1.75$ m/s and $\sigma(v_i^0) = 0.083$ m/s, $Ev_i^0 = 1.3$ m/s and $\sigma(v_i^0) = 0.066$ m/s, $Ev_i^0 = 0.96$ m/s and $\sigma(v_i^0) = 0.047$ m/s.

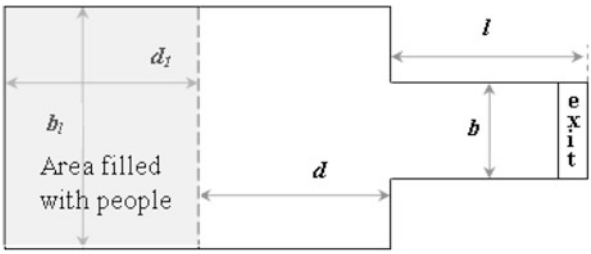

Fig. 2 Geometry set up. Parameters are: $d + d_l = 9.6\,\text{m}$; $b_l = 4\,\text{m}$; $l = 2.8\,\text{m}$; $d_l \approx 5.3\,\text{m}$

All particles have unified diameter $d_i = 0.4\,[\text{m}]$, $i = \overline{1, N}$, square projection is $0.125\,\text{m}^2$. Initially $N = 120$ people filled Grey area with close to maximum initial density, then they start to move in one time and leave the geometry through bottleneck of width b, [m] (open boundary conditions experiment).

3.2 Stochastic Properties of the Model

For each v^0 there were made simulations under different b. Model is stochastic, and one of the goals is to investigate stability of the model, to perform it 500 runs were done for each pair v^0 and b. In Fig. 3 evacuation time distributions for $v^0 = 1.3\,\text{m/s}$ (for other v^0 evacuation time distributions are similar) and different b and mean square deviations versus b are presented.

One can see dispersion goes down with increasing b. A reason is stable arc effects in front of bottleneck are pronounced more often for small b when size of particles (d_i) is comparable with b.

Arc effects realize in a way when several particles wish to move in the direction of exit but they have no enough place to do it (Fig. 4). One reason is that in the model particles (people) are considered as hard bodies and they may move through and take only free space. In real life people use squeezing to resolve arc effects, duration and frequency of such effects are lower comparing with model effects. Now the model does not realize squeezing. Arc effects disappears due to stochasticity of the model when some particles move apart the door and other particles may move in a free space. The smaller b, the higher frequency and duration of arc effects in the model.

3.3 Evacuation Time and Flow

As an estimate of evacuation time T, [s], (when last particle passes control facilities – dotted line, Fig. 2) a mode of a time density distribution was used.

Full flow rate is $J = N/T$, [pers/s], specific flow rate is $J_s = N/T/b$, [pers/s/m].

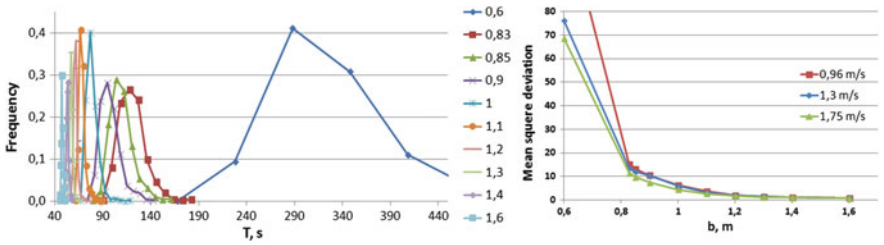

Fig. 3 Time distribution over 500 runs for each b for $v^0 = 1.3$ m/s (*left*) and mean square deviations (*right*)

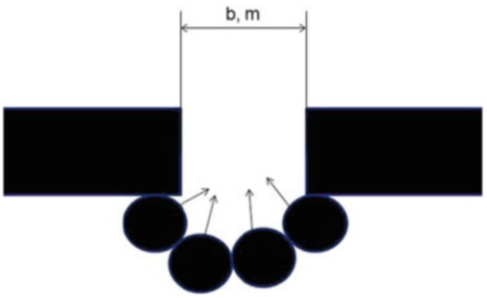

Fig. 4 Arc effect in front of the bottleneck

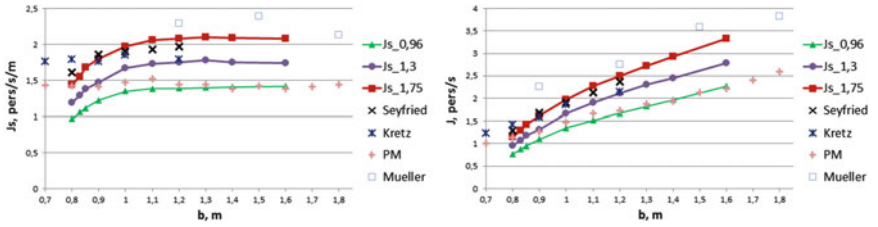

Fig. 5 Model specific (*left*) and full (*right*) flows for different b for different free movement speeds: 0.96 m/s (Js_0,96), 1.3 m/s (Js_1,3), 1.75 m/s (Js_1,75), comparing with experimental specific and full flows by other authors (http://ped-net.org)

In Fig. 5 (right picture) one can see that model full flow (for each free movement speed) rises with increasing bottleneck width b. Experimental data from web resource http://ped-net.org show similar behavior.

Model specific flow rate curves (Fig. 5 left) have two parts: they go up until some bottleneck width b and then became stable. It is explained by arc effects that appear more often in front of narrow bottlenecks. Due to model arc effects may appear in front of wide door but duration of such effect is very shot and frequency is low. With increasing bottleneck width frequency of such computational artifacts considerably decreases and model specific flow becomes approximately constant that matches with the theory of the bottleneck flows [9] and experimental data [10, 12, 13].

Conclusion
The experimental data show flow rate increasing and approximately constant specific flow rate with increasing bottleneck width. Comparison simulation results with these experimental data says that model results are within an existing conception of the bottleneck_width-flow dependence of people flow. But it was shown that there are still points to improve model.

Acknowledgements This work is supported by the Integration project of SB RAS, 49/2012.

References

1. M. Chraibi, A. Seyfried, A. Schadschneider, Generalized centrifugal-force model for pedestrian dynamics. Phys. Rev. E **82**, 046111 (2010)
2. D. Helbing, I. Farkas, T. Vicsek, Simulating dynamical features of escape panic. Nature, **407**, 487–490 (2000)
3. V. Kholshevnikov, Forecast of human behavior during fire evacuation, in *Proceedings of the International conference Emergency evacuation of people from buildings – EMEVAC*, Warsaw (Belstudio, 2011), pp. 139–153
4. V. Kholshevnikov, D. Samoshin, *Evacuation and Human Behavior in Fire* (Academy of State Fire Service, EMERCOM of Russia, Moscow, 2009)
5. E. Kirik, T. Yurgel'yan, D. Krouglov, The shortest time and/or the shortest path strategies in a ca ff pedestrian dynamics model. J. Sib. Fed. Univ. Math. Phys. **2**(3), 271–278 (2009)
6. E. Kirik, T. Yurgel'yan, D. Krouglov, On realizing the shortest time strategy in a CA FF pedestrian dynamics model. Cybern. Syst. **42**(1), 1–15 (2011)
7. E. Kirik, T. Yurgel'yan, A. Malyshev, On discrete-continuous stochastic floor field pedestrian dynamics model SIgMA.DC, in *Proceedings of the International conference Emergency evacuation of people from buildings – EMEVAC*, Warsaw (Belstudio, 2011), pp. 155–161
8. E. Kirik, A. Malyshev, E. Popel, Fundamental diagram as a model input direct movement equation of pedestrian dynamics, in *Proceedings of the International conference Pedestrian and Evacuation Dynamics'2012*, Zurich (Springer, 2014), pp. 691–703
9. V.M. Predtechenskii, A.I. Milinskii, *Planing for Foot Traffic Flow in Buildings* (American Publishing, New Dehli, 1978). Translation of Proektirovanie Zhdanii s Uchetom organizatsii Dvizheniya Lyudskikh potokov (Stroiizdat Publishers, Moscow, 1969)
10. C. Rogsch, Vergleichende Untersuchungen zur dynamischen Simulation von Personenstroumen, Diploma thesis of the University of Wuppertal and the Research Center Julich, 2005
11. A. Schadschneider, A. Seyfried, Validation of CA models of pedestrian dynamics with fundamental diagrams. Cybern. Syst. **40**(5), 367–389 (2009)
12. A. Schadschneider, W. Klingsch, H. Kluepfel, T. Kretz, C. Rogsch, A. Seyfried, Evacuation dynamics: empirical results, modeling and applications. Encycl. Complex. Syst. Sci. **3**, 3142–3192 (2009). Springer
13. A. Seyfried, T. Rupprecht, O. Passon, B. Steffen, W. Klingsch, M. Boltes, New insights into pedestrian flow through bottlenecks. Transp. Sci. **43**, 395–406 (2009)

Dynamic Data–Driven Simulation of Pedestrian Movement with Automatic Validation

Jakub Porzycki, Robert Lubaś, Marcin Mycek, and Jarosław Wąs

Abstract The article presents a dynamic data-driven simulation of pedestrian movement based on the generalized Social Distances Model, where a simulation system is continuously synchronized with current flow data, gained from Microsoft Kinect depth map. Both simulation and data analysis are real-time processes. Agent appears in simulation, as soon as consecutive pedestrians leave sensors tracking zone. Due to system architecture containing feedback loop, automatic validation and parameters calibration is possible. A new method of depth map based pedestrian tracking is proposed as well as a new algorithm of pedestrian parameters extraction for short trajectories. The paper describes in detail the proposed algorithms, system architecture and an illustrative experiment.

1 Introduction

Using of the paradigm of data-driven simulation means, that the created simulations are influenced online by the real data, not only by offline parameters or personal experience and intuition of the authors. Thus, in a data-driven approach, the simulation's input should be continually fed with actual data [2]. In crowd dynamics simulations, the sources of the data are (most commonly) attributes of pedestrians extracted from video recordings, mobile phones or, most recently, from other electronic devices like Microsoft Kinect. Thanks to such approach, it is possible to prepare short-term predictions of crowd behavior in specific, well-defined situations.

2 Related Works

Currently, one can observe significant development of real data gathering methods for crowd dynamics. For example, time-efficient automatic extraction of accurate pedestrian trajectories from video recordings is proposed in a recent work by Boltes

J. Porzycki (✉) • R. Lubaś • M. Mycek • J. Wąs
Department of Applied Computer Science, AGH University of Science and Technology,
al. Mickiewicza 30, 30-059 Kraków, Poland
e-mail: porzycki@agh.edu.pl; rlubas@agh.edu.pl; mycek@agh.edu.pl; jarek@agh.edu.pl

M. Chraibi et al. (eds.), *Traffic and Granular Flow '13*,
DOI 10.1007/978-3-319-10629-8_15

and Seyfried [1], while methodology of video analysis of high density crowd is presented in [3].

Also, low-cost sensors like Microsoft Kinect are very perspective in the context of online crowd analysis. A paper by Seer et al. [5] is devoted, inter alia, to transformation of 3D data gained from Microsoft Kinect sensor to real world coordinates and it proposes a new method for the data collection. Zhang et al. propose a water filling method for people counting using Kinect sensors [10].

Discrete methods of pedestrian dynamics are very effective in the context of data-driven simulation. One of the most known discrete models of a human crowd are based on Cellular Automata (CA) and an idea of floor field [4]. Also the Social Distances model is based on CA and floor field, although the model takes into account more accurate representation of spatial relations [9]. The Social Distances model was adapted both for simulation of mass evacuation [8], as well as for proximity estimation among people in video analyses of crowd [7].

3 System Architecture

A client-server architecture seems to be the best solution for the concept of providing data from motion sensors to dynamic data-driven simulation in real time. The scalability of this approach is an important factor, especially in terms of applying dynamic data-driven simulation methodology to larger area of interest. A simplified scheme of the system architecture can be seen in Fig. 1.

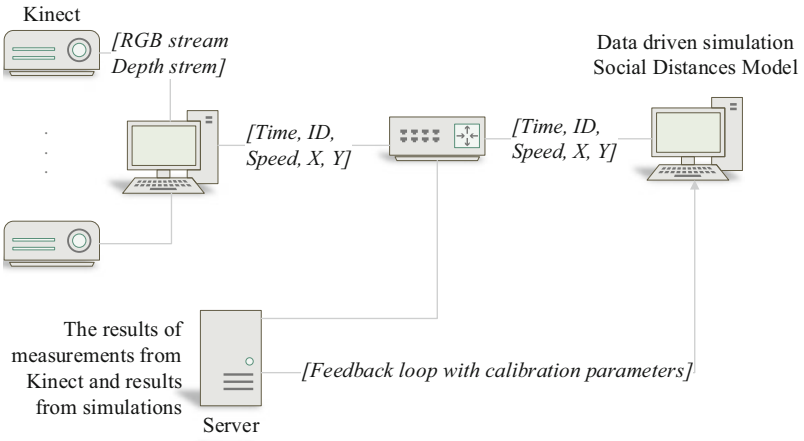

Fig. 1 A simplified scheme of the system architecture. Movement sensor client provides data about time, speed, position of the pedestrians to server, while data-driven simulation client receives pedestrian and calibration parameters

Physical elements included in the system and the connections between them:

- Microsoft Kinect (motion sensing input devices) connected to computer via USB 2.0 interface.
- Network equipment such as a Wi-Fi router to establish a local network.
- Personal computers connected to a local network. Each computer handles only one Kinect due to performance reasons.

In the application layer we provide two main components:

- The server application which takes care of the synchronization issues, exchange of information between clients and provides the feedback loop to data-driven simulation.
- Two types of client applications. The first type handles the motion sensor devices, second type is the data-driven simulation of pedestrians dynamics. Both types of clients communicate with server using the same protocol.

These applications were written in C++ programming language. To support the communication with the Kinect device we used the OpenNI library. The OpenCV library was used to handle image processing.

4 The Depth Map Analysis

The main idea behind the presented method of pedestrian tracking is the assumption that depth sensors are mounted on the ceiling, looking directly downward (Fig. 2). Therefore local minima of the depth map correspond to the top the of objects. In terms of pedestrian tracking local minima of a depth map correspond to pedestrian heads, as is shown in Fig. 3a.

Morphological erosion operation is used to detect local minima. A raw depth map is eroded using a circular structural element with diameter slightly larger than the shoulder width. In result small local minima deriving from haircut, shoulders etc. are removed. After this a binary AND operation is performed on the original and eroded image. Only pixels with the same value on both images will be detected.

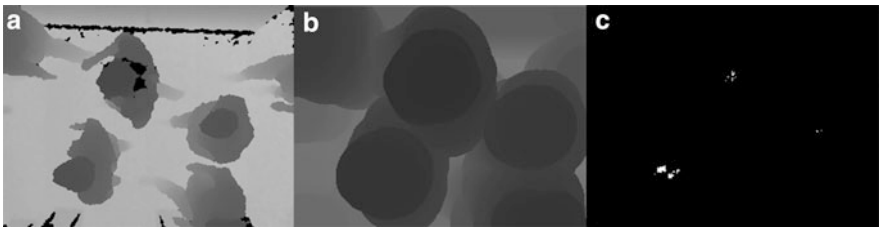

Fig. 2 Consecutive steps of local minima detection procedure. (**a**) Raw depth map, (**b**) map after erosion, (**c**) detected local minima

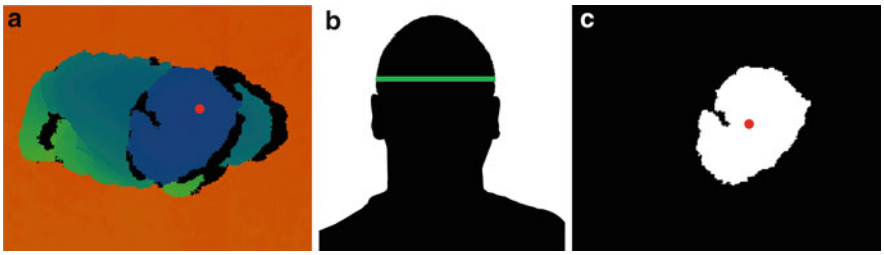

Fig. 3 Overview of Gradient Fill method: (**a**) raw depth map with minimum marked with *red dot*, (**b**) human head profile, with marked region found by Gradient Fill algorithm, (**c**) the shape determined by Gradient Fill method with the centroid marked with *red dot*

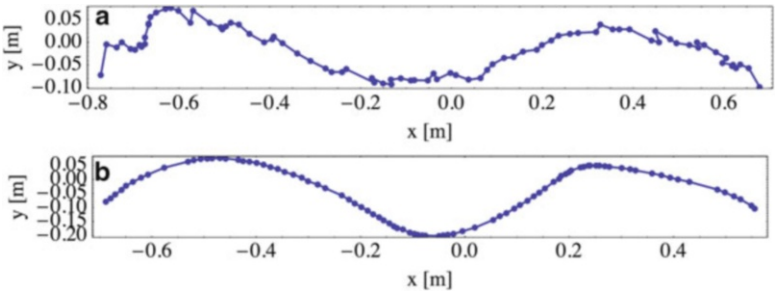

Fig. 4 Comparison of trajectories with (**b**) and without (**a**) use of Gradient Fill algorithm. Trajectory A has significant noise, while trajectory B is very smooth

Due to noise in a depth map data, as well as pedestrian swaying motion, detected local minima may not correspond exactly to head center. In consecutive frames, one can observe discontinuity of detected points. In some cases position change can be higher than actual displacement of the pedestrian. Following Gradient Fill algorithm is proposed to increase accuracy of head center detection:

- Group local minima corresponding to the same pedestrian using minimal distance method.
- For each such group find its central point and mark it as belonging to the shape.
- For any pixel already belonging to the shape, mark its neighbors as belonging to a shape, if their height difference is smaller than a given threshold (Fig. 4).
- Calculate the centroid of the shape.

To increase robustness of the Gradient Fill algorithm, an additional condition is used: difference between given pixel and local minimum also have to be below a given threshold.

There are two significant advantages of detecting shapes connected with local minima:

- Noise in head center detection is significantly reduced (Fig. 4).

- One can easily classify detected shapes, to remove from tracking furniture elements or raised hands.

Detected heads positions on consecutive frames are assembled into trajectories using minimal distance method with a given cut off threshold. Figure 4 shows the difference between trajectories obtained with (b) and without (a) use of Gradient Fill algorithm.

5 Determining Velocity and Position of the Pedestrians

People tend to sway during movement, which results in distortion of straight trajectory if the trajectory of the head is recorded. In Fig. 5 three such trajectories obtained with the Kinect device are shown. For reference one of the trajectories was recorded without the use of the Gradient Fill algorithm. In order to determine actual movement of the pedestrian, influence of the swaying has to be removed. Typical methods based on maxima of curvature [6] fail here as the recorded trajectories are very short. Because of this a new algorithm was developed for determining the center of mass movement. Due to space limit only its short description will be presented. More detailed write-up as well as mathematical background for this method will be published as a separate article.

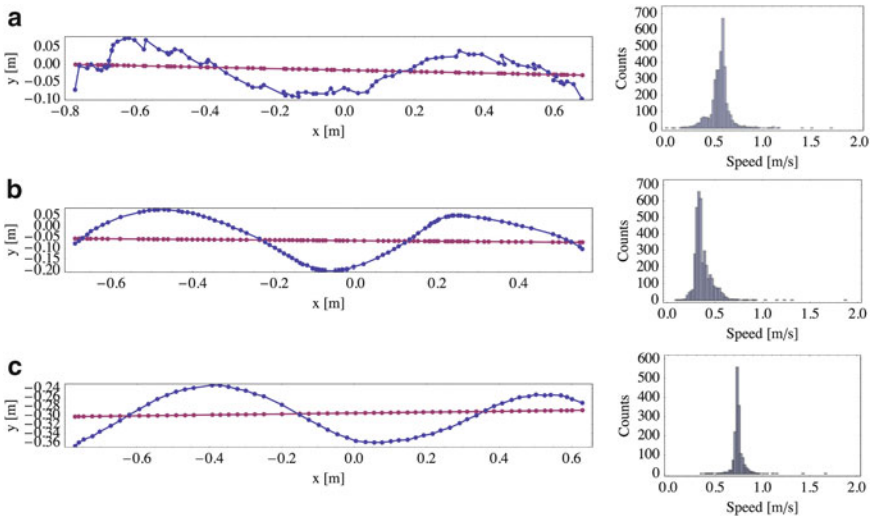

Fig. 5 In the figure three different trajectories (*blue*) recorded using a Kinect device are shown, one of them (**a**) was extracted without the use of Gradient Fill method. For each trajectory its point-to-point velocity histogram can be seen on the *right*. After removal of the swaying motion straight trajectories (*red*) are plotted against original ones

A recorded trajectory consists of 2D points $\mathbf{r}_i = (x_i, y_i)$ labeled with time t_i. The proposed algorithm can be described in the following steps:

- For each pair of points $\mathbf{r}_i, \mathbf{r}_j$ such that $i \neq j$ and $t_i > t_j$ we calculate their relative speed $\mathbf{v}_{ij} = \frac{\mathbf{r}_i - \mathbf{r}_j}{t_i - t_j}$.
- A histogram of relative speed modules is constructed. Most probable value v_p - corresponds to the center of the mass velocity. Such histograms constructed for the three earlier mentioned trajectories can be seen in Fig. 5.
- The most probable speed value v_p depends on the binning method and is always determined with small, but present systematic error. In order to mitigate this a set of values close to v_p is chosen $V_p = \{v_{ij} : \frac{\|v_{ij} - v_p\|}{\|v_p\|} \leq 0.05\}$.
- The center of mass speed $\mathbf{v}_{cm}$ - is calculated as an average of V_p.
- For each point its projection on the direction perpendicular to the $\mathbf{v}_{cm}$ can calculated in order to subtract swaying from the trajectory. Results of this procedure can be seen in Fig. 5.

After performing all steps of the algorithm a straight approximation of the center of the mass movement is obtained. As can be seen the method used is very robust and works well even for very noisy trajectories (see Fig. 5a).

6 Automatic Validation and Calibration with Feedback Loop

The architecture of the system, presented in Sect. 3 is designed to use information from depth sensors to validate and calibrate simulation models online. Both informations about tracked pedestrians and simulation results are sent to a server (see Fig. 1), which compares these results and performs quantitative validation of the simulation. This is a basis for automatic calibration of the simulation parameters.

The described system was used to conduct a simple experiment combining pedestrian tracking and crowd dynamic modeling. Two Microsoft Kinect depth sensors were mounted at two ends of a 22 m corridor (see Fig. 6). Participants were instructed to walk the corridor one by one. As they were passing under the first depth

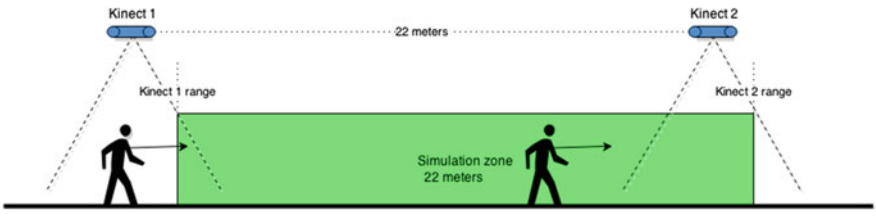

Fig. 6 An experiment overview. The experimental area consisted of a straight corridor with two Kinect depth sensors installed at both ends. Each depth sensor was used to create a tracking zone used for pedestrian tracking and speed estimation

sensor their walking speed was estimated and the moment they left the tracking zone a new agent with desired walking speed based on the measured one was added to the simulation. When pedestrians left the second tracking are their passing time was noted and compared with the simulation results. For the simulation the Social Distances model was used, which is a non-homogeneous CA model based on Hall's proxemics rules [8, 9].

The experiment described above allows an automatic validation of the simulation – as a measure an average deviation of simulated passage time from the real one was chosen:

$$\bar{d} = \frac{1}{N} \sum_{i=1}^{N} \frac{t_{pedestrian_i} - t_{simulated_i}}{t_{pedestrian_i}}. \tag{1}$$

In most models the main parameter of the pedestrians is the desired velocity v_{max}. However, only actual velocity $v_{measured}$, which is some fraction of the v_{max}, can be measured in an experiment. In the proposed setup automatic calibration is possible to mitigate this. In the simplest case this is achieved by multiplying $v_{measured}$ by a calibration parameter k:

$$v_{max} = v_{measured} \cdot k \tag{2}$$

After each group of pedestrians, the simulation was automatically calibrated – parameter k was estimated to minimize the average time deviation. Results of such procedure are shown in Fig. 7.

The authors understand that the presented case of calibration and validation is quite simple. However, this experiment shows that a data-driven approach allows automatic calibration on the fly that can be used to adjustment of the simulation tool to specific conditions.

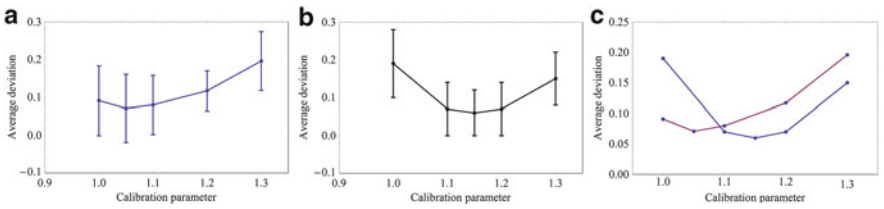

Fig. 7 Calibration results for two runs of experiment (**a**) and (**b**). Results of both runs are shown on (**c**) without uncertainties for clarity

7 Summary

The article presents a complete system of a dynamic data-driven simulation of pedestrian movement. Input data are acquired using depth sensors mounted on the ceiling. A new algorithm of depth map analysis is presented. Morphological erosion and Gradient Filling are used to obtain smooth trajectories. Body mass center trajectories and movement parameters are calculated from head trajectories using a Histogram Method – a robust algorithm, which deals even with noisy data.

Pedestrians tracking is part of a dynamic data-driven simulation. Detected individuals are used to initialize agents in the simulation. Finally, a concept of automatic validation and calibration of simulation models is demonstrated. Feedback information loop allows comparison between tracking and simulation results.

Further works are needed to enlarge possible application area of the described system. The proposed method of automatic validation and calibration should be tested in more sophisticated cases, with more than one calibration parameter. A tracking algorithm requires definition of pedestrian descriptor – vector of individual properties, to distinguish pedestrians passing under different depth sensors. Optimization and parallelization of image analysis methods may be useful in the process of creating a large scale data-driven simulation covering whole retrieved input from many sensors.

References

1. M. Boltes, A. Seyfried, Collecting pedestrian trajectories. Neurocomputing **100**, 127–133 (2013)
2. X. Hu, Dynamic data driven simulation. SCS MS Mag. 662–669 (2011)
3. A. Johansson, D. Helbing, H.Z. Al-Abideen, S. Al-Bosta, From crowd dynamics to crowd safety: a video-based analysis. Adv. Complex Syst. **11**(4), 497–527 (2008)
4. K. Nishinari, A. Kirchner, A. Namazi, A. Schadschneider, Extended floor field CA model for evacuation dynamics. IEICE Trans. **87-D**(3), 726–732 (2004)
5. S. Seer, N. Brändle, C. Ratti, Kinects and human kinetics: a new approach for studying crowd behavior (2012). arXiv:1210.2838v1
6. B. Steffen, A. Seyfried, Methods for measuring pedestrian density, flow, speed and direction with minimal scatter. Phys. A Stat. Mech. Appl. **389**(9), 1902–1910 (2010)
7. K.N. Tran, A. Gala, I.A. Kakadiaris, S.K. Shah, Activity analysis in crowded environments using social cues for group discovery and human interaction modeling. Pattern Recognit. Lett. (2013)
8. J. Wąs, R. Lubaś, Adapting social distances model for mass evacuation simulation. J. Cell. Autom. **8**(5–6), 395–405 (2013)
9. J. Wąs, B. Gudowski, P.J. Matuszyk, Social distances model of pedestrian dynamics, in *Proceedings of 7th ACRI*, Perpignan. LNCS, vol. 4173, 2006, pp. 492–501
10. X. Zhang, J. Yan, S. Feng, Z. Lei, D. Yi1, S.Z. Li, Water filling: unsupervised people counting via vertical kinect sensor, in *IEEE Ninth International Conference on Advanced Video and Signal-Based Surveillance (AVSS)*, Beijing, 18–21 Sept 2012, pp. 215–220

Crowd Research at School: Crossing Flows

Johanna Bamberger, Anna-Lena Geßler, Peter Heitzelmann, Sara Korn, Rene Kahlmeyer, Xue Hao Lu, Qi Hao Sang, Zhi Jie Wang, Guan Zong Yuan, Michael Gauß, and Tobias Kretz

Abstract It has become widely known that when two flows of pedestrians cross stripes emerge spontaneously by which the pedestrians of the two walking directions manage to pass each other in an orderly manner. In this work, we report about the results of an experiment on crossing flows which has been carried out at a German school. These results include that previously reported high flow volumes on the crossing area can be confirmed. The empirical results are furthermore compared to the results of a simulation model which successfully could be calibrated to catch the specific properties of the population of participants.

1 Introduction

1.1 Background: The Science Exchange Program Shanghai – Karlsruhe

The Science Exchange Program Shanghai – Karlsruhe is a student exchange program for students at an age of 16–17 years and come from various high schools from Karlsruhe as well as Shanghai's Jing Ye high school. It is biannually jointly organized by the Schülerakademie Karlsruhe and the Karlsruhe Institute of Technology (KIT). In 2 weeks of which one is held in Karlsruhe and one in Shanghai teams of four to eight pupils (half of them Chinese and half German) work on particular projects which are supervised by University groups, companies or research centers. In 2012 one group decided to analyze crossing pedestrian flows

J. Bamberger • A.-L. Geßler • P. Heitzelmann • S. Korn • R. Kahlmeyer
Bismarckgymnasium, D-76133 Karlsruhe, Germany

X.H. Lu • Q.H. Sang • Z.J. Wang • G.Z. Yuan
Jing Ye High School, Shanghai, China

M. Gauß
Fernstudienzentrum – Karlsruhe Institute of Technology (KIT), 76133 Karlsruhe, Germany

T. Kretz (✉)
PTV Group, D-76131 Karlsruhe, Germany
e-mail: Tobias.Kretz@ptvgroup.com

M. Chraibi et al. (eds.), *Traffic and Granular Flow '13*,
DOI 10.1007/978-3-319-10629-8_16

as their project for their week in Karlsruhe. The main part of the project was to carry out an experiment. Some simulations were done, but for this contribution additional simulations were carried out after the end of the actual student exchange program project.

1.2 History of the Research on Crossing Pedestrian Flows

In 1977 Naka [1] found that in crossing pedestrian flows stripes form which are orthogonal to the sum of the velocity vectors of the two main walking directions. This was confirmed in 1988 by Ando, Ota, and Oki [2]. However, while in the paper by Naka the stripes are sketched[1] more as extended bubbles, with a rather organic appearance, in the later paper the sketch is drawn with straight lines, strictly and clearly separating pedestrians of the two walking directions. This sketch was used in English language papers for example by Hughes [3] or Helbing et al. [4]. In this way the idea of strict and straight stripes spread and was eventually even popularized (e.g. Fisher [5]). Seeing literature evolve in this way the question emerges if the blurry, bubble-shaped stripes describe reality best and the straight stripes are maybe an urban myth resulting from a kind of Chinese Whispers Effect (here rather "Japanese Whispers Effect") or if stripes in crossing flows can actually be seen as clearly as the sketches in more recent popular publications suggest. Making another attempt to decide this question was the purpose of the experiment carried out as part of this project. Furthermore we wanted to test Naka's claim that "The total flow rate of two flows in the crossing can reach nearly the maximum of the flow rate of one direction flow".

Further notable works on crossing pedestrian flows include: an empirical study by Sano and Tatebe [6]; extensive experiments on crossing flows of various angles by Wong et al. and calibrated a simulation model with the data which then gave decreasing flows with increasing intersection angle (i.e. bi-directional flow is more reduced than orthogonally crossing flow) [7]; a work on potential benefit of crowd control by Yamamoto and Okada [8] where both, a macroscopic continuum model as well as a microscopic simulation model, yielded rather clear and straight stripes; Dias et al. found oscillating flows when two groups of ants meet in a crossing flow situation [9]; in a contribution with a theoretical focus Bärwolff et al. also present some empirical data which gives the impression that rather blurry stripes or oscillations were observed [10]. We also point out the contributions of Cividini et al. [11] and Duives et al. [12] in this proceedings book.

[1] One can assume that most readers outside Japan will only have understood the sketches in both papers, as both papers are written in Japanese.

2 Experiment

2.1 Experimental Setup

The participants were a group of 80 pupils most of them at an age of 13 or 14 years. The walking geometry as shown in Fig. 1 was about-8-shaped with a crossing area of 3×3 sq m. In the first run the access corridors had the same width (3 m) as the crossing area, in the second run two desks were added reducing the width to a total of 2.0 m, in the third run one more desk was added, resulting in a total access width of 1.5 m and in the fourth run four desks left an access width of 1.0 m. The camera was placed in a height of approximately 3.5 m above the center point of the crossing area. This was just sufficient to cover the entire crossing area.

2.2 Results of the Experiment

Figure 2 shows a still image from the third run of the experiment. The evaluation was done manually. For this the video footage was partitioned into segments of 20 s. In these 20 s the number of participants leaving the crossing area on the two outbound cross sections has been counted. This number divided by 3 m and 20 s is the specific flow of that particular segment. For density we have counted the number of pedestrians on the crossing area at times $t = 5$ s and $t = 15$ s of the particular segment. The results are displayed in Fig. 3. Segments where the participants obviously were doing other things than walking were not taken into account.

The results are not easy to interpret. With decreasing access width at first density and flow increase, then they decrease and finally the flow is decreased while the density is increased. This could be related to a learning or a tiring effect or both.

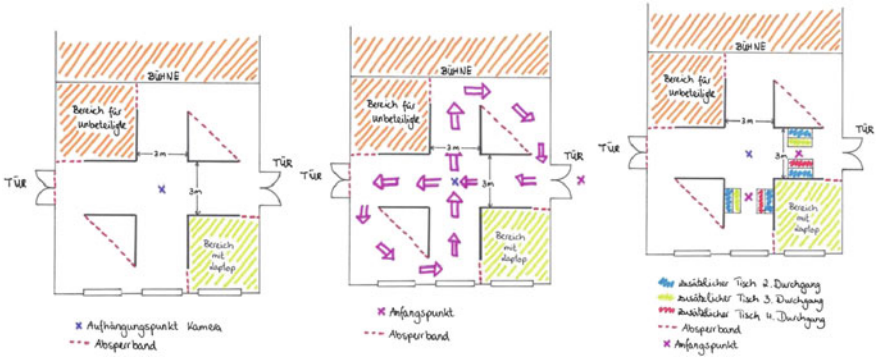

Fig. 1 Sketch of geometrical setup

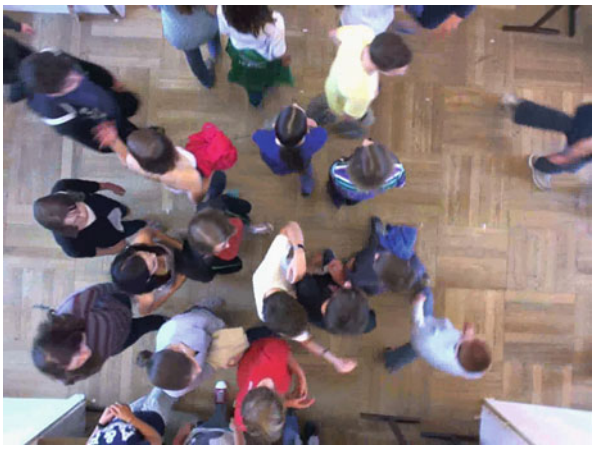

Fig. 2 Still image from the third run with three desks restricting flow into the crossing area

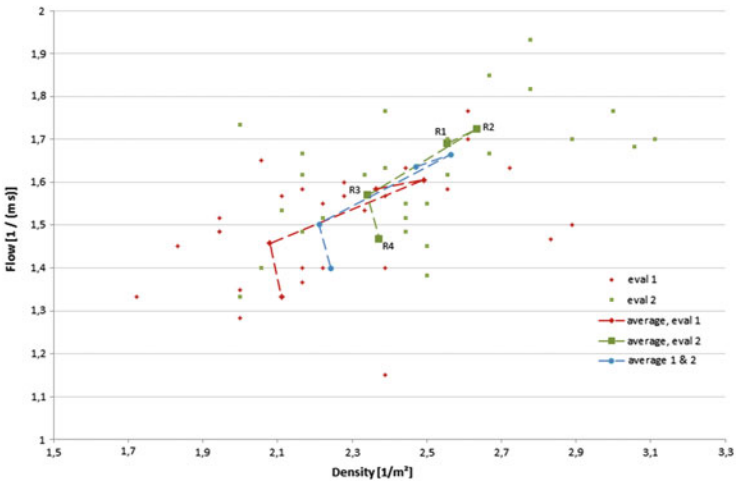

Fig. 3 Results of manual counts of two persons (*red diamond* and *green squares*) as well as their averages for each run (*R1–R4*). Note that the lower left corner of the diagram is not the offspring. The *blue circles* mark the average of both counts. It is remarkable how stable the bias between the two counting persons is. One may conjecture that it is more difficult to estimate if a person is still on the crossing area or right next to it than it appears and that each counting person has had different lines in mind to judge this

However, indisputably the specific flow is high, as Naka stated "nearly the maximum of the flow rate of one direction flow". Concerning the organization of the flow we report that to us it appeared that there were rather bubbles moving, almost oscillations of the right of way. Sometimes one could realize rather clear stripes, but these were stable only for a few seconds – about as long as it takes for a person to cross the crossing area.

3 Simulation

It is a natural next question if the empirical results can be reproduced with a simulation model of pedestrian dynamics. We have tried to do so using PTV Viswalk [13–16] and in a first attempt achieved slightly too small densities and by far a too small flow. This is, however, not a surprise, as we could not expect to have the simulation reproduce results with this special population of participants applying nothing but the default parameters. The first, obvious modification was to make the simulated pedestrians smaller than by default as the participants were all children or young youths. When we applied the changes as shown in Table 1 the results matched much better as can be seen in Fig. 4.

We have noted that it is crucial for the movement pattern how wide the distribution of desired speeds is. If everyone has (nearly) identical desired speed the emerging stripes are clear, straight, and stable. The wider the distribution is the more the stability is reduced and a deadlock consequently occurs at lower density

Table 1 Parameter modifications for calibration. Within the bounds of desired speed (v_0) and body radius the values were equally distributed in either case

Parameter	Default	Calibrated
v_0^{min}	0.72 m/s	1.25 m/s
v_0^{max}	1.61 m/s	1.53 m/s
Body radius (min)	16 cm	11 cm
Body radius (max)	23 cm	19 cm
tau	0.40 s	0.37 s
$A_{soc,iso}$	1.6 m/s^2	2.2 m/s^2
$A_{soc,mean}$	0.4 m/s^2	0.2 m/s^2
Δt (aka VD)	3 s	2 s

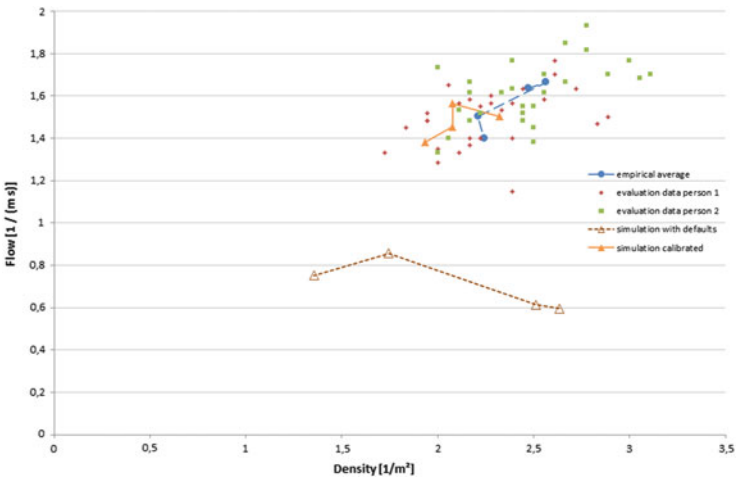

Fig. 4 Simulation and empirical results in comparison

and flow. This is – by the way – also the case for bi-directional flow for which this relation has recently been found as well in an empirical investigation [17].

It is interesting to note that the values of the A parameters had to be changed into different directions. $A_{soc,iso}$ sets the base impact of the variant of the Social Force Model as introduced in [18] while $A_{soc,mean}$ determines the strength of the elliptical specification II as introduced in [19]. This necessity for divergent modification shows how different the two variants actually are. While most parameter changes had an effect on either the density on the crossing area or the flow or both, interestingly simulation results were nearly insensitive to the choice if pedestrians followed a static or a dynamic potential [20] over the crossing area – a difference which has been found to have a heavy impact on the course of simulations of other situations [21–24]

Note that the calibration process has been carried out with regard to the empirical data of the first evaluating person. It could have been done as well according to the average or the result of evaluating person 2, but considering the large scattering of empirical data it does not make sense to attempt to achieve a very precise agreement of simulated and empirical data as obviously the empirical data yield considerable variation and potential errors. We therefore see it as sufficient agreement when the average of simulation data is within the cloud of empirical data points.

Excerpts from a simulation run with clear stripes (narrow speed distribution), excerpts from the experiment, and excerpts from the calibrated simulation can be seen in a video at this URL: youtu.be/vdjbIYpa1XE.

Conclusions

As a summary we conclude that in our experiment on crossing pedestrian flows the formerly reported high flows and densities were confirmed. We did not see, however, the formation of clear and stable stripes. The movement pattern most of the time was rather bubble-shaped towards oscillating flow directions. When there were stripes they disappeared again soon. This does not mean that there are no situations with more stable stripes. It could be that stripes emerge more clearly when the crossing area is larger. One can also argue that our population of participants was rather individualistic and rather not willing to adapt walking speeds mutually (remembering that simulations had shown that narrow distributions of desired speeds lead to a more pronounced stripe formation). Furthermore the corridors leading to the crossing area were rather short such that there was no time for the pedestrians to pre-sort themselves. Finally the demand (the inflow) on the crossing area was relatively high in all four runs. Only in the last run the access width was below half of the corridor width. This means that in the first three runs in sum demand met or was above the capacity of the crossing area and probably

(continued)

this was the case even in the last run with an access width of 2×1 m. Maybe stripes emerge rather at demands clearly below capacity.

In other words as hints for anyone who might want to do a similar experiment we note that first: it would have been interesting to do the experiment with an even smaller inflow opening width, second: to potentially allow the formation of stripes a larger crossing area was required, third: it would have been helpful for evaluation to record a larger environment of the crossing area, fourth: 80 participants was just enough or rather few for this geometry, fifth: the inflow regulating obstacles (tables) should better have been placed further upstream to allow the stream to fully expand until it reaches the crossing area.

The conclusion concerning the simulation is that it is possible to reproduce the empirically observed behavior to that degree of detail to which we analyzed the empirical data plus a visual comparison of movement patterns. The parameters of the simulation had to be adapted for this. The default parameters led to – compared to our experiment and our population of participants – clearly more conservative results.

As last conclusion we would think that the science of pedestrians (and vehicles) can contribute in many interesting ways to education at school. Pupils and students at secondary schools are involved with the topic in various ways in their everyday lives and the systems as such are well suited to introduce with them a number of concepts of mathematics and computer science.

Acknowledgements We thank Yusuke Okahira from Kozo Keikaku Engineering (KKE) for help with some of the Japanese papers.

References

1. Y. Naka, Mechanism of cross passenger frow – study on complicated passenger flow in railway station (part 1). Trans. Archit. Inst. Jpn. **258**, 93–102 (1977). In Japanese language
2. K. Ando, H. Ota, T. Oki, Forecasting the flow of people. Railw. Res. Rev. **45**(8), 8–14 (1988). In Japanese language
3. R.L. Hughes, A continuum theory for the flow of pedestrians. Trans. Res. Part B: Methodol. **36**(6), 507–535 (2002)
4. D. Helbing, L. Buzna, A. Johansson, T. Werner, Self-organized pedestrian crowd dynamics: experiments, simulations, and design solutions. Transp. Sci. **39**, 1–24 (2005)
5. L. Fisher, *The Perfect Swarm: The Science of Complexity in Everyday Life* (Basic Books, New York, 2009)
6. T. Sano, K. Tatebe, The difficulty of crossing pedestrian flow field experiment and avoidance behavior model. Bull. Aichi Inst. Technol. **35**, 167–172 (2000)
7. S.C. Wong, W.L. Leung, S.H. Chan, W.H.K. Lam, N.H.C. Yung, C.Y. Liu, P. Zhang, Bidirectional pedestrian stream model with oblique intersecting angle. J. Transp. Eng. **136**(3), 234–242 (2010)

8. K. Yamamoto, M. Okada, Continuum model of crossing pedestrian flows and swarm control based on temporal/spatial frequency, in *2011 IEEE International Conference on Robotics and Automation (ICRA)*, Shanghai (IEEE, 2011), pp. 3352–3357
9. C. Dias, M. Sarvi, N. Shiwakoti, Intersecting and merging pedestrian crowd flows under panic conditions: insights from biological entities, in *35th Australasian Transport Research Forum (ATRF)*, Perth, 2012
10. G. Bärwolff, M. Chen, F. Huth, G. Lämmel, M. Plaue, H. Schwandt, Methods for modeling and simulation of multi-destination pedestrian crowds, in *Pedestrian and Evacuation Dynamics 2012*, ed. by U. Weidmann, U. Kirsch, M. Schreckenberg (Springer, Cham, 2014)
11. J. Cividini, C. Appert-Roland, H.-J. Hilhorst, Generic instability at the crossing of pedestrian flows, in *Traffic and Granular Flow 2013*, ed. by M. Boltes, M. Chraibi, A. Schadschneider, A. Seyfried, pp. 13–20 (Springer, Berlin/Heidelberg, 2014)
12. D.C. Duives, W. Daamen, S.P. Hoogendoorn, Quantitative Estimation of Self-Organization in Bi-directional and Crossing Flows During Crowd Movements, in *Traffic and Granular Flow 2013*, ed. by M. Boltes, M. Chraibi, A. Schadschneider, A. Seyfried, pp. 251–256 (Springer, Berlin/Heidelberg, 2014)
13. T. Kretz, S. Hengst, P. Vortisch, Pedestrian flow at bottlenecks – validation and calibration of VISSIM's social force model of pedestrian traffic and its empirical foundations, in *International Symposium of Transport Simulation 2008 (ISTS08)*, ed. by M. Sarvi, page electronic publication, Gold Coast (Monash University, 2008)
14. C. Bönisch, T. Kretz, Simulation of pedestrians crossing a street, in *Traffic and Granular Flow'09*, 2011. Accepted for publication
15. A.S. Sahaleh, M. Bierlaire, B. Farooq, A. Danalet, F.S. Hänseler, Scenario analysis of pedestrian flow in public spaces, in *Proceedings of the 12th Swiss Transport Research Conference (STRC)*, Ascona, May 2012, pp. 2–4
16. T. Kretz, F. Reutenauer, F. Schubert, Multimodal simulation-based planning for pedestrians, in *92nd Annual Meeting of the Transportation Research Board*, Washington, D.C., 2013
17. M. Moussaïd, M. Guillot, E.G. Moreau, J. Fehrenbach, O. Chabiron, S. Lemercier, J. Pettré, C. Appert-Rolland, P. Degond, G. Theraulaz, Traffic instabilities in self-organized pedestrian crowds. PLoS Comput. Biol. **8**(3), e1002442 (2012)
18. D. Helbing, I. Farkas, T. Vicsek, Simulating dynamical features of escape panic. Nature, **407**(6803), 487–490 (2000)
19. A. Johansson, D. Helbing, P.K. Shukla, Specification of the social force pedestrian model by evolutionary adjustment to video tracking data. Adv. Complex Syst. **10**(supp02), 271–288 (2007)
20. T. Kretz, A. Große, S. Hengst, L. Kautzsch, A. Pohlmann, P. Vortisch, Quickest paths in simulations of pedestrians. Adv. Complex Syst. **14**, 733–759 (2011)
21. T. Kretz, S. Hengst, V. Roca, A. Pérez Arias, S. Friedberger, U.D. Hanebeck, Calibrating dynamic pedestrian route choice with an extended range telepresence system, in *2011 IEEE International Conference on Computer Vision Workshops*, pp. 166–172, 2011; *First IEEE Workshop on Modeling, Simulation and Visual Analysis of Large Crowds*, Barcelona, Nov 2011, pp. 6–13
22. T. Kretz, A. Große, From unbalanced initial occupant distribution to balanced exit usage in a simulation model of pedestrian dynamics, in *Human Behaviour in Fire Symposium*, Cambridge, ed. by T.J. Shields et al. (Interscience Communications, 2012), pp. 536–540
23. T. Kretz, Multi-directional flow as touch-stone to assess models of pedestrian dynamics, in *Annual Meeting of the Transportation Research Board*, Washington, D.C., 2013
24. T. Kretz, The effect of integrating travel time, in *Pedestrian and Evacuation Dynamics 2012*, ed. by U. Weidmann, U. Kirsch, M. Schreckenberg (Springer International Publishing, 2014), pp. 1013–1027

Stair Evacuation Simulation Based on Cellular Automata Model Considering Social Forces

Ning Ding, Tao Chen, Hui Zhang, and Peter B. Luh

Abstract Building evacuation in case of emergencies has long been recognized as a crucial issue, especially for the stair evacuation because evacuees may spend most of the evacuation time in stairs. To predict the evacuation time in stairs, simulations are commonly used, but known simulations ignore the stair structure and the fact that people may change their speeds during evacuation. As a result, how to introduce a reasonable mechanism on how evacuees change their speeds and improve the stair evacuation simulation are important. In this paper, a new Cellular Automata (CA) model where a new grid map is introduced based on the stair structure, and then the interaction among evacuees can be simulated better than the existing CA simulations. To make a reasonable mechanism of changing speed, the social forces will be introduced to the new CA model based on the advantages of social force models. However, social force model is a continuous model and CA model is a discrete model, and there is a gap to use social forces directly into a discrete model. To bridge the gap, the system time interval is shortened, and then evacuees have variable speeds by updating their positions during several intervals. To validate this simulation, an experiment was held in a high-rise building. In the fire drill, harmless smoke was released to make the drill similar to real events. The simulation results are similar to the fire drill data by comparing evacuation time.

1 Introduction

Building evacuation in case of emergencies has long been recognized as an important issue, especially for the evacuation in stairs because the stair is the only way to evacuate. For building safety, simulations are commonly used, but most

N. Ding (✉)
Center for Intelligent and Networked Systems, Tsinghua University, Beijing, China
e-mail: ding-n11@mails.tsinghua.edu.cn; dingning_hit@126.com

T. Chen • H. Zhang
Institute of Public Safety Research, Tsinghua University, Beijing, China
e-mail: chentao.a@tsinghua.edu.cn; zhhui@mail.tsinghua.edu.cn

P.B. Luh
Department of Electrical and Computer Engineering, University of Connecticut, Storrs, CT, USA
e-mail: Peter.Luh@uconn.edu

M. Chraibi et al. (eds.), *Traffic and Granular Flow '13*,
DOI 10.1007/978-3-319-10629-8_17

of the existing simulations ignore the stair structure and the fact that people may change their speeds during evacuation. As a result, how to introduce a reasonable mechanism on how evacuees change their speeds and improve the stair evacuation simulation are important.

Among the simulation models, the social force model and CA models are the most popular. Social force model [1, 2] is a continuous model, which is good at simulating the evacuation process in a room or a corridor. Several virtual forces called "social forces", which make the model reasonable to simulate human behaviors, are introduced in the model. But social force model is computational complex, and it is not appropriate for simulating stair evacuation because such kind of evacuation is always large-scale. On the contrary, CA model [3–7] is a discrete model, which is fit for both small-scale and large-scale evacuation [1, 8–12]. But the transition rule, which decides how evacuees move, is defined based on experience [2, 13, 14]. Furthermore, the existing CA simulation cannot reflect the human behaviors well in stairs based on traditional grid and cell size [7, 15, 16].

To improve stair evacuation simulation, a new CA model is established in Sect. 2. According to our previous work [17], a new simulation map is drawn according to both human body size and stair structure. To make a mechanism to change evacuees' speeds reasonably, the concept of social force will be introduced to the new CA model based on the advantages of social force models. However, as mentioned above, social force model is a continuous model and CA model is a discrete model. There is a gap to use social forces directly into a discrete model, and the system time interval is shortened to bridge the gap. Evacuees have variable speeds by updating their positions during several intervals, and social forces, such as self-driven force and push force, are used to change evacuees' speeds.

To validate this simulation in Sect. 3, an experiment held in a high-rise building was video recorded. In the experiment, 33 people evacuate from the 10th floor to the lobby. A simulation is carried out based on the experiment. The simulation results are similar to the fire drill data by comparing evacuation time.

2 Problem Formulation

A new CA model for stair egress simulation is established in this section. In Sect. 2.1, to improve the basic structure of CA model, a size of the cell and a new grid map are drawn based on the structure of stairs (tread and landing). Then the neighborhood and transition rule are introduced in Sect. 2.2. As the grid map is divided into six areas [17], the transition rule is defined separately on each area. In Sect. 2.3, several social forces are introduced in the simulation model. There are two kinds of social forces: self-driven force and push force.

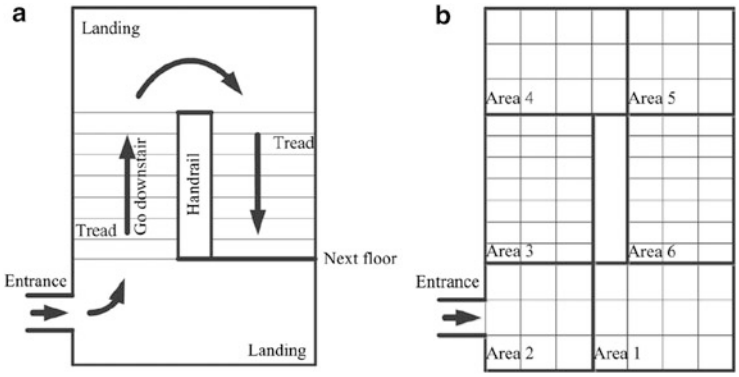

Fig. 1 The stair structure and the six areas of stair

2.1 Cell Size and Grid Map

CA model is a kind of discrete model where both the space and the time are discrete. In the existing studies, the cell size is 0.4 [4] or 0.5 m [18] which is similar to the cell size used in the corridor simulation. In our new model, the cell size is drawn based on the stair structure and human body size. Given this, the cell size of the tread area is the width of the shoulder the depth of the tread since one pedestrian can only occupy a space on one tread. Landings (as is shown in Fig. 1) are connected with treads, and the cell size of the landings is the width of the shoulder the width of the shoulder. This cell size is larger than that on the tread because it is used to simulate turning behaviors on landings. To connect the landings and the treads, the joint cell size of the landing and tread is the width of the shoulder. Stair structure is shown in Fig. 1a, and the corresponding cell space is shown in Fig. 1b. To distinguish pedestrians of different directions, the stair on between two floors is divided into six areas: Areas 1–6. The moving directions on these areas are also different, and the directions are the same as it is shown in Fig. 1a.

2.2 Neighborhood and Transition Rules

Neighborhood cells are the environment around an evacuee, and the neighborhoods on treads and landings are not the same in the model. When evacuees are going downstairs, they will move forward, left ahead or right ahead (shown in Fig. 2a) because evacuees can hardly move back, move to the left, or move to the right in stairs. As a result, the neighborhood on the treads areas is the three cells in the front of an evacuee which is shown in Fig. 2b. For landings, the neighborhood is the eight cells around a pedestrian because he/she can move to any direction on a horizontal

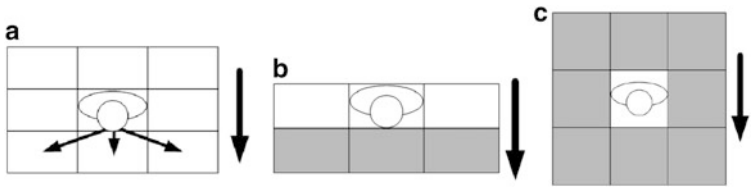

Fig. 2 Neighborhoods on treads and landings

place. This neighborhood is a typical Moore [12] neighborhood which is shown in Fig. 2c.

The rule of pedestrian's movement in the simulation is defined as transition rule, and the transition rule determines the pedestrian's moving directions and positions in the next system time interval. As the stair on each floor is divided into six areas, the transition rule of each area is defined separately to measure the probabilities of the moving directions of pedestrians in the next time interval. Take Area 3 for example, the destination of pedestrians in Area 3 is Area 4, and one pedestrian has three directions to move: straight forward, left ahead and right ahead. If one of pedestrian's moving direction is blocked, the probability of which direction he/she moves to will change. In the transition rule in Area 3, P_F, P_L, P_R, and P_S represents the probability of chosen the direction forward, left ahead,right ahead and stop, respectively. As they are probabilities of one event, we have $P_F+P_L+P_R+P_S = 1$. The transition probabilities of pedestrian movement are as follows:

$$P_F = \frac{1}{3}, p_L = \frac{1}{3} - w, P_R = \frac{1}{3} + w, P_S = 0; \tag{1}$$

$$P_F = 0, P_L = 0, P_R = 0, P_S = 1; \tag{2}$$

$$P_F = \frac{1}{2} - \frac{3w}{2}, P_L = 0, P_R = \frac{1}{2} + \frac{3w}{2}, P_S = 0; \tag{3}$$

$$P_F = 0, P_L = \frac{1}{4} - \frac{3w}{4}, P_R = \frac{3}{4} + \frac{3w}{4}, P_S = 0; \tag{4}$$

$$P_F = \frac{1}{2} + \frac{3w}{2}, P_L = \frac{1}{2} - \frac{3w}{2}, P_R = 0, P_S = 0; \tag{5}$$

$$P_F = 0, P_L = 1, P_R = 0, P_S = 0; \tag{6}$$

$$P_F = 1, P_L = 0, P_R = 0, P_S = 0; \tag{7}$$

$$P_F = 0, P_L = 0, P_R = 1, P_S = 0. \tag{8}$$

In the new model, the tendency of walking along the inner of a stair is considered in the transition rules. To simulate the tendency of walking, a parameter w is introduced with $0 \leq w \leq 1/3$. The transition rule on the landings is similar to the rule (Eqs. (1)–(8)) on the tread.

2.3 Social Forces

The basic assumption of the social force model is that the interactions among evacuees are determined by "social forces" which are not real forces, but such forces will influence people's movement. The social forces in the social force model [14] are as follows:

$$m_i \frac{d\overrightarrow{v}_i}{dt} = m_i \frac{v_i^0 \overrightarrow{e}_i^0(t) - \overrightarrow{v}_i(t)}{\tau_i} + \sum_{j \neq i} f_{ij} + \sum_{w} f_{iw}, \tag{9}$$

where m_i and $\overrightarrow{v}_i$ is the mass and velocity of pedestrian i,respectively. The desired velocity value of pedestrian i is v_i^0, and the direction of this velocity at time t is $\overrightarrow{e}_i^0(t)$. The τ_i is a relaxation time of a pedestrian to achieve the desired velocity, and it equals 0.5 s in the social force model. Social force $\overrightarrow{f}_{ij}$ reflects the forces by other pedestrians, and $\overrightarrow{f}_{iw}$ represents the force by the wall. To introduce social forces to change the speeds, variable speed is required in the new simulation model. The simulation time interval is shortened, and the pedestrians can update their positions (no more one cell) in several time intervals.

Two kinds of social forces, self-driven force and push force, will be introduced to change the pedestrians' speeds in the new simulation. Self-driven force $\overrightarrow{f}_S$ is a force driven by the inner desire, which is reflected by the concept "desired velocity" or desired speed in the paper, to move to the exits as fast as possible. The force is similar to the desired velocity mentioned in the original social force model:

$$\overrightarrow{f}_S = m_i \frac{\overrightarrow{v}_d(t) - \overrightarrow{v}_i(t)}{\tau_i}, \tag{10}$$

where $\overrightarrow{v}_d(t)$ and $\overrightarrow{v}_i(t)$ is the desired speed and current speed of pedestrian i at time t. Push forces are used to demonstrate the forces among evacuees, and such forces including two kinds: forward push force $\overrightarrow{f}_{FP}$ and backward push force $\overrightarrow{f}_{FP}$. Forward push force is the force from the people in the back, and this force is related to the speeds of a pedestrian i and a pedestrian j who is in the back of pedestrian i. If $|\overrightarrow{v}_i(t)| > |\overrightarrow{v}_j(t)|$, $\overrightarrow{f}_{FP} = 0$; otherwise, $\overrightarrow{f}_{FP}$ is as follows:

$$\overrightarrow{f}_{FP} = m_i \frac{\overrightarrow{v}_j(t) - \overrightarrow{v}_i(t)}{\tau_i}, |\overrightarrow{v}_j(t)| \leq |\overrightarrow{v}_j(t)|, \tag{11}$$

where $\overrightarrow{v}_i(t)$ and $\overrightarrow{v}_j(t)$ is the speed of pedestrian i and pedestrian j, respectively. On the contrary, the backward push force $\overrightarrow{f}_{BP}$ is the force from the people in the front, and this force is related to the speeds of a pedestrian i and a pedestrian j who is in the front of pedestrian i. If $|v_j(t)| > |\overrightarrow{v}_i(t)|$, $\overrightarrow{f}_{BP} = 0$; otherwise, $\overrightarrow{f}_{BP}$ is as follows:

$$\overrightarrow{f}_{BP} = m_i \frac{\overrightarrow{v}_j(t) - \overrightarrow{v}_i(t)}{\tau_i}, |v_j(t)| \leq |\overrightarrow{v}_i(t)|. \tag{12}$$

Above all, the final social force equation is as follow:

$$13\, m_i \overrightarrow{a}_i(t) = \overrightarrow{f}_S + \overrightarrow{f}_{FP} + \overrightarrow{f}_{BP} \tag{13}$$

where $a_i(t)$ is the acceleration of pedestrian i at time t, and the change of the speed is $\Delta v_i = a_i t$.

3 Validation and Simulation

To validate the simulation model, an experiment was held in a high-rise building, and there are 33 people took part in the experiment. The participants are all undergraduate students in Tsinghua University, and they all evacuated from the 10th floor of the building. When the alarm sounded, they start to evacuate from their rooms and all of them were told to use a specified stair in the building (a snapshot of the evacuation process is shown in Fig. 3).

The simulation is carried out according to the experiment data. The width of an evacuee's shoulder is 0.5 m and the length of the tread in the building is 0.3 m. So

Fig. 3 A snapshot of experiment process

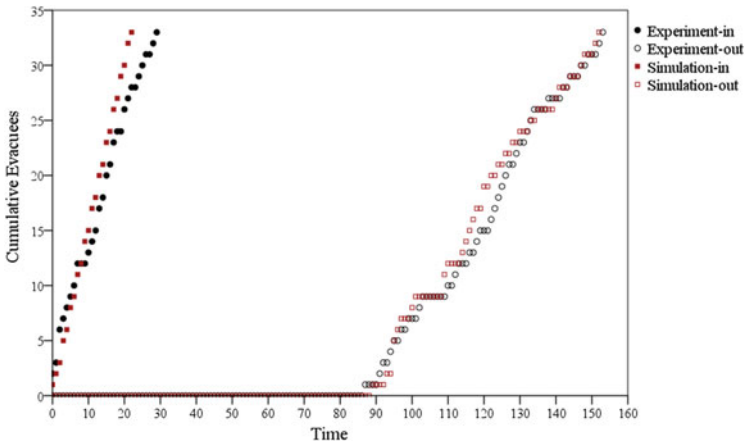

Fig. 4 Cumulative evacuees of experiment and simulation

the cell size on tread is $0.5 \times 0.3\,m^2$ and the cell size of the landing is $0.5 \times 0.5\,m^2$. Parameter w equals 0.2 to demonstrate that people incline to evacuate along the inner side of the stair. The desired speed (horizontal speed) of an evacuee is 0.85 m/s according to the free speed (tested in the building) of people in emergency conditions. The simulation is run in Matlab 7.8.0 and tested on an Intel Core i3 + 2.3 GHz Windows PC with 2 GB RAM. The simulation is run 20 times and the average CPU time is 8.32 s. Then we use IBM SPSS Statistics 19 to analyze the simulation data.

The evacuation times of the experiment data and the simulation results are shown in Fig. 4. The experiment-in and experiment-out data mean the times of evacuees entered in and exit out of the stair, so as to the simulation-in and simulation-out. The time of simulation-in is also shown in Fig. 4. The evacuation time of the experiment data is 153 s, and the result of simulation is 152 s, which is only 1 s smaller than the experiment data.

The data used for linear regression is from 87 to 153 s because the first pedestrian appears at 87 s and the last one evacuates out at 153 s. The linear regressions of the experiment-out data and the simulation-out result are as follows:

$$Experiment - out : y = 0.505x - 44.140,\ R^2 = 0.994, \tag{14}$$

$$Simulation - out : y = 0.511x - 44.054,\ R^2 = 0.993. \tag{15}$$

The slope and intercept of the experiment and simulation are similar to each other. Above all, the simulation results are similar to the experiment data according to the total evacuation times and the linear regressions.

Conclusion

This paper improves the stair evacuation simulation problem considering social forces. In the new simulation model, basic structure of the CA model is improved based on the structures of the stairs, and two kinds of social forces are introduced to change evacuees' speeds. The self-driven force is used to demonstrate the people's evacuation desire, and push forces are used to show the interactions among evacuees. To validate the new simulation, an experiment with 33 people is held in a high-rise building, and a simulation is carried out based on the experiment. Compared with the experiment data, the simulation results are accurate according to the evacuation time.

In the future, more experiments are required to validate the simulation from the micro level, and optimization guidance should be studied based on the new simulation.

References

1. D. Helbing, P. Molnár, Social force model for pedestrian dynamics. Phys. Rev. E **51**(5), 4282–4286 (1995)
2. D. Helbing, I. Farkas, P. Molnár, T. Vicsek, Simulation of pedestrian crowds in normal and evacuation situations, in *Pedestrian and Evacuation Dynamics*, ed. by M. Schreckenberg, S. D. Sharma (Springer, New York, 2002), pp. 21–58
3. A. Varas, M.D. Cornejo, D. Mainemer, B. Toledo, J. Rogan, V. Muñoz, J.A. Valdivia, Cellular automaton model for evacuation process with obstacles. Physica A **382**, 631–642 (2007)
4. A. Kirchner, K. Nishinari, A. Schadschneider, Friction effects and clogging in a cellular automaton model for pedestrian dynamics. Phys. Rev. E **67**(5), 056122 (2003)
5. A. Kirchner, A. Schadschneider, Simulation of evacuation processes using a bionics-inspired cellular automaton model for pedestrian dynamics. Physica A **312**, 260–276 (2002)
6. W.G. Weng, T. Chen, H.Y. Yuan, W.C. Fan, Cellular automaton simulation of pedestrian counter flow with different walk velocities. Phys. Rev. E **74**, 036102 (2006)
7. K. Yamamoto, S. Kokubo, K. Nishinari, Simulation for pedestrian dynamics by real-coded cellular automata (RCA). Physica A **379**(2), 654–660 (2007)
8. R.D. Peacock, J.D. Averill, E.D. Kuligowski, *Stairwell Evacuation from Buildings: What we Know we Don't Know* (U.S. Department of Commerce, National Institute of Standards and Technology, Gaithersburg, 2010)
9. S. Gwynne, E.R. Galea, M. Owen, P.J. Lawrence, L. Filippidis, A review of the methodologies used in the computer simulation of evacuation from the built environment. Build. Env. **34**(6), 741–749 (1999)
10. G. Proulx, Movement of people: the evacuation timing, in *The SFPE Handbook of Fire Protection Engineering. Society of Fire Protection Engineers* (National Fire Protection Association, Quincy/Society of Fire Protection Engineers, Bethesda, 2002), pp. 3341–3366
11. J. Lord, B. Meacham, B. Moore, R. Fahy, G. Proulx, *Guide for Evaluating the Predictive Capabilities of Computer Egress Models* (National Institute of Standards and Technology, Gaithersburg, 2005), pp. 806–886
12. N. Pelechano, A. Malkawi, Evacuation simulation models: challenges in modeling high rise building evacuation with cellular automata approaches. Autom. Constr. **17**(4), 377–385 (2008)

13. D. Helbing, L. Buzna, A. Johansson, T. Werner, Self-organized pedestrian crowd dynamics: experiments, simulations, and design solutions. Transp. Sci. **39**(1), 1–24 (2005)
14. D. Helbing, I. Farkas, T. Vicsek, Simulating dynamical features of escape panic. Nature **407**(6803), 487–490 (2000)
15. D. Helbing, A. Johansson, H.Z. Al-Abideen, Dynamics of crowd disasters: an empirical study. Phys. Rev. E **75**(4), 046109 (2007). PRE
16. S. Wolfram, Statistical mechanics of cellular automata. Rev. Mod. Phys. **55**(3), 601 (1983)
17. N. Ding, P.B. Luh, H. Zhang, T. Chen, Emergency evacuation simulation in staircases considering evacuees' physical and psychological status, IEEE International Conference on Automation Science and Engineering (IEEE CASE, 2013), pp. 741–746
18. J. Ma, S.M. Lo, W.G. Song, W.L. Wang, J. Zhang, G.X. Liao, Modeling pedestrian space in complex building for efficient pedestrian traffic simulation. Autom. Constr. **30**(0), 25–36 (2013)

Simulation of Building Evacuation Considering Information Flow

Yuan Gao, Tao Chen, Peter B. Luh, and Hui Zhang

Abstract Modeling and simulating building evacuation are effective to study human crowd and evaluate evacuation facilities. In most building evacuation models, occupants are assumed to have static information on the layout of the building. However, in reality occupants are able to obtain information from surroundings (e.g., alarms, exit signs or movement of other occupants). The information changes occupants' decision-making and movement in turn. This paper considers information flow during evacuation and combines the information flow model with a modified social force model by updating the desired velocities of occupants. Inertia is also added for occupants to maintain their desired direction so that oscillations between different targets are reduced. Several cases are studied by simulation and results show that the information significantly affects the evacuation process and with the information model, the simulation is more realistic.

1 Introduction

Modeling and simulating building evacuation are effective for evaluating evacuation facilities and analyzing risks during evacuation [11], because they cost significantly less than experiments. Many evacuation models have been developed, including network models [2], fluid dynamics models [6], route choice models [8], queuing models [10], cellular automata (CA) models [9, 13], optimal velocity models [12], and social force models [3–5]. In most of the existing models, occupants are assumed to have static information on the layout of the building. However, in reality occupants are able to obtain information from surroundings (e.g., alarms, exit

Y. Gao (✉)
Center for Intelligent and Networked Systems, Tsinghua University, Beijing, China
e-mail: y-gao06@mails.tsinghua.edu.cn

T. Chen • H. Zhang
Institute of Public Safety Research, Tsinghua University, Beijing, China
e-mail: chentao.a@tsinghua.edu.cn; hzhangsb@gmail.com

P.B. Luh
Department of Electrical and Computer Engineering, University of Connecticut, Storrs, CT, USA
e-mail: Peter.Luh@uconn.edu

M. Chraibi et al. (eds.), *Traffic and Granular Flow '13*,
DOI 10.1007/978-3-319-10629-8_18

signs or movements of other occupants), and the information changes occupants' decision-making and movement. It is also reported that a lack of information may increase individuals impatience, thus becoming the source of disorder and blocking [1] during evacuation. The information plays an important role in evacuation and occupants need to make decisions under different or even opposite information. Studies on modeling information during evacuation include CA models which described the communication between occupants using the ideas from chemotaxis [9]: every occupant is information source that sends information to the space. The information diffuses and evaporates following analogously to ant pheromones: other occupants are attracted by it. Extensions were also made [7]: a framework of swarm information models was developed which allows agents to have different views of the world, so that agents can be modelled heterogeneous. Dynamic information in the above models only affects occupants' local movement, i.e., the probability to move to the adjacent cells; and occupants may oscillate between different directions. This paper builds an information model during evacuation. This information flow model is also combined with modified social force models [3], in which desired velocity reflects occupants way finding. Inertia is also added for occupants to maintain their desired direction so that oscillations are reduced. Several cases are studied by simulation and results show that information significantly affects the evacuation process.

This paper is organized as follows: Sect. 2 provides an information model and combines it with modified social force models [3], in which occupants obtain dynamic information from their surroundings and update their movement by changing their desired velocities; Sect. 3 are case studies. Evacuation from a large room with two exits is studied. Occupants receive information from both exit signs and other occupants. By comparing the results from models with and without information, it is concluded that with the information model can describe individual occupants more precisely and more realistic.

2 Modeling

This section provides a framework of information model in Sect. 2.1 and combines it with the modified social force model in Sect. 2.2.

2.1 Framework of the Information Model

A general framework of the information model during evacuation is shown in Fig. 1. An "information field" is introduced in the framework. The information field reflects distribution of information in the space. Exit signs, alarms and occupants are all information sources that send information into the space. Occupants may have prior information of the layout of the building before evacuation, and they keep

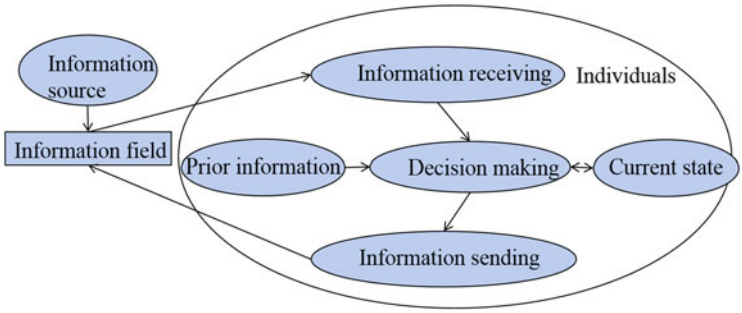

Fig. 1 The framework of the information model

on receiving information from the information field. Decisions on selecting ways to evacuate are made based on the prior information, their current states (e.g., current positions and velocities) and information they have obtained. The decisions change the movement of occupants, which in turn serves as information sources.

Information is important during the evacuation. Properties of the information include:

- Source (S). There are different types of information source, e.g., prior information, exit signs, alarms, and other occupants. The information is divided into groups indexed by s according to the source.
- Message (M). The information may lead occupants to a specified target (e.g., exit); or implicitly affect individuals movement, e.g., a lack of information may increase individuals impatience, thus becoming the source of disorder and blocking. This paper only discusses the former information, and the possible target is indexed by m
- Intensity (I): It means the audibility or visibility of the information. Generally the intensity depends on the distance from the information source. The further away from the source, the smaller the intensity of the information (With P2P communication such as by cell phone, the distribution of the intensity can be different). The intensity determines whether occupants are able to receiver the information: occupants may not be able to receive information with small intensity.

Occupants keep on analyzing the information (both received and prior) to make decisions. They have different confidence on information from different sources, e.g., the confidence on the information from exit signs may be larger than that from unfamiliar evacuees. In this model, weight values w_i^k are assigned to information i reflecting the confidence on it by occupant indexed by k. Occupants also tend to maintain his target unless they find a much better alternative, so a special weight value $w_{inertia}^k$ is assigned to the direction to current target. This inertia reduces occupants' unrealistic hesitation between different target. The weight values on

all possible targets determine the probability individuals select target m, as the following equation shows:

$$P_m^k(t) = \frac{\sum_{M_i=m} w_i^k(t) I_i^k(t)}{\sum_i w_i^k(t) I_i^k(t)} \tag{1}$$

Where the t is the time; $M_i = m$ means information i (including inertia) leads occupant k to target m; $I_i^k(t)$ is the intensity of information occupant k receives at time t.

2.2 Combination with Social Force Models

The social force model is one of the well-accepted evacuation models. In this model, occupants are driven by forces. Every individual has a desired velocity, and the difference between his/her desired velocity and actual velocity leads to self-driven forces driving him/her to achieve the desired velocity. The desired direction (i.e., the direction of the desired velocity) in the social force model points from the individuals position to the selected exit. If occupants know none of exits, the desired direction will be random initially. This paper combines the information model with the modified social force model [3] by updating the desired velocity based on the decision making process in Sect. 2.1.

3 Case Studies

In this section, two case studies are made with a simple scenario: 100 occupants, initially uniformly distributed in a room with two exits (a main exit on the right and an emergency exit on the left), start to evacuate at $t = 0$. The layout of the room is shown in Fig. 2. For simplicity, it is assumed that occupants can receive information from the information source, i.e., $I_i^k(t) = 1$, if the distance to the information source is less than 5 m; otherwise, occupants cannot obtain the information, i.e., $I_i^k(t) = 0$. The weight values of the confidence, ω on prior information, the inertial, other occupants, and observation of exits are 10.0, 5.0, 1.0, 100.0, respectively.

In the first scenario, occupants have no prior information on the positions of two exits. If there is no information model, most occupants will randomly walk to find exits. With the information model, occupants are able to know exits from other occupants. Simulation results with the information model are shown in Fig. 3. At $t = 0$ (Fig. 3a), since occupants know neither exit, their initial desired directions are randomly selected, as the arrows shown in the figure. After evacuation starts, occupants within the circle see and move to the exits. These occupants serve as information source that sends information into the space. Other occupants will

Fig. 2 Layout of the room. The size of the room is 15 m by 35 m with one main exit on the right and one emergency exit on the left. The radius of the *green semi-circle* is 5 m: occupants within the circle are able to obtain the information of the exit signs

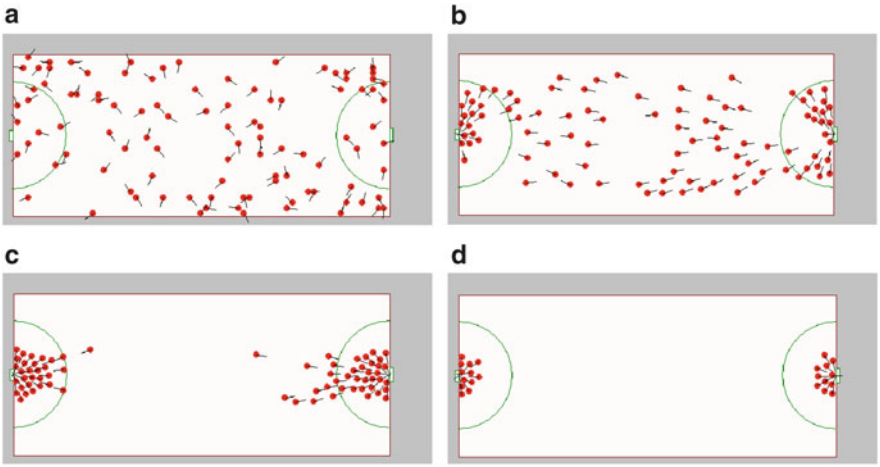

Fig. 3 Snapshots of simulation at t = 0, 3, 10 and 20 s. Nobody has prior information of exits initially. At the beginning of the evacuation, the desired directions are randomly selected. The information of the position of the exit keep on propagating throughout the whole room. This example shows that occupants can obtain dynamic information which change their movement. (**a**) $t = 0$ s. (**b**) $t = 3$ s. (**c**) $t = 10$ s. (**d**) $t = 20$ s

receive this information eventually and move to the selected exit (Fig. 3b–d). Note that the inertia reduces the hesitation of occupants on selecting exits.

In the second scenario, occupants are only familiar with the main exit. If there is no information model, occupants will use the familiar exit to evacuate. Simulation results with the information model are presented in Fig. 4. The initial desired directions all point to the main exit (Fig. 4a). As the information propagates, occupants near the emergency exit may choose this nearer exit (Fig. 4b–d).

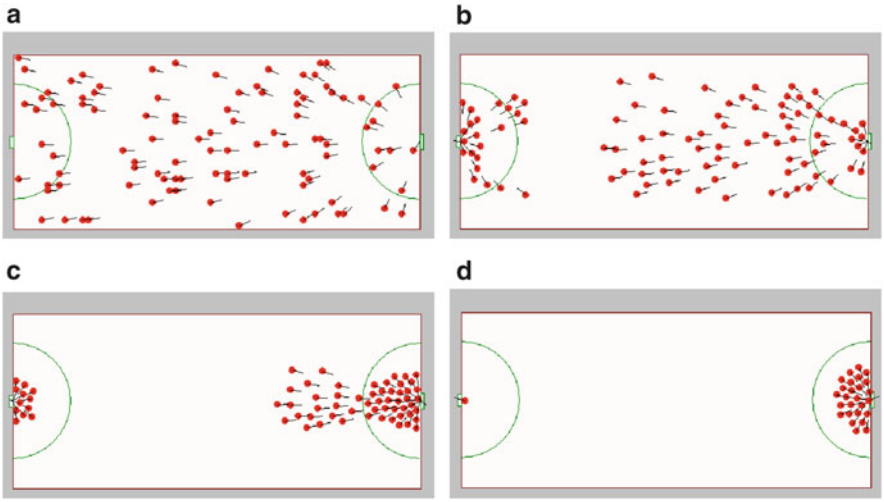

Fig. 4 Snapshots of simulation at t = 0, 3, 10 and 20 s. All occupants only know the main exit initially. (**a**) $t = 0$ s. (**b**) $t = 3$ s. (**c**) $t = 10$ s. (**d**) $t = 20$ s

Conclusion

This paper provides an information model to describe how occupants obtain information and make decisions based on the information during evacuation. Information provided in different ways have different level of confidence and distribution of intensity. The information model is also combined with the modified social force model by updating the desired directions of occupants. Inertia is added to reduce occupants' oscillation between different targets. Simulation results show that with the information model, the modified social force model achieves more realistic results.

Acknowledgements This work was supported by the project 70973062 supported by NSFC and the National Basic Research Program of China 2012CB719705 support by MOST.

References

1. R. Challenger, C.W. Clegg, M.A. Robinson, Understanding crowd behaviours: supporting evidence. Understanding Crowd Behaviours'(Crown, 2009), 1–326 (2009)
2. L.G. Chalmet, R.L. Francis, P.B. Saunders, Network models for building evacuation. Manag. Sci. **28**(1), 86–105 (1982)
3. Y. Gao, P.B. Luh, H. Zhang, T. Chen, A modified social force model considering relative velocity of pedestrians, in *IEEE International Conference on Automation Science and Engineering (CASE), 2013*, Madison, WI (IEEE, 2013), pp. 747–751

4. D. Helbing, P. Molnar, Social force model for pedestrian dynamics. Phys. Rev. E **51**, 4282 (1995)
5. D. Helbing, I. Farkas, T. Vicsek, Simulating dynamical features of escape panic, Nature **407**, 487–490 (2000)
6. L.F. Henderson, Statistics of crowd fluids. Nature **229**(5284), 381–383 (1971)
7. C.M. Henein, T. White, Information in crowds: the swarm information model, in *Cellular Automata* (Springer Berlin Heidelberg, New York, 2006), pp. 703–706
8. S.P. Hoogendoorn, P.H.L. Bovy, Pedestrian travel behavior modeling. Netw. Spat. Econ. **5**(2), 193–216 (2005)
9. A. Kirchner, A. Schadschneider, Simulation of evacuation processes using a bionics-inspired cellular automaton model for pedestrian dynamics. Phys. A **312**, 260–276 (2002)
10. G.G. Lovas, Modeling and simulation of pedestrian traffic flow. Transp. Res. B **28**, 429 (1994)
11. M. Moussaid, D. Helbing, S. Garnier, A. Johansson, M. Combe, G. Theraulaz, Experimental study of the behavioural mechanisms underlying self-organization in human crowds. Proc. R. Soc. B: Biol. Sci. **276**, 2755–2762 (2009)
12. A. Nakayama, K. Hasebe, Y. Sugiyama, Effect of attractive interaction on instability of pedestrian flow in a two-dimensional optimal velocity model. Phys. Rev. E **77**, 016105 (2008)
13. X. Zheng, W. Li, C. Guan, Simulation of evacuation processes in a square with a partition wall using a cellular automaton model for pedestrian dynamics. Phys. A **389**, 2177 (2010)

Effects of an Obstacle Position for Pedestrian Evacuation: SF Model Approach

Takashi Matsuoka, Akiyasu Tomoeda, Mayuko Iwamoto, Kohta Suzuno, and Daishin Ueyama

Abstract In order to study pedestrian dynamics, mathematical models play an important role. It is well-known that a social force model exhibits clogging or what is called the "faster-is-slower effect" (Helbing et al., Nature 407:487–490, 2000). Also, the authors in Frank and Dorso (Phys A 390:2135–2145, 2011) and Kirchner et al. (Phys Rev E 67:056122, 2003) reported that an obstacle facilitates and obstructs evacuation of pedestrians trying to get out of a room with an exit, dependently on its position, size, and shape. In particular, as stated in Frank and Dorso (Phys A 390:2135–2145, 2011), an obstacle has a strong influence on pedestrians if it is put in a site shifted a little from the front of the exit. However, it has not been shown where and how it is the most efficiency to set up an obstacle. Thus we investigate the dynamics of pedestrians and clarify the effect of a disk-shaped obstacle with various sizes placed in several positions via numerical simulations for a social force model. Finally, we calculate a leaving time of pedestrians for each size and position of an obstacle, and determine an "optimal size" of an obstacle in the case that it is set up in a site shifted from the front of the exit.

1 Introduction

A lot of mathematical models have been proposed in order to study pedestrian dynamics. One of the most successful models is the "social force model" (SF model) in [2]. Since pedestrians are thought of as particles in the

T. Matsuoka • M. Iwamoto • K. Suzuno • D. Ueyama (✉)
Graduate School of Advanced Mathematical Sciences, Meiji University, 4-21-1, Nakano, Nakano-ku, Tokyo, 164-8525, Japan
e-mail: suzunogk@meiji.ac.jp; d.ueyama@gmail.com

A. Tomoeda
Meiji Institute for Advanced Study of Mathematical Sciences, Meiji University, 4-21-1, Nakano, Nakano-ku, Tokyo, 164-8525, Japan

CREST, Japan Science and Technology Agency, 4-21-1, Nakano, Nakano-ku, Tokyo, 164-8525, Japan
e-mail: atom@isc.meiji.ac.jp

M. Chraibi et al. (eds.), *Traffic and Granular Flow '13*,
DOI 10.1007/978-3-319-10629-8_19

model, the "faster-is-slower effect" is considered as a kind of self-organized behaviors observed in granular media and has been attractive for many physicists. Also, for design of egress for places of public assembly, it is a significant issue to investigate pedestrian dynamics in facility and safety engineering [4].

In recent years, it was reported that placement of an obstacle may lead to alleviation of the faster-is-slower effect [5]. Experiments in [5] show the following two results: (i) The pedestrian outflow at a bottleneck decreases in evacuation situation when the number of pedestrians moving to an exit of a room increases. (ii) The outflow increases by putting the obstacle in front of an exit. These results indicate that the faster-is-slower effect does occur in pedestrian dynamics and an obstacle near an exit facilitate evacuation of pedestrians.

These experimental results described above were supported by theoretical approaches in [1] and [3]. Based on a cellular automaton model (CA model), the authors in [3] showed that the evacuation time is minimal if we shift the obstacle one site from the front of the exit. Similarly, it was shown in [1] via a SF model that if a panel-like or a pillar-like obstacle is placed symmetrically in front of an exit, the evacuation times are smaller than without an obstacle.

In the previous works [1] and [3], strong assumptions are made on parameters of an obstacle. The size of an obstacle is fixed in [3], and a position is chosen from three kinds of places, symmetrically in front of the exit, shifted one site and two sites. In [1], only two kinds of sizes and positions are considered at most. Then we have simple questions: where and how large obstacle facilitates evacuation of pedestrians the best. To answer these problems is our motivation in this article.

Since any CA model is completely discretized, we cannot change parameters for the size and positions of an obstacle continuously. Therefore we apply a SF model in this work, which is the same as in [2] (see Sect. 2). In order to investigate the influence of an obstacle on a leaving time of pedestrians, the size and position of an obstacle are varied in a wide range. As we show later, a leaving time tends to drastically change in the case that we put an obstacle near an exit of a room. Then we restrict the range of parameters corresponding to the size and position, and calculate a leaving time. Finally, we clarify the size of an obstacle as an average leaving time is shortest or longest.

This paper is organized as follows. In Sect. 2, we introduce a SF model and explain the settings of numerical simulations. In Sect. 3, we show our results of simulations. At first, we consider a wide range of positions of an obstacle. Then, our result implies that a leaving time changes drastically only in the case that we put an obstacle closely to an exit (Sect. 3.1). From this observation, we carry out simulations in a restricted range of parameters and calculate a leaving time in each size and position of an obstacle. Finally, we make two kinds of estimates of leaving times in Sects. 3.2 and 3.3. In section "Conclusions", we will give a conclusion.

2 Social Force Model

Collective behavior of humans in escape panic situations is described in the frame work of self-driven many particle systems, called *social force model* (see [2]) and given by

$$m\frac{\mathrm{d}\mathbf{v}_i(t)}{\mathrm{d}t} = m\frac{v_0\mathbf{e}_i^0(t) - \mathbf{v}_i(t)}{\tau} + \sum_{j(\neq i)}\mathbf{f}_{ij} + \sum_{W}\mathbf{f}_{iW}, \tag{1}$$

where $\mathbf{v}_i$ is the velocity of the i-th pedestrian. We suppose that the shapes of all pedestrians are disk, and their diameters are equal to 0.6 m. All pedestrians move with an identical desired velocity v_0 in each simulation, where v_0 is given between 1.0 and 5.0 m/s. All terms and parameters in (1) are assumed to be the same as given in [2]. So we omit an explanation of the details of (1).

We implement (1) for 200 pedestrians trying to exit from a room with size 20 × 20 m and move toward the 1.0 m-wide exit of the room, which is almost the same as in [1] and [2] (see Fig. 1). Each point in the room is given a two-dimensional coordinate, denoted by (x, y). The center of the exit is put at $(x, y) = (0, 0)$, and the wall which contains the exit is included in a line $x = 0$.

In order to clarify how an obstacle affects evacuation of pedestrians, we put an obstacle inside the room and calculate *a leaving time*. In some simulations, it is observed that pedestrians with small desired devote much time to leave the room, and some of pedestrians stop the motion. Therefore the evacuation process ran until the first 195 pedestrians left the room or the total time in a simulation achieves 300 s. Under this setting, the leaving times are calculated as shown in Table 1 when no obstacle set up in the room, denoted by T_{v_0} for each v_0, which shows the faster-is-slower effect.

In this article, we assume that the obstacle has the disk shape, and its diameter, denoted by L, is changed between $0.1 \sim 1.0$ m. Denote the position of the center of the obstacle by (x_0, y_0). Pedestrians are supposed to receive a force which is similarly defined by $\mathbf{f}_{ij}$ in (1) from the obstacle as well as other pedestrians. In other words, the obstacle is thought of as not a part of walls but one of pedestrians in simulations. The minimal distance between the surface of the obstacle and the line

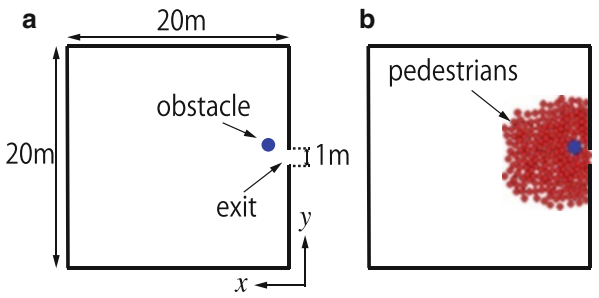

Fig. 1 (**a**) Pedestrians try to exit from a room with size 20 × 20 m^2 and move to the 1.0 m-wide exit of the room. The center of the exit is $(0, 0)$, and the x and y-directions are defined as shown in (**a**). The *blue disk* represents an obstacle. (**b**) Snapshot of the simulation with an obstacle at $t = 3.0$

Table 1 Leaving time for each desired velocity v_0. The leaving time at $v_0 = 2.0$ is smaller than at $v_0 = 5.0$ (faster-is-slower effect). We denote the leaving time for each v_0 by T_{v_0}

v_0	1.0	1.5	2.0	2.5	3.0	3.5	4.0	4.5	5.0
T_{v_0}	190	140	133	139	150	160	176	182	185

$x = 0$ is supposed to be equal to or larger than the diameter of the particle because $\mathbf{f}_{ij}$ and $\mathbf{f}_{iW}$ can generate heavy forces on pedestrians, and then particles may not be able to go through interspace. Hence we assume $x_0 - L/2 \geq 0.6$.

At the beginning of our simulations, we first put an obstacle, and set 200 particles in the room randomly as no particles overlap the obstacle. The initial velocities of all pedestrians are identically 0. For the same position and size of the obstacle, and the same desired velocity, we carry out the numerical simulations 10 times and obtain an average leaving time from the results. Numerical calculations for (1) were done by the fourth-order Runge-Kutta iterative scheme with a time step of 3.3×10^{-3} s.

3 Results

3.1 Calculation Area

Our purpose in this article is to clarify the influence of an obstacle on evacuation of pedestrians. Intuitively, an obstacle is more likely to drastically change a leaving time in the case that it is set near the exit. To check it, we assume that $L = 1.0$, $v_0 = 5.0$, $1.1 \leq x_0 \leq 3.5$, and $0 \leq y_0 \leq 2.5$, and calculation the leaving time for each (x_0, y_0). Each site in Fig. 2 is 0.1 m from neighboring sites.

The right figure in Fig. 2 shows how much the leaving time increases or decreases in the case that the obstacle is put at each position. For example, the leaving time is 145.0 s at $(x_0, y_0) = (1.2, 0.0)$, which is the shortest in the region $1.1 \leq x_0 \leq 3.5$ and $0 \leq y_0 \leq 2.5$, and we call the *optimal position*. Then the ratio of this leaving time to $T_{5.0}$ is calculated as 0.783, which is represented as the deepest red color in Fig. 2. Similarly, the leaving time at $(x_0, y_0) = (1.5, 0.0)$ is 281.935. This is the longest time, and the ratio is 1.52, which is colored by the deepest blue.

The optimal position is contained in a region around the lower right. On the other hand, colors near the upper left are relatively light, which means that the obstacle separated from the exit does not have a strong influence on pedestrians. Therefore we only consider the case that the obstacle is set near the exit, and obtain the optimal position in each parameter in the next section.

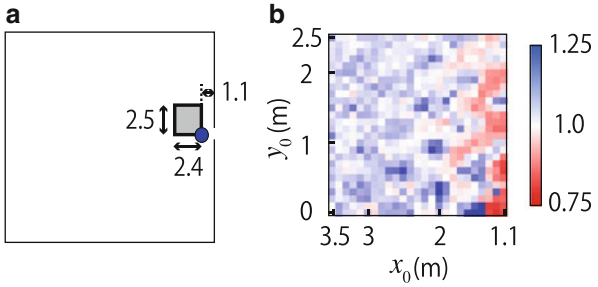

Fig. 2 Leaving times for $L = 1.0$ and $v_0 = 5.0$. (**a**) The position of an obstacle changes in the area defined by $1.1 \leq x_0 \leq 3.5$ and $0 \leq y_0 \leq 2.5$ (corresponding to the *Grey square* in (**a**)). The *blue disk* shows an obstacle set at the lower right of the area. Note that $x_0 - L/2 \geq 0.6$. (**b**) The *Grey square* in (**a**) is divided into a mesh shown in (**b**). The neighboring sites have 0.1 m distance. We calculate the leaving time for each site of (x_0, y_0) and compute the ratio of it to $T_{5.0}$. The deepest *red* and *blue* color correspond to the ratios of 0.75 and 1.25. In the case that the ratio is smaller than 0.75 or larger than 1.25, the site is also colored by the deepest *red* or *blue*

3.2 Optimal Position and Size

We compute leaving times for various desired velocities, the sizes and positions of an obstacle. Then we obtain the optimal position for each desired velocity and the size of an obstacle one by one. In the following, we assume that $1.0 \leq v_0 \leq 5.0$, $0.4 \leq L \leq 1.0$, $0.6 \leq x_0 - L/2 \leq 1.1$, and $0 \leq y_0 \leq 1$. Note that the range of x_0 should be changed for L because of the assumption $x_0 - L/2 \geq 0.6$.

Our result is shown in Table 2, which means the optimal position for each v_0 and L, respectively. For $L \leq 0.8$, almost all the y-coordinates of the optimal positions are close to 0.7 except for $L = 0.4$ and $v_0 = 3.0$. This result seems to suggest that $y_0 = 0.7$ or the neighboring sites can be a optimal position. However, this expectation is not entirely true. The graphs in Fig. 3 represent the v_0-dependency of the leaving time at the optimal position for each L. Obviously, each leaving time for $v_0 = 4.5, 5.0$ at $L = 1.0$ is the smallest in all L, respectively, while it is the largest for $v_0 = 1.5, 2.0, 2.5$. This result means that a relatively large obstacle $L = 1.0$ is the most effective for evacuation of pedestrians with higher desired velocities rather than small one while it has a small influence on pedestrians with smaller desired velocity. Therefore we state that we cannot uniquely determine such an optimal position and size of an obstacle as it is effective for all desired velocity.

Table 2 Optimal positions for various L and v_0. We calculate the leaving times in a range $0.4 \leq L \leq 1.0$, $1.0 \leq v_0 \leq 5.0$, $0.6 \leq x_0 - L/2 \leq 1.1$ and $0 \leq y_0 \leq 1.0$. A site of (x_0, y_0) has 0.05 m distance from the neighboring sites. The optimal position for each L and v_0 is shown as a two-dimensional coordinate (x_0, y_0)

$L \backslash v_0$	1.0	1.5	2.0	2.5	3.0	3.5	4.0	4.5	5.0
0.4	(0.85,0.65)	(1.05,0.7)	(0.8,0.65)	(0.8,0.75)	(1.0,0)	(0.8,0.65)	(0.8,0.6)	(0.85,0.4)	(0.85,0.55)
0.5	(0.8,0.65)	(0.8,0.7)	(0.85,0.7)	(1.05,0.7)	(0.9,0.75)	(0.95,0.7)	(0.85,0.65)	(0.85,0.65)	(0.9,0.6)
0.6	(0.9,0.65)	(0.85,0.7)	(1.05,0.7)	(1.0,0.7)	(0.95,0.7)	(0.9,0.7)	(0.9,0.65)	(0.95,0.65)	(0.9,0.65)
0.7	(0.95,0.7)	(0.9,0.7)	(1.0,0.7)	(0.95,0.7)	(1.0,0.7)	(1.0,0.65)	(0.95,0.65)	(1.0,0.6)	(0.95,0.65)
0.8	(1.0,0.6)	(0.95,0.7)	(0.95,0.7)	(0.9,0.7)	(1.0,0.7)	(1.0,0.75)	(1.0,0.6)	(1.0,0.65)	(1.0,0.6)
0.9	(1.05,0.65)	(1.0,0.7)	(0.9,0.7)	(0.85,0.7)	(1.1,0.7)	(1.2,0.05)	(1.25,0.05)	(1.2,0.05)	(1.2,0)
1.0	(1.15,0.6)	(1.1,0.65)	(1.25,0.65)	(1.1,0.65)	(1.25,0.05)	(1.3,0.05)	(1.2,0)	(1.2,0.1)	(1.25,0)

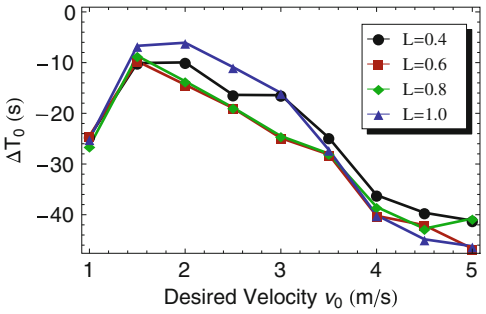

Fig. 3 Difference of leaving times with and without an obstacle. At each optimal position shown in Table 2, we also calculated the leaving time. The graphs show the results that we subtracted it from T_{v_0} for each L and v_0. The difference of the leaving times is denoted by ΔT_0

3.3 Optimal Size for an Average of Leaving Times

As described previously, it is difficult to uniquely determine such an appropriate position and size of an obstacle that pedestrians with various desired velocities evacuate from a room. Then, we first observe the optimal positions as shown in Table 2 from a different viewpoint. Next, we focus on an area around a site shifted from the front of the exit and calculate an average of the leaving times for the optimal positions. Finally, we will determine the optimal size of an obstacle in the area.

At first, we replace x_0 into $x_0 - L/2$ in Table 2. Then, counting the number of the positions $(x_0 - L/2, y_0)$ for each $0.4 \leq L \leq 1.0$ and $1.0 \leq v_0 \leq 5.0$ where the optimal position for L and v_0 is attained at (x_0, y_0), we give a score to each position $(x_0 - L/2, y_0)$ by the total number. For example, $(x_0 - L/2, y_0) = (0.7, 0.7)$ is the optimal position for $(L, v_0) = (0.7, 2.5), (0.8, 3.5)$, from which the score at the site corresponding to $(0.7, 0.7)$ is 2 (colored by light Grey in Fig. 4).

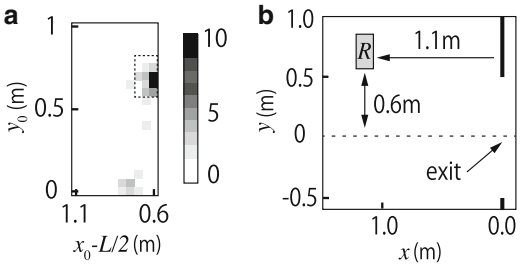

Fig. 4 (**a**) Concentration of the optimal positions in a region. For the optimal position (x_0, y_0) shown in Table 2, we calculate $(x_0 - L/2, y_0)$ and count the number of it. The number of most sites is less than 5, but only the sites at $(x_0 - L/2, y_0) = (0.6, 0.65), (0.6, 0.7)$ are 15, 18, which are colored by *black*. The *square surrounded by a dashed line* is denoted by Region R. (**b**) Position of Regions R in the room for $L = 1.0$. The region R changes its position dependently on L. The right figure (**b**) shows the position of R in the room as an example

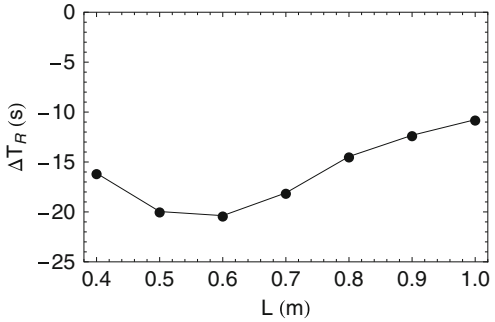

Fig. 5 Average leaving time T_R in all sites of R and desired velocities. The graph shows the L-dependency of the difference of T_R and $\overline{T}$

Our result is shown in Fig. 4, which implies that sites with high scores concentrate in a region surrounded by a dashed line. We denote this region by R, shifted from the front (see (b) in Fig. 4). More precisely, R is defined by $R = \{(x_0, y_0) \mid 0.6 \leq x_0 - L/2 \leq 0.75, 0.6 \leq y_0 \leq 0.8\}$. Indeed, the total number of parameter sets is 63 and the total score included in this region is 50, which implies that almost 80 % of the optimal positions is contained in R. Hence to set an obstacle in R is the most effective in evacuation. Thus we focus on the region R.

We first calculate an average of the leaving times in all sites of R and all desired velocities for each L. Denote the average time by T_R. Similarly, we compute an average of T_{v_0} for all v_0 and denote it by $\overline{T}$. Then we obtain the difference of T_R and $\overline{T}$ for each L, denoted by ΔT_R. Figure 5 shows the L-dependency of ΔT_R. Obviously, ΔT_R has a minimum at $L = 0.6$, which implies that the obstacle with $L = 0.6$ is the most efficiency for evacuation of pedestrians with various desired velocity. Therefore we conclude that the optimal size of a disk-shaped obstacle is $L = 0.6$.

Conclusions

The faster-is-slower effect can be observed in the pedestrians dynamics, mainly in mathematical models [2] and [5]. As is well-known, the higher desired velocity pedestrians have, the more slowly they evacuate under the situation that the faster-is-slower effect occurs. In the previous works [1, 3], it was shown that an obstacle can alleviate this effect. However, it has not been shown where and how it is the most efficient to set up an obstacle in a room for pedestrians. Thus we investigate the dynamics of pedestrians and clarify the effect of a disk-shaped obstacle with various sizes put in several positions via numerical simulations for a social force model.

For each desired velocity, size and position of the obstacle, we calculated a leaving time one by one. At first, we see that the optimal position drastically changes dependently on the desired velocity and the size of an obstacle. In addition, as far as we calculated, many optimal positions concentrate in an area around a site shifted from the front of the exit, which corresponds to the result reported in [1] although a cellular automaton model was applied in [1]. Then, instead of uniquely determining the optimal position and size of the obstacle, we focus on an area around a site shifted from the front of the exit. By calculating an average leaving time of all optimal positions in the area and desired velocities for each size of the obstacle, the average leaving time becomes the smallest when the diameter of the obstacle is 0.6 m. Therefore we conclude that the optimal size of the obstacle is 0.6 m in evacuation of pedestrians.

Acknowledgements T. Matsuoka would like to thank Meiji University Graduate School to support him. He also thanks Professor K. Ikeda in Meiji University for valuable comments and advice.

References

1. G.A. Frank, C.O. Dorso, Room evacuation in the presence of an obstacle. Physica A **390**, 2135–2145 (2011)
2. D. Helbing, I. Farkas, T. Vicsek, Simulating dynamical features of escape panic. Nature **407**, 487–490 (2000)
3. A. Kirchner, K. Nishinari, A. Schadschneider, Friction effects and clogging in a cellular automaton model for pedestrian dynamics. Phys. Rev. E **67**, 056122 (2003)
4. X. Pan, C.S. Han, K. Dauber, K.H. Law, A multi-agent based framework for the simulation of human and social behaviors during emergency evacuations. AI Soc. **22**, 113–132 (2007)
5. D. Yanagisawa, A. Kimura, A. Tomoeda, R. Nishi, Y. Suma, K. Ohtsuka, K. Nishinari, Introduction of frictional and turning function for pedestrian outflow with an obstacle. Phys. Rev. E **80**, 036110 (2009)

Realistic Stride Length Adaptation in the Optimal Steps Model

Isabella von Sivers and Gerta Köster

Abstract Pedestrians move freely in an open space by stepping forward. When the navigational situation becomes difficult, say in a dense crowd, they adjust their stride length and speed. The Optimal Steps Model uses local optimization on a circle around a pedestrian to determine the next position. The target function is a navigational field. Each individual's stride length, that is, the circle radius depends on his or her speed. This introduces a delay in adaptation, because all speed measurements involve the past. A real person, however, is more likely to react instantaneously. We model this effectively by optimizing on a disk instead of a circle. The radius is chosen in accordance with the pedestrian's free-flow velocity. A two dimensional continuous optimization problem ensues that we solve efficiently thus maintaining fast computational speed. Our simulations closely match real walking behavior which we demonstrate for navigation around a column in a narrow corridor and behavior at a bottleneck.

1 Introduction

Modeling pedestrian motion has become an integral part of methods to mitigate risks for life and health in crowded situations. Therefore, accurate models of human behavior and movement are needed. Most state-of-the-art models suffer from undesirable artifacts: such as inaccuracies and oscillations in social force type models [1, 6] or grid restrictions as in cellular automaton models [4, 10].

The Optimal Steps Model, introduced in [10] avoids both types of side effects. It is inspired by the intuitive rules often used in cellular automaton models [5], but the pedestrians are not restricted to a grid. The next position of a pedestrian is chosen on a circle where the radius depends on the stride length of that pedestrian. The stride length either depends on the pedestrian's free-flow velocity or on the actual speed [10]. The first approach does not adapt the stride length to the actual situation; the latter introduces a delay in adaptation because the speed can only be measured in the past.

I. von Sivers (✉) • G. Köster
Munich University of Applied Sciences, Lothstr. 64, 80335 München, Germany
e-mail: isabella.von_sivers@hm.edu; gerta.koester@hm.edu

M. Chraibi et al. (eds.), *Traffic and Granular Flow '13*,
DOI 10.1007/978-3-319-10629-8_20

A real person is more likely to reduce his or her normal step length immediately when there is no room to move or navigation is difficult. This can be modeled effectively if the next pedestrian position is determined on a disk instead of a circle. The impact of this seemingly small extension of the Optimal Steps Model is strong: The virtual pedestrians move in a significantly more realistic way.

The paper is structured as follows: Sect. 2 gives a short introduction to the Optimal Steps Model. In Sect. 3 we formulate the search for the next position of the pedestrian's foot as a two-dimensional optimization problem. We also present its numerical solution. Section 4 shows how the new stride length adaptation leads to more realistic pedestrian movement. Section "Conclusion" summarizes the results and gives an outlook on further work.

2 The Optimal Steps Model

In the Optimal Steps Model [10], virtual pedestrians navigate along a floor field. The field is constructed by superposing scalar fields that represent the orientation towards a target, the need for personal space between pedestrians and, finally, the avoidance of obstacles. We interpret the navigational field as a utility function. Pedestrians seek the most advantageous position in their reach.

A wave front propagating from the target (see Fig. 1) as introduced in [2, 13] expresses the target orientation. Let $\Omega \subset \mathbb{R}^2$ be the area of the scenario with boundary $\partial\Omega$ and let $\Gamma \subset \partial\Omega$ be the boundary of the target. The arrival time $\Phi : \Omega \to \mathbb{R}$ of a wave front starting from Γ is given by the solution of the eikonal equation (1) with traveling speed $F : \Omega \to \mathbb{R}_+$. We set $F \equiv 1$ outside obstacles so that the wave propagates uniformly. With that assumption, a pedestrian navigating

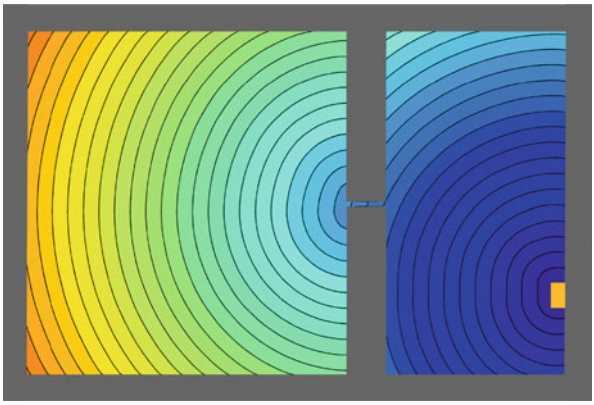

Fig. 1 Wave front propagating from the target (*small orange rectangle*, on the right)

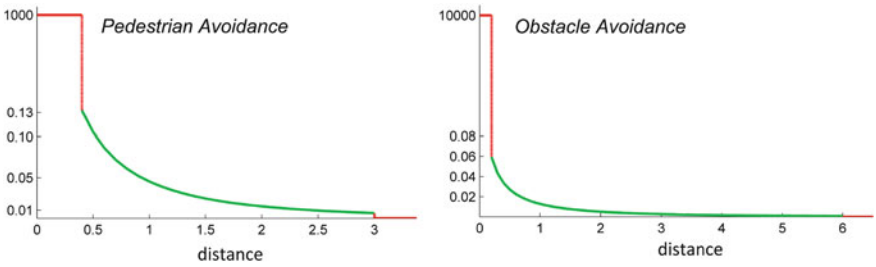

Fig. 2 The 'pedestrian avoidance' and the 'obstacle avoidance' in the Optimal Steps Model

along the floor field defined by Φ takes the shortest path to the target. The eikonal equation with boundary conditions is given by

$$F(x)\|\nabla\Phi(x)\| = 1 \qquad \text{for } x \in \Omega \tag{1}$$

$$\Phi(x) = 0 \qquad \text{for } x \in \Gamma. \tag{2}$$

Sethian's fast marching algorithm [11, 12] efficiently solves the eikonal equation on a grid. We use a bilinear interpolation between grid points [2, 10] to define the utility function $P_t(x)$ for target orientation for every point $x \in \Omega$. The floor field also contains utility functions for pedestrian avoidance and obstacle avoidance [10].

'Pedestrian avoidance' (see Fig. 2) stands for the need for personal space between persons. It is modeled through 'punishing' functions carried around by each pedestrian:

$$P_p^j(x) := \begin{cases} \mu_p & \text{if } \delta_p^j(x) \le g_p, \\ v_p \cdot \exp\left[-a_p \cdot \delta_p^j(x)^{b_p}\right] & \text{if } g_p < \delta_p^j(x) \le g_p + h_p, \\ 0 & \text{else.} \end{cases} \tag{3}$$

$P_p^j(x)$ depends on the Euclidean distance $\delta_p^j(x)$ between the center of pedestrian j and position x; g_p is the torso diameter of the pedestrian. Here it is chosen identical for all pedestrians. We prevent pedestrians from overlapping by setting the avoidance value μ_p to an extremely high value. We cut off outside a radius of influence $g_p + h_p$. The strength of the avoidance, that is, the need for personal space of a pedestrian, can be regulated by the parameters v_p, a_p and b_p. Obstacle avoidance is formulated in an analogous fashion to pedestrian avoidance [10]. Superposition of the target orientation, pedestrian avoidance and obstacle avoidance gives the navigational field $P_i(x)$ for pedestrian i for any point $x \in \Omega$ [10].

$$P_i(x) = P_t(x) + \sum_{j=1, j\neq i}^{n} P_p^j(x) + \sum_{k=1}^{m} P_o^k(x), \tag{4}$$

3 Optimization Problem

Navigation in the Optimal Steps Model depends on a balance of conflicting goals: reaching the target, avoiding fellow pedestrians and avoiding obstacles. Superimposing the functions associated with these goals means to interpret the floor field, or rather its negative, as an utility function. Function $-P_i$ measures the degree of the attraction for pedestrian i.

Following this idea, each virtual pedestrian seeks the position with the lowest value of P within his or her reach. In the original model formulation [10], the reachable area is a circle of radius r around the pedestrian that represents the individual's stride length. Finding the next position is an one-dimensional minimization problem on the circle. The pedestrian just moves if, and only if, the minimum value on the circle is lower than the one at the actual position. This algorithm significantly improved on former models [10] but left unsolved the problem of immediate stride adaptation to the navigational situation.

We propose to search the next position on a disc [14] with radius r so that the maximum stride length corresponds to the correct length for the pedestrian's free-flow velocity. A two-dimensional optimization problem with one inequality constraint ensues:

$$\begin{aligned} &\min_{x \in \Omega} P_i(x) \\ \text{s.t.} \quad &\delta_p^i(x) - r \leq 0 \quad . \end{aligned} \tag{5}$$

With our choice of the floor field, the objective function P_i (4) is nonlinear, non-differentiable and discontinuous. Hence, we can't use optimization algorithms that need the derivatives of the objective function. We implemented three of the most common methods that are suitable to solve such a problem: a direct search on a grid, a basic evolution strategy and the Nelder-Mead simplex algorithm [9] and compare the error and the computational speed.

In our experiments, we require a maximum error in position of 10^{-2}, that is, a distance of 1 cm between the numerical approximation to the minimum and the true minimum. The direct search and the evolution strategy need significantly more evaluations of the objective functions than the Nelder-Mead simplex algorithm before they satisfy our error bound (see Fig. 3). We observe this behavior consistently in our experiments [14]. Thus, we choose the Nelder-Mead simplex as default method in our experiments.

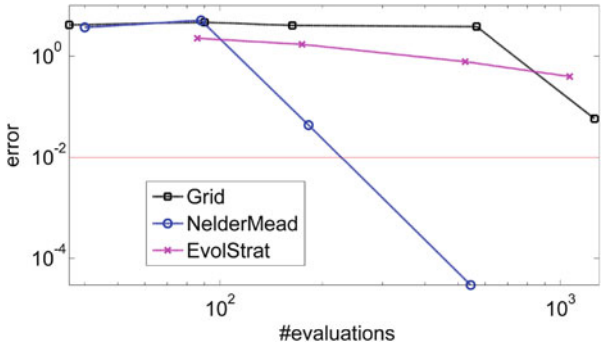

Fig. 3 Number of function evaluations necessary to reach a maximum error of 1 cm in an example scenario with the Himmelblau function [3] as floor field: direct search on a grid, evolution strategy and Nelder-Mead. The *thin (red) horizontal line* indicates the error bound

4 Results

In this section we compare the performance of the two step types in the Optimal Steps Model, the optimization on the circle as presented in the original model [10] and the optimization on the disk proposed here [14]. For this, we look at a column in a narrow corridor that needs to be skirted. Then we show how immediate stride length adaptation results in a realistic movement of pedestrians at a bottleneck.

In the first scenario a column is placed in the middle of a corridor. The opening between the column and the wall is so small that only one pedestrian can walk through it at the same time. This scenario is inspired by an experiment in [8], where the column was represented by a person and the trajectories form an 'eye' around the person.

Figure 4 shows the trajectories of ten single pedestrians with the two different step types. The pedestrians start one after another so that they have no effect on each other. When we use optimization on a circle, the step lengths remain unnaturally big near the column and coarse in front of it (Fig. 4a). The trajectories for the optimization on a disc are smoother. When necessary, the pedestrian make small adjusting steps while squeezing through the opening (Fig. 4b). The latter is, in our opinion, how people move in reality.

When ten pedestrians start at the same time, they get in each others way. See Fig. 5. Again, the behavior of the Optimal Steps Model with fixed and adaptive stride length is compared. With a fixed stride length virtual pedestrians sometimes get stuck for a while in front of the narrowing (Fig. 5a). The floor field in the area between the pillar and the wall forms a narrow valley. The optimization algorithm has to find the intersection of the valley ground with the circle line. This search may fail unless the grid is extremely fine or the algorithm. Seitz and Köster [10] restart the algorithm while disturbing the grid with each search which results in a solution after few attempts. Thus the pedestrian is not held up for long. Nevertheless, stalling

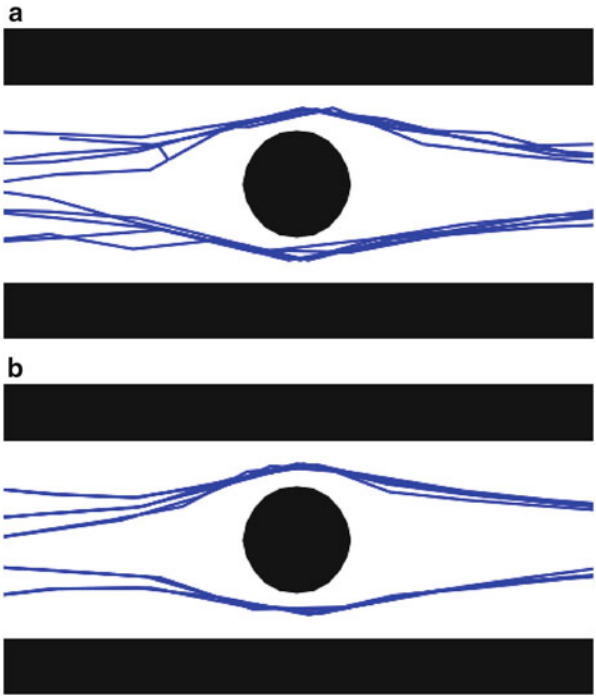

Fig. 4 Navigation around a column: Trajectories for ten single pedestrians walking from left to right. The opening between the wall and the pillar is exactly the torso diameter. (**a**) Optimization on the circle. (**b**) Optimization on the disk

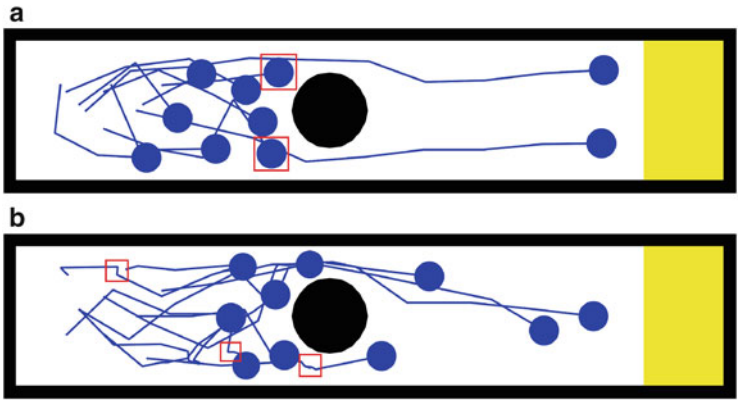

Fig. 5 Navigation around a column for a small crowd: 10 Pedestrians start all at the same time walking from left to right. The opening between the wall and the pillar is equal to the torso diameter. (**a**) Optimization on the circle: pedestrians get stuck for a while in front of the pillar (*red rectangles*) because of the small opening. (**b**) Optimization on the disk: pedestrians make smaller, sometimes evasive steps (*red rectangles*) to navigate in crowded and difficult situations

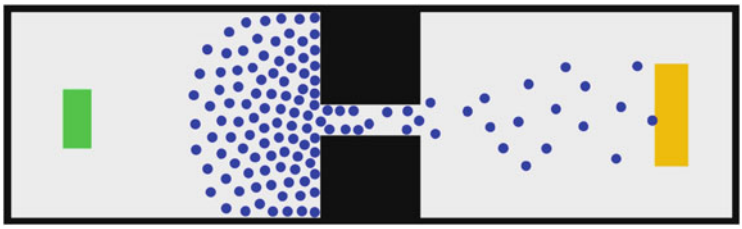

Fig. 6 Simulation with the Optimal Steps Model with the optimization on the disk. One hundred and eighty pedestrians walk from left to the target on the right through a smaller corridor of width 1.2 m

in front of the opening looks unnatural. We think that real pedestrians make evasive steps in dense crowds to achieve more personal space and short navigational steps while rounding the pillar. See Fig. 5b. That is exactly what the optimization on the disk yields.

The second scenario is inspired by an experiment by [7]. One hundred and eighty pedestrians start in a room and walk through a bottleneck of width 1.2 m to the target on the right. We expect to see an increase of density in front of the bottleneck which is impossible to map with a cellular automaton model. Figure 6 is a screen shot of a simulation with the Optimal Steps Model with immediate stride length adaptation. We observe a concentration in front of the opening and a loser spacing on the fringe of the crowd Fig. 6. Our virtual pedestrians are able to make smaller steps when a situation becomes tight. Thus, they move closer together in front of the narrowing which, in our opinion, matches reality.

Conclusion

In this paper, we showed how a simple extension of the Optimal Steps Model leads to more realistic behavior in the simulation of pedestrian motion. In the original formulation of the Optimal Steps Model [10] pedestrians move forward like real humans, stepping freely in continuous space. This was achieved by optimizing the next position on a circle around the pedestrian. We proposed to optimize on a disk instead. With that, pedestrians are now able to adjust their stride length and speed depending on the navigational situation. The two-dimensional optimization problem was solved efficiently with the Nelder-Mead simplex algorithm. We saw in our simulation results that locomotion of the has become even more realistic matching human locomotion very well. We will use this as a basis for our further work, the integration of sociological and psychological aspects of human behavior into models of pedestrian motion.

Acknowledgements This work was funded by the German Federal Ministry of Education and Research through the project MEPKA on mathematical characteristics of pedestrian stream models (grant number 17PNT028).

References

1. M. Chraibi, A. Seyfried, A. Schadschneider, Generalized centrifugal-force model for pedestrian dynamics. Phys. Rev. E **82**(4), 046111 (2010)
2. D. Hartmann, Adaptive pedestrian dynamics based on geodesics. New J. Phys. **12**, 043032 (2010)
3. D.M. Himmelblau, *Applied Nonlinear Programming* (McGraw-Hill, New York, 1972)
4. G. Köster, D. Hartmann, W. Klein, Microscopic pedestrian simulations: from passenger exchange times to regional evacuation, in *Operations Research Proceedings 2010: Selected Papers of the Annual International Conference of the German Operations Research Society*, ed. by B. Hu, K. Morasch, S. Pickl, M. Siegle (Springer, Berlin/Heidelberg/New York, 2011), pp. 571–576
5. G. Köster, M. Seitz, F. Treml, D. Hartmann, W. Klein, On modelling the influence of group formations in a crowd. Contemp. Soc. Sci. **6**(3), 397–414 (2011)
6. G. Köster, F. Treml, M. Gödel, Avoiding numerical pitfalls in social force models. Phys. Rev. E **87**(6), 063305 (2013)
7. J. Liddle, A. Seyfried, B. Steffen, W. Klingsch, T. Rupprecht, A. Winkens, M. Boltes, Microscopic insights into pedestrian motion through a bottleneck, resolving spatial and temporal variations (2011). arXiv, 1105.1532v1
8. M. Moussaïd, D. Helbing, G. Theraulaz, How simple rules determine pedestrian behavior and crowd disasters. Proc. Nat. Acad. Sci. **108**(17), 6884–6888 (2011)
9. J.A. Nelder, R. Mead, A simplex method for function minimization. Comput. J. **7**, 308–313 (1965)
10. M.J. Seitz, G. Köster, Natural discretization of pedestrian movement in continuous space. Phys. Rev. E **86**, 046108 (2012)
11. J.A. Sethian, A fast marching level set method for monotonically advancing fronts. Proc. Nat. Acad. Sci. **93**(4), 1591–1595 (1996)
12. J.A. Sethian, *Level Set Methods and Fast Marching Methods: Evolving Interfaces in Computational Geometry, Fluid Mechanics, Computer Vision, and Materials Science* (Cambridge University Press, Cambridge/New York, 1999)
13. A. Treuille, S. Cooper, Z. Popović, Continuum crowds. ACM Trans. Graph. (SIGGRAPH 2006) **25**(3), 1160–1168 (2006)
14. I. von Sivers, Numerische Methoden zur Optimierung der Schrittrichtung und -weite in einem Modell der Personenstromsimulation. Master's thesis, Fernuniversität in Hagen, 2013

A Discrete Spheropolygon Model for Calculation of Stress in Crowd Dynamics

Fernando Alonso-Marroquín, Jonathan Busch, Álvaro Ramírez-Gómez, and Celia Lozano

Abstract Several models have been presented to evaluate flow rates in pedestrian dynamics, yet very few focus on the calculation of the stress experienced by pedestrians under high density. With this aim, a pedestrian dynamics model is implemented to calculate the stress developed under crowd conditions. The model is based on an extension of a granular dynamics model to account contact forces, ground reaction forces and torques in the pedestrians. Contact stiffness is obtained from biomedical journal articles, and coefficient of restitution is obtained by direct observations of energy loss in collisions. Existing rotational equations of motion are modified to incorporate a rotational viscous component, which allows pedestrians to come to a comfortable stop after a collision rather than rotating indefinitely. The shape of the pedestrian is obtained from a bird's eye, cross sectional view of the human chest cavity and arms, which was edited to produce an enclosed shape. This shape is them approximated by a *spheropolygon*, which is a mathematical object that allows real-time simulation of complex-shape particles. The proposed method provides real benefits to the accuracy on particle shape representation, and rotational dynamics of pedestrians at micro-simulation level. It provides a new tool to calculate the risk of injuries and asphyxiation when people are trapped in dense crowds that lead to development of high pressure.

1 Introduction

Since its inception in the 1950s [1], numerous methods have been developed to best describe pedestrian behavior, including the Social Force Model, cellular automaton, as well as fluid and gas representations. The study of pedestrian panic, however,

F. Alonso-Marroquín (✉) • J. Busch
School of Civil Engineering, The University of Sydney, Sydney, NSW, Australia
e-mail: fernando.alonso@sydney.edu.au

Á. Ramírez-Gómez
Escuela Técnica Superior de Ingeniería y Diseño Industrial, Universidad Politécnica de Madrid, Madrid, Spain

C. Lozano
Facultad de Ciencias, Departamento de Física, Universidad de Navarra, Navarra, Spain

M. Chraibi et al. (eds.), *Traffic and Granular Flow '13*,
DOI 10.1007/978-3-319-10629-8_21

began later in the 1990s in response to many of history's horrific crowd stampedes [2]. Typically pedestrian panic events occur in crowds with high density, at points where flows of people conflict with one another, or at doorways and corridors where the flow is constrained. Despite improvements in crowd management, 2,000 deaths annually occur in incidents owing to crowding. Hsieh et al. study considered 215 reports on stampedes occurred at sporting, musical, political and religious [3]. It was found that panic events at religious events were the most severe, with an average of 12 fatalities per stampede. Fewer fatalities are reported in political, sport and musical events, which produce 6, 5 and 3 deaths per stampede. The Muslim pilgrimage to Mecca (also known as the 'Hajj'), is a site with a long history of deaths due to stampedes resulting from panic events. Over the past three decades, nearly 3,000 people have been killed in stampedes during the Hajj; the one in 2006 causing at least 345 fatalities [4].

The numerical study of pedestrian panic has arisen because traditional methods did not attempt to describe the collision or interaction forces between pedestrians. Pedestrian panic models can quantify the interaction forces and stress distributions as pedestrians come into contact with one another. The model proposed in this paper is based on a Discrete Element Model (DEM) developed for granular materials. This approach takes advantage of the computationally efficient and accurate calculation of the interaction forces provided by the well-developed study of granular material. The computer simulations in this model will be based on a complex-shapes particle method, which use spheropolygons instead of rigid discs as discrete elements. This allows for a more accurate pedestrian shape that reflects the morphology of the human chest. The behavior of pedestrians in this model will be governed by a modified form of the DEM which will include a driven force, collision forces, rotational equations of motion, as well as friction and viscous forces.

2 State-of-the-Art of Pedestrian Dynamic Modeling

Pedestrian dynamic modeling simulations have been developed since the pioneer work of Helbing who have been responsible for numerous advances in the field from the mid to end 1990s until now [4–8]. During this time, the key challenge in the pedestrian dynamic modeling has been to achieve rules that guide how the agents considered particles in many cases interact with each other in a way that faithfully reproduces behaviors commonly observed in reality. Earliest studies suggested that motion of pedestrians can be described as if they would be subject to the so-called social forces [5]. These forces would not be directly exerted by the pedestrians' personal environment, but they would be a measure for the internal motivations of the agents to perform movements. The social force model of Helbing and Molnar [5] is one of the best known approaches to simulate pedestrian motion, a collective phenomenon with nonlinear dynamics. The social force model considers that the Newtonian laws of motion mostly carry over to pedestrian motion. Therefore, human trajectories can be computed solving a set of ordinary differential equations

for position and velocity. Earliest studies of evacuation [9,10] were based on a lattice gas model of pedestrian flows. Many observations of the dynamics of pedestrian crowds have been successfully described by simple many-particle models. Xia et al. [11] developed a macroscopic model for pedestrian flow using the dynamic continuum modeling approach. Chraibi et al. [12] introduced a spatially continuous force-based model for simulating pedestrian dynamics, Guy et al. [13] proposed a simple and intuitive formulation based on biomechanical measurements and the principle of least effort. Baglietto and Parisi [14] presented an off-lattice automaton for modeling pedestrian dynamics. Here, pedestrians are represented by disks. The more recent model of Alonso-Marroquín et al. [15] accounts for particle shape using spheropolygons and calculate the full visco-elastic forces.

3 Methodology

The proposed model is based on a modified DEM model that reflects the properties of pedestrians in dense crowds. The so-called spheropolygons are used to represent particles. A spheropolygon is the object generated by sweeping a disk along a polygon [16]; contact forces between spheropolygons are calculated from the vertex-edge distance between their polygons [17]. By including ground-reaction forces and torques, one can simulate dynamics of pedestrian using spheropolygons [15]. These studies represent granular flow in two dimensions, which is convenient to adapt to pedestrians, whose interactions with obstacles and other agents can generally be simplified to two dimensions.

In adapting granular force to pedestrians, the typical gravity force was taken to be analogous to the pedestrian driven force which is a subset of the social forces proposed by Helbing [18]. The agents' desired speed is equivalent to the terminal velocity of particle immersed in a viscous fluid. The cross-section of a pedestrian was derived using an image of a cross section of human thorax and arms. The image was scaled to reflect typical sternum width, and simplified into a closed curve which is then approximated by a spheropolygon, see Fig. 1. The interaction includes contact forces, and self-driven forces, and torques accounting shoulder rotation. A visco-elastic force analogous to the granular force is applied at each physical contact between pedestrians. This force consists of an elastic spring and a damper that accounts restitution after collision [15]; The self-driven force accounts the desired walking speed in a direction chosen by the pedestrian. The motive torque is used by the agent to rotate from their current to their desired orientation was derived using methods proposed by Korohonen et al. [19] and Langston et al. [20]:

$$T = \frac{\lambda I}{\tau^2}[1 - exp(-\frac{v}{v_0})](\theta - \theta_D) - \frac{I}{\tau}\omega \tag{1}$$

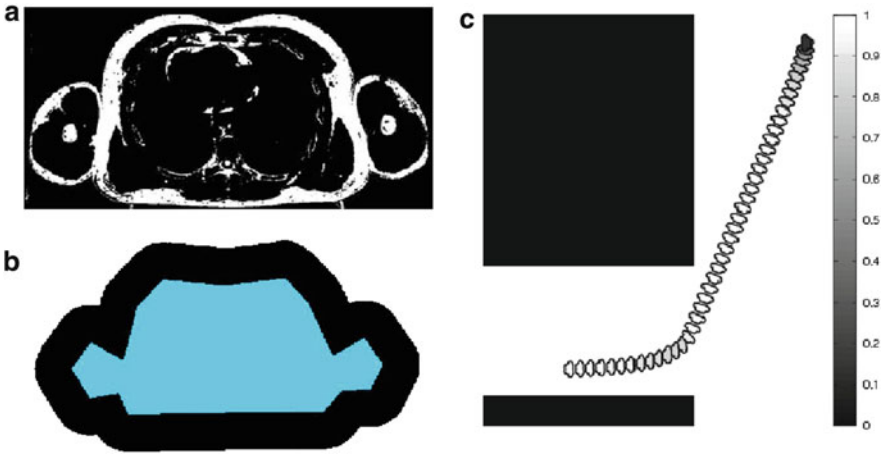

Fig. 1 (**a**) Boundary of the cross-section chest derived from US National Library Image of Thorax; and (**b**) representation of the thorax shape using a spheropolygon with 18 vertices and a spheroradius of 0.05 m. (**c**) Time lapse snapshots of the pedestrian displacement of reorientation. The color bar encodes velocity [m/s] the frame rate is 0.25 s

Table 1 Summary of the model parameters and agent properties

Parameter	Name	Value	Obtained from
k_n	Normal stiffness	10^5 N/m	Force-displacement relation
ρ	Agent density	10^3 kg/m^2	Average mass divided by average area
τ	Reaction time	0.5 s	Time required to reach the desired speed
μ	Coefficient of friction	0.4	Tables of friction between clothes
ϵ	Coefficient of restitution	0.3	Observations of energy loss after collisions
λ	Torsion stiffness	25	Comparison of simulation with video footage

The first term is the ground reaction torque that was considered to arise solely from the pedestrian's desire to face toward their preferred destination. θ is the orientation of the pedestrian and θ_D is the angle to the walking direction. τ is the relaxation time of rotation, and I is the moment of inertia. In Eq. 1, the constant λ is a dimensionless constant that is derived by comparison of simulations with real pedestrian rotation. The exponential factor is used to account for lower motive torque at lower speeds. This is a reflection of higher rotation observed in pedestrians at lower velocities. In this factor, we include the pedestrian speed v and the terminal speed v_0. The second term in Eq. 1 allows the pedestrian to reach their desired angular velocity. As pedestrians prefers not to rotate, the desired angular velocity was set to zero. As a consequence, the pedestrian comes to a comfortable stop after a collision rather than continuing to rotate.

The parameters of the contact force model were chosen as follows, see Table 1: the thorax responses to forces are taken from medical data on thorax deformation [21]; the coefficient of friction $\mu = 0.4$ is close to the coefficient of friction between

pieces of cloth fabric. Since little information is available regarding the coefficient of restitution between pedestrians, we performed observations of pedestrian collisions and obtained coefficients of restitution within the range 0.1–0.5. The parameters of the torque were obtained from video footage observation, as explained in the Table 1. For the simulation presented here, each pedestrian has an initial acceleration of 1 m/s^2 and a terminal velocity if $v_0 = 2$ m/s.

The in-house object-oriented computer program SPOLY was used to conduct the simulations. SPOLY simulates the pedestrian dynamics based on spheropolygons and a five-order predictor-corrector numerical integration. The use of a neighbor table and Verlet distances allows real-time simulation with up to 400 pedestrians. For large-scale simulations with around ten thousands pedestrians the algorithm executes around 1 min of simulations per hour. Details relating to the SPOLY code are found in [16, 17, 22].

4 Results

On the first test, we present the movement of a single pedestrian, as shown in the Fig. 1. Initially, the pedestrian is facing west and its desired direction of motion is towards the center of the exit to a hallway. Initially, the pedestrian rotates their shoulders parallel to its desired direction of motion. Then, the pedestrian accelerates until it reaches its desired speed. When the agent enters the hallways region, the pedestrian turns to east. Here we notice a slight deceleration, as the desired direction is not smooth at the exit. The deviation was not significant relative to forces observed under panic conditions.

Using these results, we simulate the evacuation of a room, and calculate the severity of the contact forces acting on the pedestrians during the process. A total of 500 agents were used in simulations. The room's dimensions were set to 20×24 m, with the exit width varying between 1 and 3 m. All widths lead to a bottleneck forming. As expected, the flow rate increases as the width is increased. When the exit is 1 m width, the system clogs due to interlocking between chest and arm arrangements. Interestingly, this clogging seems to be stable to small perturbations such as slightly shaking of the pedestrians. In reality, we expect the pedestrians will be able to break that arch that is formed on the exit, but breaking is not an instantaneous process, and stresses due to contact forces will persist over minutes during evacuation. The contact forces create an intricate network as shown in Fig. 2. Each link in this network is constructed by connecting the center of mass of the pedestrian with the contact point; the thickness of the width encodes the magnitude of the contact force. We separate the contact forces into severe $F > 400\ N$, mild $40\ N < F < 400\ N$, and low $F < 40\ N$. Severe forces are observed in all simulations. Intuitively, large forces remain for short time in wide corridors, while they are long-lasting in small ones. These long-lasting severe forces are more likely to produce injuries by asphyxiation, especially besides walls and near to the exits.

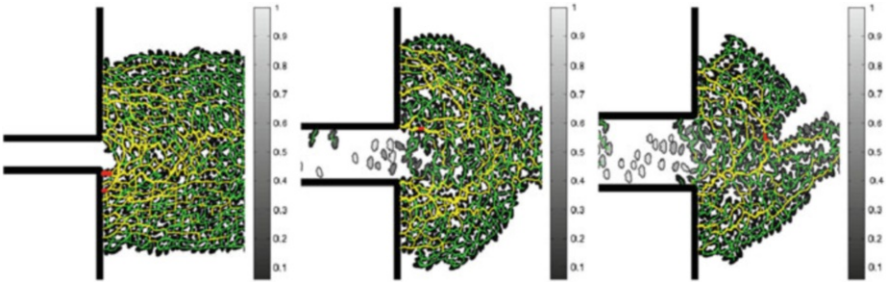

Fig. 2 Snapshot of crowd configuration after 1 min of evacuation of a room. The width of the exit is 1, 2, 2.5 and 3 m. The lines encode the magnitude of contact forces that are classified as severe (*red*) mild (*yellow*) and low (*green*). The color of the pedestrians encodes their speed

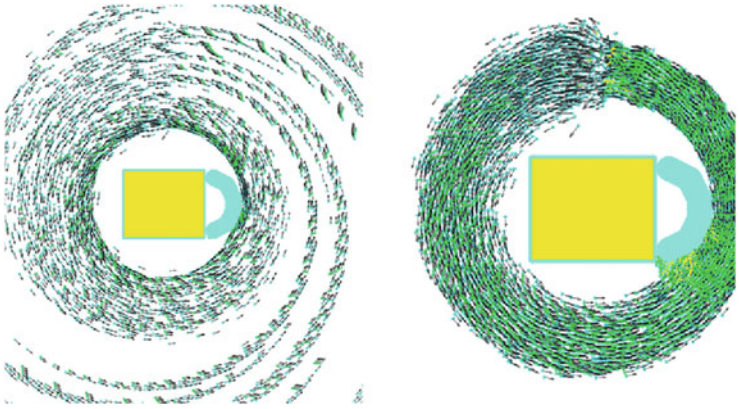

Fig. 3 Snapshots of the simulation of the circling of the Kaaba in the Muslin Hajj peregrination. Besides the rectangular box (Kaaba) lies the semi-circular wall (Hatim). The *arrows* represent the velocity of pedestrians. The snapshots are taken after 5 and 10 min

Understanding how the contact network evolves in pedestrian dynamics is a key factor for calculating probability of injuries in crowd.

The final simulation prepared was the circling of the Kaaba in the muslin Hajj pilgrimage to Mecca, Saudi Arabia. This is the largest mass gathering in the world. The Kaaba is a cube shaped building that act as the direction of muslin prayer. In the Grand Mosque, the pilgrims circle seven times counterclockwise. In the preliminary simulation of this event, we represent both the Kaaba and the Hatim (the semi-circular wall besides the Kaaba) by fixed spheropolygons, see Fig. 3. A total of 6,800 pilgrims were distributed around the Kaaba. The desired direction of motion of a pedestrian is given by the vector $\mathbf{e} = \mathbf{k} \times \mathbf{r} - 0.1\mathbf{r}$; where $\mathbf{r}$ connects the center of the Kaaba to the center of mass of the pedestrian, and $\mathbf{k}$ is a unit vector perpendicular to the floor, pointing upwards. The first component of this equation accounts for the circulation of the pilgrim; and the second one accounts for the tendency to get approach the Kaaba.

Figure 3 shows two snapshots at an early and advanced stage of simulation. The spiral-like pattern results from the combined rotation and attraction of the pilgrims around the Kaaba. Note that the Hatim acts an obstacle that keeps the pilgrims away from the Kaaba. After few minutes, the simulation reach a stationary stage as shown in Fig. 3b. The Hatim helps to create ordered lanes where the pedestrian are in a comfortable contact with each other. These lanes break down spontaneously after a certain point, leading to a less dense configuration where the pedestrian are almost in no contact. The stresses developed in the circling of the Kaaba are quite low (below $F = 40\ N$), which indicate low probability of injuries under this ritual, which is consistent with the lower levels of injuries observed in this ritual. It is expected that major risks of fatalities are likely in the corridor and hallways used by the pilgrims to complete the whole Hajj ritual, and should be investigated in future research.

Conclusions

The extension of the discrete spheropolygon method to simulate pedestrian dynamics provided an improved model in terms of the rotational motion, pedestrian shape, and interaction via contact forces. The rotational equations of motion produced behavior that is consistent with pedestrian rotation. Contact parameters yielded a typical collision with a low coefficient of restitution which was indicated by research, and the shape improvements allowed for a more accurate description of the packing arrangements of panic disasters. The main difficulties with implementing the model were the inherent limitations from using a granular model with insufficient capacity to capture route choice behavior. These restrictions did not, however, obscure the benefits of the proposed improvements to simulate escape dynamics under panic situations. With this aim, we are calling for real case scenarios of crowd dynamics to be simulated with our in-house software, SPOLY. We have capabilities to model real geometry based on scale plans. Besides, complex behavioral rules of the pedestrian can be introduced via ground reaction torques and forces. In addition, more customized pedestrians could be modeled including those that deviate from the crowd's speed to determine the behavior of a more complex crowd. Finally, a more general implementation of the crowd dynamic could be included to increase pedestrian avoidance at low speeds so that behavior is more streamlined and efficient. The field of pedestrian dynamics still has many opportunities for advances in the ever on-going pursuit of accurate modeling methods that inform safe design practices and describes crowd behavior.

Acknowledgements We thank the input Mustafa El Cherkawi in the modelling of Hajj's peregrination, and the discussion with Chraibi Mohcine and Daniel Parisi.

References

1. B.D. Hankin, R.A. Wright, Passenger flow in subways. Oper. Res. Soc. **9**(2), 81–88 (1958)
2. S.A.H. Algadhi, H.S. Mahmassani, Modelling crowd behavior and movement: application to makkah pilgrimage. Trans. Traffic Theory **1990**, 59–78 (1990)
3. Y.-H. Hsieh, K.M. Ngai, F.M. Burkle, E.B. Hsu, Epidemiological characteristics of human stampedes. Disaster Med. Public Health Prep. **3**(04), 217–223 (2009)
4. D. Helbing, A. Johansson, H.Z. Al-Abideen, Dynamics of crowd disasters: an empirical study. Phys. Rev. E **75**(4), 046109 (2007)
5. D. Helbing, P. Molnar, Social force model for pedestrian dynamics. Phys. Rev. E **51**(5), 4282 (1995)
6. D. Helbing, I. Farkas, T. Vicsek, Simulating dynamical features of escape panic. Nature **407**(6803), 487–490 (2000)
7. D. Helbing, R. Jiang, M. Treiber, Analytical investigation of oscillations in intersecting flows of pedestrian and vehicle traffic. Phys. Rev. E **72**(4), 046130 (2005)
8. D. Helbing, A. Johansson, J. Mathiesen, M.H. Jensen, A. Hansen, Analytical approach to continuous and intermittent bottleneck flows. Phys. Rev. Lett. **97**(16), 168001 (2006)
9. D. Helbing, M. Isobe, T. Nagatani, K. Takimoto, Lattice gas simulation of experimentally studied evacuation dynamics. Phys. Rev. E **67**(6), 067101 (2003)
10. M. Isobe, D. Helbing, T. Nagatani, Experiment, theory, and simulation of the evacuation of a room without visibility. Phys. Rev. E **69**(6), 066132 (2004)
11. Y. H. Xia, S.C. Wong, C.-W. Shu, Dynamic continuum pedestrian flow model with memory effect. Phys. Rev. E **79**(6), 066113 (2009)
12. M. Chraibi, A. Seyfried, A. Schadschneider, Generalized centrifugal-force model for pedestrian dynamics. Phys. Rev. E **82**(4), 046111 (2010)
13. S.J. Guy, S. Curtis, M.C. Lin, D. Manocha, Least-effort trajectories lead to emergent crowd behaviors. Phys. Rev. E **85**(1), 016110 (2012)
14. G. Baglietto, D.R. Parisi, Continuous-space automaton model for pedestrian dynamics. Phys. Rev. E **83**(5), 056117 (2011)
15. F. Alonso-Marroquin, C. Lozano, A. Ramirez-Gomez, J. Busch, Simulation of counter flow pedestrian dynamics in hallways using spheropolygons (2013). arXiv preprint arXiv:1310.8482
16. F. Alonso-Marroquin, Spheropolygons: a new method to simulate conservative and dissipative interactions between 2d complex-shaped rigid bodies. EPL (Europhys. Lett.) **83**(1), 14001 (2008)
17. F. Alonso-Marroquin, Y.C. Wang, An efficient algorithm for granular dynamics simulations with complex-shaped objects. Granul. Matter **11**(5), 317–329 (2009)
18. D. Helbing, I.J. Farkas, P. Molnar, T. Vicsek, Simulation of pedestrian crowds in normal and evacuation situations. Pedestr. Evacuation Dyn. **21**, 21–58 (2002)
19. T Korhonen, S Heliovaara, S. Hostikkaa, H Ehtamo, Counterflow model for agent-based simulation of crowd dynamics. Saf. Sci. (2010)
20. P.A. Langston, R. Masling, B.N. Asmar, Crowd dynamics discrete element multi-circle model. Saf. Sci. **44**(5), 395–417 (2006)
21. C.-H. Chi, J.-Y. Tsou, F.-C. Su, Effects of rescuer position on the kinematics of cardiopulmonary resuscitation (cpr) and the force of delivered compressions. Resuscitation **76**(1), 69–75 (2008)
22. F. Alonso-Marroquin, A. Ramirez-Gomez, C. Gonzalez-Montellano, N. Balaam, D.A.H. Hanaor, E.A. Flores-Johnson, Y. Gan, S. Chen, L. Shen, Experimental and numerical determination of mechanical properties of polygonal wood particles and their flow analysis in silos. Granul. Matter **15**(6), 811–826 (2013)

Pedestrian Behavior Analysis in Crowds Using Image-Based Methods

Saira Saleem Pathan and Klaus Richter

Abstract In this paper, we aim to investigate the image-based approaches and propose a framework to examine the pedestrian flow in crowds on various real situations. This research is inclined on two main aspects: first, an in-depth analysis of image-based approaches is given particularly for the situation containing large number of pedestrians (i.e., crowds) and second, our proposed approach which mainly focuses on computing the flow data, modeling, and classifying the corresponding behaviors of pedestrians in a crowd. The dynamic data of underlying crowd scenes establish a large cloud of information (i.e., correlated or un-correlated data). Therefore, it is essential to extract the meaningful information from the data cloud however the selection of criteria is a crucial task which is answered in the first part of the paper. Moreover, in crowded scenes, it is challenging to extract individual characteristics (e.g., head, torso, or leg count) of every pedestrian forming the crowd. Because, the pedestrians do not own these characteristics while moving in the form of groups. Therefore, we can not rely on such individual information of every pedestrian for longer time instances. Based on this fact, in this research, we measure the dynamic contents over consecutive frames. After this, we model this information by computing the Histogram of Flow (HOF) for each time instance. Later, we classify these HOF features according to our behavior-specific classes. We have tested the proposed approach on the dataset recorded with the help of approximately 30 volunteers. In the context of pedestrian behaviors characterization, we have employed Support Vector Machines on our recorded dataset and achieved 91 % classification rate.

1 Crowd Behavior Analysis in Computer Vision

In crowded scenes, behavior understanding of pedestrians is an emerging research domain in computer vision. The process of pedestrians behavior detection includes basic components of image processing, such as motion analysis, feature extraction and classification of behaviors (e.g., normal, abnormal, running, and dispersion) at

S.S. Pathan (✉) • K. Richter
Fraunhofer Institute for Factory Operation and Automation, Magdeburg, Germany
e-mail: Saira_Saleem.Pathan@iff.fraunhofer.de; Klaus.Richter@iff.fraunhofer.de

M. Chraibi et al. (eds.), *Traffic and Granular Flow '13*,
DOI 10.1007/978-3-319-10629-8_22

individual and collective level. However, research in pedestrians behavior analysis itself poses significant challenges due to the inherent self-governing movement of pedestrians in crowds. In literature, robust automated surveillance systems for crowded situations are almost non-existent when taking a quick glance over the literature and industrial applications [1]. In this paper, we provide a detailed analysis of recent research in computer vision for pedestrians behavior analysis in crowds. We have categorized the research of pedestrians behavior understanding in crowded scenes based on the methodology that each work has used to solve this task. Afterwards, the proposed approach is described which is based on simple but yet practical solution to the problem of pedestrians behavior analysis.

1.1 Behavior Analysis with Individual Detection

Motivated with pedestrian-specific recognition of events in non-crowded scenes, the aim of these approaches is to detect activities of pedestrians in crowds. For instance, a model-based segmentation scheme is suggested to localize the pedestrians in crowded scenes by Zhao et al. [2] in a Bayesian framework. With similar goal, a global annealing optimization framework is proposed by Tu et al. [3] using the clustering of interest points based on their (i.e., among) geometric associations to segment the pedestrians in crowds. Also, Brostow et al. [4] proposed an unsupervised Bayesian clustering framework for grouping the trajectories of moving entities based on their space-proximity. Stalder et al. [5] proposed an adaptive grid-based classifier for pedestrians detection in crowds based on the local context. In their approach, different classifiers are trained incorporating various contexts over time, such as scene specific samples from the background, and object class.

1.1.1 Discussion

The main drawback of these methods is that they tend to be impractical in dense crowded scenes because of their inherent limitation when the pedestrians are moving with free style dynamics resulting severe occlusions. Moreover, the computed features, such as interest points, localized heads, and specific human classifiers become unreliable. To overcome this shortcoming, we argue that detection of pedestrian is not crucial; instead modeling the crowd at a global level is more practical in the dense crowd where pedestrians possessing the complex interactions.

1.2 Behavior Analysis with Trajectory Modeling

Over years, tracking algorithms are focused to perform surveillance on non-crowded scenes. Surprisingly, little work has been reported in exploiting high level cues

for human detection, tracking, and behavior analysis for crowded situations. For instance, Antonini et al. [6] proposed a method for detecting and tracking pedestrian behavioral patterns using discrete choice models for crowded scenes. Rodriguez et al. [7] proposed a framework for tracking pedestrians in unstructured crowded scenes by employing the Correlated Topic Model. With similar motivation, Wu et al. [8], proposed a framework for tracking and modeling the trajectories to localize the anomalies in crowds with a three layers framework: (1) particles are advected, (2) grouping of similar trajectories to extract the chaotic dynamics, and (3) these chaotic features are learned by probabilistic model, and a maximum likelihood estimation criterion is adopted to classify the scene behavior state.

1.2.1 Discussion

The individuals in crowds are highly anticipated, and it is difficult to determine the low level features (i.e., color, spatial templates, interest points, contours, etc.) owned by the specific pedestrian. Moreover, due to the complex interaction of pedestrians in the crowds, severe occlusions are observed frequently; therefore, tracking over longer time durations is difficult. Moreover, the resulting track of pedestrians (i.e., trajectories) are highly inconsistent and unable to discriminate between usual and unusual events. Therefore, we contend that the tracking-based models may disregard the important correlation between pedestrian within close proximity and is impractical to handle a wide range of situations under flexible assumptions.

1.3 Behavior Analysis with Modeling Crowd Flow

In earlier attempts, Boghossian et al. [9] proposed a technique to model the pedestrian dynamics such as circular flow paths or emerging and diverging points of the scene using hough voting. Later, Andrade et al. [10] employed optical flow and used generative model (i.e., ergodic HMM) at a global level for normal motion patterns of pedestrians where the anomaly is treated as outliers. With a different perspective, Kratz et al. [11] model the statistics of spatio-temporal gradients (i.e., cuboids) with coupled HMM to characterize the behaviors in dense crowds. Taking inspirations from pedestrian behavioral modeling, Mehran et al. [12] suggested a social force model with the optical flow based particle advection technique and simulate the normal social forces of particles implicitly to detect the deviations from pre-trained parameters. Further, these particle forces are modeled for normal behaviors where bag of words approach is employed to classify the normal and abnormal characteristic of crowd. In their later work by Wu et al. [8], trajectories of advected particles are modeled to localize the abnormality. However, the resulting tracks on the test dataset are highly inconsistent as it is difficult to determine the pedestrian at the pixel level and their associations in next frames. Albio et al. [13]

measure the optical flow at corner points and constitutes histograms to detect the deviations and abnormalities on PETS2009 [14] dataset. In similar context, Benabbas et al. [15] build the online probabilistic models for both density and orientation of flow patterns to detect the crowd activities. Another work is presented by Chan et al. [16] to holistically model the crowd flow in the scene using the dynamic texture model where Nearest Neighbour (NN) and Support Vector Machines (SVM) are used as classifiers to detect the events in crowds. Similarly, Mahadevan et al. [17] proposed a framework to model the normal dynamics of the crowd using mixtures of the dynamic textures hypotheses. The experiments are demonstrated on a new dataset containing the different definitions of anomalies such as walking in wrong direction or vehicles over walking area.

1.3.1 Discussion

In pedestrian (or crowd) behavior analysis, the term anomaly (i.e., abnormal: both terms used interchangeably, unless specified) is formalized as an outlier detection problem. In video streams, capturing certain motion properties in situations containing concurrent and sparse pedestrian activities are extremely difficult. For example, in coherent crowds (e.g., marathon), the pedestrians may move with common dynamics which is relatively easy to model. But many scenes (e.g., shopping centers) contain completely random movement of pedestrians resulting in a complicated dynamics, and it is difficult to model the overall dynamics. In the literature, generative modeling approaches [10, 11] (i.e., HMM and LDA) require stringent conditional independence among the observed flow fields for more tractable joint distributions. On the contrary, Mehran et al. [12] assume the particles as pedestrian but they are not able to detect anomaly due to the multiple interacting crowd because it requires the knowledge about physical quantities making this approach impractical.

2 Proposed Framework

In this paper, we propose a framework to detect pedestrian behavior in crowds using image-based methods. The proposed framework is staged in several phases to model and characterize the behaviors in crowded scenes. The measured optical flow over each frame in the video stream is modeled by computing the histogram at flow values defining the distinct feature for the each block. Next, the corresponding crowd behavior is detected through SVM classifier. Finally, the cumulative behaviors are inferred for each time instance.

2.1 Histogram of Flow and Behavior Classification

In this paper, the dynamic information over the consecutive frames is computed by optical flow approach [18]. The observed flow cloud data is transformed into a flow vector $f = (v_x, v_y)$ where v_x and v_y represent the velocities along the horizontal and vertical axis of the motion field. Next, each frame is sectioned into $N \times M$ blocks of size (i.e., $size = 16$), selected after conducting empirical studies over our dataset. Mathematically,

$$\mathbf{V} = [I_1, \ldots, I_K], \quad I_k = \{B_1, \ldots, B_L\} \; and \quad B_l = (f_1, \ldots, f_P)$$

where $\mathbf{V}$ is the video sequence containing K frames, B_L are the flow blocks in the K-th frame. Each flow block keeps P cloud of flow data which serves as a fundamental information for the analysis of pedestrian's behaviors in crowd.

The cloud of flow data P in each flow block represents the dynamic content. The flow cloud data is defined as 2d flow vectors (i.e., $f = (v_x, v_y)$) in each flow block as random variables which are extended over frames (i.e., K). But, the direct use of raw optical flow data in each flow block is not very useful, as it can be significantly different and correlated. However, it is important to note that the optical flow profiles vary according to the context and situation. Later, HOF is computed over the flow data which is spatially differentiated by making flow blocks in each frame. Each flow vector $f = (v_x, v_y)$ in flow block is binned according to its orientation $\theta = \arctan(\frac{v_y}{v_x})$ and magnitude $m = \sqrt{v_x^2 + v_y^2}$. The histogram is formed for each flow block by directional binning (i.e., with $\theta = 45$ making 8 bins) of orientation corresponding to its magnitude. By doing so, we are able to handle the optical flow uncertainties because the noisy flow values have an insignificant effect on the observed histogram as well. Finally, we pick the bin with the highest frequency and take its magnitude and direction as a representative features for the corresponding flow block.

After the feature extraction, the next step is to classify pedestrian behaviors in the crowd as normal and abnormal to analyze the overall situation of the scene. We use the magnitude from the HOF as our main representative feature for each flow block. For the classification SVM [19], a supervised learning technique for optimal modeling of data is used with Radial Basis Function as a kernel. In the experiments, each flow block is classified as normal or abnormal as shown in Fig. 2.

3 Experimental Results

The results of the proposed approach is tested on our record dataset where 30 volunteers are depicting the actions of various kinds (i.e., group walk or run). The normal situations are represented by the usual walk of large number of pedestrians whereas the corresponding abnormal situations (i.e., running, panic and dispersion)

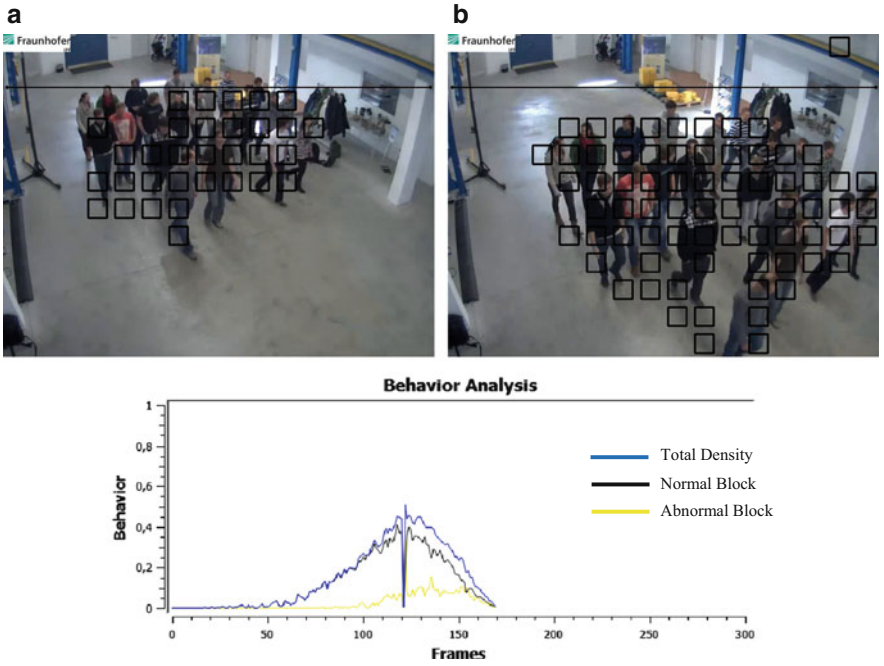

Fig. 1 (**a**) and (**b**) shows the results where normal behaviors are indicated by *black blocks* (Photo:Fraunhofer IFF)

are observed when pedestrians or groups of pedestrians deviate from the normal behavior. Figure 1 shows the results on our dataset where pedestrians are moving with normal behavior while moving in groups. In contrast, Fig. 2 presents the results when the pedestrians are having abnormal state due to any unknown reason. In Fig. 2a, the group of pedestrians are entering whereas after some instance of time, it can be observed that all the pedestrians are running with a common goal as shown in Fig. 2b. The graphs in Figs. 1 and 2 present the overall detection of corresponding pedestrian behaviors (i.e., yellow curve shows anomaly, black curve shows normal, and blue curve shows the density of pedestrians in the crowd) at each time instance.

As described in an earlier section, the definition of anomaly (i.e. abnormality) is context specific. We assume that the categorization of pedestrian behavior in a scene as normal and abnormal is somehow fuzzy. Therefore, we provide the information of both behaviors to scene analyst through the graphical and visual representation. For this purpose, a statistical analysis with an option of defining a threshold (i.e., if abnormal behavior is more than 50 %) is provided by computing $\%Anomaly = \frac{AbNB}{Nb+AbNB} * 100$. Where $\%Anomaly$ defines the total abnormal behavior of pedestrians in the scene which is computed as the ratio of total flow blocks detected as abnormal ($AbNB$) relative to the total ($Nb+AbNB$) normal and abnormal

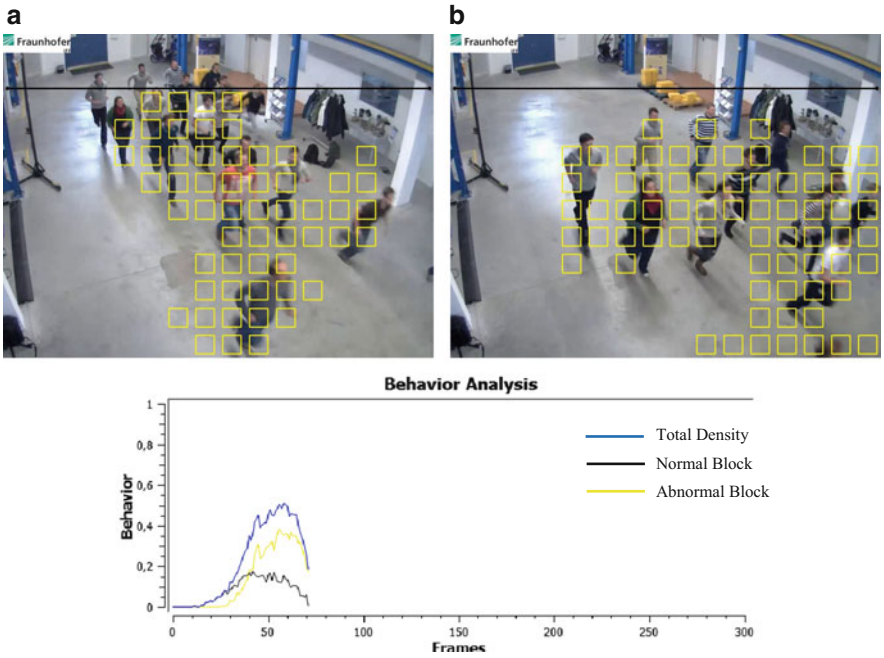

Fig. 2 (**a**) and (**b**) shows the results where abnormal behaviors are indicated by *yellow blocks* (Photo:Fraunhofer IFF)

classified flow blocks. In our proposed approach, we aimed to address the issues of pedestrian behavior analysis (i.e., in the context of crowd analysis) and achieved our defined objectives. However, the proposed approach has certain limitations for instance, detection of high level events like recognition of paths blocking or falling down of pedestrians in crowd. However, further interpretations can be built on top of the proposed approach by employing the strong assumptions according to the social behaviors of pedestrians in crowds and the contexts of application.

Conclusion

In this paper, we introduced a method to identify the behaviors of pedestrians in crowds. A top to down methodology is adapted which captures the dynamic characteristics of pedestrians in the form of flow data and computes features with HOF approach. The SVM classifier is used to localize the specific and overall behavior of the pedestrians in crowds. The results show that our approach successfully identifies the behaviors of pedestrians in crowds.

Acknowledgements The authors are partially funded by the Federal Ministry of Education and Research (BMBF) within the project ViERforES (No. 01IM08003C).

References

1. B. Zhan, D. Monekosso, P. Remagnino, S. Velastin, L. Xu, Crowd analysis: a survey. Mach. Vis. Appl. **19**, 345–357 (2008)
2. T. Zhao, R. Nevatia, Tracking multiple humans in complex situations. IEEE Trans. Pattern Anal. Mach. Intell. **26**, 1208–1221 (2004)
3. P.H. Tu, J. Rittscher, Crowd segmentation through emergent labeling, in Statistical Methods in Video Processing ed. by D. Comaniciu, R. Mester, K. Kanatani, D. Suter. Lecture Notes in Computer Science (Springer, Berlin/Heidelberg, 2004), pp. 187–198
4. G.J. Brostow, R. Cipolla, Unsupervised bayesian detection of independent motion in crowds, in *Proceedings of IEEE Computer Society Conference on Computer Vision and Pattern Recognition (CVPR) – Volume 1*. New York (IEEE Computer Society, 2006), pp. 594–601
5. S. Stalder, H. Grabner, L.V. Gool, Exploring context to learn scene specific object detectors, in *IEEE International Workshop on Performance Evaluation of Tracking and Surveillance*, Miami, 2009
6. G. Antonini, S. Martinez, V. Santiago, M. Bierlaire, J. Thiran, Behavioral priors for detection and tracking of pedestrians in video sequences. Int. J. Comput. Vis. **69**, 159–180 (2006)
7. M. Rodriguez, S. Ali, T. Kanade, Tracking in unstructured crowded scenes, in *Proceeding of IEEE International Conference on Computer Vision*, Kyoto, pp. 1389–1396, 2009
8. S. Wu, B.E. Moore, M. Shah, Chaotic invariants of lagrangian particle trajectories for anomaly detection in crowded scenes, in *IEEE Conference on Computer Vision and Pattern Recognition*, San Francisco, 2010
9. A. Boghossian, A. Velastin, Motion-based machine vision techniques for the management of large crowds, in *Proceedings of 6th IEEE International Conference on ICECS Electronics, Circuits and Systems*, Pafos, vol. 2, pp. 961–964, 2002
10. E.L. Andrade, B. Scott, R.B. Fisher, Hidden markov models for optical flow analysis in crowds, in *Proceedings of the 18th International Conference on Pattern Recognition*, Hong Kong (IEEE Computer Society, 2006), pp. 460–463
11. L. Kratz, K. Nishino, Anomaly detection in extremely crowded scenes using spatio-temporal motion pattern models, in *IEEE Conference on Computer Vision and Pattern Recognition*, Miami, pp. 1446–1453, 2009
12. R. Mehran, A. Oyama, M. Shah, Abnormal crowd behavior detection using social force model, in *IEEE Computer Society Conference on Computer Vision and Pattern Recognition*, Miami, vol. 0, pp. 935–942, 2009
13. A. Albiol, M. Silla, A. Albiol, J. Mossi, Video analysis using corner motion statistics, in *Performance Evaluation of Tracking and Surveillance Workshop at CVPR 2009,* Miami, Florida, pp. 31–37, 2009
14. J. Ferryman, A. Shahrokni, PETS 2009 (2009). http://www.cvg.rdg.ac.uk/PETS2009
15. Y. Benabbas, N. Ihaddadene, C. Djeraba, Global analysis of motion vectors for event detection in crowd scenes, in *Performance Evaluation of Tracking and Surveillance Workshop at CVPR 2009,* Miami, Florida, pp. 109–116, 2009
16. A.B. Chan, M. Morrow, N. Vasconcelos, Analysis of crowded scenes using holistic properties, in *Performance Evaluation of Tracking and Surveillance Workshop at CVPR*, pp. 31–37, 2009
17. V. Mahadevan, W. Li, V. Bhalodia, N. Vasconcelos, Anomaly detection in crowded scenes, in *Proceedings of IEEE Conference on Computer Vision and Pattern Recognition*, San Francisco, pp. 1975–1981, 2010
18. G. Farnebäck, Two-frame motion estimation based on polynomial expansion, in *Proceedings of the 13th Scandinavian Conference on Image Analysis (SCIA'03)*, Halmstad (Springer, Berlin/Heidelberg, 2003), pp. 363–370
19. N. Cristianini, J. Shawe-Taylor, *An Introduction to Support Vector Machines: And Other Kernel-Based Learning Methods*, 1st edn. (Cambridge University Press, Cambridge/New York, 2000)

Dynamic Structure in Pedestrian Evacuation: Image Processing Approach

Kohta Suzuno, Akiyasu Tomoeda, Mayuko Iwamoto, and Daishin Ueyama

Abstract We show that there exists a typical dynamic arch-shape structure in pedestrian evacuation system governed by the social force model. It is well known that the simulation of pedestrian evacuation from a square room using the social force model shows arch-shape formation and clogging in front of the exit. It is also known experimentally and numerically that an obstacle near the exit could improve the flow rate, but detailed mechanism of this effect is not clear. In this paper, we show the existence of the "dynamic arch", the typical structure in the long term, by using the social force model and the image processing. The time-averaged image of the system shows us the existence of the typical structure in the system and it can be interpreted as the probability distribution of the arch formation. With this method, we discuss the possible physical mechanism of the effect of an obstacle in the pedestrian system. From the observation of the morphological feature of the arch obtained by the simulation and image processing, we show that the obstacle affects the structure of the arch in three ways. These effects could lead the easy-to-break arch that enhances the flow rate of the system.

1 Introduction

Congestion of particles at a bottleneck is one of the major problems in granular and pedestrian systems. Let us consider the discharge of dissipative particles from a square box through a single narrow exit. Such a system sometimes shows clogging when many particles rush to the exit simultaneously. We can see such phenomena in the granular systems (the silo, the glass hour) and the pedestrian systems

K. Suzuno (✉) • M. Iwamoto • D. Ueyama
Graduate School of Advanced Mathematical Sciences, Meiji University, 4-21-1 Nakano, Nakano-ku, Tokyo, 164-8525, Japan
e-mail: suzunogk@meiji.ac.jp

A. Tomoeda
Meiji Institute for Advanced Study of Mathematical Sciences, Meiji University, 4-21-1 Nakano, Nakano-ku, Tokyo, 164-8525, Japan

CREST, Japan Science and Technology Agency, 4-21-1 Nakano, Nakano-ku, Tokyo, 164-8525, Japan

M. Chraibi et al. (eds.), *Traffic and Granular Flow '13*,
DOI 10.1007/978-3-319-10629-8_23

(the evacuation from a room or through a corridor). In many cases, this clogging leads undesirable results so that the mechanism should be clarified to improve the particle flow.

One possible cause for the phenomena is the existence of the dynamic arch, the arch-shaped dynamic structure [1]. The arch is formed and broken repeatedly, and this structure decreases the flow rate.

On the other hand, we also have some hopeful solutions for that situation. Some experimental and numerical studies have shown that one possible solution is to place an obstacle near the exit [3, 6, 7]. It is said that the obstacle absorbs pressure [3] and enhances smooth evacuation. But the effect of the obstacle depends on the configuration of the obstacle (the shape, the position, and others) so that we need to clarify how the obstacle works.

In this paper, we discuss this obstacle effect from the viewpoint of the dynamic arch by using the social force model (SFM) [4] and the image processing technique. Inspired by the work that visualize the static clogging of granular media [2], we show the existence of the long-term structure of the dynamic arch in the evacuation system by using the SFM and the image processing. By this, we give the visualization of the dynamic arch and investigate the relation between the position of the obstacle and the structure of the arch. In this study, we use quite simple geometry and focus only on the effect of the position of the obstacle. Generally, the pedestrian system has many parameters and they affect the efficiency of the evacuation in a complicated way. For example, the relation among the driving force, the position of the obstacle, and the size of the obstacle is also important aspect of the system [5]. But the main purpose of this paper is to discuss the relation between the structure of the arch and the flow rate, so that we just focus on the effect of the obstacle position, and we also pay attention to the small area just in front of the exit.

2 Methods

Let us consider the discharge of the self-driven particles from a box-shape room through a single narrow exit. Let the motion of the particles be governed by the SFM [4]. The situation of the system is described in Fig. 1. The size of the particles are uniform, and the self-driven force for each particle is set to 3 m/s. The number of particles is 150. The particles distribute randomly in the room as an initial condition. The SFM parameters used here are based on Helbing et al. [4]. In this study, we use the periodic boundary to keep the number of particles inside the room constant to remove the N dependence of the flow rate. The numerical scheme is RK2 with $dt = 0.001$ s.

From this simulation, we generate many snapshots and investigate them. But what we are interested in here is the dynamic formation of the particles, thus we depict the contact network of the particles instead of the shape of the particles. If any two particles have the overlap above a given threshold, we draw a line that connects two particles. Here the threshold is set to 0.01 m to visualize the dominant

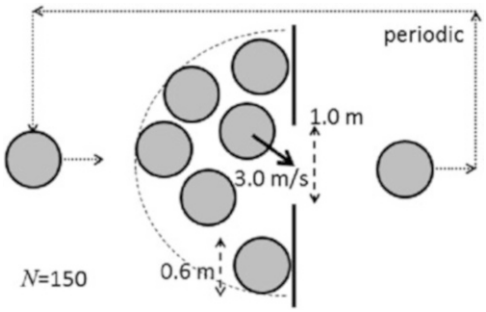

Fig. 1 Details of the system. The self-driven particles rush to the exit and evacuate from the room. All particles have the same diameter (0.6 m) and the self-driven force (3.0 m/s). They go out through the exit (1.0 m) and return to the room from the opposite side of the exit. The number of particles is 150. We observe this evacuation process up to 300 s

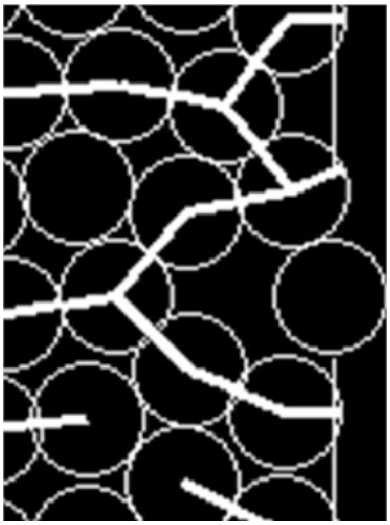

Fig. 2 Example of contact force network. The particles move from left to right side of the picture. When two particles have penetrated, the *white line* that connects two particles is depicted, and the system shows the network structure. In this calculation, the thickness of the line does not depend on the magnitude of force for simplicity. Note that the shape of the particles (*circles* in the picture) is depicted in this example picture for clarification, but it is not drawn in the actual calculation

connection in the system and to remove the "light touch" connection between particles. As a result, we obtain the pictures that show the connection of the particles for each time step (Fig. 2).

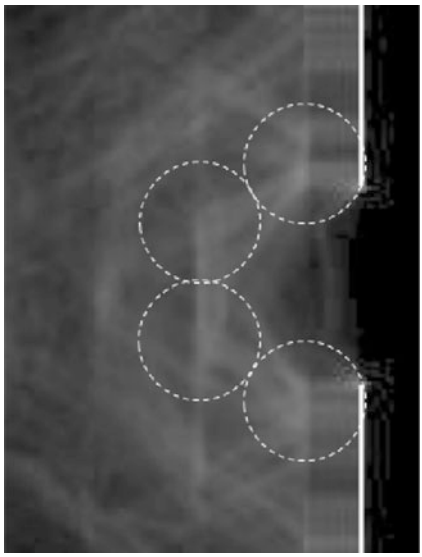

Fig. 3 Example of time-averaged network. The *white lines* show the averaged contact network in this many-particle system. Here gamma correction ($\gamma = 2.0$) is used and the additional *circles* are depicted for visibility. The four-particle arch is the most frequently occurred structure. The picture also shows the vague triangular lattice in the bulk region (behind the arch), and it reflects the mono-disperse property (all particles have the same diameter) of the system

Next, we perform the following image processing technique. Let us denote the pixel value in the position (i, j) on the picture taken at time t as $I_{ij}(t)$. Then we generate the time-averaged image

$$< I >_{ij} = \frac{1}{N} \sum_{n=1}^{N} I_{ij}(ndt), \tag{1}$$

where N is the number of images generated from the simulation, and dt is the time step. The resulting image means the probability distribution of the contact network. We assume that the structure presented in the resulting image can be interpreted as the dynamic arch of the system. The image obtained by the above method visualizes the possible dynamic structure and its frequency in the system. The typical result is given in Fig. 3.

As we can see, it shows many types of arch-like structures in front of the exit. It implies that the arch that consist of four particles is the most frequently observed structure. Around the arch, many faint triangles are observed and they are the results of mono-disperse property of the system.

3 On the Effect of the Obstacle

By using the above technique, we investigate visually the effect of the obstacle on the structure of the arch. We place the obstacle near the exit in our system which shape is the same as the particles. Then we conduct the simulations with different

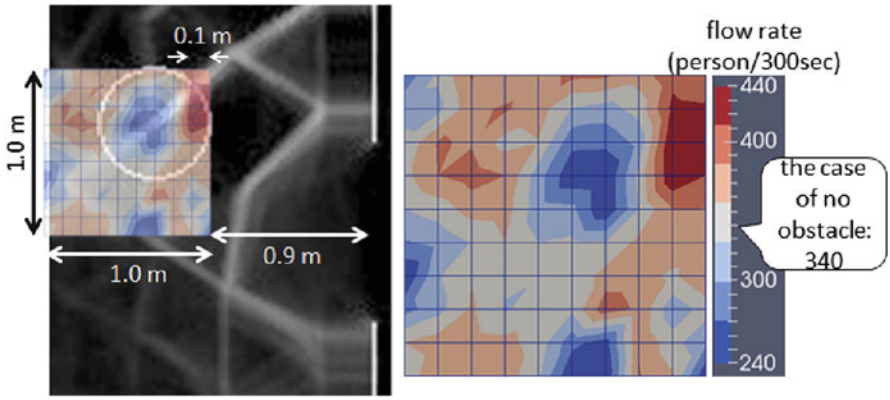

Fig. 4 Results of the numerical simulation. We calculate the flow rate by using the SFM with different configuration of the obstacle. The size of the obstacle is the same as the particles. (*Left*) The position of the obstacle considered here is shown as the lattice point in the figure. The *circle* in the figure is the example of the obstacle. (*Right*) The color distribution shows the flow rate for each obstacle position. *White area* correspond to the flow rate without obstacle (340 person/300 s)

position of the obstacle and obtain the distribution of the flow rate as a function of the obstacle position. We place the obstacle inside the following region: $0.9\,\mathrm{m} \leq X \leq 1.9\,\mathrm{m}$ and $0.0\,\mathrm{m} \leq Y \leq 1.0\,\mathrm{m}$, where X and Y are the distance from the center of the exit. The resulting flow rate is given in Fig. 4.

The distribution of the flow rate shows that the obstacle improves the flow rate in many cases. But we also have some "spots" where the flow rate decreases compare to the no-obstacle case. As we can see, these spots are distributed in a triangular manner, and their positions correspond to the case of the most packing situation. In such cases, the obstacle enhances the closely-packed dense configuration of the particles. Another notable feature in the figure is the top-right area where the flow rate improves considerably due to the obstacle. This means that the shifted obstacle (not just in front of the exit) leads better flow rate.

4 Possible Mechanisms of the Obstacle Effect

We performed simulations with different positions of the obstacle, and compared the results of the shape of the arch. Figure 5 shows the case of no-obstacle and the case that attain the highest flow rate. Comparing these results, we can extract three morphological factors of the shape of the arch. The flow rate increases when (i) the arch has a space to deform, (ii) the position of the arch is shifted, and (iii) the arch is distorted. If there is a enough space around the exit, the arch can be deformed easily and the symmetry is broken. The obstacle could take a role as a barrier from the particles behind, protect the arch, and make a room to deform. The existence of

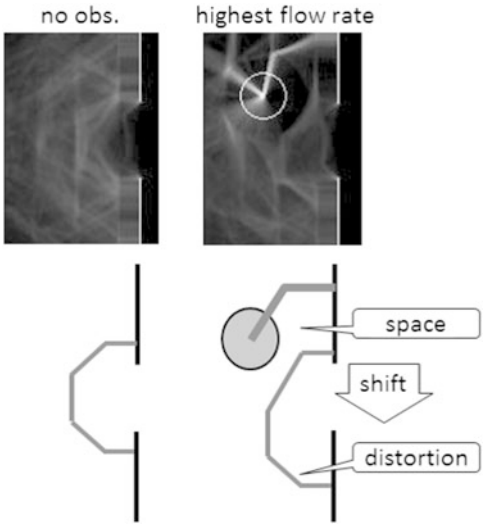

Fig. 5 Morphological observation of the arch. In no-obstacle case (*top-left*), the shape of the arch is almost symmetric. On the other hand, the situation that attain the highest flow rate (*top-right*) shows asymmetric arch. Here gamma correction is used for visibility ($\gamma = 2.0$). The obstacle covers the arch in front of the exit and protect it from the particles behind. The obstacle makes a space, and it also allows the arch to be shifted and distorted (*bottom*)

the obstacle also breaks the symmetry of the force from behind so that the center-of-mass of the arch is shifted to one side and one of the leg of the arch is on the edge of the exit. Furthermore, asymmetric force leads the distorted arch, and the combination of these factors result in an easy-to-break arch. The improvement of the flow rate occurs when we place the obstacle at an appropriate position where the above three factors are realized.

Conclusion

We investigated the dynamic arch by combining the simulation with the image processing. By using these techniques, we qualitatively clarified the effect of the obstacle in the pedestrian simulation. The morphological observation of the result from the SFM and the time-averaged image is performed, and the results imply that the flow improvement by the obstacle comes from (i) the space around the arch (these might be equivalent to the pressure absorption [3] or dilatancy), (ii) the shift of the center of the arch, and (iii) the distortion of the arch. Note that the study presented here has many simplifications. We focus only on the physical properties of the system, and neglect some social aspects. The contact force network we investigate here does not reflect the magnitude of force (so called force chain). We need to include these factors for further quantitative investigation of the effect of the obstacle.

Acknowledgements This work is supported by the Meiji University Global COE Program "Formation and Development of Mathematical Sciences Based on Modeling and Analysis."

References

1. C.M. Carlevaro, L.A. Pugnaloni, Eur. Phys. J. E **35**, 44 (2012)
2. A. Garcimartín, I. Zuriguel, L.A. Pugnaloni, A. Janda, Phys. Rev. E **82**, 031306 (2010)
3. D. Helbing, L. Buzna, A. Johansson, T. Werner, Trans. Sci. **39**, 1 (2005)
4. D. Helbing, I. Farkas, T. Vicsek, Nature (London) **407**, 487 (2000)
5. T. Matsuoka, A. Tomoeda, M. Iwamoto, K. Suzuno, D. Ueyama, in Traffic and Granular Flow '13, ed. by M. Chraibi, M. Boltes, M. Schadschneider, A. Seyfried (Springer, 2014)
6. D. Yanagisawa, R. Nishi, A. Tomoeda, K. Ohtsuka, A. Kimura, Y. Suma, K. Nishinari, SICE J. Control Meas. Syst. Integr. **3**(6), 395 (2010)
7. I. Zuriguel, A. Janda, A. Garcimartín, C. Lozano, R. Arévalo, R. Maza, Phys. Rev. Lett. **107**, 278001 (2011)

Human-Ant Behavior in Evacuation Dynamics

Daniel R. Parisi and Roxana Josens

Abstract Recently, it has been shown that ants evacuate efficiently during a life-and-death situation displaying an unselfish behavior (Boari et al., PlosOne 8:11, 2013, e81082). Here, we model this ant behavior and compare it with the more expected selfish (human) behavior by considering different mixtures of evacuating agents with both kind of behaviors. Two unselfish behaviors were studied using the social force model as physical bases. For the *ant-like* behavior, an optimum mixture is found at 80 %. In the case of *living-obstacle* behavior, only 29 % is required to achieve the minimum evacuation time. In general, the simulations with a mixture of selfish and unselfish behavior show improvement in the evacuation time and blockage probability of the exit.

1 Introduction

The main motivation of our work is to investigate the highly competitive egress of people through narrow doors, which can display clogging, jamming and blockage with the consequent loss of capacity and increased risk. What we understand by highly competitive behavior is a pushing life-and-death behavior that would be present if the estimated time to egress [1] is greater than or similar to the estimated Available Safe Egress Time [2]. This kind of behavior was also named as "impatient" in Ref. [3] and "selfish evacuation behavior" in Ref. [4].

Because controlled experiments in laboratory conditions of this system have several complications, we decided to study simpler and somehow similar systems such as granular matter [5] and ants [4, 6]. Unfortunately, these social insects have demonstrated efficient evacuations [6] and, unlike most of the animals, ants display

D.R. Parisi (✉)
Instituto Tecnológico de Buenos Aires, 25 Mayo 444, (C1002ABJ) C. A. de Buenos Aires, Argentina
e-mail: dparisi@itba.edu.ar

R. Josens
Instituto de Fisiología, Biología Molecular y Neurociencias, FCEN – UBA, Pabellon II, Ciudad Universitaria, (C1428EHA) C. A. de Buenos Aires, Argentina
e-mail: roxy@bg.fcen.uba.ar

M. Chraibi et al. (eds.), *Traffic and Granular Flow '13*,
DOI 10.1007/978-3-319-10629-8_24

neither selfish evacuation behavior, nor highly competitive egress, nor jamming or clogging near the door [4, 6]. In consequence, we claim that humans and ants have a mismatched behavior.

In normal conditions, clearly ants cannot model humans because their fundamental diagram has a very different nature, i.e., the speed of ants does not depend on their density [7] contrary to what occurs in vehicle and pedestrian traffic. Moreover, ants do not produce jamming [7, 8]. But not only in normal conditions are ants so different to humans, they are perhaps more different under emergency situations.

On the one hand, in the presence of a real danger most animal species, and human beings in particular, behave individually trying to escape from the danger as soon as possible, in a direct path to the exit. In this extreme circumstance the survival of the individual prevails. This statement is supported by the following examples:

1. Stampedes during real catastrophes such as the one that occurred at "The Station Night Club" fire (Rhode Island, USA, 20 Feb 2003), which has been uploaded (http://www.youtube.com/watch?v=OOzfq9Egxeo). People that tried to egress simultaneously through the main door caused the blockage of that door [9].
2. Saloma et al. [10] found this response when studying the egress of mice from a water pool.
3. Zuriguel et al. [11] also observed the same response when studying the passage of sheep through a narrow door.
4. Most of the pedestrian egress models consider this behavior, for example in the seminal paper of Helbing et al. [12].
5. Under threatening conditions, in principle, people could rush or not toward the exit. As this decision has an impact on the payoffs of each agent and the whole group, it can be studied from the point of view of game theory. Heliövaara et al. [3] have shown that jamming and clogging may be caused by people acting rationally, even when this rational individual behavior results in a bad strategy for the group.

In all these cases, jamming and clogging are generated upstream the exit door causing the loss of evacuation efficiency.

On the other hand, ants do not follow a direct path to the exit under emergency egress conditions and thus, clogging and jamming at the door are not observed. This fact can be seen, for example, in the following articles:

1. A complete evacuation process of one of the experiments conducted by Altshuler et al. [13] can be seen on the journal's Web site. There, it is possible to observe that ants did not produce jamming near the doors.
2. In Fig. 3 of Ref. [14] it can be seen that the exits do not show a higher density than the rest of the surrounding areas.
3. In Ref. [4] it was explicitly stated that ants did not generate jamming near the exit, for none of the intensities of the aversive stimulus studied (different citronella concentrations). Moreover, in this work it was warned that ant models should not be used for validating human egress simulations.

4. Also, the behavioral pattern of not following a direct path to the exit, and not clogging or jamming, was observed in Argentine ants (*Linepithema humile*) stressed with high temperature [6]. In this paper it was found that ants, even under a life-and-death situation, egress efficiently displaying a *faster is faster* effect.

Furthermore, in any of these examples it is important to differentiate similar physical observables from the microscopic mechanism that creates them. In the case of the *faster is slower* (FIS) effect observed in ants [4], it was highlighted that the cause that originates the FIS effect is different from that in crowd simulations, because in the latter system the FIS effect is generated by high tangential friction [15] and in ants it is not, as can be observed in the examples mentioned above. Similarly, the improvement by placing a column upstream the door [14] is not for the same reason as in the social force model simulation or granular matter experiment [16–18]. In these two systems the column reduces the pressure before the exit while, again, in the ant system no such pressure exists because ants do not produce jamming or high frictional contact.

Considering these differences, we discourage the approach proposed in Ref. [14, 19, 20] where it is claimed that results from ant experiments can be directly extrapolated to human systems. This approach is not justified and its application could lead to grievous errors of design.

Instead, we propose studying ant egress, given that they display an efficient evacuation behavior, and try to use its mechanism to enhance human evacuation protocols. Our approach is to model ant behavior when evacuating through a narrow door and then study pedestrian simulations by varying the fraction of agents with selfish and unselfish (ant-inspired) behavior. In this sense, valid questions about individual and collective ant behavior can be posed, such as: Is this behavior better than the selfish one? Is there an optimum mix of both behaviors in a population?

2 Ant Behavioral Model

In this section we propose a very simple phenomenological model for describing ant behavior when evacuating under an emergency situation. As physical background we will use the social force model [12] describing simulated pedestrians with a high desired velocity of 6 m/s. The rest of the parameters are the same as in that paper considering a 20×20 m room with a 1.2 m door and 200 agents. The behavior is defined only through the direction of the driving force and there are, in principle, two possible behaviors: (a) selfish evacuation behavior: the agent goes directly toward the door from the beginning of the evacuation and (b) *ant-like* behavior: the agent does not go toward the door from the start of the evacuation, but some time later.

In the *ant-like* behavior, the criterion for deciding when to go directly toward the door is based on the following fact. In the ant evacuation experiments performed using citronella as aversive stimuli [4], it was observed that the discharge curve, i.e.,

the number of ants inside the room as a function of time, follows an exponential decay law (Parisi et al., Unpublished). It was also observed that ants move fast during emergency but do not follow a direct path to the door [4, 6] displaying exploratory trajectories by going to undefined points inside the room. From these observations we propose the following *ant-like* behavior:

1. Initially, agents move toward random points inside the room.
2. Every second, each agent can change its state with probability λ.
3. If agent i changes its state, it moves toward the door and gets out.

The results of simulating this behavior, for a given value of λ, are depicted in Fig. 1. Typical snapshots obtained at different times are shown in Fig. 1a, b. Figure 1c displays the whole population of agents inside the room and the group going directly toward the door as a function of time. Clearly, higher values of λ will increase the rate at which agents begin to try to exit, and thus, increasing jamming and clogging will occur with the consequent increase of the partial evacuation time (PET). On the

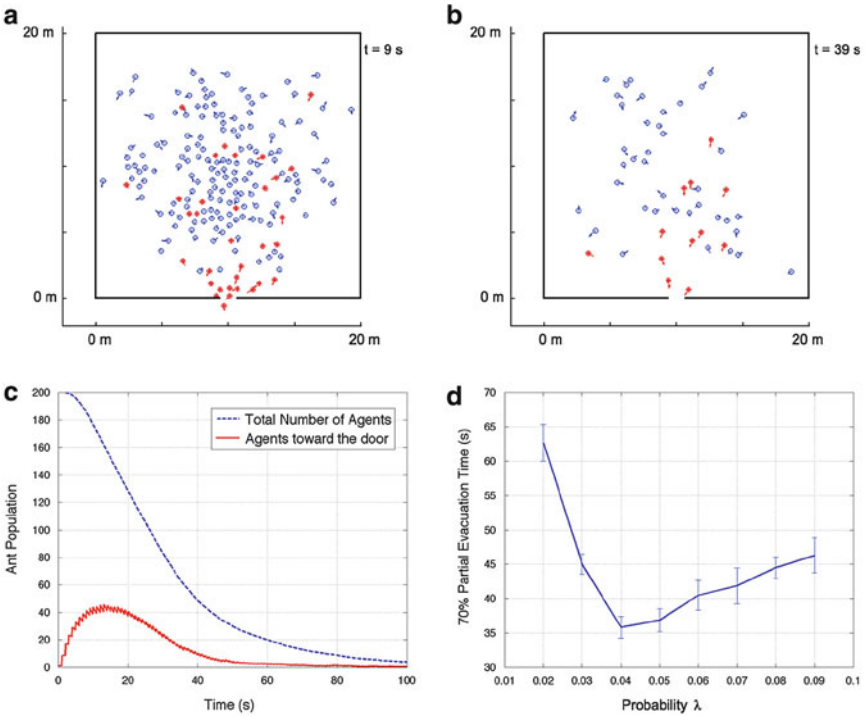

Fig. 1 Results of simulations of agents with pure *ant-like* behavior. (**a**) and (**b**) Snapshots at times 9 and 39 s. The *red* (*filled*) agents are going toward the door and the *blue* (*empty*) agents are wondering around inside the room. *Arrows* display instant velocities. (**c**) Evolution of the total number of agents inside the room (*blue-dashed line*) and the ones heading to the door (*red-solid line*). (**d**) PET for the first 70 % of the initial population as a function of the probability λ

other hand, with small values of λ very few agents will try to exit simultaneously and the capacity of the door will not be totally used. In Fig. 1d the PET is studied as a function of λ and there exists an optimum λ at which the PET is minimum. In consequence, we will center our attention on the probability $\lambda = 0.04$ for the simulations investigating different mixtures of selfish and *ant-like* behavior.

3 Simulation Results

In this section we will theoretically investigate the evacuation performance for a group of agents having a fraction of the population behaving selfishly and the rest following unselfish behaviors. The set-up for the simulation is the one outlined in Sect. 2 and it corresponds to a life-and-death situation leading to highly competitive egress as described in Sect. 1. We will call *selfish* or *human* behavior the one displayed by agents going directly to the door from the start of the evacuation.

The performance of the evacuation process will be characterized by means of two physical observables: (a) partial evacuation time (PET) and (b) blocking cluster probability (BCP). The first one (a) considers the time elapsed until the first 70 % of the initial population has egressed in accordance with the studies presented for ants in Ref. [4]. The blocking cluster probability (b) was introduced in Ref. [21]. A blocking cluster is the subset of particles in contact with each other and closest to the door whose first and last components are in contact with walls on both sides of the door. This structure will be of certain duration (t_{bc}). Summing up for all the durations t_{bc} during an evacuation process that lasts a time T, we compute the blocking cluster probability as: $BCP = \sum t_{bc} / T$. In other words, the BCP is the fraction that the system lay blocked.

Figure 2 shows the results of simulations considering a population with mixed types of behaviors. Panel A displays a snapshot of the systems, with 50 % mixture of selfish and *ant-like* behavior, at the start of the evacuation process showing that there is a fraction of agents in the state of going toward the door from the very beginning. Panel B shows the same system after 6 s, where a big cluster of agents near the door can be observed, in contrast to what occurs in Fig. 1a, b. Figure 2c shows the PET as a function of the human fraction behavior of the population. It can be seen that for zero human fraction (100 % ant behavior) the optimum λ is 0.04, as was already shown in Fig. 1d. An important result is that 100 % *ant-like* behavior produces a better PET than in the case of 100 % selfish behavior. As the fraction of human behavior increases, the PET decreases to reach a minimum at 20 % selfish behavior. The same qualitative characteristic is observed for the other values of λ and it can be verified that $\lambda = 0.04$ produces the better combination of behaviors. Looking at the BCP (Fig. 2d) it can be seen that the duration of these clusters increases monotonically with the fraction of human behavior present in the population. Focusing on $\lambda = 0.04$, it can be observed that when the human or selfish behavior is the majority (greater than 50 %), the PET and BCP are big and do not change too much. In order to improve both physical observables, the human

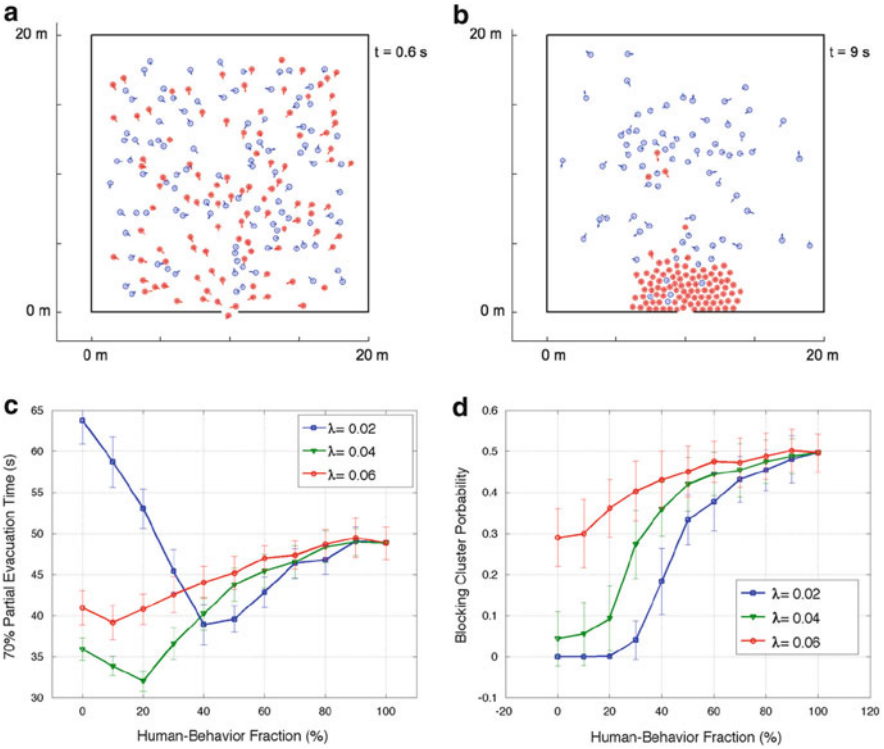

Fig. 2 Results of simulations with different mixtures of agents displaying human and *ant-like* behavior. (**a**) and (**b**) snapshots at 0.6 and 9 s for a realization with 50 % human behavior. (**c**) and (**d**) 70 % PET and BCP as a function of the human behavior fraction of the population

fraction has to be the minority of the population (less than 30 %). Thus, this result indicates that if we tried that a fraction of evacuating people change their selfish behavior during an emergency for an *ant-like* behavior, it would only be useful if a majority of the population follows the instructions. Because it is not probable that this occurs, we continue one step further looking for another behavior that could be more useful for practical purposes.

In Fig. 2b we can see that there are two factors contributing to the improvement of the evacuation metrics when *ant-like* behavior is present. One is that because *ant-like* agents do not go immediately toward the door, they decrease the cluster size near the door and thus the pressure and friction reduce the BCP. The other factor is that there are trapped agents inside the cluster, wanting to go everywhere inside the room but not to the door, and thus pushing in opposite direction of the clustered agents trying to exit. So, these trapped agents act as *living-obstacles* and also reduce the pressure over the door.

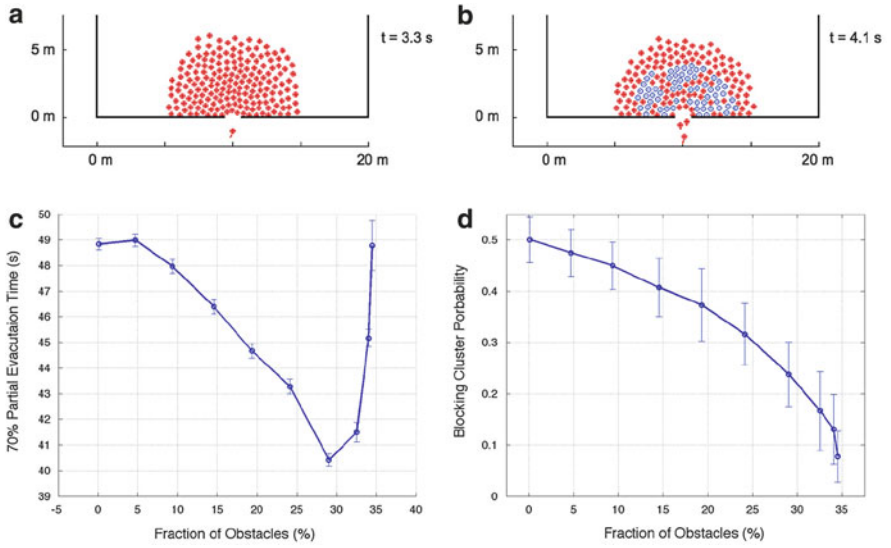

Fig. 3 Results of simulations with different mixtures of agents with selfish and *living-obstacle* behavior. (**a**) and (**b**) snapshots at 3.3 and 4.1 s. (**c**) and (**d**) show the PET and BCP, respectively, as a function of the fraction of agents displaying *living-obstacle* behavior

Inspired by this observation, we defined a *living-obstacle* behavior that is as follows. At the start of the evacuation all agents behave selfishly and go directly toward the door, forming the typical big cluster. After 3.5 s a fraction of agents inside the cluster change their states and become living obstacles trying to maintain the position (i.e., the driving force points toward the position they were when they changed state). If the selfish agents push obstacle agents outside the room, the obstacle agent goes on and does not try to reenter. In this behavior no λ parameter is involved. Figure 3 illustrates the agents' behavior in panels a and b. The impact of the different fractions of agents behaving as obstacles can be seen in Fig. 3c and d. Now the unselfish behavior necessary to minimize the PET is only 29 %, which is a clear minority. Moreover, this fraction of obstacle behavior also reduce the BCP to one half with respect to pure selfish behavior, resulting in a more applicable strategy that could be followed by instructed pedestrians evacuating during a life-and-death emergency.

Conclusions

Inspired by the observation of the cooperative behavior of ants when evacuating under threatening conditions, we define two unselfish behaviors: the *ant-like* and the *living-obstacle* behaviors, which were implemented by

(continued)

adjusting the driving force in the social force model. The room evacuation problem was studied using populations with different fractions of selfish and unselfish behavior.

If all agents follow *ant-like* behavior, the PET and the BCP are much better than in the case of all agents behaving selfishly. From the point of view of the PET, a mixture with a majority of unselfish behavior (80 %) would be optimum. Conversely, a minor fraction, only 29 % of agents, is required to follow *living-obstacle* behavior in order to decrease the PET by 18 % and the BCP by 50 %. Therefore, this is potentially more applicable if evacuating pedestrians should follow the instruction of not pushing toward the door but trying to keep their position near it.

Finally, we remark that it is necessary to extend this investigation with an experimentally validated model of evacuation under highly competitive conditions through narrow doors.

Acknowledgements Authors are members of the CONICET, Argentina. We acknowledge financial support from grants PICT 2011-1238 (BID-ANPCyT Argentina), PIP 2010-0304 (CONICET, Argentina).

References

1. D. Helbing, A. Johansson, J. Mathiesen, M.H. Jensen, A. Hansen, Analytical approach to continuous and intermittent bottleneck flows. Phys. Rev. Lett. **97**, 168001 (2006)
2. H.E. Nelson, F.W. Mowrer, Emergency movement, in *SFPE Handbook of Fire Protection Engineering*, ed. by P.J. DiNenno, W. Douglas Walton, 3rd edn. (National Fire Protection Association, Quincy, 2002), pp. 3–367
3. S. Heliövaara, H. Ehtamo, D. Helbing, T. Korhonen, Patient and impatient pedestrians in a spatial game for egress congestion. Phys. Rev. E **87**, 012802 (2013)
4. S.A. Soria, R. Josens, D.R. Parisi, Experimental evidence of the "Faster is Slower" effect in the evacuation of ants. Saf. Sci. **50**(7), 1584–1588 (2012)
5. P.A. Gago, D.R. Parisi, L.A. Pugnaloni, 'Faster is Slower' effect in granular flows, in *Traffic and Granular Flow '11*, ed. by V.V. Kozlov, A.P. Buslaev, A.S. Bugaev, M.V. Yashina, A. Schadschneider, M. Schreckenberg. Springer, Berlin, 317–324 (2013)
6. S. Boari, R. Josens, D.R. Parisi, Efficient egress of escaping ants stressed with temperature. PlosOne, **8**, 11 (2013). e81082
7. A. John, A. Schadschneider, D. Chowdhury, K. Nishinari, Trafficlike collective movement of ants on trails: absence of jammed phase. Phys. Rev. Lett. **102**, 108001 (2009)
8. A. Dussutour, V. Fourcassi, D. Helbing, J.L. Deneubourg, Optimal traffic organization in ants under crowded conditions. Nature **428**, 70–73 (2004)
9. R.F. Fahy, G. Proulx, L. Aiman, Panic or not in fire: clarifying the misconception. Fire Mater. (Spec. Issue Spec. Issue Hum. Behav. Fire) **36**(5–6), 328338 (2012)
10. C. Saloma, G.J. Perez, G. Tapang, M. Lim, C.P. Saloma, Self-organized queuing and scale-free behavior in real escape panic. Proc. Nat. Acad. Sci. **100**, 11947–11952 (2003)
11. I. Zuriguel, A. Garcimartín, A. Janda, C. Lozano, D. Maza, Clogging in bottlenecks: from vibrated silos to room evacuation. In this proceedings TFG 2013 Conference, Jülich, Germany, (2014)

12. D. Helbing, I. Farkas, T. Vicsek, Simulating dynamical features of escape panic. Nature **407**(6803), 487–490 (2000)
13. E. Altshuler, O. Ramos, Y. Nez, J. Fernndez, A.J. Batista-Leyva, C. Noda, Symmetry breaking in escaping ants. Am. Nat. **166**, 643–649 (2005). http://www.jstor.org/stable/3491227?seq=1
14. N. Shiwakoti, M. Sarvi, G. Rose, M. Burd, Animal dynamics based approach for modeling pedestrian crowd egress under panic conditions. Trans. Res. Part B **45**, 14331449 (2011)
15. D.R. Parisi, C.O. Dorso, Morphological and dynamical aspects of the room evacuation process. Phys. A Stat. Mech. Appl. **385**, 343–355 (2007)
16. B. Zelinski, E. Goles, M. Markus, Maximization of granular outflow by oblique exits and by obstacles. Phys. Fluids **21**, 031701 (2009)
17. I. Zuriguel, A. Janda, A. Garcimartn, C. Lozano, R. Arvalo, D. Maza, Silo clogging reduction by the presence of an obstacle. Phys. Rev. Lett. **107**, 278001 (2011)
18. C. Lozano, A. Janda, A. Garcimartn, D. Maza, I. Zuriguel, Flow and clogging in a silo with an obstacle above the orifice. Phys. Rev. E **86**, 031306 (2012)
19. N. Shiwakoti, M. Sarvi, Enhancing the panic escape of crowd through architectural design. Trans. Res. Part C 37, 260–267 (2013)
20. C. Dias, M. Sarvi, N. Shiwakoti, O. Ejtemai, M. Burd, Investigating collective escape behaviours in complex situations. Saf. Sci. **60**, 87–94 (2013)
21. D.R. Parisi, C.O. Dorso, Microscopic dynamics of pedestrian evacuation. Physica A **354**, 606–618 (2005)

Escape Velocity of the Leader in a Queue of Pedestrians

Akiyasu Tomoeda, Daichi Yanagisawa, and Katsuhiro Nishinari

Abstract The relaxation process in a queue is very important for the smooth movement of pedestrians. As previously reported, the propagation speed of a starting wave, that is, a wave of people's successive reactions in the relaxation process of a queue, and the initial density of a queue are fundamentally related by a power law. In addition, when the walking velocity of the leader of a queue, called "escape velocity", is optimal, the flow of the queue is maximized and the queue is not separated. In order to investigate how the behaviour of the followers in a queue changes with the leader's velocity, we performed experimental measurements on real pedestrians. In our experiment, we set the walking velocity of the leader of a queue using three metronome tempos (fast, normal, and slow) transmitted through earphones. The experimental results show that the escape velocities corresponding to the fast and slow tempos cause empty spaces in a queue and limit the walking velocities of the queue members, respectively.

1 Introduction

In recent decades, considerable research on the collective motion of self-driven particles (SDPs), including the dynamics of traffic flow and pedestrian behaviour, has been conducted from the viewpoint of mathematical sciences [2, 3, 5]. In particular, the interdisciplinary research field concerning the dynamics of jamming

A. Tomoeda (✉)
Meiji Institute for Advanced Study of Mathematical Sciences, Meiji University, 4-21-1, Nakano, Nakano-ku, Tokyo, 164-8525, Japan

CREST, Japan Science and Technology Agency, 4-21-1, Nakano, Nakano-ku, Tokyo, 164-8525, Japan
e-mail: atom@isc.meiji.ac.jp

D. Yanagisawa
College of Science, Ibaraki University, 2-1-1, Bunkyo, Mito, Ibaraki, 310-8512, Japan

K. Nishinari
Research Center for Advanced Science and Technology, The University of Tokyo, 4-6-1, Komaba, Meguro-ku, Tokyo, 153-8904, Japan

M. Chraibi et al. (eds.), *Traffic and Granular Flow '13*,
DOI 10.1007/978-3-319-10629-8_25

phenomena in the collective motion of SDPs, called "Jamology", has progressed owing to sophisticated, experimentally-validated mathematical models.

In the case of one-dimensional jamming phenomena, the key concept in studying queues of vehicles and pedestrians is called "slow-in fast-out". This concept is a simple idea derived from queuing theory: the length of the queue decreases when the departure rate is greater than the arrival rate. A slow-in strategy for traffic was proposed in [4] and demonstrated by the experiment reported in [7]. We, on the other hand, have focused on the fast-out strategy. In our previous study [8], we investigated the dynamics of the propagation speed of a starting wave, which is defined by people's successive reactions in the relaxation process of a queue. The fundamental relation between the propagation speed of a starting wave (a) and the initial density of a queue (ρ) is characterized by the power law $a = \alpha\rho^{-\beta}$ ($\beta \neq 1$), where α and β are positive parameters. This characterization elucidates the dynamics of a queue before pedestrians start to walk. As a next step, we investigate the dynamics after pedestrians start to walk. This behaviour depends on the walking velocity of the leader of a queue, called the "escape velocity".

The escape velocity is significant from the viewpoint of controlling a queue, especially in an emergency situation, because it affects the walking behaviour of followers. An appropriately controlled escape velocity will result in the ideal situation, in which the flow of a queue is maximized and the queue is not separated. For example, if the leader moves very fast, it becomes difficult for followers in the queue to keep up. On the other hand, if the leader moves very slowly, the walking velocity of followers is limited by the leader. In order to investigate how the behaviour of followers changes with the leader's velocity, we performed experimental measurements on real pedestrians. In this study, we focus on the relation between the escape velocity and the walking behaviour of followers.

2 Experiments

2.1 Settings

Figure 1 shows the passage in our experiment. The lengths of the initial queue (l_1), the walking passage (l_2), and the total length of the passage (L) are 11.0, 15.0, and

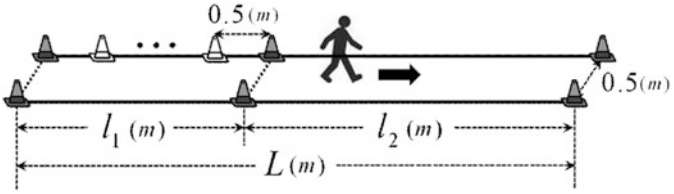

Fig. 1 Setting of our experimental passage

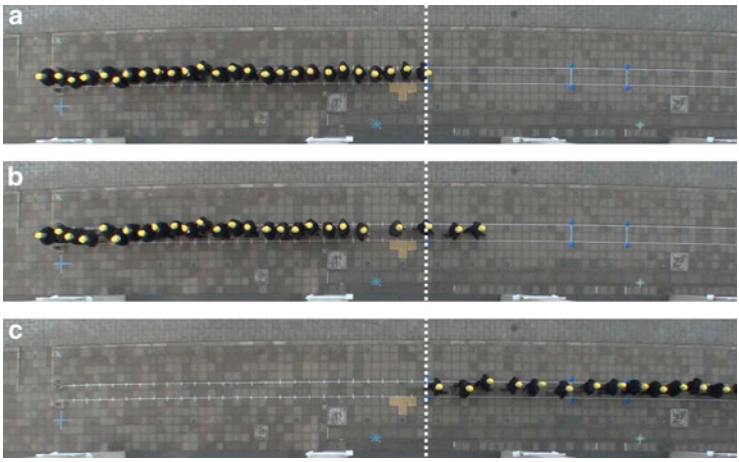

Fig. 2 Snapshots taken during our experiment. The *dashed line* corresponds to the position of the leader of the initial queue. (**a**) Initial position of the pedestrians in a queue. (**b**) Starting wave propagates backwards in the queue after the leader starts to move. (**c**) The last pedestrian passes the starting position of the leader

26.0 m, respectively. The width of the passage is 0.5 m. We mounted two cameras on the windows of the fifth floor of a building, which is 20.35 m above the ground, to track the movements of pedestrians in a queue. Snapshots obtained from an overhead camera are shown in Fig. 2. As shown in Fig. 2, each pedestrian wore a black t-shirt and a yellow knitted hat. Data sets comprising the exact positions of all pedestrians on the pathway at each frame were obtained from the recorded video data by detecting the pedestrians' hats using PeTrack software [1].

As an initial condition, all pedestrians (N in total) stood in line with the same headway distance; that is, the density of the initial queue was constant and uniform throughout the queue (see Fig. 2a). We fixed the number of pedestrians and the density as $N = 22$ (average height: 1.73 m) and $\rho = 2.0\,\mathrm{m}^{-1}$, respectively. The leader adjusted the walking velocity according to the beats of an electronic metronome transmitted through a headset. The relation between the walking velocity of the leader and the metronome frequency in our experiment is shown in Fig. 3. We found that the walking velocity of the leader increased approximately linearly with metronome tempo. The dashed line is a fitting function based on the linear relation between walking velocity $V(x)$ and tempo x, that is, $V(x) = ax + b$. The parameters (a, b) are $(0.012, -0.091)$. A similar relation was reported in [6], which experimentally studied the effect of music on individual pedestrians and showed that walking tempo is proportional to music tempo in the majority of cases. These results indicate that changing the tempo is a suitable method for controlling the walking velocity of the leader of a queue. Thus, the escape velocity is controlled using three different tempos: slow (50 BPM), normal (140 BPM), and fast (208 BPM). Here, BPM denotes beats per minutes. The leader started to move after

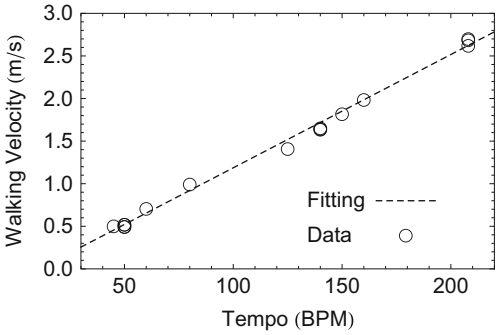

Fig. 3 The relation between walking velocity and tempo (BPM)

the tempo was arbitrarily chosen, and then the followers moved forward in order, beginning at the front of the queue. Therefore, following pedestrians knew neither the escape velocity nor the time at which the leader started walking. In this process, we observed that the starting wave propagates backward in a queue (see Fig. 2b). Figure 2c shows the moment when the last follower passes the head position of the initial queue.

2.2 Results

Typical spatio-temporal plots for each walking velocity are shown in Fig. 4. In the case of fast walking velocity, the time difference between the leader and the last follower in a queue was large. Additionally, some of the distances between successive pedestrians were large. That is, the walking velocity of the leader was too high for some of the following pedestrians to keep up. In the case of normal walking velocity, there was no significant time difference between the leader and the last follower, and the trajectories of all pedestrians were mostly linear and parallel. That is, all pedestrians could walk with constant headway and velocity. In the case of slow walking velocity, the trajectories were not linear, and the time differences at the end of the passage were small. The former result indicates that the followers could not walk at a natural constant velocity, because there was a difference between their natural walking velocity and the real walking velocity. The latter result indicates that the followers had space to move. Note that the behaviour of the followers is nearly independent of the escape velocity because the starting time of the last pedestrian is almost identical in each situation.

Figure 5 shows time lapse plots for two measurement positions: (I) the starting point and (II) the end of the passage. In case (I), at the starting point, the time lapse T_I in the case of slow escape velocity is quite larger than that for the other two escape velocities. Therefore, the slow escape velocity is slower than the natural walking velocity of pedestrians. On the other hand, in case (II), at the end of the passage, the normal escape velocity appears most likely to achieve smooth

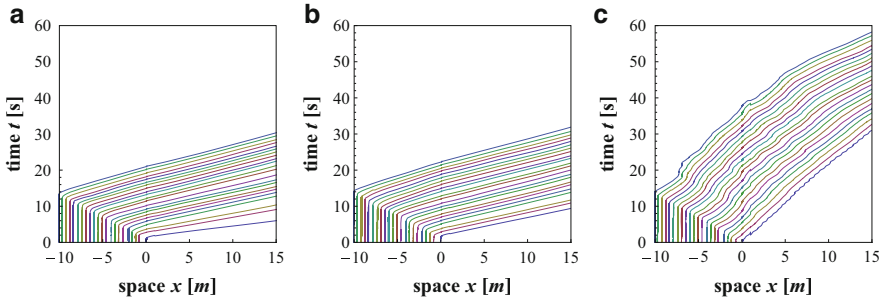

Fig. 4 The spatio-temporal plots for three cases: (**a**) fast escape velocity, (**b**) normal escape velocity, and (**c**) slow escape velocity. Zero point of space corresponds to the head position of the initial queue

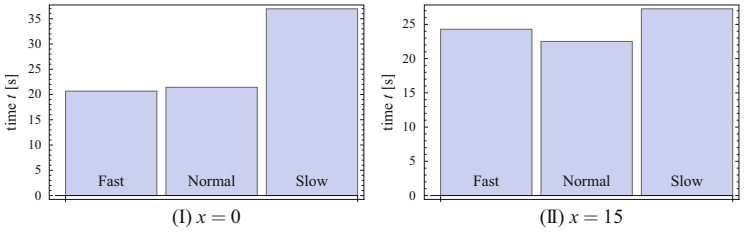

Fig. 5 The time lapse plots for two points: (*I*) time elapsed after the leader starts and before the last follower passes $x = 0$ m (starting position) and (*II*) time elapsed after the leader starts and before the last follower passes $x = 15$ m (end of the passage)

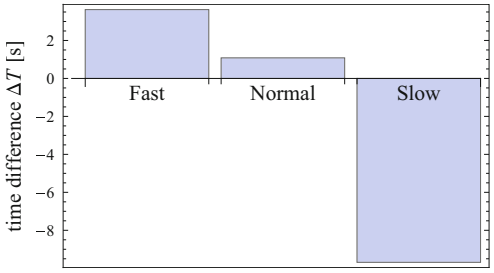

Fig. 6 The difference in time elapsed between $x = 0$ m (start) and $x = 15$ m (end), i.e., (I)–(II) for each escape velocity in Fig. 5

movement because the time lapse T_{II} in the normal case is minimized. Moreover, Fig. 6 shows the time difference ΔT between cases (I) and (II), which is calculated by $\Delta T = T_{II} - T_I$. From this result, we find that the time difference in the case of slow escape velocity is negative. In this situation, the escape velocity is slower than the natural walking velocity. In the case of fast escape velocity, the time difference is a large positive value. When the escape velocity is higher than the natural walking velocity, a vacant space is created in the queue, which negatively affects smooth

movement. As observed above, we found that the slow and fast escape velocities are not optimal for smooth movement of a queue, because they limit walking speed and create vacant space, respectively.

Conclusions
In order to achieve a smooth movement of a queue, the escape velocity is appropriately controlled to the optimal velocity, at which the flow in the queue is maximized and the queue is not separated. In this study, we experimentally investigated following pedestrians' behaviour in three situations: fast, normal, and slow escape velocities. The position data of the pedestrians in our experiment were obtained using the image processing capabilities of PeTrack software. Comparing followers' behaviour in the three situations, we found that the slow and fast escape velocities are not optimal for smooth movement of a queue, because they limit walking speed and create vacant space, respectively. This result indicates that an optimal escape velocity indeed exists. We will demonstrate the existence of the optimal escape velocity analytically and quantitatively in the near future.

Acknowledgements We are greateful to Maik Boltes, Mohcine Chraibi, and Kazumichi Ohtsuka for their kind supports in our experiments. One author (AT) was supported by a Grant-in-Aid for Young Scientists (B) (Grant Number: 25790099) from the Japan Society for the Promotion of Science.

References

1. M. Boltes, A. Seyfried, Collecting pedestrian trajectories. Neurocomput. Spec. Issue Behav. Video **100**, 127 (2013)
2. D. Chowdhury, L. Santen, A. Schadschneider, Statistical physics of vehicular traffic and some related systems. Phys. Rep. **329**, 199 (2000)
3. D. Helbing, Traffic and related self-driven many-particle systems. Rev. Mod. Phys. **73**, 1067 (2001)
4. R. Nishi, A. Tomoeda, K. Shimura, K. Nishinari, Theory of jam-absorption driving. Trans. Res. B **50**, 116 (2013)
5. A. Schadschneider, D. Chowdhury, K. Nishinari, *Stochastic Transport in Complex Systems – From Molecules To Vehicles* (Elsevier, Amsterdam/Oxford, 2010)
6. F. Styns, L. van Noorden, D. Moelants, M. Leman, Walking on music. Hum. Mov. Sci. **26**, 769 (2007)
7. Y. Taniguchi, R. Nishi, A. Tomoeda, K. Shimura, K. Nishinari, A demonstration experiment of a theory of jam-absorption driving, in *Traffic and Granular Flow'13*, eds. by Chraibi, M., Boltes, M., Schadschneider, A., Seyfried, A. (Springer, 2014)
8. A. Tomoeda, D. Yanagisawa, T. Imamura, K. Nishinari, Propagation speed of a starting wave in a queue of pedestrians. Phys. Rev. E **86**, 035113 (2013)

Experimental Study on the Interaction Mechanism of Cross-Walking Pedestrians

Wei Lv, Xiaoge Wei, and Weiguo Song

Abstract In the field of pedestrian dynamics, the interaction mechanism among pedestrians is significant for both system modelling and evacuation designing. In this study, a cross-walking experiment is conducted in two crossed passageways to investigate the microscopic interactions between individuals. Trajectories of 51 groups of pedestrians' movements are extracted by means of image processing. Four main behaviours, i.e. accelerating, decelerating, detour and keep-walking, are identified when pedestrians walk crosswise. The pair velocities before and after the cross point are also calculated and classified to three modes: the first mode is one accelerating with the conflicting partner decelerating, the second mode is accelerating together or decelerating together, and the third mode is one keeping speed with the conflicting partner accelerating or decelerating. It is found that to avoid conflict, 90.2 % of participants take accelerated behaviour or decelerated behaviour and only 5.9 % of participants take detour behaviour, which implies pedestrians prefer to adjust their speeds rather than change their directions when facing potential conflict. Particularly, 64.7 % of groups of pedestrian avoid the conflict through the coordination mode, i.e. one accelerating with the other decelerating, which indicates the major self-organized behaviour of pedestrian. Two kinds of detour behaviour are also observed from the experiment: detouring ahead the conflicting partner and detouring behind the conflicting partner. It is found the detour ahead the conflicting pedestrian would induce an approximate lateral movement of 0.65–0.75 m, larger than that of 0.55 m when detouring behind the conflicting pedestrian. It is hoped that this study would provide some useful experimental data or conclusions for the research field of pedestrian traffic.

W. Lv • X. Wei • W. Song (✉)
State Key Laboratory of Fire Science, University of Science and Technology of China, Hefei 230026, China
e-mail: weil232@mail.ustc.edu.cn; wxg2010@mail.ustc.edu.cn; wgsong@ustc.edu.cn

M. Chraibi et al. (eds.), *Traffic and Granular Flow '13*,
DOI 10.1007/978-3-319-10629-8_26

1 Introduction

Large crowds or high density crowds have been considered as a headache of the large event organizers, the administrators and the activity managers. The large-scale gathering or the uncontrolled crowds, especially in panic, are extremely likely to cause stampede accident or traffic interruption. People may lose their lives and traffic facilities could be destroyed, just because these large crowd disasters. Therefore, to avoid such disasters and save people's lives, some measures should be adopted. Such as disaster prediction, risk assessment, anomaly identification and detection, route planning, density control, evacuation, and so on. These approaches may be important and practical, while all of them based on the researches of the pedestrian dynamics.

In the research field of pedestrian dynamics, there have been two basic methods to use for the majority of scholars. One is experiment [1, 3, 4], and the other is modelling [2, 5, 6]. Experiment is an effective way to validate the accuracy of the model because it can provide useful parameters for modelling. Meanwhile, new models require more reasonable experiments to be designed or conducted. Therefore, it is no doubt that experiment could promote modelling and the models verified through experiment are more reliable and credible.

Pedestrian's walking is complex and its mechanism involves several scientific issues. First and foremost, the velocity and direction changing mechanism should be revealed so as to accurately predict pedestrian's movement. In addition, the collision avoidance mechanism and the interaction mechanism also should be explained so as to help facility design or crowd intervention. Therefore, experiments that can reveal the walking mechanism of pedestrian are valuable and necessary.

In this paper, we focus on the cross-walking pedestrians through conducting a cross-walking experiment, and try to answer what action would people take and what is the major way to avoid collision when they are facing potential conflict.

2 Experiment

2.1 Experimental Scene and Organization

The experiment is carried out on an outdoor ground in a college campus of China. The sketch of the experiment can be seen in Fig. 1. Two cameras were fixed at the roof of one four-layers building that beside the ground, vertically shoot to the ground. The experimental scene is composed of two crossing passageways that marked by color lines on the ground. Each passageway has a length of 8 m and a width of a half meter. In the experiment, a group of two participants are required to walk from one side of each passageway to another side from the same start time.

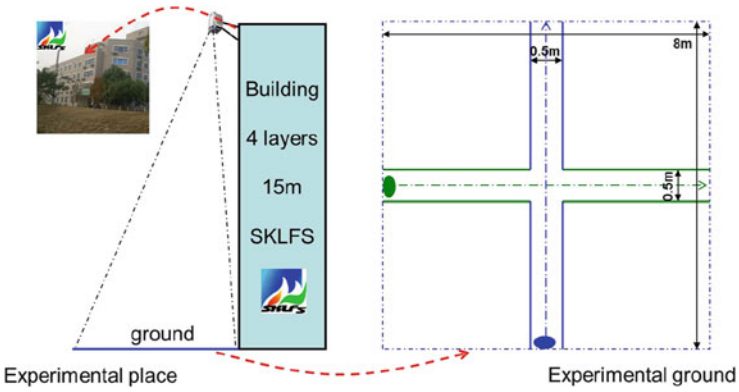

Fig. 1 Scene of the cross-walking experiment

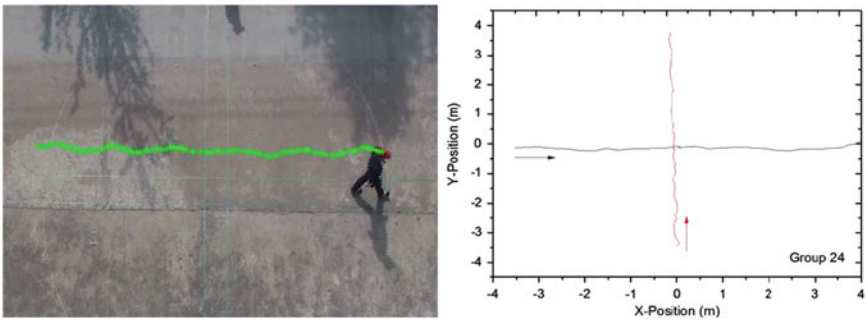

Fig. 2 Image positions of a pedestrian (*left*) and real trajectories of a group of pedestrians

It should be pointed that the participants were not forbidden to walk out the marked passageways, that is, they could walk out the passageway boundaries at any time if they want (Fig. 2).

The experiment was conducted by the research group of Prof. Song Weiguo, in the University of Science and Technology of China, in October, 2011. There were 34 college students participate the experiment, including 17 males and 17 females. At the beginning of the experiment, a group of two students were arranged to stand at each side of the two passageways. When the organizer announced 'GO!', the two students began to walk towards to the other side of the passageway. This walking process was recorded by the cameras, and can be seen as one time experiment. In this experiment, 34 students were divided into 17 groups and each group repeated this process three times, so total 51 recordings were obtained finally.

2.2 Data Processing

The target of data processing is to obtain real movement trajectories of the participants in each group, which include three steps. First, the recordings were converted into frame images with a speed of 25 fps. Then, the positions of the red or yellow cap in each frame image were tracked manually with the software Matlab. Third, the Direct Linear Transformation method was used to rectify the image positions to match the real space coordinate. Finally, we could use the trajectories composed of the real positions to analyze the cross walking.

3 Results and Discussion

In the experiment, the cross walking would generate a potential conflict at the crossing center. How to avoid the potential collision? What actions would be taken?

3.1 Three Modes of Cross Walking

We investigate the pedestrian's reaction from the view of the velocity changes. We focus on two velocities, as shown in Fig. 3, one is the mean velocity of the pedestrian in the one-meter-distance before the center of the passageway, and the other is the mean velocity of the pedestrian in the one-meter-distance after the center of the passageway. As the area after the crossing center can be seen as collision-free area, we consider the second velocity V_B as pedestrian's normal speed, so if the first velocity V_A lager than V_B, it indicates the pedestrian accelerate before crossing the intersection. According these two velocities, it is clear to see there are three kinds of velocity changes: accelerating, decelerating and keeping speed.

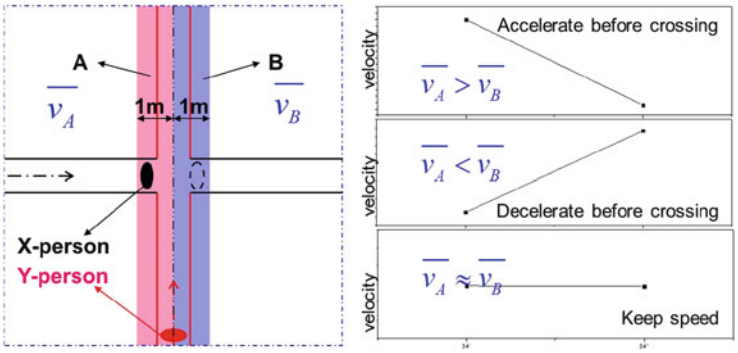

Fig. 3 Velocity changes near the crossing center

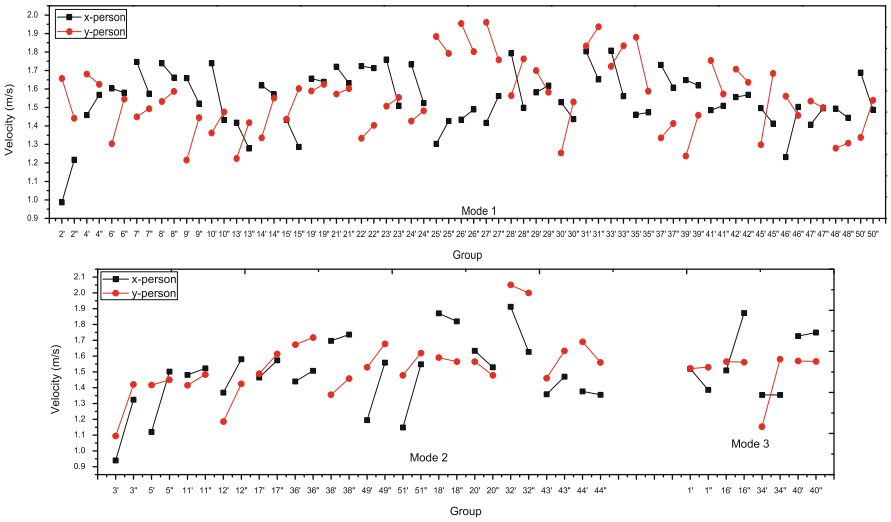

Fig. 4 Three modes of the cross walking

Using this method, we calculate the two velocities of all pedestrians. And three modes of the cross walking can be identified. Figure 4 shows these modes and the explanations are as follows,

Mode 1: One pedestrian accelerate with the conflicting partner decelerate. This mode was adopted by 64.7 % of pedestrians, which indicates it is the major way for cross-walking pedestrian to avoid potential collisions.

Mode 2: Both pedestrians accelerate or decelerate. It can be seen in this mode, more pedestrians chose the decelerating behaviour to avoid conflict with the partner. Only a few pedestrians both chose acceleration and these persons may be more aggressive.

Mode 3: One keep speed, the other accelerates or decelerates. This mode occupies only 5.9 % of participants, but it is indeed reflect real situations. One's acceleration can provide the space for the other to keep speed, while one's keeping speed can also occupy the other's walking space and decelerate him.

3.2 Four Behaviors in the Cross Walking

We also extract the four main behaviours in the cross-walking pedestrians: accelerate, decelerate, keep speed and detour. The first three behaviours can be seen as velocity adjustment, while the detour behaviour is essentially a direction-changing

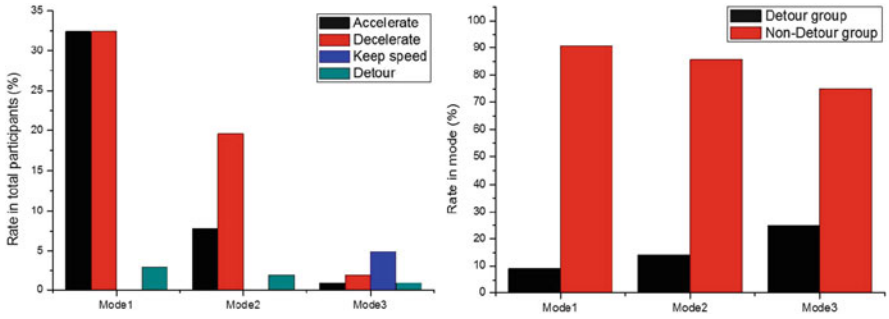

Fig. 5 Rate of each behaviour in total participants and mode

method. Figure 5 shows the rates of each behaviour in the total participants and in three modes, it can be seen 90.2 % of participants take accelerated behaviour or decelerated behaviour and only 5.9 % of participants take detour behaviour. This result indicates that pedestrian prefer to adjust speed rather than change direction when facing potential conflict.

3.3 Detour Analysis

As mentioned above, detour behaviour was taken by few participants in the cross-walking experiment, but as one direction-changing method, it is indeed reflect some characteristics of pedestrian walking. In our study, we find the detour behaviours exist in all modes, but the mode 3 contains the most detour behaviour. The experiment also shows two types of detouring behaviour. One is detouring ahead the partner's direction (type 1), the other is detouring behind the partner's direction (type 2), as shown in Figs. 6 (left) and 7 (left). Meanwhile, Figs. 6 (right) and 7 (right) exhibit the velocities of the two pedestrians in the whole cross-walking process. The results shows similar movement characteristic, i.e., the detouring walker accelerates when detour but the crossing walker's speed would be reduced.

To further investigate the difference of the two types of detour, we define the detour magnitude as the maximum offset of the person to the crossing center, as shown in Fig. 8. And we find detouring ahead causes about 0.65–0.75 m offset, larger than 0.55 m that caused by detouring behind.

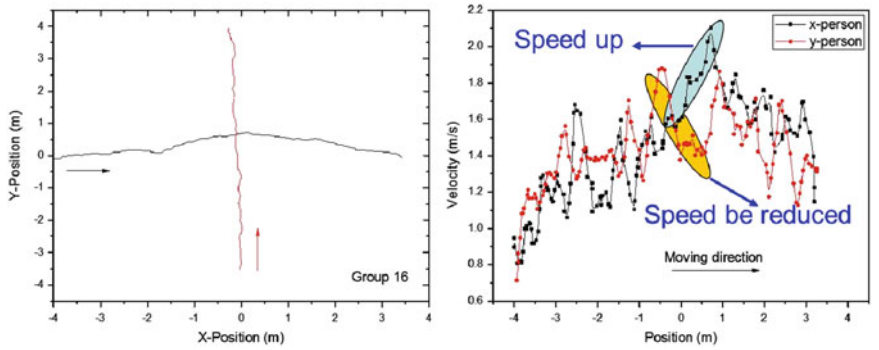

Fig. 6 Trajectory and velocity of the detour type 1

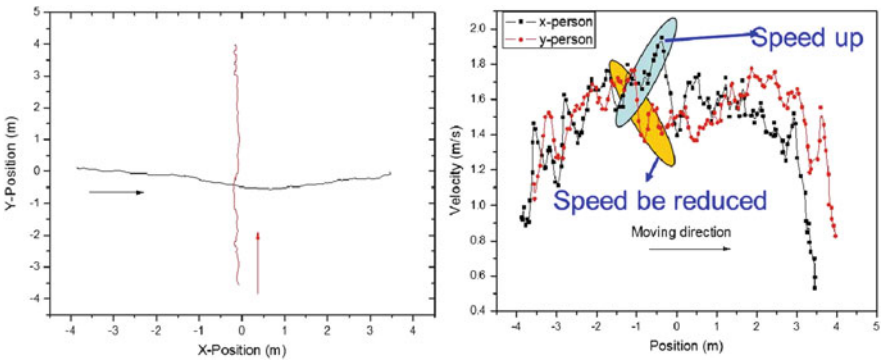

Fig. 7 Trajectory and velocity of the detour type 2

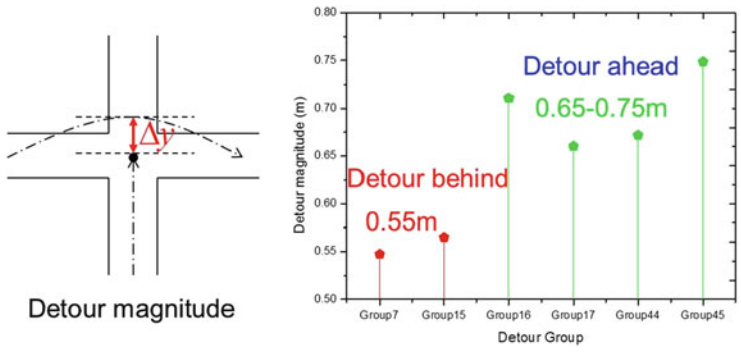

Fig. 8 Detour magnitude of the two detour types

3.4 Arriving Time Interval

We also briefly study the arriving time interval of the two cross-walking pedestrians. The arriving time interval can be calculated using the mean velocities of the two pedestrian before arriving at the crossing center. The result shows that the intervals in the experiment arrange from 0.4 to 1.3 s, with a mean value of 0.66 s. This also implies that at least 0.4 s interval difference could ensure the cross-walking pedestrians to avoid each other.

4 Summary

In this paper, we conduct a cross-walking experiment to study the interaction mechanism of cross-walking pedestrians. By analyzing the trajectories of the cross-walking pedestrians, we found three cross-walking modes, i.e., one accelerating and the crossing walker decelerating, accelerating or decelerating together, and one keeping speed with the crossing walker accelerating or decelerating. Statistical results show the first mode is the major self-organized mode in cross-walking. Comparing the rates of four main behaviours, it is found pedestrians prefer to avoid conflict by adjusting velocity rather than changing direction. In addition, two kinds of detour behaviours are identified and compared, and it indicates the detouring usually along with self-accelerating but other's decelerating. The brief discussion of arriving time interval shows at least 0.4 s interval should be ensured for avoiding conflict.

Experiments involve the movement characteristics of pedestrians and the interaction between pedestrian, especially at the individual level, are valuable and essential for pedestrian dynamics study. It is hoped more experiments and further analysis would be done in our future work.

Acknowledgements This work is supported by the National Natural Science Foundation of China (51178445) and the Fundamental Research Funds for the Central Universities (WK2320000014).

References

1. C.R. Childs, T. Fujiyama, N. Tyler, *Pedestrian and Evacuation Dynamics 2008*, p. 249–255 (2010)
2. H.J. Hilhorst, C. Appert-Rolland, J. Stat. Mech. Theory Exp. 2012, P06009 (2012)
3. J. Ma, W. Song, Z. Fang, S. Lo, G. Liao, Build. Environ. **45**, 2160–2169 (2010)
4. M. Moussaid, D. Helbing, S. Garnier, A. Johansson, M. Combe, G. Theraulaz, Proc. R. Soc. B Biol. Sci. **276**, 2755–2762 (2009)
5. W. Lv, W. Song, J. Ma, Z.M. Fang, IEEE Trans. Intell. Trans. Syst. **99**, 1–11 (2013)
6. W. Lv, W. Song, F. Huo, Appl. Mech. Mater. **444–445**, 1690–1694 (2014)

Inflow Process: A Counterpart of Evacuation

Takahiro Ezaki, Kazumichi Ohtsuka, Daichi Yanagisawa, and Katsuhiro Nishinari

Abstract We propose a new concept,"inflow process" of pedestrians as a counterpart of an evacuation process. In the inflow process, pedestrians enter a limited area without hurrying. This type of pedestrian motion can be observed in our daily life, e.g. in elevators, trains, etc. From experimental observation, we found intriguing behaviors, including pedestrians' preference for boundaries, collective orientation, etc. Besides, the inflow process has contrastive aspects to evacuation process. For this reason the process is important for the pedestrian dynamics field.

1 Introduction

For human society, investigation on collective behaviors of walking people has been of great importance since people started to live in a densely populated world. Over recent decades, analyzing such phenomena from a physical perspective has attracted interests of researchers, and numerous studies have been reported [1, 2]. One of the main focus of these researches is on "evacuation process" that has been an important topic for security purposes [3–9]. On the other hand, recently we proposed a new important research topic, "inflow process". The inflow process is a process in which pedestrians enter a limited area and finally stop walking after they find their comfortable positions [10], which is observed when people use elevators, trains, etc. In the previous work [10], we reported some fundamental phenomena, including pedestrians' preference for boundaries of an area, with a discrete model.

T. Ezaki (✉)
Department of Aeronautics and Astronautics, School of Engineering, The University of Tokyo, 7-3-1, Hongo, Bunkyo-ku, Tokyo 113-8656, Japan

Japan Society for the Promotion of Science, 5-3-1, Ichibancho, Kojimachi, Chiyoda-ku, Tokyo 102-0083, Japan
e-mail: ezaki@jamology.rcast.u-tokyo.ac.jp

K. Ohtsuka • K. Nishinari
Research Center for Advanced Science and Technology, The University of Tokyo, 4-6-1, Komaba, Meguro-ku, Tokyo 153-8904, Japan

D. Yanagisawa
College of Science, Ibaraki University, 2-1-1, Bunkyo, Mito, Ibaraki 310-8512, Japan

M. Chraibi et al. (eds.), *Traffic and Granular Flow '13*,
DOI 10.1007/978-3-319-10629-8_27

As the next step, we have conducted an experiment of an inflow process. In this article, we formulate the process in comparison with evacuation process, and show its characteristics observed in an experiment.

2 Evacuation Process and Inflow Process

This section is devoted to describe the inflow process and its contrastive aspects to the evacuation process. First, the directions of motion are opposite in the two processes: inflow and outflow. Second, one can see the difference between their relationships to our daily life. We experience inflow process almost everyday, while evacuation process only in cases of emergency. In contrast, the fatality of evacuation is high while normal inflow process is never fatal. For its fatality, evacuation process has been considered to be an important problem; however, considering its frequency, inflow process also has a certain impact on our life. Finally, from a scientific point of view, we discuss driving force that acts upon pedestrians. In an evacuation process, the most predominant motivation of pedestrians is to get out of a certain area as quickly as possible. For this reason, pedestrian might push each other and clog exits. In contrast, in an inflow process, people do not have a clear destination in the area, but instead, they try to save a desirable position where they can secure their own personal space. Namely, in this process pedestrians are driven by a psychological repulsive force between others.

Many pedestrian models have adopted the idea that pedestrian motion is driven by three factors [10–14]; desire to destination, physical contact force, and psychological repulsion force. In an evacuation process the former two factors are predominant, while in an inflow process the last factor drives the system dynamics. Due to these differences, investigation on an inflow process requires different approaches from conventional ones. Psychological repulsion force is well associated with *proxemics* [15], which is a concept proposed by Hall [16]. To understand the inflow process we have to deal with its dynamic behavior on the proxemics theory, which is not yet accessible at the moment (Table 1).

Table 1 Comparison between the inflow process and evacuation process

	Inflow process	Evacuation process
Direction of motion	In	Out
Fatality	Low	High
Frequency	High	Low
Driving force	Psychological repulsion	Destination/physical contact

3 Features of Inflow Process

In this article, we report fundamental characteristics of the inflow process observed in our last experiment. From a queue, 25 participants were asked to enter an area (3.6×3.6 m) that was enclosed within walls, in the same manner as elevators (Fig. 1). They wore a cap for video tracking, and their trajectories have been collected using the PeTrack [17] software.

Figure 2 (left) shows the trajectories of all pedestrians. In contrast to direct motion in evacuation, pedestrians walk indirectly to their final positions. This reflects the fact that they do not have clear destinations and adopt the environment while walking.

As predicted in our previous work [10], pedestrians tend to attracted by boundary because their personal space is not intruded by others from the wall direction. From Fig. 2 (right) we can see that the first half of pedestrians entered the area are at the walls, and latter half goes inside the area that is open at the time. Each Voronoi cell (see Appendix) indicates the space allocated to the corresponding pedestrian. Due to the incapability and laziness of pedestrians to distribute uniformly, the area is not equally divided into 25 pedestrians.

Interestingly, after acquiring their place, pedestrians turn around for the entrance to see incoming pedestrians. Besides, for a pedestrian coming after, almost all the pedestrians are facing the opposite direction, which makes him/her uncomfortable, contributing the urge to turn around. This phenomenon can be observed even if the direction of the exit (after the entrance) is not shown.

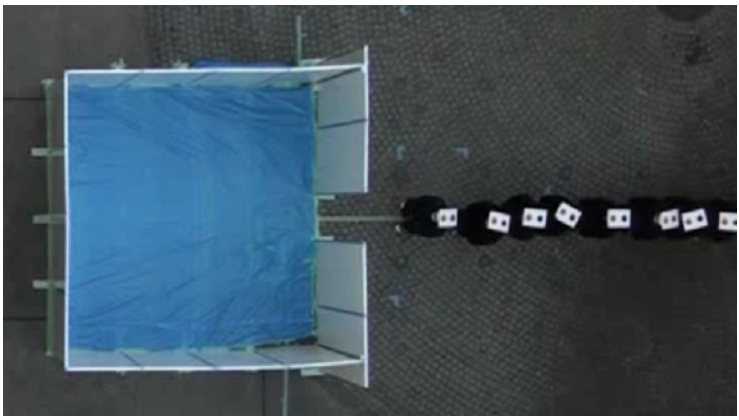

Fig. 1 Experimental setup. An are of 3.6×3.6 m is enclosed with walls of 2.0 m high. At the initial state, in front of the entrance set at the center of one boundary, 25 participants wait in a line with a 0.5 m gap between next one. In the experiment, they are asked to start walking simultaneously and enter the area one by one

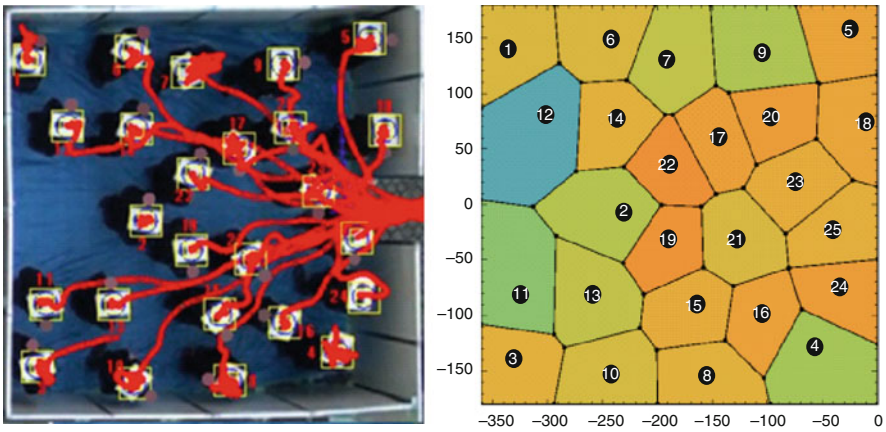

Fig. 2 Spatial distribution of pedestrians in the final state with trajectory lines (*left*) and Voronoi division (*right*). Pedestrians enter the area from the center of the right boundary (0, 0). The entrance order of pedestrian is shown with numbers on *black circles* in the *right panel*

4 Summary and Outlook

In this article we have presented a new concept, inflow process. This process has not been well focused on so far, in spite of its importance. Difficulty in investigating this process lies in its driving force. Different from other topics of pedestrian dynamics including the evacuation process and directional flow in corridor, pedestrians do not have a clear destination in the inflow process. This implies that over all motion of a pedestrian cannot be described by a sum of "forces". Instead, we have to consider several distinct phases of a pedestrian: perception, decision making for destination, interaction between other pedestrians, stopping, direction change, and adaptation to incoming people. We now have to uncover how transitions between these phases occur (or some could occur simultaneously), and how they drive the system. A present task for understanding them is analyze trajectory of pedestrians obtained by experiments, and abstract results one by one.

Acknowledgements We appreciate Mohcine Chraibi and Maik Boltes for their technical support for performing the experiment and tracking.

Appendix: Voronoi Diagram

In this appendix we present the definition of a Voronoi diagram [18]. For a given area X and points $P_1, P_2, \cdots, P_n \in X$, a Voronoi domain for each P_i $(1 \leq i \leq n)$ is defined as

$$V(P_i) = \{P \in X | d(P, P_i) \leq d(P, P_j), j \neq i\}, \tag{1}$$

where $d(\cdot, \cdot)$ is a distance between two points. Namely, $V(P_i)$ is a set of points whose distance to P_i is smaller than to other points P_j $(j \neq i)$. A set of $V(P_i)$ defines a Voronoi diagram for X and P_i $(1 \leq i \leq n)$. This Voronoi diagram has been used to calculate the area used by one pedestrian [19]. In the inflow process, since the final spacial distribution of pedestrians is of great interest, the diagram is a powerful tool for evaluating it.

References

1. D. Helbing, Rev. Mod. Phys. **73**, 1067 (2001)
2. T. Nagatani, Rep. Prog. Phys. **65**, 1331 (2002)
3. A. Kirchner, A. Schadschneider, Physica A **321**, 260 (2002)
4. A. Kirchner, K. Nishinari, A. Schadschneider, Phys. Rev. E **67**, 056122 (2003)
5. D.R. Parisi, C.O. Dorso, Physica A **606**, 606 (2005)
6. R.Y. Guo, H.J. Huang, Physica A **387**, 580 (2008)
7. D. Yanagisawa, K. Nishinari, Phys. Rev. E **76**, 061117 (2007)
8. D. Yanagisawa, A. Kimura, A. Tomoeda, R. Nishi, Y. Suma, K. Ohtsuka, K. Nishinari, Phys. Rev. E **80**, 036110 (2009)
9. T. Ezaki, D. Yanagisawa, K. Nishinari, Phys. Rev. E **86**, 026118 (2012)
10. T. Ezaki, D. Yanagisawa, K. Ohtsuka, K. Nishinari, Physica A **391**, 291–299 (2012)
11. D. Helbing, I. Farkas, T. Vicsec, Nature **407**, 487 (2000)
12. A. Seyfried, B. Steffen, T. Lippert, Physica A **368**, 232 (2006)
13. M. Chraibi, A. Seyfried, A. Schadschneider, Phys. Rev. E **82**, 046111 (2010)
14. R. Löhner, Appl. Math. Model. **34**, 366 (2010)
15. J. Was, B. Gudowski, P.J. Matuszyk, *ACRI 2006*. LNCS, vol. 4173 (Springer, Heidelberg, 2006), pp. 492–501
16. E.T. Hall, *The Hidden Dimension* (Anchor Press, New York, 1962)
17. M. Boltes, A. Seyfried, Neurocomputing **100**, 127–133 (2013)
18. F. Aurenhammer, ACM Comput. Surv. **23**, 345 (1991)
19. J. Zhang, W. Klingsch, A. Schadschneider, A. Seyfried, J. Stat. Mech. P06004 (2011). doi:10.1088/1742-5468/2011/06/P06004, http://iopscience.iop.org/1742-5468/2011/06/P06004

Mobility Modelling in a Process Constrained Environment: Modelling the Movements of Nurses in a Neonatal Intensive Care Unit

David Greenwood, Shrikant Sharma, and Anders Johansson

Abstract Understanding the movement of people constrained by process is of practical importance. It may enable process improvements and more accurate provision of space in buildings (such as hospitals, laboratories and airports) and thus contribute to making safer and more efficient built environments. We present an empirical study of the movement of nurses working at a neonatal intensive care unit (NICU) within a UK hospital. The aim of this study is to model the mobility of individuals within a process constrained built environment. Our objective is to create a model that recreates room occupancy distributions – this implies that we require a room transition model that predicts a person's next destination as well as a dwell time model that predicts how long a person will stay in a room. This class of situation is of theoretical and practical significance because nurses' movements are driven by sequences of purposeful activity that are spatially, logically and temporally constrained i.e. process constrained. We used Ekahau Wi-Fi location tracking tags to collect room transitions of 10 day-shift nurses within a NICU for a period of 28 days. We use this dataset to evaluate four proposed models of room transition: (1) random model; (2) an occupancy and distance model; (3) an attractiveness model; (4) a Markov model. We evaluate the models' goodness-of-fit by comparing our empirical dataset with model predictions.

1 Introduction

Pedestrian mobility models have traditionally focused on helping planners and architects create efficient, comfortable and safe operating environments in pedestrian facilities such as transport hubs, sports stadia and shopping malls. These environments all share a key challenge which is how to manage large volumes

D. Greenwood (✉) • A. Johansson
Faculty of Engineering, University of Bristol, Merchant Venturers Building, Woodland Road, Bristol BS8 1UB, UK
e-mail: dg12208@bristol.ac.uk; a.johansson@bristol.ac.uk

S. Sharma
Buro Happold, 230 Lower Bristol Road, Bath, BA2 3DQ, UK
e-mail: Shrikant.Sharma@BuroHappold.com

M. Chraibi et al. (eds.), *Traffic and Granular Flow '13*,
DOI 10.1007/978-3-319-10629-8_28

of people and therefore a significant volume of research has been concerned with understanding high volume flows or evacuations [2,3,6]. Perhaps due to the focus on these environments, pedestrian mobility models have largely ignored the challenges of environments where pedestrian movements are logically, spatially and temporally constrained because the pedestrians are behaving in accordance to some process. Some notable attempts to address this chalenge include [5, 7].

Process constrained environments are environments where a pedestrian's behaviour is contingent on the outcome of a previous activity such as in hospitals, scientific labs, airports and retail environments. Take a hospital for instance, a nurse may arrive in the morning, change in the staff area, attend a hand-over meeting and then go on to perform planned activities such as preparing and checking medication, administering intravenous fluids, giving blood products, record keeping, and cleaning clinical areas. Emergent events will also occur and are responded to such as drops in heart rate and blood oxygen saturation levels. This process of performing planned activities and responding to unplanned events is often repeated numerous times.

At present, pedestrian movement simulators are typically driven by an origin-destination matrix that sets a pedestrian's start-point, end-point and way-points. However, in process constrained situations these types of models have limitations because whilst the start-point and end-point is often known, the journey by which a pedestrian goes from start to end is contingent upon the outcome of the activities along the way. This paper contributes to addressing this challenge by aiming to model the mobility of individuals within a process constrained built environment and in doing so contributes to exploring the challenges of modelling process constrained environments. Our objective is to create a model that recreates room occupancy distributions – this implies that we require a room transition model that predicts a person's next destination as well as a dwell time model that predicts how long a person will stay in a room.

2 Research Method

This section of the paper introduces the reader to the case study environment, our method of data capture, our proposed models and our model evaluation approach.

2.1 The Case Study Environment: NICU

The case study process constrained environment is a neonatal intensive care unit (NICU) of a major UK hospital. The NICU comprises a system with the purpose of caring for seriously ill or prematurely born infants. The environment is typically staffed by neonatologists, nurses, pharmacists and respiratory therapists. The nurses, whom are the subject of this study, are responsible for performing

activities at scheduled times as well as responding to emergent events such as a deterioration in state of an infant. Planned activities include preparing and checking medication, administering intravenous fluids, giving blood products, record keeping, and cleaning the infants. Emergent events typically comprise responding to alarms such as drops in infants' heart rate and blood oxygen saturation levels.

The NICU comprises a process constrained environment because the nurses room transitions are logically, spatially and temporally constrained. For example, the nurses must administer medicines at set intervals during the day according a prescription (temporal constraint), the nurses can only collect medicines from certain rooms and administer them to infants in the clinical rooms (spatial constraints), the nurses' behaviour is constrained by a logical order in which tasks are performed e.g. when administering a medicine they must first collect it from the equipment store, administer it in a clinical area and then dispose of waste in the dirty utility room (logical constraints).

The environment featured in this case study (Fig. 1) comprises of 21 rooms. Rooms 1–6 are clinical rooms consisting of nurseries, other significant rooms include the nurse station which acts as an information hub, the clean utility where clean materials can be found, the dirty utility where used materials are disposed, the milk kitchen where nutrition is prepared and the staff room where breaks may be taken or meetings held.

2.2 Data Capture

We used Ekahau Wi-Fi location tracking tags to collect room transitions and dwell times of 10 day-shift nurses within a NICU for a period of 28 days from 08:00 Tuesday 14th June 2011 to 20:00 Monday 11th July 2011. The data collected provided a unique identifier for each nurse during a single day and consisted of the time they entered a room and their duration of stay. We used this dataset to identify and evaluate the proposed models of room transition.

2.3 Models and Model Evaluation Method

The models described below were evaluated for their goodness-of-fit with the empirical dataset. The goodness-of-fit criteria used was their success rate at predicting the next room a nurse will visit. This criteria was selected on the basis that if a model can predict each nurses' subsequent room transition then at the macro-level the model will be able to provide accurate room visitation statistics.

We decided to evaluate the following models' ability at predicting the nurses' room transitions: (1) random model; (2) occupancy distance model; (3) attractiveness model; (4) Markov model.

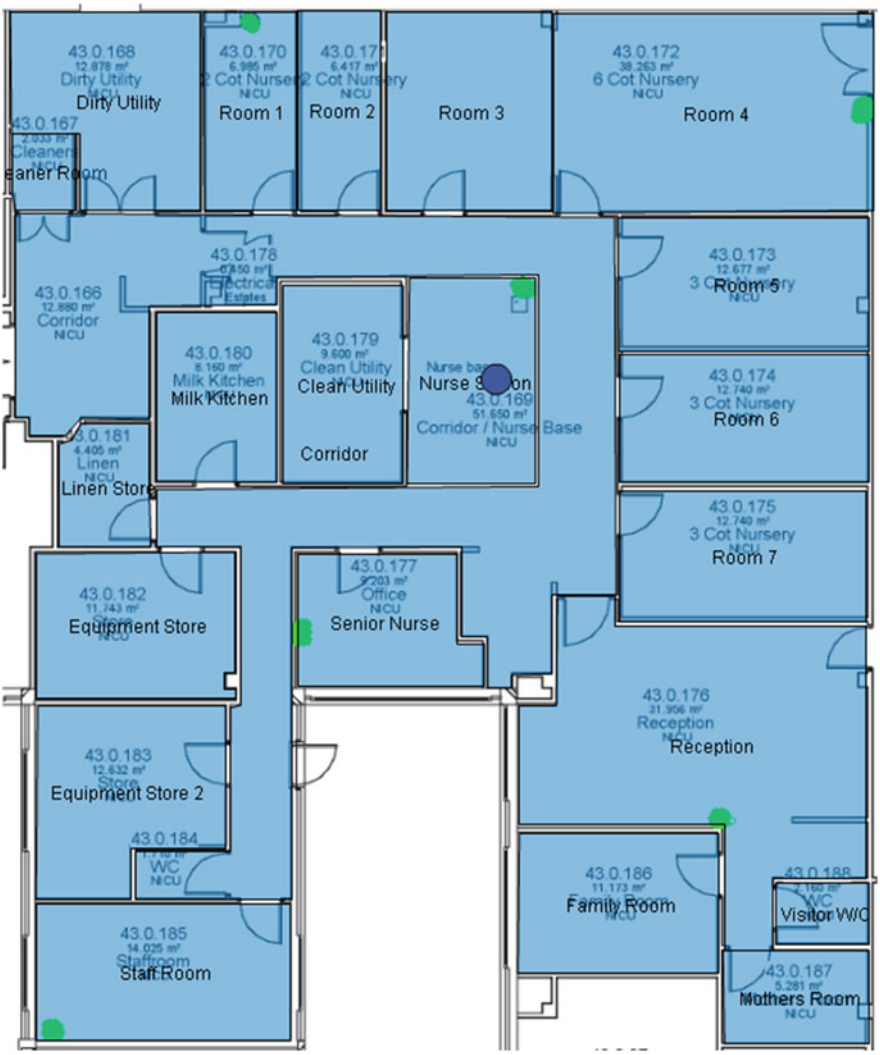

Fig. 1 Layout of case study NICU department

2.3.1 Random Model

A random model was proposed to act as a simple baseline to evaluate the performance of the other room transition models against. According to the random model all the rooms were equally probable e.g. $p_{ij} = 1/N$ where p_{ij} is the probability of transitioning from a room i to a room j and N = number of rooms.

2.3.2 Occupancy-Distance Model

An occupancy-distance model (Eqs. (1)–(4)) was evaluated to understand to what extent nurse room transitions can be predicted on the basis of the distance between rooms and the number of other nurses in a room. The notion behind this model is to understand whether distance, or numbers of other nurses in a room, is an attractor and also to understand if there are any interactions between the two variables. This model is intended to provide an indication of the solitary vs collectivist nature of the environment as well as a distance dependency within the environment e.g. distance dependent vs distance independent.

$$p_{ij} = \frac{U_{ij}}{\sum_j U_{ij}} \tag{1}$$

$$U_{ij} = U_o(o_j) + U_d(d_{ij}) \tag{2}$$

$$U_o(o_j) = \alpha_0 + \alpha_1 o_j + \alpha_2 o_j^2 \tag{3}$$

$$U_d(d_{ij}) = \beta_0 + \beta_1 d_{ij} + \beta_2 d_{ij}^2 \tag{4}$$

U_{ij} is the utility of a nurse transitioning from a room i to a room j; $U_o(o_j)$ represents the utility derived from being in a room with an occupancy o_j ; $U_d(d_{ij})$ represents the utility derived from moving a distance d_{ij}. The parameters α and β are to be discovered by fitting them to our empirical dataset using the Nelder Mead method of non-linear optimisation [4].

2.3.3 Attractiveness Model

An attractiveness model (Eq. (5)) was evaluated to understand whether some rooms are more intrinsically attractive than others ignoring all information other than the number of room visitations. The notion behind this model is to understand to what extent a room transition is contingent upon the intrinsic attractiveness of a room.

$$A_j = \frac{\sum_i C_{ij}}{\sum_i \sum_j C_{ij}} \tag{5}$$

In the equations above A_j represents the intrinsic attractiveness of a room j and C_{ij} represents the number of times a nurse has transitioned from room i to room j.

2.3.4 Markov Model

A Markov Chain model [1] was evaluated to understand to what extent the room transitions by nurses is dependent on their current room location. The notion behind this model is to understand to what extent the system is 'memoryless' in the sense that future behaviour can be accurately predicted using only current location state information.

$$p_{ij} = \frac{C_{ij}}{\sum_j C_{ij}} \tag{6}$$

3 Results

The results indicate that Markov Chain models can be used to generate empirically adequate room occupancy distributions in a process constrained environment (Table 1).

The poor goodness-of-fit metric of the attractiveness model is indicative that the NICU environment modelled is indeed a process constrained environment because the intrinsic attractiveness of rooms accounts for only a 17 % goodness-of-fit indicating that room transition behaviour is not random but neither is it determined by intrinsic room attractiveness suggesting transition behaviour is contingent on the current or prior states of the system such as number of nurses in rooms, distances between rooms, or the nurse's mental models of purposeful activity.

The results of the occupancy distance model (See Fig. 2a) suggests that distance plays a small role in the room transition behaviour of nurses. However, the number of nurses in a room did play a strong role – the greater the number of nurses in a room the greater the likelihood that another nurse would also enter the room. This finding is likely to be explained by the fact that the nurses have team meetings or hand-over meetings at certain points during the day so when the number of nurses in a room increases the probability that it is one of these all hands meetings also increases and so it is likely that more nurses will transition to the room. The fact that distance plays a small role is also very informative about the nurse room transition behaviour as it is indicative that the nurses are not moving between rooms due to their physical proximity but are transitioning on the basis of other factors one

Table 1 Model goodness-of-fit

Model name	Goodness-of-fit (%)	Improvement vs. baseline
Random	~5	Baseline
Attractiveness	~17	3.2 x
Occupancy distance	~31	6.2x
Markov chain	~39	7.8x

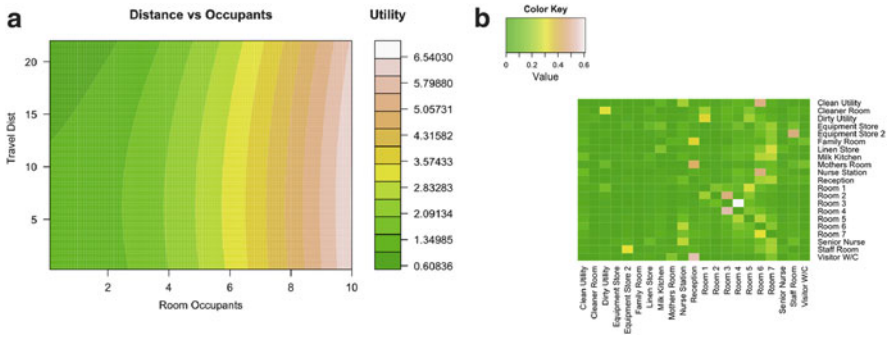

Fig. 2 (**a**) Contour map of utility as calculate using distance and occupancy metrics. (**b**) Heat map of room transition probabilities

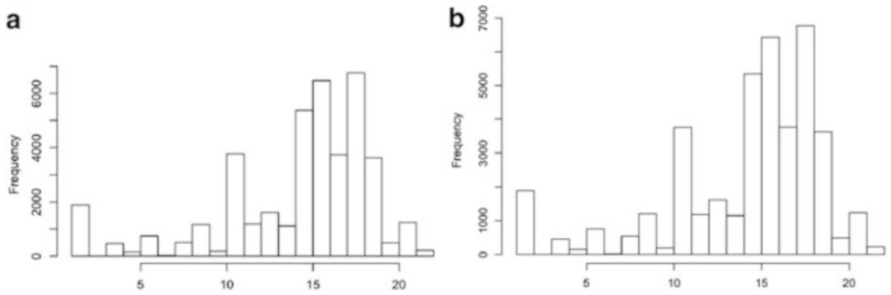

Fig. 3 Comparison of empirical vs simulated distributions. (**a**) Empirical room occupancy distribution. (**b**) Markov chain model occupancy distribution

of which we have identified is related to the number of other nurses in a room. Combining this information with the fact that intrinsic room attractiveness has poor goodness-of-fit it strongly suggests that the nurse room transition behaviour is being driven by current or prior states of the system such as numbers of nurses in a room and potentially the nurse's mental model of purposeful activity.

The results of the Markov Chain model goodness-of-fit (39 %) was 7.8× baseline suggesting that nurses' room transition is strongly contingent on current room location – see Fig. 2b. This finding is strongly suggestive that the nurses room transitions are process constrained because the probability of transitioning to a room j is contingent on the nurses current room (but not due to distance).

To investigate whether the Markov Chain model is sufficiently representative of the environment to be able to generate empirically adequate room occupancy distributions we simulated a 28 day time series of room transitions and compared it to the empirical dataset. It can be seen from the histograms that the Markov Chain model creates empirically adequate room transition distributions – see Fig. 3a, b.

Conclusions and Further work

The aim of this paper was to model the mobility of pedestrians within a process constrained built environment and in doing so to explore the challenges of modeling process constrained environments. Our objective was to create a model that recreates observed room occupancy distributions. We conclude that Markov Chain models are able to capture sufficient information about the NICU environment to generate empirically adequate room occupancy distributions. Through this case study investigation we illustrated that modelling a process constrained environment is non-trivial. Whilst we were able to generate high-level room occupancy distributions we were only able to predict the next room transition of nurse with an accuracy of 39 %. This suggests that there is significant scope for future work. Modellers may wish to consider developing models that are not 'memoryless' and that take into account temporal dimensions for example taking into account that certain rooms, such as staff rooms, are more likely to be visited at certain times of day. Modellers may also consider developing models where the process is known along with the number of pedestrians but room occupancy distributions and corridor congestion is unknown.

Acknowledgements This work is supported by the Systems Centre, the EPSRC funded Industrial Doctorate Centre in Systems (Grant EP/G037353/1), and Buro Happold.

References

1. C. Bishop, *Pattern Recognition and Machine Learning* (Springer, New York, 2006)
2. A. Johansson, D. Helbing, Analysis of empirical trajectory data of pedestrians, in *Pedestrian and Evacuation Dynamics 2008*, ed. by W.W.F. Klingsch, C. Rogsch, A. Schadschneider, M. Schreckenberg (Springer, Berlin/Heidelberg, 2010), pp. 203–214. doi:10.1007/978-3-642-04504-2_15
3. B. Maury, J. Venel, Handling of contacts in crowd motion simulations, in *Traffic and Granular Flow 07*, ed. by C. Appert-Rolland, F. Chevoir, P. Gondret, S. Lassarre, J.P. Lebacque M. Schreckenberg (Springer, Berlin/Heidelberg, 2009), pp. 171–180. doi:10.1007/978-3-540-77074-9_15
4. J.A. Nelder, R. Mead, A simplex method for function minimization. Comput. J. **7**(4), 308–313 (1965). doi:10.1093/comjnl/7.4.308
5. S. Paris, D. Lefebvre, S. Donikian, Simulem: introducing goal oriented behaviours in crowd simulation, in *Pedestrian and Evacuation Dynamics 2008*, ed. by W.W.F. Klingsch, C. Rogsch, A. Schadschneider, M. Schreckenberg (Springer, Berlin/Heidelberg, 2010). pp. 479–490. doi:10.1007/978-3-642-04504-2_40

6. A. Seyfried, B. Steffen, A. Winkens, T. Rupprecht, M. Boltes, W. Klingsch, Empirical data for pedestrian flow through bottlenecks, in *Traffic and Granular Flow 07*, ed. by C. Appert-Rolland, F. Chevoir, P. Gondret, S. Lassarre, J.P. Lebacque, M. Schreckenberg (Springer, Berlin/Heidelberg, 2009), pp. 189–199. doi:10.1007/978-3-540-77074-9_17
7. V. Tabak, B. Vries, J. Dijkstra, Rfid technology applied for validation of an office simulation model, in *Pedestrian and Evacuation Dynamics 2008*, ed. by W.W.F. Klingsch, C. Rogsch A. Schadschneider, M. Schreckenberg (Springer, Berlin/Heidelberg, 2010), pp. 269–275. doi:10.1007/978-3-642-04504-2_23

From Drivers to Athletes: Modeling and Simulating Cross-Country Skiing Marathons

Martin Treiber, Ralph Germ, and Arne Kesting

Abstract Traffic flow of athletes in classic-style cross-country ski marathons, with the Swedish *Vasaloppet* as prominent example, represents a non-vehicular system of driven particles with many properties of vehicular traffic flow such as unidirectional movement, the existence of lanes, and, moreover, severe traffic jams. We propose a microscopic acceleration and track-changing model taking into account different fitness levels, gradients, and interactions between the athletes in all traffic situations. The model is calibrated on microscopic data of the *Vasaloppet 2012*. Using the multi-model open-source simulator MovSim.org, we simulate all 15,000 participants of the Vasaloppet during the first 10 km.

1 Introduction

Traffic jams are not only observed in vehicular traffic but also in the crowd dynamics of mass-sport events, particularly cross-country ski marathons. The Swedish *Vasaloppet*, a 90-km race with about 15,000 participants, is the most prominent example (cf. Fig. 1). Several other races attract up to 10,000 participants. Consequently, "traffic jams" among the athletes occur regularly. They are not only a hassle for the athletes but also pose organisational or even safety threats. While there are a few scientific investigations of the traffic around such events [1], we are not aware of any investigations on the crowd dynamics of the skiers *themselves*.

Unlike the athletes in running or skating events [2], the skiers in Marathons for the classic style (which is required in the Vasaloppet main race) move along fixed tracks, i.e., the traffic flow is not only unidirectional but *lane based*. This allows us to generalize car-following and lane changing models [3] to formulate a microscopic model for the motion of skiers.

M. Treiber (✉) • R. Germ
Technische Universität Dresden, 01 062 Dresden, Germany
e-mail: treiber@vwi.tu-dresden.de

A. Kesting
TomTom Development Germany GmbH, An den Treptowers 1, 12 435 Berlin, Germany
e-mail: mail@akesting.de

M. Chraibi et al. (eds.), *Traffic and Granular Flow '13*,
DOI 10.1007/978-3-319-10629-8_29

Fig. 1 Starting phase of the Vasaloppet 2012

Simulating the model allows event managers to improve the race organization by identifying (and possibly eliminating) bottlenecks, determining the optimum number of starting groups and the maximum size of each group, or optimizing the starting schedule [2].

We propose a microscopic acceleration and track-changing model for cross-country skiers taking into account different fitness levels, gradients, and interactions between the athletes in all traffic situations. After calibrating the model on microscopic data of jam free sections of the *Vasaloppet 2012*, we apply the open-source simulator MovSim.org [4] to simulate all 15,000 participants of the Vasaloppet during the first 10 km. The simulations show that the initial jam causes a delay of up to 40 min which agrees with evidence from the data.

The next section introduces the model. In Sect. 3, we describe the calibration, the simulation, and the results. Section "Conclusion" concludes with a discussion.

2 The Model

Unlike the normal case in motorized traffic, the "desired" speed (and acceleration) of a skier is restricted essentially by his or her performance (maximum mechanical power $P = P_{\max}$), and by the maximum speed v_c for active propulsion ($P = 0$ for $v \geq v_c$). Since, additionally, $P \to 0$ for $v \to 0$, it is plausible to model the usable power as a function of the speed as a parabola,

$$P(v, v_c) = 4P_{\max}\frac{v}{v_c}\left(1 - \frac{v}{v_c}\right)\theta(v_c - v), \tag{1}$$

where $\theta(x) = 1$ if $x \geq 0$, and zero, otherwise. While the maximum mechanical power is reached at $v_c/2$, the maximum propulsion force $F_{\max} = 4P_{\max}/v_c$, and the

maximum acceleration

$$a_{\max} = \frac{4P_{\max}}{mv_c}, \tag{2}$$

is reached at zero speed. The above formulas are valid for conventional techniques such as the "diagonal step" or "double poling". However, if the uphill gradient (in radian) exceeds the angle $\alpha_{\text{slip}} = a_{\max}/g$ (where $g = 9.81\,\text{m/s}^2$), no forward movement is possible in this way. Instead, when $\alpha > \alpha_{\max}/2$, athletes use the slow but steady "fishbone" style described by (1) with a lower maximum speed V_{c2} corresponding to a higher maximum gradient $4P_{\max}/(gmv_{c_2})$. In summary, the propulsion force reads

$$F(v,\alpha) = \begin{cases} P(v,v_c)/v & \alpha < \alpha_{\max}/2 \\ P(v,v_{c2})/v & \text{otherwise.} \end{cases} \tag{3}$$

Balancing this force with the inertial, friction, air-drag, and gravitational forces defines the free-flow acceleration $\dot{v}_{\text{free}}$:

$$m\dot{v}_{\text{free}} = F(v) - \frac{1}{2}c_d A\rho v^2 - mg(\mu_0 + \alpha). \tag{4}$$

If the considered skier is following a leading athlete (speed v_l) at a spatial gap s, the free-flow acceleration is complemented by the decelerating interaction force of the intelligent-driver model (IDM)[1] leading to the full longitudinal model

$$\frac{\mathrm{d}v}{\mathrm{d}t} = \min\left\{\dot{v}_{\text{free}},\, a_{\max}\left[1 - \left(\frac{s^*(v,v_l)}{s}\right)^2\right]\right\}, \tag{5}$$

where the desired dynamical gap of the IDM depends on the gap s and the leading speed v_l according to

$$s^*(v,v_l) = s_0 + \max\left(0,\, vT + \frac{v(v_l - v)}{2\sqrt{a_{\max}b}}\right). \tag{6}$$

Besides the ski length, this model has the parameters $c_d A\rho/m$, μ_0, $P_{\max}/m$, v_c (defining $a_{\max}$), v_{c2}, s_0, T, and b (see Table 1). It is calibrated such that the maximum unobstructed speed $v_{\max}$ on level terrain, defined by $F(v_{\max},0) - c_d A\rho v_{\max}^2/2 - mg\mu_0 = 0$, satisfies the observed speed distributions on level unobstructed sections (Fig. 2).

Table 1 Model parameters of the proposed longitudinal model

Parameter	Typical value (fourth starting group)
ski length l	2 m
Mass m incl. equipment	80 kg
Air-drag coefficient c_d	0.7
Frontal cross section A	1 m^2
Friction coefficient μ_0	0.02
Maximum mechanical power P_{max}	150 W
Limit speed for active action v_c	6 m/s
Time gap T	0.3 s
Minimum spatial gap s_0	0.3 m
Normal braking deceleration b	1 m/s^2
Maximum deceleration b_{max}	2 m/s^2

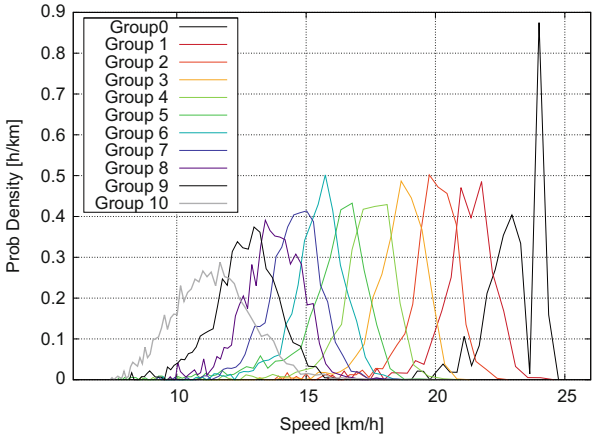

Fig. 2 Speed density functions for the section between Station 1 and 2 for each starting group. No jams were observed in this section

2.1 *Lane-Changing Model*

We apply the general-purpose lane-changing model MOBIL [3]. Generally, lane changing and overtaking is allowed on either side. Crashes are much less avoided than in vehicular traffic, so, the symmetric variant of the model with zero politeness and rather aggressive safety settings is appropriate. Lane changing takes place if it is both safe and advantageous. The safety criterion is satisfied if, as a consequence of the change, the back skier on the new track is not forced to decelerate by more than his or her normal deceleration ability b:

$$\frac{\mathrm{d}v_{\mathrm{back,new}}}{\mathrm{d}t} \geq -b. \tag{7}$$

A change is advantageous if, on the new track, the athlete can accelerate more (or needs to decelerate less) than on the old track:

$$\frac{\mathrm{d}v_{\mathrm{front,new}}}{\mathrm{d}t} \geq \frac{\mathrm{d}v_{\mathrm{actual}}}{\mathrm{d}t} + \Delta a, \tag{8}$$

where the only new parameter Δa represents some small threshold to avoid lane changing for marginal advantages. Note that for mandatory lane changes (e.g., when a track ends), only the safety criterion (7) must be satisfied.

3 Simulation Results

We have simulated all of the 15,000 athletes of the Vasaloppet 2012 for the first 10 km (cf. Fig. 3) by implementing the model into the open-source traffic simulator MovSim.org. The starting field includes 70 parallel tracks (cf. Fig. 1) where the 10 starting groups (plus a small elite group) are arranged in order. Further ahead, the number of tracks decreases gradually down to eight tracks at the end of the uphill section for $x \geq 7$ km. The uphill gradients and the course geometry (cf. Fig. 3) were obtained using Google Earth.

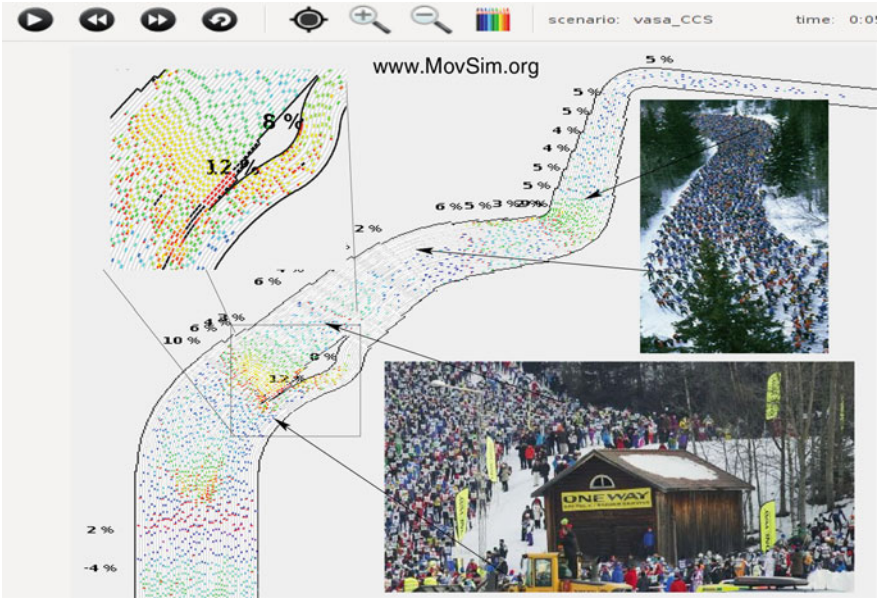

Fig. 3 Screenshot of the MovSim Simulation of the first 10 km of the Vasaloppet 2012 (*center*) with an enlargement of the diverge-merge section (*left top*). Also shown are two photos of the crowd flow at the corresponding sections (*right*)

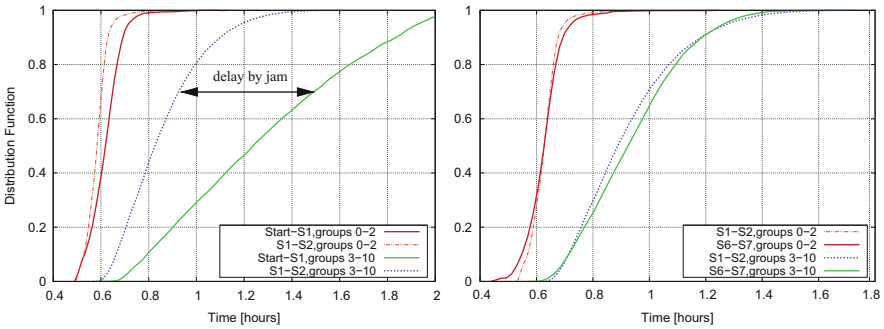

Fig. 4 Distribution functions of the split times from the start to Station S1 (*left*), S1–S2 (*left* and *right*), and S6–S7 (*right*), shown separately for the fastest groups (elite and groups 1 and 2) and the remaining groups 3–10. All three sections take about the same time. Major jams occur only for the groups 3–10 and only between the start and S1

As in the real event, we simulated a mass start. While the initial starting configuration dissolves relatively quickly, massive jams form at the beginning of the gradient section, particularly at the route divide (inset of Fig. 3). In summary, the delays due to the jams accumulated up to 40 min for the last starting groups which agrees with the macroscopic flow-based analysis of the split-time data (Fig. 4).

Conclusion

Using the open-software MovSim, we have quatitatively reproduced the congestions and stop-and-go waves on the first 10 km of the Vasaloppet Race 2012. The jams leading to a delay of up to 40 min are caused a steep uphill section and a simultaneous reduction of the number of tracks. Further simulations have also shown that eliminating the worst bottlenecks by locally adding a few tracks only transfers the jams to locations further downstream. In contrast, replacing the mass start (which is highly controversial) by a wave start with a 5-min delay between the starting groups would essentially eliminate the jams without the need to reduce the total number of participants.

References

1. P. Ahmadi, Analysis of traffic patterns for large scale outdoor events a case study of vasaloppet ski event in sweden, Thesis, Royal Institute of Technology
2. M. Treiber, Crowd flow modeling of athletes in mass sports events – a macroscopic approach, in *Traffic and Granular Flow '13* ed. by M. Chraibi, M. Boltes, A. Schadschneider, A. Seyfried (Springer, *Traffic Flow Dynamics: Data, Models and Simulation*, 2014)

3. M. Treiber, A. Kesting, *Traffic Flow Dynamics: Data, Models and Simulation* (Springer, Berlin, 2013)
4. A. Kesting, R. Germ, M. Budden, M. Treiber, MovSim – multi-model open-source vehicular simulator. www.movsim.org

Quantitative Estimation of Self-Organization in Bi-directional and Crossing Flows During Crowd Movements

Dorine C. Duives, Winnie Daamen, and Serge P. Hoogendoorn

Abstract Understanding emerging phenomena in crowd movements is necessary to understand how pedestrians behave during these movements under different circumstances and over time. Measures able to identify self-organization patterns are currently scarce. In the present study the way in which three measures (the cluster-method (Moussaid, et al. PLoS Comput Biol 8(3):e1002442, 2012), Efficiency (Helbing (1997) Verkehrsdynamik – Neue physikalische Modellierungskonzepte, 1st edn. Springer, Berlin/Heidelberg, p. 46), and Polarization (Hemelrijk and Hildenbrandt, PLoS ONE 6(8):e22479, 2011)) identify the presence of self-organization within crowd movements. Trajectory data sets resulting from a laboratory experiment and several simulations are used as a basis for the assessment. It was found for all three methods that the extent to which self-organization can be accurately predicted depends on the flow situation. Furthermore, two out of three methods were able to detect the presence of self-organization in pedestrian flows at all.

1 Introduction

Self-organization patterns in moving human crowds have been studied for more than a decade. Self-organization has been defined as a process in which a pattern at the global level of a system emerges solely from numerous interactions among the lower-level components of the system [2]. Several of these patterns were also found to appear in crowds, such as bi-directional lane formation and stripe formation. Depending on the angle at which pedestrian flows intersect either the first or the latter pattern arises [1, 7]. An understanding of how pedestrian flows behave under different circumstances and develop over time is required in order to accurately predict pedestrian crowd movements. Yet, until now quantitative research of the self-organization patterns during large-scale crowd movements has been limited. Measures to identify the extent of self-organization patterns are scarce. Biologists

D.C. Duives (✉) • W. Daamen • S.P. Hoogendoorn
Delft University of Technology, Stevinweg 1, 2628 CN Delft, The Netherlands
e-mail: d.c.duives@tudelft.nl; w.daamen@tudelft.nl; s.p.hoogendoorn@tudelft.nl

M. Chraibi et al. (eds.), *Traffic and Granular Flow '13*,
DOI 10.1007/978-3-319-10629-8_30

have studied self-organisation patterns within complex biological systems in a quantitative manner for some time now by means of a method named "Polarization". Traffic related research has focused more on the stability and efficiency of pedestrian flows. Helbing [5] and Hoogendoorn and Daamen [7] mention quantitative measures which might, when interpreted differently, also indicate the presence of self-organisation. Currently, the quantitative assessment of the presence of self-organisation is not trivial. Therefore, the present study investigates the extent to which the three measures are capable of identifying the presence of self-organization within crowd movements. It can be assumed that a form of self-organisation is present, when one of the two before mentioned patterns is visible (i.e. ground truth). The quantitative result of the three measures is compared for the time periods that self-organisation is visually perceptible.

2 Discussion of Measures that Indicate Self-Organisation

In literature, three computational methods have been presented that can possibly be used to analyze the extent to which pedestrian movements are self-organizing. In this paper, the three methods are put to the test. In the following the efficiency measure [5], the cluster-method [8], and the Polarization measure [6] are reviewed. In the subsections underneath the three methods are explained further.

2.1 Efficiency

Helbing [5] introduces a method that determines the efficiency of a pedestrian flow. In this case, if all pedestrians in the flow have the ability to walk in the direction they prefer while adopting their preferred free speed, a flow is seen as efficient. In an inefficient flow situation, pedestrians are assumed to deviate either from their preferred direction or walking speed. See Eq. 1 for the mathematical formulation.

$$Efficiency < E >= \lim_{T \to \infty} \frac{1}{T} \int_0^T dt \frac{1}{N} \sum_{i=1}^{N} \frac{\mathbf{v_i(t)} * e_i}{\mathbf{v_o}} \tag{1}$$

Where N is the number of pedestrians in the systems, T the time period for which the Efficiency is computed, v_o is the average velocity at which a pedestrian moves in its target direction and v_i the velocity of the pedestrian at timestep i. When assuming that self-organized flows are per definition more efficient than unorganized flows, the method proposed by [5] can be used to determine the extent to which a flow situation is self-organized. In this sense, $E = 1$ refers to lane and/or stripe formation, while $E = 0$ corresponds to a crystalline non-moving state.

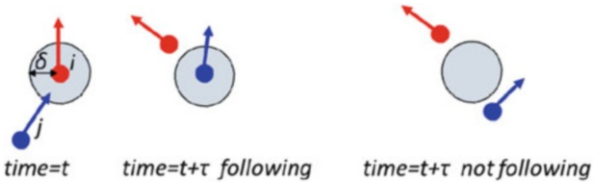

Fig. 1 Clustering method according to [8]. Two pedestrians i and j belong to the same cluster if one follows the other. In this study also t = 1 s and d = 0.6 m are the two clustering parameters used

2.2 Cluster-Method

In order to analyse the instabilities in a self-organized pedestrian crowd, [8] proposed a method to determine when groups of pedestrians formed that followed a similar trajectory. The method is visually explained in Fig. 1, which is adopted from this paper. When assuming that the extent of self-organisation is related to the average size of the groups of pedestrians who follow each other, the Cluster-method can serve as a proxy for the extent of self-organization within a flow situation.

2.3 Polarization

Biologists have studied the self-organisation of biological social systems for more than a decade. Several methods have been proposed to quantitatively determine the extent of self-organization within moving self-driven particle systems. Since pedestrians are also self-driven particles, this method might also be used to determine self-organisation in pedestrian flows. Most proposed methods are slightly different versions of the mathematical formula proposed by [6]. The 'Polarization' of a system, extent to which all individuals in a system move in one direction, is defined by average deviation of all individuals velocity from the systems average course; see Eq. 2 for the mathematical formulation.

$$Polarization < \Phi(d) >= \frac{1}{N(d)} \sum_{i \in D} \frac{\mathbf{v_i(d)}}{||\mathbf{v_i(d)}||} \frac{\bar{\mathbf{v(d)}}}{||\bar{\mathbf{v(d)}}||} \tag{2}$$

In this formulation of Polarization, $\mathbf{v_i(d)}$ is the current velocity of pedestrian i who is part of flow direction d and $\bar{\mathbf{v(d)}}$ the average movement velocity of all pedestrians that are part of a certain flow. This method assumes that in a system that is self-organized all pedestrians part of a certain flow direction move in exactly the same direction due to the lack of disturbances. Since self-organized pedestrian crowd movements know large groups of pedestrians which follow a similar path, this assumption also holds for pedestrian crowds. In the formula, $\Phi(d) = 1$ refers to complete organisation of the walking direction (i.e. self-organisation is present),

while $\Phi(d) = 0$ corresponds to total chaos. When accounting for all movements in the system, total self-organisation is accounted for by $\Phi(total) = 0$ for bi-directional flow situations and $\Phi(total) = 0.707$ for intersecting flows.

3 Methodology of Comparison

Trajectory data sets resulting from a laboratory experiment and several simulation data sets are used as the basis for this assessment. In this study, trajectory data sets predicted by the calibrated microscopic pedestrian simulation model NOMAD [3] are used. However, since it is unknown to the authors whether any simulation model is capable of representing self-organization correctly, this study does not only rely on computer generated trajectories. Additionally, experimental data sets are used, which resulted from the pedestrian walking experiments performed by the Delft University of Technology [4].

In both the laboratory and simulation study two flow patterns were generated, being orthogonal intersecting flows (90° angle) and bi-directional flows (180° angle). The demand of both experiments and simulation study followed a similar pattern. Visually self-organisation is recognized in all trajectory data sets used in the comparison of the methods. To review the methods specified in Sect. 2, the measures are computed using the trajectory data sets. Accordingly the results over time are compared with respect to each other, and a visual analysis of the situation.

4 Results

In the analysis of the results it was found that the three methods display similar trends for both the simulation and the experimental data sets with respect to the quantitative representation of self-organisation for respectively bi-directional and intersecting flows. In order to explain the results, the graphs in Fig. 2 represent the computational results from two of the simulation experiments.

The results from the Efficiency method suggest that the self-organisation of the flows decreases over time, while the other two methods (correctly) indicate that self-organisation increases over time. The Polarization method does indicate a slight decrease of self-organisation for intersecting flows. A visual analysis of the trajectory data of the bi-directional experiments shows that self-organisation comes into existence after 120 s. In these experiments the average number of pedestrians that are part of a cluster increases around the same period of time. Furthermore, the increase of the polarization per direction (see Fig. 2e) indicates that the directionality of the pedestrian movement becomes more smooth from this moment in time onwards. Even though the system is more organized, Fig. 2a shows that the efficiency of the overall movement decreases. For bi-directional flow situations both the Cluster-method (see Fig. 2c) and the Polarization indicate

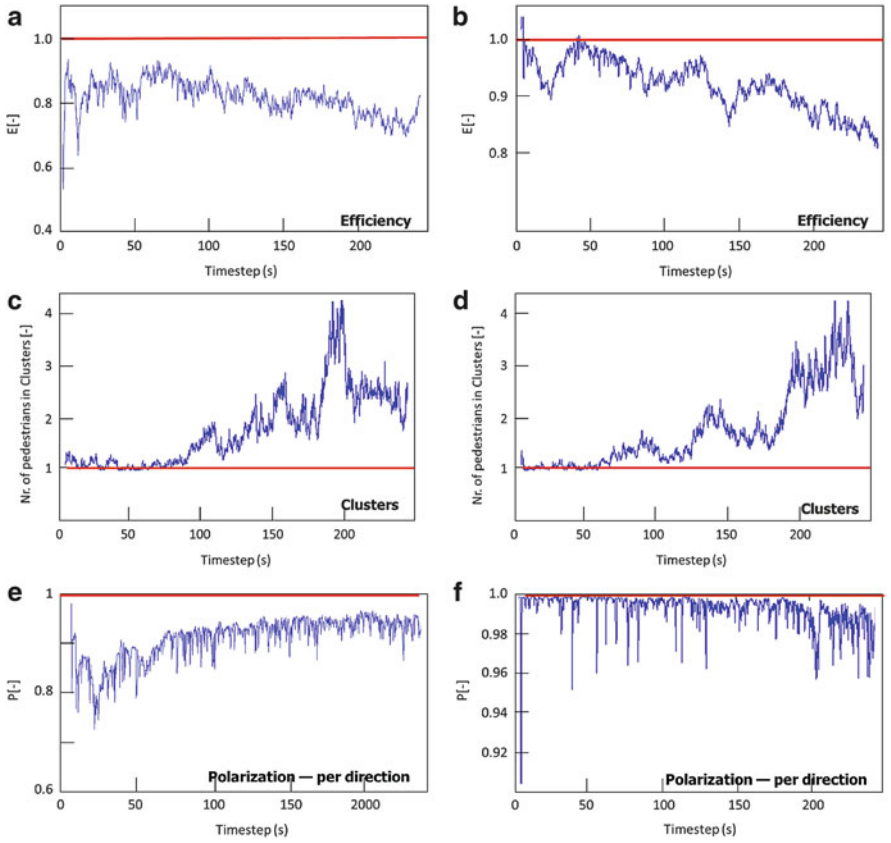

Fig. 2 Simulation results bi-directional (*left*) and 90 intersecting flows (*right*). (**a**) and (**b**) Efficiency of total system, (**c**) and (**d**) Number of pedestrians in a cluster, (**e**) and (**f**) Polarization for pedestrians part of one of the directions

the presence of self-organisation. The Cluster-method indicates the presence of self-organisation at the moment that the average cluster size increases. The extent to which is visualized through size of the clusters. The Polarization graph does also indicate the presence of self-organisation. But besides the extent to which self-organisation is present, the graph also provides more information about the disturbance in the system. In a sense, directionally non-uniform movements indicate the angular deviation of pedestrians and as such friction between the directional groups.

The results from the visual analysis of the simulations featuring intersecting flows show that self-organisation comes into existence after 150 s. At this moment in time the average number of pedestrians in clusters increases (Fig. 2d). Additionally, Fig. 2f shows that the polarization per direction decreases, which indicates the pedestrians move less uniformly. Based on these results, one can conclude that

pedestrians need to twist, turn and decrease their velocity more in order to cross the intersection. As a result, the efficiency of the entire system decreases, which is indeed seen in Fig. 2b. Of the three measures, only the Cluster-method actually give an indication of the exact moment that self-organization arises in the system, as the graph features a sudden increase in amount of pedestrians in a cluster.

Conclusions

The outcome of the three proposed methods depends on the shape of the flow situation. It is found that two out of three methods are capable of detecting the presence of the self-organization in pedestrian flows. Especially the measures Average cluster size and Polarization can do so. Where Polarization is a more effective method to identify of the average operational interactions within pedestrian flows (directionality), the Cluster-method can only identify whether self-organization is present. The Efficiency measure indicates whether the pedestrian flow is effective. However, using this last method one is not capable to identify the tipping point between non-organized and self-organized behaviour.

This research has indicated the possibilities to use contemporary quantitative measures to indicate the presence of self-organisation in pedestrian crowd movements. These measures can be implemented in order to assess the chaos within a pedestrian movement system with a limited number of directed flows. Yet, more research is needed to fully understand how, why and when self-organisation plays an important role in crowd movement dynamics.

References

1. K. Ando, H. Ota, T. Oki, Forecasting the flow of people (in Japanese). R.R.R. Railw. Res. Rev. **45(8)**, 8–1 (1988)
2. S. Camazine, J.-L. Deneubourg, N.R. Franks, J. Sneyd, G. Theraula, E. Bonabeau, *Self-Organization in Biological Systems* (Princeton University Press, Princeton/Oxford, 2003). p. 7
3. M. Campanella, S.P. Hoogendoorn, W. Daamen, Improving the Nomad microscopic walker model, in *12th IFAC Symposium on Control in Transportation Systems (CTS'09)*, Redondo Beach (2009)
4. W. Daamen, S. Hoogendoorn, Controlled experiments to derive walking behavior. Eur. J. Transp. Infrastruct. Res. (EJTIR) **3**(1), 39–54 (2003)
5. D. Helbing, *Verkehrsdynamik – Neue physikalische Modellierungskonzepte*, 1st edn. (Springer, Berlin/Heidelberg, 1997), p. 46
6. C.K. Hemelrijk, H.Hildenbrandt, Some causes of the variable shape of flocks of brids. PLoS ONE **6**(8), e22479 (2011)
7. S.P. Hoogendoorn, W. Daamen. Self-organization in walker experiments, in *Proceedings of the 5th Symposium on Traffic and Granular Flow*, Delft (2004)
8. M. Moussaid, E. Guillot, M. Moreau, J. Fehrenbach, O. Chabiron, S. Lemercier, G. Theraulaz, Traffic instabilities in self-organized pedestrian crowds. PLoS Comput. Biol. **8**(3), e1002442 (2012)

An Expanded Concept of the "Borrowed Time" in Pedestrian Dynamics Simulations

Marcin Mycek, Robert Lubaś, Jakub Porzycki, and Jarosław Wąs

Abstract Discretization in numerical simulations holds big advantage of decreasing complexity of calculations, allowing for faster and larger-scale simulations. However, such a procedure leads to emergence of unwanted phenomena due to finite space and/or time resolution. For this reason when space is discretized usually regular lattices are used as they preserve highest rotational and translational symmetry. Highest natural isotropy is obtained by using hexagonal grid. However, for pedestrian dynamics applications due to natural tendency of humans to build square-based buildings and typical big size of the cell square grid allows drastically better space representation. This paper describes how a borrowed time concept can be used to reduce anisotropy in pedestrian dynamics simulations using regular square grid without increasing complexity of the calculation. A simple case of pedestrian movement using expanded borrowed time concept is described and compared with basic approach. A method for generating static potential field with higher isotropy is shown as well.

1 Introduction

Currently, the simulation of pedestrian dynamics is an issue of growing interest and importance. Reliable results of the simulations enable: architects, safety engineers or managers of public facilities to test influence of space arrangement and possible scenarios on key characteristics of pedestrian flow. Regarding discrete, lattice-based pedestrians simulations, a close attention should be drawn to issue of isotropy of moving particles representing pedestrians.

M. Mycek (✉) • R. Lubaś • J. Porzycki • J. Wąs
Department of Applied Computer Science, AGH University of Science and Technology,
al. Mickiewicza 30, 30-059 Kraków, Poland
e-mail: mycek@agh.edu.pl; rlubas@agh.edu.pl; porzycki@agh.edu.pl; jarek@agh.edu.pl

M. Chraibi et al. (eds.), *Traffic and Granular Flow '13*,
DOI 10.1007/978-3-319-10629-8_31

The term *isotropy* is a combination of two Greek words (presented below in Latin transcription): isos – equal and tropos – way. In general, it means *having the same value when measured in different directions*.

2 Related Works

Different approaches to the anisotropy reduction were presented by various authors. For microscopic discrete simulations it was shown that introducing randomness of any kind – be it a random distribution of active grid cells [6], a randomized space discretization [7], introducing random walk [9], using inherent randomness such as in lattice-gas automata [1] or asynchronous dynamics [10] can highly reduce unwanted effects of discretization, while Kirchner et al. [3] analyzed issue of discretization of different models of pedestrian dynamics. Kretz and Schreckenberg in [5] discussed problems of symmetry and influence of neighborhood schemes on discrete models of pedestrian dynamics.

In pedestrian dynamics topic of isotropy was undertaken from different angles as most of the previously mentioned methods are not applicable due to typical large grid cell size. Kretz and Schreckenberg [5] addressed this issue by analyzing impact of higher speed of pedestrians i.e. allowing them to move larger, but discrete number of steps in one round of simulation. Klüpfel [4] considered a basic borrowed time approach, but only one step corrections were considered, which are not enough to achieve high isotropy [8]. Hartmann [2] proposed first-order movement algorithm for determining accurate shortest paths and presented it for a hexagonal grid.

3 An Expanded Concept of Borrowed Time

A full mathematical background of a borrowed time concept has been described in detail in [8], in this article only key points will be briefly described.

For any regular grid one can define **an optimal path** from a cell A to a cell B:

Definition 1 For a path P_{AB} between two given cells A and B: if there does not exist a path connecting between those two cells with a shorter time than P_{AB}, it is called **an optimal path** and denoted by P_{AB}^{op}, with its time (length) labeled t_{AB}^{op}.

For such paths between cells A and B **an average speed** $\bar{V}_{AB}$ can be defined as:

$$\bar{V}_{AB} = \frac{dist(AB)}{t_{AB}^{op}}, \tag{1}$$

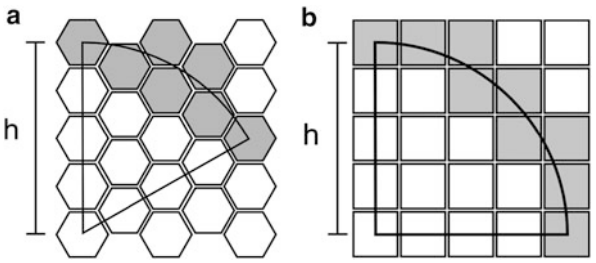

Fig. 1 A horizon $H(4)$ for a hexagonal (**a**) and a square (**b**) grid. For clarity only part of the whole horizon has been shown

with $dist(AB)$ being Euclidean distance between cells centers. To measure relative quantities we can introduce **the average speed deviation** D_{AB}:

$$D_{AB} = \frac{\bar{V}_{AB} - 1}{1}. \tag{2}$$

In order to define a measure of isotropy a set over which it can be measured needs to be constructed as well:

Definition 2 For a given cell A and distance h, a set of all cells having at least one common point with a circle with radius h and center in the middle of the cell A is called **a horizon** and denoted by $H_A(h)$.

How horizons are shaped for both square and hexagonal grid can be seen in Fig. 1. Finally **a measure of the average speed isotropy** – $I_A(h)$ can be introduced:

Definition 3

$$I_A(h) = \frac{1}{\#H_A(h)} \sum_{C \in H_A(h)} D_{AC}^2. \tag{3}$$

The main problem with anisotropy of a square grid comes from diagonal moves. Typical grid cell size in pedestrian dynamics is too big to disallow diagonal movement, while pedestrians in simulation during such steps cover significantly more distance. The proposed solution is to allow pedestrian to "borrow" time for diagonal moves in order to keep average speed similar in all directions, thus regaining isotropy. If the amount of time borrowed by the agent exceeds whole time step, to compensate this the pedestrian is frozen for one round of simulation. There are two approaches to the amount of time agent should borrow during diagonal moves. First one is to optimize first step, i.e., $I_A(1)$[4], the second one is to optimize $I_A(\infty)$[8]. How does $I_A(h)$ and D_{AB} look like for both cases and for a case without any modifications (i.e., pure Moore neighborhood) can be seen in Fig. 2.

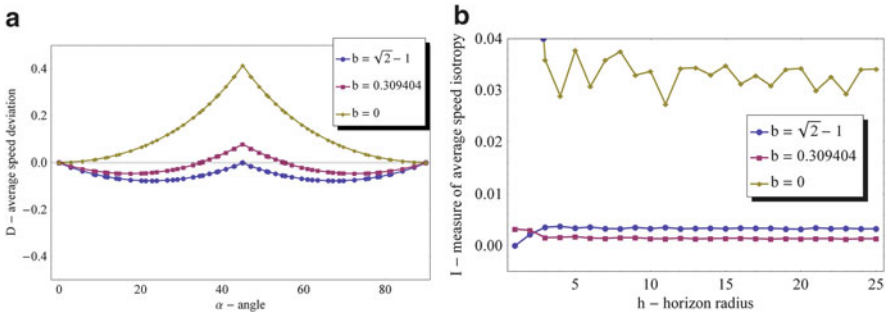

Fig. 2 (**a**) – dependence of average speed deviation D on angle for different borrowed time parameter values. (**b**) – relation between a measure of the average speed isotropy I_A and a horizon radius h. Values of $b_1 = \sqrt{2} - 1$ and $b_\infty = 0.309404$ correspond to first and infinite step improvement correspondingly, $b = 0$ correspond to pure Moore neighborhood without any modifications

4 Applications

Lets consider pedestrians on a square grid moving toward a point at different angles, but with the same distance to the target, i.e., with starting points from the same horizon. The situation is depicted in Fig. 3 with a target cell marked green and $H(16)$ marked dark gray. Two potential fields are marked on the picture. The first one (red) was calculated using Dijkstra algorithm with $\sqrt{2}$ distance on diagonal connections. For the second one (black) $1 + b_\infty$ value was used instead.

Lets study movement of eight pedestrians with their initial positions marked by $(1, 2, 3, 4, 4', 3', 2', 1')$. All pedestrians in typical way choose in each time step a destination a cell with the smallest potential value in Moore neighborhood. Their chosen trajectories are marked blue. The dark blue cells show where and when a pedestrian movement is temporary frozen due to borrowing more then one whole time step. The borrowed time parameter b was different for each potential field as well – b_1 and b_∞ for respectively. We see that while for pedestrians close to main axes $(1, 1', 2, 2')$ the difference is negligible, it is more visible the closer the movement is to diagonal – pedestrians 4 and $4'$ reach target after 18 and 19 simulation steps respectively

Not only on the operational level the concept of borrowed time can be used, but also to improve isotropy of static potential fields generated with local greedy method such as a Dijsktra algorithm. Depending on assumed neighborhood and diagonal distance the shape of the determined potential can be very different. In Fig. 4 four different ways of generating potential field are shown, namely for von Neumann

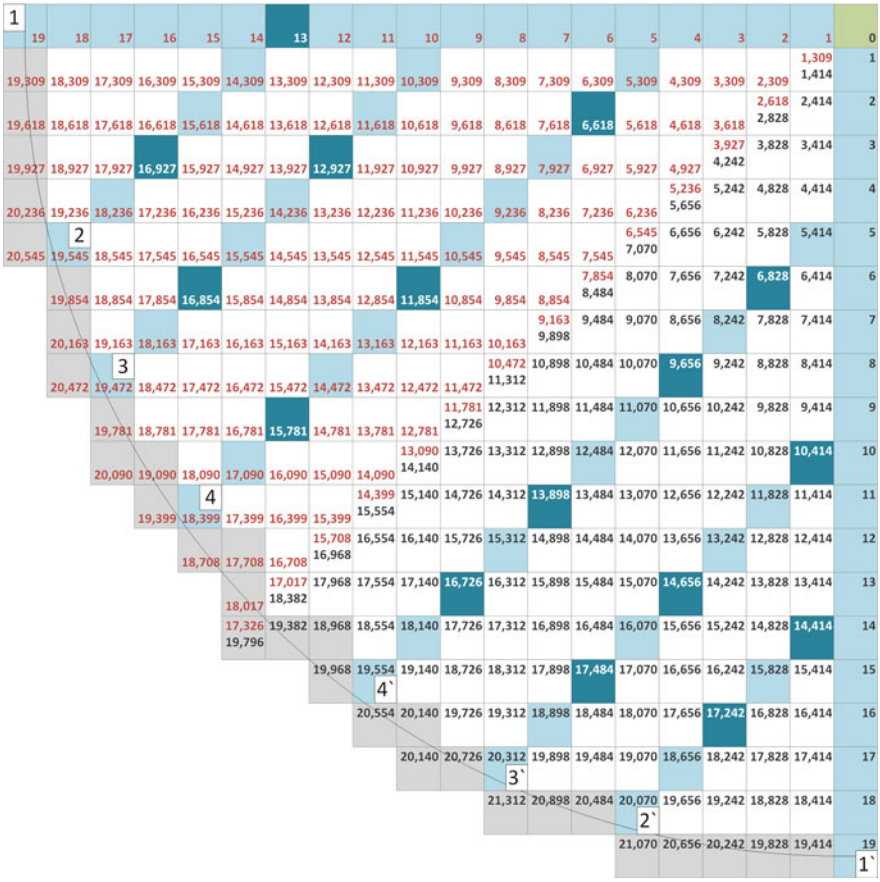

Fig. 3 An illustration of pedestrian trajectories for basic and an expanded borrowed time concept. All pedestrians start in the same distance (*grey cells*) to the target point (*green*). (1, 2, 3, 4, 4′, 3′, 2′, 1′) depict starting positions of eight pedestrians with their trajectories marked *blue*. *Dark blue cells* highlight where and when pedestrian movement was stopped due to borrowing too much time

neighborhood (a) and Moore neighborhood (b) with diagonal distance of 1 and for Moore neighborhood with diagonal distance of $1 + b_1$ (c) and $1 + b_\infty$. To highlight the differences two last cases are compared in Fig. 5 with a reference circular shape. As can be seen for $1 + b_1$ the shape is always inside a circle. This means that we make a systematic error always with the same sign. On the other hand for $1 + b_\infty$ the absolute error is lower and mean error is very close to zero [8].

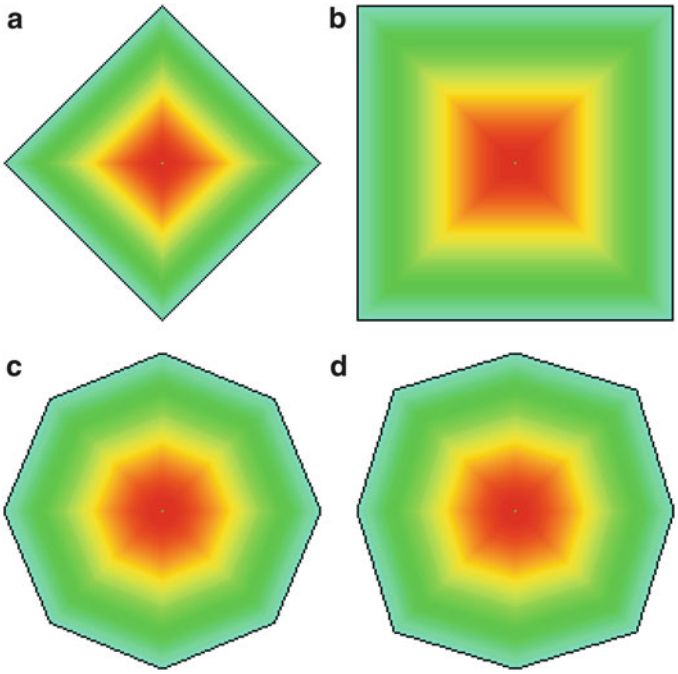

Fig. 4 A comparison of four potential fields, all generated using a Dijkstra algorithm, but with a different neighborhood and a diagonal distance. (**a**) von Neumann neighborhood with a diagonal distance 1. (**b**) Moore neighborhood with a diagonal distance 1. (**c**) Moore neighborhood with a diagonal distance $1 + b_1$. (**d**) Moore neighborhood with a diagonal distance $1 + b_\infty$

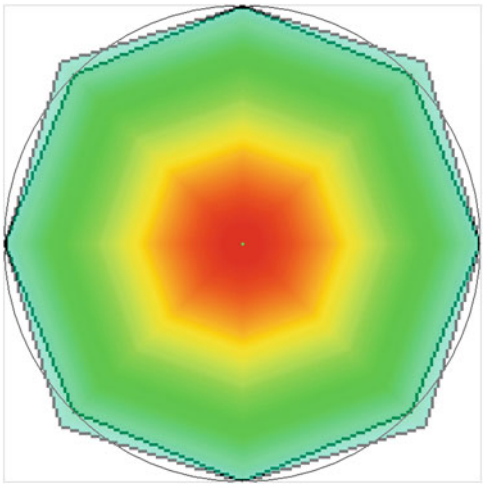

Fig. 5 A comparison of static potential fields generated with a Dijkstra algorithm for a Moore neighborhood with different diagonal distance – $1 + b_1$ (*inner*) and $1 + b_\infty$ (*outer*). A *circular shape* for corresponding perfect shape is shown

5 Summary

The article described how an expanded concept of borrowed time can be used to reduce anisotropy in pedestrian dynamics simulations. To potential applications in pedestrian movement and static field generation were presented. Especially isotropy of the shapes obtained by different approaches to Dijkstra algorithm were compared, with the clear advantage of the approach based on an expanded concept of the borrowed time.

It should be noted that while proposed solutions are very similar to the methods based on solving Eikonel equations proposed in [2], they are the best zero order solution in comparison to the first order method of [2].

References

1. U. Frish, B. Hasslacher, Y. Pomeau, Lattice-gas automata for the Navier-Stokes equation. Phys. Rev. Lett. **56**(14), 1505–1508 (1986)
2. D. Hartmann, Adaptive pedestrian dynamics based on geodesics. New J. Phys. **12**(4), 043032 (2010)
3. A. Kirchner, H. Kluepfel, K. Nishinari, A. Schadschneider, M. Schreckenberg, Discretization effects and the influence of walking speed in cellular automata models for pedestrian dynamics. J. Stat. Mech.: Theory Exp. **2004**(10), P10011 (2004). http://iopscience.iop.org/1742-5468/2004/10/P10011/cites
4. H. Klüpfel, A Cellular Automaton Model for Crowd Movement and Egress Simulation. Dissertation, University Duisburg-Essen (2003)
5. T. Kretz, M. Schreckenberg, Moore and more and symmetry, in *Pedestrian and Evacuation Dynamics 2005*, ed. by N. Waldau et al. (Springer, Berlin/Heidelberg, 2005), pp. 297–308
6. C. Kurrer, K. Schulten, Propagation of chemical waves in discrete excitable media: anisotropic and isotropic wave fronts, in *Nonlinear Wave Processes in Excitable Media*, ed. by M.M. Holden, A.V. Othmer, H.G. Othmer (Plenum Press, New York, 1991)
7. M. Markus, Dynamics of a cellular automaton with randomly distributed elements, in *Mathematical Population Dynamics*, A.D.E. Arino, O. Kimmel, M. Kimmel (Marcel Dekker, New York, 1991)
8. M. Mycek, An expanded concept of the borrowed time as a mean of increasing the average speed isotropy on regular grids, new results in dependability and computer systems. Adv. Intell. Syst. Comput. **224**, 315–324 (2013)
9. A. Nishiyama, T. Tokihiro, Construction of an isotropic cellular automaton for a reaction-diffusion equation by means of a random walk. J. Phys. Soc. Jpn. **80**, 054003 (2010)
10. B. Schonfisch, Anisotropy in cellular automata. Biosystems **41**(1), 29–41 (1997)

Measuring Disaster Preparedness of UK Cities from Open Spatial Databases

Bharat Kunwar and Anders Johansson

Abstract In recent years, we have seen a surge in the number of natural disasters (Munich, Loss events worldwide 2013, 2013). Rapid urbanisation and population growth are contributing factors. However, the planning tools available are usually specific to a region and incompatible in new areas. Therefore, aim of the overall project is to utilise growing wealth of crowd-sourced open spatial databases like OpenStreetMap (OSM) (Haklay and Weber, Pervasive Comput IEEE 7(4):12–18, 2008), computational mobility and behavioural models to achieve rapid simulation of large-scale evacuation effort in response to major crises. As part of an initial effort to gain insight into disaster resilience of various UK cities, 7 amenities across 11 cities have been studied. Correlations between population count (GPWv3) (Center for International Earth Science Information Network (CIESIN)/Columbia University and Centro Internacional de Agricultura Tropical (CIAT), Gridded Population of the World, Version 3 (GPWv3): Population Density Grid, 2005) and number of critical amenities that have the potential to suffer increase in demand during a crisis have been looked at. Similarly, correlations between pairs of potentially interdependent population weighted amenities have also been investigated by working with the assumption that if they are spatially well correlated, they can work better. As the work is ongoing, a worldwide geographically specific 'Evacuation-Friendliness Index' is envisioned at the end of this project. As the research focus expands take suitability of road networks for emergency evacuation and dynamic effects using agents based models, the outcome is expected to have implication on emergency planning in the short term by testing multiple strategies in the run up to a disaster and influence policy makers in the long term by identifying weakest links and bottlenecks in a city system.

1 Introduction

In recent years, we have seen a surge in the number of natural disasters [1]. In early November 2013, Typhoon Haiyan, an exceptionally powerful tropical cyclone devastated portions of Southeast Asia killing at least 6,000 people with UN estimate

B. Kunwar (✉) • A. Johansson
University of Bristol, Bristol, UK
e-mail: b.kunwar@bristol.ac.uk; a.johansson@bristol.ac.uk

M. Chraibi et al. (eds.), *Traffic and Granular Flow '13*,
DOI 10.1007/978-3-319-10629-8_32

suggesting that around 11 million people have been affected by it and many have been left homeless. While rapid urbanisation and population growth are contributing factors, it is also a call for urgent action.

Lämmel et al., [2] carried out evacuation simulation in the Indonesian city of Padang for Last Mile Evacuation Project. However, such planning tools rely on a large amount of information gathering which requires an equally large amount of time. They are also usually constrained to specific geographical regions and difficult to keep up to date with new data.

As a result, the aim is to provide an interface where a region of interest anywhere on the planet can be selected under risk of a type of disaster (e.g. flooding or earthquake), and within matter of minutes, have an evacuation model running for that region using combination of well studied approaches like Agent Based Modelling (ABM) and road network analysis on a world-wide scale.

Initial work is an examination of Points Of Interest (POI) within various UK cities to uncover potential socioeconomic insights from spatial data and whether their disaster critical POI are best spatially located to serve their purpose.

An extract of OpenStreetMap (OSM) [3] spatial database for Great Britain (great-britain-26072012.osm.pbf – 570.7 MB compressed as of 26 July 2013) [4] is used.

The OSM database schema contains three primary tables for points, lines and polygons. POI information is accessed from the points table.

To enable comparison with distribution of population, Gridded Population of the World, Version 3 Future Estimates (GPWv3FE) [5] is used, which consists of estimates of human population for the years 2015 at 2.5 arc-min resolution.

Table 1 enlists sample size of amenities according to OSM database. The cities are in the order of population size. Note that the OSM database entries do not necessarily explicitly replicate reality and may be incomplete, as a consequence of which the later results may be skewed, especially for cities with few samples.

Table 1 Sample size of amenities in the given cities (OSM) in the order of population size (GPWv3) that are covered in this report

	Population	Fuel	Police	Fire_station	Hospital	School	atm	Post_box
London	8,555,606	341	79	33	76	657	642	5,232
Birmingham	1,379,033	42	12	3	12	47	104	858
Leeds	1,000,671	51	8	9	9	107	119	782
Manchester	615,549	27	8	4	11	63	21	83
Liverpool	532,449	16	11	4	11	52	20	308
York	347,195	13	2	1	3	8	40	210
Nottingham	313,880	20	7	1	1	27	36	271
Bristol	253,664	23	8	4	5	60	47	425
Cardiff	198,112	12	3	1	2	16	32	85
Oxford	158,451	9	3	1	1	5	40	209
Chester	23,644	12	1	1	2	10	7	31

Amenities like 'police', 'hospital' and 'fire_station' that have the potential to be a critical infrastructure during a crisis are examined here. Some are non-critical amenities, e.g. 'atm' and 'post_box', but they provide good control group to compare against, (e.g. 'school' vs 'post_box'). This is to help highlight the more useful correlations between amenities such as 'fire_station' and 'hospital'.

2 Methodology

The population density raster map $p(i, j)$ that falls within the extent of the geographical map is resized using a 'bicubic' interpolation method which consistently yields the lowest error compared to other ways of interpolation methods like 'bilinear', 'box' and 'nearest'. It is converted to population count map, $P(i, j)$ by multiplying each cell using the average area of a grid cell, $S_{average}$ to give,

$$p(i, j) \times S_{average} = P(i, j) \tag{1}$$

Similarly, the number of amenities that fall within the extent of these cells are counted and saved to an integer matrix to obtain an amenity count grid $A(i, j)$. It may also be represented in terms of population weighted amenity $\frac{A}{P}(i, j)$ as follows,

$$\frac{A(i, j)}{P(i, j)} = \frac{A}{P}(i, j), \quad if \quad P(i, j) \geq 1 \tag{2}$$

Then, using data on population and amenity count in the scope, correlation coefficient between them are calculated using Eq. 3 where i is the cell index and n is the number of cells.

$$r_{xy} = \frac{\sum_{i=1}^{n}(x_i - \bar{x})(y_i - \bar{y})}{\sqrt{\sum_{i=1}^{n}(x_i - \bar{x})^2 \sum_{i=1}^{n}(y_i - \bar{y})^2}} \tag{3}$$

'Population-Amenity' correlation analysis (r_{PAC}) aims to look at the relative difference between various places and make a qualitative inference of places that might be better prepared for disasters than others. To do this, correlation is established between $P(i, j)$ and $A(i, j)$ to see if there are links between how well the critical amenities and population centres are correlated as a measure of how they are intrinsically prepared in response to various crises by having the necessary amenities within reach of where they are most needed. Higher r_{PAC} could mean greater preparedness by having the necessary amenities within close proximity of most people. However, it could also be problematic by inhibiting access to critical amenities due to denser population.

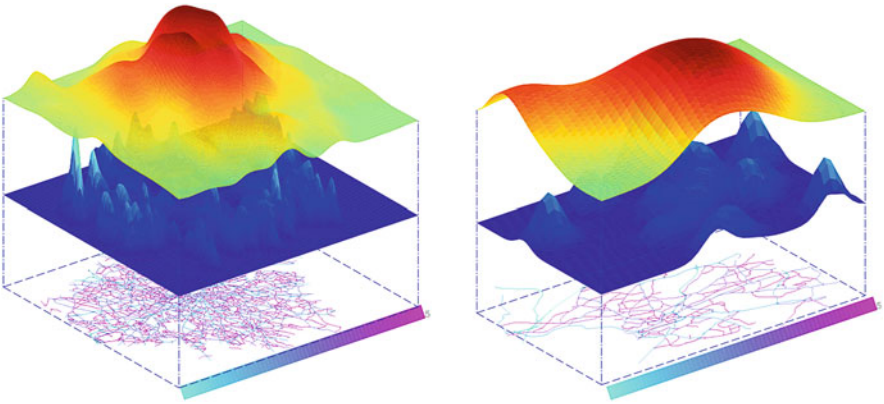

Fig. 1 Example cases of various interacting Highway (*bottom*), Amenity (*middle*) and Population (*top*) layers for London (*left*) and Bristol (*right*). Highway and Amenity layers come from OSM. Population layer comes from GPWv3 [5]. The size of the peaks on Amenity and Population layers simply indicate the relative maximum and minimum points for the purpose of demonstration only

'Amenity-Amenity' correlation analysis (r_{AAC}) examines the possibility of a similar disaster preparedness indicator to r_{PAC} by working with the assumption that if two critical highly interdependent amenities in a city are within good proximity of each other, it is indicative of a greater disaster preparedness but potentially also reduce resilience as both could fail simultaneously. This is done by establishing correlation between pairs of $\frac{A}{P}(i, j)$ dataset belonging to various amenities (Fig. 1).

3 'Population-Amenity' Correlation Results

Figure 2 shows median r_{PAC} of seven correlations per city for each amenity. It ranks 'London' with a median $r_{PAC} \approx 0.8$ at the top and 'Chester' with a median $r_{PAC} \approx -0.3$ at the bottom. All the leading cities from 'London' to 'Bristol' have a strong median r_{PAC}, roughly following the trend of population size, with the exception of 'Oxford'.

Figure 3 shows median r_{PAC} of 11 correlations per amenity for each city. Amenity 'post_box' is best correlated with population count with a median $r_{PAC} \approx 0.6$. Amenity 'hospital' and 'fire_station' share the least correlation with a median $r_{PAC} \approx 0.3$. The range of values lean towards a positive correlation.

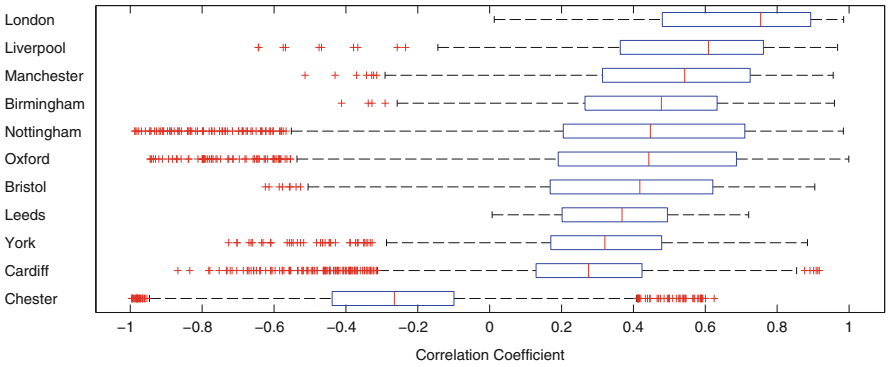

Fig. 2 Distribution of mean r_{PAC} of the 7 amenities on x-axis for each of the 11 cities on y-axis. −1.0 is maximum anti-correlation, 0 is no correlation and 1.0 maximum correlation. The *red etches* indicate the median of seven analyses per city for each amenity

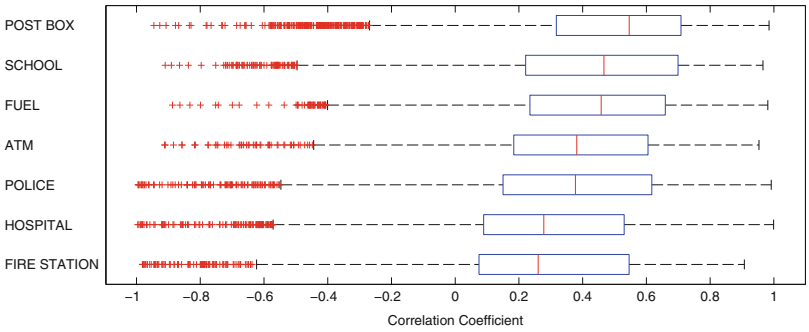

Fig. 3 Distribution of mean r_{PAC} of the 11 cities on x-axis for each of the 7 amenities on y-axis. −1.0 is maximum anti-correlation, 0 is no correlation and 1.0 maximum correlation. The *red etches* indicate the median of 11 analyses per amenity for each city

4 'Amenity-Amenity' Correlation Results

Figure 4 shows medians of 21 unique correlations per city between amenity pairs that are not self-referential. 'Leeds' and 'Manchester' rank high with a median $r_{AAC} \approx 0.7$ while 'Oxford' with a median $r_{AAC} \approx 0.1$ falls at the bottom.

Figure 5 shows median of r_{AAC} for 66 unique correlations per amenity between amenity pairs across cities. Amenity 'post_box' is most correlated with other amenities with a median $r_{AAC} \approx 0.6$. Amenities 'fire_station' and 'hospital' share the lowest median correlation $r_{AAC} \approx 0.25$. The range of values lean towards a positive correlation.

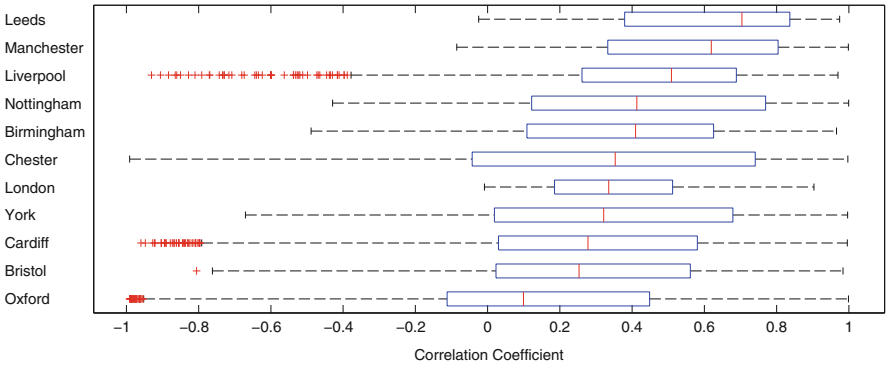

Fig. 4 Distribution of mean r_{AAC} of the 7 amenities on x-axis for each of the 11 cities on y-axis. −1.0 is maximum anti-correlation, 0 is no correlation and 1.0 maximum correlation. The *red etches* indicate the median of 21 unique correlations per city between amenity pairs

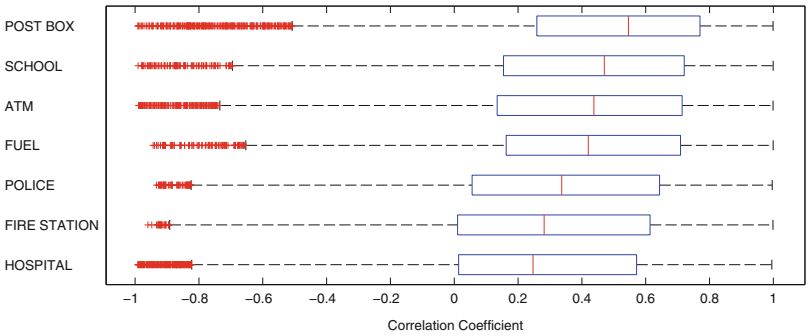

Fig. 5 Distribution of mean r_{AAC} of the 11 cities on x-axis for each of the 7 amenities on y-axis. −1.0 is maximum anti-correlation, 0 is no correlation and 1.0 maximum correlation. The *red etches* indicate the median of 66 unique correlations per amenity between amenity pairs across cities

5 Conclusion

'Population-Amenity' correlations seem to increase with population size of the UK cities in the study scope with greater certainty due to smaller inter-quartile range (attribute of a bigger sample size). 'London' and 'Chester' rank at the top and bottom respectively. The highest correlation can be seen for 'fuel' stations, indicating ease of access. The lowest correlation can be seen for 'hospital' and 'fire_station' indicating presence away from dense population centres, indicating that services are less likely to be hindered.

'Amenity-Amenity' correlations rank 'Leeds' and 'Manchester' at the top, and 'Bristol' and 'Oxford' at the bottom. The amenity 'post_box' is best correlated with all the other amenities across all cities. However, 'fire_hospital' and 'hospital' rank at the bottom, following the same trend as 'Population-Amenity' correlation. It is

probably a good idea that these critical amenties are not spatially coupled with other critical amenities in the face of a disaster as multiple failure could be even more disastrous.

6 Current Limitations and Future Work

Small sample size of amenities for some of the cities and use of low resolution GWPv3FE population data in this work are limiting factors.

However, as incorporation of ABM is the next step, layers such as 'urban centres', 'altitude', etc. will be added. A taxonomy of various types of disasters is also pending so that scarce resources can be identified, e.g. earthquakes may increase demand for open spaces. Road networks will also be analysed to get an idea of relative robustness of road networks in world cities.

Acknowledgements BK acknowledges funding from EPSRC Doctoral Training Grant and Systems Centre, University of Bristol.

References

1. R.E. Munich, Loss events worldwide 2013, 2013
2. G. Lämmel, M. Rieser, K. Nagel, H. Taubenböck, G. Strunz, N. Goseberg, T. Schlurmann, H. Klüpfel, N. Setiadi, J. Birkmann. Emergency Preparedness in the Case of a Tsunami – evacuation analysis and traffic optimization for the Indonesian city of Padang, in *Pedestrian and Evacuation Dynamics 2008* (Springer, Berlin/Heidelberg, 2010), pp. 171–182
3. M. Haklay, P. Weber, Openstreetmap: user-generated street maps. Pervasive Comput. IEEE **7**(4), 12–18 (2008)
4. Geofabrik, OpenStreetMap Data Extracts, 2013
5. Center for International Earth Science Information Network (CIESIN)/Columbia University and Centro Internacional de Agricultura Tropical (CIAT), Gridded Population of the World, Version 3 (GPWv3): Population Density Grid, 2005

Heterogeneous Pedestrian Walking Speed in Discrete Simulation Models

Stefania Bandini, Luca Crociani, and Giuseppe Vizzari

Abstract Discrete pedestrian simulation models are viable alternatives to particle based models, employing a continuous spatial representation and they are able to reproduce realistic pedestrian dynamics from the point of view of a number of observable properties. The effects of discretisation, however, also imply difficulties in modelling some phenomena that can be observed in reality. This paper presents a discrete model extending the floor field approach allowing heterogeneity in the walking speed of the simulated population of pedestrians. Whereas some discrete models allow pedestrians to move more than a single cell per time step, in the present work we maintain a maximum speed of one cell per step but we model lower speeds by having pedestrians yielding their movement in some turns. Different classes of pedestrians are associated to different desired walking speeds and we define a stochastic mechanism ensuring that they maintain an average speed close to this threshold.

1 Introduction

Discrete pedestrian simulation models are viable alternatives to particle based models that employ a continuous representation (see, e.g., [4]) and they are able to reproduce realistic pedestrian dynamics from the point of view of a number of observable properties. The effects of discretisation, however, also imply difficulties in modelling some phenomena that can be observed in reality. This paper focuses on the possibility of modelling heterogeneity in the walking speed of the simulated population of pedestrians by modifying an existing multi-agent model extending the floor field approach [6]. Whereas some discrete models allow pedestrians (or cars, when applied to traffic modelling) to move more than a single cell per time step (as discussed in [1]), in the present work we maintain a maximum speed of one cell per step, but we model lower speeds by having pedestrians yielding their movement in some turns. Different classes of pedestrians are associated to different desired

S. Bandini (✉) • L. Crociani • G. Vizzari
Department of Informatics, Systems and Communications, Complex Systems and Artificial Intelligence Research Center, University of Milano-Bicocca, Viale Sarca 336, 20126 Milano, Italy
e-mail: bandini@disco.unimib.it; crociani@disco.unimib.it; vizzari@disco.unimib.it

M. Chraibi et al. (eds.), *Traffic and Granular Flow '13*,
DOI 10.1007/978-3-319-10629-8_33

walking speeds and we define a stochastic mechanism ensuring that they maintain an average speed close to this threshold. In the paper we will formally describe the model and we will show the results of its application in benchmark scenarios (single and counter flows in simple scenarios).

2 A Discrete Model with Heterogeneous Speeds

The method described in this paper has been developed on the computational model described in [6]. For reasons of space, we will omit the discussion of this baseline and we will only explain the general characteristics of the discrete environment, fundamental for the understanding of the proposed method for managing speed heterogeneity. The environment is represented by a grid of 40 cm sided square cells. Moore neighbourhood structure is used for describing the agents movement capabilities at each time step. Finally, update of agents intentions and positions at each step are managed with the parallel update strategy, with rules for conflict management based on the notion of friction [2].

In the literature, discrete models generally assume only one speed profile for all the population and this is considered a strong limitation of this approach; efforts towards the modelling of different speed profiles consider two main approaches: (i) *increasing agents movement capabilities* [1] (i.e. they can move more than 1 cell per time step), according to their *desired speed*; in this way, given k the side of cells and n the maximum number of movements per step, it is possible to obtain n different speed profiles, less or equal to $n \cdot k$ m/step; (ii) modifying the current time scale, making it possible to cover the same distance in less time and achieving thus a higher maximum speed profile but at the same time allowing each pedestrian to *yield their turn in a stochastic way* according to an individual parameter, achieving thus a potentially lower speed profile.

The method supporting movements of more than a single cell can be effective, but it leads to complications and increased computational costs for the managing of micro-interactions and conflicts: in addition to already existing possible conflicts on the destination of two (or more) pedestrian movements, even potentially illegal crossing paths must be considered, effectively requiring the modelling of sub-turns. In addition, the expressiveness of this method is still limited: the maximum number of movements allowed per time step determines the number of speed profiles reproducible with simulations (e.g., with $v_{max} = 4$ cell per step and a turn duration of 1 s, simulations can be configured with 0.4, 0.8, 1.2 and 1.6 m/s).

For these reasons, we decided to retain a maximum velocity of one cell per turn, allowing the model to reproduce lower speed profiles by introducing a stochastic yielding mechanism.

The baseline computational model has been modified in several parts. Each agent has a new parameter $Speed_d$ in its *State*, describing its desired speed. For the overall scenario, a parameter $Speed_m$ is introduced for indicating the maximum speed allowed during the simulation (described by the assumed time scale). In order

Algorithm 1 Life-cycle update with heterogeneous speed

```
if Random() ≤ α/β then
    if updatePosition() == true then
        α ← α − 1
    else
        β ← β + 1
    end if
end if
β ← β − 1
if β == 0 then
    (α, β) = Frac(ρ)
end if
```

to obtain the desired speed of each pedestrian during the simulation, the agent life-cycle is then *activated* according to the probability to move at a given step $\rho = \frac{Speed_d}{Speed_m}$.

By using this method, the speed profile of each pedestrian is modelled in a fully stochastic way and, given a sufficiently high number of step, their effective speed will be equal to the wanted one. But it must be noted that in several cases speed has to be rendered in a relatively small time and space window (think about speed decreasing on a relatively short section of *stairs*).

In order to overcome this issue, we decided to consider ρ as an indicator to be used to decide if an agent can move according to an *extraction without replacement* principle. For instance, given $Speed_d = 1.0\,\mathrm{m/s}$ of an arbitrary agent and $Speed_m = 1.6\,\mathrm{m/s}$, ρ is associated to the fraction $5/8$, that can be interpreted as an **urn model** with 5 *move* and 3 *do not move* events. At each step, the agent extracts once event from its urn and, depending on the result, it moves or stands still. The extraction is initialised anew when all the events are extracted. The mechanism can be formalised as follows:

- Let $Frac(r) : \mathbb{R} \to \mathbb{N}^2$ be a function which returns the minimal pair $(i, j) : \frac{i}{j} = r$.
- Let *Random* be a pseudo-random number generator in $[0, 1]$.
- Given ρ the probability to activate the life-cycle of an arbitrary agent, according to its own desired speed and the maximum speed configured for the simulation scenario. Given (α, β) be the result of $Frac(\rho)$, the update procedure for each agent is described by the pseudo-code of Algorithm 1. The method *updatePosition*() describes the attempt of movement by the agent: in case of failure (because of a conflict), the urn is not updated.

This basic mechanism allows synchronisation between the effective speed of an agent and its desired one every τ steps, which in the worst case (informally when $\frac{Speed_d}{Speed_m}$ cannot be reduced) is equal to $Speed_m \cdot 10^{\iota}$ step, where ι is associated to the maximum number of decimal positions considering $Speed_d$ and $Speed_m$. For instance, if the desired speed is fixed at $1.3\,\mathrm{m/s}$ and the maximum one at $2.0\,\mathrm{m/s}$,

the resulting $Frac(\rho) = \frac{13}{20}$, therefore the agent average velocity will match its desired speed every 20 steps.

As discussed in [3, 5], an effect of the discretisation of the environment is the fact that diagonal movements generate a higher movement speed. In order to face this issue, this mechanism can be improved by considering these movements as a different kind of event during the extraction. With this strategy, each diagonal movement carried out by an agent decreases its probability to move in the next steps according to the ratio $\Delta = \frac{0.4*\sqrt{2}-0.4}{Speed_d*timeScale}$, where $timeScale = 0.4/Speed_m$ (considering the adopted scale of spatial discretisation). This fraction represents the relationship between the additional covered space, due to the diagonal movement, and the desired speed of the agent expressed in step. In this way Δ represents the exact number of steps the agent will have to stand still to achieve a synchronisation of desired and actual speed. In order to discount diagonal movements, therefore, we introduced in the agents' state a parameter *diagPenalty*, initially set to 0, which is increased by Δ each diagonal movement. Whenever $diagPenalty \geq 1$, the probability to move is decreased by adding in the urn of extraction one *do not move* event or, in reference to Algorithm 1, by increasing of 1 unit the parameter β after *updatePosition*() invocation, decreasing *diagPenalty* by 1.

This method is now consistent for reproducing different speeds for pedestrians in a discrete environment also considering the Moore neighbourhood structure. It must be noted, however, that if it is necessary to simulate very particular velocities (consider for instance a finer grained instantiation of a population characterised by a normal distribution of speed profiles), $Frac(\rho)$ is such that a large number of turns is needed to empty the urn, that is, to achieve an average speed equal to the desired one. This means that locally in time the actual speed of a pedestrian could differ in a relatively significant way from this value. To avoid this effect, during the life of each agent the fraction describing the probability is updated at each step and in several cases it will reach unreduced forms, with $GCD(\alpha, \beta) > 1$. These situations can be exploited by splitting the urn into simpler sub-urns according to the *GCD* value. For example, given a case with $Frac(\rho) = \frac{5}{11}$, after one movement the urn will be associated to $\frac{4}{10}$; since $GCD(4, 10) = 2$ the urn can be split into 2 sub-urns containing 2 *move* and 3 *do not move* events that will be consumed before restarting from initial urn. The effect of this subdivision is to preserve a stochastic decision on the actual movement of the pedestrian but to avoid excessive local diversions from the desired speed. Improvements obtained with this method (from here called *sub-urn* method) are discussed in the next section.

3 Simulation Results

With the results shown in this section we want to exemplify the reliability of the proposed method: to verify the correct reproduction of the agents speed, as well as the average error generated by discrete space and time, two sets of stress tests

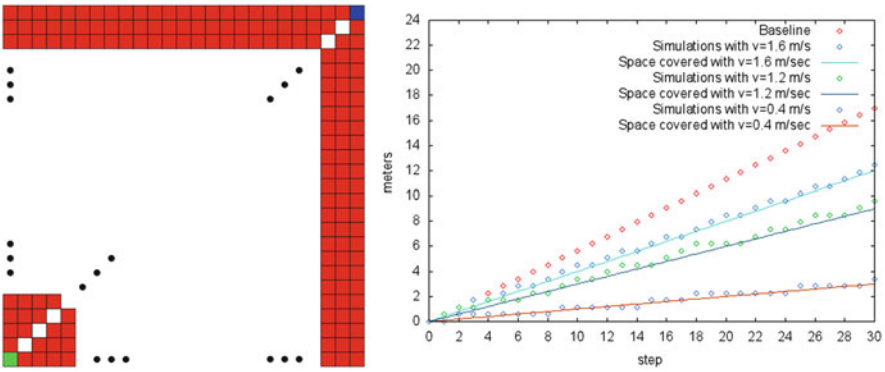

Fig. 1 Space covered by the agent, per step, in a scenario where only diagonal movements are possible, shown on the *left*

have been performed in two ad hoc scenarios. For both of them, only one agent is present in the environment in order to avoid the influence caused by conflicts. In the first scenario, depicted in Fig. 1 on the left, the agent can only perform diagonal movements (either towards the destination or, less likely, backwards). Three desired speeds have been considered – 1.6, 1.2 and 0.4 m/s – with a turn duration of 0.25 s; test results are shown in Fig. 1 on the right. Baseline data represents the space covered by the agent with desired speed of 1.6 m/s without using the proposed method for the penalisation of diagonal movements: the additional space covered by means of diagonal movement causes the agent to achieve a speed of 2.26 m/s. By applying the proposed method the error in the actual speed is significantly reduced: the mean absolute error in the distance covered at each step was about 0.25 m for desired speed of 1.6 m/s, 0.35 m for desired speed of 1.2 m/s and 0.18 m for 0.4 m/s. Maximum errors have been, respectively, of 0.54, 0.83 and 0.56 m for the lowest desired speed.

To evaluate the improvements given by the sub-urn method a second scenario has been executed in a linear environment which constrains the agent to perform only non-diagonal movements. Desired speed of the agent has been configured to 1.31 m/s, which causes and initial urn of 160 events, where 131 of them are *moves* (i.e., the agent will assume exactly 1.31 m/s every 160 steps). Figure 2 illustrates the aggregation of the results of 30 different runs of the simulation by using (darker dots) and not adopting (lighter dots) the proposed method. Results emphasize that the sub-urn method leads to a more accurate simulation of the desired speed: darker dots are in fact much closer to the line describing the distance covered with 1.31 m/s in a continuous space. This result is also described by a lower mean and maximum absolute error: the proposed method produced a mean and maximum error of 0.23 and 1.34 m against 0.56 and 2.49 m for the baseline approach.

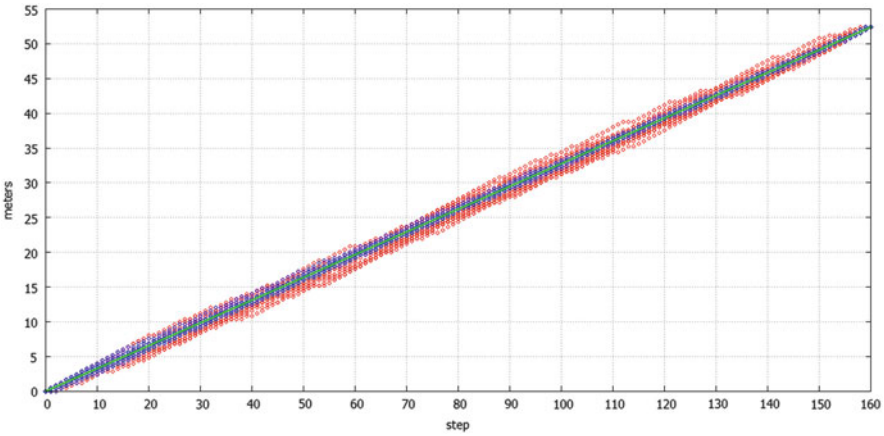

Fig. 2 Space covered by the agent in the second set of tests. *Blue dots* are obtained with the *suburn* method, while *red* ones without. The *green line* describes 1.31 m/s

Conclusions

This paper discussed an approach for reproducing different speeds in discrete pedestrian simulation models preserving a maximum movement of one cell per step, avoiding thus the need to manage conflicts that arise with higher maximum velocities. The proposed technique is simple yet effective, as explained with the proposed test results. It allows discrete computational models (not only the one adopted for the tests) to simulate more heterogeneous pedestrian populations, and it will also make possible the modelling of portions on the environment that alter pedestrian speed like stairs.

References

1. A. Kirchner, H. Klüpfel, K. Nishinari, A. Schadschneider, M. Schreckenberg, Discretization effects and the influence of walking speed in cellular automata models for pedestrian dynamics. J. Stat. Mech.: Theory Exp. **2004**(10), P10011 (2004). http://stacks.iop.org/1742-5468/2004/i=10/a=P10011
2. A. Kirchner, K. Nishinari, A. Schadschneider, Friction effects and clogging in a cellular automaton model for pedestrian dynamics. Phys. Rev. E **67**, 056122 (2003). http://link.aps.org/doi/10.1103/PhysRevE.67.056122
3. T. Kretz, M. Kaufman, M. Schreckenberg, Counterflow extension for the f.a.s.t.-model, in *ACRI*, ed. by H. Umeo, S. Morishita, K. Nishinari, T. Komatsuzaki, S. Bandini. Lecture Notes in Computer Science, vol. 5191 (Springer, Berlin/Heidelberg, 2008), pp. 555–558

4. A. Schadschneider, W. Klingsch, H. Klüpfel, T. Kretz, C. Rogsch, A. Seyfried, Evacuation dynamics: empirical results, modeling and applications, in *Encyclopedia of Complexity and Systems Science*, ed. by R.A. Meyers (Springer, New York, 2009), pp. 3142–3176
5. M. Schultz, H. Fricke, Stochastic transition model for discrete agent movements, in *ACRI*, ed. by S. Bandini, S. Manzoni, H. Umeo, G. Vizzari. Lecture Notes in Computer Science, vol. 6350 (Springer, Berlin/Heidelberg, 2010), pp. 506–512
6. G. Vizzari, L. Manenti, L. Crociani, Adaptive pedestrian behaviour for the preservation of group cohesion. Complex Adapt. Syst. Model. **1**, 7 (2013)

Stochastic Headway Dependent Velocity Model and Phase Separation in Pedestrian Dynamics

Christian Eilhardt and Andreas Schadschneider

Abstract The occurrence of phase separation into a jammed phase and a free-flow phase with non-interacting agents is a common feature observed in vehicular traffic. Experiments have shown a similar behavior for pedestrians, though the situation in pedestrian dynamics is more complicated. The two separate phases in one-dimensional "single-file" pedestrian movement are a jammed high-density phase and a phase of medium to high density with slowly moving pedestrians. Both phases consist of interacting agents. In order to understand this phenomenon we develop the one-dimensional Stochastic Headway Dependent Velocity Model which is continuous in space but discrete in time. The velocity of each agent depends on its headway and on its velocity: standing agents are subjected to a slow-to-start rule. The model can reproduce the experimentally observed phase separation at high densities.

1 Experimental Data

Experiments with single-file pedestrian traffic performed by Seyfried et al. [1] in 2006 with up to 70 pedestrians have provided strong evidence for phase separation in these systems. The length of the experimental setup was approximately 26 m including a 4 m long measurement section in which the pedestrian trajectories have been measured by automatically tracking the pedestrian heads [2]. The resulting trajectories at high density, shown together with the fundamental diagram and the velocity distribution in Sect. 3, indicate a separation into a jammed phase and a phase of slowly moving pedestrians. This is rather different from the phase separation observed in vehicular traffic where the coexistence of a jam with free flow is observed (see e.g. [3] and references therein). Here we introduce a simple model which tries to capture the main features leading to this unconventional form of phase separation.

The experimental data only extends over the small time-scale of 140 s and small spatial scales of 26 m of the whole experimental setup and only 4 m of

C. Eilhardt (✉) • A. Schadschneider
University of Cologne, Institute of Theoretical Physics, 50937 Köln, Germany
e-mail: ce@thp.uni-koeln.de; as@thp.uni-koeln.de

M. Chraibi et al. (eds.), *Traffic and Granular Flow '13*,
DOI 10.1007/978-3-319-10629-8_34

the measurement section. This prevents judging the stability of the empirical phase separation. Firstly, it is unclear whether phase separation remains for longer timescales. Secondly, we do not know whether the observed jam in the measurement section is the only jam in the experimental setup. The existence of additional jams would be an indication that jams might be forming and decaying dynamically.

2 Model Definition

The Stochastic Headway Dependent Velocity (SHDV) model is a space-continuous model with discrete time in one dimension. It therefore incorporates aspects of both continuous models such as the Generalized Centrifugal Force Model [4] or the Optimal Velocity Model [5, 6] and discrete models, e.g. cellular automata such as [7] or the Floor Field model [8]. Other models with discrete time and continuous space are discussed in [9] and [10]. The SHDV model also includes a variant of a slow-to-start rule used in vehicular traffic models [11–13].

Time is divided into discrete timesteps which can be identified with the reaction time of a pedestrian. This is equivalent to the time-discreteness in cellular automata models. The length of a timestep is $\Delta t = 0.3\,\mathrm{s}$. Each pedestrian is represented by an agent and moves through a continuous but finite one-dimensional space. Periodic boundary condition are used which correspond to the circular course in the experiments. All simulations are performed with a system length of 26 m equal to the length of the experimental setup.

The initial configuration for the simulations is very similar to that in the experiments and resembles an 'almost homogeneous' state. This is achieved via a two-step process: The agents are first distributed homogeneously. Then each agent's position is shifted slightly according to a Gauss distributed random variable. The Gauss distribution is cut off to prevent overlapping of agents.

For modeling purposes, the agents are assumed to be point-like. In each timestep the velocity is calculated as a function of the headway. Here we choose a piecewise linear form of the velocity function $v(h)$. A graphical representation is given in Fig. 1. The velocity function is characterized by five parameters $v_{\max}$, $v_{\min}$, d, d_c, and α. Only four of these are independent, e.g. d_c can be expressed in terms of the other parameters as

$$d_c = d + \frac{1}{\alpha}(v_{max} - v_{min})\,. \tag{1}$$

Each agent has a maximum velocity $v_{\max}$ and minimum velocity $v_{\min}$. An agent i is only allowed to move if its headway h_i exceeds a lower threshold $d = 0.4\,\mathrm{m}$. Note that this distance includes the space occupied by the pedestrian itself. We will later see that the model dynamics leads to a minimum distance $d_{\min}$ between agents that is a little bit smaller than d. Agents that have headways larger than the interaction

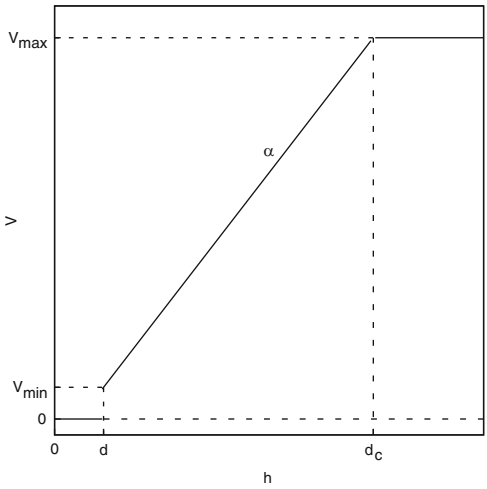

Fig. 1 Relation between headway and velocity used in the simulations

range d_c move interaction-free with maximum velocity. The final parameter that characterizes the velocity function is its slope α.

Additionally a slow-to-start rule is applied: with probability $p_0 = 0.5$ the velocity of an agent that did not move in the last timestep remains zero.

The following algorithm describes the update of the SHDV model: In each timestep, a parallel update of all agents is performed by executing the following steps in order:

1. First the headway h_i of each pedestrians i is calculated.
2. The velocity v_i of each agent i is calculated according to the velocity function $v(h_i)$ depicted in Fig. 1:

$$v_i = v(h_i), \qquad v(h) = \begin{cases} 0\ , h \leq d \\ \alpha(h-d) + v_{\min}\ , d < h < d_c \\ v_{\max}\ , h \geq d_c \end{cases} \tag{2}$$

3. If the agent did not move in the last timestep, its velocity remains zero with the stopping probability p_0 and with probability $1 - p_0$ it takes the value given by Eq. (2).
4. Each agent moves with velocity v_i determined in the previous step and its position changes by $\Delta x = v_i \cdot \Delta t$.
5. Time is advanced by Δt: $t \to t + \Delta t$.

The simulations in this contribution are performed with parameter values $d = 0.4\,\text{m}$, $v_{\max} = 1.2\frac{m}{s}$, $v_{\min} = 0.1\frac{m}{s}$, $\alpha = \frac{1}{2}s^{-1}$, $p_0 = 0.5$, and $\Delta t = 0.3\,\text{s}$, resulting in $d_c = 2.6\,\text{m}$.

Due to the discrete timestep, the actual minimum distance between agents can be smaller than the lower threshold d. Consider an agent i with a headway $h_i = d + \epsilon$

slightly larger than d following an agent $i+1$ that has a headway smaller than d. In the next timestep agent $i+1$ does not move whereas agent i moves with velocity $v_i = v(h_i)$. This results in a new headway that is smaller than d. In the limit $h_i \to d$ this is the minimum possible distance in the SHDV model and given by

$$d_{\min} \geq d + \epsilon - v(d+\epsilon) \cdot \Delta t \to d - v_{min} \cdot \Delta t = 0.37\,\text{m}. \tag{3}$$

The Stochastic Headway Dependent Velocity Model can – in contrast to typical continuous models – be implemented exactly as stated here without the need for approximations, e.g. discretization of time. This prevents the emergence of artifacts which depend on the implementation such as the details of the time discretization.

3 Results

3.1 Fundamental Diagram

To obtain the fundamental diagram of the stationary state we start the measurement after 100,000 s and average over the next 100 s. Figure 2 shows fundamental diagrams of the SHDV model as well as the fundamental diagram obtained from the experimental data. The global fundamental diagram is obtained by using the averaged velocity and the global density corresponding to the number N of pedestrians. For each N, 10 simulation runs have been performed. The local fundamental diagram uses local velocity and density values. For each timestep in

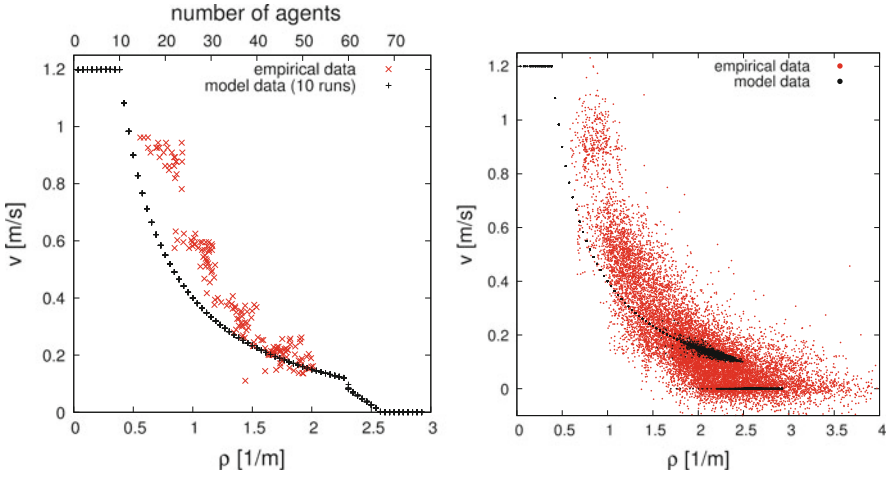

Fig. 2 Global (*left*) and local (*right*) fundamental diagrams of both simulation and experimental data

the simulation or for each frame of the experimental data, we get a data point for every pedestrian.

The fundamental diagram of the SHDV model features three distinct regimes. At low densities each agent moves interaction-free with a constant velocity equal to the maximum velocity. In this density regime the movement is completely deterministic with large headways that allow free flow.

At intermediate densities the fundamental diagram shows a $1/x$ curve. This can be directly explained by the model dynamics. The density is too large to allow free-flow of all agents, therefore interactions start to happen. In the stationary state the agents are spaced evenly within the simulation area. The density is then equal to the reciprocal of the headway, $\rho = \frac{1}{h}$. The velocity of each agent is proportional to its headway h and therefore proportional to $\frac{1}{\rho}$. The movement is deterministic and there are no standing agents.

At high densities there are two branches in the local fundamental diagram. Some agents have velocity $v = 0$ and some agents are moving slowly. The global fundamental diagram, on the other hand, shows an approximately linear decline due to the averaging of standing and moving agents. At higher densities the fraction of moving agents as well as the velocity of the moving agents decrease. This can be seen in more detail in the velocity distribution (Fig. 3). The gap in the fundamental diagram at the start of the linear decline stems from the beginning influence of the stopping probability. The size of the gap depends on the value of p_0. Stochasticity plays a role for the model dynamics at high densities, leading to a cloud of data points in the local fundamental diagram and to fluctuations in the global fundamental diagram.

The experimental fundamental diagram does not show these clearly distinct sections. This is expected due to measurement errors and the resulting scatter of the data points on the one hand and the lack of data for very large densities on the other.

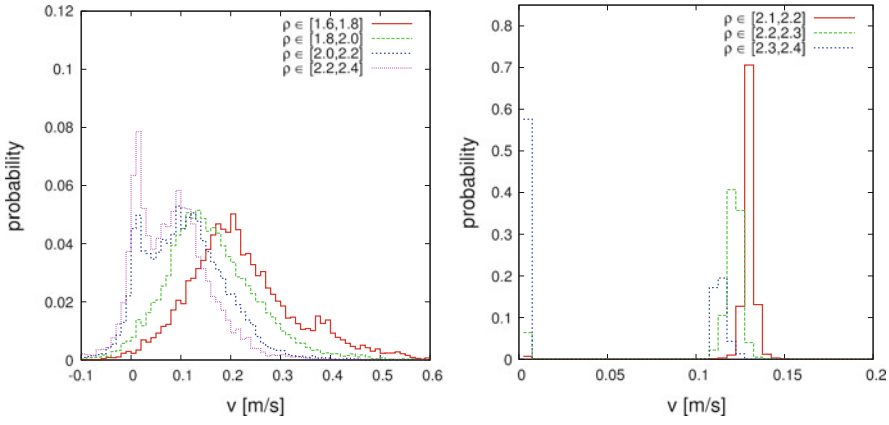

Fig. 3 Velocity distribution of the experiment (*left*) and of the model (*right*)

Note that the model is not designed to perfectly reproduce the fundamental diagram but to recreate the observed phase separation in single-file pedestrian flows at high densities. However, there is still a reasonable qualitative agreement between the experimental fundamental diagram and the fundamental diagram of the Stochastic Headway Dependent Velocity Model.

3.2 Velocity Distribution

The distribution of velocities based on the local density definition is shown in Fig. 3 for several density intervals. The size of each velocity bin is $0.005\ \frac{m}{s}$. Note that the density bins are different for the experimental and model data. This is necessary because the change from a completely jammed state (at very high density) to a state in which all agents move (at a smaller density) happens in a smaller density interval in the model than in the experiment. The differently sized density bins lead to sharper and more pronounced peaks in the model data compared to the broader experimental data. The difference is amplified by the intrinsic stochasticity of real pedestrians and the measurement process. For technical reasons, the experiment did not track the center of mass, but the head of each pedestrian. Therefore additional head movement (swaying) leads to a broadening of the measured velocity distribution. This also explains the negative velocities in the experimental data. A variation of the stopping probability p_0 to larger values increases the density range in which phase separation happens and thereby results in a broader model velocity distribution than shown here. It does however also lead to more unrealistic pedestrian behavior.

The general structure of the velocity distribution is however very similar. Both model and experimental data include two peaks at $v = 0$ and at $v = 0.1 - 0.15\ \frac{m}{s}$, respectively. The height of the first peak and thus the fraction of standing agents increases with increasing density. A higher local density means on average a smaller headway and thus a lower velocity. The position of the second peak therefore shifts to the left for higher densities.

3.3 Trajectories

A good agreement of fundamental diagram and velocity distribution with the empirical data does not ensure realistic dynamics on a microscopic scale. To achieve a deeper understanding of pedestrian behavior we consider individual trajectories. The model fundamental diagram as well as the velocity distribution show a coexistence of moving and standing agents at high densities. Whether the moving and standing agents are condensed in distinct phases or not can be analyzed by looking at the trajectories. A state with a lot of small jams and congested areas

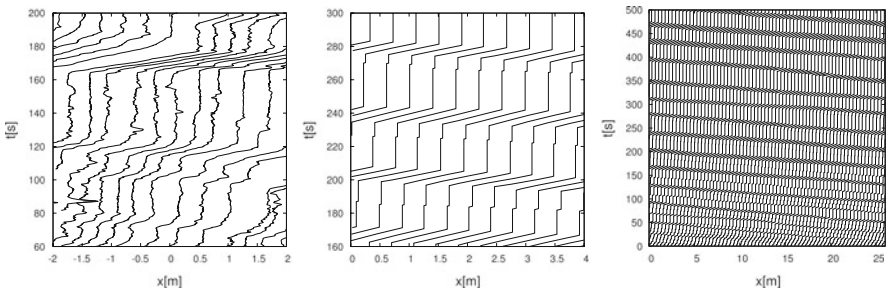

Fig. 4 Trajectories of the experiment (*left*), model trajectories zoomed in to an equivalent area (*middle*), and model trajectories of the whole simulation area

in the system and a state with only one big jam in the system may result in the same fundamental diagram and velocity distributions.

Both experimental and model data shown in Fig. 4 feature a separation into two distinct phases: a standing phase and a phase with slowly moving pedestrians. Small movements in the experimental trajectories come from head movements of the pedestrians. Note that the separation in two distinct phases in the model happens at a slightly lower density ($\rho = 2.5\,\mathrm{m}^{-1}$) than in the experiment ($\rho = 2.7\,\mathrm{m}^{-1}$).

The model trajectories are shown at a later time because it takes a short time for the phase separation to form, see the global trajectories in Fig. 4. In the first 50–100 s the system organizes into a phase separated state. At each point in time after that there is only one jammed phase and one moving phase in the system.

The details of the phase separation depend on the density. The size of the standing phase increases with increasing density: both the fraction of standing agents and the number of timesteps they remain standing increases. The velocity in the slow-moving phase decreases a little bit with increasing density. There is only a relatively small density interval in which phase separation occurs. The movement is homogeneous for smaller densities and the system comes to a complete standstill at larger densities. The phase separated state is unchanged even after long simulation times over 100,000 s.

Conclusions and Outlook

The trajectories of single-file pedestrian movement at high densities develop into a phase-separated state with coexisting jammed and slowly-moving phases. To understand the emergence of this kind of phase separation, we propose the Stochastic Headway Dependent Velocity Model. Starting from an 'almost homogeneous' initial condition the model develops a single jam in the simulated system as well as a region of congested pedestrians. This leads to a good qualitative agreement with current experimental data for

(continued)

the fundamental diagram, the velocity distribution, and the trajectories. The behavioral change from free-flow to phase separation with standing agents happens within a smaller density range than in the experiment.

The fundamental diagram and velocity distribution alone do not explain how the moving and standing agents are distributed in the system. Instead a detailed analysis of individual trajectories is necessary. This can be done in a more quantitative way by defining an order parameter similar to [14]. A detailed definition and discussion can be found in [15]. The order parameter describes the inhomogeneity of the system and distinguishes between states with one large jam in the system on the one hand and states with two or more distinct jams or a random mix of standing and moving agents on the other, thereby identifying phase separation.

In upcoming work we plan to implement and analyze several modifications of the model in order to identify which aspects of the model are required for the development of pedestrian phase separation.

Acknowledgements We thank the Deutsche Forschungsgemeinschaft (DFG) for support under the grant "Scha 636/9-1".

References

1. A. Seyfried, A. Portz, A. Schadschneider, Phase coexistence in congested states of pedestrian dynamics. Lect. Notes Comput. Sci. **6350**, 496–505 (2010)
2. M. Boltes, A. Seyfried, B. Steffen, A. Schadschneider, Using stereo recordings to extract pedestrian trajectories automatically in space, in *Pedestrian and Evacuation Dynamics*, ed. by R.D. Peacock, E.D. Kuligowski, J.D. Averill, (Springer, New York, 2010), pp. 751–754
3. A. Schadschneider, D. Chowdhury, K. Nishinari, *Stochastic Transport in Complex Systems. From Molecules to Vehicles* (Elsevier Science, Amsterdam/Oxford, 2010)
4. M. Chraibi, A. Seyfried, A. Schadschneider, The generalized centrifugal force model for pedestrian dynamics. Phys. Rev. E **82**, 046111 (2010)
5. M. Bando, K. Hasebe, A. Nakayama, A. Shibata, Y. Sugiyama, Structure stability of congestion in traffic dynamics. Jpn. J. Indust. Appl. Math. **11**, 203–223 (1994)
6. M. Bando, K. Hasebe, A. Nakayama, A. Shibata, Y. Sugiyama, Dynamical model of traffic congestion and numerical simulation. Phys. Rev. E **51**, 1035–1042 (1995)
7. V.J. Blue, J.L. Adler, Cellular automata microsimulation for modeling bidirectional pedestrian walkways. Transp. Res. B **35**, 293–312 (2001)
8. C. Burstedde, K. Klauck, A. Schadschneider, J. Zittartz, Simulation of pedestrian dynamics using a two-dimensional cellular automaton. Physica A **295**, 507–525 (2001)
9. Z. Fang, W. Song, X. Liu, W. Lv, J. Ma, X. Xiao, A continuous distance model (CDM) for the single-file pedestrian movement considering step frequency and length. Physica A **391**, 307–316 (2012)
10. S. Tadaki, M. Kikuchi, Y. Sugiyama, S. Yukawa, Noise induced congested traffic flow in coupled map optimal velocity model. J. Phys. Soc. Jpn. **68**, 3110–3114 (1999)
11. K. Nagel and M. Schreckenberg: *A cellular automaton model for freeway traffic*. J. Phys. I France **2**, 2221–2229 (1992)

12. S.C. Benjamin, N.F. Johnson, P.M. Hui, Cellular automata models of traffic flow along a highway containing a junction. J. Phys. A **29**, 3119 (1996)
13. M. Takayasu, H. Takayasu, 1/f noise in a traffic model. Fractals **1**, 860–866 (1993)
14. Y. Ikura, E. Heisler, A. Awazu, H. Nishimori, S. Nakata, Collective motion of symmetric camphor papers in an annular water channel. Phys. Rev. E **88**, 012911 (2013)
15. C. Eilhardt, Computer simulation of pedestrian dynamics at high densities. Ph.D. thesis, Universität zu Köln, 2014. To be published

Simulation of Merging Pedestrian Streams at T-Junctions: Comparison of Density Definitions

Matthias Craesmeyer and Andreas Schadschneider

Abstract We study merging pedestrian streams at T-junctions using the Floor Field Cellular Automata Model. The discreteness of the underlying lattice of the cellular automaton model limits the resolution of the predicted densities. We therefore compare different methods for the determination of the density. In particular we consider a discrete version of the Voronoi method which allows to define individual densities for each pedestrian.

1 Introduction

The increasing number of mass events and planning of public buildings require complex evacuation strategies. Escape routes should be optimized for pedestrian traffic and (ideally) be dynamically adjusted in real-time. In the near future, new techniques will allow us to track people by cameras and calculate optimal evacuation strategies from this data based on computer simulations.

The models used for the planning of mass events or evacuation strategies for public buildings have to be validated and calibrated. There are different approaches to model pedestrian dynamics. Here we will use the Floor Field Model (FFM) [1, 2] which is arguably the most popular cellular automaton (CA) approach to pedestrian dynamics. Our focus is on a generic structure which appears in almost all evacuation scenarios, namely T-junctions. Despite its importance there are only few works dealing with this scenario [3–6]. From a theoretical point of view T-junctions are relevant since this is one of the simplest scenarios where several pedestrian streams merge.

2 Floor Field Model

The floor field model (FFM) is a cellular automaton model for pedestrian dynamics and has been introduced in [1, 2]. The space is divided into cells of size (40 cm) × (40 cm) where each cell can be occupied by at most one pedestrian.

M. Craesmeyer (✉) • A. Schadschneider
Institut für Theoretische Physik, Universität zu Köln, 50937 Köln, Germany
e-mail: mc@thp.uni-koeln.de; as@thp.uni-koeln.de

M. Chraibi et al. (eds.), *Traffic and Granular Flow '13*,
DOI 10.1007/978-3-319-10629-8_35

The motion of each pedestrian is determined by simple stochastic rules which take into account the interactions with other pedestrians and the infrastructure. This is encoded in two fields, the static and the dynamic floor field S_{ij} and D_{ij}, respectively, which determine the transition probabilities to one of the nearest neighbour cells (i, j):

$$p_{ij} = N \cdot \exp(k_s \cdot S_{ij}) \cdot \exp(k_d \cdot D_{ij}) \cdot (1 - n_{ij}) \cdot \xi_{ij} \,. \tag{1}$$

Here n_{ij} is the occupation number of the target cell, ξ a wall factor which is 0 for inaccessible cells (e.g. walls) and 1 otherwise, and N normalisation constant. k_s and k_d are coupling constants to the two floor fields. The static floor field S_{ij} is usually determined by the distance of the cell (i, j) to the exit. The dynamic floor field D_{ij} is created by moving pedestrian and has its own dynamics (diffusion and decay). It encodes the tendency of pedestrians to follow moving persons. In addition to the above parameters the transition probability depends on a friction parameter μ which decides whether it comes to a transition in the event of a conflict [2].

For the T-junction scenario we have to specify the sites where pedestrian enter the junction. These entry cells are occupied with a certain probability α in each time step. At the exit cells pedestrians are removed from the system with probability β (Fig. 1).

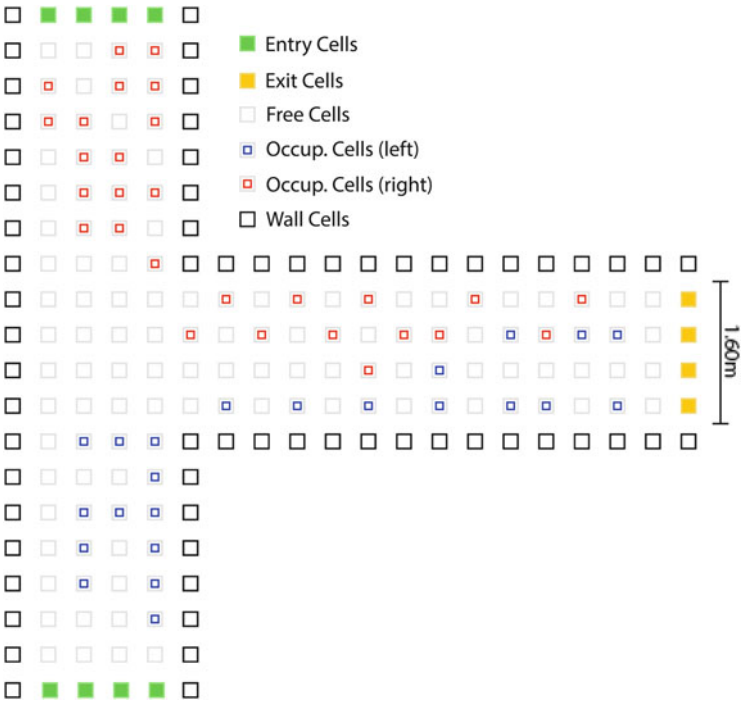

Fig. 1 Space discretisaton of the T-junction as used for the simulations with the FFM. The *color code* indicates the entry and exit cells and walls

3 Density Definitions in CA Models

There are several density definitions that have been used for pedestrian systems, but all of them have certain limitations. For a more complete discussion, see [7,8]. Here we discuss and compare density definitions specifically in CA models where the discreteness of space leads to additional problems.

3.1 Standard Method

The simplest method to determine the density $\rho(\mathbf{r})$ uses the number of persons in $N(A)$ a predefined area A, i.e.

$$\rho(\mathbf{r}, t) = \frac{N(A)}{A}. \tag{2}$$

This density is usually assigned to the position $\mathbf{r}$ in the center of the area. In CA models this definition is based on a neighbourhood of a cell. In the simplest case the area consist of just one cell. Then, at any time, only two densities are possible (0 or 1). The standard choice is therefore based on the Moore neighbourhood of the center cell. For a square lattice it consists of 9 cells. The density is then quantized in multiples of $1/9$, i.e. $\rho(\mathbf{r}) = n/9$ with $n = 0, 1, \ldots, 9$. Additional problems arise for cells near walls as illustrated in Fig. 2. Therefore the main disadvantages of the standard method are the low resolution and the tendency to artefacts due to the edge effects (Fig. 3).

3.2 Voronoi Method

The Voronoi method introduced in [8] has been shown to have several advantages over the standard method. Here we adopt it for CA models. First, Voronoi cells for all pedestrians are determined. Then the density is calculated from the surface area

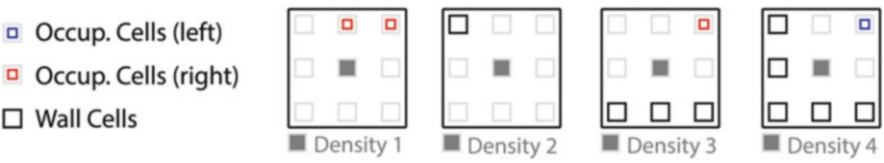

Fig. 2 The density definition based on the Moore neighbourhood leads to a quantization of the density values. The density for the center cell in the four examples is $\rho_1 = 2/9$, $\rho_2 = 1/8$, $\rho_3 = 1/6$ and $\rho_4 = 1/4$, respectively

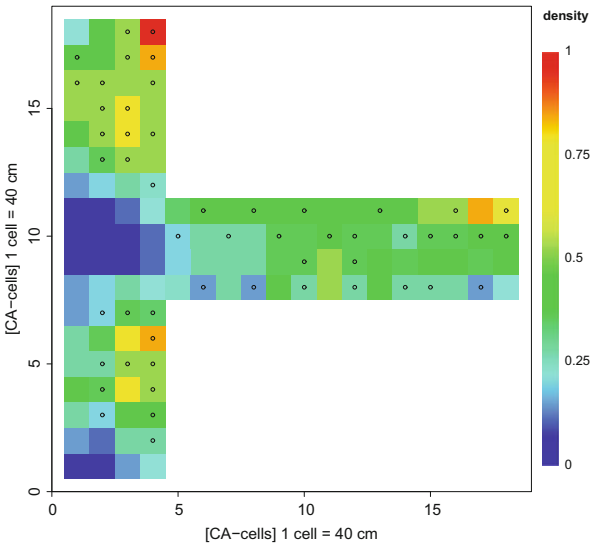

Fig. 3 Density for the configuration shown in Fig. 1 as determined by standard method

A_j of the Voronoi cell of pedestrian j. The density of the area covered by Voronoi cell j is given by

$$\rho_j = \frac{1}{A_j} . \tag{3}$$

The Voronoi method can be implemented in different ways.

3.2.1 Exact Method

First cells are determined by the algorithm of Fortune [9]. The algorithm receives the coordinates of the occupied positions as input. The output is a list of edges which are assigned to the occupied positions in CA. Because the algorithm does not consider margins, the obtained edges are generally not finite. Therefore infinite edges have to be pruned to borders. After this procedure it is possible to extract closed cells provided that the border is a convex polygon. In the case of a T-junction, the boundary is not convex which means that there is no general algorithmic solution to close the cells. A possible solution is the restriction to convex subregions. Nevertheless the algorithm we developed works fine for most cases. Limitations occur in cases of small densities. If the cells have been correctly determined, the areas of each cell (irregular polygons) can be calculated by triangulation. Because the exact determination (Fig. 4) does not work for all situations we tested another approach where the cells are determined approximately on a refined grid (Fig. 5).

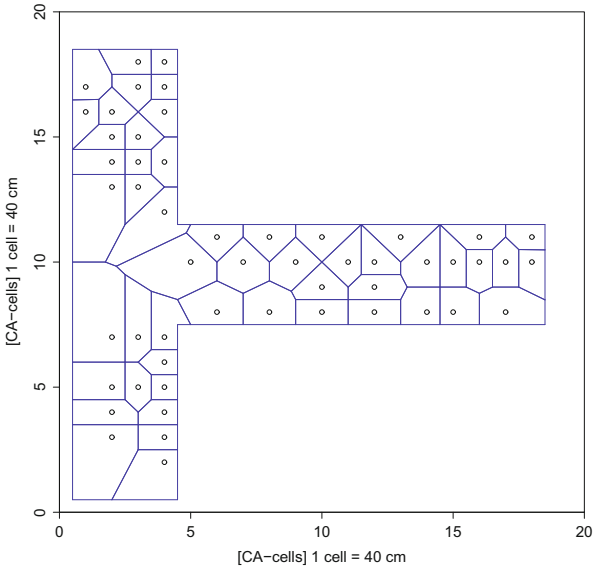

Fig. 4 Exact Voronoi decomposition of the configuration shown in Fig. 1

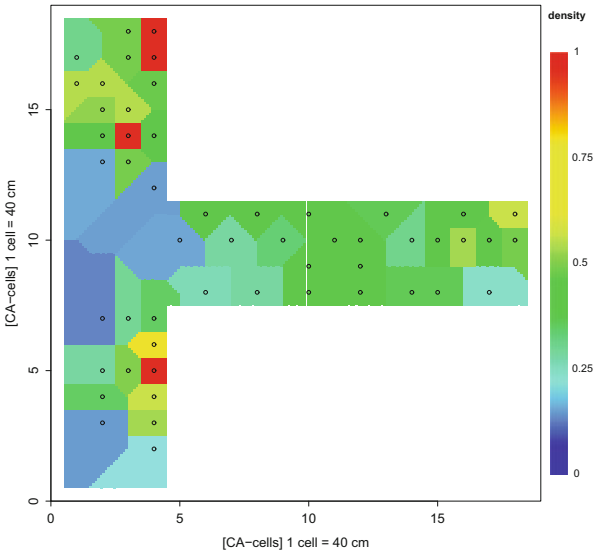

Fig. 5 Density for the configuration in Fig. 1 calculated by approximate Voronoi method

3.2.2 Approximate Method (Flood Fill Algorithm)

In the first step, the resolution is refined by a factor of 10 by dividing each cell of the FFM into 10×10 subcells. In the flood fill algorithm, occupied cells propagate on the refined grid to their Moore neighbourhood. The propagation ends at walls or when propagation fronts from different occupied cells meet. The disadvantage of this method is the ambiguity at the cell boundaries. When two growing regions

spread simultaneously to a cell, there will be a conflict which leads to ambiguities. The conflict can be resolved by choosing the dominant region in the Moore neighbourhood. As can be seen in Fig. 5, only angles of 0°, 45°, 90° between the regions are possible. This effect leads to deviations from the exact determination, particularly at low densities.

3.3 Comparison

In the comparison of the methods one should take into account the meaning of density in pedestrian dynamics. It provides information on the available space and thus the mobility of the individuals. In the standard method the density is a local measure for the mobility since it is determined only by the Moore neighborhood of a cell. Information about the mobility beyond this neighbourhood is not considered. In contrast, in the Voronoi method the area which determines the density is dynamic and depends on the distribution of occupied positions. In this sense, the Voronoi method takes into account global information. To compare the methods, the average deviation over all positions is determined. These average deviations are considered as a function of the global density which is defined here as the fraction of occupied cells of the CA model.

The comparison of the two methods is shown in Figs. 6 and 7. It is noticeable that the absolute difference is especially large for medium global densities. For high densities, square Voronoi cells arise and consequently small deviations from the standard method appear. For small densities, absolute deviations are small, but the relative deviations with respect to the global density are rather large, as can be seen in Fig. 7. On the other hand, there is no big difference between the relative deviations with respect to the global and the average Voronoi.

The extension of the Voronoi cells and their associated densities provide information about the number of time steps a pedestrian can move without conflict.

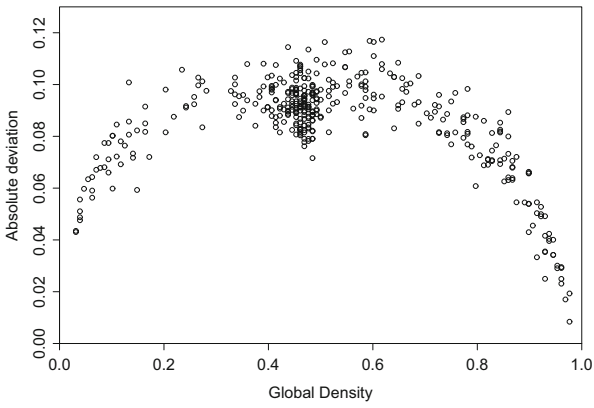

Fig. 6 Absolute deviation: Standard and Voronoi method

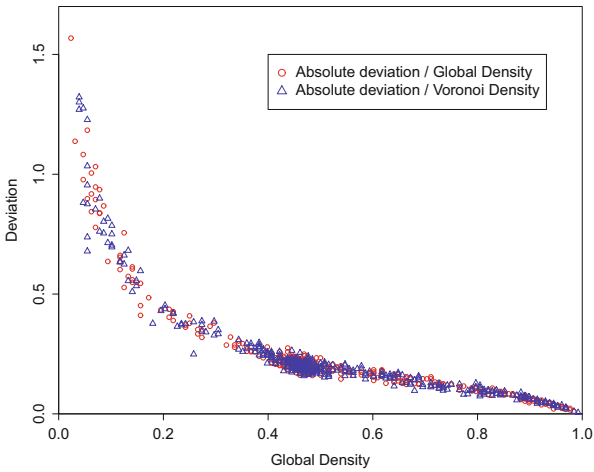

Fig. 7 Relative deviation: Standard and Voronoi method

This gives a very good representation of the mobility. Furthermore it is possible to achieve a more accurate classification by the refinement. For these reasons, the Voronoi method is preferred.

4 Results and Outlook

Like in any other model, quantities in CAs should be introduced in a way which allows good comparability with data from experiments. The Voronoi method can be applied to data from CAs, as well as to data from experiments in a very similar manner. Quantization effects, which arise from the discreteness of the CAs, do not play a major role here. However, some technical problems in the determination of the Voronoi decomposition for general (non-convex) geometries remain open for the time being. In such cases. the flood fill algorithm was shown to provide good approximate results.

Acknowledgements We thank the Deutsche Forschungsgemeinschaft (DFG) for support under the grant“Scha 636/9-1”.

References

1. C. Burstedde, K. Klauck, A. Schadschneider, J. Zittartz, Simulation of pedestrian dynamics using a two-dimensional cellular automaton. Physica A **295**, 507 (2001)
2. A. Kirchner, K. Nishinari, A. Schadschneider, Friction effects and clogging in a cellular automaton model for pedestrian dynamics. Phys. Rev. E **67**, 056122 (2003)

3. J. Zhang, W.W.F. Klingsch, A. Schadschneider, A. Seyfried, Transitions in pedestrian fundamental diagrams of straight corridors and T-junctions. J. Stat. Mech. P06004 (2011)
4. J. Zhang, W.W.F. Klingsch, A. Schadschneider, A. Seyfried, Experimental study of pedestrian flow through a T-junction. in *Traffic Granular Flow'11* (Springer, Berlin/Heidelberg, 2013), p. 241
5. Y.-C. Peng, C.-I. Chou, Simulation of pedestrian flow through a "T" intersection: a multi-floor field cellular automata approach. Comput. Phys. Commun. **182**, 205 (2011)
6. Y. Tajima, T. Nagatani, Clogging transition of pedestrian flow in T-shaped channel. Physica A **303**, 239 (2002)
7. A. Schadschneider, W. Klingsch, H. Klüpfel, T. Kretz, C. Rogsch, A. Seyfried, Evacuation dynamics: empirical results, modeling and applications, in *Encyclopedia of Complexity and System Science*, ed. by R.A. Meyers (Springer, New York/London, 2009), p. 3142
8. B. Steffen, A. Seyfried, Methods for measuring pedestrian density, flow, speed and direction with minimal scatter. Physica A **389**, 1902 (2010)
9. S. Fortune, A sweepline algorithm for Voronoi diagrams, in *Proceedings of 2nd Annual Symposium on Computational Geometry*, Yorktown Heights, 1986, p. 313

Exclusive Queueing Process: The Dynamics of Waiting in Line

Chikashi Arita and Andreas Schadschneider

Abstract The dynamics of pedestrian crowds has been studied intensively in recent years, both theoretically and empirically. However, in many situations pedestrian crowds are rather static, e.g. due to jamming near bottlenecks or queueing at ticket counters or supermarket checkouts. Classically such queues are often described by a M/M/1 queue which neglects the internal structure (density profile) of the queue by focussing on the queue length as the only dynamical variable. This is different in the exclusive queueing process (EQP) in which we consider the queue on a microscopic level. It is equivalent to a totally asymmetric exclusion process (TASEP) of varying length. The EQP has a surprisingly rich phase diagram with respect to the arrival probability α and the service probability β. The behavior on the phase transition line is much more complex than for the TASEP with a fixed system length. It is nonuniversal and depends strongly on the update procedure used.

1 Introduction

Queueing processes have been studied extensively [1, 2]. Although originally developed to describe problems of telecommunication, they have been applied later also to various kinds of jamming phenomena, e.g. supply chains [3] and vehicular traffic [4, 5]. However, classical queueing theory neglects the spatial structure of queues and the particles in the queues do not interact with each other. The length L_t of the queue is the only dynamical variable and the density along the queue is constant. Therefore an extension of the classical M/M/1 queueing process has been introduced recently [6, 7]. It takes into account particle interactions through the excluded-volume effect and leads to nontrivial density profiles of the queue.

C. Arita (✉)
Theoretische Physik, Universität des Saarlandes, 66041 Saarbrücken, Germany
e-mail: c.arita@physik.uni-saarland.de

A. Schadschneider
Institut für Theoretische Physik, Universität zu Köln, 50937 Köln, Germany
e-mail: as@thp.uni-koeln.de

M. Chraibi et al. (eds.), *Traffic and Granular Flow '13*,
DOI 10.1007/978-3-319-10629-8_36

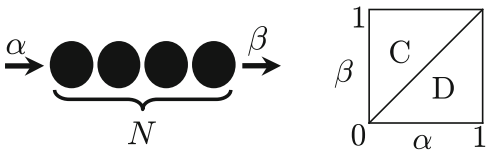

Fig. 1 Definition of M/M/1 queue (*left*) and its phase diagram (*right*). When the arrival probability α is larger than service probability β, the queue diverges (D). It converges when $\alpha < \beta$ (C)

2 M/M/1 Queue

The M/M/1 queueing process describes the dynamics of a single queue with Markovian arrival and service processes. It is defined by the arrival probability α and service probability β [1, 2]. Customers (= particles) arrive with probability α at the end of the queue and are serviced (= removed) with probability β at the front of the queue (Fig. 1).

The M/M/1 queue has two phases separated by the *critical line* $\alpha = \beta$: for $\alpha > \beta$ the average length $\langle L_t \rangle$ of the queue (at time t) diverges, i.e. $\lim_{t\to\infty}\langle L_t \rangle = \infty$, whereas for $\alpha < \beta$ it converges: $\lim_{t\to\infty}\langle L_t \rangle = L_\infty < \infty$ (Fig. 1). In the M/M/1 queueing process, the internal structure of the queue is not considered, i.e. the queue has density 1 everywhere and the number of particles N_t is equal to the length L_t.

3 Exclusive Queueing Process (EQP)

The EQP is defined on a semi-infinite chain where sites are labeled by natural numbers from right to left (Fig. 2). The dynamics of the model is defined as follows:

(i) *Input:* a particle is inserted with probability α on the site just behind the last particle in the queue,
(ii) *Hopping:* particles behind an empty site move forward with probability p
(iii) *Output:* a particle at site 1 is serviced with probability β.

For parallel update these rules are applied simultaneously to all sites. In the case of backward-sequential update, first (i) and (iii) are carried out. Then (ii) is applied sequentially to all sites starting at site $j = 1$. The dynamics of the particle hopping we use is of the totally asymmetric simple exclusion process (TASEP) [8–12]. The TASEP with input and output of particles has been intensively studied, in particular from statistical-physics point of view. However, the TASEP is usually defined on a chain of fixed length with input and output at the fixed ends. Therefore the EQP can be interpreted as a TASEP of variable length.

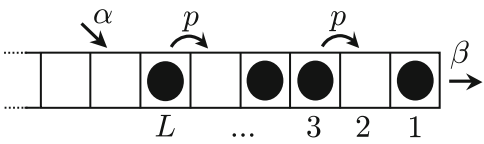

Fig. 2 Definition of the Exclusive Queueing Process (EQP). The length L is defined by the position of the last (*leftmost*) particle

4 Phase Diagram of EQP

The known exact solutions for the stationary state of the TASEP with a fixed system length [13, 14] can be generalized to the EQP [6, 15]. Exact stationary states for parallel and continuous-time updates of the EQP have been found in matrix product forms. In the case of parallel dynamics, an exact time-dependent solution is also known for deterministic hopping $p = 1$ in the bulk [16].

By changing the input and output probabilities α and β the EQP shows boundary-induced phase transitions. The phases are classified according to different criteria:

- *Queueing classification:* convergent (C) or divergent (D) queue length.
  In the divergent case the length behaves as $\langle L_t \rangle = V \cdot t + o(t)$, whereas $\langle L_t \rangle \to L_\infty$ in the convergent phase.
- *TASEP classification:* maximal current (MC) or high-density (HD).
  In the maximal current phase, the current J_{out} of particles going through the right end is independent of both α and β. In the high-density phase the current depends only on β, but is independent of α [17].
- *Classification according to density profile:* The divergent phase can be divided into subphases according to the number of plateaus in the density profile [18]. The rescaled profile has the form of a rarefaction wave [19]. It is cut-off at some point of the general profile shown in Fig. 3 which depends on the values of the parameters α and β. The velocity V of the growth of the system length has up to three different forms, which are denoted by I, II and III in Fig. 3.

The convergent and divergent phases are separated by a critical line whose precise location depends on the update type. For all updates, the critical line consists of a curve connecting $(\alpha, \beta) = (0, 0)$ and $(\alpha, \beta) = (\alpha_c, \beta_c)$ and a straight line $\alpha = \alpha_c$ and $\beta > \beta_c$ with critical values

$$\alpha_c = \begin{cases} (1 - \sqrt{1-p})/2 & \text{(parallel)}, \\ (1 - \sqrt{1-p})^2/p & \text{(backward)}, \end{cases} \qquad \beta_c = 1 - \sqrt{1-p}\,. \tag{1}$$

For the parallel update and the continuous-time case, the critical line can be obtained exactly by evaluating the normalization of the exact stationary state [6, 15].

The phase diagram is found to be dependent on the update rule. In the parallel update case we find seven subphases (Fig. 3). For backward-sequential dynamics one has to distinguish the cases $p < 1/2$ and $p > 1/2$. The latter shows the same seven phases as the parallel update, but the two III-phases vanish for $p < 1/2$ (Fig. 3).

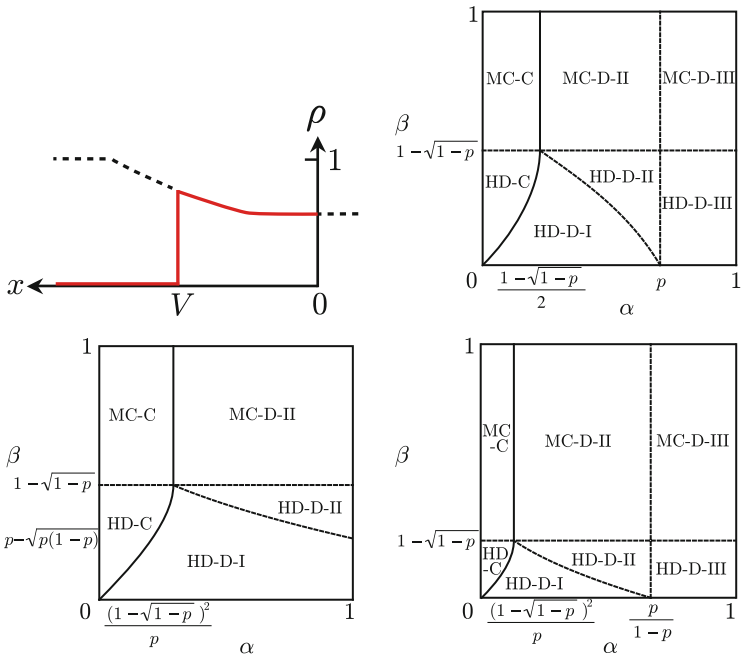

Fig. 3 A schematic picture for the density profile in the divergent phase (*top-left*), where x is the rescaled position j/t, and the phase diagrams of the EQP with parallel (*top-right*) and backward-sequential dynamics for $p < 1/2$ (*bottom-left*) and $p > 1/2$ (*bottom-right*). According to the injection probability (rate) α, the rarefaction wave is "cut" by the leftmost customer ($x = V$) and the server ($x = 0$). The end of the queue can be in three different regimes, (plateau at density $\rho < 1$, regime of increasing density or plateau at density $\rho = 1$), which defines the regions I, II, III., respectively. The density profile shown here belongs to II

5 Critical Line: Non-universal Behavior

In the divergent phase the average length $\langle L_t \rangle$ and the average number of particles $\langle N_t \rangle$ diverge linearly in time. On the phase transition line separating the convergent and divergent phases the growth is slower than linear, i.e.

$$\langle X_t \rangle = O(t^{\gamma_X}) \qquad (X = L, N), \tag{2}$$

where the critical exponents γ_X are smaller than 1.

Figure 4 shows the time-dependence of the average system length obtained by Monte Carlo simulations. As one can observe in these log-log plots, the slopes depend both on the update type and the location on the critical line (curved part

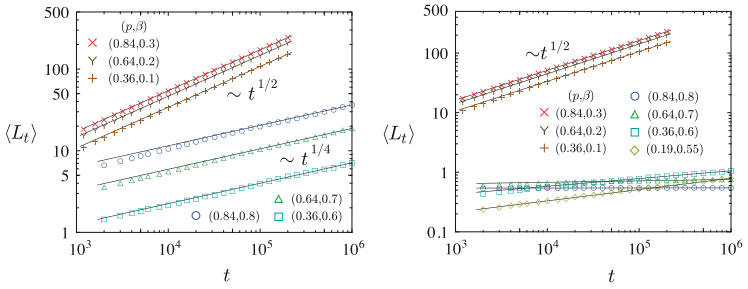

Fig. 4 Time-dependence of average system length $\langle L(t) \rangle$ for parallel dynamics (*left*) and backward dynamics (*right*)

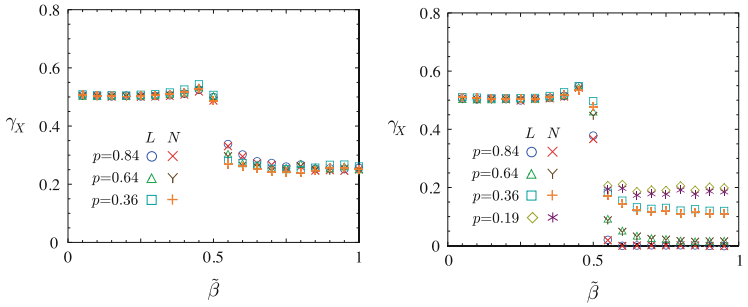

Fig. 5 Exponents γ_X for parallel dynamics (*left*) and backward dynamics (*right*). β has been rescaled so that $\tilde{\beta} = 0, 1/2, 1$ corresponds to $\beta = 0, \beta_c, 1$, respectively

$\beta < \beta_c$ or straight part $\beta > \beta_c$). Figure 5 also provides simulation results of the exponents. Depending on the update rule, the exponents have different values:

$$\text{parallel:} \qquad \gamma_X = \begin{cases} 1/2 & (\text{for } \beta < \beta_c) \\ 1/4 & (\text{for } \beta > \beta_c) \end{cases} \tag{3}$$

$$\text{backward:} \qquad \gamma_X = \begin{cases} 1/2 & (\text{for } \beta < \beta_c), \\ f(p) & (\text{for } \beta > \beta_c, p < p_c) \\ 0 & (\text{for } \beta > \beta_c, p > p_c) \end{cases} \tag{4}$$

with some function $f(p) \in (0, 1/4)$, whose explicit form is not known. The nonuniversal behavior (4) and the existence of the critical point p_c for the backward case has been tested by simulations, see [20] for detailed discussions.

6 Discussion

The exclusive queueing process (EQP) can be considered as a minimal model of pedestrian queues which takes into account the internal dynamics of the queue. We have found that the EQP has a rich phase diagram. Surprisingly, it shows a strong dependence of its critical properties on the update scheme. This is rather different from the TASEP with a fixed system length. The order of the phase transition between the diverging and converging phases can also be different.

Besides application to pedestrian queues, variants of the EQP might have interesting applications to biological processes. Similar models of varying system length have already been studied e.g. in [21–25]. We expect that transport models with varying system lengths will show many other interesting phenomena.

Acknowledgements AS is supported by Deutsche Forschungsgemeinschaft (DFG) under grant "Scha 636/8-1".

References

1. J. Medhi, *Stochastic Models in Queueing Theory* (Academic, San Diego, 2003)
2. T.L. Saaty, *Elements of Queueing Theory With Applications* (Dover, New York, 1961)
3. W.J. Hopp, M.L. Spearman, *Factory Physics* (McGraw-Hill, Boston, 2008)
4. D. Heidemann, Transp. Sci. **35**, 405 (2001)
5. F.C. Caceres, P.A. Ferrari, E. Pechersky, J. Stat. Mech. P07008 (2007)
6. C. Arita, Phys. Rev. E **80**, 051119 (2009)
7. D. Yanagisawa, A. Tomoeda, R. Jiang, K. Nishinari, JSIAM Lett. **2**, 61 (2010)
8. B. Derrida, J. Stat. Mech. P07023 (2007)
9. G.M. Schütz, in *Phase Transitions and Critical Phenomena*, ed. by C. Domb, J.L. Lebowitz, vol. 19 (Academic, San Diego, 2001)
10. R.A. Blythe, M.R. Evans, J. Phys. A: Math. Gen. **40**, R333 (2007)
11. T.M. Liggett, *Stochastic Interacting Systems: Contact, Voter and Exclusion Processes* (Springer, New York, 1999)
12. A. Schadschneider, D. Chowdhury, K. Nishinari, *Stochastic Transport in Complex Systems: From Molecules to Vehicles* (Elsevier Science, Amsterdam, 2010)
13. B. Derrida, M.R. Evans, V. Hakim, V. Pasquier, J. Phys. A **26**, 1493 (1993)
14. M.R. Evans, N. Rajewsky, E.R. Speer, J. Stat. Phys. **95**, 45–96 (1999)
15. C. Arita, D. Yanagisawa, J. Stat. Phys. **141**, 829 (2010)
16. C. Arita, A. Schadschneider, Phys. Rev. E **84**, 051127 (2011)
17. C. Arita, A. Schadschneider, Phys. Rev. E **83**, 051128 (2011)
18. C. Arita, A. Schadschneider, J. Stat. Mech. P12004 (2012)
19. P.L. Krapivsky, S. Redner, E. Ben-Naim, *A Kinetic View of Statistical Physics* (Cambridge University Press, Cambridge, 2010)
20. C. Arita, A. Schadschneider, EPL **104**, 30004 (2013)
21. K. Sugden, M.R. Evans, W.C.K. Poon, N.D. Read, Phys. Rev. E **75**, 031909 (2007)
22. S. Dorosz, S. Mukherjee, T. Platini, Phys. Rev. E **81**, 042101 (2010)
23. D. Johan, C. Erlenkämper, K. Kruse, Phys. Rev. Lett. **108**, 258103 (2012)
24. A. Melbinger, L. Reese, E. Frey, Phys. Rev. Lett. **108**, 258104 (2012)
25. M. Schmitt, H. Stark, EPL **96**, 28001 (2011)

Air Traffic, Boarding and Scaling Exponents

Reinhard Mahnke, Jevgenijs Kaupužs, and Martins Brics

Abstract The air traffic is a very important part of the global transportation network. In distinction from vehicular traffic, the boarding of an airplane is a significant part of the whole transportation process. Here we study an airplane boarding model, introduced in 2012 by Frette and Hemmer, with the aim to determine precisely the asymptotic power–law scaling behavior of the mean boarding time $\langle t_b \rangle$ and other related quantities for large number of passengers N. Our analysis is based on an exact enumeration for small system sizes $N \leq 14$ and Monte Carlo simulation data for very large system sizes up to $N = 2^{16} = 65{,}536$. It shows that the asymptotic power–law scaling $\langle t_b \rangle \propto N^{\alpha}$ holds with the exponent $\alpha = 1/2$ ($\alpha = 0.5001 \pm 0.0001$). We have estimated also other exponents: $\nu = 1/2$ for the mean number of passengers taking seats simultaneously in one time step, $\beta = 1$ for the second moment of $\langle t_b \rangle$ and $\gamma \approx 1/3$ for its variance. We have found also the correction–to–scaling exponent $\theta \approx 1/3$ and have verified that a scaling relation $\gamma = 1 - 2\theta$, following from some analytical arguments, holds with a high numerical accuracy.

1 Introduction

Recently, following the paper of Frette and Hemmer [1] there has been a spurt of activity regarding airplane boarding, resulting in five papers in Phys. Rev. E [1–5] in roughly 16 months. In the model considered by Frette and Hemmer [1], N passengers have reserved seats, but enter the airplane in arbitrary order ($N!$ possibilities). A simplified situation is considered with a single isle of rows and only one seat in each row. It is assumed that a passenger occupies a place equal

R. Mahnke (✉) • M. Brics
Institute of Physics, Rostock University, D–18051 Rostock, Germany
e-mail: reinhard.mahnke@uni-rostock.de; martins.brics2@uni-rostock.de

J. Kaupužs
Institute of Mathematical Sciences and Information Technologies, University of Liepaja, Liepaja LV–3401, Latvia

Institute of Mathematics and Computer Science, University of Latvia, LV–1459 Riga, Latvia
e-mail: kaupuzs@latnet.lv

M. Chraibi et al. (eds.), *Traffic and Granular Flow '13*,
DOI 10.1007/978-3-319-10629-8_37

to the distance between rows. In addition, he or she requires one time step to place carry-on luggage and get seated, the time for walking along the isle being neglected. However, a passenger must wait for a possibility to move forwards to his or her seat if the motion is blocked by other passengers staying or taking seats in front of him or her (see [1] for more details and examples). The number of seats is equal to the number of passengers in this model. In [4], the same process has been considered with more than one seat per row. It has been also discussed there what happens if only some fraction p of the passengers occupy the seats. In a series of works [1,2,4], a non-random ordering of passengers has been also considered. One of the basic quantities of interest is the boarding time t_b of an airplane. All these papers deal with a numerical estimation of the mean boarding time $\langle t_b \rangle$, stating that it is more ore less well consistent with the power law $\langle t_b \rangle = cN^{\alpha}$. Estimates $\alpha = 0.69 \pm 0.01$ and $c = 0.95 \pm 0.02$ have been obtained in [1] from the data with a small number of passengers, $2 < N < 16$.

Later on, it has risen an interesting discussion [2–4] about the value of the exponent α, describing the asymptotic power law at $N \to \infty$. It has been found that the numerical estimates converge to a remarkably different from 0.69 value $\alpha = 1/2$ for large N. In particular, $\alpha = 0.5001 \pm 0.0001$ has been found in [3] from the Monte Carlo simulation data up to $N = 2^{16}$. In fact, $\alpha = 1/2$ is exactly the analytical value reported earlier in [6]. As explained in [4], the $\propto N^{1/2}$ asymptotic behavior follows from the mathematical theorem reported already in [7, 8]. In [6], the proportionality coefficient $c = 4 - 2\ln 2$ has been also found. Corrections to scaling have been considered in [3], as well as in [6]. Numerical estimation in [3] suggests that correction–to–scaling exponent θ in $\langle t_b \rangle = cN^{\alpha}\left(1 + \mathcal{O}\left(N^{-\theta}\right)\right)$ is approximately $1/3$. It has been also numerically found there that the variance of t_b scales with a similar exponent $\gamma \approx 1/3$. In [6] it has been argued that $\alpha - \theta$ is larger than $1/6$, i.e., $\theta < 1/3$. The question about the precise values of θ and γ is interesting and merits further investigation.

2 Exact Results for Boarding with Small Number of Passengers

Here we consider in some detail the simple model introduced by Frette and Hemmer [1]. For a small number of passengers N, it is possible to consider all $N!$ permutations and count exactly the number of realizations $m(N, t_b)$, corresponding to certain boarding time t_b, where $1 \leq t_b \leq N$, by an appropriate numerical algorithm. The probability to have the boarding time t_b then is $P(N, t_b) = m(N, t_b)/N!$.

The results $P(N, t_b)$ for $N \leq 4$ are collected in Table 1 (left). The number of sequences of passengers with increasing seat numbers s is also interesting, since these passengers always get seated simultaneously. This point has been discussed in [1], reporting some exact results. In this case the seats are numbered from left

Table 1 The number of realizations $m(N, t_b)$ for boarding of N passengers in t_b time steps (*left table*), and the number of realizations $m(N, s)$ with s sequences of increasing seat numbers (*right table*). $P(N, t_b) = m(N, t_b)/N!$ in the *left table* is the probability that the boarding time is just t_b, and $P(N, s) = m(N, s)/N!$ in the *right table* is the probability that there are just s sequences

N	t_b	$m(N, t_b)$	$P(N, t_b)$
1	1	1	1
2	1	1	0.5
	2	1	0.5
3	1	1	0.25
	2	4	0.75
	3	1	0.25
4	1	1	$1/24 \approx 0.04167$
	2	12	0.5
	3	10	$5/12 \approx 0.41667$
	4	1	$1/24 \approx 0.04167$

N	s	$m(N, s)$	$P(N, s)$
1	1	1	1
2	1	1	0.5
	2	1	0.5
3	1	1	0.25
	2	4	0.75
	3	1	0.25
4	1	1	$1/24 \approx 0.04167$
	2	11	$11/24 \approx 0.45833$
	3	11	$11/24 \approx 0.45833$
	4	1	$1/24 \approx 0.04167$

to right, passengers enter the airplane from the left hand side, and we are looking for sequences of passengers also from left to right. A sequence of passengers is represented by the corresponding sequence of seat numbers. For example, the sequence 1 2 3 4 represents a queue of $N = 4$ passengers, where the last passenger staying in the queue has the seat number 1, the passenger staying in front of him or her has the seat number 2, and so on. In this case there is only one sequence of increasing seat numbers ($s = 1$) when looking from left to right, which means that all passengers get seated simultaneously in one time step, i.e., the boarding time is $t_b = 1$. A naive guess would be that $t_b = s$. The number of realizations $m(N, s)$, corresponding to certain s, as well as the probability $P(N, s)$ to have just s sequences of passengers with increasing seat numbers, can be easily calculated for a small N.

The results $P(N, s)$ for $N \leq 4$ passengers are collected in Table 1 (right). The probability distribution $P(N, s)$ is always symmetric, as it follows from the exact results of [1]. It is seen also in Table 1. On the other hand, it is evident from this table that already at $N = 4$ the probability distribution $P(N, t_b)$ is asymmetric, which means that $t_b \neq s$. This effect appears because of merging of the sequences with increasing seat numbers. For $N = 4$ such a merging occurs only for one of $4! = 24$ possible permutations, i.e., for the arrangement 2 1 4 3 with $s = 3$. In this case, the passenger with seat number 1 gets seated simultaneously with the passenger with seat number 3, although these two passengers belong to two different sequences with increasing seat numbers. As a result, two sequences merge after the first step, and the remaining two passengers get seated simultaneously in the second step. It means that $t_b = 2 < s$ holds in this case.

Such cases of merging makes the problem non-trivial and does not allow us to obtain an exact solution for arbitrary N analytically. The number of merging increase very significantly for larger N. The exactly enumerated values of $m(N, t_b)$ and the corresponding values of $P(N, t_b)$ are collected in Table 2 for $5 \leq N \leq 13$.

Table 2 The number of realizations $m(N, t_b)$ for boarding of N passengers in t_b time steps. $P(N, t_b) = m(N, t_b)/N!$ is the probability that the boarding time is just t_b

t_b	$m(N, t_b)$	$P(N = 5, t_b)$
1	1	0.00833
2	33	0.275
3	66	0.55
4	19	0.15833
5	1	0.00833

t_b	$m(N, t_b)$	$P(N = 6, t_b)$
1	1	0.00139
2	88	0.12222
3	372	0.51667
4	227	0.31528
5	31	0.04306
6	1	0.00139

t_b	$m(N, t_b)$	$P(N = 7, t_b)$
1	1	0.00020
2	232	0.04603
3	1,956	0.38810
4	2,218	0.44008
5	586	0.11627
6	46	0.00913
7	1	0.00020

t_b	$m(N, t_b)$	$P(N = 8, t_b)$
1	1	0.00002
2	609	0.01510
3	9,973	0.24735
4	19,587	0.48579
5	8,824	0.21885
6	1,261	0.03127
7	64	0.00159
8	1	0.00002

t_b	$m(N, t_b)$	$P(N = 9, t_b)$
1	1	2.7557×10^{-6}
2	1,596	0.00440
3	50,236	0.13844
4	163,969	0.45185
5	117,589	0.32404
6	27,006	0.07442
7	2,397	0.00661
8	85	0.00023
9	1	2.7557×10^{-6}

t_b	$m(N, t_b)$	$P(N = 10, t_b)$
1	1	2.7557×10^{-7}
2	4,180	0.00115
3	252,299	0.06953
4	1,335,180	0.36794
5	1,460,396	0.40245
6	503,411	0.13873
7	69,057	0.01903
8	4,166	0.00115
9	109	0.00003
10	1	2.7557×10^{-7}

t_b	$m(N, t_b)$	$P(N = 11, t_b)$
1	1	2.5052×10^{-8}
2	10,945	0.00027
3	1,268,890	0.03179
4	10,731,205	0.26884
5	17,405,710	0.43605
6	8,630,106	0.21620
7	1,707,964	0.04279
8	155,075	0.00388
9	6,767	0.00017
10	136	3.4071×10^{-6}
11	1	2.5052×10^{-8}

t_b	$m(N, t_b)$	$P(N = 12, t_b)$
1	1	2.0877×10^{-9}
2	28,656	0.00006
3	6,402,738	0.01337
4	85,860,395	0.17925
5	202,624,251	0.42301
6	140,460,107	0.29324
7	38,400,800	0.08017
8	4,898,366	0.01023
9	315,693	0.00066
10	10,426	0.00002
11	166	3.4655×10^{-7}
12	1	2.0877×10^{-9}

t_b	$m(N, t_b)$	$P(N = 13, t_b)$
1	1	1.6059×10^{-10}
2	75,024	0.00001
3	32,435,686	0.00521
4	687,285,783	0.11037
5	2,329,632,160	0.37412
6	2,213,481,380	0.35546
7	811,899,122	0.13038
8	139,225,896	0.02236
9	12,374,938	0.00199
10	595,214	0.00010
11	15,396	2.4725×10^{-6}
12	199	3.1957×10^{-8}
13	1	1.6059×10^{-10}

Table 3 The number of realizations $m(N = 14, t_b)$ for boarding of $N = 14$ passengers in t_b time steps (left table), and the number of realizations $m(N = 14, s)$ with s sequences of increasing seat numbers (right table). $P(N = 14, t_b) = m(N = 14, t_b)/N!$ in the left table is the probability that the boarding time is just t_b, and $P(N = 14, s) = m(N = 14, s)/N!$ in the right table is the probability that there are just s sequences for $N = 14$

t_b	$m(N = 14, t_b)$	$P(N = 14, t_b)$
1	1	1.1471×10^{-11}
2	196,417	2.2530×10^{-6}
3	164,973,584	0.00189
4	5,519,763,360	0.06332
5	26,642,715,539	0.30561
6	34,207,960,967	0.39239
7	16,491,836,851	0.18917
8	3,688,831,863	0.04231
9	432,622,448	0.00496
10	28,312,826	0.00032
11	1,055,151	0.00001
12	21,957	2.5186×10^{-7}
13	235	2.6956×10^{-9}
14	1	1.1471×10^{-11}

s	$m(N = 14, s)$	$P(N = 14, s)$
1	1	1.1471×10^{-11}
2	16,369	1.8776×10^{-7}
3	4,537,314	0.00005
4	198,410,786	0.00228
5	2,571,742,175	0.02950
6	12,843,262,863	0.14732
7	27,971,176,092	0.32085
8	27,971,176,092	0.32085
9	12,843,262,863	0.14732
10	2,571,742,175	0.02950
11	198,410,786	0.00228
12	4,537,314	0.00005
13	16,369	1.8776×10^{-7}
14	1	1.1471×10^{-11}

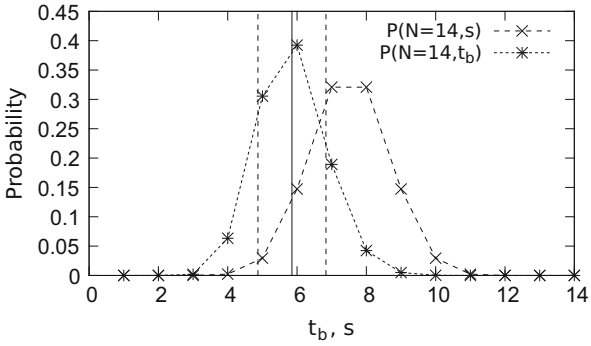

Fig. 1 The probability distributions $P(N, t_b)$ and $P(N, s)$ for $N = 14$ passengers. The mean boarding time $\langle t_b \rangle = 5.85212$ is shown by a *vertical solid line*, the range $\pm\sigma$ of one standard deviation $\sigma = 0.98116$ from the mean value is indicated by *vertical dashed lines*

In Table 3, the results for $N = 14$ are shown, including also those for $m(N = 14, s)$ and $P(N = 14, s)$. The probability distributions $P(N = 14, t_b)$ and $P(N = 14, s)$ are depicted in Fig. 1, showing also the mean value and the standard deviation for the boarding time distribution.

3 Mapping to the Two-Dimensional Problem of the Longest Increasing Sequence

A passenger sequence can be rendered as a two-dimensional scatter plot. Each passenger is represented by a point with coordinates $x = i/N$ and $y = j/N$, where i is his/her sequential index in the queue and j is his/her seat number. Note that in this case the passenger, who enters the airplane first has the index $i = 1$, the passenger behind him or her has the index $i = 2$, and so on. In the asymptotic limit $N \to \infty$, an averaged over ensemble of sequences density of points $(i/N, j/N)$, normalized by N, gives the probability density function $p(x, y)$.

According to the mathematical theorem in [7, 8], the length of the longest increasing subsequence asymptotically scales as $N^{1/2}$, provided that $p(x, y)$ is finite. A subsequence $\{(x_{i_1}, y_{j_1}), (x_{i_2}, y_{j_2}), \ldots, (x_{i_l}, y_{j_l})\}$ of pairs of real numbers with $0 \le x_i \le 1$ and $0 \le y_i \le 1$ for $i = 1, 2, \ldots, N$ is called an increasing subsequence, if $x_{i_m} < x_{i_{m+1}}$ and $y_{i_m} < y_{i_{m+1}}$ holds for $m = 1, 2, \ldots, l-1$, where i_m is a sequence of non-repeated indices between 1 and N. In the considered here model, the distribution of points in the xy plane is fully random, so that $p(x, y) \equiv 1$ is indeed finite.

The papers [4–6] deal with claim that the length l of the longest increasing sequence is equal to the boarding time t_b. We have check it for $N = 4$, considering the two-dimensional scatter plots for all $4! = 24$ permutations in Fig. 2. In each of the cases, the longest increasing sequence is shown by connecting the points of this sequence by lines. The number of points in this graph is equal to l. In one of the cases no lines are present, implying that $l = 1$. In the cases, where there are several sequences with the same maximal length, different lines are used to distinguish them. In 23 of 24 cases we can see that t_b is indeed equal to the length l of the longest increasing sequence. However, there is one exception, corresponding to the sequence 3 1 4 2 in the notations of Sect. 2. In this case, the seat numbers are $j_1 = 2$, $j_2 = 4$, $j_3 = 1$ and $j_4 = 3$ for passengers numbered sequentially from right to left, as considered in this section. The corresponding scatter plot is the second one in the third row in Fig. 2. Evidently, the boarding time in this case is $t_b = 3$, but $l = 2$.

This exception shows that the mapping of the original problem to the problem of finding the longest increasing sequence is not exact. Nevertheless, it is possible that the asymptotic scaling of $\langle l \rangle$ and $\langle t_b \rangle$ is described by the same exponent α, e.g., if t_b/l is finite (and nonzero at $N \to \infty$) in a fraction of cases which tends to unity at $N \to \infty$. According to the above mentioned theorem of [7, 8], $\langle l \rangle$ scales with the exponent $\alpha = 1/2$ at $N \to \infty$. It is also very plausible that $\langle t_b \rangle$ scales with the same exponent owing to the mentioned here reason, since $\alpha = 1/2$ is accurately confirmed by Monte Carlo simulations [3].

The ensemble of realizations, illustrated in Fig. 2, is unchanged if each of the plots is mirror-reflected with respect to the diagonal $y = x$. The same is true for the mirror–reflection with respect to the other diagonal $y = 1 - x$. Thus, the mirror–symmetric with respect to each other plots appear with equal probability. This is an evident symmetry property for any passenger number N in the considered

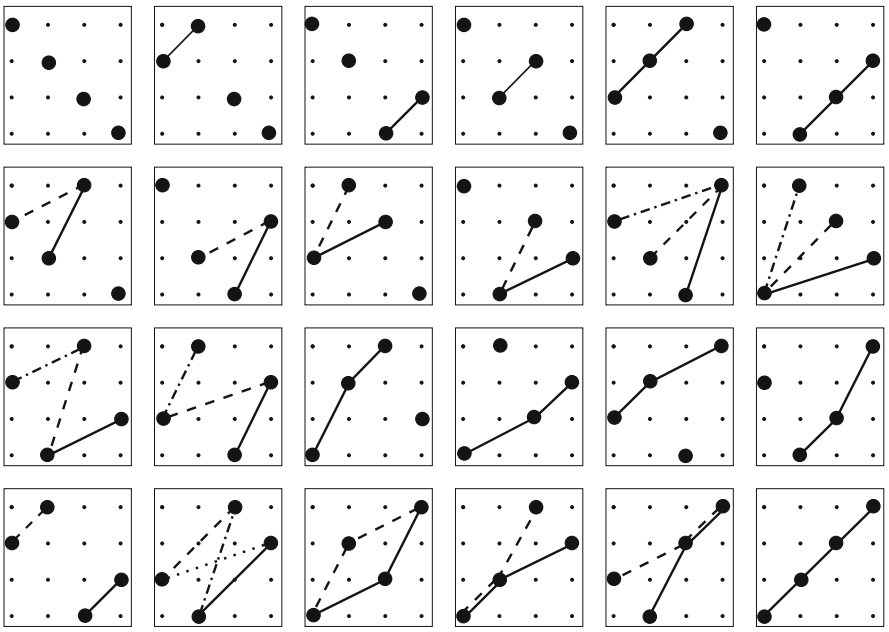

Fig. 2 Scatter plots with horizontal and vertical axes representing the sequential number and the seat number for each of $N = 4$ passengers, plotted by *solid circles*. The connecting lines are used to show the longest increasing sequences

here mapping, where the number of seats is equal to the number of passengers N and all $N!$ permutations are equally probable. Therefore, if in the asymptotic limit $N \to \infty$ the plot of the longest increasing sequence follows certain curve $y = f(x)$, then there exist also mirror–symmetric curves with respect to both diagonals, representing equivalent plots of increasing sequences of the same (i.e., maximal) length. Hence, the curve $y = f(x)$ is unique only if it follows the diagonal $y = x$ (it cannot follow the other diagonal $y = 1 - x$, since it must be increasing).

Because it turns out that the often used [4–6] and tested here mapping to the problem of finding the longest increasing sequence is inexact, and we also cannot see how the analytical solutions of [5, 6] reflect the outlined here symmetry of such a mapping in the simplest case, we mainly rely on our simulation results.

4 Asymptotic Scaling Results for Airplane Boarding with Large Number of Passengers

According to [3], the mean boarding time $\langle t_b \rangle$ and its second moment $\langle t_b^2 \rangle$ for large N values about 2^{16} are very accurately described by asymptotic formulas

$$\langle t_b \rangle = At^{\alpha} \left(1 + a_1 N^{-\theta} + a_2 N^{-2\theta} + o\left(N^{-2\theta}\right)\right) \quad (1)$$

$$\langle t_b^2 \rangle = Bt^{\beta} \left(1 + b_1 N^{-\theta} + b_2 N^{-2\theta} + o\left(N^{-2\theta}\right)\right) \quad (2)$$

with the exponents $\beta = 2\alpha = 1$ and $\theta \approx 1/3$. Since the boarding time distribution is asymptotically sharp at $N \to \infty$, the relation $B = A^2$ holds for the coefficients. The exponent $\alpha = 1/2$ agrees with the results of [2, 4–6]. The coefficient A has been estimated in [3] (see Fig. 1 there) to be $A = 2.6092 \pm 0.0002$, which is similar to $A = 4 - 2\ln 2 \approx 2.6137$ of [6]. We consider also the variance of the boarding time, which scales as

$$\mathrm{var}(t_b) = \langle t_b^2 \rangle - \langle t_b \rangle^2 \propto N^{\gamma} \quad (3)$$

at large N. According to (1) and (2), where $B = A^2$ and $\beta = 2\alpha = 1$, we have $\gamma = 1 - \theta$ if $b_1 - 2a_1 \neq 0$, and $\gamma = 1 - 2\theta$ if $b_1 - 2a_1 = 0$ and $b_2 - 2a_2 - a_1^2 \neq 0$ hold. Our numerical estimation supports the second possibility, as we find that the relation

$$\gamma = 1 - 2\theta \quad (4)$$

is satisfied within the small error bars of the estimates $\theta = 0.330 \pm 0.001$ (see Fig. 2 in [3]) and $\gamma = 0.343 \pm 0.001$ given in [3]. The agreement of these values with $1/3$, however, is not perfect, and we allow a possibility that $\theta < 1/3$ and $\gamma > 1/3$ hold.

5 Discussions and Application

The growing need for mobility through the world shows no sign of slowing down. Applications of stochastic processes to transport problems in a large variety of complex systems, including vehicular and pedestrian traffic, are well known [9, 10]. Here we focus on the air traffic and boarding of an airplane as a significant part of the global transportation process. Our Monte Carlo simulation and analysis is one of numerous applications of stochastic methods to study the behavior of complex systems. From the theoretical point of view, it is tightly related to the power–law scaling and universality problems in many–particle systems. From a practical point of view, it could help to understand the boarding process in order to optimize it.

Acknowledgements We thank E. Bachmat for fruitful discussions via e–mail. This research is supported by the Baltic–German University Liaison Office through German Academic Exchange Service (DAAD) with funds from the Foreign Office of the Federal Republic of Germany.

References

1. V. Frette, P.C. Hemmer, Time needed to board an airplane: a power law and the structure behind it. Phys. Rev. E **85**, 011130 (2012)
2. N. Bernstein, Comment on 'Time needed to board an airplane: a power law and the structure behind it'. Phys. Rev. E **86**, 023101 (2012)
3. M. Brics, J. Kaupužs, R. Mahnke, Scaling behavior of an airplane-bording-model. Phys. Rev. E **86**, 042117 (2013)
4. Y. Baek, M. Ha, H. Jeong, Impact of sequential disorder on the scaling behavior of airplane boarding time. Phys. Rev. E **87**, 052803 (2013)
5. E. Bachmat, V. Khachaturov, R. Kuperman, Optimal back-to-front airplane boarding. Phys. Rev. E **87**, 062805 (2013)
6. E. Bachmat, D. Berend, L. Sapir, S. Skiena, N. Stolyarov, Analysis of airplane boarding via space-time geometry and random matrix theory. J. Phys. A **39**, L453–459 (2006)
7. A.M. Vershik, C.V. Kerov, Asymptotics of the Plancherel measure of the symmetric group and the limiting form of Young tables. Dokl. Acad. Nauk SSSR **233**, 1024 (1977); Sov. Math. Dokl. **18**, 527 (1977)
8. J.-D. Deushel, O. Zeitouni, Limiting curves for I.I.D. records. Ann. Prob. **23**, 852 (1995)
9. A. Schadschneider, D. Chowdhury, K. Nishinari, *Stochastic Transport in Complex Systems. From Molecules to Vehicles* (Elsevier, Amsterdam, 2011)
10. R. Mahnke, J. Kaupužs, I. Lubashevsky, *Physics of Stochastic Processes. How Randomness Acts in Time* (Wiley, Weinheim, 2009)

Part II
Highway and Urban Vehicular Traffic

Time Evolution of Road Networks

Marc Barthelemy

Abstract Urbanization is a fundamental phenomenon which however still remains poorly quantitatively characterized. An important facet of this phenomenon is the road network which co-evolves with other urban structures and we review here the most recent results about the structure and the evolution of these important infrastructures. These studies suggest that the natural evolution of a road network is governed by two elementary processes: (i) 'densification', which corresponds to an increase in the local density of roads around existing central points and (ii) 'exploration' which consists in new roads triggering the spatial evolution of the urbanization front. However, interventions of central, top-down planning could modify this simple picture of a natural evolution and we will present the example of the street network of Paris (France), which during the nineteenth century experienced large modifications supervised by a central authority, the 'Haussmann period'. In this case, the usual network measures display a smooth behavior and the most important quantitative signatures of central planning are the spatial reorganization of centrality and the modification of the block shape distribution. Such effects can only be obtained by structural modifications at a large-scale level, with the creation of new roads not constrained by the existing geometry. These different results suggest that the evolution of a road network results from the superimposition of continuous, local growth processes and punctual changes operating at large spatial scales, opening new directions for the modelling of these systems.

1 Quantitative Urbanism

Urbanization is a fundamental process in human history, and is increasingly affecting our environment and societies. The portion of the world population living in urban areas has just grown beyond the 50 % and is expected to rapidly increase in the next future [1]. The challenges posed by such a fast urbanizing world are well known, and range from an increasing dependence of cities on fossil fuels,

M. Barthelemy (✉)
Institut de Physique Théorique, CEA, CNRS-URA 2306, F-91191, Gif-sur-Yvette, France
e-mail: marc.barthelemy@cea.fr

M. Chraibi et al. (eds.), *Traffic and Granular Flow '13*,
DOI 10.1007/978-3-319-10629-8_38

to socio-spatial inequalities and economical uncertainties. Controlling urbanization has already proven to be a difficult task, and will become even harder in the next future due to the larger and unprecedented scale of the phenomenon. In addition, urbanization is often accompanied by massive poverty at an equally unprecedented scale, expanding corruption and weaknesses of the local planning systems (in particular in developing countries). Understanding how urbanization and land use change under different circumstances, and what are the dominant mechanisms and, if any, the 'universal' features of such large-scale self-organized processes, is more important than ever as policy makers, professionals and the scientific community are actively looking for new paradigms in urban planning and land management [2, 3].

The search for a quantitative theory of cities is a long time story (see the recent book by Batty [4]) with noticeable periods of activity. Quantitative geography in the 1960s was very active [5], and after a quieter period, there is currently a renewal of interest about this subject mainly triggered by the availability of data. 'Big data' about cities allow now to construct models and to test them, a necessary condition for knowledge evolution. More precisely, these different datasets inform us about various aspects of cities and their analysis will lead to stylized facts and will help us to build models with a small number of assumptions and parameters and with testable predictions.

We can divide the available data about cities according to their temporal scale and some of the recent results pertaining to this new science of cities are the following ones, from time scales of order a day to long times such as decades and centuries (Fig. 1).

- At a typical time scale of the order the hour to a day, mobility data gathered by mobile phones, GPS, or RFIDs inform us about where and when people move in the city, revealing in depth the spatio-temporal structure of activities in a city and statistical patterns of mobility. The availability of mobility data renewed the interest for understanding the laws governing the trips of individuals, such as the gravity law, and questioned its validity, leading to new, more accurate models. Also, these datasets provide a clear picture of the spatial distribution of activities, and of the existence of multiple activity subcenters, allowing us to discuss the possibility of a typology of cities in terms of degree of polycentrism [6].
- At a larger time scale, of a month to a year, socio-economical surveys provide us with relevant informations such as the total yearly gasoline consumption, the total yearly number of miles driven, the relation between density and area, etc. The key of understanding how these different quantities scale with population is the mobility spatial pattern [7, 8].

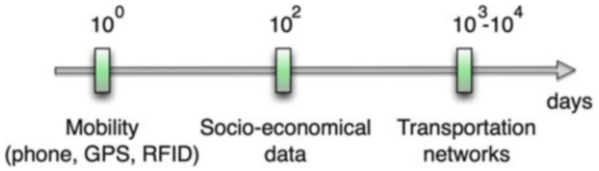

Fig. 1 We can divide the available data about cities according to their temporal scale, from time scales of order a day to long times such as decades and centuries

- Finally at very long time scales such as decades and centuries, remote sensing and the recent digitization of old maps allow us to study the evolution of urbanized areas, transportation and road networks. We can then observe that large subway networks seem to converge to the same structure [9], characterized by similar values of morphological indicators, revealing the existence of dominant mechanisms independent from cultural and historical considerations. We can also observe the large-scale evolution of road networks – that we will describe in more detail in this paper – allowing us to characterize quantitatively the natural, 'organic' evolution of an urban system and the influence of urban planning.

2 Road Network: Static Properties

Despite the peculiar geographical, historical, social-economical mechanisms that have shaped distinct urban areas in different ways (see for example [10] and references therein), recent empirical studies [11–22] (see also the review [23]) have shown that, at least at a coarse grained level, unexpected quantitative similarities exist between road networks of very different cities. The simplest description of the street network consists of a graph whose links represent roads, and vertices represent roads' intersections and end points. For these graphs, links intersect essentially only at vertices and are thus planar. The degree of a node is then the number of roads intersecting at it. Planarity can be violated due to bridges but can be in general considered as a good approximation [16]. Measuring spatial properties of cities through the analysis of the street network is not new and was popularized some time ago by Hillier and Hanson [24] under the term 'space syntax'. In this chapter, we will discuss different recent measures of these networks in the light of our current understanding of the structure of networks.

2.1 Degrees, Lengths, and Cell Area Distribution

In [14, 17] measurements for different cities in the world are reported. Based on the data from these sources, the authors of [19] plotted (Fig. 2a) the number of roads E (edges) versus the number of intersections N. The plot is consistent with a linear fit with slope ≈ 1.44 (which is consistent with an average degree value $\langle k \rangle \approx 2.5$ measured in [17]). The quantity $e = E/N = \langle k \rangle /2$ displays values in the range $1.05 < e < 1.69$, in between the values $e = 1$ and $e = 2$ that characterize tree-like structures and $2d$ regular lattices, respectively. In a study of 20 German cities, Lämmer et al. [16] showed that most nodes have four neighbors (the full degree distribution is shown in Fig. 3a) and that for various world cities the degree rarely exceeds 5 [14]. These values are however not very indicative: planarity imposes severe constraints on the degree of a node and on its distribution which is generally peaked around its average value.

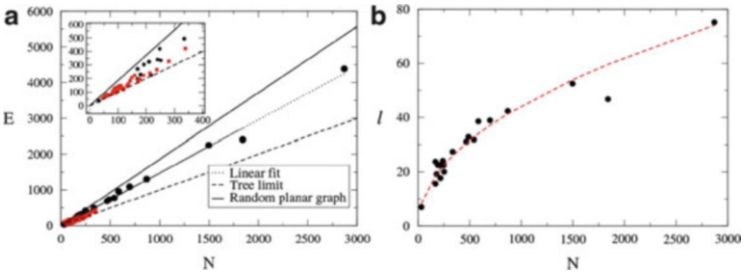

Fig. 2 (**a**) Number of roads versus the number of nodes (i.e. intersections and centers) for data from [14] (*circles*) and from [17] (*squares*). In the *inset*, we show a zoom for a small number of nodes. (**b**) Total length ℓ_T versus the number of nodes. The line is a fit which predicts a growth as $\sqrt{N}$ (Data from [14] and figures from [19])

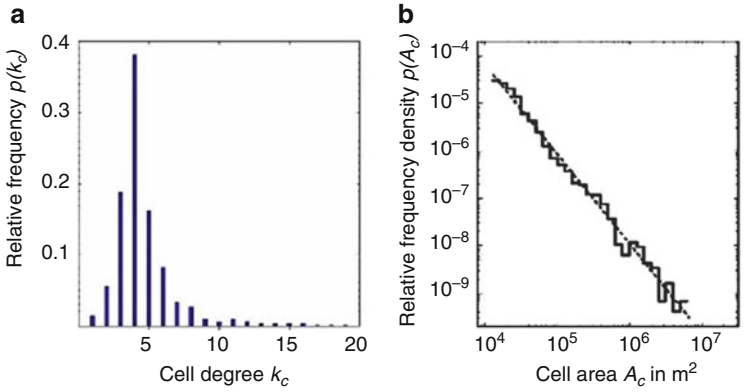

Fig. 3 (**a**) Degree distribution of degrees for the road network of Dresden. (**b**) The frequency distribution of the cell's surface areas A_c obeys a power law with exponent $\alpha \approx 1.9$ (for the road network of Dresden) (From [16])

In Fig. 2b, we show the total length ℓ_T of the network versus N for the towns considered in [14]. Data are well fitted by a power function of the form

$$\ell_T = \mu N^{\beta} \tag{1}$$

with $\mu \approx 1.51$ and $\beta \approx 0.49$. In order to understand this result, one has to focus on the street segment length distribution $P(\ell_1)$. This quantity has been measured for London in [25] and decreases rapidly, implying that both the average and the dispersion are finite. If we assume that this result extends to other cities, the typical distance between connected nodes then naturally scales as

$$\ell_1 \sim \frac{1}{\sqrt{\rho}} \tag{2}$$

where $\rho = N/L^2$ is the density of vertices and L the linear dimension of the city. This implies that the total length scales as

$$\ell_T \sim E\ell_1 \sim \frac{\langle k \rangle}{2} L\sqrt{N} \tag{3}$$

This simple argument reproduces well the $\sqrt{N}$ behavior observed in Fig. 2b and also the value (given the error bars) of the prefactor $\mu \approx \langle k \rangle/2$.

The simplest hypothesis consistent with all the data presented so far, at this stage, is that the road network is a statistically homogeneous and translational invariant structure. However, this network naturally produces a set of non overlapping cells – or blocks – encircled by the roads themselves and covering the embedding plane, and surprisingly, the distribution of the area A of such cells measured for the city of Dresden in Germany (Fig. 3b) has the form

$$P(A) \sim A^{-\alpha} \tag{4}$$

with $\alpha \simeq 1.9$. This seems to be in sharp contrast with the simple picture of an almost regular lattice which would predict a distribution $P(A)$ peaked around ℓ_1^2, but if we assume that $A \sim 1/\ell_1^2 \sim 1/\rho$ and that ρ is distributed according to a distribution $f(\rho)$ (with a finite $f(0)$), a simple calculation gives

$$P(A) \sim \frac{1}{A^2} f(1/A) \tag{5}$$

which behaves as $P(A) \sim 1/A^2$ for large A. This simple argument thus suggests that the observed value $\approx$2.0 of the exponent is universal and reflects the random variation of the density. More measurements are however needed at this point in order to test the validity of this hypothesis.

The authors of [5, 16] also measured the distribution of the form factor for a cell defined as

$$\phi = \frac{4A}{\pi D^2} \tag{6}$$

which is the ratio of the area A of the cell to the area of the circumscribed circle of diameter D. The value of the shape factor is in general higher for regular convex polygons, and tends to 1 when the number of sides in the polygons increases. They found that most cells have a form factor between 0.3 and 0.6, suggesting a large variety of cell shapes, in contradiction with the assumption of an almost regular lattice. This fact thus call for a model radically different from simple models of regular or perturbed lattices.

2.2 Betweenness Centrality

The importance of a road can be characterized by its traffic which can be measured by sensors or surveys, but if we assume that the traffic between all pairs of nodes is the same, a natural proxy for the traffic is the betweenness centrality (BC) defined as [26]

$$g(i) = \sum_{s \neq t \neq i} \frac{\sigma_{st}(i)}{\sigma_{st}} \tag{7}$$

(up to a normalization factor) where $\sigma_{st}(i)$ is the number of shortest paths from s to t going through i (and σ_{st} is the number of shortest paths between s and t). A node with a large BC is important in the structure of shortest paths and will very likely correspond to a node that is very congested in reality. At least, even if the underlying assumptions are not correct the spatial distribution of the betweenness centrality gives important information about the coupling between space and the structure of the road network.

Lämmer et al. [16] studied the German road network and obtained very broad distributions of betweenness centrality with a power law exponent in the range $[1.279, 1.486]$ (for Dresden ≈ 1.36). These broad distributions of the betweenness centrality signals the strong heterogeneity of the network in terms of traffic, with the existence of a few very central roads which very probably points to some congestion traffic problems. Also the absence of a scale in a power law distribution suggests that the importance of roads is organized in a hierarchical way, a property expected for many transportation networks [27]. The broadness of the betweenness centrality distribution does not seem however to be universal. Indeed, in [13, 28], the betweenness centrality distribution is peaked (depending on the city, either exponentially or according to a Gaussian) which signals the existence of a scale and therefore of a finite number of congested points in the city.

The betweenness centrality is in itself interesting since it points to the important zone which potentially are congested. The Fig. 4 displays the spatial distribution of the betweenness centrality for the city of Dresden (Germany). As expected zones which are central from a geographical point of view also have a large betweenness centrality. We however see that other roads or zones can have a large betweenness centrality pointing to a complex pattern of flow distribution in cities.

In addition to have a relation with the traffic and possibly with congestion, a recent paper [29] proposes an interesting direction which is in the general context of connecting topological measures of the networks and socio-economical indices. In particular, these authors show that there is a clear correlation between the betweenness centrality and the presence of commercial activities.

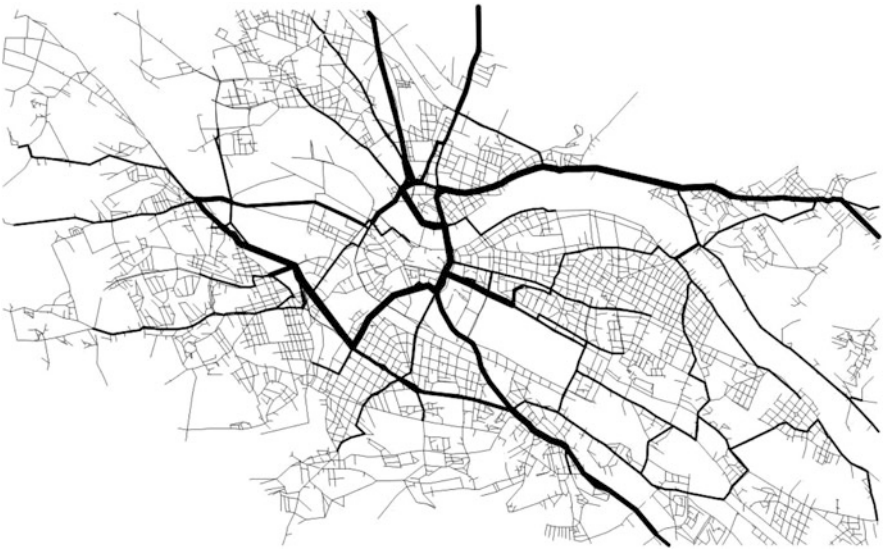

Fig. 4 Betweenness centrality for the city of Dresden. The width of the links corresponds to the betweenness centrality (Figure taken from [16])

3 Evolution of Road Networks

Street networks coevolve as with urban systems and understanding their growth represents an important piece of the puzzle of urbanization. The recent digitization and georeferentiation of old maps enable us to measure this evolution and we will here consider the evolution over almost 200 years of two different systems. The first one corresponds to the evolution of a large system made of many small towns in the region of Groane (Italy) and not controlled by any central authority. In contrast, we will also present the case of Paris (France) which during the nineteenth century experienced large transformations controlled by a central authority.

We notice that for both systems (Fig. 6a) that the that the number of nodes N is proportional to the population P (for the first case of the italian Groane region it is of order $dN/dP \approx 0.019$ and for central Paris $dN/dP \approx 0.0021$). In other words, the number of people per road intersection remains constant over time. To be able to compare these systems at different points of their evolution, we thus adopt the number of nodes N as the natural internal clock of the system, and we study the change of various network properties as a function of N.

Finally we note that, interestingly, the total road network length growth rate (averaged over the total period of order 200 years) is of the same order of magnitude for both systems

$$\frac{\Delta \ell_T}{\Delta t} \simeq \begin{cases} 4.6\,\text{km/year} & \text{(Groane, Italy)} \\ 1.6\,\text{km/year} & \text{(Paris, France)} \end{cases} \tag{8}$$

3.1 Elementary Processes

3.1.1 Characterizing Network Growth

In this part we will focus on the evolution, over two centuries, of the road network in a large area of 125 km^2, located north of Milan (Italy). In Fig. 5 we show the street networks obtained at seven different times from 1833 to 2007. In the period under consideration, we observe an uninterrupted network growth. In two centuries, the total number of nodes N in the road network grows by a factor of 20, from the original 255 nodes present at $t = 1833$ to more than 5,000 nodes at $t = 2007$. However, this growth is not regular: it is slow from 1833 to 1933, fast from 1933 to 1994, and slow again from 1994 to 2007 (Fig. 5).

The number of links K grows almost linearly with N (Fig. 6b, top), showing that the average degree is roughly constant despite massive historical changes, with a slight increase from $\langle k \rangle \simeq 2.57$ to 2.8 when going from 1914 to 1980 (Fig. 6b, bottom). Moreover, in Fig. 6c we observe that the total network length increases as N^{ν} where $\nu \simeq 0.54$ and, accordingly, the average length of links decreases as $N^{\nu-1}$. This result is consistent with the evolution of two-dimensional lattices with a peaked link length distribution [19, 23] which are described by a value $\nu = 1/2$. The quantity

$$r_N = \frac{[N(1) + N(3)]}{N} \tag{9}$$

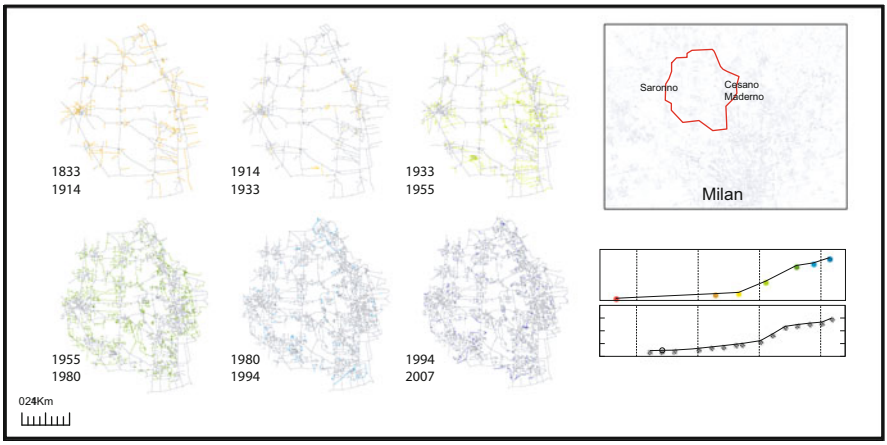

Fig. 5 Evolution from 1833 to 2007 of the road network in the region of Groane (Italy). On each map we report in grey all the nodes and links already existing at the previous time, and we indicate in color the new streets added in the time window under consideration. The *bottom right panel* reports, as a function of time, the total number of nodes N of the graph and the total population in the area obtained from census data. The map on *top-right panel* shows the location of the area under study in the metropolitan region of Milan

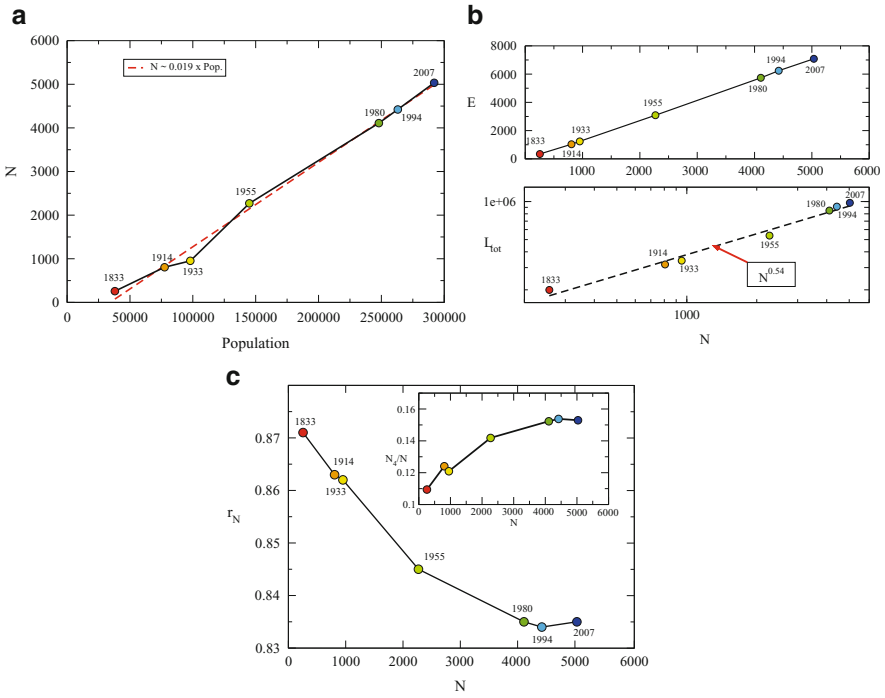

Fig. 6 (**a**) Number of nodes N versus total population (*continuous line with circles*) and its linear fit (*red dashed line*). (**b**) Total number of edges E, and the total network length L_{tot} (*upper panel*) versus the number of nodes. The total length scales with N as a power law with exponent close to $1/2$. (**c**) As the network grows, the value of the ratio r_N decreases, indicating the presence of a higher number of 4-ways crossings. In the inset we report the percentage of nodes having degree $k = 4$ as a function of N. Notice that the relative abundance of four-ways crossings increases by 5% in two centuries

where $N(k)$ is the number of nodes of degree k, gives additional information on the structure of the network. Indeed, the plot of r_N versus N (Fig. 6d) shows that it steadily decreases from $r_N \simeq 0.87$ at $t = 1833$ to $r_N \simeq 0.835$ at $t = 2007$. In the inset we report the relative abundance of four-ways crossings, i.e. N_4/N. We notice a substantial increase from $N_4/N \simeq 11\,\%$ at $t = 1833$ to $N_4/N \simeq 15.5\,\%$ at $t = 2007$. This trend is the signature of a historical transition from a pre-urban to an urban phase.

3.1.2 Evolution of Cells: Towards Homogenization

Road networks can be considered as planar graphs consisting of a series of cells surrounded by street segments. The statistics on area and shapes of cells can be used to distinguish regular lattices from very heterogeneous patterns. In particular, we saw above that cell areas seem to be distributed in general as a power-law $P(A) \sim A^{-\gamma}$, with an exponent $\gamma \simeq 1.9$ [16]. In Fig. 7a we show that the distribution of the

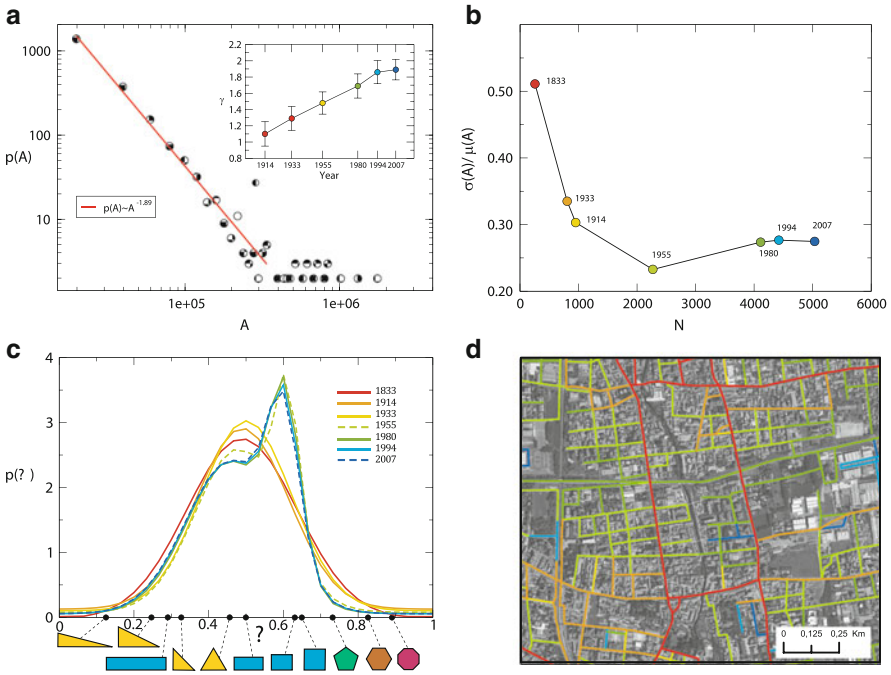

Fig. 7 (**a**) The size distribution of cell areas at $t = 2007$ can be fitted with a power-law $p(A) \sim A^{-\gamma}$, with an exponent $\gamma \simeq 1.9$. The values of γ increase over the years as shown in the *inset*. (**b**) Relative dispersion in the distribution of areas as a function of the network size N. (**c**) Distribution of cell shapes at each time, as quantified by the shape factor Φ. We also report, as a reference, the values of shape factors corresponding to various convex regular polygons. (**d**) The map shows some typical cell shapes at different times with the same color-code as in the previous panels

cell areas at $t = 2007$ is a power law with the same exponent $\gamma = 1.9 \pm 0.1$. As reported in the inset, the exponent however changes in time: it takes a value $\gamma \simeq 1.2$ at $t = 1833$ and converges towards $\gamma \simeq 1.9$ as the network grows. Because a larger exponent indicates a higher homogeneity of cell areas, we are thus witnessing here a process of homogenization of the size of cells. This appears to be a clear effect of increasing urbanization in time, with the fragmentation of larger cells of natural land into smaller urbanized ones. Accordingly, the relative dispersion of cell areas, shown in Fig. 7b, decreases from 0.5 at $t = 1833$ to 0.26 at $t = 2007$, indicating that the variance of the distribution becomes smaller as N increases.

The diversity in the cells shape can be quantitatively characterized by the so-called shape factor ϕ (see above). The distributions $P(\phi)$ reported in Fig. 7c clearly reveals the existence of two different regimes: for $t \leq 1933$ the distribution is well approximated by a single Gaussian function with an average of about 0.5 and a standard deviation of 0.25. Conversely, for $t \geq 1955$ the distribution of shape factors displays two peaks and can be fitted by the sum of two Gaussian functions. The first peak coincides roughly with the one obtained for $t \leq 1933$, while the second peak,

centered at 0.62, signals the appearance for $t \geq 1955$ of an important fraction of regular shapes such as rectangles with sides of similar lengths. In Fig. 7d we show some examples of the cell shapes at different times.

3.1.3 Properties of New Links: Elementary Processes of Urbanization

We focus here on the properties of the new links at a given time by looking at their length and centrality. We show in [21] that the average length of new links decreases over time, as expected. The nature of the growth process can be characterized quantitatively by looking at the centrality of streets. More precisely, we quantify the relative impact $\delta_b(e)$ of each new link e on the overall BC of the network at time t, essentially by looking at the difference in total centrality of the network caused by the hypothetical removal of the link [21]. Remarkably, the distribution of this quantity $\delta_b(e)$ displays two well-separated peaks (Fig. 8), with the first peak tending to increase in time while the second peak decreases, until they merge into only one peak in the last time-section (1994–2007).

In order to understand this remarkable dynamics and the nature of these two peaks, we focus on the geographical location of new links according to their impact on BC. We map in green the links whose centrality impact falls in the range of

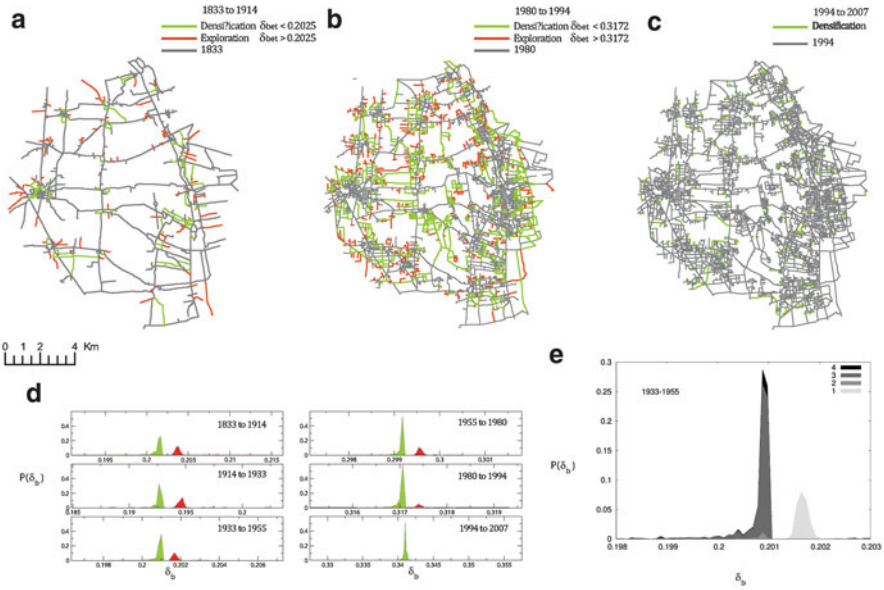

Fig. 8 The two phases of densification (*green*) and exploration (*red*), illustrated for the network at 1914 (**a**), 1994 (**b**), and 2007 (**c**). (**d**) We show the probability distribution of the BC impact $\delta_b(e)$ for the different time snapshots. The red peak corresponds to exploration, and the green peak to densification. Notice that the red peak becomes smaller and smaller with time, and completely disappears in the last snapshot. In (**e**) we show zoom on the period 1933-1955

the first peak (or is lower) and in red the links whose δ_b falls in the range of the second peak (or is larger). In Fig. 8a, b we can see that green links (small δ_b, first peak) tend to bridge already existing streets while red links (large δ_b, second peak) usually connect existing edges to new nodes. The distribution of BC impact thus suggests that the evolution of the road network is essentially characterized by two distinct, concurrent processes: one of 'densification' (green links, first peak, lower impact on centrality) which corresponds to an increase of local density of the urban texture, and one of 'exploration' (red links, second peak, higher impact on centrality) which corresponds to the expansion of the network towards previously non-urbanized areas. Obviously, since the amount of available land decreases over time, at earlier time-sections (such as in 1833) the fraction of exploration is higher, while in the 1980s it becomes smaller until it completely disappears in 2007.

Finally, there is a relation between the age of a street and its centrality. In [21], we show that highly central links usually are also the oldest ones. In particular, the links constructed before $t = 1833$ have a much higher centrality than those added at later time-sections. More precisely, the historical structure of oldest links mostly coincides with the highly central links at $t = 2007$. For this region, more than 90 % of the 100 most central links in 2007 (and almost 60 % of the top 1,000) were already present in 1833.

3.2 Planning Versus Self-Organization

A city is a highly complex system where a large number of agents interact, leading to a dynamics seemingly difficult to understand. Many studies in history, geography, spatial economics, sociology, or physics discuss various facets of the evolution of the city [30–38]. From a very general perspective, the large number and the diversity of agents operating simultaneously in a city suggest the intriguing possibility that cities are an emergent phenomenon ruled by self-organization [34]. On the other hand, the existence of central planning interventions might minimize the importance of self-organization in the course of evolution of cities. Central planning – here understood as a top-down process controlled by a central authority – plays an important role in the city, leaving long standing traces, even if the time horizon of planners is limited and much smaller than the age of the city. One is thus confronted with the question of the possiblity of modelling a city and its expansion as a self-organized phenomenon. Indeed central planning could be thought of as an external perturbation, as if it were foreign to the self-organized development of a city.

3.2.1 The Case of Paris

We consider here the evolution of the street network of Paris over more than 200 years with particular focus on the nineteenth century, a period when Paris experienced large transformations under the guidance of Baron Haussmann [39].

It would be difficult to describe the social, political, and urbanistic importance and impact of Haussmann works in a few lines and we refer the interested reader to the existing abundant literature on the subject (see [39, 40] and references therein). Essentially, until the middle of the nineteenth century, central Paris has a medieval structure composed of many small and crowded streets, creating congestion and, according to some contemporaries, probably health problems. In 1852, Napoleon III commissioned Haussmann to modernize Paris by building safer streets, large avenues connected to the new train stations, central or symbolic squares (such as the famous place de l'Etoile, place de la Nation and place du Panthéon), improving the traffic flow and, last but not least, the circulation of army troops. Haussmann also built modern housing with uniform building heights, new water supply and sewer systems, new bridges, etc. Hausmann plan implied a large number of destruction and rebuilding: approximately 28,000 houses were destroyed and 100,000 were built [40].

The case of Paris under Haussmann provides an interesting example where changes due to central planning are very important and where a naive modelling is bound to fail. We analyze here in detail the effect of these planned transformations on the street network. By introducing physical quantitative measures associated with this network, we are able to compare the effect of the Hausmann transformation of the city with its 'natural' evolution over other periods.

By digitizing historical maps into a Geographical Information System (GIS) environment, we reconstruct the detailed road system (including minor streets) at six different moments in time, $t = 1, 2, \ldots, 6$, respectively corresponding to years: 1789, 1826, 1836, 1888, 1999, 2010. It is important to note that we have thus snapshots of the street network before Haussmann works (1789–1836) and after (1888–2010). In Fig. 9a, we display the map of Paris as it was in 1789 on top of the current map (2010). In order to use a single basis for comparison, we limited our

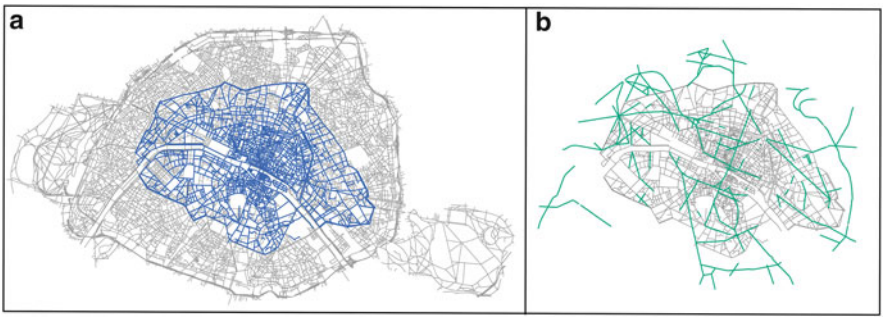

Fig. 9 (**a**) Map of Paris in 1789 superimposed on the map of current 2010 Paris. In the whole study, we focus on the Haussmann modifications and limited ourselves to the 1789 portion of the street network. (**b**) Map of Haussmann modifications. The *grey lines* represent the road network in 1836, the *green lines* represent the Haussmann modifications which are basically all contained in the 1789 area

study over time to the portion corresponding to 1789. We note here that the evolution of the outskirts and small villages in the surroundings has certainly an impact on the evolution of Paris and even if we focus here (mainly because of data availability reasons) on the structural modifications of the inner structure of Paris, a study at a larger scale will certainly be needed for capturing the whole picture of the evolution of this city. We then have six maps for different times and for the same area (of order 34 km^2). We also represent on Fig. 9b, the new streets created during the Haussmann period which covers roughly the second half of the nineteenth century. Even if we observe some evolution outside of this portion, most of the Haussmann works are comprised within this portion.

3.2.2 Simple Measures

In the following we study the structure of the graph G_t at different times t, having in mind that our goal is to identify the most important quantitative signatures of central planning during the evolution of this road network. First basic measures include the evolution of the number of nodes N, edges E, and total length ℓ_T of the networks (restricted to the area corresponding to 1789). In Fig. 10 we show the results for these indicators which display a clear acceleration during the Haussmann period (1836–1888). The number of nodes increased from about 3,000 in 1836 to about 6,000 in 1,888 and the total length increase from about 400 kms to almost 700 kms, all this in about 50 years. As noted above, the node increase corresponds essentially to an important increase in the population, and the results versus the number of nodes shown Fig. 10d–f display a smoother behavior. In particular, E is a linear function of N, demonstrating that the average degree is essentially constant $\langle k \rangle \approx 3.0$ since 1789. The total length versus N also displays a smooth behavior consistent with a perturbed lattice [23] of the form $\ell_T = \frac{\langle k \rangle}{2} \sqrt{AN}$ (A is the area considered here). A fit of the type $a\sqrt{N}$ is shown in Fig. 10d and the value of a measured gives an estimate of the area $A \simeq 29.7\,\text{km}^2$, in agreement with the actual value $A = 33.6\,\text{km}^2$ (for the 1789 portion). This agreement demonstrates that all the networks at different times are not far from a perturbed lattice.

We also plot the average route distance d_R defined as the average over all pairs of nodes of the shortest route between them (see Methods for more details). For a two dimensional spatial network, we expect this quantity to scale as $d_R \sim \sqrt{N}$ and thus increases with N. The ratio $d_R/\sqrt{N}$ is thus better suited to measure the efficiency of the network and we observe (Fig. 10c, f) that it decreases with time and N. This result simply demonstrate that if we neglect delays at junctions, it becomes easier to navigate in the network as it gets denser.

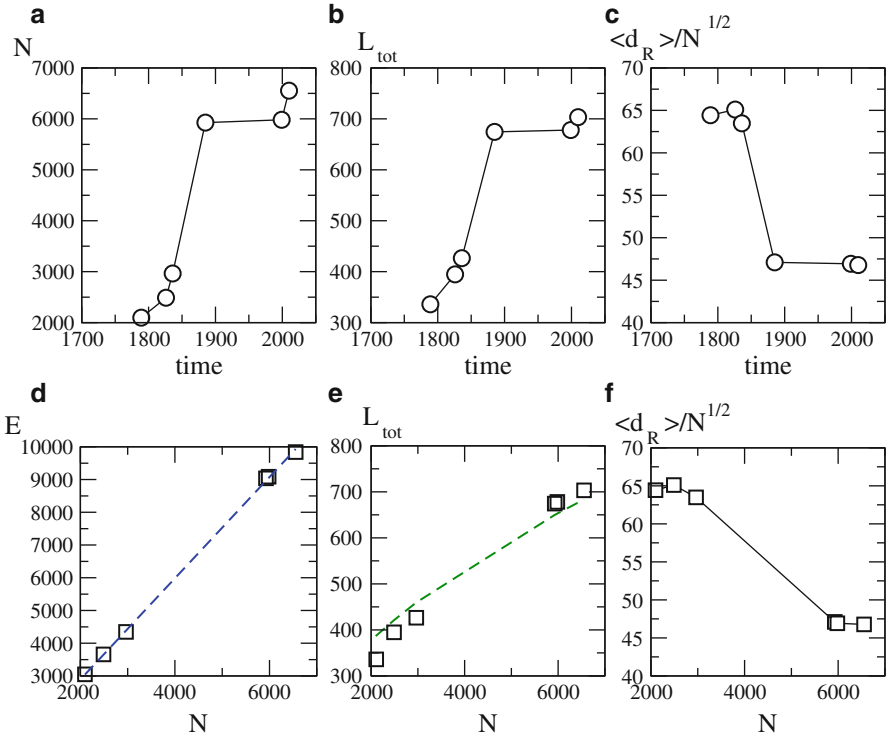

Fig. 10 Top panels: Number of (**a**) nodes, (**b**) total length (kms), and (**c**) rescaled average route distance versus time. Bottom panels: Number of (**d**) edges, (**e**) total length (kms), and (**f**) the rescaled average route distance versus the number of nodes N. In (**d**) the dashed (*blue*) line is a linear fit with slope 1.55 ($r^2 = 0.99$) consistent with constant average degree of order $\langle k \rangle \approx 3$, and in (**e**) the *dashed (green) line* a square root fit of the form $a\sqrt{N}$ with $a = 8.44$ kms ($r^2 = 0.99$). Based on a perturbed lattice picture this gives an area equal to $A \simeq 29.7\,\text{km}^2$ consistent with the actual value ($A = 33.6\,\text{km}^2$). In (**f**), we show the rescaled average shortest route versus N which decreases showing that the denser the network and the easier it is to navigate from one node to the other (if delays at junctions are neglected)

3.2.3 Evolution of the Spatial Distribution of Centrality

We now consider the time evolution of the node betweenness centrality. We note that in our case where we consider a limited portion of a spatial network, it is important to bear in mind that the BC has then to be used here as a structural probe of the network, enabling us to track the important modifications.

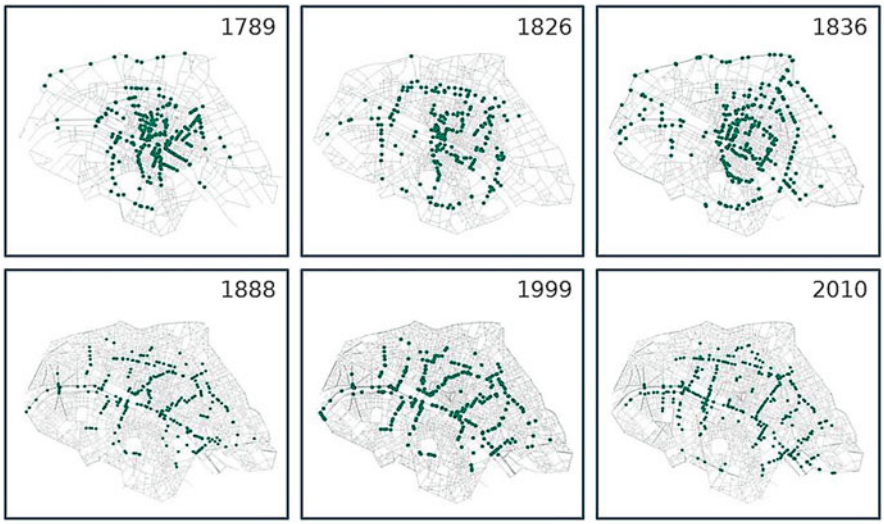

Fig. 11 Spatial distribution of the most central nodes (with centrality g_v such that $g_v > \max g_v/10$). We observe for the different periods important reorganizations of the spatial distribution of centrality, corresponding to different specific interventions. In particular, we observe a very important redistribution of centrality during the Haussmann period with the appearance of a reticulated structure on the 1888 map

In [21], we show the tail of the BC distribution remains constant in time, showing that the statistics of very central nodes is not modified. From this point of view, the evolution of the road network follows a smooth behavior, even in the Haussmann period. So far, most of the measures indicate that the evolution of the street network follows simple densification and exploration rules and is very similar to other areas studied [21]. At this point, it appears that Haussmann works didn't change radically the structure of the city. However, we can suspect that Haussmann's impact is very important on congestion and traffic and should therefore be seen on the spatial distribution of centrality. In the Fig. 11, we show the maps of Paris at different times and we indicate the most central nodes (such that their centrality $g_v(i)$ is larger than $\max g_v/\alpha$ with $\alpha = 10$). We can clearly see here that the spatial distribution of the BC is not stable, displays large variations, and is not uniformly distributed over the Paris area. In particular, we see that between 1836 and 1888, the Haussmann works had a dramatical impact on the spatial structure of the centrality, especially near the heart of Paris. Central roads usually persist in time [21], but in our case, the Haussmann reorganization was acting precisely at this level by redistributing the shortest paths which had certainly an impact on congestion inside the city. After Haussmann we observe a large stability of the network until nowadays.

It is interesting to note that these maps also provide details about the evolution of the road network of Paris during other periods which seems to reflect what happened in reality and which we can relate to specific local interventions. For example, in the period 1789–1826 between the French Revolution and the Napoleonic empire, the maps shown in Fig. 11 display large variations with redistribution of central nodes which probably reflects the fact that many religious and aristocratic domains and properties were sold and divided in order to create new houses and new roads, improving congestion inside Paris. During the period 1826–1836 which corresponds roughly to the beginning of the July Monarchy, the maps in Fig. 11 suggests an important reorganization on the east side of Paris. This seems to correspond very well to the creation during that period of a new channel in this area (the 'Canal Saint Martin') which triggered many transformations in the eastern part of the network.

It is visually clear in Fig. 11, that there is a large concentration of centrality in the center of Paris until 1836 at least. The natural consequence of this concentration is that the center of Paris was very probably very congested at that time. In this respect, what happens under the Haussmann supervision is natural as he acts on the spatial organization of centrality. We see indeed that in 1888, the most central nodes form a more reticulated structure excluding concentration of centrality. A structure which remained stable until now. Interestingly, we note that Haussmann's new roads and avenues represent approximately 6 % of the total length only (compared to nowadays network), which is a small fraction, considered that it has a very important impact on the centrality spatial organization.

This reorganization of centrality was undertaken with creation of new roads and avenues destroying parts of the original pattern (see Fig. 9b) resulting in the modification of the geometrical structure of blocks (defined as the faces of the planar street network). The effect of Haussmann modifications on the geometrical structure of blocks can be quantitatively measured by the distribution of the shape factor ϕ shown in Fig. 12 (top). We see that before the Haussmann modifications, the distribution of ϕ is stable and is essentially centered around $\phi = 0.5$ which corresponds to rectangles. From 1888, the distribution is however much flatter showing a larger diversity of shapes. In particular, we see that for small values of $\phi < 0.25$ there is an important increase of $P(\phi)$ demonstrating an abundance of elongated shapes (triangles and rectangles mostly) created by Haussmann's works. These effects can be confirmed by observing the angle distribution of roads shown on Fig. 12 (bottom) where we represent on a polar plot $r(\theta) = P(\theta)$ with $P(\theta)$ the probability that a road segment makes an angle θ with the horizontal line. Before Haussmann's modifications, the distribution has two clear peaks corresponding to perpendicular streets and in 1888 we indeed observe a more uniform distribution with a large proportion of various angles such as diagonals.

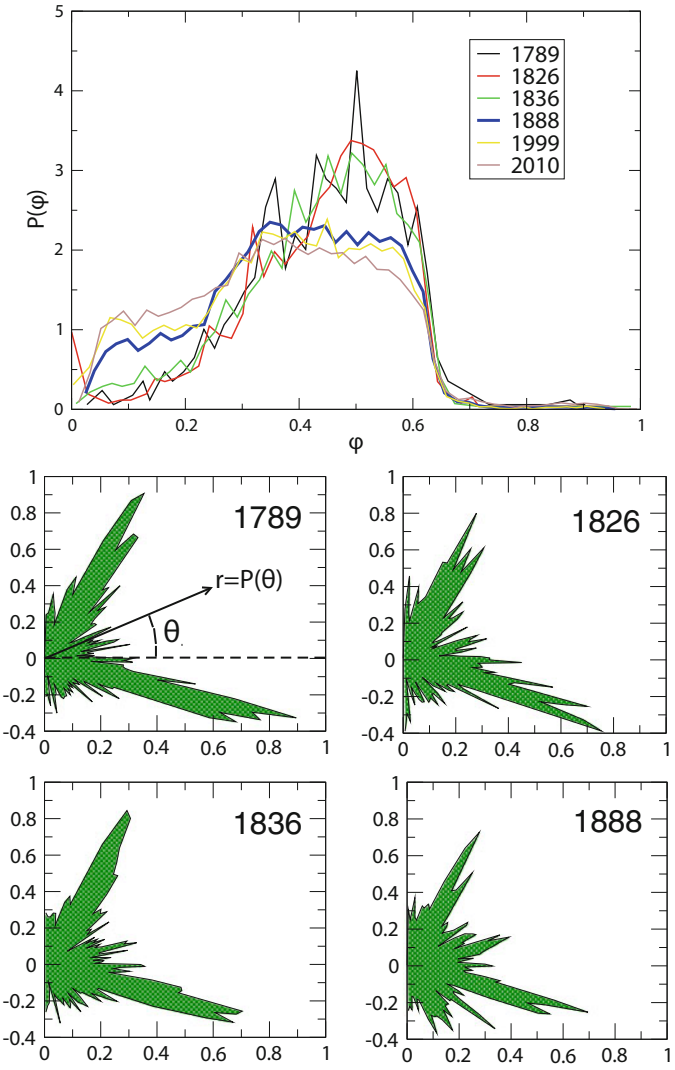

Fig. 12 (*Top*) Probability distribution of the ϕ shape factor for the blocks at different years. Until 1836, this distribution is stable and we observe a dramatical change during the Haussmann period with a larger abundance of blocks with small value of ϕ. These small values correspond to elongated rectangle or triangles created by streets crossing the existing geometry at various angles. (*Bottom*) Radial representation of the angle distribution of road segments for 1789, 1826, 1836, 1888. The radial distance r in this plot represents the probability to observe a street with angle θ: $r = P(\theta)$ with $\theta \in [-\pi/2, \pi/2]$ and $P(\theta)$ is the probability to observe an oriented road with angle θ with the *horizontal line* (see first panel, *top left*). Until 1836, the distribution is peaked around two values separated by approximately 90° and in 1888, we observe an important fraction of diagonals and other lines at intermediate angles

4 Discussion and Perspectives

We described quantitatively the evolution of the street network in two different cases. In general, we observe a trend towards a larger number of 4-ways junctions, as opposed to an earlier structure of 3-ways junctions. Our results also reveal a clear signature of urbanization on the evolution of the shape and size of land cells, which become more homogeneously distributed and square-shaped. These structural transformations appear to be the result of the interplay between two concurrent dynamics, namely densification and exploration. While exploration is typical of the earliest historical periods of urbanization, densification predominates in the latest.

Another interesting feature of the evolution of theses systems is the stability of the structure of most central streets over time: the most central streets largely coincide with the oldest ones. This is a quite remarkable result if we consider the huge modifications that can happen during 200 years of evolution. Central roads appear therefore to constitute a robust spatial backbone which remains stable over time, and characterizes the evolution of the road system as a continuous expansion and reinforcement of pre-existing structures rather than as a sharp switch towards radically new configurations.

In the particular case of the city of Paris, we could quantify the effect of central planning. Our results reveal that most indicators follow a smooth evolution, dominated by a densification process, despite the important perturbation that happened during Haussmann. The important quantitative signature of central planning appears to be the spatial reorganization of the most central nodes, in contrast with other regions where self-organization dominated and which didn't experience such a large-scale structure modification. This structural reorganization was obtained by the creation at a large scale of new roads and avenues (and the destruction of older roads) which do not follow the constraints of the existing geometry. These new roads do not follow the densification/exploration process but appear at various angles and intersect with many other existing roads.

While the natural, self-organized evolution of roads seems in general to be local in space, Haussmann modifications took place during a relatively short time and at a large spatial scale by connecting important nodes which are far away in the network. Following the Haussmann interventions, the natural processes take over on the modified substrate. It is unclear at this stage if Haussmann modifications were optimal and more importantly, if they were at a certain point inevitable and would have happened anyway (due to the high level of congestion for example). More work, with more data on a larger spatial scale are probably needed to study these important questions.

All these different results suggest that the evolution of a road network results from the superimposition of continuous, local growth processes and punctual changes operating at large spatial scales, opening new directions for the modelling of these systems.

Acknowledgements I thank my collaborators, colleagues, students and postdocs for stimulating discussions on street networks and other urban subjects: M. Batty, H. Berestycki, P. Bordin, R. Gallotti, M. Gribaudi, V. Latora, T. Louail, R. Louf, V. Nicosia, S. Porta, C. Roth, E. Strano.

References

1. UN Population division, http://www.unpopulation.org (accessed october 2014)
2. UN-Habitat, *Planning Sustainable Cities* (United Nations Human Settlements Programme, Nairobi, 2010)
3. B.L. Turner II, E.F. Lambin, A. Reenberg, The emergence of land change science for global environmental change and sustainability. Proc. Natl. Acad. Sci. (USA) **104**, 20666 (2007)
4. M. Batty, *The New Science of Cities* (MIT, Cambridge, 2013)
5. P. Haggett, R.J. Chorley, *Network Analysis in Geography* (Edward Arnold, London, 1969)
6. T. Louail et al., From mobile phone data to the spatial structure of cities. arXiv:1401.4540 (2014)
7. R. Louf, M. Barthelemy, Modeling the polycentric transition of cities. Phys. Rev. Lett. **111**, 198702 (2013)
8. R. Louf, M. Barthelemy, From mobility patterns to scaling in cities. arXiv preprint arXiv:1401.8200 (2014)
9. C. Roth, S.M. Kang, M. Batty, M. Barthelemy, A long-time limit of world subway networks. J. R. Soc. Interface **9**, 2540–2550 (2012)
10. F. Xie, D. Levinson, Modeling the growth of transportation networks: a comprehensive review. Netw. Spat. Econ. **9**(3), 291–307 (2009)
11. B. Jiang, C. Claramunt, Topological analysis of urban street networks. Environ Plan B Plan Design **31**, 151–162 (2004)
12. S. Marshall, *Streets and Patterns* (Spon Press, Abingdon, 2006)
13. P. Crucitti, V. Latora, S. Porta, Centrality measures in spatial networks of urban streets. Phys. Rev. E **73**, 0361251-5 (2006)
14. A. Cardillo, S. Scellato, V. Latora, S. Porta, Structural properties of planar graphs of urban street patterns. Phys. Rev. E **73**, 066107 (2006)
15. S. Porta, P. Crucitti, V. Latora, The network analysis of urban streets: a primal approach. Environ Plan B Plan Design **33**, 705–725 (2006)
16. S. Lämmer, B. Gehlsen, D. Helbing, Scaling laws in the spatial structure of urban road networks. Physica A **363**, 89 (2006)
17. J. Buhl, J. Gautrais, N. Reeves, R.V. Soé, S. Valverde, P. Kuntz, G. Theraulaz, Topological patterns in street networks of self-organized urban settlements. Eur. Phys. J. B **49**, 513 (2006)
18. F. Xie, D. Levinson, Measuring the structure of road networks. Geogr. Anal. **39**, 336–356 (2007)
19. M. Barthelemy, A. Flammini, Modeling urban street patterns. Phys. Rev. Lett. **100**, 138702 (2008)
20. T. Courtat, C. Gloaguen, S. Douady, Mathematics and morphogenesis of cities: a geometrical approach. Phys. Rev. E **83**, 036106 (2011)
21. E. Strano, V. Nicosia, V. Latora, S. Porta, M. Barthelemy, Elementary processes governing the evolution of road networks. Sci. Rep. **2**, 296 (2012)
22. M. Barthelemy, P. Bordin, H. Berestycki, M. Gribaudi, Self-organization versus top-down planning in the evolution of a city. Sci. Rep. **3**, 2153 (2013)
23. M. Barthelemy, Spatial networks. Phys. Rep. **499**, 1–101 (2011)
24. B. Hillier, J. Hanson, *The Social Logic of Space* (Cambridge University Press, Cambridge, 1984)
25. A.P. Masucci, D. Smith, A. Crooks, M. Batty, Random planar graphs and the London street network. Eur. Phys. J. B **71**, 259 (2009)

26. L.C. Freeman, A set of measures of centrality based on betweenness. Sociometry **40**, 35 (1977)
27. B.M. Yerra, D.M. Levinson, The emergence of hierarchy in transportation networks. Ann. Reg. Sci. **39**(3), 541 (2005)
28. S. Scellato, A. Cardillo, V. Latora, S. Porta, The backbone of a city. Eur. Phys. J. B **50**, 221–225 (2006)
29. S. Porta, V. Latora, F. Wang, S. Rueda, E. Strano, S. Scellato, L. Latora, Street centrality and the location of economic activities in Barcelona. Urban Stud. **49**(7), 1471–1488 (2012)
30. P. Geddes, R.T. LeGates, F. Stout, *Cities in Evolution*, vol. 27 (Williams & Norgate, London, 1949)
31. L. Mumford, *The City in History* (Harcourt Brace, New York, 1961)
32. H.A. Makse, S. Havlin, H.E. Stanley, Modelling urban growth patterns. Nature **377**, 608 (1995)
33. M. Fujita, P.R. Krugman, A.J. Venables, *The Spatial Economy: Cities, Regions and International Trade* (MIT, Cambridge, 2001)
34. M. Batty, *Cities and Complexity* (MIT, Cambridge, 2005)
35. S. Angel, S.C. Sheppard, D.L. Civco, *The Dynamics of Global Urban Expansion* (The World Bank, Washington, DC, 2005)
36. L.M.A. Bettencourt, J. Lobo, D. Helbing, C. Kuehnert, G.B. West, Growth, innovation, scaling, and the pace of life in cities. Proc. Natl. Acad. Sci. (USA) **104**, 7301 (2007)
37. M. Batty, S. Marshall, Centenary paper: the evolution of cities: Geddes, Abercrombie and the new physicalism. Town Plan. Rev. **80**, 551 (2009)
38. E. Glaeser, Cities, productivity, and quality of life. Science **333**, 592 (2011)
39. D. Jordan, *Transforming Paris: The Life and Labors of Baron Haussmann* (University of Chicago Press, Chicago, 1995)
40. I. Samuels, P. Panerai, J. Castex, J.C.C. Depaule, *Urban Forms* (Routledge Publishers, Abingdon, 2012)

Spatio-Temporal Traffic Pattern Recognition Based on Probe Vehicles

Hubert Rehborn and Micha Koller

Abstract Ubiquitous mobile probe data give new opportunities for the precise reconstruction of congested traffic situations. Kerner's three-phase traffic theory (Kerner, The physics of traffic. Springer, Berlin/Heidelberg/New York, 2004; Introduction to modern traffic flow theory and control. Springer, Berlin/Heidelberg, 2009) is the theoretical fundament for a review of the probe data analysis presented in this paper. The methodology of the approach developed initially in Kerner et al. (Physica A 392:221–251, 2013), will be illustrated and evaluated with empirical examples from a German field trial. The mobile probes are processed with a three-phase traffic state recognition while the vehicles drive through a spatio-temporal congested traffic pattern, i.e., they pass synchronized flow regions and/or wide moving jams. In the traffic control center, the traffic states from all communicating mobile probes are fused depending on the related traffic phase. The quality of the reconstructed traffic pattern using the mobile probes can be correlated with the reconstruction based on stationary detectors. Therefore, we can conclude which amount of mobile probes give the same information accuracy as roadside detectors at certain distances. A microscopic traffic simulation based on Kerner-Klenov traffic model (Kerner and Klenov, J Phys A Math Gen 35:L31–L43, 2002; Phys Rev E 68:036130, 2003; J Phys A Math Gen 37:8753–8788, 2004; Phys Rev E 80:056101, 2009) has given us an environment for developing, testing and evaluation of the traffic reconstruction algorithms. The car-to-infrastructure field trial with more than 120 vehicles communicating with the traffic control center for the duration of 6 month in the German federal state of Hessen produces a huge amount of empirical data. The paper illustrates results of the congested traffic recognition and jam front detection. We will show that 2 % communicating probe vehicles of the total flow rate give the opportunity of precise jam front warnings and, in addition, the same data quality as detectors of 1–2 km distances.

H. Rehborn (✉) • M. Koller
Daimler AG, HPC: 059-X832, D-71063 Stuttgart, Germany
e-mail: hubert.rehborn@daimler.com; micha.koller@daimler.com

M. Chraibi et al. (eds.), *Traffic and Granular Flow '13*,
DOI 10.1007/978-3-319-10629-8_39

1 Introduction

Nowadays the stationary detectors that are often installed, used and have their data offered by public authorities will become more and more superfluous for traffic services because mobile probes from vehicles (i.e., "probe vehicles") are made available anywhere in the road network. It has been a widely discussed question how much probe vehicle data is needed to replace such detector data. We believe that spatio-temporal traffic patterns should be recognized in a certain quality based on a sufficient penetration rate of probe vehicles in the traffic flow. This paper reveals a data fusion approach which combines stationary and mobile probe data and compares the reconstruction quality which can be achieved with each of the two sources.

2 Elements of Kerner's Three-Phase Traffic Theory

Figure 1 shows a spatio-temporal diagram which explains qualitatively Kerner's three phase traffic theory. Free flow is drawn as white. At a specific time and location a traffic breakdown occurs, which is a phase transition from free to synchronized flow (drawn as yellow area). Synchronized flow stays primarily fixed at a bottleneck and disappears after several hours only. Within the area of synchronized flow caused by further disturbances a wide moving jam can emerge (marked as red area). Wide moving jams propagate upstream over time with a constant velocity of the downstream front of the wide moving jam. The downstream front propagation speed is a characteristic parameter of this congested traffic phase and about −15 km/h (e.g., [1,2]). The black line in the diagram symbolizes one probe vehicle. The vehicle has to decelerate sharply if it reaches the upstream front of the wide moving jam and only after passing it can accelerate again to free flow. A larger number of vehicles would allow reconstructing the congested traffic pattern if the traffic state changes are combined with a specific data fusion algorithm.

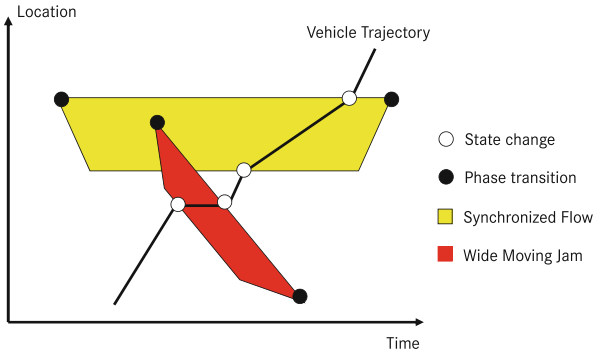

Fig. 1 Traffic state changes and traffic phase transitions a vehicle experiences on its way through a spatio-temporal congested traffic pattern

3 Methodology of the Data Fusion Approach

The overview of the approach is illustrated in Figs. 2 and 3. A stochastic Kerner-Klenov traffic simulation [3–6] allows an analysis of the microscopic vehicle behavior which has led to a congested pattern which is qualitatively similar to Fig. 1. In the microscopic data analysis we can change the penetration rate of probe vehicles in the total traffic flow and, therefore, the reconstruction algorithms can be developed and tested. Details of those traffic phase dependent algorithms can be found in [8] and [9]. Basically, the probe vehicles send their individual driving paths to the control center, the traffic state changes are derived there and then all these traffic state changes will be composed in a meaningful way, i.e., regions of synchronized flow and wide moving jams are built-up by a number of traffic state changes which are spatio-temporally close enough together in the neighborhood. Probe vehicles at closer distances pass the same traffic phase region and this fact has been used to develop the fusion algorithms (see [8] for details).

To realize jam front warnings it is enough to have vehicle probe data of 2 % of the current traffic flow available at a control center because the fronts of propagating wide moving jams can then be observed with sufficient accuracy (Fig. 3). To know currently and precise the very dangerous and sharp fronts between free flowing traffic and a wide moving jam would be very important for the safety of each driver: an upstream warning could be given that a wide moving jam front propagates upstream in the direction of the individual driver. The vehicle and/or the driver could

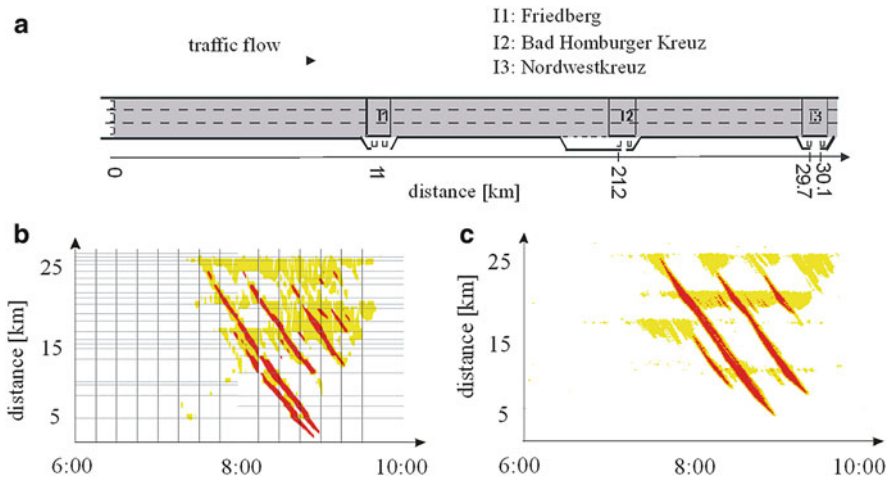

Fig. 2 Methodology: (**a**) A5 highway section. (**b**) ASDA/FOTO [1, 2, 7] pattern reconstruction based on detector data on 10th Dec., 2009. (**c**) Simulations of (**b**) with Kerner-Klenov stochastic microscopic three-phase traffic flow model

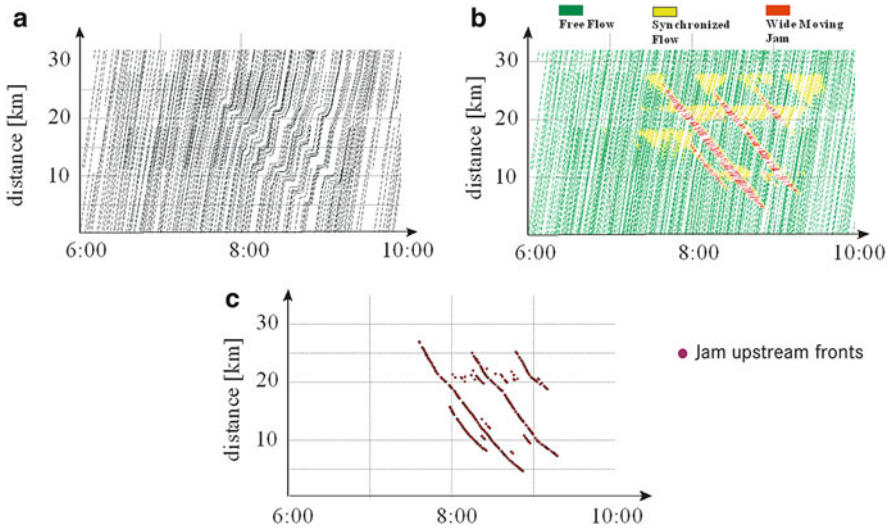

Fig. 3 Methodology: (**a**) Simulated vehicle trajectories of random distributed 2 % probe vehicles within the congested pattern in Fig. 2c. (**b**) Traffic state detection for probe vehicles in (**a**). (**c**) Jam warning messages by probe vehicles in (**a**)

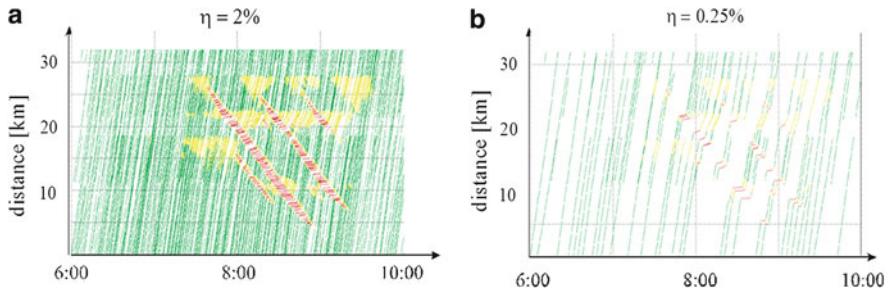

Fig. 4 Results of traffic state detection at different penetration rates of probe vehicles: (**a**) 2 % and (**b**) 0.25 %

be informed about the upcoming front before it is detectable and/or visible for the vehicle. If we use a traffic state detection algorithm for probe vehicle data and vary the penetration rates, one can see that qualitatively the congested pattern can be reconstructed at high quality with 2 % of probe vehicles (Fig. 4a) – less percentages would mean less quality and with 0.25 % it is very difficult to understand and detect any current traffic congestion. The details of these investigations with a mathematical analysis can be found in [9].

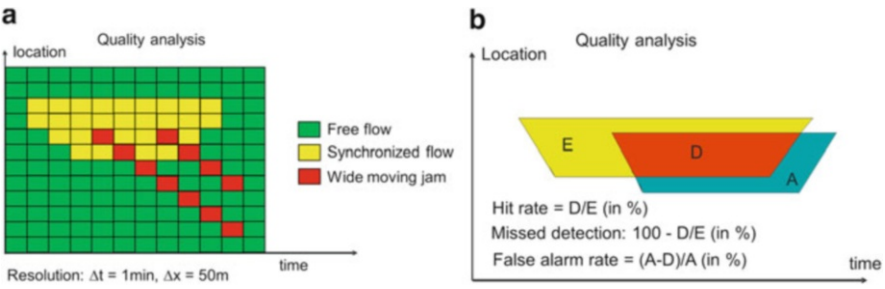

Fig. 5 (**a**) Time and space resolution of empirical data. (**b**) Definition of hit and failure rates

4 Reconstruction Quality

To explain the approach to determine the reconstruction quality, Fig. 5a shows a spatial and temporal discrete resolution of a congested traffic pattern: each reconstructed congestion has in each rectangle of this resolution one of three traffic states which then can be compared to each other. For the calculation of the related hit and failure rates we use a general definition illustrated in Fig. 5b: if we detect a kind of "ground truth" reality, e.g., by detectors and ASDA/FOTO models (shown in yellow), the data source of the probe vehicles can give a detection rate, missed detection rate and the false alarm rate, which is very important for the traffic service quality: because traffic congestion is a more or less negative information and a driver would probably less accept a high number of false alarms, but is interested in a very high detection rate. In our data fusion software solution it is possible to change the data sources for the evaluation approach: the probe data can be chosen as "ground truth" reality and be compared with the detector data and vice versa.

5 Field Trial Results

Within the simTD-field trial ("Sichere und Intelligente Mobilität – Testfeld Deutschland") up to 120 vehicles have been equipped to send their driving paths via WLAN/GSM communication to the traffic control center. The examination of possibilities of the traffic data fusion from different sources was one part of the field trial. Therefore, it was necessary that the vehicles test drives should be organized to have as much as possible of probe vehicles on the same road section in a shorter time interval during traffic congestion. One day has been the 29th, Nov. 2012 on the A5-South road section (Fig. 6): on the left the reconstructed congestion based on detectors and ASDA/FOTO models, on the right the green trajectories of the probes and the reconstruction of congested traffic phases. The related hit and failure rates reveal that the hit rates for wide moving jams are higher (and the failure rates

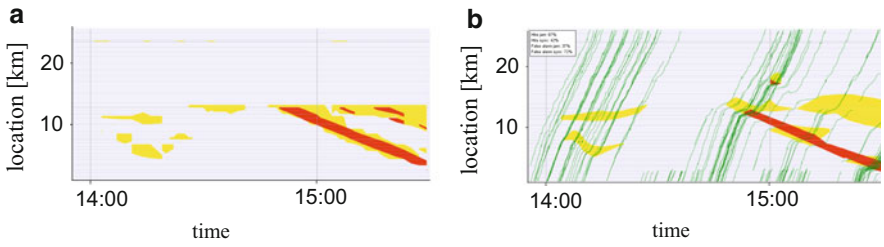

Fig. 6 (**a**) Traffic state reconstruction based on detectors on A5-South, 29th Nov., 2012 (**b**) Achieved hit and failure rates: Hit rate for wide moving jam is 67 %, hit rate for synchronized flow is 42 %, false alarm rate for wide moving jam is 37 % and false alarm rate for synchronized flow is 72 %

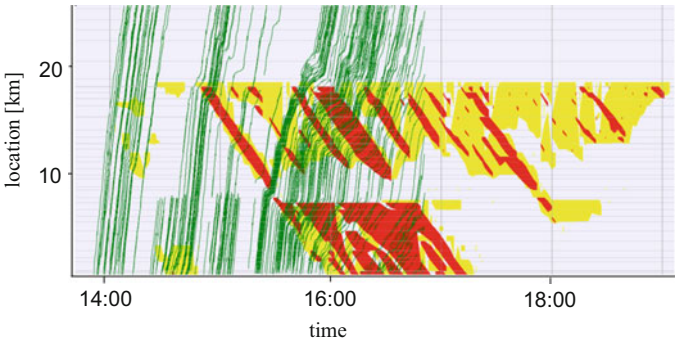

Fig. 7 Overview on traffic situation reconstructed based on detectors on A5-South, 29th Nov., 2012

lower) in comparison to synchronized flow: the propagating structure of the wide moving jams can be detected more easy due to its stability while the synchronized flow regions are more difficult to reconstruct with the same amount of probe data.

Figure 7 shows the overview of the total congested situation of the same day as in Fig. 6: the green trajectories show the time interval when vehicle tests have been performed. It is obvious here in this case that the congestion duration is longer than the field driving tests. Therefore, the total traffic congestion over time can in this example only be reconstructed with the roadside detectors and the ASDA/FOTO models [7].

As one final technical space-time diagram of this paper illustrating a variety of data sources with comparable results, Fig. 8 shows three different data sources for the same traffic congestion on a 50 km road stretch of the A5 on 12th May, 2010. Figure 8a shows more than 6 h of traffic congestions reconstructed with ASDA/FOTO models: several wide moving jams are following one another in a stable propagating over the whole freeway section (in addition, independent from bottlenecks like on- and off-ramps). Figure 8b presents the TomTom GPS-based probe data from navigation applications like personal navigation devices (PND)

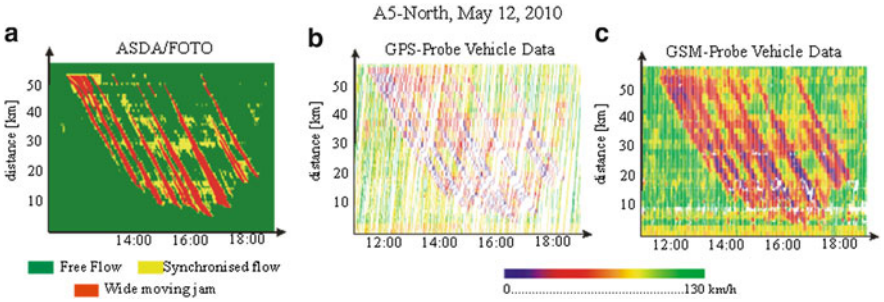

Fig. 8 Comparison of congested traffic pattern measured on 12th May, 2010 on A5-North, Germany with detector data processed with (**a**) ASDA/FOTO models (**b**) with on-line TomTom's GPS and (**c**) GSM probe vehicle data for this day

or navigation applications used in smartphones: these data are sent as vehicle trajectories with probe data in 10 sec intervals transferred to the control center every 2 min. Technically, Fig. 8c pictures GSM-probe vehicle data from TomTom which allow a precise reconstruction especially of the wide moving jams: on-call data from base stations of the GSM mobile network make the propagation of several wide moving jams visible [10]. In the given example, the number of GPS probes is in the order of 1 % (i.e. about 40–60 probe vehicles per hour on a three-lane highway with a maximum flow rate of about 6,000 vehicles per hour) and the number of GSM probes has been even more than three times higher.

Conclusions

This paper reveals that traffic congestion recognition will be performed in the future more and more based on mobile probe data. We show that a Kerner-Klenov-Wolf traffic model can simulate a microscopic driver behavior leading to a collective congestion which is in good accordance with a real congested traffic situation measured by detectors and reconstructed by the models ASDA/FOTO [7].

The three-phase traffic theory gives the fundament for the development of data fusion algorithm for both stationary detector data and mobile probe data. The German field trial with about 120 vehicles has produced a large amount of empirical data which we have used to develop, test and evaluate the data fusion algorithms.

The reconstruction quality of a congested traffic situation using 2 % communicating probe vehicles of the total flow rate is similar to the quality of a traffic situation which was reconstructed based on data from stationary detectors which has 1–2 km distances. Examinations show that today a traffic service provider like TomTom is able to provide probe data of high quality

(continued)

up to 2 % of the total flow rates on all highways at any time. Such high penetration rates of probe vehicles will offer future opportunities for new traffic services, e.g., precise jam front warnings.

Acknowledgements We would like to thank the federal government of Hessen for their permission of our participation in the field trial project and TomTom for the preparation of their anonymous aggregated probe vehicle data.

References

1. B.S. Kerner, *The Physics of Traffic* (Springer, Berlin/Heidelberg/New York, 2004)
2. B.S. Kerner, *Introduction to Modern Traffic Flow Theory and Control* (Springer, Berlin/Heidelberg, 2009)
3. B.S. Kerner, S.L. Klenov, J. Phys. A Math. Gen. **35**, L31–L43 (2002)
4. B.S. Kerner, S.L. Klenov, Phys. Rev. E **68**, 036130 (2003)
5. B.S. Kerner, S.L. Klenov, J. Phys. A Math. Gen. **37**, 8753–8788 (2004)
6. B.S. Kerner, S.L. Klenov, Phys. Rev. E **80**, 056101 (2009)
7. B.S. Kerner, H. Rehborn, M. Aleksic, A. Haug, Transp. Res. C **12**, 369–400 (2004)
8. B.S. Kerner, H. Rehborn, R.P. Schäfer, S.L. Klenov, J. Palmer, S. Lorkowski, N. Witte, Physica A **392**, 221–251 (2013). doi:10.1016/j.physa.201207.070
9. J. Palmer, Fahrzeugautonome und verteilte Erkennung räumlich-zeitlicher Verkehrsmuster zur Nutzung in Fahrerassistenzsystemen. PhD thesis, University of Tübingen, 2012
10. R.P. Schäfer, S. Lorkowski, N. Witte, J. Palmer, H. Rehborn, B.S. Kerner, A study of TomTom's probe vehicle data with three phase traffic theory. Traffic Eng. Control **52**(5), 225–230 (2011)

From Random Walker to Vehicular Traffic: Motion on a Circle

Hans Weber, Reinhard Mahnke, and Jevgenijs Kaupužs

Abstract Driving of cars on a highway is a complex process which can be described by deterministic and stochastic forces. It leads to equations of motion with asymmetric interaction and dissipation as well as to new energy flow law already presented at previous TRAFFIC AND GRANULAR FLOW meetings. Here we consider a model, where motion of an asymmetric random walker on a ring with periodic boundary conditions takes place. It is related to driven systems with active particles, energy input and depot. This simple model can be further developed towards more complicated ones, describing vehicular or pedestrian traffic. Three particular cases are considered, starting with discrete coordinate and time, then making time continuous and, finally, considering a drift–diffusion equation in a continuum limit.

1 Introduction

Inspired by our previous work on models of vehicular motion and traffic breakdown in one–dimensional systems with periodic boundary conditions [1, 2]; we turn our attention to a different set of models obeying the same geometrical constraints. Random walk is one of basic models in understanding processes across a wide spectrum of scientific disciplines with a large variety of different applications [3, 4]. Random walk of independent particles is an important first step towards understanding of stochastic transport in more complex systems with interactions [5]. Our aim is to

H. Weber (✉)
Department of Physics, Luleå University of Technology, SE–97187 Luleå, Sweden
e-mail: Hans.Weber@ltu.se

R. Mahnke
Institute of Physics, Rostock University, D–18051 Rostock, Germany
e-mail: reinhard.mahnke@uni-rostock.de

J. Kaupužs
Institute of Mathematical Sciences and Information Technologies, University of Liepaja, Liepaja LV-3401, Latvia

Institute of Mathematics and Computer Science, University of Latvia, LV–1459 Riga, Latvia
e-mail: kaupuzs@latnet.lv

M. Chraibi et al. (eds.), *Traffic and Granular Flow '13*,
DOI 10.1007/978-3-319-10629-8_40

consider asymmetric random walks of different type and find relations between them. In particular, we consider different cases, where each of two variables – position and time, can be either discrete or continuous. The following idea is to develop these models of independent random walk towards models of traffic flow.

2 Stochastic Motion on a Ring with Discrete Position and Time

We start our consideration with a discrete model of asymmetric random walk on a ring. The probability $P(x_m, t_n)$ to find the walker at a position x_m at time moment t_n is given by Markov chain

$$P(x_m, t_n + \tau) = p\, P(x_m - a, t_n) + q\, P(x_m + a, t_n)\ , \tag{1}$$

where p and q are jumping probabilities for $x_m \to x_m + a$ and $x_m \to x_m - a$, respectively, such that $p + q = 1$. The discrete position and time are given by

$$x_m = a\, m \quad , \quad m = 0, 1, 2, \ldots, M - 1 \tag{2}$$

$$t_n = \tau\, n \quad , \quad n = 0, 1, 2, \ldots \tag{3}$$

The motion takes place on a ring of length $x_M = a\, M = L$, with periodic boundary condition $P(x_m, t_n) = P(x_m + L, t_n)$, starting at certain position x_0, which is not necessarily zero. Thus the initial condition is

$$P(x_m, t_0 = 0) = \delta_{x_m, x_0}\ . \tag{4}$$

In the following, we use the spatial Fourier transformation

$$\tilde{P}(k, t_n) = \sum_{m=0}^{M-1} P(x_m, t_n)\, e^{ikx_m}\ , \tag{5}$$

$$P(x_m, t_n) = \frac{1}{M} \sum_{k} \tilde{P}(k, t_n)\, e^{-ikx_m}\ . \tag{6}$$

with M discrete wave numbers $k = 2\pi l / L$ for $l = 0, 1, \ldots, M - 1$. It leads to the Markov chain

$$\tilde{P}(k, t_n + \tau) = \left(p\, e^{ika} + q\, e^{-ika}\right) \tilde{P}(k, t_n) \tag{7}$$

in the discrete k–space. Taking into account the initial condition (Eq. 4), we obtain

$$\tilde{P}(k, t_n) = \left(p\, e^{ika} + q\, e^{-ika}\right)^{t_n/\tau}\, e^{ikx_0} \ . \tag{8}$$

The inverse transformation (Eq. 6) generates the following solution

$$P(x_m, t_n) = \frac{1}{M} \sum_k \left(p\, e^{ika} + q\, e^{-ika}\right)^{t_n/\tau}\, e^{-ika(x_m - x_0)/a} \tag{9}$$

with

$$k' \equiv ka = 2\pi l/M \qquad , \qquad l = 0, 1, 2, \ldots, M-1 \ . \tag{10}$$

To consider the limit $M \to \infty$ we replace the sum by the integral as follows

$$\frac{1}{M} \sum_{k'} \ldots \quad \to \quad \frac{1}{2\pi} \int_{-\pi}^{\pi} \ldots \, dk' \ . \tag{11}$$

The periodic solution (Eq. 9) shows the diffusive relaxation from the initial sharp peak (Eq. 4) to steady state with or without drift depending on the asymmetry parameter $\Delta = p - q$. Using Δ instead of $p = 1 - q$ we get

$$\left(p\, e^{ika} + q\, e^{-ika}\right) = \cos(ka) + i\,\Delta \sin(ka) \tag{12}$$

and receive the solution (Eq. 9) in the following notation

$$P(x_m, t_n) = \frac{1}{M} \sum_k e^{-(\lambda'_k - i\,\lambda''_k)t_n}\, e^{-i\,k(x_m - x_0)} \tag{13}$$

$$= \frac{1}{M} \sum_k e^{-\lambda'_k t_n} \left[\cos(\lambda''_k t_n)\cos(k(x_m - x_0)) + \sin(\lambda''_k t_n)\sin(k(x_m - x_0))\right] \tag{14}$$

with

$$\lambda'_k = -\frac{1}{\tau} \ln\left(\sqrt{\cos^2(ka) + \Delta^2 \sin^2(ka)}\right) \ , \tag{15}$$

$$\lambda''_k = \frac{1}{\tau} \arctan\left(\Delta \tan(ka)\right) \ . \tag{16}$$

This rotating ($\Delta \neq 0$) random walker is, of course, not a model of traffic flow. This stochastic process explains drift–diffusive motion without interaction and active behaviour.

3 Stochastic Motion on a Ring with Discrete Position and Continuous Time

Let us now consider a model, where position is discrete, but the time t is continuous. In this case we have the master equation

$$\frac{\partial}{\partial t}P(x_m,t) = w_+ P(x_{m-1},t) + w_- P(x_{m+1},t) - [w_+ + w_-]P(x_m,t)\ . \tag{17}$$

Here $x_m = ma$, $m = 0, 1, 2, \ldots, M-1$ are the discrete coordinates, whereas w_+ and w_- are transition rates, which in this case are assumed to be constant. As before, motion is on a ring of length L (periodic boundary condition), starting at x_0. The solution of this problem for $x_0 = 0$ is given in [5] (Sect. 3.1), using somewhat different notations than here.

To obtain the solution, we use the Fourier transformation

$$\tilde{P}(k,t) = \sum_{m=0}^{M-1} P(x_m,t)e^{ikx_m} \tag{18}$$

$$P(x_m,t) = \frac{1}{M}\sum_k \tilde{P}(k,t)e^{-ikx_m} \tag{19}$$

with $k = 2\pi l/L$ for $l = 0, 1, 2, \ldots, M-1$. It gives the equation in the k–space

$$\frac{\partial \tilde{P}(k,t)}{\partial t} = \left[w_+ e^{ika} + w_- e^{-ika} - (w_+ + w_-)\right]\tilde{P}(k,t) = -\lambda_k \tilde{P}(k,t)\ , \tag{20}$$

where

$$\lambda_k = w_+(1 - e^{ika}) + w_-(1 - e^{-ika})\ . \tag{21}$$

The complex solution reads

$$\tilde{P}(k,t) = \tilde{P}(k,0)e^{-\lambda_k t}\ . \tag{22}$$

Using the initial condition $P(x_m,0) = \delta_{x_m,x_0}$ and (Eq. 18), we get $\tilde{P}(k,0) = e^{ikx_0}$. Inserting this and (Eq. 22) into (Eq. 19), we obtain the solution in the coordinate space,

$$\begin{aligned} P(x_m,t) &= \frac{1}{M}\sum_k e^{-\lambda_k t - ik(x_m - x_0)} \\ &= \frac{1}{M}\sum_k e^{-\lambda'_k t}\Big(\cos(\lambda''_k t)\cos(k[x_m - x_0]) + \sin(\lambda''_k t)\sin(k[x_m - x_0])\Big)\ . \end{aligned} \tag{23}$$

Here λ_k is the complex rate parameter, which is represented as $\lambda_k = \lambda'_k - i\lambda''_k$, where

$$\lambda'_k = (w_+ + w_-)(1 - \cos(ka)) \,, \tag{24}$$

$$\lambda''_k = (w_+ - w_-)\sin(ka) \,. \tag{25}$$

4 From Discrete to Continuous Time

The solution $P(x_m, t_n)$ (Eq. 14) of the model with discrete time and coordinate is different for odd and even n, i.e., it always makes jumps in time in such a way that it is zero for odd m and nonzero for even m at one time step and vice versa at the next time step. Therefore, we consider the probability function

$$\bar{P}(x_m, t_n) = \frac{1}{2}\Big(P(x_m, t_n) + P(x_m, t_n + \tau)\Big) \,, \tag{26}$$

which is obtained by an averaging over two successive time steps. This function is expected to be smoother in time. Considering two successive steps of the Markov chain (Eq. 1), we obtain the Markov chain

$$\bar{P}(x_m, t_n + \tau) = p\,\bar{P}(x_m - a, t_n) + q\,\bar{P}(x_m + a, t_n) \tag{27}$$

for $\bar{P}(x_m, t_n)$. If the initial condition for $P(x_m, t_n)$ is $P(x_m, 0) = \delta_{x_m, x_0}$, then for $\bar{P}(x_m, t_n)$ we have

$$\bar{P}(x_m, 0) = \frac{1}{2}\Big(q\,\delta_{x_m, x_0 - a} + \delta_{x_m, x_0} + p\,\delta_{x_m, x_0 + a}\Big) \,. \tag{28}$$

Taking into account that $p + q = 1$, we can write

$$\frac{\bar{P}(x_m, t_n + \tau) - \bar{P}(x_m, t_n)}{\tau} = \frac{p}{\tau}\,\bar{P}(x_m - a, t_n) + \frac{q}{\tau}\,\bar{P}(x_m + a, t_n) - \frac{p + q}{\tau}\,\bar{P}(x_m, t_n) \,. \tag{29}$$

The expression on the left hand side of (Eq. 29) is approximately equal to the time derivative $\partial\bar{P}(x_m, t)/\partial t$ at $t = t_n$ for $\tau \ll t_n$, i.e., for a large number of time steps or large time scale, when the probability distribution $\bar{P}(x_m, t)$ (but not $P(x_m, t)$) changes very slightly in one time step. It leads to the master equation

$$\frac{\partial\bar{P}(x_m, t)}{\partial t} = w_+\,\bar{P}(x_m - a, t) + w_-\,\bar{P}(x_m + a, t) - (w_+ + w_-)\,\bar{P}(x_m, t) \,, \tag{30}$$

where $w_+ = p/\tau$ and $w_- = q/\tau$ are the transition rates. Here we consider the limit $t/\tau \to \infty$ for a finite τ, since the transition rates have to be finite.

5 Stochastic Motion on a Ring with Continuous Position and Time

We consider now the limit $a \to 0$ in the master equation (Eq. 17) or (Eq. 30). These two equations are similar, with the only difference that (Eq. 30) is for the averaged over two successive time steps probability distribution. We can rewrite (Eq. 17) as

$$\frac{\partial P(x_n,t)}{\partial t} = a^2 \frac{w_+ + w_-}{2} \frac{P(x_n+a,t) - 2P(x_n,t) + P(x_n-a,t)}{a^2} - a\,(w_+ - w_-) \frac{P(x_n+a,t) - P(x_n-a,t)}{2a} . \tag{31}$$

Considering the probability density $p(x,t) = P(x,t)/a$ as a continuous function of coordinate x and taking the limit $a \to 0$, we obtain from (Eq. 31) the drift–diffusion equation

$$\frac{\partial p(x,t)}{\partial t} = D \frac{\partial^2 p(x,t)}{\partial x^2} - v_{\text{drift}} \frac{\partial p(x,t)}{\partial x} \tag{32}$$

with the diffusion coefficient D and drift coefficient v_{drift} given by

$$D = \frac{a^2}{2}\Big(w_+ + w_-\Big) \tag{33}$$

$$v_{\text{drift}} = a\,(w_+ - w_-) . \tag{34}$$

To solve (Eq. 32) with the initial condition $p(x,0) = \delta(x - x_0)$, we use the Fourier transformation

$$\tilde{p}(k,t) = \int_0^L p(x,t) e^{ikx} dx \tag{35}$$

$$p(x,t) = \frac{1}{L} \sum_k \tilde{p}(k,t) e^{-ikx} dk , \tag{36}$$

where $k = 2\pi l/L$ with $l = 0, \pm 1, \pm 2, \ldots$ The Fourier–transformed drift–diffusion equation reads

$$\frac{\partial \tilde{p}(k,t)}{\partial t} = (-Dk^2 + ik\, v_{\text{drift}})\, \tilde{p}(k,t) . \tag{37}$$

The solution is

$$\tilde{p}(k,t) = \tilde{p}(k,0)\, e^{-\lambda_k t} \ , \tag{38}$$

where the complex rate parameter $\lambda_k = \lambda_k' - i\,\lambda_k''$ is given by

$$\lambda_k' = Dk^2 \ , \tag{39}$$

$$\lambda_k'' = k\, v_{\text{drift}} \ . \tag{40}$$

Using the initial condition $p(x,0) = \delta(x - x_0)$, we obtain $\tilde{p}(k,0) = e^{ikx_0}$ and thus

$$\tilde{p}(k,t) = e^{-\lambda_k t + ikx_0} \ . \tag{41}$$

The solution in the coordinate space

$$\begin{aligned} p(x,t) &= \frac{1}{L}\sum_k e^{-(\lambda_k' - i\,\lambda_k'')t}\, e^{-ik(x-x_0)} \\ &= \frac{1}{L}\sum_k e^{-\lambda_k' t}\Big(\cos(\lambda_k'' t)\cos(k[x-x_0]) + \sin(\lambda_k'' t)\sin(k[x-x_0])\Big) \end{aligned} \tag{42}$$

is obtained via the transformation (Eq. 36).

6 The Optimal Velocity Model for Highway Traffic

There are several models for highway traffic. We will restrict ourselves to a model for vehicular traffic on a single lane. Vehicles in the model are subjected to periodic boundary conditions and they cannot overtake. The vehicle, in the absence of other vehicles, drives at its maximum velocity. If other vehicles are present the 'driver' has to take into account a safety distance to the next vehicle in front. This leads to an adaption of speed, the optimal velocity, as a vehicle in front is approached.

A widely used model in this context is the optimal velocity model (OVM) by Bando et al. [6, 7]. This is microscopic model assigning to each vehicle a velocity and a position. The motion is controlled by a set of coupled differential equations (Eq. 43). We integrate out the equations of motion of the OV model by a Runge

Kutta 4th order scheme. The Bando OVM is a deterministic model for traffic flow and is given by the equations

$$\begin{cases} \frac{d}{dt}v_i = \frac{1}{\tau}\left(v_{opt}(\Delta x_i) - v_i\right) & \frac{d}{dt}u_i = \left(u_{opt}(\Delta y_i) - y_i\right) \quad (a) \\ \frac{d}{dt}x_i = v_i & \frac{d}{dt}y_i = \frac{1}{b}u_i \quad (b) \\ v_{opt}\left(\Delta x_i\right) = v_{max}\frac{(\Delta x)^2}{D^2+(\Delta x)^2} & u_{opt}\left(\Delta y_i\right) = \frac{(\Delta y)^2}{1+(\Delta y)^2} \quad (c) \\ & b = \frac{D}{v_{max}\tau} \quad (d) \end{cases} \tag{43}$$

In the equations above the leftmost set defines the OV model. The velocity of the car i is v_i and its position is x_i. The control parameters are the maximum velocity v_{max}, τ and D (interaction distance), $v_{opt}(\Delta x)$ is the optimal velocity function and $\Delta x_i = x_{i+1} - x_i$ is the headway (bumper-to-bumper distance). The average homogeneous density of cars is $c = \frac{N}{L}$. The rightmost set of equations (43) are the same equations as the leftmost but in a dimensionless form. The dimensionless velocity of car i is u_i and its position is y_i. There is only one control parameter $b = \frac{D}{v_{max}\tau}$ in this formulation.

In Fig. 1 we illustrate by a series of 'snapshots' taken at different times in the development of a traffic configuration. The dimensionless set of equations (43) have been integrated out to give results for the density of vehicles as a function of position at three different instants of time. The parameters used are $N = 90$ the number of vehicles, $L = 61$ the length of the circular road and $b = 1.25$ as control parameter. In Fig. 1 we see a distinct feature, a maximum in the density of vehicles. Vehicles that have entered into this stretch of the circular road where the density is increased are in a queue. Whilst in the queue the vehicle has a low velocity. In the low density region the vehicles are more or less in the free flow regime and move with a velocity close the v_{max}.

Vehicles enter the queue from the left and exit on the right of the maximum density. The queue shifts its position to the left in the figures as time evolves. The leftmost figure is a snapshot of the earliest configuration of the three snapshots and the rightmost is the latest.

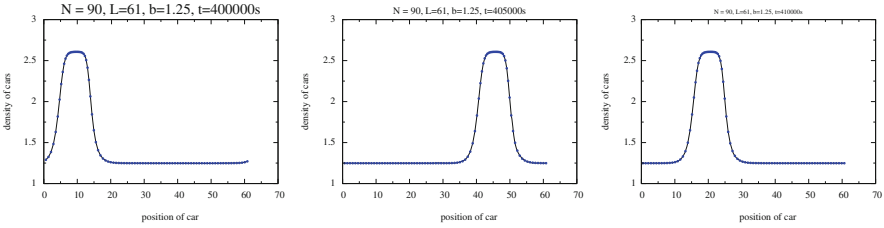

Fig. 1 The time development of a traffic queue, shown at three different instants. The equations (43) for $N = 90$, $L = 61$ and $b = 1.25$

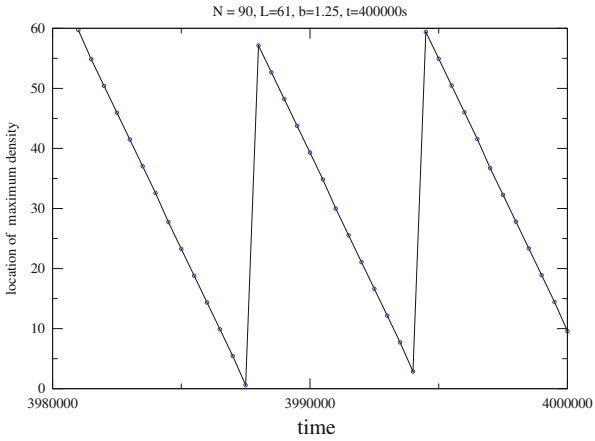

Fig. 2 The position of the maximum in Fig. 1 as a function of time. The slope is the velocity with which the maximum moves to the left

A property of the OV model is that the configuration of the queue in the limit $t \to \infty$ is stable as time evolves, ie the queue does not disperse. From the previous graphs Fig. 1 we can construct a figure that shows how the position of the maximum of the density evolves as a function of time t. In Fig. 2 the drift of the queue is shown as a function of time. The position of the queue is identified by the maximum of the distribution if Fig. 1. The drift velocity is the slope of the lines in Fig. 2. Note the slope is negative number as cars drive into the queue from the left (in Fig. 1) and exit on the right. Therefore the position of the maximum moves to the left in Fig. 1

7 Numerical Solutions for the Random Walker Model

In this section we will make a comparison between three simple models of random walkers constrained to move on a one dimensional road with periodic boundary conditions.

- Model 1: A random walker with discrete time and position defined by the equations in Sect. 2.
- Model 2: A random walker with continuous time and discrete position defined by the equations in Sect. 3.
- Model 3: A random walker with continuous time and position defined by the equations in Sect. 5.

7.1 Discrete Time and Position

The solution (Eq. 14) for a discrete asymmetric random walker on a ring is illustrated in Fig. 3. The probabilities are set to $p = 0.74$ for a step to the right

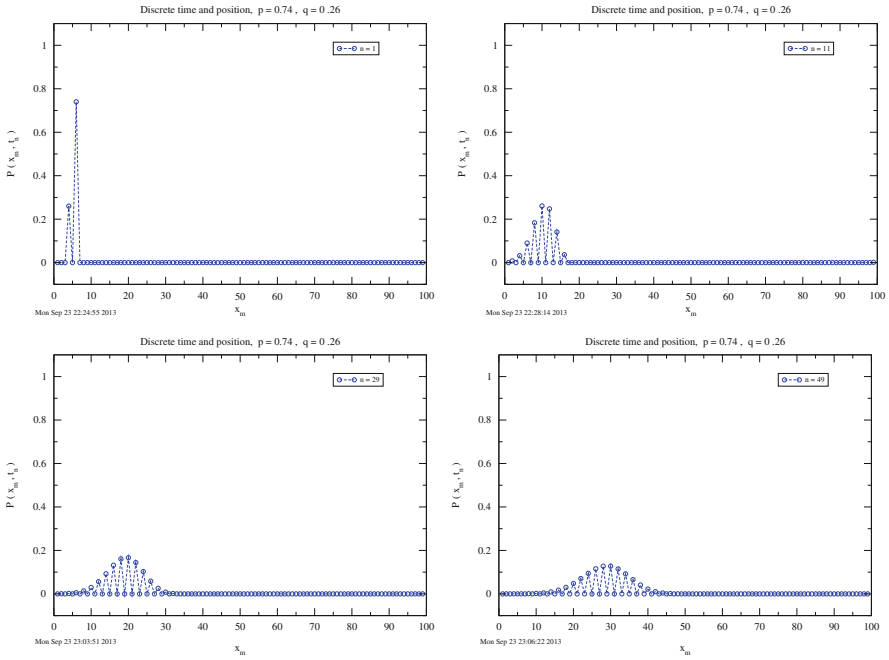

Fig. 3 The probability $P(x_m, t_n)$, given by Eq. (14), for a random asymmetric ($p = 0.74, q = 0.26$) walker to be at a position x_m at two different time moments. The initial starting position is set to $x_0 = 5$ at time $t = 0$

and $q = 0.26$ for a step to the left. The initial position of the walker is set to $x_0 = 5$. If one takes a careful look at Fig. 3 there seems to be a spiky appearance of the probability. This can easily be explained by the discreteness of the model. After one time step the walker will occupy positions 4 and 6. The walker jumps from odd to even positions and vice versa every time step, hence the spiky appearance of the probability.

7.2 Discrete Position and Continuous Time

The solution (Eq. 23) for a discrete asymmetric random walker with transition rates $w_+ = 0.75$ and $w_- = 0.25$ on a ring is illustrated in Fig. 4. The walker is started at position $x_m = 5$ at $t = 0$ and the graphs show the development of the probability distribution (Eq. 23) at four instants of time in units of τ.

From the graphs we can note two characteristics. The position of the maximum slowly drifts to the right as the walker is asymmetric and also that the distribution of the probability $P(x_m, t)$ gets smeared out as time increases.

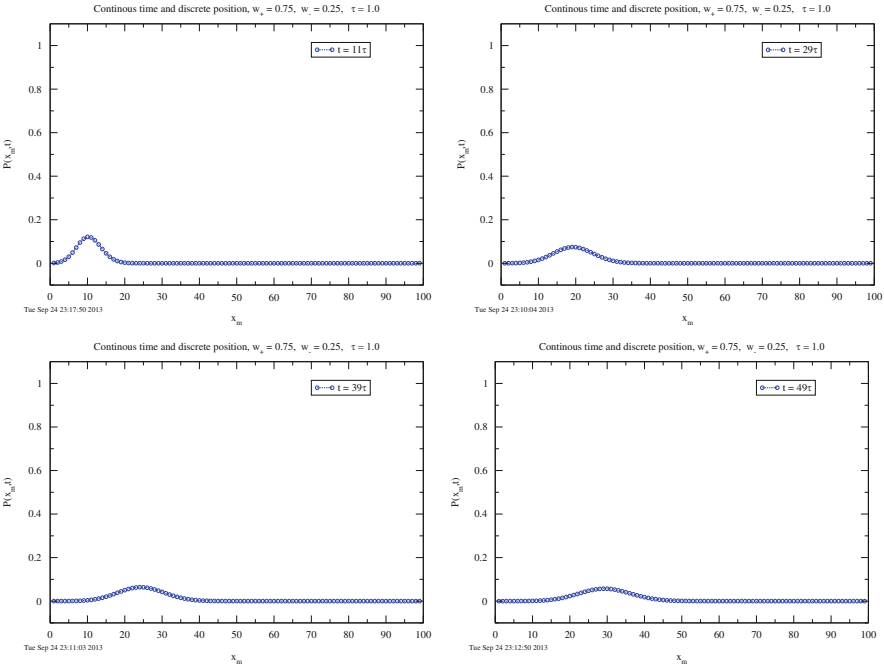

Fig. 4 The probability $P(x_m, t)$, given by Eq. (14), for a random asymmetric ($w_+ = 0.75, w_- = 0.25$) walker to be at a position x_m at two different time moments. The initial starting position is given by $x_0 = 5$ at time $t = 0$. The four graphs are for times $t = 11, 29, 39$ and $t = 49$ in units of τ

7.3 *Continuous Position and Time*

The solution Eq. (42) for the motion of a random walker on a ring with continuous position and time is illustrated in Fig. 5. The figures have the same appearance as the one (Fig. 4) for the discrete walker with continuous time presented in Sect. 7.2.

For the three random walker models discussed above we can note two characteristic features. As all three models where put into an asymmetric state the position of the maximum slowly drifts to the right in the Figs. 3–5. We can also tell that all three models have a dispersing distribution of the probability $P(x_m, t)$ as time increases. Eventually the homogeneous distribution will be reached as time goes to infinity.

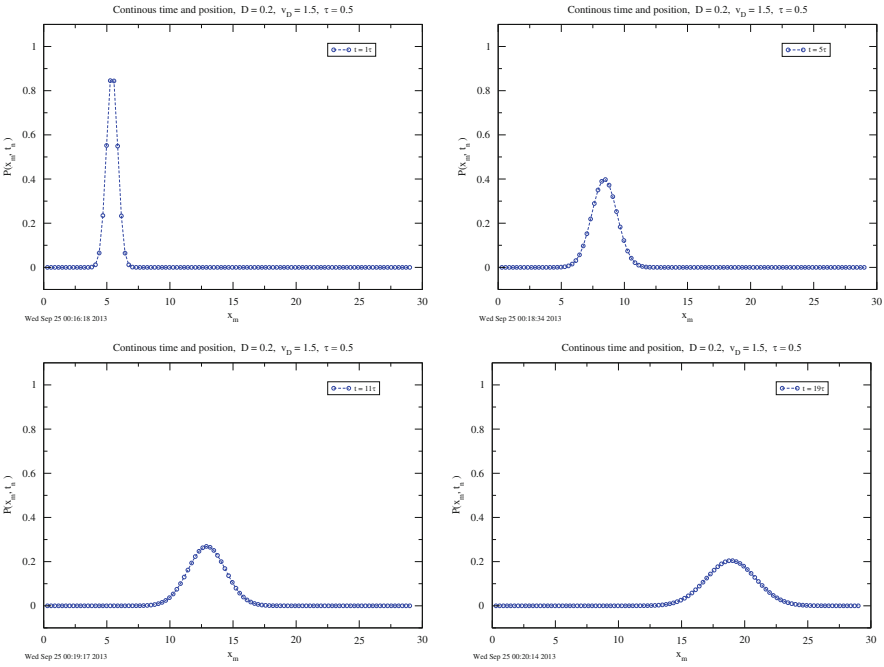

Fig. 5 The probability $P(x,t)$, given by (42), for a random ($v_D = 1.5, D = 0.2$) walker to be at a position x at four different time moments. The parameters of the models are $N = 99$ and $L = 29$. The initial starting position is given by $x_0 = (L-1)/6 = 4\frac{2}{3}$

8 Discussion

All the considered models in Sects. 2–5 describe a random walk of a single particle or, equivalently, of independent particles. These models include an asymmetry of the walker as a very important feature of traffic or pedestrian flow. However one should be careful as the three random walker models presented are not real models of traffic flow. Indeed, the considered solutions spread out with time due to the diffusion, and the long–time equilibrium state is described by a uniform distribution of the probability or probability density.

Continuous stochastic model of Ornstein-Uhlenbeck type [8] with 'staying together parameter' γ, drift or speed v, diffusion or stochasticity D

$$\frac{\partial}{\partial t}p(x,t) = -v\frac{\partial}{\partial x}p(x,t) + \gamma\frac{\partial}{\partial x}\left(xp(x,t)\right) + D\frac{\partial^2}{\partial x^2}p(x,t) \tag{44}$$

would be an appropriate extension of the drift–diffusion equation (Eq. 32), allowing us to describe a stable spatially non-homogeneous density distribution corresponding to a traffic jam, coexisting with free flow, or to stop–and–go waves.

Properties of the different models

- In the 'Bando Model' a steady state does not disperse. Whereas in the different realisations of the random walker there is dispersion. Except for special cases like $p = 0$ or $w_+ = 0$.
- The 'Bando Model' and the all the different realisations of the random walker show a well defined linear drift with a well defined drift velocity.

References

1. R. Mahnke, J. Kaupužs, J. Hinkel, H. Weber, Eur. Phys. J. B **57**, 463–471 (2007)
2. Ch. Liebe, R. Mahnke, J. Kaupužs, H. Weber, Vehicular motion and traffic breakdown: evaluation of energy balance, in *Traffic and Granular Flow'07* (Springer, Berlin, Orsay, France, 2009), pp. 381–388
3. C.W. Gardiner, *Handbook of Stochastic Methods* (Springer, Berlin, 2004)
4. J. Rudnick, G. Gaspari, *Elements of the Random Walk* (Cambridge University Press, Cambridge, 2004)
5. A. Schadschneider, D. Chowdhury, K. Nishinari, *Stochastic Transport in Complex Systems. From Molecules to Vehicles* (Elsevier, Amsterdam, 2011)
6. M. Bando, K. Hasebe, A. Nakayama, A. Shibata, Y. Sugiyama, Jpn. J. Indust. Appl. Math. **11**, 203 (1994); Phys. Rev. E **51**, 1035 (1995)
7. M. Bando, K. Hasebe, K. Nakanishi, A. Nakayama, A. Shibata, Y. Sugiyama, J. Phys. I Fr. **5**, 1389 (1995)
8. R. Mahnke, J. Kaupužs, I. Lubaschevsky, *Physics of Stochastic Processes. How Randomness Acts in Time* (Wiley-VCH, Weinheim, 2009)

Different Approaches to the Multilane Traffic Simulation

Antonina Chechina, Natalia Churbanova, and Marina Trapeznikova

Abstract The paper deals with development of both macroscopic and microscopic approaches to the mathematical modeling of multilane vehicular traffic on city roads and highways. The macroscopic model considers synchronized traffic flow, uses the continuum approach and is based on the original quasi-gas-dynamic (QGD) system of equations. The distinguishing feature of the model is the variable transverse velocity reflecting the speed of lane changing. The numerical implementation is explicit, the similarity with kinetically consistent finite difference schemes is used. The microscopic model is based on the cellular automata theory and presents generalization of Nagel-Schreckenberg model to the multilane case. The computational domain is the 2D lattice where two directions correspond to the road length and width. The number of cells in the transverse direction corresponds to the number of lanes. Each cell of the lattice can be either empty or occupied by one vehicle. Such a model allows vehicles to change lanes and to overtake one another. The algorithm of cell state update is formed by two components: lane change (if it is necessary and possible), movement along the road by the rules of N-S model.

1 Introduction

There are two main approaches to traffic flow modeling: macroscopic approach, in which vehicle flow is considered as a compressible fluid or gas flow, and a microscopic one, where each car is considered separately. Macroscopic models describe congested traffic, when distance between cars and their size have the same order. Commonly in macroscopic models all the drivers have the same strategies and behavior. The computational cost in such approach does not depend on the amount of vehicles in the network, that is why it is usually used for traffic simulation on large road networks. In microscopic approach there are no restrictions concerning flow density, but computational cost increases if more cars are added in simulation. There is a possibility to take into account different drivers behavior and car properties, so we can get a detailed picture of traffic flow as a result of simulation.

A. Chechina (✉) • N. Churbanova • M. Trapeznikova
Keldysh Institute of Applied Mathematics RAS, 4 Miusskaya Square, Moscow 125047, Russia
e-mail: chechina@imamod.ru; nata@imamod.ru; marina@imamod.ru

M. Chraibi et al. (eds.), *Traffic and Granular Flow '13*,
DOI 10.1007/978-3-319-10629-8_41

In this article macroscopic [1] and microscopic [2] models proposed by authors earlier received further development.

2 Macroscopic Model

The majority of macroscopic models are one-dimensional, i.e. lane changing is not considered. Therefore, the real road geometry is not taken into account. Developing two-dimensional macro model is not easy because of inequivalence of movement along and across the road.

As is standard, we deal with the density of cars $\rho(x, y, t)$, i.e. the number of cars per lane per length unit and the flow velocity consisting of two components: $u(x, y, t)$ is the speed along the road, $v(x, y, t)$ is the speed across the road. As said before, the continuum approach can be applied only in case of congested (synchronized) traffic state. Under these conditions all drivers have to maintain the same strategies:

- To move with the speed providing safe traffic,
- To move to the lane with lower density and/or higher speed,
- To approach planned destination.

The main difference between gas dynamics equations and traffic flow equations is in the terms that describe human will, for example, acceleration/deceleration force:

$$f_x = a_x \cdot \rho, \quad f_y = a_y \cdot \rho; \tag{1}$$

Acceleration depends on the difference between the real and equilibrium speed, the last one is the specific speed of movement at the exact value of ρ:

$$a_x = \frac{u_{eq} - u}{T_x}, \quad a_y = \frac{v_{eq} - v}{T_y}; \tag{2}$$

Equilibrium speed along the road:

$$u_{eq} = u_f \cdot \left(1 - \frac{\rho}{\rho_{jam}}\right); \tag{3}$$

where u_f is the free flow speed, ρ_{jam} is the jam density, i.e. the density of traffic jam, the maximum density of vehicular flow.

T_x and T_y – relaxation (driver reaction) times:

$$T_x = t_{0x} \cdot \left(1 + \frac{r\rho}{\rho_{jam} - r\rho}\right), \quad T_y = t_{0y} \cdot \left(1 + \frac{r\rho}{\rho_{jam} - r\rho}\right); \tag{4}$$

t_{0x}, t_{0y} and r – phenomenological constants.

Equilibrium speed across the road consists of three terms:

- Movement to the lane with higher speed –

$$v_u = k_u \cdot \frac{\partial u}{\partial y}, \tag{5}$$

- Movement to the lane with lower density –

$$v_\rho = -k_\rho \cdot \frac{\partial \rho}{\partial x}, \tag{6}$$

- Movement towards desired destination –

$$v_{des} = min\left(k_{des} \cdot \frac{u}{x_{des} - x}, 1\right) \cdot u \cdot \frac{y_{des} - y}{x_{des} - x}; \tag{7}$$

here k_u, k_ρ, k_{des} – phenomenological constants and (x_{des}, y_{des}) – coordinates of desired destination point.

$$v = v_u + v_\rho + v_{des}. \tag{8}$$

Speed limitation due to safety conditions:

$$0 \le u \le u_{max}, \quad -v_{max} \le v \le v_{max}; \tag{9}$$

The analogue of pressure is introduced into the model to represent the driver's reaction on the road conditions downstream and on the neighbouring lanes:

$$p_x = \lambda_x \frac{\rho^{\beta_x}}{\beta_x}, \quad p_y = \lambda_y \frac{\rho^{\beta_y}}{\beta_y}; \tag{10}$$

where λ_x, λ_y, β_x, β_y – phenomenological constants.

We consider the Knudsen number Kn that is the ratio between the typical scale of the medium and the typical scale of the flow. In hydrodynamics, $Kn < 10^{-3}$; however, for traffic flow $Kn \sim 0.1$, which is the reason we use kinetically consistent difference schemes (KCDS) [3] in this work, as they work well within the wide range of Knudsen numbers.

In addition, we introduce the minimal time scale to meet the approximation of the continuous medium. We take the time instant when the given point of the road is crossed by several cars as such a time.

$$\tau_x \sim \frac{\delta(u)}{u}, \quad \tau_y \sim \frac{1}{v} \tag{11}$$

To simplify the model, we treat τ_x and τ_y as constants.

Special term is included in continuity equation providing solution smoothing along the road:

$$W_x = \frac{\tau_x}{2} \cdot \frac{\partial}{\partial x} \left(\rho u^2 + p_x \right). \tag{12}$$

Additional diffusional flow connected with vehicle movement across the road:

$$W_y = \frac{\tau_y}{2} \cdot \frac{\partial}{\partial y} \left(\rho v^2 + p_y \right). \tag{13}$$

Generalizing the assumptions (1)–(13), we obtain system of flow dynamics equations:

$$\begin{aligned} \frac{\partial \rho}{\partial t} + \frac{\partial \rho u}{\partial x} + \frac{\partial \rho v}{\partial y} = \frac{\partial}{\partial x}\frac{\tau_x}{2}\left(\frac{\partial}{\partial x}\left(\rho u^2 + p_x\right) - f_x + \frac{\partial}{\partial y}\left(\rho u v\right)\right) \\ + \frac{\partial}{\partial y}\frac{\tau_y}{2}\left(\frac{\partial}{\partial y}\left(\rho v^2 + p_y\right) - f_y + \frac{\partial}{\partial x}\left(\rho u v\right)\right) \end{aligned} \tag{14}$$

$$\begin{aligned} \frac{\partial \rho u}{\partial t} + \frac{\partial}{\partial x}\left(\rho u^2 + p_x\right) - f_x + \frac{\partial}{\partial y}\left(\rho u v\right) \\ = \frac{\partial}{\partial x}\frac{\tau_x}{2}\left(\frac{\partial}{\partial x}\left(\rho u^3 + 3 p_x u\right) - 3 f_x u\right) + \frac{\partial}{\partial y}\frac{\tau_y}{2}\left(\frac{\partial}{\partial y}\left(\rho u v^2 + p_y u\right) - f_y u\right) \\ + \frac{\partial}{\partial x}\frac{\tau_x}{2}\left(\frac{\partial}{\partial y}\left(\rho u^2 v + p_y v\right) - f_y v\right) + \frac{\partial}{\partial y}\frac{\tau_y}{2}\left(\frac{\partial}{\partial x}\left(\rho u^2 v + p_x v\right) - f_x v\right) \end{aligned} \tag{15}$$

$$\begin{aligned} \frac{\partial \rho v}{\partial t} + \frac{\partial}{\partial x}\left(\rho v^2 + p_y\right) - f_y + \frac{\partial}{\partial x}\left(\rho u v\right) \\ = \frac{\partial}{\partial x}\frac{\tau_x}{2}\left(\frac{\partial}{\partial x}\left(\rho u^2 v + p_x v\right) - f_x v\right) + \frac{\partial}{\partial y}\frac{\tau_y}{2}\left(\frac{\partial}{\partial y}\left(\rho v^3 + 3 p_y v\right) - 3 f_y v\right) \\ + \frac{\partial}{\partial x}\frac{\tau_x}{2}\left(\frac{\partial}{\partial y}\left(\rho v^2 u + p_y u\right) - f_y u\right) + \frac{\partial}{\partial y}\frac{\tau_y}{2}\left(\frac{\partial}{\partial x}\left(\rho v^2 u + p_x u\right) - f_x u\right) \end{aligned} \tag{16}$$

Model includes several constants and parameters that can be obtained only from experimental and statistical data. We used the following values:

$$\lambda_x = 60\frac{\text{km}^2}{\text{h}^2}, \quad \lambda_y = 4\frac{\text{km}^2}{\text{h}^2}, \quad \beta_x = 2, \quad \beta_y = 1, \quad \tau_x = 2 \cdot 10^{-3}\,\text{h}, \quad \tau_y = 3 \cdot 10^{-4}\,\text{h},$$

$$t_{0x} = 50\,\text{s}, \quad t_{0y} = 7.5\,\text{s}, \quad r = 0.95, \quad \rho_{jam} = 120\frac{\text{veh}}{\text{km} \cdot \text{lane}}, \quad u_{max} = 90\frac{\text{km}}{\text{h}},$$

$$u_f = 120\frac{\text{km}}{\text{h}}, \quad v_{max} = 20\frac{\text{km}}{\text{h}}$$

3 Microscopic Model

The proposed microscopic model is based on Nagel-Schreckenberg model [4] using cellular automata (CA) theory.

The original 1D model was extended by authors to the multilane case. The computational domain is 2D lattice, each cell is 7.5 m long and 1 lane wide, it can either contain a car or be empty. Time and speed are also discrete, speed v of each vehicle can take one of the integer values $v = 0, 1, \ldots, v_{max}$ (each vehicle can have its own v_{max}), it denotes how many cells the vehicle overpasses during a time step.

Cell state update algorithm consists of two steps:

1. Lane change (if it is necessary and possible);
2. Movement along the road by the rules of one-lane traffic.

Change of lanes should happen during a time step. If there are more than two lanes in one direction, a conflict can occur when two vehicles from extreme lanes tend to the inner lane and try to occupy one and the same cell. The rule like the next one could help to resolve such a situation: vehicles change to the right only on even time steps and change to the left on odd steps. In general rules and conditions for changing lanes are as follows:

- Vehicle is located in the domain where lane change is allowed;
- Lane change leads to increase of the speed (decrease of the density) or is necessary to reach the destination (to achieve the goal);
- Target cell is empty;
- Safety condition is satisfied – on the target lane the distance behind the vehicle is greater or equal to v_{max}, in front of the vehicle it is greater or equal to v_n, then the change takes place with some probability.

If x_n and v_n are the position and the speed of the current n-th vehicle, d_n is the distance between the current vehicle and the vehicle in front of it, then at each time step $t \to t + 1$ the algorithm of the vehicle arrangement update consists of the next stages:

1. Acceleration $v_n \to min(v_{n+1}, v_{max})$
2. Deceleration $v_n \to min(v_n, d_{n-1})$
3. Randomization $v_n \to max(v_{n-1}, 0)$ with some probability p
4. Vehicle movement $x_n \to x_n + v_n$

The first stage reflects the common tendency of all drivers to move as fast as possible, the second one guarantees avoiding collisions, the third one takes into account randomness in driver behavior, and the skip itself takes place on the fourth stage – each vehicle is moved forward according to its new velocity.

4 Test Results

Several test problems were solved in order to verify our models and make a comparison between them and with standard program package Aimsun TSS [5].

4.1 Local Widening of the Road

The first test problem is vehicle movement on the road with local widening. The corresponding road configuration is shown in Fig. 1.

Figure 2 demonstrates the density field obtained by macroscopic simulation. The density of vehicles decreases at the wide part of the road but then increases significantly near the narrowing point. Thus, the total time required to pass the given road interval grows as compared with the road without widening.

The same test problem has been solved using the microscopic model. The average density is depicted in Fig. 3. Here is the same tendency: the maximal density is located at the end of widening. Moreover the density at the road exit exceeds the enter density.

In Fig. 4 the simulation results via Aimsun TSS, the widely used commercial traffic modeling software, are shown. There is no possibility to get the detailed picture of density distribution along and across the road using Aimsun, only average density on large road fragments is depicted. However, the density increases in the wider part leading to capacity reduction.

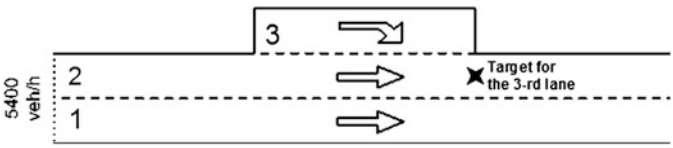

Fig. 1 Local widening: the problem statement

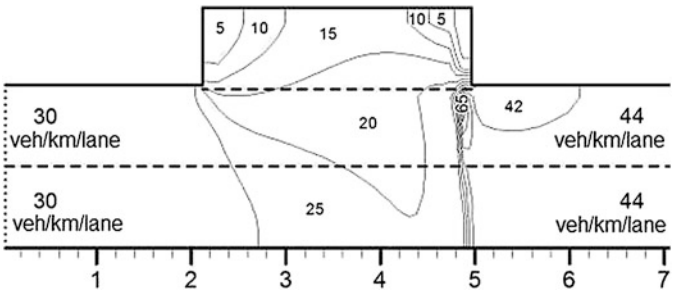

Fig. 2 Density field obtained via the macroscopic model

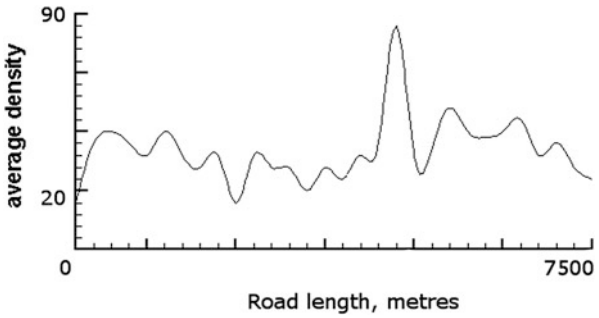

Fig. 3 Density field obtained via the microscopic model

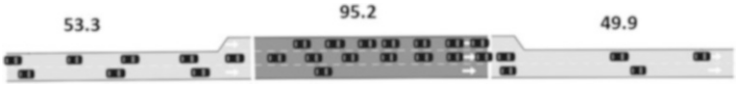

Fig. 4 Density field obtained via Aimsun

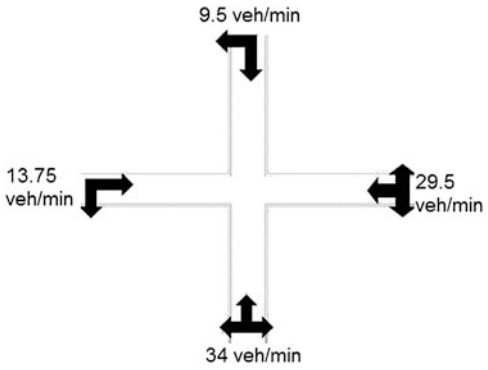

Fig. 5 Entering flows and permitted directions on the signalized intersection

4.2 Traffic Lights on the Crossroad

The second problem to be considered is the simulation of traffic on a crossroad at different traffic lights regimes using the above microscopic model. The problem involves obtaining the optimal traffic lights regime namely the signal durations to ensure the minimal time of stay on the crossroad for all traffic participants (Fig. 5).

In Fig. 6 the capacity of the signalized intersection in case of different traffic lights regimes is shown. Fifteen regimes obtained by changing durations of traffic light phases were explored using microscopic model and Aimsun. As is seen from the picture, though the absolute values of capacity obtained via Micro and Aimsun differ in the same regimes (this is a calibration problem), the results show good agreement.

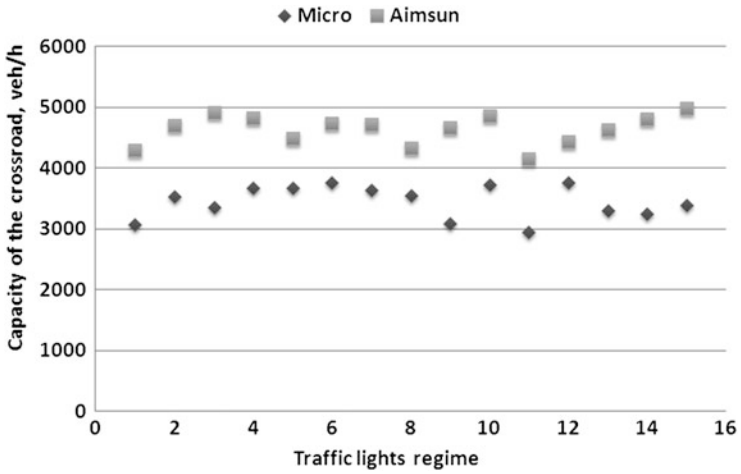

Fig. 6 Capacity of the signalized intersection. Results for 15 configurations of traffic lights regimes obtained via Micromodel and Aimsun TSS

Conclusions

- The models and algorithms developed showed results comparable with the simulation by the standard program software but demonstrated more detailed description of the traffic flow and its evolution in time. They can be implemented as a program package for traffic modeling.
- Due to inner parallelism and simplicity of numerical algorithms of the models the calculations can be carried out using high performance supercomputers on large-scale road networks. The capacity and performance of modern multicore hybrid computer systems allows real time predictions.

References

1. A. Sukhinova, M. Trapeznikova, B. Chetverushkin, N. Churbanova, Two-dimensional macroscopic model of traffic flows. Math. Models Comput. Simul. **1**(6), 669–676 (2009)
2. M. Trapeznikova, I. Furmanov, N. Churbanova, R. Lipp, Simulating multilane traffic flows based on cellular automata theory. Math. Models Comput. Simul. **4**(1), 53–61 (2012)
3. B.N. Chetverushkin, Application of the kinetic schemes for simulation of viscous gas dynamics problems. CFD J. (Jap. Sos. of CFD) **10**(3), 363–371 (2001)
4. K. Nagel, M. Schreckenberg, A cellular automation model for freeway traffic. J. Phys. I Fr. **2**, 2221 (1995)
5. http://www.aimsun.com

Empirical and Theoretical Fundamentals for Reliable Control and Optimization of Vehicular Traffic and Transportation Networks

Boris S. Kerner

Abstract As explained in a TGF'13 talk and Kerner (Physica A 392:5261–5282, 2013), generally accepted fundamentals and methodologies of traffic and transportation theory have failed by their applications for traffic network optimization and control in the real world. In comparison with a full version of the review Kerner (Physica A 392:5261–5282, 2013) with about 540 references, in this short paper we formulate and discuss empirical and theoretical fundamentals, which can be used for the development of reliable control and optimization of vehicular traffic and transportation networks.

1 Introduction

In the review [1] it has been shown that the generally accepted fundamentals and methodologies of traffic and transportation theory are not consistent with the set of the fundamental empirical features of traffic breakdown at a highway bottleneck. In this article, based on the results of three-phase traffic theory, we discuss briefly empirical and theoretical fundamentals of reliable control and optimization of vehicular traffic and transportation networks.

B.S. Kerner (✉)
Physik von Transport und Verkehr, Universität Duisburg-Essen, 47048 Duisburg, Germany
e-mail: boris.kerner@uni-due.de

M. Chraibi et al. (eds.), *Traffic and Granular Flow '13*,
DOI 10.1007/978-3-319-10629-8_42

2 The Fundamental Empirical Basis for Reliable Control and Optimization of Vehicular Traffic and Transportation Networks

Users of traffic and transportation networks would expect that through the use of traffic control, dynamic traffic assignment and other methods of dynamic optimization traffic breakdown can be prevented, i.e., free flow can be maintained in the network. This is because due to traffic breakdown congested traffic occurs in which travel time, fuel consumption as well as other travel costs increase considerably in comparison with travel costs in free flow. Therefore, any traffic and transportation theory, which is claimed to be a basis for the development of reliable methods and strategies for dynamic traffic assignment as well as network optimization and control should be consistent with the fundamental empirical features of traffic breakdown at a road bottleneck.

- The fundamental empirical basis for reliable control and optimization of vehicular traffic and transportation networks is the set of empirical features of traffic breakdown at a road bottleneck.

Consequently, we can also make the following conclusion:

- Traffic and transportation theories, which are not consistent the set of the fundamental empirical features of traffic breakdown at a bottleneck, cannot be applied for the development of reliable management, control, and organization of traffic and transportation networks.

3 The Set of Empirical Features of Traffic Breakdown at Highway Bottlenecks

The set of fundamental empirical features of traffic breakdown at a highway bottleneck, which is found from a study of traffic breakdown at a given bottleneck during many different days (and years) of traffic breakdown observations (see, e.g., [2–11]), is as follows [12, 13]:

1. Traffic breakdown at a highway bottleneck is a local phase transition from free flow (F) to congested traffic whose downstream front is usually fixed at the bottleneck location (see, e.g., [2–11] and references there). Such congested traffic we call synchronized flow (S) [12, 13] (Fig. 1).
2. At the same bottleneck, traffic breakdown can be either spontaneous (Fig. 1a) or induced (Fig. 1b) [12, 13].
3. The probability of traffic breakdown is an increasing flow rate function [6–11].
4. There is a well-known hysteresis phenomenon associated with traffic breakdown and a return transition to free flow (e.g., [2–4]).

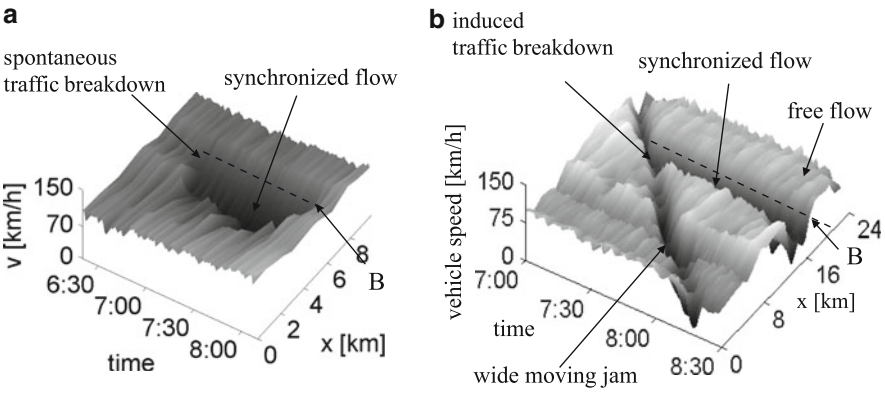

Fig. 1 Empirical examples for spontaneous (**a**) and induced traffic breakdown (**b**) at highway bottlenecks (Taken from [12])

4 Failure of Generally Accepted Fundamentals and Methodologies of Traffic and Transportation Theory

Traffic researchers have developed a huge number of traffic theories for optimization and control of traffic and transportation networks. In particular, to generally accepted fundamentals and methodologies of traffic and transportation theory belong the following theories and associated methodologies:

(i) The Lighthill-Whitham-Richards (LWR) model introduced in 1955–1956 [14, 15]. In 1994–1995, Daganzo introduced a cell-transmission model (CTM) that is consistent with the LWR model [16, 17]. Currently, Daganzo's CTM is widely used for simulations of traffic and transportation networks (see references in [1]).

(ii) A traffic flow instability that causes a growing wave of a local reduction of the vehicle speed. This classical traffic flow instability was introduced in 1959–1961 in the General Motors (GM) car-following model by Herman, Gazis, Montroll, Potts, and Rothery [18–20]. With the use of very different mathematical approaches, this classical traffic flow instability has been incorporated in a huge number of traffic flow models that can be considered belonging to the GM model class. This is because (as found firstly in [21, 22]) in all these very different traffic flow models the traffic flow instability causing a growing wave of a local reduction of the vehicle speed leads to a moving jam (J) formation in free flow (F→J transition) (see references in [1]).

(iii) The understanding of highway capacity as a *particular value*. This understanding of road capacity was probably introduced in 1920–1935 (e.g., [23] and references in [2, 24–26]). Recently due to empirical results of Elefteriadou et al. [5, 7, 26], Persaud et al. [6] as well as Brilon et al. [8–11] it has been assumed this the particular highway capacity is a stochastic value: At any time

instant, there is some particular value of highway capacity, however, we know the capacity with some probability only [6–11, 26].

(iv) Wardrop's user equilibrium (UE) and system optimum (SO) principles for traffic and transportation network optimization and control introduced in 1952 [27]. The Wardrop's UE and SO principles are the basis for a huge number of models for dynamic traffic assignment, control and optimization of traffic and transportation networks (see references in [1]).

There are many achievements of these generally accepted fundamentals and methodologies of traffic and transportation theory, which have made a great impact on the understanding of many traffic phenomena as emphasized in [1]. Because of these achievements of generally accepted classical traffic and transportation theories, a question arises:

- Why does the author state in [1] that the generally accepted classical traffic and transportation theories are not consistent with the set of empirical features of traffic breakdown and, therefore, they are not applicable for a reliable description of traffic breakdown, capacity, traffic control, and optimization of real traffic and transportation networks?

The failure of the generally accepted classical traffic flow models is explained as follows [1]:

1. The LWR-theory ([14–17] and references in [1, 2]) fails because this theory cannot show induced traffic breakdown observed in real traffic (Fig. 1b).
2. Two-phase traffic flow models of the GM model class (see references in [1, 2, 12, 13]) fail because traffic breakdown in the models of the GM class is an F→J transition. In contrast with this model result, real traffic breakdown is a phase transition from free flow (F) to synchronized flow (S) (F→S transition) (Fig. 1).
3. The understanding of highway capacity as a particular value [2, 6–11, 24–26] fails because this assumption about highway capacity contradicts the empirical evidence that traffic breakdown that limits highway capacity can be induced at a highway bottleneck as observed in real traffic (Fig. 1b).
4. Dynamic traffic assignment or/and any kind of traffic optimization and control based on Wardrop's SO or UE principles (see references in [1]) fail because of random transitions between the free flow and synchronized flow at highway bottlenecks. Due to such random transitions, the minimization of travel cost in a traffic network is not possible.

This can explain why network optimization and control approaches based on these fundamentals and methodologies have failed by their applications in the real world. Even several decades of a very intensive effort to improve and validate network optimization models have no success. Indeed, there can be found no examples where on-line implementations of the network optimization models based on these fundamentals and methodologies could reduce congestion in real traffic and transportation networks.

This is not surprising: The fundamental empirical features of traffic breakdown at highway bottlenecks have been understood only during last 20 years. In contrast, the generally accepted fundamentals and methodologies of traffic and transportation theory have been introduced in the 1950s–1960s. Thus the great scientists whose pioneering ideas led to these fundamentals and methodologies of traffic and transportation theory [14, 15, 18–20, 23, 27] could not know the fundamental empirical basis for reliable control and optimization of vehicular traffic and transportation networks.

5 Basic Theoretical Fundament for the Development of Reliable Control and Optimization of Traffic and Transportation Networks

To explain the set of the fundamental empirical features of traffic breakdown at network bottlenecks, the author has introduced three-phase traffic flow theory [12, 28–30].

- The main reason for the three-phase theory is the explanation of the set of the fundamental empirical features of traffic breakdown, rather than the features of traffic congestion.

In three-phase theory, an F→S transition explains traffic breakdown at a highway bottleneck: The terms $F \rightarrow S$ *transition* and *traffic breakdown at a highway bottleneck* are synonyms. The F→S transition (traffic breakdown) occurs in metastable free flow (Fig. 2) [12, 13]. The term *metastable free flow* with respect to an F→S transition means that a small enough disturbance for free flow at a bottleneck decays; therefore, in this case free flow persists at the bottleneck over time. However, when a critical disturbance (or a disturbance that is larger than the critical one) for free flow appears in a neighborhood of the bottleneck, traffic breakdown occurs at the bottleneck.

The metastability of free flow explains both spontaneous (Fig. 2a) and induced (Fig. 2b) traffic breakdowns leading to the emergence of synchronized flow at the bottleneck (empirical features 1 and 2 of traffic breakdown of Sect. 3). The theoretical probability of spontaneous traffic breakdown at the bottleneck found firstly from simulations of a microscopic stochastic three-phase traffic flow model by Kerner, Klenov and Wolf [31] (Fig. 2c) is a growing flow-rate function as in empirical observations [6] (empirical feature 3 of traffic breakdown of Sect. 3). This theoretical dependence of the probability of spontaneous breakdown on the flow rate q_{sum} downstream of a bottleneck is well fitted by a function [31]

$$P^{(\mathrm{B})} = \frac{1}{1 + \exp[\alpha(q_{\mathrm{P}} - q_{\text{sum}})]}, \tag{1}$$

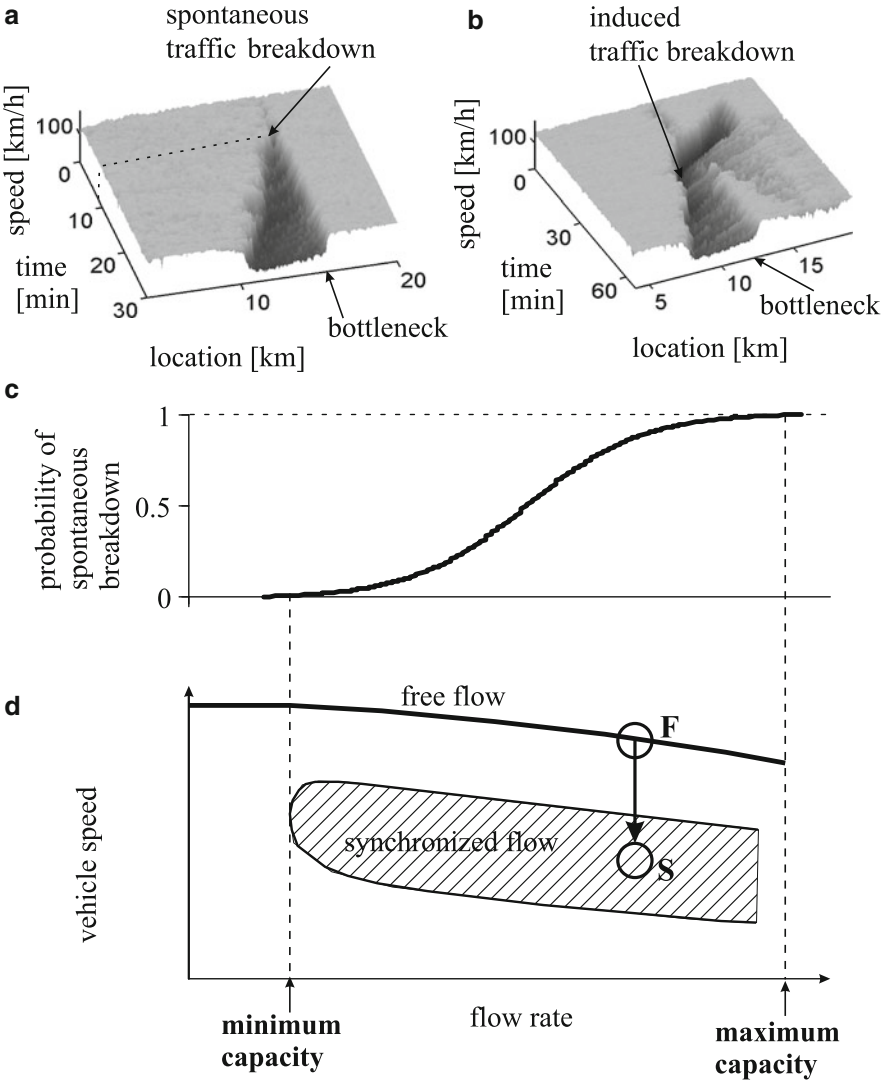

Fig. 2 Explanations of the fundamental empirical features of traffic breakdown at a highway bottleneck based on the assumption of three-phase theory about the metastability of free flow at the bottleneck with respect to an F→S transition (Taken from [1]): (**a**, **b**) Simulations of spontaneous (**a**) and induced (**b**) breakdown at on-ramp bottleneck. (**c**) Simulations of the probability of spontaneous traffic breakdown at on-ramp bottleneck on a single-lane road taken from [31]. (**d**) Qualitative Z-speed–flow-rate characteristic for traffic breakdown; *F* – free flow, *S* – synchronized flow (simulations of the Z-speed–flow-rate characteristic for traffic breakdown can be seen in Fig. 3.17b of [13])

where α and q_P are parameters. Qualitatively the same growing flow-rate function for the breakdown probability has later been found in measured traffic data [8–10].

The explanation of traffic breakdown at a highway bottleneck by an F→S transition in a metastable free flow at the bottleneck is the basic assumption of three-phase theory (Fig. 2) [12, 28–30]. Because none of the earlier traffic flow theories includes this basic assumption of three-phase theory, in accordance with the classical book by Kuhn [32], the three-phase theory is *incommensurable* with all other traffic flow theories.

The possibility of induced traffic breakdown at a bottleneck (Fig. 1b) leads to the following conclusion of three-phase theory: At the same flow rate on a network link, traffic flow at the bottleneck can be either in the free flow phase (F) or in the synchronized flow phase (S) (Fig. 2d). This fact is responsible for the existence of the range of the infinite number of highway capacities in three-phase theory: At any time instant, there are the infinite number of highway capacities within a range of the flow rate between the minimum highway capacity and the maximum highway capacity (Fig. 2c, d); within this flow range, traffic breakdown can be induced at the bottleneck. Thus, the theoretical fundament resulting from three-phase theory for the development of reliable control and optimization of traffic and transportation networks is as follows.

- At any time instant, there are the infinite number of the flow rates in free flow at a highway bottleneck at which traffic breakdown can be induced at the bottleneck. These flow rates are the infinite number of the capacities of free flow at the bottleneck. The range of these capacities of free flow at the bottleneck is limited by a minimum capacity and a maximum capacity (Fig. 2d).

Recently, this conclusion has been generalized for a city bottleneck due to traffic signal [33–36].

Conclusions

- The fundamental empirical basis for reliable control and optimization of vehicular traffic and transportation networks is the set of empirical features of traffic breakdown at a road bottleneck.
- The theoretical fundament resulting from three-phase theory for the development of reliable control and optimization of traffic and transportation networks is the existence of the range of the infinite number of highway capacities: At any time instant, there are the infinite number of highway capacities within a range of the flow rate between the minimum highway capacity and the maximum highway capacity (Fig. 2c, d); within this flow range, traffic breakdown can be induced at the bottleneck.

(continued)

- The explanation of traffic breakdown at a highway bottleneck by an F→S transition in a metastable free flow introduced in three-phase theory is responsible for the incommensurability of three-phase theory with all other traffic flow theories.

Acknowledgements We thank our partners for their support in the project "UR:BAN – Urban Space: User oriented assistance systems and network management", funded by the German Federal Ministry of Economics and Technology by resolution of the German Federal Parliament.

References

1. B.S. Kerner, Physica A **392**, 5261–5282 (2013)
2. A.D. May, *Traffic Flow Fundamentals* (Prentice-Hall, Englewood Cliffs, 1990)
3. F.L. Hall, K. Agyemang-Duah, Trans. Res. Rec. **1320**, 91–98 (1991)
4. F.L. Hall, V.F. Hurdle, J.H. Banks, Transp. Res. Rec. **1365**, 12–18 (1992)
5. L. Elefteriadou, R.P. Roess, W.R. McShane, Transp. Res. Rec. **1484**, 80–89 (1995)
6. B.N. Persaud, S. Yagar, R. Brownlee, Trans. Res. Rec. **1634**, 64–69 (1998)
7. M. Lorenz, L. Elefteriadou, Transp. Res. Circ. **E-C018**, 84–95 (2000)
8. W. Brilon, M. Regler, J. Geistefeld, Straßenverkehrstechnik, Heft **3**, 136 (2005)
9. W. Brilon, H. Zurlinden, Straßenverkehrstechnik, Heft **4**, 164 (2004)
10. W. Brilon, J. Geistefeldt, M. Regler, in *Traffic and Transportation Theory*, ed. by H.S. Mahmassani (Elsevier, Amsterdam, 2005), pp. 125–144
11. J. Geistefeldt, W. Brilon, in *Transportation and Traffic Theory*, ed. by W.H.K. Lam, S.C. Wong, H.K. Lo (Springer, Dordrecht/Heidelberg/London/New York, 2009), pp. 583–602
12. B.S. Kerner, *The Physics of Traffic* (Springer, Berlin/Heidelberg/New York, 2004)
13. B.S. Kerner, *Introduction to Modern Traffic Flow Theory and Control* (Springer, Heidelberg/Dordrecht/London/New York, 2009)
14. M.J. Lighthill, G.B. Whitham, Proc. R. Soc. A **229**, 281–345 (1955)
15. P.I. Richards, Oper. Res. **4**, 42–51 (1956)
16. C.F. Daganzo, Trans. Res. B **28**, 269–287 (1994)
17. C.F. Daganzo, Transp. Res. B **29**, 79–93 (1995)
18. R. Herman, E.W. Montroll, R.B. Potts, R.W. Rothery, Oper. Res. **7**, 86–106 (1959)
19. D.C. Gazis, R. Herman, R.B. Potts, Oper. Res. **7**, 499–505 (1959)
20. D.C. Gazis, R. Herman, R.W. Rothery, Oper. Res. **9**, 545–567 (1961)
21. B.S. Kerner, P. Konhäuser, Phys. Rev. E **48**, 2335–2338 (1993)
22. B.S. Kerner, P. Konhäuser, Phys. Rev. E **50**, 54–83 (1994)
23. B.D. Greenshields, Highw. Res. Board Proc. **14**, 448–477 (1935)
24. Highway Capacity Manual 2000, National Research Council, Transportation Research Board, Washington, DC, 2000
25. Highway Capacity Manual 2010, National Research Council, Transportation Research Board, Washington, DC, 2010
26. L. Elefteriadou, *An Introduction to Traffic Flow Theory*. Springer Optimization and Its Applications, vol. 84 (Springer, Berlin, 2014)
27. J.G. Wardrop, in *Proceedings of the Institution of Civil Engineers II*, vol. 1, (London, UK, 1952), pp. 325–378
28. B.S. Kerner, Trans. Res. Rec. **1678**, 160–167 (1999)
29. B.S. Kerner, Phys. World **12**, 25–30 (1999)

30. B.S. Kerner, in *Transportation and Traffic Theory*, ed. by A. Ceder (Elsevier, Amsterdam, 1999), pp. 147–171
31. B.S. Kerner, S.L. Klenov, D.E. Wolf, J. Phys. A Math. Gen. **35**, 9971–10013 (2002)
32. T.S. Kuhn, *The Structure of Scientific Revolutions*, 4th edn. (The University of Chicago Press, Chicago/London, 2012)
33. B.S. Kerner, Physica A **397**, 76–110 (2014)
34. B. S. Kerner, Phys. Rev. E **84**, 045102(R) (2011)
35. B. S. Kerner, Europhys. Lett. **102**, 28010 (2013)
36. B. S. Kerner, S. L. Klenov, M. Schreckenberg, J. Stat. Mech. P03001 (2014)

Simulation Model for Traffic Using Network Fundamental Diagrams

Victor L. Knoop and Serge P. Hoogendoorn

Abstract Traditionally, traffic is described at the level of an individual vehicle (microscopic) or at the level of a link (macroscopic). This paper introduces a traffic flow simulation model at a higher, subnetwork scale. The network is split in cells (subnetworks), and for each of the cells the Network Fundamental Diagram (NFD) is determined. Each time step, the flow from one cell to another is determined by the NFD, separated in a demand and a supply. For the demand, the border capacity between two cells plays a role. Opposed to the cell transmission model, the demand is decreasing for overcritical accumulation in cell i due to accumulation effects. This model can be used to quickly determine effects of network wide traffic control.

1 Introduction

Nowadays, due to increased communication techniques, traffic control measures can be coordinated over larger areas. For this, control concepts need to be developed. Moreover, these concepts needs to be tested, possibly on-line, for which traffic simulation programs are used. We argued earlier [5] that the larger the area, the longer the look-ahead period. For larger areas and longer time intervals, microscopic (vehicle-based) or macroscopic (link-based) simulation programs are too slow.

On an aggregate level there is a relation between the number of vehicles and their speeds [2,4], the Network Fundamental Diagram (NFD). Although some basic calculations have been describing the dynamics of a network by NFDs, none of these describe a multi-zone network, taking physical effects of the limited boundary capacity into account. This paper develops such a model. This model is useful for on-line optimization of traffic management measures. The paper also shows the application of the model in Sect. 5.

V.L. Knoop (✉) • S.P. Hoogendoorn
Transport & Planning, Delft University of Technology, Stevinweg 1, 2628 CN Delft, The Netherlands
e-mail: v.l.knoop@tudelft.nl; s.p.hoogendoorn@tudelft.nl

M. Chraibi et al. (eds.), *Traffic and Granular Flow '13*,
DOI 10.1007/978-3-319-10629-8_43

2 Simulation of Traffic Flow Dynamics

In traffic flow theory, several macroscopic models are available. One of the most intuitively understandable is the cell transmission model (CTM) [1]. In this model, the road is split in cells. The flow between cells is based on an upstream demand and a downstream supply (see also [6]). Up to the critical density, demand is an increasing function. For densities higher than the critical density, the demand is equal to the capacity of the road. The supply equals the capacity of the road up to the critical density. For higher densities, the supply decreases. The flow from one cell to the next is the minimum of the upstream demand and the downstream supply.

The above models describe how traffic flows on links. A network model also needs to describe how traffic behaves at nodes. A good overview of node models and their requirements is given by [8].

In this paper, we combine the concepts of the cell transmission model and good node models and apply it to a model describing the network dynamics, called the Network Transmission Model.

3 Traffic Coding

The basis of the model are subnetworks, called cells in the description of the computational methodology. The basic quantities used in this paper are accumulation K and performance P, which can be seen as weighted average density and flow, respectively. Note that performance is the flow which exits a network, rather than the internal flows. It has been shown that the performance is strongly correlated with the internal flow, the production [4]. The accumulation K in each cell A is the average density k for all links Z in the cell weighted to their length L and the number of lanes l. This total weighting factor is indicated by w

$$w_A = \sum_{Z \in A} L_Z l_Z \tag{1}$$

The accumulation is now calculated as

$$K = \frac{\sum_{Z \in A} k_Z L_Z l_Z}{w_A} \tag{2}$$

For each cell, it is registered which fraction of the vehicles (and thus accumulation) is heading towards which destination s; this is called ζ_s. The routing from cell A to the destination is coded by the next neighboring cell B in so called destination-specific splitfractions $\eta_{s,A,B}$. All neighbouring cells of A are indicated by the set $\mathscr{B}$. The fraction $\eta_{s,A,B}$ lies between 0 and 1, and all vehicles should be heading somewhere, so $\sum_{B \in \mathscr{B}} \eta_{s,A,B} = 1$. In our formulation, vehicles are assumed

to have arrived their destination once they arrive somewhere in the cell. This could be changed in a future version.

4 Traffic Dynamics

Let's now consider the traffic dynamics. The flow diagram of the model can be found in Fig. 1. The dynamics of traffic are simulated in these subnetwork, using properties of the NFD in each subnetwork. For these cells the NFD is assumed to be known. The flow from cell A to cell B is determined by the minimum of three elements

1. The capacity of the boundary between cell A and cell B, C_A^B; this is determined exogenously
2. The demand from cell A to cell B, D_A^B
3. The supply in cell B, related to the total demand to cell B

The demand from A to B D_A^B is determined based on the NFD, the function which relates production P to the accumulation K: $P = P(K)$. This NFD has to be determined exogenously, for which are several methods, empirically [4] or theoretically [7]. Now, a demand and supply scheme similar to the cell transmission model [1] is constructed. The supply S can be determined in the same way as in the cell transmission model, that is, it is at capacity if the accumulation in the receiving cell is lower than the critical density and equal to NFD for higher accumulations:

$$S = \begin{cases} P_{\text{crit}} & \text{if } K \leq K_{\text{crit}} \\ P(K) & \text{if } K > K_{\text{crit}} \end{cases} \tag{3}$$

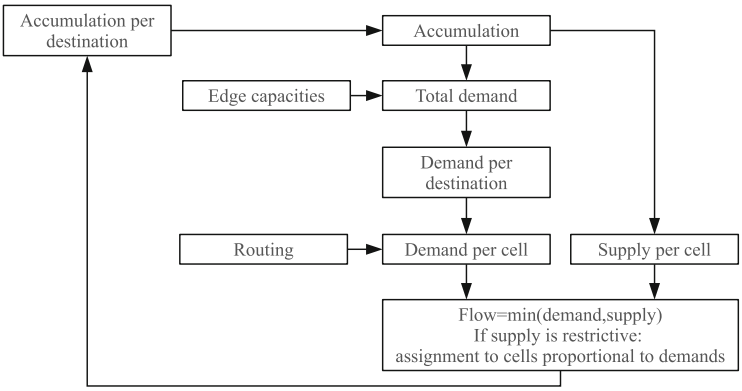

Fig. 1 A graphical representation of the steps taken in the computation scheme

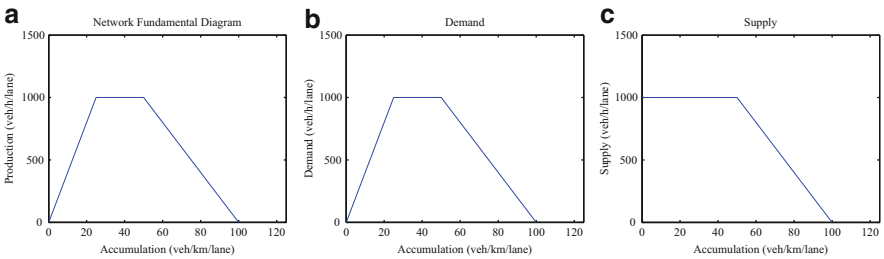

Fig. 2 The factors determining the flow. (**a**) Network Fundamental Diagram. (**b**) Demand. (**c**) Supply

Contrary to the CTM, the demand in a cell *decreases* with an increasing accumulation at values over the critical accumulation. This is because there is internal congestion in the cell, limiting the potential outflow. We thus have: $D = P(K)$, graphically shown in Fig. 2. Additionally, a minimum flow can be defined. This would allow a demand even from a completely full cell.

The total demand from cell A to cell B, D_A^B is only a part of the total demand in cell A, D_A. In fact, we consider the destinations separately. Hence, the demand in A for each of the destinations is

$$D_{A,s} = \zeta_s D_A \tag{4}$$

For each of these partial demands, the fraction heading to neigbouring cell B is indicated by $\eta_{A,s}^B$ The demand from cell A towards cell B hence is $D_A^B = \sum_{\text{all destinations } s} \eta_{A,s}^B D_{A,s}$. This is now limited to the capacity of the boundary between A and B, C_A^B, giving the effective demand $\tilde{D}_A^B = \min\left\{D_A^B, C_A^B\right\}$ The fraction of traffic allowed over the boundary between A and B, θ_A^B, is now calculated as: $\theta_A^B = \min\left\{\frac{\tilde{D}_A^B}{D_A^B}, 1\right\}$ As an intermediate step, we now have the effective demand from cell A to destination s via cell B:

$$\tilde{D}_{A,s}^B = D_{A,s}\eta_{A,s}^B\theta_A^B \tag{5}$$

The total demand towards cell B (D^B) is determined by adding all effective demands towards cell B, i.e. for all destinations and origin cells A. This is compared with the supply in cell B. If the supply is larger, the flow is unrestricted. However, if the supply is lower, the fraction of the flow which can flow into cell B ψ^B is calculated: $\psi^B = \min\left\{\frac{S^B}{D^B}, 1\right\}$.

All cells B, neighbours of A, which have effective demand $\tilde{D}_A^B$ larger than zero are combined in set $\mathscr{B}$. It is now calculated what is the lowest of these outflow fractions. This will be the restricting factor for the flow from cell A: Ψ_A: $\Psi_A = \min_{B\in\mathscr{B}}\left\{\Psi^B\right\}$. If the supply restricts the flow, demand to all neighboring cells in $\mathscr{B}$ is scaled down with this factor Ψ_A. Now, the flow from A to B is set as the minimum

of demand and supply. This flow is assumed to be constant between two consecutive time steps. The accumulation in any cell A towards destination s can now be updated based on the flows from B to A with destination s, indicated $q^A_{B,s}$ and the flow in the opposite direction, $q^B_{A,s}$:

$$K^s_A(t+\tau) = K^s_A(t) + \left(\sum_{B \in \mathscr{B}} q^A_{B,s} - \sum_{B \in \mathscr{B}} q^B_{A,s} \right) \tau / w_A \tag{6}$$

From the flow, vehicles have to be translated into accumulation using the simulation time step τ and the road length w_A.

5 Application on a Case Study

For the case study we set up a network with 10×10 cells, each representing an area and all having the same characteristics. The cells have a size of 1×1 km and 10 kms of roadway length. The NFD of the cells is shown in Fig. 2a. The capacity on the boundary between two cells is high enough that it does not restrict the flow. The time step used in the case study is 15 s.

A cross-network demand is loaded onto the network, shown graphically in Fig. 3a. The arrow width indicates the size of the demand. The base demand for directions top-down and left-right is 625 veh/h, to left is 833 veh/h and the demand bottom-up is 312 veh/h. To this base demand, an extra demand is added, representing the loading onto the network, and then gradually reducing. After the demand has decreased to zero, the simulation continues to empty the network.

For the routing we use the Floyd Warshal algorithm [3]. Travel costs per cell are updated on-line, based on the time it costs to cross a cell. Routing variation is ensured by doing a probit assignment with 10 % error in the perceived travel costs.

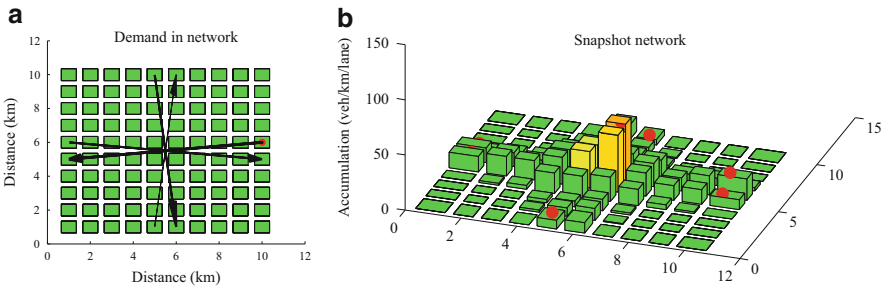

Fig. 3 Case study. (**a**) Demands in the network. (**b**) Case study network

Figure 3b shows a snapshot of the model during the simulation. It shows that traffic is clustering around the middle cells, and due to the congestion there, traffic is taking alternative routes around the city center. This shows the model works in practice and shows plausible results.

Conclusions
This paper introduced the Network Transmission Model describing the traffic flow dynamics on an aggregate level. The network was splitted into cells and for the traffic flow dynamics a numerical approach based on the MFD was introduced. The model is face valid, but further studies should test the model and calibrate and validate it against real data or more often used traffic simulation programs. Once done, the model seems promising to test network traffic control using model predictive control.

Acknowledgements This work is supported by the Netherlands Organisation for Scientific Research (NWO) in grant "There is plenty of room in the other lane".

References

1. C.F. Daganzo, The Cell transmission model: a dynamic representation of highway traffic consistent with the hydrodynamic theory. Transp. Res. Part B **28B**(4), 269–287 (1994)
2. C.F. Daganzo, Urban gridlock: macroscopic modeling and mitigation approaches. Transp. Res. Part B Methodol. **41**(1):49–62 (2007)
3. P. Floyd, Algorithm 97: shortest path. Commun. ACM **5**, 345 (1962)
4. N. Geroliminis, C.F. Daganzo, Existence of urban-scale macroscopic fundamental diagrams: some experimental findings. Transp. Res. Part B Methodol. **42**(9), 759–770 (2008)
5. V.L. Knoop, J.W.C. van Lint, J. Vries, L. Kester, I. Passchier, Relationship between application scale and maximum time latency in Intelligent Transport Solutions, Transp. Res. Rec. No. 2380, 1–9 (2013)
6. J.P. Lebacque, The Godunov scheme and what it means for first order traffic flow models, in *Proceedings of the 13th International Symposium on Transportation and Traffic Theory* (Lyon, France, 1996)
7. L. Leclercq, N. Geroliminis, Estimating MFDs in simple networks with route choice, in *Proceedings of the 20th International Symposium on Transportation and Traffic Theory*, ed. by S.P. Hoogendoorn, V.L. Knoop, H. Van Lint (Noordwijk, the Netherlands, 2013)
8. C.M.J. Tampère, R. Corthout, D. Cattrysse, L.H. Immers. A generic class of first order node models for dynamic macroscopic simulation of traffic flows. Transp. Res. Part B 45:289–309 (2011)

A Model of Car-Following Behavior at Sags

Bernat Goñi Ros, Victor L. Knoop, Wouter J. Schakel, Bart van Arem, and Serge P. Hoogendoorn

Abstract Sags are bottlenecks in freeway networks. The main reason is that the increase in slope has a negative effect on vehicle acceleration, which results in local changes in car-following behavior that reduce traffic flow capacity. Existing car-following models are not able to reproduce the acceleration behavior of drivers at sags and the resulting traffic flow dynamics in a sufficiently realistic way. This paper presents a new car-following model that aims to fill that gap. The model assumes that drivers have a limited ability to compensate for the negative effect that an increase in gradient has on vehicle acceleration. Compensation is assumed to be linear over time; the maximum compensation rate is defined as a parameter. The paper presents the results of a case study using the proposed car-following model. The study site is a particular sag in Japan. Similar traffic flow patterns are observed in simulation and in empirical data from that site. In particular, the model generates a bottleneck caused by the increase in freeway slope, reproducing its location very accurately.

1 Introduction

Sags are freeway sections along which the slope changes significantly from downwards to upwards. Sags are bottlenecks in freeway networks [1, 2]. The main cause is that the increase in freeway slope has a negative effect on vehicle acceleration, which results in local changes in car-following behavior that reduce traffic flow capacity [3–5]. In this contribution, we identify two characteristics of traffic flow at sags that existing car-following models are not able to reproduce in a sufficiently realistic way. The first characteristic is that drivers change their car-following behavior only on the lower part of the uphill section, regaining their normal driving behavior farther up the hill [4, 5]. The second characteristic is that, at sags, the capacity bottleneck is located 500–1,000 m downstream of the bottom of the sag [2, 4]. In this paper, we present a new car-following model that aims to

B. Goñi Ros (✉) • V.L. Knoop • W.J. Schakel • B. van Arem • S.P. Hoogendoorn
Faculty of Civil Engineering and Geosciences, Department of Transport and Planning, Delft University of Technology, Stevinweg 1, 2628 CN, Delft, The Netherlands
e-mail: b.goniros@tudelft.nl; v.l.knoop@tudelft.nl; w.j.schakel@tudelft.nl; b.vanarem@tudelft.nl; s.p.hoogendoorn@tudelft.nl

M. Chraibi et al. (eds.), *Traffic and Granular Flow '13*,
DOI 10.1007/978-3-319-10629-8_44

reproduce traffic flow dynamics at sags, including the two phenomena mentioned above. We present the results of a case study using the new model. The study site is the Yamato sag (Tomei Expressway, Japan). Analyses of empirical traffic data from that site are available [2,6]. The results of the case study show that the model is able to reproduce the traffic flow patterns observed in empirical data. Particularly, the model generates a bottleneck caused by the increase in freeway slope, and it predicts the location of that bottleneck very accurately. We conclude that the proposed model is able to reproduce traffic flow dynamics at sags more realistically than existing models.

2 Background

Empirical studies show that drivers change their car-following behavior when they reach the uphill section of sags. Drivers tend to reduce speed [4, 7] and keep longer headways than expected given their speed [3]. These local changes in car-following behavior occur because drivers are unable to accelerate sufficiently to immediately compensate for the increase in resistance force resulting from the increase in freeway slope [5]. Capacity decreases as a result of the above-mentioned changes in car-following behavior, which causes congestion in conditions of high traffic demand [1,2]. Generally, in congested conditions, the head of the queue (i.e., the bottleneck) is located 500–1,000 m downstream of the bottom of the sag [2,4].

Several car-following models have been developed in the last decades with the objective of reproducing traffic flow dynamics at sags. Koshi et al. [1] and Komada et al. [8] propose two different models that assume that drivers do not explicitly compensate for the limiting effect that a positive freeway gradient has on vehicle acceleration. Therefore, those models assume that a constant slope has a constant influence on vehicle acceleration. This assumption is not consistent with empirical observations, which show that drivers generally regain their normal car-following behavior as they climb the uphill section [4, 5]. Yokota et al. [9] present a car-following model that assumes that drivers explicitly compensate for the limiting effect that an increase in gradient has on vehicle acceleration. The model assumes that drivers are able to fully compensate for changes in slope with a certain time delay. Hence a constant slope has a decreasing influence on vehicle acceleration. This is more in line with empirical observations. However, an important disadvantage of that model is that it does not accurately reproduce the location of the bottleneck at sags. The model generates a bottleneck around the bottom of the sag [9].

In order to model traffic operations at sags, it is necessary to develop a car-following model that reproduces the following two phenomena: (i) drivers regain their normal car-following behavior as they climb the uphill section of sags; (ii) at sags, the bottleneck is located 500–1,000 m downstream of the bottom of the sag. In the next section, we present a car-following model that aims to fill that gap.

3 Car-Following Model

The model describes vehicle acceleration ($\dot{v}$) based on a two-term additive function:

$$\dot{v}(t) = f_{\mathrm{r}}(t) + f_{\mathrm{g}}(t) \,. \tag{1}$$

The first term (f_{r}) describes regular car-following behavior. Its formulation is based on the IDM model [10], and it accounts for the influence of speed (v), relative speed to the leading vehicle (Δv) and net distance headway (s) on acceleration:

$$f_{\mathrm{r}}(t) = a \cdot \left[1 - \left(\frac{v(t)}{v_{\mathrm{des}}(t)} \right)^4 - \left(\frac{s_{\mathrm{des}}(t)}{s(t)} \right)^2 \right] , \tag{2}$$

where the dynamic desired net distance headway (s_{des}) is:

$$s_{\mathrm{des}}(t) = s_0 + v(t) \cdot T(t) + \frac{v(t) \cdot \Delta v(t)}{2 \cdot \sqrt{ab}} \,. \tag{3}$$

The parameters in Eqs. 2–3 are: desired speed (v_{des}), maximum acceleration (a), maximum comfortable deceleration (b), net distance headway at standstill (s_0), and safe time headway (T). Note that we specified a different value for T depending on the traffic state. If $v(t) \geq v_{\mathrm{crit}}$ (uncongested traffic conditions), $T = T_0$. If $v(t) < v_{\mathrm{crit}}$ (congested conditions), the value of T is higher ($T = \gamma \cdot T_0$, where $\gamma > 1$).

The second term in Eq. 1 (f_{g}) accounts for the influence of freeway gradient on vehicle acceleration. At a given time t, that influence is the gravity acceleration ($g = 9.81\,\mathrm{m/s^2}$) multiplied by the difference between the gradient at the location where the vehicle is at that time ($G(t)$) and the gradient compensated by the driver until that time ($G_{\mathrm{c}}(t)$):

$$f_{\mathrm{g}}(t) = -g \cdot [G(t) - G_{\mathrm{c}}(t)] \,. \tag{4}$$

The *compensated gradient* (G_{c}) is a variable that accounts for the fact that drivers have a limited ability to compensate for the negative effect that an increase in freeway slope has on acceleration [5]. The model assumes that drivers compensate for any increase in slope linearly over time with a maximum gradient compensation rate defined by parameter c (and they fully compensate for any decrease in slope):

$$G_c(t) = \begin{cases} G(t) & \text{if } G(t) \leq G(t_{\mathrm{c}}) + c \cdot (t - t_{\mathrm{c}}) \\ G(t_{\mathrm{c}}) + c \cdot (t - t_{\mathrm{c}}) & \text{if } G(t) > G(t_{\mathrm{c}}) + c \cdot (t - t_{\mathrm{c}}) \,, \end{cases} \tag{5}$$

where:

$$t_{\mathrm{c}} = \max(t \mid G_{\mathrm{c}}(t) = G(t)) \,. \tag{6}$$

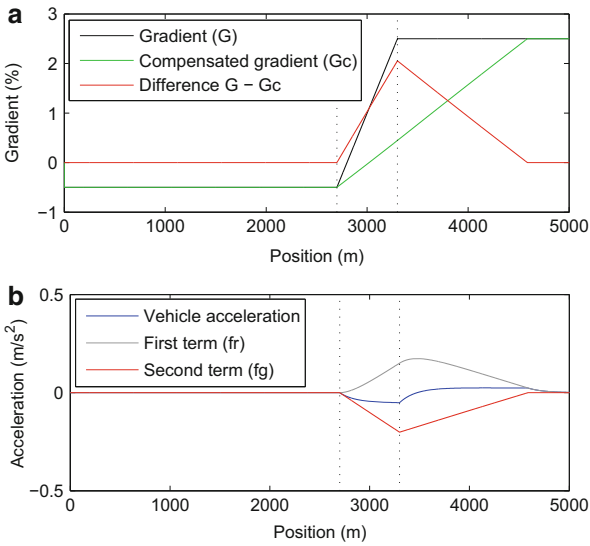

Fig. 1 Influence of an increase in gradient on the acceleration of a single vehicle driving on a sag. (**a**) Gradient and compensated gradient over distance. (**b**) Vehicle acceleration over distance

The properties of the model are as follows. If the gradient profile of a sag is such that the rate at which the freeway slope increases is lower than the driver's maximum gradient compensation rate (c), then $G_c(t) = G(t)$ at any time t. Therefore, in such a sag, $f_g(t) = 0$ at any time t, which implies that vehicle acceleration is not affected at all by the increase in slope. However, at sags where the gradient increase rate is higher than the driver's maximum gradient compensation rate (see example in Fig. 1a), $G_c(t) < G(t)$ for a certain period of time $t = [t_c, t_f]$. Time t_c is the time at which the driver could no longer fully compensate for the increase in gradient, and time t_f is the time at which the driver fully compensates for the whole increase in gradient. In Fig. 1a, t_c corresponds to the time at which the vehicle is at location $x = 2.7$ km, and t_f corresponds to the time at which the vehicle is at location $x \approx 4.8$ km. During period $t = [t_c, t_f]$, the compensated gradient (G_c) increases linearly over time (see Fig. 1a), but f_g is negative (see Fig. 1b). Note that the acceleration limitation caused by a negative f_g may reduce the vehicle speed and/or increase the distance to the leading vehicle, which are regular car-following behavior incentives to accelerate. Therefore, in our model, a negative f_g generally causes an increase in f_r. Acceleration is the combination of the influence of regular car-following behavior incentives and the influence of gradient (Eq. 1). As shown in Fig. 1b, $f_r(t) + f_g(t) < 0$ during the time the vehicle is within the freeway section with increasing degree of gradient; therefore, the vehicle decelerates on that section. Once the vehicle gets on the freeway section with constant positive slope, $f_r(t) + f_g(t)$ becomes positive; hence the vehicle re-accelerates and normal car-following behavior is eventually restored. Note that the acceleration limitation is maximum at the location where the gradient increase rate becomes lower than the driver's maximum gradient compensation rate (i.e., $x = 3.3$ km in Fig. 1b), because the difference between G and G_c is maximum at that location (see Fig. 1a).

4 Case Study

4.1 Site

The study site is the Yamato sag (Tomei Expressway, Japan), which has three lanes. Analyses of empirical traffic data from that site are available [2, 6]. According to those data, the bottleneck at the Yamato sag is located on the uphill section, 500 m downstream of the bottom of the sag. The free flow capacity and the queue discharge capacity of the bottleneck are around 5,400 and 4,800 veh/h, respectively. Therefore, the capacity drop is approximately 11 %. The process of congestion formation consists of two phases: first, traffic flow becomes congested on the median lane (which is the busiest lane in high demand conditions); then, congestion spreads to the other lanes as a result of lane changes.

4.2 Model Setup

We simulate traffic on a 5-km freeway stretch that has a layout similar to that of the Yamato sag. The freeway stretch has three lanes and the following gradient profile (Fig. 1a): (a) 2.7-km section with a constant slope of −0.5 %; (b) 0.6-km section where slope increases linearly from −0.5 % to +2.5 %; and (c) 1.7-km section with a constant slope of +2.5 %. We defined two vehicle classes (i.e., cars and trucks), which have different vehicle length (4 and 15 m, respectively) and different speed limit (100 and 85 km/h, respectively). Furthermore, we defined three classes of car drivers and one class of truck driver. The drivers' car-following behavior is determined by the model presented in Sect. 3. Lane-changing behavior is determined by the LMRS model [11]. The values of the parameters of the car-following and lane-changing models for each vehicle-driver class are shown in Table 1. Those values were selected based on [11]; however, it is important to remark that the car-following and lane-changing models have not been specifically calibrated for the study site. Note that some of the parameters are stochastic. More specifically, the values of parameters v_{des}, a, b, T_0, c, T_{min} for car drivers (only parameter v_{des} for truck drivers) are Gaussian distributed. The values of the stochastic parameters shown in Table 1 correspond to their mean values. The simulation period is 100 min. Total demand increases linearly from 3,000 to 5,200 veh/h between $t = 0$ and $t = 75$ min. From $t = 75$ min on, total demand is constant (5,200 veh/h). The distribution of the total demand across the three lanes at location $x = 0$ is determined by Wu's lane flow distribution model [12]. The composition of the traffic demand is the following: (a) 10 % trucks and 90 % cars with drivers of class I on the shoulder lane; (b) 5 % trucks and 95 % cars with drivers of class II on the center lane; and (c) 100 % cars with drivers of class III on the median lane. After entering the network, drivers are free to change lanes according to the lane-changing model.

Table 1 Parameters of the car-following model and the lane-changing model[a]

Vehicle class	Car			Truck
Driver class	Class I	Class II	Class III	
a (m/s^2)	1.15	1.21	1.29	0.50
b (m/s^2)	1.66	1.75	1.85	1.50
T_0 (s)	1.58	1.24	1.12	1.50
s_0 (m)	3	3	3	3
v_{des} (km/h)	92	97	103	85
v_{crit} (km/h)	60	60	60	60
c (s^{-1})	0.00039	0.00041	0.00043	0.00042
γ (-)	1.15	1.15	1.15	1.15
T_{min} (s)	0.61	0.58	0.54	0.56
τ (s)	25	25	25	25
x_0 (m)	200	200	200	200
v_{gain} (km/h)	70	50	50	70
d^{ij}_{free} (-)	0.365	0.365	0.365	0.365
d^{ij}_{sync} (-)	0.577	0.577	0.577	0.577
d^{ij}_{coop} (-)	0.788	0.788	0.788	0.788

[a]A description of the lane-changing model parameters can be found in [11]

4.3 Results

The model generates a bottleneck around the location where gradient becomes constant on the uphill section, i.e., 500 m downstream of the bottom of the sag (see Figs. 1a and 2). Traffic breaks down at that location when the total flow approaches 5,200 veh/h (see Fig. 3b), which can be considered as the free flow capacity of the bottleneck. The process of congestion formation is as follows. First, traffic breaks down on the median lane (see Figs. 2 and 3a). Then, some drivers move from the median lane to the other lanes in order to avoid queuing. This increases the flow on the center and shoulder lanes, as observed in Fig. 3a. The capacity of those lanes is exceeded and traffic breaks down there as well (see Fig. 3a). Note that the occurrence of congestion on a lane causes a reduction in lane flow (capacity drop). When congestion has spread to all lanes, the total outflow from the bottleneck is around 5,000 veh/h, i.e., 4 % lower than the total demand (see Fig. 3b). As a result, a queue forms upstream of the bottleneck. The head of the queue stays at $x \approx 3.3$ km, as observed in the speed contour plot of the median lane (Fig. 2). The speed contour plots of the other lanes (not shown) are very similar to that of the median lane.

The traffic flow patterns observed in simulation are similar to those observed in empirical data (see Sect. 4.1). The model generates a bottleneck and reproduces its location very accurately, although the simulated free flow capacity (5,200 veh/h) is lower than in empirical data (5,400 veh/h). Also, the model reproduces the capacity drop in congestion, although the magnitude of the drop (around 4 %) is lower than in empirical observations (11 %). Finally, the car-following model (combined with a lane-changing model) is able to reproduce the process of congestion formation.

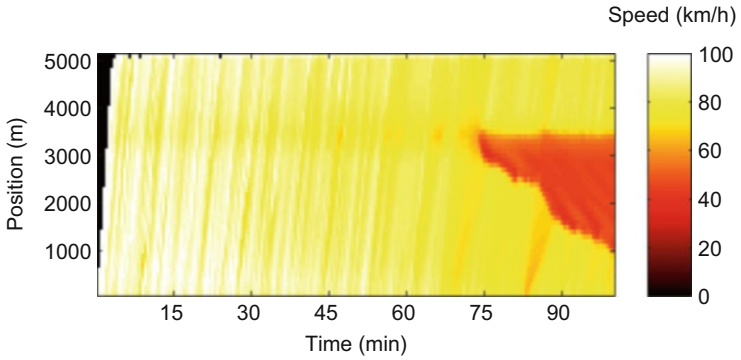

Fig. 2 Speed contour plot of the median lane

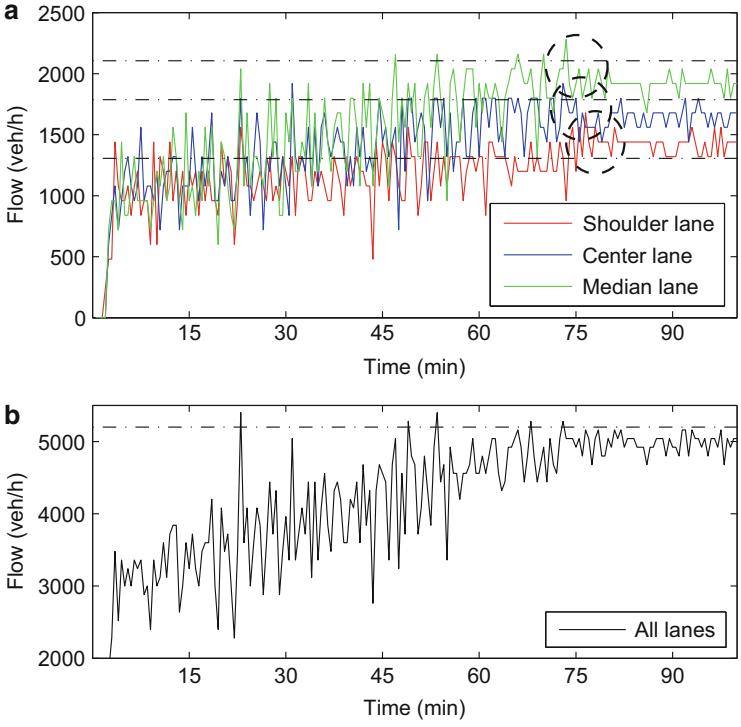

Fig. 3 Flows at $x = 3.2$ km (*dashed lines* indicate the average inflow at $x = 0$ after $t = 75$ min). (**a**) Flow per lane. (**b**) Total flow on all lanes

Conclusions
This contribution presented a new model describing car-following behavior at sags. The model assumes that drivers have a limited ability to compensate for the negative effect that an increase in freeway slope has on vehicle acceleration. Compensation is assumed to be linear over time. The maximum compensation rate is defined as a parameter. The difference between actual gradient and compensated gradient is the variable that limits vehicle acceleration. A case study was carried out in order to test the model. The study site is a particular sag of a Japanese freeway. Similar traffic flow patterns are observed in the simulation output data and empirical data from the study site. More specifically, the model generates a capacity bottleneck caused by the increase in gradient, reproducing its location very accurately. Although the proposed model still needs to be calibrated, we conclude that it is able to reproduce traffic flow dynamics at sags more realistically than existing models. The assumption of a bounded gradient compensation rate appears to be more realistic than the behavioral assumptions of other models, such as a fixed compensation time delay [9]. This finding suggests that the magnitude of the gradient change over distance has a strong influence on the location and capacity of the bottleneck at sags.

Acknowledgements This research was sponsored by Toyota Motor Europe.

References

1. M. Koshi, M. Kuwahara, H. Akahane, Capacity of sags and tunnels on Japanese motorways. ITE J. **62**(5), 17–22 (1992)
2. A.D. Patire, M.J. Cassidy, Lane changing patterns of bane and benefit: observations of an uphill expressway. Trans. Res. B **45**(4), 656–666 (2011)
3. M. Koshi, An interpretation of a traffic engineer on vehicular traffic flow, in *Traffic and Granular Flow'01*, ed. by M. Fukui, Y. Sugiyama, M. Schreckenberg, D.E. Wolf (Springer, Berlin, Nagoya, Japan, 2003), pp. 199–210
4. W. Brilon, A. Bressler, Traffic flow on freeway upgrades. Trans. Res. Rec. **1883**, 112–121 (2004)
5. R. Yoshizawa, Y. Shiomi, N. Uno, K. Iida, M. Yamaguchi, Analysis of car-following behavior on Sag and curve sections at intercity expressways with driving simulator. Int. J. Intel. Trans. Syst. Res. **10**(2), 56–65 (2012)
6. B. Goñi Ros, V.L. Knoop, B. van Arem, S.P. Hoogendoorn, Empirical analysis of the causes of stop-and-go waves at sags. IET Intell. Transp. Syst. **8**(5), 499–506 (2014)
7. T. Furuichi, S. Yamamoto, M. Kotani, M. Iwasaki, Characteristics of spatial speed change at motorway sag sections and capacity bottlenecks, in *Proceedings of the 82nd Annual Meeting Transportation Research Board*, Washington, DC, 2003
8. K. Komada, S. Masukura, T. Nagatani, Effect of gravitational force upon traffic flow with gradients. Physica A **388**, 2880–2894 (2009)

9. T. Yokota, M. Kuwahara, H. Ozaki, A study of AHS effects on traffic flow at bottlenecks, in *Proceedings of the 5th ITS World Congress*, Seoul, 1998
10. M. Treiber, A. Hennecke, D. Helbing: Congested traffic states in empirical observations and microscopic simulations. Phys. Rev. E **62**(2), 1805–1824 (2000)
11. W. Schakel, V.L. Knoop, B. van Arem, Integrated lane change model with relaxation and synchronization. Trans. Res. Rec. **2316**, 47–57 (2012)
12. N. Wu, Equilibrium of lane flow distribution on motorways. Trans. Res. Rec. **1965**, 48–59 (2006)

Multi-anticipative Car-Following Behaviour: Macroscopic Modeling

G. Costeseque and Jean-Patrick Lebacque

Abstract In this work we will deal with a macroscopic model of multi-anticipative car-following behaviour i.e. driving behaviour taking into account several vehicles ahead. Some empirical studies have suggested that drivers not only react to the closest leader vehicle but also anticipate on traffic conditions further ahead. Using a recent mathematical result of homogenization for a general class of car-following models (and also available for multi-anticipative models), we will deeply investigate the effects of multi-anticipation at the microscopic level on the macroscopic traffic flow. To investigate multi-anticipation behaviour may be fundamental to understand better cooperative traffic flow dynamics.

1 Introduction

1.1 Motivation

Our motivation comes from the sky-rocketing development of new technologies in transportation leading to the multiplication of Intelligent Transportation Systems (ITS). More precisely we would like to assess the impact of cooperative systems on general traffic flow. Cooperative systems include vehicle-to-vehicle (V2V) or vehicle-to-infrastructure (V2I) communications, generally designated as V2X technologies. There is a fast growing literature about cooperative systems. The interested reader can refer for instance to [13] and references therein.

The fact that the observed headway between two consecutive vehicles is often strictly less than the reaction time of the drivers, suggests that drivers anticipate

G. Costeseque
Université Paris-Est/Ecole des Ponts ParisTech/CERMICS, Marne-la-Vallée, France

Université Paris-Est/IFSTTAR/GRETTIA, 14-20 Boulevard Newton, Marne-la-Vallée Cedex 2, France
e-mail: costeseg@cermics.enpc.fr

J.-P. Lebacque (✉)
Université Paris-Est/IFSTTAR/GRETTIA, 14-20 Boulevard Newton, Marne-la-Vallée Cedex 2, France
e-mail: jean-patrick.lebacque@ifsttar.fr

M. Chraibi et al. (eds.), *Traffic and Granular Flow '13*,
DOI 10.1007/978-3-319-10629-8_45

on more than one leader. Indeed, if not, the proportion of accidents should be dramatically increased. The multi-anticipation has been shown as a key element for the stabilization of traffic flow, above all in dense traffic situations.

However multi-anticipation behaviour has only been taken into consideration at a microscopic scale. Indeed such macroscopic models as the Payne-Whitham one only account for anticipation in time. The macroscopic issues encompass multi-lane traffic with lane changing and assignment but also multi-anticipation on each lane or the combination of those both processes. In classical approaches, the whole traffic is projected on a single line to simplify the problem in a one-dimensional framework.

1.2 Notations

Let x denote the position and $t > 0$ the time. $x_i(t)$ refers to the trajectory of the vehicle $i \in \mathbb{Z}$. The speed and the acceleration of vehicle i are described by the first and second derivative of x_i w.r.t. time. Notice that we also introduce a time delay $T \geq 0$.

We assume that the vehicles are labelled according to a snapshot of a section of road from upstream to downstream (see Fig. 1). Vehicle labels increase with x. Thus $(x_{i+1} - x_i)(t)$ is the spacing and $(\dot{x}_{i+1} - \dot{x}_i)(t)$ the relative speed at time t between vehicle i and its leader $(i+1)$. We also denote by $m \geq 1$ the total number of leaders that are considered by vehicle $i \in \mathbb{N}$.

At the macroscopic level, we denote respectively the density and the flow of vehicles at location x and time t as $\rho(x,t)$ and $Q(x,t)$.

1.3 Main Results and Organization of the Paper

As a main result we describe a new macroscopic model that encompass multi-anticipative car-following behaviour that are classically taken into account only at the microscopic scale. Moreover our model is able to consider multi-lane dynamics.

The rest of the paper is organized as follows: we first recall some existing multi-anticipative car-following models in Sect. 2. We particularly highlight what we think to be the seminal form of such a model. In Sect. 3, we describe the formal mathematical result that allows us to pass from microscopic models to equivalent

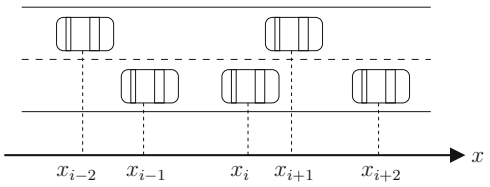

Fig. 1 Notations for the microscopic car-following models

macroscopic ones. Our macro model is also described in Sect. 4. Finally we provide some numerical considerations in section "Conclusion and Future Directions" before to discuss the results and to conclude.

2 Multi-anticipative Traffic Modelling: An Introduction

Multi-anticipative models The main existing multi-anticipative car-following models come from adaptations of classical car-following ones with a single leader vehicle. We recall below some examples. The interested reader could refer to [4] for references. We can quote for instance

- The model of Bexelius extends the car-following model of Chandler et al.
- Lenz et al. extend the model of Bando et al. yielding a second order multi-anticipative model.
- Hoogendoorn et al. [7] propose an extension of the model of Helly

$$\ddot{x}_i(t+T) = \sum_{j=1}^{m_1} \alpha_j \left(\dot{x}_{i+j} - \dot{x}_i\right)(t) + \sum_{j=1}^{m_2} \beta_j \left[\left(x_{i+j} - x_i\right)(t) - S_0 - jT\dot{x}_i(t)\right], \tag{1}$$

  with two different number of considered leaders $m_1 \geq 1$ and $m_2 \geq 1$ according to either speed variations or headway variations.
- Treiber et al. introduces the Human Driver Model (HDM) as an extension of his well-known Intelligent Driver Model (IDM).
- Farhi et al. [4] describes a first order model that extends the Min-Plus car-following model. This model is described in Sect. 3. As it is based on Min-Plus algebra, it is easy to check its global properties.

Remark 1 The additive form in the multi-anticipative models yields models which are easier to study analytically. But the minimum form expresses the fact that a driver will adapt its velocity (or equivalently its acceleration) according to the worst behaviour of all the considered leaders and thus offers more physical interpretation.

Experimental results In [6, 14], the model (1) is calibrated on real data and it fits best for $m_1 = 3$ and $m_2 = 1$, meaning that the drivers are more sensitive to speed variations than headway variations. It is also shown that the multi-anticipative models improves the representation of driving behaviour. However there is a high variance in driving behaviour which is not totally accounted for.

In many studies (for instance [13, 16] and references therein), platoon stability (on a single lane) is shown to decrease when the reaction time increases, and to increase when the spatial and/or temporal anticipation are increased.

3 Macroscopic Model for Multi-anticipative Traffic

3.1 First Result in the Min-Plus Algebra

First order multi-anticipative models can be viewed as high-viscosity approximation of second order models (such as the Frenkel-Kontorova model studied in [5]). For instance, in [4] the model is a first order and based on a piecewise linear fundamental diagram (FD). The velocity is computed by taking the minimum of all constraints imposed by preceding vehicles. The model is expressed in the Min-Plus algebra as follows

$$x_i(t+1) = x_i(t) + \min_{1\leq j\leq m} (1+\lambda)^{m-1} \min_{v\in\mathcal{U}} \max_{w\in\mathcal{W}} \left[\alpha_{vw} \left(\frac{x_{i+j}(t) - x_i(t)}{j} \right) + \beta_{vw} \right] \tag{2}$$

where $\mathcal{U}$ and $\mathcal{W}$ are two finite sets of indices. The $\lambda \geq 0$ is a discount parameter favouring closer leaders over the farther ones.

The authors obtain semi-analytical results concerning the stability of the model and the existence of fixed points. These fixed points match invariant states for the macroscopic traffic flow.

Notice moreover that the simulation results in [4] show the smoothing effects of multi-anticipative driving on the macroscopic traffic flow.

3.2 Multi-anticipative First Order Models and Hamilton-Jacobi Equation

One approach to micro-macro passage relies on the mathematical homogenization of car-following models into Hamilton-Jacobi equation.

Let us first consider the following first order multi-anticipative model

$$\dot{x}_i(t+T) = \max \left[0, V_{max} - \sum_{j=1}^{m} f\left(x_{i+j}(t) - x_i(t)\right) \right] \tag{3}$$

with $T \geq 0$ and with $f : \mathbb{R}_+^* \mapsto \mathbb{R}_+$ which needs to be a non-negative and non-increasing function describing the speed-spacing relationship. Let us choose

$$f(r) = \beta \exp(-\gamma r), \quad \text{for any} \quad r > 0, \tag{4}$$

with $\beta, \gamma > 0$. This choice is mathematically convenient because if we set

$$F\left(\{x_k\}_k\right) := V_{max} - \sum_{j=1}^{m} f\left(x_{i+j}(t) - x_i(t)\right),$$

then we can check that $\dfrac{\partial F}{\partial x_k} \geq 0$, for any $k = \{i, \ldots, i+m\}$. Thus, it is possible to recover (at least formally) homogenization results.

Remark 2 Notice that qualitatively this choice of an exponential speed-spacing fundamental diagram (FD) implies that the more the vehicles anticipate on their leaders, the lower their speeds and the higher their spacings. However one would expect that multi-anticipation allows shorter spacing and with high speeds.

Remark 3 (Equivalence result) One can check that if we consider a piecewise linear speed-spacing relationship, then the model (3) can be approximated by the Min-Plus model (2).

Let us consider the model (3). If we apply an unzooming procedure by introducing the rescaled position of vehicles as follows

$$X^{\varepsilon}(y,t) = \varepsilon x_{\lfloor \frac{y}{\varepsilon} \rfloor}\left(\frac{t}{\varepsilon}\right), \quad \text{for} \quad y \in \mathbb{R}, \quad t \in [0, +\infty) \tag{5}$$

where $\lfloor . \rfloor$ denotes the floor integer, then we can recover a Hamilton-Jacobi equation by homogenization when the scale factor ε goes down to zero:

$$\frac{\partial X^0}{\partial t} = \bar{V}\left(\frac{\partial X^0}{\partial n}, m\right) \tag{6}$$

with m the number of considered leaders and the (macroscopic) flow speed as follows

$$\bar{V}(r,m) = \max\left[0, V_{max} - \sum_{j=1}^{m} f(jr)\right].$$

The unknown $X^0(n,t)$ denotes the position of the vehicle labelled n at time t:

$$\frac{\partial X^0}{\partial t} = v \quad \text{and} \quad \frac{\partial X^0}{\partial n} = r,$$

where v and r describe respectively the speed and the spacing.

We recover the classical LWR model (standing for Lighthill, Whitham [12] and Richards [15]) in Lagrangian coordinates (n,t) that is

$$\begin{cases} \partial_t r + \partial_n v = 0, \\ v = \bar{V}(r,m). \end{cases} \tag{7}$$

We recall that the LWR model in Eulerian coordinates (t, x) expresses the conservation of vehicles on a section

$$\begin{cases} \partial_t \rho + \partial_x (\rho v) = 0, \\ v = V(\rho, m) := \bar{V}(1/\rho, m). \end{cases}$$

with ρ the density of vehicles and the *modified* speed-density fundamental diagram (FD) $V : (\rho, m) \mapsto V(\rho, m)$ which is non-negative and non-increasing w.r.t. ρ.

This homogenization result is fully described in [1] and Khoshyaran, Lebacque and Monneau (Private communications, 2010). Homogenization is a general technique which has been used for several different models involving interactions with a finite number of particles. The interested reader is referred to [5] and references therein.

3.3 General Multi-lane Traffic Flow Model with Multi-anticipation

We consider a multi-lane road section and we consider the projection of vehicles on the spatial axis as in Fig. 1. Assume that the traffic flow on such a section is composed of a mixture of multi-anticipative vehicles. The model (7) implies that low anticipation vehicles will be stuck behind high anticipation vehicles. In the case of multi-lane traffic such behaviour is precluded by the fact that vehicles can overtake each other.

Therefore let us denote by χ_j the fraction of j-anticipative vehicles. Then the traffic flow is the superposition of traffic of j-anticipative vehicles, i.e.

$$\chi = (\chi_j)_{j=1,\dots,m},$$

with $0 \leq \chi_j \leq 1$ for any $j = \{1, \dots, m\}$ and $\sum_{j=1}^{m} \chi_j = 1$. It is then obvious that the composition is advected with the traffic flow. We can express this concept using a model of the Generic Second Order Modelling (GSOM) familly as it has been introduced by Lebacque et al. in [10]. The driver attribute is the composition χ. We get the following expression

$$\begin{cases} \partial_t \rho + \partial_x (\rho v) = 0, \\ v := \sum_{j=1}^{m} \chi_j V(\rho, j) = \sum_{j=1}^{m} \chi_j \bar{V}(1/\rho, j), \\ \partial_t (\rho \chi) + \partial_x (\rho \chi v) = 0. \end{cases} \tag{8}$$

Let us set

$$W(\rho,\chi)=\sum_{j=1}^{m}\chi_j\,\bar{V}(1/\rho,j),\quad\text{and}\quad\overline{W}(r,\chi)=W(1/r,\chi)=\sum_{j=1}^{m}\chi_j\,\bar{V}(r,j).$$

We can check that the third line in Eq. (8) could be rewritten as a simple advection equation

$$\partial_t\chi+v\partial_x\chi=0.$$

As it has been already shown (see for instance [10]), the system (8) admits only two kinds of waves:

- Kinematic waves (rarefaction or shock) for the vehicles density, similar to kinematic waves for the LWR model. Through such a wave, the composition of traffic χ is preserved but not the speed;
- Contact discontinuities for the composition of traffic. In this case, the wave velocity is equal to the speed of traffic v which is conserved through the wave.

In Lagrangian coordinates (t,n), with n the label of cars, the flux variable is v and the stock variable is the spacing $r=1/\rho$. The model can be recast as:

$$\begin{cases}\partial_t r+\partial_n v=0\\ v=\overline{W}(r,\chi)\\ \partial_t\chi=0\end{cases}\tag{9}$$

The model (8) and (9) is new in the sense that there already exist some multilanes models such as the model of Greenberg, Klar and Rascle (see [10] and references therein) which belong to the GSOM family. However to the authors best knowledge, there does not exist any macroscopic PDE model taking into consideration multi-anticipative behaviour in a multi-lane context.

4 Numerical Approaches

To numerically solve the system (8), we can use classical GSOM methodologies [10, 11] that encompass:

- Godunov-like schemes for which we need to introduce finite time and space steps Δt, Δx_k that need to satisfy a CFL condition. Consider the following scheme

$$\begin{cases}\rho_k^{t+1}=\rho_k^t+\dfrac{\Delta t}{\Delta x_k}\left[q_k^t-q_{k+1}^t\right],\\ q_k^t:=\min\left\{\Delta_k\left(\rho_k^t,\chi_k^t\right),\Sigma_{k+1}\left(\rho_{k+1}^t,\chi_{k+1}^t\right)\right\},\\ \rho_k^{t+1}\chi_k^{t+1}=\rho_k^t\chi_k^t+\dfrac{\Delta t}{\Delta x_k}\left[q_k^t\chi_k^t-q_{k+1}^t\chi_{k+1}^t\right].\end{cases}\tag{10}$$

We also need to define the supply and demand functions as in [9]

$$\Delta_k(\rho,\chi) = \max_{0\le\xi\le\rho} \left[\xi W_k(\xi,\chi)\right], \quad \text{and} \quad \Sigma_k(\rho,\chi) = \max_{\xi\ge\rho} \left[\xi W_k(\xi,\chi)\right].$$

- Variational formulation and dynamic programming techniques [2].
- Particle methods in the Lagrangian framework (t,n). A standard way of obtaining these (refer to [10, 11]) is to apply a Godunov scheme to (9). This is easy: the supply is simply v_{max}, the demand is W, because $r \mapsto \overline{W}(r,\chi)$ is increasing. Since a cell can be associated to a packet of Δn vehicles having a total spacing r_n^t and tail position x_n^t, a simple car-following like model (11) is derived. Considering Lagrangian finite difference methods, we can either deal with a vectorial attribute χ or with an integer $j = 1,\dots,m$ with randomization of probability χ_j. We opt here for the first option. The resulting model is described hereafter:

$$\left|\begin{array}{l} x_n^{t+1} = x_n^t + \Delta t\, \overline{W}\left(r_n^t, \chi_n^t\right) \\ r_n^t = \left(x_{n+1}^t - x_n^t\right)/\Delta n \\ \chi_n^{t+1} = \chi_n^t \end{array}\right. \tag{11}$$

The Lagrangian method (11) is more precise (less smoothing of waves) than (10) and easier to calculate (the demand being the speed).

4.1 Choice of the Fundamental Diagram

For this numerical example, we have used the speed-spacing function described in (4) that is

$$\bar{V}(r,m) = \max\left[0, V_{max} - \sum_{j=1}^{m} \beta \exp(-\gamma j r)\right]$$

with $\beta, \gamma > 0$. As we consider that those coefficients are strictly independent of the number of considered leaders $j \in \{1,\dots,m\}$, one can easily check that

$$\beta = V_{max} \exp\left(\gamma r_{min}\right)$$

where r_{min} is the minimal spacing between two consecutive vehicles. The maximal speed V_{max} is equal to 25 m/s and γr_{min} is fixed to 0.18 in order to ensure a proper critical density. The maximal number of considered leaders m is equal to 5.

Note that the fundamental diagrams plotted on Fig. 2 are intended for a single lane. Then the higher the number of considered leaders, the higher the critical spacing (or equivalently the lower the critical density) per single lane.

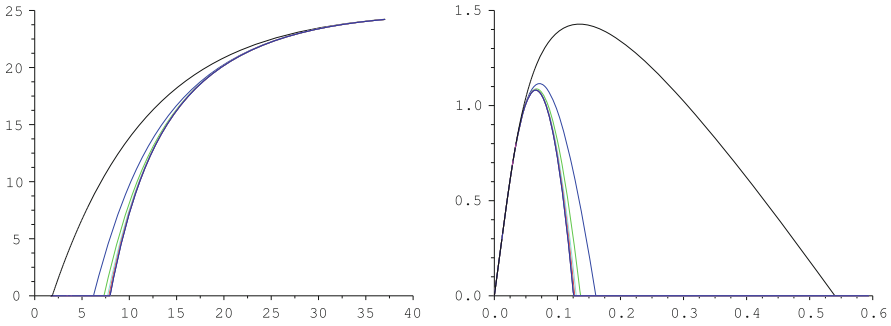

Fig. 2 Speed-spacing fundamental diagram $r \mapsto \bar{V}(r, \kappa)$ (*left*) and Flow-density fundamental diagram $\rho \mapsto \rho V(\rho, \kappa)$ (*right*) for different values of κ

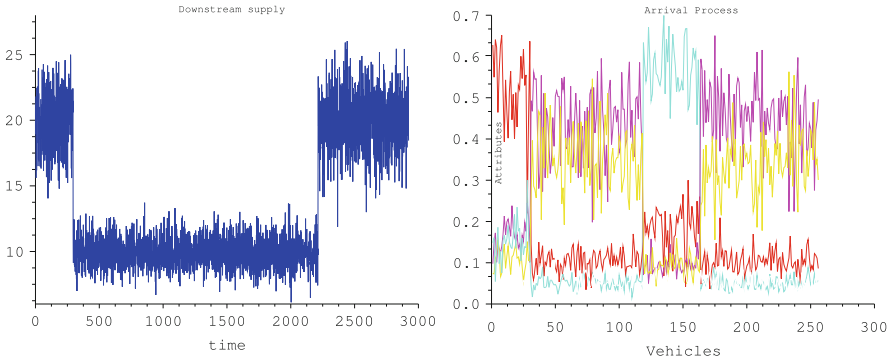

Fig. 3 Downstream supply value (*left*) and traffic composition attribute χ (*right*)

4.2 *Description of the Use Case*

Let us consider a traffic flow on a multi-lane road section. Roughly speaking, assume that entering the section we have two distinct compositions of traffic: high anticipatory, then low anticipatory, then high anticipatory again (see Fig. 3). The downstream supply is formulated in terms of speed, which is more convenient in the Lagrangian framework. The supply is assumed to drop in the middle of the considered period (from times $t = 250$ to $t = 2{,}200$), generating a high-density wave propagating backwards.

This shock wave interacts with the contact discontinuities carried by the incoming traffic (at times $t = 1{,}000$ and $t = 1{,}800$). Note that the increase of downstream supply at time $t = 2{,}200$ generates also a rarefaction wave (see Fig. 4).

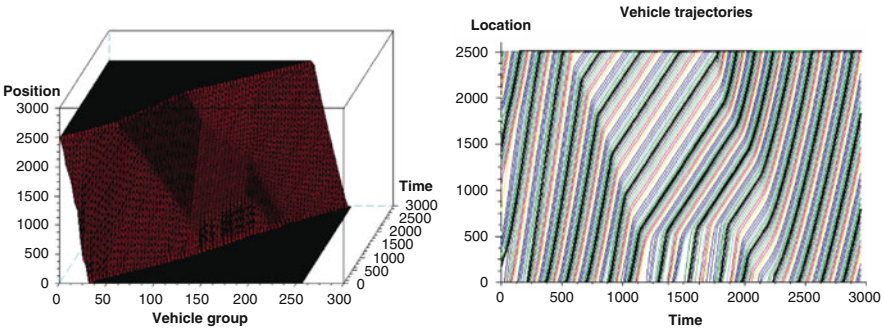

Fig. 4 Positions in Lagrangian framework (*left*) and Eulerian trajectories (*right*)

This simple numerical example shows that the low anticipatory fraction of the traffic allows to reduce or annihilate the shock wave because drivers accept lower critical spacings. This effect results is strongly dependent on our choice of the speed-spacing relationship $\bar{V}$ which implies that less anticipative drivers driver faster, take more risks. The inclusion of stochastic effects [8] would show another effect: that multi-anticipation smoothens traffic.

Conclusion and Future Directions

Possible extensions include adding source terms for the equation of advection of the composition. This could account for the spatial variability of multi-anticipatory behaviour. See for instance [11]. Moreover our model should be tested on real measurement data. The main problem is the identification of instantaneous traffic composition χ as well the speed-spacing function parameters as it was done in [4].

Another study should be based on the analysis of individual trajectories to recover the results of previous studies which state that the multi-anticipative car-following models improve the representation of individual driving behaviour. While the existing experiments only take into account already congested situations, these works should extend the results by considering for congested and also fluid traffic flow situations. Such a study could also confirm or infirm the impact of anticipatory traffic on the driving behavior (see Remark 2).

Acknowledgements The authors are grateful to Prof. Régis Monneau. We also want to thank the organizers of the Conference on Traffic and Granular Flow (TGF'13) in Jülich, Germany.

This work was partially supported by the ANR (Agence Nationale de la Recherche) through HJnet project ANR-12-BS01-0008-01.

References

1. R. Monneau, Homogenization of some traffic vehicular models, private lectures (2011)
2. G. Costeseque, J.P. Lebacque, A variational formulation for higher order macroscopic traffic flow models: numerical investigation, Transp. Res. B, **70** 112–133 (December 2014)
3. N. Farhi, Piecewise linear car-following modeling. Transp. Res. Part C Emerg. Technol. **25**, 100–112 (2012)
4. N. Farhi, H. Haj-Salem, J.P. Lebacque, Multi-anticipative piecewise linear car-following model. Presented at the 91st Transportation Research Board Annual Meeting (No. 12-3823), Washington, DC, 2012, arXiv:1302.0142 [math.OC] (2012)
5. N. Forcadel, C. Imbert, R. Monneau, Homogenization of accelerated Frenkel-Kontorova models with n types of particles. Trans. Am. Math. Soc. **364**(12), 6187–6227 (2012)
6. S.P. Hoogendoorn, S. Ossen, M. Schreuder, Empirics of multianticipative car-following behavior. Transp. Res. Rec. J. Transp. Res. Board **1965**(1), 112–120 (2006)
7. S.P. Hoogendoorn, S. Ossen, M. Schreuder, Properties of a microscopic heterogeneous multi-anticipative traffic flow model, in *Transportation and Traffic Theory*, ed. by R.E. Allsop, M.G.H. Bell, B.G. Heydecker (Elsevier, Amsterdam, 2007)
8. M.M. Khoshyaran, J.P. Lebacque, A stochastic macroscopic traffic model devoid of diffusion, in *Traffic and Granular Flow'07*, ed. by C. Appert-Rolland, F. Chevoir, P. Gondret, S. Lassarre, J.-P. Lebacque, Michael Schreckenberg (Springer, Berlin/Heidelberg, 2009), pp. 139–150
9. J.P. Lebacque, The Godunov scheme and what it means for first order traffic flow models, in *Transportation and Traffic Theory, Proceeding of the 13th ISTTT*, Lyon (Elsevier, 1996), pp. 647–677
10. J.P. Lebacque, S. Mammar, H. Haj Salem, Generic second order traffic flow modelling, in *Transportation and Traffic Theory 2007*. Papers Selected for Presentation at ISTTT17, 2007
11. J.P. Lebacque, M.M. Khoshyaran, GSOM traffic flow models with eulerian source terms, Presentation at TGF'2013 (2013, in preparation)
12. M.J. Lighthill, G.B. Whitham, On kinematic waves. II. A theory of traffic flow on long crowded roads. Proc. R. Soc. Lond. Ser. A Math. Phys. Sci. **229**(1178), 317–345 (1955)
13. J. Monteil, R. Billot, N.E. El Faouzi, Véhicules coopératifs pour une gestion dynamique du trafic: approche théorique et simulation. Recherche Transports Sécurité, **29** 47–58 (2013)
14. S. Ossen, S.P. Hoogendoorn, Multi-anticipation and heterogeneity in car-following empirics and a first exploration of their implications, in *Intelligent Transportation Systems Conference, ITSC'06*, Toronto (IEEE, 2006), pp. 1615–1620
15. P.I. Richards, Shock waves on the highway. Oper. Res. **4**(1), 42–51 (1956)
16. M. Treiber, A. Kesting, D. Helbing, Delays, inaccuracies and anticipation in microscopic traffic models. Physica A Stat. Mech. Appl. **360**(1), 71–88 (2006)

A Simple Statistical Method for Reproducing the Highway Traffic

Luis Eduardo Olmos and José Daniel Muñoz

Abstract Some of the most important questions concerning the traffic flow theory are focused on the correct functional form of the empirical flow-density fundamental diagram. Although most cellular automata intend to reproduce this diagram by measuring the limit steady-states from the dynamic simulation, real roads are constantly perturbed by external factors, driving the system to explore a much broader phase space. Hereby, we show that a Monte Carlo sampling of all states compatible with a driving rule (previously derived for Bogota) actually reproduces the measured fundamental diagram, both in mean values and dispersion, when all such states are assumed equally probable. Even more, by using the Wardrop's relation, the same gathered data also approximates the general form of the *time-mean* fundamental diagrams. These results suggest that driving rules are much richer in information than usually expected and, that the assumption of equally probable states plus a finite length of road may be a first model for the statistical description of highways.

1 Introduction

Since the beginnings the investigation in traffic flow is mainly focused on the functional relationships between the flow q, the space-mean speed v_s and the density of vehicles on a road ρ and even Greenshields [1] found a linear relationship between speed and density. The first fundamental diagrams were found just by fitting a relation $q(\rho) = \rho \cdot v(\rho)$ of the empirical data, where $v(\rho)$ is again the fitted empirical velocity-density relationship. However, this is much more complex than just a well-defined function. It is discontinuous and, for high densities, the data are widely scattered, which is usually interpreted as an effect of fluctuations or of an instability in vehicle dynamics. This property shows that rather than the fundamental diagram, the microscopic structure is the key for the understanding of the traffic flow characteristics. That is why microscopic models have been more successful over other models. Among those, cellular automata models (CA) have been some of the most fruitful, as they have reproduced the more complex properties of the

L.E. Olmos (✉) • J.D. Muñoz
Universidad Nacional de Colombia, Av. Carrera 30 # 45 Bogotá, Colombia
e-mail: leolmoss@unal.edu.co; jdmunozc@unal.edu.co

M. Chraibi et al. (eds.), *Traffic and Granular Flow '13*,
DOI 10.1007/978-3-319-10629-8_46

traffic flow. The success of these models is due to its simplicity and flexibility in the introduction of individual driving features, which are ultimately the responsible for the complex behaviour. Nevertheless, the traffic flow is a open system that, in general, is continuously perturbed at random by real factors (like pedestrians, or road imperfections) which make the system walks about several states. This arises the question of which traffic features can be reproduced by a Monte Carlo exploration of the phase space allowed by the driving rules.

2 Data Collection

Most empirical data are collected by stationary inductive loops at many highway locations. The loop detects a vehicle, it records the time of passing and it can also calculated the vehicle speed v_i. Quantities as q and v can be derived and presented in aggregated values for a time period, for instance, 1 or 5 min. The flow q is given by the number of cars $N(\Delta t)$ passing the detector per time interval Δt, i.e. $q = \frac{N(\Delta t)}{\Delta t}$. The time-mean speed, v_t, is obtained as the arithmetic average $v_t = \frac{1}{N}\sum_{i=1}^{N} v_i$. However, the determination of density is rather problematic. The difficulty arises from the fact the density is derived from the hydrodynamic relation $\rho = \frac{q}{v}$ and, when v_t is used, standing or slow cars are not detected, so then density is underestimated. By assuming stationary conditions, some authors avoid this difficulty by computing the space-mean speed as the harmonic mean of the time measurements [2, 4, 6, 10]:

$$v_s = \frac{1}{\frac{1}{N}\sum_{i=1}^{N}\frac{1}{v_i}} \quad . \tag{1}$$

The harmonic mean value corrects the detection of slow cars, but it does not allow to account for standing cars. Even so, this relation is the mostly used in the empirical data analysis. On respect to the differences between these two speed averages Wardrop [11] found that under homogeneous and stationary conditions:

$$v_t = \frac{\sigma_s^2}{v_s} + v_s \quad , \tag{2}$$

where σ_s^2 is the variance of space mean speed. Equation 2 is not useful if one has just local measurements (real case). This difficulty makes the single-vehicle data more interesting over aggregated data for the study of traffic flow. In other words, the histograms of quantities such as the time interval between consecutive cars (*temporal-headway*) or the spatial distance between them, *distance-headway* or *gap*, contains much more valuable information that simple relationships among average values [2, 6].

3 Methods

Let us implement a simple Monte Carlo sampling from the driving rules to generate at random the traffic states on the road in such a way that the states so obtained fulfill the driving rules. With this aim, the road is represented by a one-dimensional lattice of L sites with periodic boundaries. Since the empirical data are aggregated for short time periods we must use small road sizes, otherwise, the data dispersion would be reduced. Then, we choose a number of cars N and throw them randomly into the road. After that, each car computes its distance headway and takes the maximal allowed velocity v_{com} (comfort velocity) according to the rules of the CA model we are studying. So, we are absorbing both the non-equilibrium characteristic of traffic and the fact that drivers want to move as fast as possible. For each state so generated, it measured the spatial variables ρ and q which corresponds to a point in the fundamental diagram. The process is repeated many times for each number of cars $N \leq L$ and the fundamental diagram was obtained by cumulating these samples onto a two-dimensional histogram on the flow-density map (see Fig. 1). The main assumption of this work is that all randomly generated configurations, understood as the disposition of the cars on the road, are equally probable. But it is not the same for the macroscopic states of the traffic defined by the value of q, v and ρ. Figure 1 right shows that for a value of ρ there is a value of q more probable which just depends on the driving rules. We identify the most likely regions as the realistic states observed in empirical measurements.

We studied the driving rules of two CA models. The first one is the deterministic case of the well known NaSch model [5] where $v_{com} = gap$ for $gap \leq v_{max}$ and $v_{com} = v_{max}$ for $gap > v_{max}$. The second one is the Olmos-Muñoz model [7, 8] which was developed and implemented by the authors for reproducing the behavior of traffic flow in Bogota. This model keep in mind the particularities of Bogotan drivers, measured directly inside a car running on Bogota's highways. In this model, each car occupies two cells, and the gaps the driver uses to decide to brake or

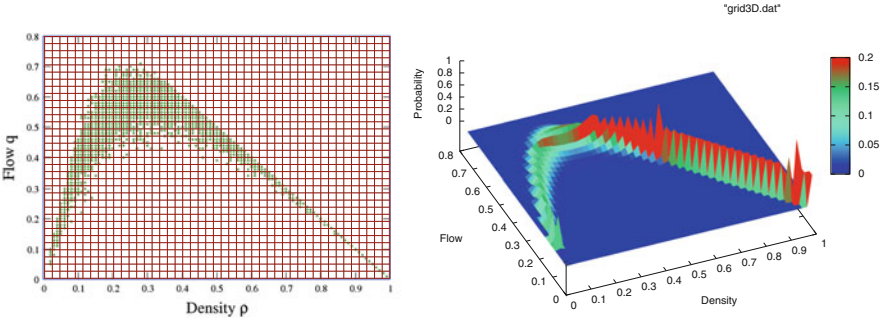

Fig. 1 Monte Carlo sampling from driving rules to generate at random the traffic states of the road. Scatter plot of the fundamental diagram (*left*) and density of states (*right*) obtained from the highway traffic states of these random configurations

Table 1 Values of v_{com} for each *gap* in the Olmos Muñoz model

Gap	v_{com}	Gap	v_{com}
0 or 1	0	6	6
2	1	7	7
3	2	8	9
4	3	9	9
5	4	10	10

accelerate are different for each speed. Then, if the headway distance is less or equal to the brake gap, the car brakes, and if it is greater than the accelerate gap, it accelerates; otherwise, the speed remains constant. Here, the comfort speed v_{com} corresponds to the largest one at which the gap ahead is lower or equal than the accelerate gap. The other two elements are delay time on the acceleration (the time it takes the car to reach the next discrete speed value) and break lights that force to brake when the car ahead breaks. Since these last two elements have a dynamical nature, they cannot be included in our method. This model is not as simple as the NaSch model but the value of v_{com} is summarized in the Table 1.

4 Results for the Fundamental Diagram

Figure 2 up shows the contour graph obtained for the frequency to obtain states with flux q at density ρ for the driving rules of the deterministic NaSch model. This is compared to the steady states of the dynamic simulation of the cellular automata. It is clear that around the value of maximum flow the most probable states do not match with the equilibrium states of the dynamical simulation. This could be expected, since there is not disorder in the deterministic NaSch model and, thus, it describes an unrealistic traffic flow. Nevertheless, by setting a non-zero value for the stochastic parameter, the match can improve. Figure 2 down shows the comparison between the empirical fundamental diagram measured for Bogota (built from *space-mean* measures in [7]) and the result obtained with the Monte Carlo method by using the Olmos-Muñoz driving rules (Table 1). This figure shows that the most likely states of the system (red color region) match in a good agreement to the real data measurements of a non-equilibrium system.

As we mentioned above, this method build the fundamental diagrams from *space-mean* variables. This arises the question of how a fundamental diagram is based on *time-mean* quantities. Although our method is not dynamic, we can compute the local quantities by using the Eq. 2, since σ_s^2 can be estimated from the histogram by computing standard deviations on horizontal sections of the diagram. So then, v_t can be obtained from v_s, the flow q remains the same but the density is recalculated from $\rho = \frac{q}{v_t}$. This step is included in the method before computing the density of the states. Figure 3 shows the surprising result. We obtain a fundamental diagram very similar to those measured empirically using temporal

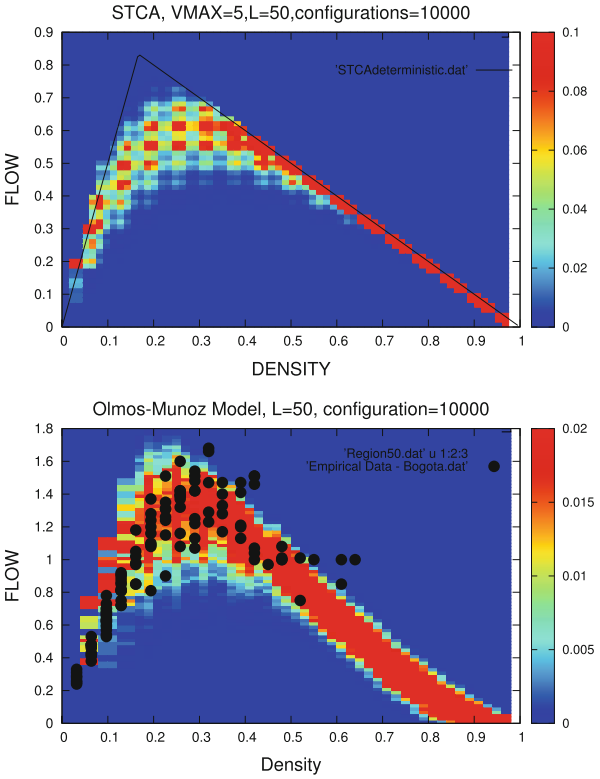

Fig. 2 Contour graph of the fundamental diagram obtained from the driving rules of the deterministic NaSch model (*top*) and of the Olmos-Muñoz model (*down*) for $L = 50$. *Top*: the right line corresponds to the steady state from a cellular automata simulation. *Down*: the *black dots* correspond to the empirical fundamental diagram measured in Bogota

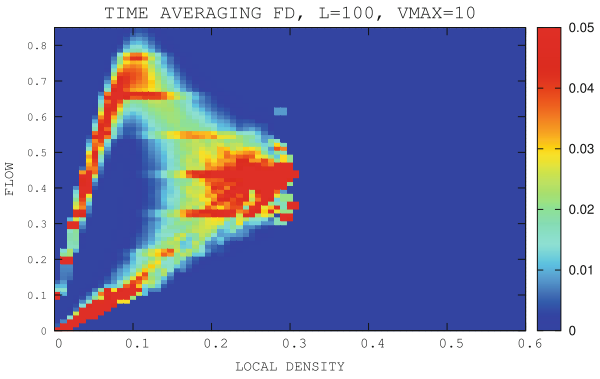

Fig. 3 Contour plot of the fundamental diagram obtained by transforming the *space-mean* variables in *time-mean* by using the Eq. 2 and the driving rules of the NaSch model. It is clear the similarity to those measured empirically using temporal averaged variables. It should remark that the discontinuity emerges naturally as a region of unlikely states

averaged variables. Focusing on the most likely states, one can distinguish the free-flow branch with high-flow states, and separated from this, a wide dispersed data appears as the synchronized phase under the perspective of the three-phases theory [3]. Therefore, the discontinuity appears naturally as a region of unlikely states. Besides that, it appears a region with low flow and a underestimated density, in similarity with the real collected data.

5 Analytical Approach and Distribution of Spatial Headways

We are also interested in the features of the microscopic structure that this method can reproduce. Clearly, the *spatial-headway distribution* is the characteristic that we can study directly. Due to the assumption of equally probable microstates, this method neglects the correlation between the gaps in front of successive cars. If we assume further that the length of the road $L \to \infty$, one can analytically derive that the gaps distribute as

$$\wp(gap) = \rho \cdot (1-\rho)^{gap} \text{ and, therefore, } \langle gap \rangle = \sum_{gap=0}^{\infty} gap \cdot \wp(gap) = \frac{1-\rho}{\rho} \qquad (3)$$

However, the empirical distribution of distance-headways reveals the inadequacy of this equation. As Fig. 4 left shows, this distribution is surprisingly broad. Even so, it is interesting to see that the right hand of the Eq. 3 predicts an average gap decreasing with the inverse density $\frac{1}{\rho}$, as Tilch and Helbing reported [10]. Thus, let us go more deeply with the idea. Since the v_{com} is related with the *gap*, we can study the distribution of speeds. The distribution of speeds $\wp(v_{com})$ for the deterministic NaSch model, for instance, is the same $\wp(gap)$ for $v_{com} < v_{max}$ and $\wp(v_{max}) = \sum_{i=v_{max}}^{\infty} i \cdot \rho \cdot (1-\rho)^i$ for v_{max}. Then, the average speed can be written as

$$\langle v \rangle = \frac{1-\rho}{\rho} \cdot (1-(1-\rho)^{v_{max}}) \quad , \qquad (4)$$

and one can obtain the flow immediately as $q = \rho \cdot \langle v \rangle$. Note that Eq. 4 with $v_{max} = 1$ reproduces Greenshield's model, and even other empirical models can be reproduced with other values of v_{max}. The kind of analytical calculations resulting in Eq. 4 are typical of the naive mean-field theory[1] and its generalizations [9]. These

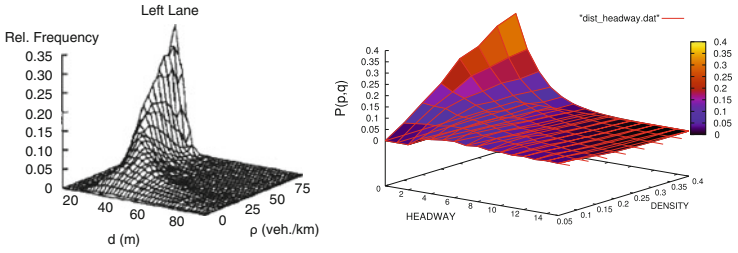

Fig. 4 The broad distribution of vehicle distance-headways at all densities ρ. *Left*: Empirical distribution from Tilch and Helbing [10]. *Right*: Distance-headways distribution just for most likely states in the Monte Carlo sampling of the NaSch model. Figure shows the same broad distribution observed in empirical data

[1] Actually our calculations are more naive than the naive mean-field theory.

theories were applied with success to the NaSch model at the beginning of the past decade but, as we already noted, they could not reproduce the distance-headway distribution of the stationary states of the CA model on a large system. Nevertheless, we are not interested in the stationary states of a cellular automaton but in the most likely states one would measure in reality. Therefore, we computed the distance-headway distribution for a finite system just for most likely states (the red color regions in Fig. 2 up). The results, in Fig. 4 right, shows the same broad distribution observed in empirical data.

Conclusions

Hereby, we have showed that a Monte Carlo exploration of the driving rules can reproduce the empirical fundamental diagram. Indeed, by generating states according with the Olmos-Muñoz model, and assuming that all these microstates are equally probable, we have reproduced with good agreement the capacity and the data dispersion of the fundamental diagram measured for Bogota city. Even more, by using the Wardrop's relation (Eq. 2), our data also approximates the general form of the *time-mean* fundamental diagrams, revealing a naturally emergence of both the discontinuity between free-flow and congested phases, and the high-flow states in this diagram as a consequence of such relation. In addition, by computing the *distance-headways* distribution according to the driving rules of NaSch model and just for the most likely states of a finite road, we have reproduced the broad distribution observed in reality. All this result suggests that the non-dynamical driving rules are more than a simulation mechanism; they can give valuable information about the macroscopic behaviour of the highway traffic flow. In addition, they also suggest that the assumption of equal probabilities for all states compatible with the driving rule plus a finite length of road may be a first model for the statistical description of highways. Of course, this hypothesis should be validated on other roads with other automaton rules, and this will be an interest subject of future work.

References

1. B.D. Greenshields, A study of traffic capacity, in *Highway Research Board Proceedings*, vol. 14, (Washington DC, 1935), p. 448
2. D. Helbing, Traffic and related self-drive many-particle systems. Rev. Mod. Phys. **73**, 1067–1141 (2001)
3. B. Kerner, *The Physics of Traffic: Empirical Freeway Pattern Features, Engineering Applications and Theory*. Understanding Complex Systems (Springer, 2004)
4. V. Knoop, S.P. Hoogendoorn, H. van Zuylen, Empirical differences between time mean speed and space mean speed, in *Traffic and Granular Flow'07 Proceedings* (Springer, Orsay, France, 2008), pp. 351–356

5. K. Nagel, M. Schrekenberg, A cellular automaton model for freeway traffic. J. Phys. I Fr. **2**, 2221–2229 (1992)
6. L. Neubert, L. Santen, A. Schadschneider, M. Schreckenberg, Single-vehicle data of highway traffic: a statistical analysis. Phys. Rev. E **60**, 6480 (1999)
7. L.E. Olmos, J.D. Muñoz, Traffic flow in Bogotá, in *Traffic and Granular Flow'05 Proceedings* (Springer, Berlin, Germany, 2006), p. 403
8. L.E. Olmos, J.D. Muñoz, A cellular automaton model for the traffic flow in Bogotá. Int. J. Mod. Phys. C **15**, 1397 (2004)
9. A. Schadschneider, Traffic flow: a statistical physics point of view. Physica A **313**, 153–187 (2002)
10. B. Tilch, D. Helbing, Evaluation of single vehicle data in dependence of the vehicle-type, lane, and site, in *Traffic and Granular Flow'99* (Springer, Berlin, Stuttgart, Germany, 2000), p. 333
11. J.G. Wardrop, Some theoretical aspects of road traffic research, in *Proceedings of the Institution of Civil Engineers*, vol. 1 of 2, (London, Great Britain, 1952)

Controlling of Vehicular Traffic Flow at an Intersection Via Two Schemes of Traffic Lights

Somayyeh Belbasi and M. Ebrahim Foulaadvand

Abstract By means of extensive Monte Carlo simulation, we have investigated the traffic flow characteristics in a single signalised intersection via developing Nagel-Schreckenberg cellular automata model. A set of traffic lights operating in two schemes controls the traffic flow. A closed boundary condition is applied to the streets, each of which conducts a unidirectional flow. It is shown that there exists a plateau region in fundamental diagrams inside which the total outflow remains almost.

1 Introduction

Simulation of urban traffic flow is becoming an essential tool for optimisation purposes as the number of vehicles increases continuously and traffic conditions deteriorate, both for vehicles and pedestrians. Modelling the dynamics of vehicular traffic flow by cellular automata has constituted the subject of intensive research by statistical physics during the past years [1–3]. City traffic was an early simulation target for statistical physicists [4–11]. Recently, physicists have notably attempted to simulate the traffic flow at intersections and other traffic designations such as roundabouts [12–20].

The vehicular flow at the intersection of two roads can be controlled via two distinctive schemes. In the first scheme, the traffic is controlled without traffic lights [19, 21]. In the second scheme, signalised traffic lights control the flow. Our objective in this paper is to study in some depth, the characteristics of traffic flow and its optimisation in a single intersection

S. Belbasi (✉) • M.E. Foulaadvand
University of Zanjan, Zanjan, IRAN
e-mail: s_belbasi@znu.ac.ir; foolad@iasbs.ac.ir

M. Chraibi et al. (eds.), *Traffic and Granular Flow '13*,
DOI 10.1007/978-3-319-10629-8_47

2 Description of the Problem

Consider a traffic flow at the intersection of two streets. Each street conduct a unidirectional traffic flow and has two lanes. The flow directions are taken south-north in street one and east-west in street two. Vehicles can turn when reaching to the intersection. A northward moving car can turn right left and a westward moving car can turn right when reaching to the intersection. We model each street lane by a chain of L sites. The chains of perpendicular streets intersect each other at the middle sites $i_1 = i_2 = \frac{L}{2}$. The discretisation of space is such that each car occupies five cells. Time elapses in discrete steps of Δt and velocities take discrete values $0, 1, 2, \cdots, v_{max}$ in which v_{max} is the maximum velocity measured in unit of $\frac{\Delta x}{\Delta t}$ in which Δx is the cell length. In the first scheme, fixed time signalization of lights, the lights periodically turn into red and green. The period T, hereafter referred to as *cycle time*, is divided into two phases. In the first phase with duration T_g, the lights are green for the northward street and red for the westward one. In the second phase which lasts for $T - T_g$ timesteps the lights change their colour i.e.; they become red for the northward and green for the westward street. The gap of all cars are update with their leader vehicle except those two which are the nearest approaching cars to the intersection. These two cars need special attention. For these approaching cars gap should be adjusted with the signal in its red phase. In this case, the gap is defined as the number of cells right after the car's head to the intersection point $\frac{L}{2}$. The system is update for 2×10^5 time steps. After transients, two streets maintain steady-state currents denoted by J_1 and J_2 which are defined as the number of vehicles passing from a fixed location per time step. They are functions of global densities ρ_1 and ρ_2 and signal times T and T_g. Figures 1–3 show the fundamental diagrams for specified parameters.

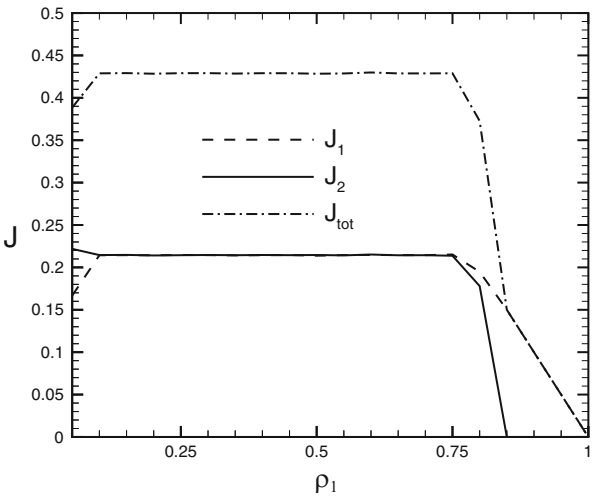

Fig. 1 Current versus ρ_1 for $T = 30$, $T_g = 15$ and $\rho_2 = 0.1$

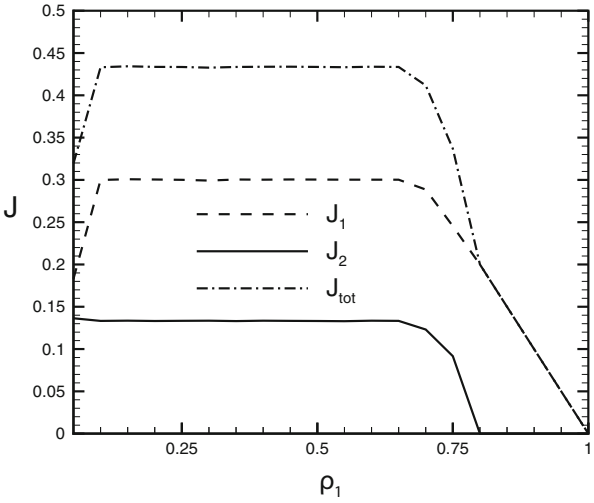

Fig. 2 Current versus ρ_1 for T = 30, $T_g = 20$ and $\rho_2 = 0.1$

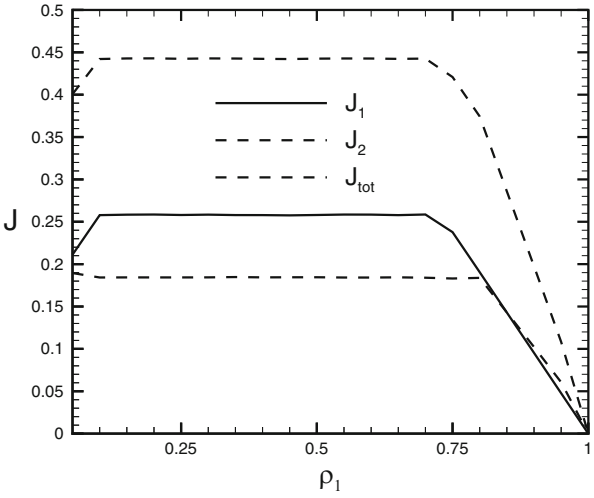

Fig. 3 Current versus ρ_1 for T = 35, $T_g = 20$ and $\rho_2 = 0.1$

We observe that for each T_g, J_1 linearly increase then a lengthy plateau region is formed. It seems the plateau region is natural because by increasing T_g the model tends to a normal NS model. The emergence of a plateau region is associated to defect-like role of the crossing point. After the plateau, J_1 exhibits linear decrease versus ρ_1 in the same manner as in the fundamental diagram of a single road. Concerning the variation of cycle time T, increasing the cycle time T gives rise, on an equal basis, to increase both in the green and in the red portion of the cycle allocated to each street. The results show a notable increase in flows when T is increased. This observation does not seem to comply to reality. The reason is due to unrealistic nature of NS rules.

Although ρ_2 remains constant J_2 is affected by density variations in street 1. For each T_g, J_2 as a function of ρ_1 exhibits two regimes. In the first regime, J_2 is almost independent of ρ_1 and remains constant up to high ρ_1. Afterwards in the second regime, J_2 exhibits a linearly decreasing behaviour towards zero. Analogous to J_1, the existence of a wide plateau region indicates that street 2 can maintain a constant flow capacity for a wide range of density variations in the first street. If T_g is increased, the green time allocated to the second street decrease so we expect J_2 to exhibit a diminishing behaviour.

In general, the dependence of total current on J_1 depends on the value of T_g. Except for small values of T_g, total current increases with ρ_1 then it becomes saturated at a lengthy plateau before it starts its linear decrease.

In the second scheme, intelligent controlling scheme, the signalisation of traffic lights is simultaneously adapted to traffic status in the vicinity of intersection. There exist numerous schemes in which traffic responsive signalisation can be prescribed. Here for brevity we discuss only one of these methods. To be precise, we define a cut-off queue length. The signal remain red for a street until the length of the corresponding queue formed behind the red light exceeds the cut-off length. At this moment the lights change colour. Apparently due to stochastic nature of cars movement, the cycle time will be subjected to variations and will no longer remain constant. In Figs. 4 and 5 we exhibit J versus ρ_1 for various values of cut-off lengths.

Analogous to fixed-time scheme, for given ρ_2 a lengthy plateau in J_{tot} forms. The plateau height as well as its length show a significant dependence on queue length. Higher queue length are associated with smaller length and higher current. We have also examined larger values of ρ_2. The results are qualitatively analogous the above

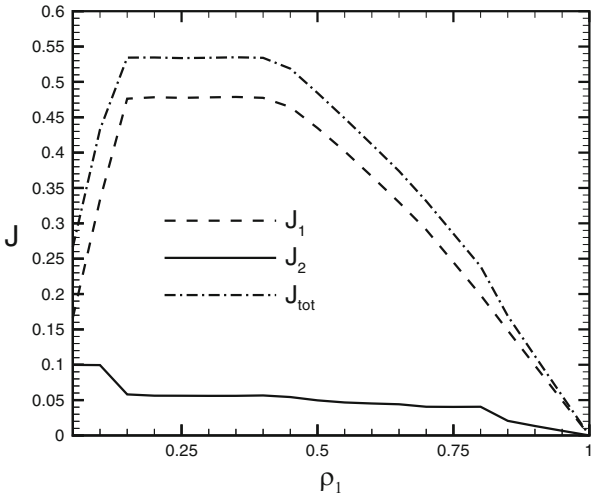

Fig. 4 Total current versus ρ_1 for $\rho_2 = 0.03$ and queue length = 8

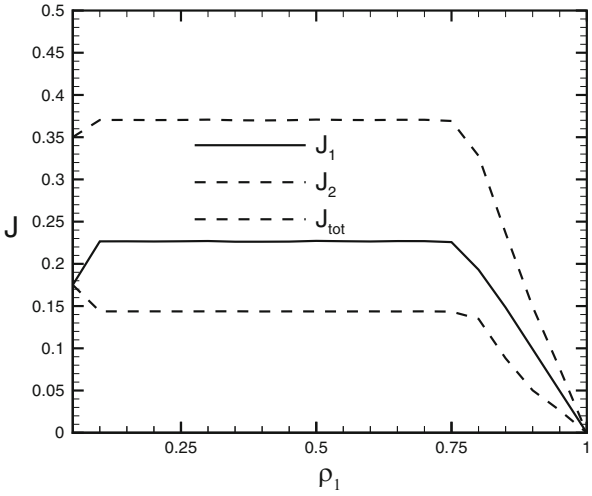

Fig. 5 Total current versus ρ_1 for $\rho_2 = 0.05$ and queue length = 5

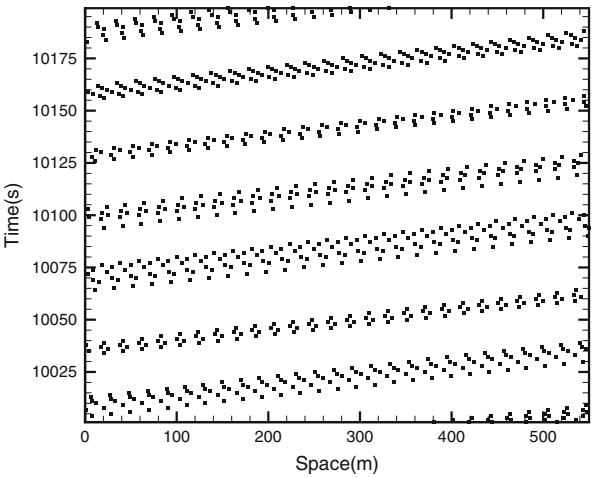

Fig. 6 Space-time plot for $\rho_1 = 0.9$, $\rho_2 = 0.9$, T = 30 and $T_g = 15$

graphs. The notable point is that for ρ_2 larger than 0.1, J_{tot} do not show a significant dependence on ρ_2.

To shed some light onto the problem, we sketch space-time plots of vehicles in Figs. 6 and 7. It is oberved that in traffic responsive scheme, the cars spatial distribution is more homogeneous which is due to randomness in cycle times.

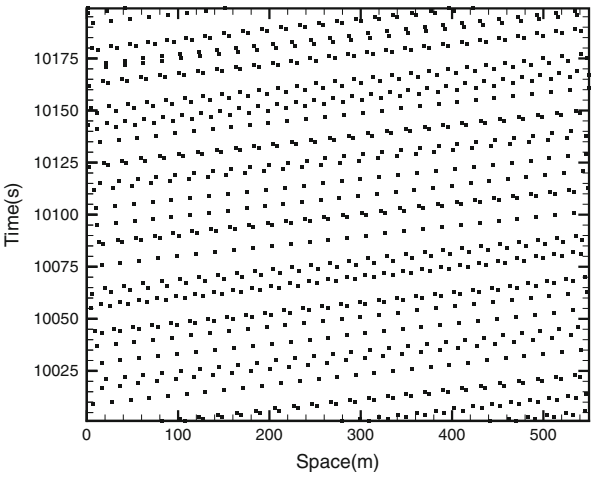

Fig. 7 Space-time plot for $\rho_1 = 0.9$, $\rho_2 = 0.9$ and queue length = 5

Conclusion

Our finding show that hindrance of cars upon reaching the red light gives rise to the formation of plateau regions in the fundamental diagrams. This is reminiscent of the conventional role of a single impurity in one-dimensional out of equilibrium systems. The existence of a wide plateau region in the total system current shows the robustness of the controlling scheme to the density fluctuations. The overall throughput from the intersection exhibits a significant dependence on the cycle time in the fixed time scheme and on the queue cut-off length in the responsive scheme.

References

1. D. Chowdhury, L. Santen, A. Schadschneider, Phys. Rep. **329**, 199 (2000)
2. D. Helbing, Rev. Mod. Phys. **73**, 1067 (2001)
3. C. Apert-Rolland, F. Chevior, P. Godret, S. Lasarre, J.-P. Lebacque, M. Schreckenberg (eds.), *Traffic and Granular Flow'07*, University of Paris-Sud, Orsay, France (Springer, 2009)
4. O. Biham, A. Middleton, D. Levine, Phys. Rev. A **46**, R6124 (1992)
5. T. Nagatani, J. Phys. Soc. Jpn. **63**, 1228 (1994); J. Phys. Soc. Jpn. **64**, 1421 (1995)
6. J.A. Cuesta, F.C. Martines, J.M. Molera, A. Sanchez, Phys. Rev. E **48**, R4175 (1993)
7. J. Freund, T. Pöschel, Physica A **219**, 95 (1995)
8. B. Chopard, P.O. Luthi, P.A. Queloz, J. Phys. A **29**, 2325 (1996)
9. S. Tadaki, Phys. Rev. E **54**, 2409 (1996); J. Phys. Soc. Jpn. **66**, 514 (1997)
10. J. Török, J. Kertesz, Physica A **231**, 515 (1996)
11. E. Brockfeld, R. Barlovic, A. Schadschneider, M. Schreckenberg, Phys. Rev. E **64**, 056132 (2001)
12. S. Lämmer, H. Kori, K. Peters, D. Helbing, Physica A **363**, 39 (2006)
13. R. Jiang, D. Helbing, P. Kumar Shukla, Q.-S. Wu, Physica A **368**(2), 567 (2006)

14. B. Ray, S.N. Bhattacharyya, Phys. Rev. E **73**, 036101 (2006)
15. R.X. Chen, K.Z. Bai, M.R. Liu, Chin. Phys. **15**(7), 1471 (2006)
16. R. Wang, M. Liu, R. Kemp, M. Zhou, Int. J. Mod. Phys. C **18**(5), 903 (2007)
17. D.W. Huang, Physica A **383**(2), 603 (2007)
18. M. Najem, Int. J. Mod. Phys. C **18**(6), 1047 (2007); **19**(6), 947 (2008)
19. M.E. Foulaadvand, S. Belbasi, J. Phys. A Math. Theor. **40**, 8289 (2007)
20. K.-Z. Bai, R.-X. Chen, M.-R. Liu, L.-J. Kong, R.-S. Zheng, Acta Phys. Sin. **58**(7), 4500 (2009)
21. M.E. Foulaadvand, M. Neek Amal, Eur. Phys. Lett. **80**(6), Article number 6002 (2007)

Equation-Free Analysis of Macroscopic Behavior in Traffic and Pedestrian Flow

Christian Marschler, Jan Sieber, Poul G. Hjorth, and Jens Starke

Abstract Equation-free methods make it possible to analyze the evolution of a few coarse-grained or macroscopic quantities for a detailed and realistic model with a large number of fine-grained or microscopic variables, even though no equations are explicitly given on the macroscopic level. This will facilitate a study of how the model behavior depends on parameter values including an understanding of transitions between different types of qualitative behavior. These methods are introduced and explained for traffic jam formation and emergence of oscillatory pedestrian counter flow in a corridor with a narrow door.

1 Introduction

The study of pedestrian and traffic dynamics leads naturally to a description by a few macroscopic, e.g., averaged, quantities of the systems at hand. On the other hand, so-called microscopic models, e.g., multi-agent systems, inherit individual properties of the agents and can therefore be made very realistic. Among more successful microscopic models are social force models for pedestrian dynamics [1–3] and optimal velocity models in traffic dynamics [4–8]. Although computer simulations of microscopic models for specific scenarios are straightforward to perform it is often more relevant and useful to look at the systems on a coarse scale, e.g., to investigate a few macroscopic quantities like first-order moments of distributions or other macroscopic descriptions which are motivated by the application.

The analysis of the macroscopic behavior of microscopically defined models is possible by the so-called *equation-free* or *coarse analysis*. This approach is motivated and justified by the observation, that multi-scale systems, e.g., many-

C. Marschler (✉) • P.G. Hjorth • J. Starke
Department of Applied Mathematics and Computer Science, Technical University of Denmark, DK-2800 Kongens Lyngby, Denmark
e-mail: chrms@dtu.dk; pghj@dtu.dk; jsta@dtu.dk

J. Sieber
College of Engineering, Mathematics and Physical Sciences, University of Exeter, EX4 4QF Exeter, UK
e-mail: j.sieber@exeter.ac.uk

M. Chraibi et al. (eds.), *Traffic and Granular Flow '13*,
DOI 10.1007/978-3-319-10629-8_48

particle systems, often exhibit low-dimensional behavior. This concept is well known in physics as slaving of many degrees of freedom by a few slow variables, sometimes referred to as "order parameters" (see e.g. [9, 10]) and is formalized mathematically for slow-fast systems by Fenichel's theory [11]. These methods aim for a description of the system in terms of a small number of variables, which describe the interesting dynamics. This results in a dimension reduction from many degrees of freedom to a few degrees of freedom. For example, in pedestrian flows, we reduce the full system of equations of motion with equations of motion for each single pedestrian to a low-dimensional system for weighted mean position and velocity of the crowd.

A difficulty for such a macroscopic analysis is that governing equations for the coarse variables, i.e., the order parameters, are often not known. Those equations are often very hard or sometimes even impossible to derive from first principles especially in models with complicated microscopic dynamics. To extract information about the macroscopic behavior from the microscopic models equation-free methods [12–15] can be used. This is done by using a special scheme for switching between microscopic and macroscopic levels by restriction and lifting operators and suitably initialized short microscopic simulation bursts in between. Problems with the initialization of the microscopic dynamics, i.e., the so-called lifting error, have been studied in [8]. An *implicit equation-free method* for simplifying the lifting procedure has been introduced, allowing for avoiding lifting errors up to an error which can be estimated for reliable results [8]. The equation-free methodology is most suitable in cases where governing equations for coarse variables are either not known, or when one wants to study finite-size effects if the number of particles is too large for investigation of the full system, but not large enough for a continuum limit. It is even possible to apply equation-free and related techniques in experiments, where the microscopic simulation is replaced by observations of an experiment [16–18].

For pedestrian and for traffic problems, a particularly interesting case is a systematic study of the influence of parameters on solutions of the system. This leads to equation-free bifurcation analysis. One obtains qualitative as well as quantitative information about the solutions and their stability. Furthermore, it saves computational time and is therefore advantageous over a brute-force analysis or computation. The knowledge of parameter dependence and the basin of attraction of solutions is crucial for controlling systems and ensuring their robustness. Changes of solutions are summarized in bifurcation diagrams and solution branches are usually obtained by means of numerical continuation. These techniques from numerical bifurcation analysis can be combined with equation-free methods to gain insight into the macroscopic behavior in a semi-automatic fashion.

In the following, we apply *equation-free bifurcation analysis* to two selected problems in traffic and pedestrian dynamics. Section 2 gives a short overview about equation-free methods. The methods introduced in Sect. 2 are then applied to study traffic jams in the optimal velocity model (cf. [4, 8]) in Sect. 3. Section 4 describes the macroscopic analysis of two pedestrian groups in counterflow through

a bottleneck (cf. [3]) and the section "Discussion and Conclusion" concludes the paper with a brief discussion and an outlook on future research directions.

2 Equation-Free Methods

Equation-free methods have been introduced (cf. [14, 15] for reviews) to study the dynamics of multi-scale systems on a macroscopic level without the need for an explicit derivation of macroscopic equations from the microscopic model. The necessary information is obtained by suitably initialized short simulation bursts of the microscopic system at hand. Equation-free methods assume that the system under investigation can be usefully described on a coarse scale. Evolution equations on the macroscopic level are not given explicitly. A big class of suitable systems are slow-fast systems, which have a separation of time scales. Under quite general assumptions (cf. [11]) these systems quickly converge to a low-dimensional object in phase space, the so-called *slow manifold* (cf. Fig. 1). The long-term dynamics (i.e., the macroscopic behavior) happens on this slow manifold, which is usually of much lower dimension than the overall phase space (of the microscopic system). The goal of equation-free methods is to gain insight into the dynamics on this slow manifold.

In the following we discuss the equation-free methodology in detail. The construction of a so-called macroscopic time stepper requires three ingredients to be provided by the user: the lifting $\mathscr{L}$ and restriction $\mathscr{R}$ operators to communicate between the microscopic and macroscopic levels and vice versa, and the microscopic time stepper M. Due to a separation of time scales, it is possible to construct the macroscopic time stepper by a *lift-evolve-restrict-scheme*. This scheme is subsequently used to perform bifurcation analysis and numerical continuation.

2.1 Microscopic Time Stepper M

To be specific, let us consider a microscopic model in the form of a high-dimensional system of N differential equations

$$\dot{u} = f(u). \tag{1}$$

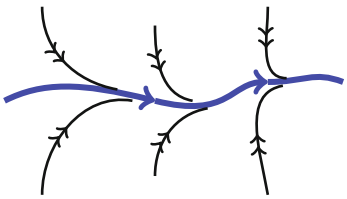

Fig. 1 Fast convergence to a slow manifold (*thick blue curve*). Trajectories in many dynamical systems converge very quickly to a slow manifold, along which the long-time macroscopic behavior takes place

This can be any model of traffic or pedestrian dynamics, possibly depending on a set of parameters. We generally assume that the number of degrees of freedom and thereby the dimension N of u is large. Note that a second-order model, e.g., the social force model with forces $f_{\text{force}}(x)$, can be written as a first-order model of the type (1) by including the velocities $\dot{x} = v$ into the equation. Then u has the form $u = (x, v)$, and the right-hand side is $f(u) = f((x, v)) = [v, f_{\text{force}}(x)]$. We assume that a microscopic time stepper M for model (1) is available. That is, we have a routine M (usually a simulation or software package) with two inputs: the time $t \in \mathbb{R}$ by which we want to evolve and the initial state $u_0 \in \mathbb{R}^N$ from which we start. The output $M(t, u_0) \in \mathbb{R}^N$ is defined by the relation

$$u(t_0 + t) = M(t, u(t_0)). \tag{2}$$

That is $M(t, u_0)$ is the state u of (1) after time t, starting from u_0 at time t_0.

2.2 Separation of Time Scales

We also assume that the dynamics on the macroscopic scale can be described by a few macroscopic variables $x \in \mathbb{R}^n$, where n is much smaller than the phase space dimension N of the microscopic model. This assumption is typically true in many-particle systems, e.g., pedestrian flow and traffic problems. The goal of equation-free methods is then to construct a time stepper for x on the macroscopic level,

$$x(t_0 + t) = \Phi(t, x(t_0)), \tag{3}$$

based on repeated and appropriately initialized runs, i.e., simulation bursts, of the microscopic time stepper M for u. In practice, a user of equation-free methods begins with the identification of a map, the so-called restriction operator

$$\mathscr{R} : \mathbb{R}^N \to \mathbb{R}^n,$$

which reduces a given microscopic state $u \in \mathbb{R}^N$ to a value of the desired macroscopic variable $x \in \mathbb{R}^n$. The assumption about the variables x describing the dynamics at the macroscopic scale has to be made more precise. We require that for all relevant initial conditions u and a sufficiently long transient time t_{skip} the result of the microscopic time stepper (2) is (at least locally and up to a small error) uniquely determined by its restriction, i.e., its macroscopic behavior. That is, if for two initial conditions u_0 and u_1 the relation

$$\begin{aligned} &\mathscr{R}M(t_{\text{skip}}; u_0) = \mathscr{R}M(t_{\text{skip}}; u_1) \quad \text{holds, then} \\ &|\mathscr{R}M(t_{\text{skip}} + t; u_0) - \mathscr{R}M(t_{\text{skip}} + t; u_1)| < C \exp(\varepsilon t - \gamma\, t_{\text{skip}}) \end{aligned} \tag{4}$$

for all $t \geq 0$. In (4) the pre-factor C should be of order unity and independent of the choice of t, u_0 and u_1. The growth rate ε is also assumed to be smaller than the decay rate γ. This is what we refer to as *separation of time scales* between macroscopic and microscopic dynamics. Requirement (4) makes the statement "the dynamics of u on long time scales can be described by the macroscopic variable $x = \mathscr{R}u$" more precise. We also see that the error in this description can be made as small as desired by increasing the *healing time* t_{skip}. In fact, requirement (4) determines what a good choice of t_{skip} is for a given problem.

In order to complete the construction of the macroscopic time stepper Φ, the user has to provide a lifting operator

$$\mathscr{L} : \mathbb{R}^n \to \mathbb{R}^N,$$

which reconstructs a microscopic state u from a given macroscopic state x. See [19–21] for proposals how to construct good lifting operators for explicit equation-free methods (see Eq. (6) below). In the case of implicit equation-free methods the choice of a lifting operator is not as delicate [8]. Also note that the choice of lifting operator is not unique.

2.3 Macroscopic Time Stepper Φ

We can now assemble the approximate macroscopic time stepper Φ for x by applying the steps *Lift-Evolve-Restrict*, as illustrated in Fig. 2 in a judicious manner (cf. Fig. 3 for a detailed construction): the time-t image $y = \Phi(t; x)$ of an initial condition $x \in \mathbb{R}^n$ is defined as the solution y of the implicit equation

$$\mathscr{R}M(t_{\text{skip}}; \mathscr{L}y) = \mathscr{R}M(t_{\text{skip}} + t; \mathscr{L}x). \tag{5}$$

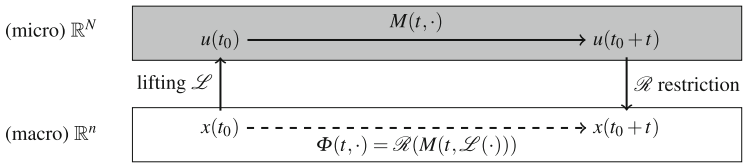

Fig. 2 Scheme for construction of the macroscopic time stepper Φ using the lifting $\mathscr{L}$ and restriction operator $\mathscr{R}$ for switching between microscopic and macroscopic levels. M denotes the microscopic time stepper

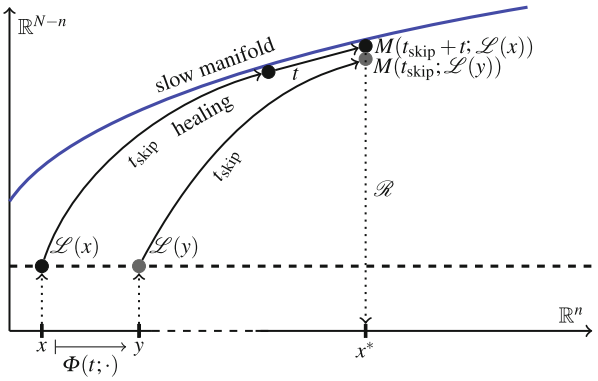

Fig. 3 Visualization of the implicit scheme (5). The macroscopic time stepper Φ maps the macroscopic state x to the yet unknown macroscopic state y. The scheme *lift-evolve-restrict* is applied to both states. Additionally to the healing step t_{skip} the dynamics on the slow manifold are observed for state x for an additional (long) time t. Both "paths" are compared at the macroscopic end point x^*. Note, that this scheme defines y implicitly

Note, that the macroscopic time stepper has originally been introduced as the explicit definition (cf. also Fig. 2)

$$\tilde{\Phi}(t;x) = \mathscr{R}M(t;\mathscr{L}x). \tag{6}$$

The explicit method (6) requires that the lifting operator maps onto (or very close to) the slow manifold for every macroscopic point x. The implicit method (5) does not have this requirement and should be the method of choice (cf. the discussion in Sect. 3). The implementation of the explicit and implicit time stepper is further illustrated in Table 1 using pseudocode. Equation (5) is a nonlinear but in general regular system of n equations for the n-dimensional variable y. Note that the construction (5) does not require an explicit derivation of the right-hand side $F : \mathbb{R}^n \to \mathbb{R}^n$ of the assumed-to-exist macroscopic dynamical system

$$\dot{x} = F(x). \tag{7}$$

However, it can be used to evaluate (approximately) the right-hand side F in desired arguments x (see below). The convergence of the time stepper Φ to the correct time-t map Φ_* of the assumed-to-exist macroscopic equation (7) is proven in detail in [8]. The error $|\Phi(t;x) - \Phi_*(t;x)|$ is of order $\exp(\varepsilon t - \gamma t_{\text{skip}})$.

2.4 Advantages of Equation-Free Methods

What additional benefits can the macroscopic time stepper Φ have beyond simulation of the low-dimensional dynamics (which could have been accomplished by running long-time simulations using M directly)?

Table 1 Pseudocode algorithm for computing the macroscopic solution y after time t using the macroscopic time stepper for the solution x using the explicit (6) and implicit (5) scheme, respectively. The implicit scheme uses a Newton iteration with a given tolerance `tol` to find y. For one-dimensional y the Jacobian `dF` is given by `(F(y[n]+dy)-F(y[n]))/dy`. Note, that the complexity of the implicit scheme stems mainly from the Newton iteration, which is not specific for equation-free computations

Required functions: lift, evolve, restrict (cf. main text)
solution at time t0: x

```
function res = Phi(t,x)
u1 = lift(x); u2 = evolve(t,u1); res = restrict(u2);
end
```

Explicit scheme	Implicit scheme

`y = Phi(t,x);`	`choose dy, tol, y[0] = x, n = 0, err = 2*tol`
	
	`function res = F(y)`
	`  res = Phi(tskip,y) - Phi(tskip+t,x);`
	`end`
	
	`while err > tol`
	`  Fy = F(y[n]);`
	`  dF = Jacobian(F,y[n],dy);`
	`  y[n+1] = y[n] - (dF)^-1*(Fy);`
	`  err = abs(y[n+1] - y[n]);`
	`  n = n+1;`
	`end`
	`y = y[n];`

- *Finding locations of macroscopic equilibria* regardless of their dynamical stability: macroscopic equilibria x are given by solutions to the n-dimensional implicit equation $\Phi(t_0; x) = x$, or, in terms of lifting and restriction:

$$\mathscr{R}M(t_{\text{skip}} + t_0; \mathscr{L}x) = \mathscr{R}M(t_{\text{skip}}; \mathscr{L}x) \tag{8}$$

for a suitably chosen time t_0 (a good choice is of the same order of magnitude as t_{skip}). The stability of an equilibrium x, found by solving (8), is determined by solving the generalized eigenvalue problem $Ax = \lambda Bx$ with the Jacobian matrices

$$A = \frac{\partial}{\partial x}\mathscr{R}M(t_{\text{skip}} + t_0; \mathscr{L}x), \quad B = \frac{\partial}{\partial x}\mathscr{R}M(t_{\text{skip}}; \mathscr{L}x).$$

Stability is determined by the modulus of the eigenvalues λ (where $|\lambda| < 1$ corresponds to stability).

- *Projective integration* of (7): one can integrate the macroscopic system (7) by point-wise approximation of the right-hand side F and a standard numerical integrator. For example, the explicit Euler scheme for (7) would determine the value $x_{k+1} \approx x((k+1)\Delta t)$ from $x_k \approx x(k\Delta t)$ implicitly by approximating

$$F(x_k) = \frac{1}{\delta}\left[\mathscr{R}M(t_{\text{skip}} + \delta; \mathscr{L}x_k) - \mathscr{R}M(t_{\text{skip}}; \mathscr{L}x_k)\right]$$

  with a small time δ, and then solving the implicit equation

$$\mathscr{R}M(t_{\text{skip}}; \mathscr{L}x_{k+1}) - \mathscr{R}M(t_{\text{skip}}; \mathscr{L}x_k) = F(x_k)\Delta t$$

  with respect to x_{k+1}. Projective integration is useful if the macroscopic time step Δt can be chosen such that $\Delta t \gg \delta$, or for negative Δt, enabling integration backward in time for the macroscopic system (7).
- *Matching the restriction*: Sometimes it is useful to find a "realistic" microscopic state u, corresponding to a given macroscopic value x. "Realistic" corresponds in this context to "after rapid transients have settled". This can be accomplished by solving the nonlinear equation

$$\mathscr{R}M(t_{\text{skip}}; \mathscr{L}y) = x \tag{9}$$

  for y and then setting $u = M(t_{\text{skip}}; \mathscr{L}y)$.

The formulas (8) and (9) have already been presented and tested in [22], where they were found to have vastly superior performance compared to alternative proposals for consistent lifting (such as presented in [19–21]).

2.5 Bifurcation Analysis and Numerical Continuation

Building on top of the basic uses of the macroscopic time stepper Φ, one can also use advanced tools for the study of parameter-dependent systems. Suppose that the microscopic time stepper M (and, thus, the macroscopic time stepper Φ) depends on a system parameter p. We are interested in how macroscopic equilibria and their stability change as we vary p. In the examples in Sects. 3 and 4 the primary system parameter is the target velocity (traffic) and door width (pedestrians), respectively.

When tracking equilibria in a parameter-dependent problem one may start at a parameter value p_0, where the desired equilibrium x_0 (given by $\Phi(t_0; x_0, p_0) = x_0$) is stable so that it can be found by direct simulations. This achieves a good initial guess, which is required to solve the nonlinear equations (8) reliably with a Newton iteration for near-by p close to p_0. In the traffic system studied in Sect. 3 the equilibrium corresponding to a single phantom jam undergoes a saddle-node bifurcation (also called fold, that is, the equilibrium turns back in the parameter

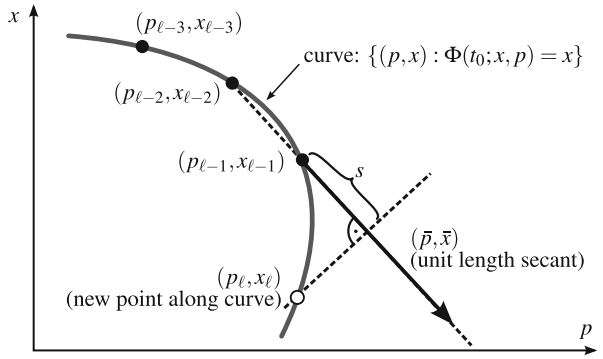

Fig. 4 Pseudo-arclength continuation of a curve of fixed points $\{(p, x) : \Phi(t_0; x, p) = x\}$ of the macroscopic time stepper Φ. A new point $(\bar{p}, \bar{x})$ is computed along the secant through $(p_{\ell-2}, x_{\ell-2})$ and $(p_{\ell-1}, x_{\ell-1})$ in a so-called predictor step. The following corrector step solves the equilibrium condition (cf. (10)) in the perpendicular direction to find the next equilibrium (p_ℓ, x_ℓ) on the curve

changing its stability, see Fig. 5a for an illustration). In order to track equilibria near folds one needs to extend the nonlinear equation for the macroscopic equilibrium with a so-called pseudo-arclength condition, and solve for the equilibrium x and the parameter p simultaneously [23, 24]. That is, suppose we have already found a sequence (p_k, x_k), $k = 1, \ldots, \ell - 1$, of equilibria and parameter values (see Fig. 4). We then determine the next pair (p_ℓ, x_ℓ) by solving the extended system for (p_ℓ, x_ℓ):

$$\begin{aligned} 0 &= \Phi(t_0; x_\ell, p_\ell) - x_\ell && \text{equilibrium condition} \\ s &= \bar{p}_\ell(p_\ell - p_{\ell-1}) + \bar{x}_\ell^T(x_\ell - x_{\ell-1}) && \text{pseudo-arclength condition.} \end{aligned} \tag{10}$$

The vector

$$(\bar{p}_\ell, \bar{x}_\ell^T) = \frac{(p_{\ell-1} - p_{\ell-2}, x_{\ell-1}^T - x_{\ell-2}^T)}{|(p_{\ell-1} - p_{\ell-2}, x_{\ell-1}^T - x_{\ell-2}^T)|} \tag{11}$$

is the secant through the previous two points, scaled to unit length, and s is the approximate desired distance of the newly found point (p_ℓ, x_ℓ) from its predecessor $(p_{\ell-1}, x_{\ell-1})$. The continuation method (10) permits one to track equilibria through folds such as shown in Fig. 5a or Hopf bifurcations such as shown in Fig. 6b (where the equilibrium becomes unstable and small-amplitude oscillations emerge). For a more detailed review on methods for bifurcation analysis the reader is referred to standard references, e.g., [23, 24].

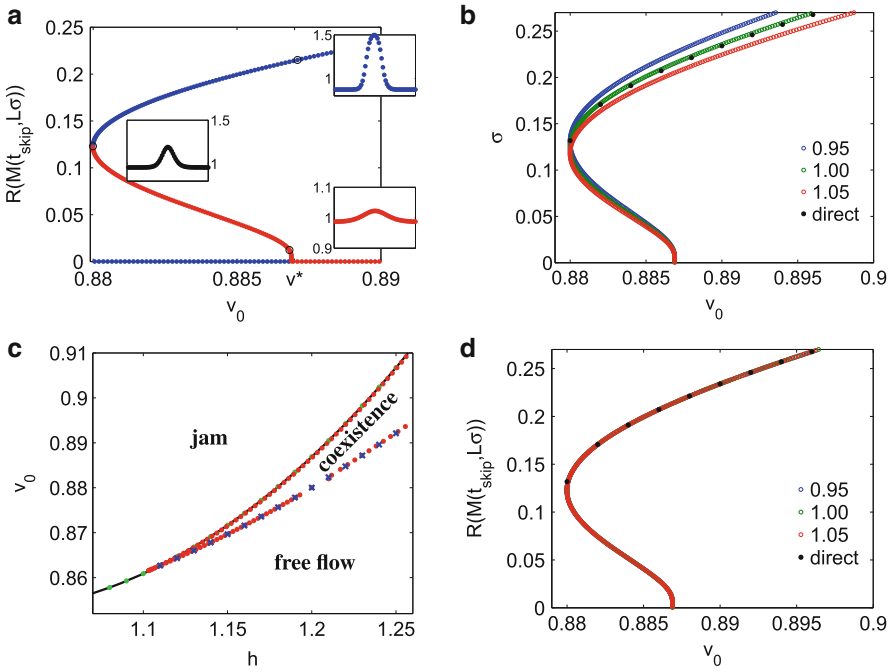

Fig. 5 Equation-free bifurcation analysis for the optimal velocity model (12). (**a**) Bifurcation diagram in healed quantities for $h = 1.2$. Headway profiles are shown for selected points (*black circles*) along the branch. *Blue* and *red dots* denote stable and unstable solutions, respectively. (**b**) and (**d**) show bifurcation diagrams for different lifting operators. Healed values in (**d**) lie exactly on the same branch and recover the results from direct simulation (*black dots*). Thus, the choice of lifting operator $\mathscr{L}$ does not affect the results if one reports the healed values (in contrast to (**b**), reporting the solutions σ of (8)). (**c**) Two-parameter bifurcation diagram for continuation of the fold point. Saddle-node (*blue crosses*) and Hopf points (*green dots*) from measurements in one-dimensional diagrams are in perfect agreement with the continuation in two parameters h and v_0 (*red dots*) and the analytical curve (*black line*)

3 Traffic Models

We apply the methods introduced in Sect. 2 to the optimal velocity (OV) model [4] as an example of microscopic traffic models. The model captures the main features of experiments of cars on a ring road [6]. We exploit equation-free numerical bifurcation analysis to answer the following questions; (1) for which parameter values in the OV model do we expect traffic jams and (2) how severe are they?

The equations of motion for car n in the OV model are

$$\tau \ddot{x}_n + \dot{x}_n = V(x_{n+1} - x_n), \qquad V(\Delta x_n) = v_0(\tanh(\Delta x_n - h) + \tanh(h)), \qquad (12)$$

where $\tau = 0.588$ is the reaction time and V is the optimal velocity function depending on the velocity parameter v_0 and inflection point h. Periodic boundary conditions $x_{n+N} = x_n + L$ are used for $N = 60$ cars on a ring road of length $L = 60$. Depending on the choice of v_0 and h one observes uniform flow, i.e., all cars have *headway* $\Delta x_n = 1$, or a traffic jam, i.e., a region of high density of cars. It is worth noting, that bistable parameter regimes can exist, i.e., a stable uniform flow and a stable traffic jam coexist and one or the other emerges, depending on initial conditions.

First, we fix $h = 1.2$ and study the bifurcation diagram in dependence of v_0. Before we are able to apply the algorithms presented in Sect. 2, we have to define the lifting and restriction operators.

3.1 The Restriction and Lifting Operators

The restriction operator $\mathscr{R}$, used to compute the macroscopic variable to describe phenomena of interest (here the deviation of the density profile from a uniform flow) of the microscopic model on a coarse level, is chosen as the standard deviation of the distribution of headway values

$$\mathscr{R}(u) = \sigma = \sqrt{\frac{1}{N-1}\sum_{n=1}^{N}(\Delta x_n - \langle \Delta x \rangle)^2}, \tag{13}$$

where $\langle \Delta x \rangle$ is the mean headway.

As the numerical continuation operates in a local neighborhood of the equilibrium states, the lifting operator can be based on a previously computed microscopic reference state $\tilde{u} = (\tilde{x}, \tilde{y})$ for positions $\tilde{x}$ and velocities $\tilde{y}$ and its macroscopic image under $\mathscr{R}$, $\tilde{\sigma} = \mathscr{R}\tilde{u}$. We use $\tilde{u}$ and $\tilde{\sigma}$ to obtain a microscopic profile u for every $\sigma \approx \tilde{\sigma}$:

$$\mathscr{L}_\mu(\tilde{u}, \sigma) = u = (x, y) = (x_{\text{new}}, V(x_{\text{new}})), \quad x_{\text{new}} = \frac{\mu\sigma}{\tilde{\sigma}}(\Delta\tilde{x} - \langle \Delta\tilde{x} \rangle) + \langle \Delta\tilde{x} \rangle. \tag{14}$$

We let the lifting $\mathscr{L}_\mu$ depend on an artificial parameter μ. We will vary μ later to demonstrate that the resulting bifurcation diagram is independent of the particular choice of $\mathscr{L}$.

3.2 Numerical Results

The results of the equation-free bifurcation analysis are shown in Fig. 5. The bifurcation diagram for fixed $h = 1.2$ (cf. Fig. 5a) shows a stable traffic jam for parameter values $v_0 > v^* = 0.887$. By continuation of the solution from a

stable traffic jam towards smaller values of v_0 a saddle-node bifurcation is found at $v_0 = 0.88$. The traffic jam loses stability and an unstable solution exists for $v_0 \in [0.88, 0.887]$. Continuing further along the branch, a Hopf bifurcation, i.e., a macroscopic pitchfork bifurcation, where traffic jams are born as small-amplitude time-periodic patterns, is found at $v_0 = 0.887$. At this point, stable uniform flow solutions ($\sigma = 0$) change their stability to unstable uniform flow solutions. For $v_0 \in [0.88, 0.887]$ two stable solutions coexist. In this one-dimensional system, the unstable solution separates the stable and the unstable fixed point, acting as a barrier. Thus, the bifurcation diagram also informs us about the magnitude of the disturbance necessary to change the behavior of the system from a stable traffic jam to a stable free flow. Headway profiles are shown for selected points along the branch to illustrate the microscopic solutions. In Fig. 5b, d the comparison of different lifting operators is shown. While the unhealed values σ (cf. Fig. 5b) of the equilibrium depend on the choice of μ, the healed values $\mathscr{R}M(t_{\text{skip}}; \mathscr{L}\sigma)$, used in the implicit equation-free methods (cf. Fig. 5d and [8]) are in perfect agreement with results from direct simulations (black dots).

In order to study the dependence on both parameters v_0 and h simultaneously, we use an extended set of equations to continue the saddle-node bifurcation point in Fig. 5c. Blue crosses and green dots denote measurements of the saddle-node and Hopf points from one-parameter continuations, respectively. The two-parameter continuation (red dots) is in perfect agreement with the measurements. As a check of validity, the Hopf curve (black line below red dots) can be computed analytically (cf. e.g., [8]) and is shown for comparison.

In conclusion, the analysis pinpoints the parameter values for the onset and collapse of traffic jams. This information is of potential use to understand the role of speed limits. The two-parameter bifurcation diagram in Fig. 5c shows a free flow regime for small v_0 and large h (bottom right part of the diagram). On the other hand, a large velocity parameter v_0 and a small safety distance h lead to traffic jams (top left part). In between, a coexistence between free flow and traffic jams is found. The final state depends on the initial condition. A speed limit lower than the saddle-node values is necessary to assure a global convergence to the uniform free flow.

4 Pedestrian Models

For further demonstration of the equation-free bifurcation analysis, we also apply it to a social force model describing pedestrian flow [1, 25]. A particular setup with two crowds passing a corridor with bottleneck [26] from opposite sites (the crowd marked blue moving to the right, the crowd marked red moving to the left) is analyzed with respect to qualitative changes of the system behavior [3, 27]. To this end, a coarse bifurcation analysis is used to determine which bifurcations occur and thereby to understand which solutions are expected to exist. Details about the model and the analysis of the bottleneck problem can be found in [3]. Here, we focus on the coarse analysis of the problem.

Two parameters have been chosen as the main bifurcation parameters; the ratio of desired velocities of the two crowds $r_{v_0} = v_0^r / v_0^b$ and the width of the door w acting as a bottleneck. Microscopic simulations of the model for two crowds of size $N = 100$ reveal two fundamentally different regimes of the dynamics. One finds a blocked state and a state that is oscillating at the macroscopic level (cf. Fig. 6a) for small and large door widths, respectively. The question we would like to answer is: how and where does the transition from a blocked to an oscillating state happen? In mathematical terms the question is, where is the bifurcation point and what type of bifurcation is observed at the transition?

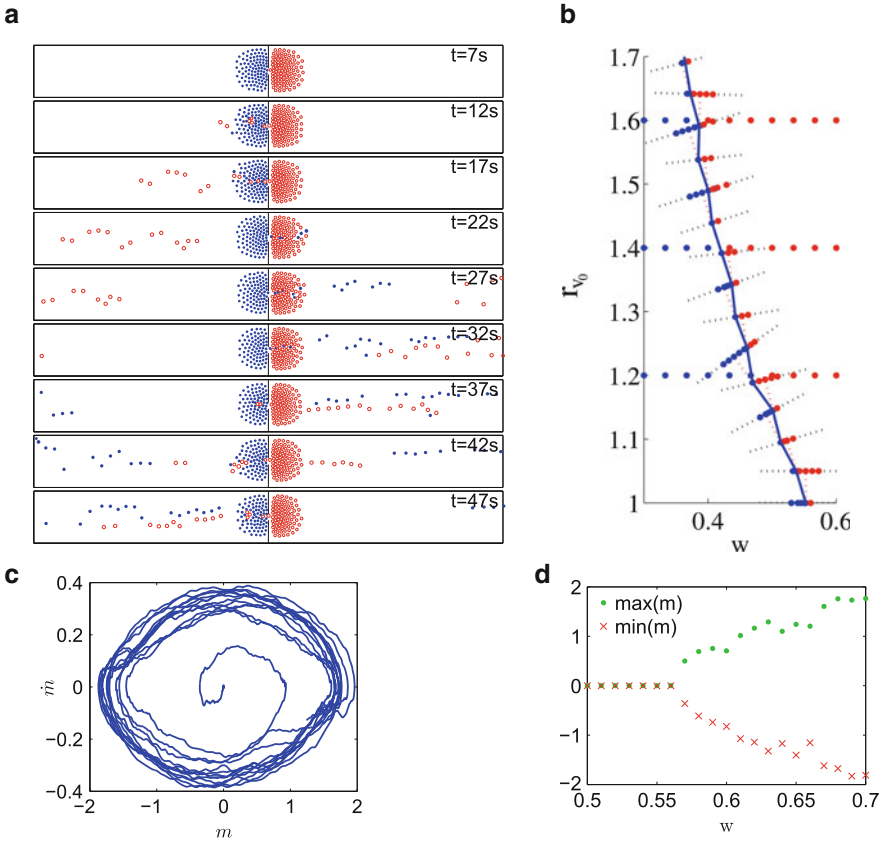

Fig. 6 Coarse analysis of the pedestrian dynamics in a corridor with bottleneck. (**a**) Snapshots of a microscopic simulation show oscillating behavior for large enough door width $w = 0.6$. (**b**) Two-parameter plane explains the dynamics of the system and the point for the Hopf bifurcation. (**c**) Transient and limit cycle in the macroscopic description for $w = 0.7$. (**d**) The coarse bifurcation diagram reveals a Hopf bifurcation at a critical door width $w = 0.56$

4.1 The Restriction and Lifting Operators

We define the macroscopic quantity m as

$$m = \frac{m_r + m_b}{2}, \qquad m_{(r,b)} = \frac{\sum_{i\in(r,b)} \kappa(x_i)x_i}{\sum_{i\in(r,b)} \kappa(x_i)}, \tag{15}$$

where $m_{(r,b)}$ is a weighted average of the longitudinal component for the blue and red pedestrian crowd, respectively. The function κ gives more weight to pedestrians close to the door (see [3] for details). Since we expect oscillations from microscopic observations the pair of variables $(m, \dot{m})$ is used as the macroscopic variable for the equation-free methods. The transient from the initial condition to a limit cycle in the macroscopic description is shown for $w = 0.7$ in Fig. 6c. The restriction operator $\mathscr{R} = (m, \dot{m})$ is therefore defined by the macroscopic description (15) and its derivative.

The lifting operator $\mathscr{L}$ uses information about the distribution of the pedestrians in front of the door to initialize a sensible microscopic state. The distribution of positions of pedestrians along the corridor is known from numerical studies and is observed to be well-approximated by a linear density distribution, i.e., the distribution is of the form $p(|x|) = a|x| + b$, where $|x|$ is the distance from the door along the corridor axis. The slope a and interception b are determined by simulations for all parameter values of interest. The lifting uses these distributions to map, i.e., lift $(m, \dot{m})$ to a "physically correct" microscopic state. All velocities are initially set to 0, such that we lift to a microscopic state with $\dot{m} = 0$ (see [3] for details).

4.2 Numerical Results

Using equation-free bifurcation analysis, the bifurcation diagram is computed for the fixed ratio $r_{v_0} = 1$. Figure 6b shows the maximum and minimum of $m(t)$ as a function of w. The transition from a blocked state to an oscillating state is clearly observed and the bifurcation point is found to be at $w = 0.56$. The transition is analyzed in detail in [3] and the bifurcation point is identified as a Hopf bifurcation point using Poincaré sections, i.e., a discretization of the recurrent dynamics in time. This method is also implicit with a healing time t_{skip} determined by the first crossing of the Poincaré section. The Hopf bifurcation gives rise to macroscopic oscillations for large door width w emerging from a stable blocked state for w small enough.

Let us now study the influence of r_{v_0} on the location of the bifurcation point. The system for macroscopic continuation is analyzed by a predictor-corrector method using a linear prediction and a subspace search for the correction in order to study the two-parameter problem and to continue the Hopf point. The results are shown in Fig. 6a. Keeping the other model parameters fixed, this gives an overview of the behavior of the system on a macroscopic level in two parameters.

The application of equation-free analysis is not limited to pedestrians in a bottleneck scenario. One could also think of applications in evacuation scenarios (see, e.g., [28,29]), where parameter regimes with blocked states have to be avoided at all cost. It is also possible to apply equation-free analysis to discrete models, e.g., cellular automaton models [30, 31]. This motivates further studies using equation-free methods in traffic and pedestrian flow in order to systematically investigate and finally optimize the parameter dependencies of the macroscopic behavior of such microscopic models.

Discussion and Conclusion

We have demonstrated, that equation-free methods can be useful to analyze the parameter dependent behavior in traffic and pedestrian problems. Implicit methods allow us to improve the results further by reducing the lifting error. The comparison between traffic and pedestrian dynamics shows that both problem classes can be studied with the same mathematical tools. In particular, the use of coarse bifurcation analysis reveals some information about the system that could not be obtained by simpler means, e.g., direct simulations of a microscopic model, since they cannot investigate unstable solutions. Nevertheless, unstable solutions are important in order to understand the phase space and parameter dependence of the dynamics. In particular, in the case of a one-dimensional macroscopic dynamics the unstable solutions act as barriers between separate stable regimes defining reliable operating ranges. The knowledge of their locations can be used to systematically push the system over the barrier to switch to another more desirable solution, e.g., leading to a transition from traffic jams to uniform flow. In the application to two-dimensional macroscopic dynamics, we find the precise dividing line between oscillations and blocking in two parameters.

Finally, let us contrast equation-free analysis to the most obvious alternative. A common approach to determining the precise parameter value at which the onset of oscillations occurs, is to run the simulation for sufficiently long time and observe if the transient behavior vanishes. This approach suffers from two problems. First, close to the loss of linear stability in the equilibrium (i.e. close to the bifurcation point) the rate of approach to the stable orbit or fixed point is close to zero as the Jacobi matrix becomes singular. This makes the transients extremely long, resulting in unreliable numerics. Second, even eventually decaying transients may grow intermittently (the effect of *non-normality*) such that the criteria for the choice of the transient time to observe are non-trivial. Equation-free computations working on the macroscopic level in a neighborhood of the slow manifold do not suffer from these long transients, as they are based on direct root-finding methods.

(continued)

In conclusion coarse bifurcation analysis can be used in future research to improve safety in traffic problems and evacuation scenarios of large buildings in case of emergency. The main advantage is, that realistic models can be used and a qualitative analysis of the macroscopic behavior is still possible. The method works almost independent of the underlying microscopic model and has a significant potential for helping traffic modellers to gain insight into previously inaccessible scenarios.

Acknowledgements The authors thank their collaborators R. Berkemer, A. Kawamoto and O. Corradi. The research of J. Sieber is supported by EPSRC grant EP/J010820/1. J. Starke was partially funded by the Danish Research Council under 09-065890/FTP and the Villum Fonden (VKR-Centre of Excellence "Ocean Life").

References

1. D. Helbing, P. Molnár, Phys. Rev. E **51**, 4282 (1995)
2. D. Helbing, Rev. Mod. Phys. **73**, 1067 (2001)
3. O. Corradi, P. Hjorth, J. Starke, SIAM J. Appl. Dyn. Syst. **11**(3), 1007 (2012)
4. M. Bando, K. Hasebe, A. Nakayama, A. Shibata, Y. Sugiyama, Phys. Rev. E **51**(2), 1035 (1995)
5. I. Gasser, G. Sirito, B. Werner, Phys. D: Nonlinear Phenom. **197**, 222 (2004)
6. Y. Sugiyama, M. Fukui, M. Kikuchi, K. Hasebe, A. Nakayama, K. Nishinari, S.i. Tadaki, S. Yukawa, New J. Phys. **10**(3), 033001 (2008)
7. G. Orosz, B. Krauskopf, R. Wilson, Phys. D: Nonlinear Phenom. **211**, 277 (2005)
8. C. Marschler, J. Sieber, R. Berkemer, A. Kawamoto, J. Starke, SIAM J. Appl. Dyn. Syst. **13**(3), 1202–1238 (2014)
9. H. Haken, *Synergetics: An Introduction* (Springer, Berlin, 1983)
10. H. Haken, *Advanced Synergetics* (Springer, Berlin, 1983)
11. N. Fenichel, J. Differ. Equ. **31**, 53 (1979)
12. I.G. Kevrekidis, C.W. Gear, J.M. Hyman, P.G. Kevrekidis, O. Runborg, C. Theodoropoulos, Commun. Math. Sci. **1**, 715 (2003)
13. I.G. Kevrekidis, C.W. Gear, G. Hummer, AIChE J. **50**(7), 1346 (2004)
14. I.G. Kevrekidis, G. Samaey, Annu. Rev. Phys. Chem. **60**(1), 321 (2009)
15. Y. Kevrekidis, G. Samaey, Scholarpedia **5**(9), 4847 (2010)
16. J. Sieber, B. Krauskopf, Nonlinear Dyn. **51**(3), 365 (2008)
17. E. Bureau, F. Schilder, I.F. Santos, J.J. Thomsen, J. Starke, J. Sound Vib. **332**(22), 5883 (2013)
18. D.A.W. Barton, J. Sieber, Phys. Rev. E **87**, 052916 (2013)
19. C.W. Gear, T.J. Kaper, I.G. Kevrekidis, A. Zagaris, SIAM J. Appl. Dyn. Syst. **4**, 711 (2005)
20. A. Zagaris, C.W. Gear, T.J. Kaper, Y.G. Kevrekidis, ESAIM: Math. Model. Numer. Anal. **43**(04), 757 (2009)
21. A. Zagaris, C. Vandekerckhove, C.W. Gear, T.J. Kaper, I.G. Kevrekidis, Discret. Contin. Dyn. Syst. Ser. A **32**(8), 2759 (2012)
22. C. Vandekerckhove, B. Sonday, A. Makeev, D. Roose, I.G. Kevrekidis, Comput. Chem. Eng. **35**(10), 1949 (2011)
23. W.J. Beyn, A. Champneys, E. Doedel, W. Govaerts, Y.A. Kuznetsov, B. Sandstede, in *Handbook of Dynamical Systems*, vol. 2, ed. by B. Fiedler (Elsevier Science, Amsterdam/Boston, 2002), pp. 149–219

24. Y.A. Kuznetsov, *Elements of Applied Bifurcation Theory*. Applied Mathematical Sciences, vol. 112, 3rd edn. (Springer, New York, 2004)
25. A. Seyfried, B. Steffen, T. Lippert, Phys. A: Stat. Mech. Appl. **368**(1), 232 (2006)
26. J. Zhang, W. Klingsch, A. Schadschneider, A. Seyfried, J. Stat. Mech. Theory Exp. **2012**(02), P02002 (2012)
27. C. Marschler, J. Starke, P. Liu, I.G. Kevrekidis, Phys. Rev. E **89**, 013304 (2014)
28. D. Helbing, I.J. Farkas, P. Molnar, T. Vicsek, Pedestr. Evacuation Dyn. **21**, 21 (2002)
29. A.U.K. Wagoum, M. Chraibi, J. Mehlich, A. Seyfried, A. Schadschneider, Comput. Animat. Virtual Worlds **23**(1), 3 (2012)
30. C. Burstedde, K. Klauck, A. Schadschneider, J. Zittartz, Phys. A: Stat. Mech. Appl. **295**(3–4), 507 (2001)
31. S. Nowak, A. Schadschneider, Phys. Rev. E **85**, 066128 (2012)

Dynamical Systems on Honeycombs

Valery V. Kozlov, Alexander P. Buslaev, Alexander G. Tatashev, and Marina V. Yashina

Abstract Stochastic and deterministic versions of a discrete dynamical system on a necklace network are investigated. This network contains several contours. There are three cells and a particle on each contour. The particle occupies one of the cells and, at each step, it makes an attempt to move to the next cell in the direction of movement. As well as on neighboring contours the particles move in accordance with rules of stochastic or deterministic type. We prove that the behavior of the model with a rule of the first type is stochastic only at the beginning, and after a time interval the behavior becomes purely deterministic. The system with a rule of the first type reaches a stationary mode which depends on the initial state. The average velocity of particles and other characteristics of the dynamical systems are studied.

1 Introduction

Dynamical systems of different nature have been used in studies of physical phenomena, see e.g. the work of Kac [1] and Kozlov [2]. A type of dynamical systems was introduced by Nagel and Schreckenberg in [3]. These systems are used as traffic models and have been investigated by many authors [3–10]. Exact mathematical results for characteristics of deterministic versions of these models have been proved by Blank [11, 12]. In [11], monotonic walks of particles on a one-dimensional lattice (a ring or a straight line) were considered. Each particle moves a position at every step, in the direction of movement, with probability 1, if the cell ahead is vacant. A formula has been proved which describes the dependence of the average velocity of particles on the flow density. In [12] the formula, proved in [11], is generalized in the case when each cell can contain no more than a fixed number of particles.

V.V. Kozlov
Steklov Mathematical Institute, Russian Academy of Sciences, Moscow, Russia

A.P. Buslaev (✉) • A.G. Tatashev • M.V. Yashina
MADI, MTUCI, Moscow, Russia
e-mail: apal2006@yandex.ru

M. Chraibi et al. (eds.), *Traffic and Granular Flow '13*,
DOI 10.1007/978-3-319-10629-8_49

Some exact results for stochastic models have been obtained in our papers [13–15]. In [13], a monotonic random walks of particles on a ring was investigated. In this model, each particle moves a position at every step, with a fixed probability if the cell ahead is vacant. A formula has been found for the average velocity of particles. In [14] the model considered in [13] is investigated in the case of the big number of cells and fixed density. In this limit a formula has been found for the average velocity of particles. In [15], the formula has been obtained for the average velocity of particles in a model with maximum distance jumps of particles. In this model the probability of each jump depends on the type of the particle and the cell occupied by the particle. In [16, 17] some cluster models have been introduced as a continuous analogue of totally – connected monotonic walks. In [17, 18], cluster models on planar networks of contours (chainmails) are investigated.

The average characteristics, in first place the velocity, are studied in [17, 18]. The studies of conditions of *collapse* (all particles do not move) and of *synergy* (all particles move at each step) are of considerable interest. Numerous results and computer simulations show that, in the symmetrical case (identical circles and masses), half circle and quarter circle are the critical values for a periodical chain of rings (*necklace*) and for a periodical two-dimensional network of rings (*chainmail*). The phase transitions take place in a neighborhood of these values.

As proven in [18], some models of particles walk on a network are equivalent stochastically to some discrete time queueing systems, the behavior of which has been studied [19]. In the models introduced in [3], particles move on a one-dimensional circular lattice. These models can be considered as Markov chains [20]. All possible states of these Markov chains have positive stationary probabilities. Some network traffic models with symmetrical periodic structures were studied in [21] using simulations.

2 Honeycomb Networks

We will consider networks made of honeycombs (Fig. 1, left) where network nodes (small circles) and cells (small squares) are alternating (ANC). The other kind of honeycomb networks are networks, where nodes and cells coincide (NC) (Fig. 1, right).

In presented fragments of networks every internal contour has three neighboring contours (network of index 3). The networks of indexes 2 (necklace) and 4 (chainmail) were considered in [17, 18, 22–24]. The direction of movement and cell numbering on contours are coordinated. At every step a particle moves to the next cell in the direction of movement, if the next cell is vacant and there is no conflict for the node ahead. Conflict rules are given below.

We consider symmetrical structures of NC and ANC honeycombs networks. If we identify the opposite nodes on horizontal and vertical lines in Fig. 1 then we obtain NC and ANC honeycomb networks on horizontal and vertical lines, on a torus

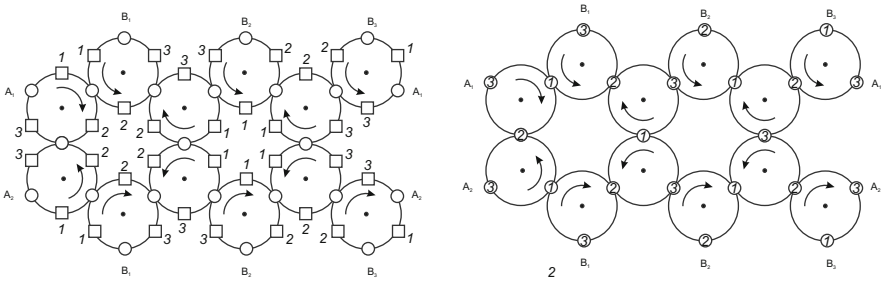

Fig. 1 *Left*: Alternating honeycomb network (ANC). *Right*: Coinciding honeycombs network (NC)

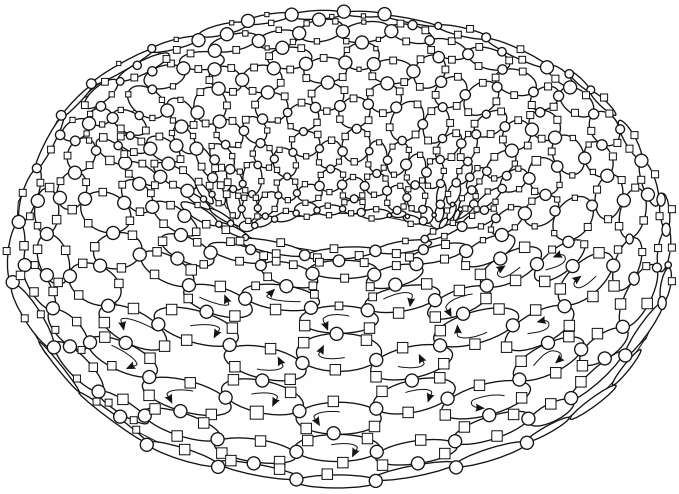

Fig. 2 Honeycomb network on a torus

(Fig. 2). If we continue periodically the blocks in Fig. 1 on horizontal and vertical lines, then we obtain NC and ANC honeycomb networks with multiple sizes.

3 Quantitative Characteristics of Particle Flow

We introduce the concept of the *velocity* in case of a network with n contours and one particle on each contour. Suppose $S_i(T)$ is the number of of transitions of the particle of the contour i (the particle i) for the time interval $[0, T)$ (for $i = 1, \ldots, n$). The *average velocity* $v_i^*(T)$ *of the particle* i *on the time interval* $[0, T)$ is defined as

$$v_i^*(T) = \frac{S_i(T)}{T}, \qquad (i = 1, \ldots, n). \tag{1}$$

The limit

$$v_i^* = \lim_{T\to\infty} v_i^*(T), \qquad (i = 1, \dots, n), \tag{2}$$

is called the *velocity* v_i^* of the particle i, if this limit exists.

We introduce also the *velocity* $\theta_i(T)$ *of the particle* i *at the time instant* T. Let by definition $\theta_i(T) = 1$, if at fixed initial condition and at the instant T the particle i is in the state, when it moves to next step, and $\theta_i(T) = 0$ otherwise ($T = 0, 1, 2, \dots$) *The average velocity by coordinates* $\overline{v}(T)$ *of particles at the instant* T is defined as

$$\overline{v}(T) = \frac{1}{n}\sum_{i=1}^{n} \theta_i(T)\,. \tag{3}$$

The average velocity in the system on time axis v^* is defined as arithmetic average of individual velocities:

$$v^* = \frac{1}{n}\sum_{i=1}^{n} v_i^* = \lim_{T\to\infty} \frac{1}{n}\sum_{i=1}^{n}\left(\frac{1}{T}\sum_{k=1}^{T}\theta_i(k)\right) = \frac{1}{nT}\lim_{T\to\infty}\sum_{i=1}^{n}\sum_{k=1}^{T}\theta_i(k). \tag{4}$$

We say that the system, since some instant, is in the state of *synergy* if $\exists\ T^*$ such that for all $T > T^*$

$$\overline{v}(T) \equiv 1. \tag{5}$$

The system, since the instant, is in the state of *collapse* if there $\exists\ T^*$ such that $\forall\ T > T^*$

$$\overline{v}(T) \equiv 0. \tag{6}$$

If the system, since the instant, comes to the state of synergy, then $v_i^* = 1$, $\forall\ i$, $v = 1$.

4 Star of David as the Minimum Alternating Honeycomb Network

4.1 David Star

Consider an alternating honeycomb network of minimum size, which contains six contours (Fig. 3 (left)). We consider a rule of behavior of conflict particles that the results can be generalized to any dimension. There are common cells of contour i and contour $i + 1$ and of contour i and contour $i + 3$, respectively (the addition is

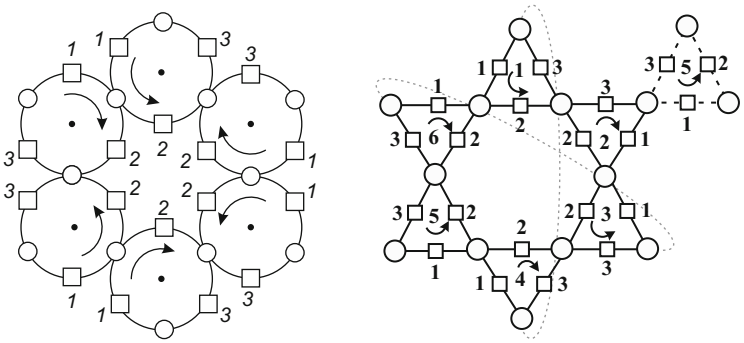

Fig. 3 *Left*: The minimum cell of an alternating honeycomb network. *Right*: Star of David

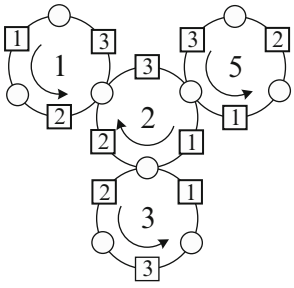

Fig. 4 Non-priority contour between three priority contours

meant modulo six). There is a particle on each contour which occupies one of three cells at each time instant. A particle moves clockwise if the index of the contour is odd, and counter-clockwise if the index is even. At every step, each particle moves one cell forward, if the neighboring particle does not have to move through the same node. In the latter case, one of two particles moves in accordance with a rule of behavior of particles in the case of a conflict.

The considered network system is topologically equivalent to a network in which arcs of contours between nodes are replaced by segments resulting in a six-pointed star. We enumerate each triangular contour as shown in Fig. 3 (right).

4.2 David Star with FM-Rule

We consider the behavior of the system in the case of the *"father–mother"* rule. Particles of the contour with an odd index (a particle "father") have priority. In the case of this rule, each particle moves at each step. We can consider the behavior of non-priority particles ("mother"). The behavior of each mother-particle does not depend on other non-priority particles, and depends only on the behavior of three priority particles (Fig. 4). Therefore we can consider only the behavior of four

particles, one of which is mother-particle. Suppose the mother-particle is on the contour 2. Suppose the vector (i_1, i_2, i_3, i_5) corresponds to the state of the four such that the particle of the contour j occupies the cell i_j. There are 81 states of the 4.

Theorem 1 *1. If the initial state (i_1, i_2, i_3, i_5) of the four contours is such that there are, in set of numbers i_1, i_3, i_5, at least two the same, then the system comes to the state of synergy after a finite time interval. There are 63 such the states.*

2. *There are 9 initials states (i_1, i_2, i_3, i_5) such that all the numbers i_1, i_3, i_5 are different and the velocity of each mother-particle equals 2/3. For these states, we can get the permutation (i_1, i_3, i_5) from the permutation $(3, 2, 1)$ with cyclical shift.*
3. *There are also 9 initials states (i_1, i_2, i_3, i_5) such that all the numbers i_1, i_3, i_5 are different and the velocity of each mother-particle equals 1/2. For these states, we can get the permutation (i_1, i_3, i_5) from the permutation $(1, 2, 3)$ with cyclical shift.*
4. *If all possible initial states are equiprobable, then the expectation of the average velocity of mother particles is 49/54, and the expectation of the average velocity of the particles in the network is equal to 103/108.*

Proof If the initial state (i_1, i_2, i_3, i_5) is such that all numbers i_1, i_3, i_5 are different, then, after a finite number of steps, the value of i_2 will differ from any value i_1, i_3, i_5, and the mother particle will move at every step.

For nine initial states, the mother particles will move at every second step, and we can the permutations corresponding to vectors of these states from the permutation $(1, 2, 3)$ with cyclical shift. Indeed, we have the following sequence of transitions

$$\begin{aligned}
&(1,1,2,3) \to (2,1,3,1) \to (3,2,1,2) \to (1,2,2,3)\\
&\qquad\qquad \to (2,3,3,1) \to (3,3,1,2) \to (1,1,2,3)\ldots,\\
&(1,3,2,3) \to (2,1,3,1)\ldots,\\
&(2,2,3,1) \to (3,3,1,2)\ldots,\\
&(1,3,2,3) \to (2,1,3,1)\ldots
\end{aligned} \tag{7}$$

For nine initial states, the mother particles will move at two steps from each three steps, and we can do the permutations corresponding to the vectors of these states from the permutation $(3, 2, 1)$ with cyclical shift. Indeed, we have the following sequence of transitions

$$\begin{aligned}
(1,1,3,2) &\to (2,1,1,3) \to (3,2,2,1) \to (1,3,3,2) \to\\
&\to (2,3,1,3) \to (3,1,2,1) \to (1,2,3,2) \to \cdots \to\\
&\to (2,2,1,3) \to (3,3,2,1) \to (1,1,3,2) \to \ldots
\end{aligned} \tag{8}$$

If all possible initial states are equiprobable, then the velocity, with probability 7/9, is equal to 1, with probability 1/9, is equal to 2/3, and, with probability 1/9, is equal

to 1/2. Thus the expectation of the average velocity of the mother particle equals 49/54. As the number of father particles equals the number of mother particles, and the velocity of mother particle equals 1, then the expectation of the average velocity of particles in the network equals 103/108. Thus Theorem 1 has been proved.

Remark When we consider the behavior of a mother particle, we do not take into account the dimension of the network and the existence of the network save the considered four. Therefore the velocity of the non-priority particle is the same at the same state of the four, and the velocity is the same still at the same state of the networks of the minimum dimension and any dimension. Taking into account that there exist the same 81 states of the 4 in the case of any alternating honeycomb network, we can generalize the result to the case of structures of an arbitrary size.

4.3 David Star with Egalitarian Rule

We can consider a similar dynamical system with the *egalitarian rule* of behavior of particles in the case of conflict. In accordance with this rule, each of two conflicted particles has the priority with probability 1/2. In this case we can formulate the following.

Hypothesis 1 Suppose the egalitarian rule is used in the alternating honeycombs network star of David. Then, for any initial state, the system comes to the state of synergy for a time interval with a finite time interval.

5 Necklaces with Displaced Centers

Consider (non-symmetrical) periodical structures which are closed chains of contours. Each contour has common cells with two neighboring contours. There is a common cell of each two neighboring contours. Examples of a symmetrical structure of such type are the *elementary necklace*, which was considered in [22], and the *system of pendulums* considered in [23]. Non-symmetrical networks can be considered as fragments of two-dimensional structures called “chainmail” and are considered in [24]. We will discuss the non-symmetrical necklace as a fragment of a honeycomb network on a torus in more detail below.

Consider a dynamical system, in which particles move on M contours. Suppose there are 3 cells and a particle on each contour (Fig. 5). This system is similar to the system considered in Sect. 2 as there are three cells on each contour of both the system. The system time is discrete. At every step, each particle moves a cell forwards in the direction of movement, if the cell ahead is vacant, and this particle and the particle of the neighboring contour are in conflict. In the latter case, one of two these particle moves. Suppose that each of two conflicted particles has has the priority with probability 1/2, i.e., we consider the case of the *egalitarian* rule.

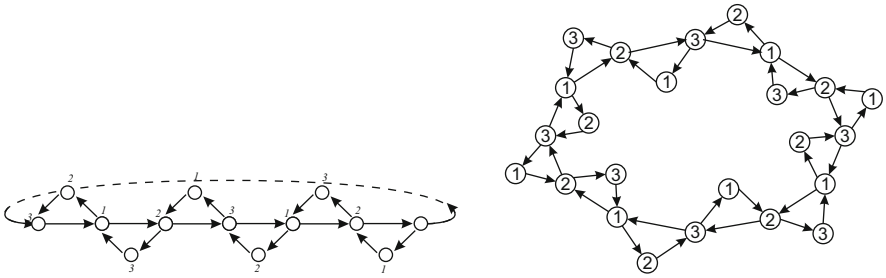

Fig. 5 *Left*: Necklace with $M = 6$. *Right*: Non-symmetrical necklace, $M = 12$

The indexes of cells are such that the common cell of contours i and $i + 1$ has the same index on both the contours. We suppose M is multiple of 6. In this case, the indexes of the cells 1 and M are the same too (Fig. 5).

Suppose the vector $(i_1, \ldots, i_n)$ corresponds to the network state at that the particle of the contour j occupies the cell i_j, $j = 1, \ldots, M$.

Theorem 2 *Suppose $M = 6$, and the egalitarian rule is used.*

1. *There is a unique state of collapse.*
2. *There exist classes of corresponding states such that there are six states at each class. If the system is at one of this state, the sequence of states alternate with period six, and there are three transitions of each particles per period, i.e., the velocity of particles is equal to 1/2.*

Proof The state $(3, 1, 2, 3, 1, 2)$ is the unique state of collapse. If $(2, 1, 2, 3, 2, 1)$ is the initial state, then we have the sequence of transitions

$$(2,1,2,3,2,1) \to (3,1,2,1,3,1) \to (3,1,3,2,3,2) \to (3,2,1,2,1,2)$$
$$\to (1,3,1,3,1,2) \to (2,3,2,3,1,3) \to (2,1,2,3,2,1)\ldots \quad (9)$$

Thus the initial state is repeated. The sequence of states is repeated with period six. There are three transitions of each particle per period. The velocity of particles equals 1/2. Thus Theorem 2 has been proved.

Theorem 3 *Suppose $M = 6$ and the egalitarian rule is used.*

There are initial states from that the system, after the finite time interval, comes, with positive probability, to the state of collapse, and, with positive probability, comes to the class of corresponding states, where the velocity of particles is equal to 1/2.

Proof Suppose $(2, 3, 1, 3, 1, 1)$ is the initial state. From this state the system, with probability 1/2, comes to the state of collapse $(3, 1, 2, 3, 1, 2)$. With probability 1/2 the system comes to the state $(3, 1, 2, 3, 2, 1)$, and then to the state $(3, 1, 2, 1, 3, 1)$.

This state belongs, in accordance with Theorem 2, to the class of corresponding states in that the velocity of particles equals 1/2. Thus Theorem 3 has been proved.

Let us formulate some hypotheses. Suppose m is any multiple of 6.

Hypothesis 2 Suppose $M \geq 4$, and the egalitarian rule.

1. There is a unique state of collapse.
2. There is no state of synergy.
3. The "yellow" particles disappear after a time interval with a finite time interval, but, for any k, "yellow" particles can appear after the time instance k with positive probability.
4. There are initial states such that the system, with probability 1, comes to the state of collapse after a finite number of steps.
5. There exist initial states such that, with probability 1, the system comes to the class of corresponding states, where the velocity of every particle is non-zero.
6. There exist initial states such that the system, with a positive probability, and, with a positive probability, comes to the class of corresponding states, where the velocity of every particle is non-zero.

We return to the example of repeating sequences of six states. Mark out the coordinates corresponding to "red" particles:

$$\begin{aligned}(2, \mathbf{1}, \mathbf{2}, 3, 2, \mathbf{1}) \to (\mathbf{3}, \mathbf{1}, 2, 1, \ \mathbf{3}, 1) \to\to (\mathbf{3}, 1, 3, \mathbf{2}, 3, \mathbf{2}) \to (\mathbf{3}, 2, 1, \mathbf{2}, 1, \mathbf{2}) \\ \to (1, 3, \mathbf{1}, 3, \mathbf{1}, \mathbf{2}) \to (\mathbf{2}, 3, \mathbf{2}, \mathbf{3}, 1, 3) \to (2, \mathbf{1}, \mathbf{2}, 3, 2, \mathbf{1}) \ldots \quad (10)\end{aligned}$$

We see that the configuration of marked coordinates is shifted a position at each step. This allows to formulate the following

Hypothesis 3 1. If the system is at the state of corresponding states such that there are "green" and "red" particles, but there are no "yellow" particles, then the configuration of coordinates corresponding to non-moving particles is shifted a position at each step, and the sequence of states alternate with period M. There are $3i$ transitions of each particle per period ($i = 1, 2, \ldots, (M/3) - 1$).
2. When steady periodic movement occurs, the velocity of each particle is the same. The possible values of velocities are $3i/M$, ($i = 0, 1, \ldots, (M/3) - 1$). There are no other possible values of velocities.

6 Honeycomb Networks with Coincided Nodes and Cells

We consider a honeycomb network with joined nodes and cells (Fig. 6 (left)). Consider a system with six contours (star of David with joined nodes and cells) similar to a non-symmetrical necklace but the non-common cell of the contour i is

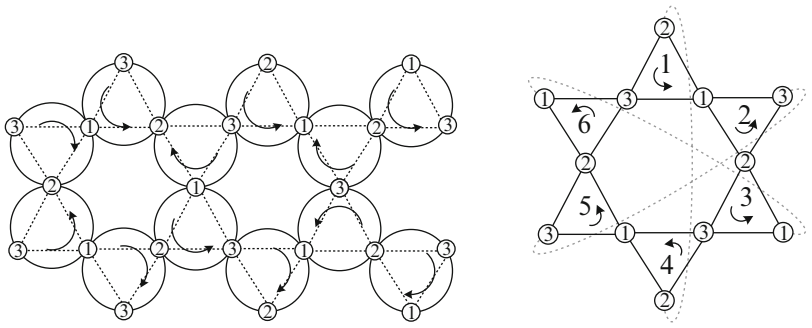

Fig. 6 *Left*: Development of NC-network on torus. *Right*: Minimum non-symmetrical necklace with coincided cells and nodes

common with a cell of the contour $i+3$, $i = 1, \ldots, 6$ (the addition is meant modulo 6) (Fig. 6 (right)). This system can be considered as a fragment of a honeycomb network with joined cells and nodes (Fig. 6 (right)).

In the system in Fig. 6 (right) the particles on every contours move to opposite directions. In this case the numbering of cells is the same as for the non-symmetrical necklace with six contours, which was considered in Sect. 4. On the network in Fig. 6 (left) the particle movement is co-directed and the numbering of cells corresponding to alternating honeycomb network.

Theorem 4 *1. There exist the collapse states.*

2. *There exist classes of communicating states such that in each class there are six states. As well as if the system is in one of these states, then state sequence repeats with period six, and for the period three transferences of each particle. i.e. velocity of each particle is equal to 1/2.*

Proof The examples for a collapse state and a state, when every particle moves with velocity 1/2, are presented in the proof of Theorem 2. These also hold for the considered system. Thus Theorem 4 is proved.

Theorem 5 *The collapse state is not unique.*

Proof Before the collapse state $(3, 1, 2, 3, 1, 2)$, that is the unique state of collapse for corresponded non-symmetrical necklace, in this case the collapse state is, for example, the state $(1, 3, 3, 2, 2, 1)$. Thus Theorem 5 is proved.

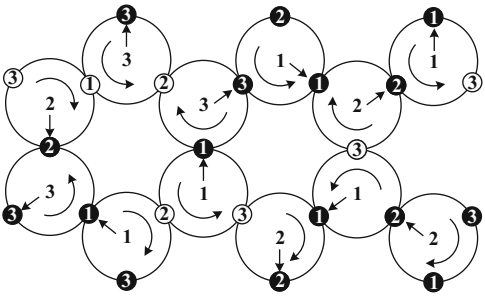

Fig. 7 Dynamical system on torus with coincided cells and nodes

Remark In Fig. 7 the development of minimal network with coincided nodes and cells on a torus is shown. It is easy to see that reasoning of Sect. 4 is useful to this case. In particular, on one of the horizontal placed non-symmetrical necklace a collapse state can be obtained, while the dynamical system on another necklace will be independent.

References

1. M. Kac, *Probability and Related Topics in Physical Sciences* (Interscience Publishers, New York/London, 1958)
2. V. Kozlov, Statistical irreversibility of the Kac reversible circular model. Rus. J. Nonlinear Dyn. **7**, 101–117 (2011)
3. K. Nagel, M. Schreckenberg, A cellular automaton model for freeway traffic. J. Phys. I Fr. **2**, 1221 (1992)
4. A. Schadschneider, M. Schreckenberg, Cellular automaton models and traffic flow. J. Phys. **A26**, L679 (1993)
5. M. Schreckenberg, A. Schadschneider, K. Nagel, N. Ito, Discrete stochastic models for traffic flow. Phys. Rev. E **51**, 2939 (1995)
6. M. Rickert, K. Nagel, M. Schreckenberg, A. Latour, Two lane traffic simulations using cellular automata. Physica A **231**, 534 (1996)
7. K. Nagel, D. Wolf, P. Wagner, P. Simon, Two-lane traffic rules for cellular automata: a systematic approach. Phys. Rev. E **58**, 1425 (1998)
8. P. Simon, K. Nagel, A simplified cellular automation model for city traffic. Phys. Rev. E **58**, 1286 (1998)
9. M.V. Evans, N. Rajewsky, E.R. Speer, Exact solution of a cellular automation for traffic. J. Stat. Phys. **95**, 45 (1999)
10. L. Gray, D. Griffeath, The ergodic theory of traffic jams. J. Stat. Phys. **105**, 413 (2001)
11. M. Blank, Exact analysis of dynamical systems arising in models of traffic flow. Russ. Math. Surv. **55**(3), 333 (2000)
12. M. Blank, Dynamics of traffic jams: order and chaos. Mosc. Math. J. **1**(1), 1–26 (2001)
13. A.P. Buslaev, A.G. Tatashev, Particles flow on the regular polygon. J. Concr. Appl. Math. **9**, 290 (2011)
14. A.P. Buslaev, A.G. Tatashev, Monotonic random walk on a one-dimensional lattice. J. Concr. Appl. Math. **10**, 130 (2012)
15. A.P. Buslaev, A.G. Tatashev, On exact values of monotonic random walks characteristics on lattices. J. Concr. Appl. Math. **11**, 17 (2013)

16. A.P. Buslaev, A.G. Tatashev, M.V. Yashina, Cluster flow models and properties of appropriate dynamic systems. J. Appl. Funct. Anal. **8**, 54–76 (2013)
17. A.S. Bugaev, A.P. Buslaev, V.V. Kozlov, A.G. Tatashev, M.V. Yashina, Traffic modelling: monotonic random walks on a network. Matematicheskoe modelirovanie **25**, 3 (2013)
18. V.V. Kozlov, A.P. Buslaev, A.G. Tatashev, *Monotonic Random Walks and Clusters Flows on Networks*. Models and Applications (Lambert Academician Publishing, Saarbrücken, 2013). No. 78724, ISBN:978-3-659-33987-5
19. H. Daduna, *Queuing Networks with Discrete Time Scale: Explicit Expression for the Steady State Behavior of Discrete Time Stochastic Networks* (Springer, Berlin, 2001)
20. A. Feller, *An Introduction to Probability Theory and Its Applications* (Wiley, New York, 1968)
21. K.K. Glukharev, N.M. Ulyukov, A.M. Valuev, I.N. Kalinin, On traffic flow on the arterial network model, in *Traffic and Granular Flow '11*, ed. by V.V. Kozlov, A.P. Buslaev, A.S. Bugaev, M.V. Yashina, A. Schadschneider, M. Schreckenberg (Springer, Berlin/Heidelberg, 2013), pp. 399–411. ISBN: 978-3-642-39668-7 (Print), 978-3-642-39669-4 (Online), http://link.springer.com/book/10.1007/978-3-642-39669-4
22. V.V. Kozlov, A.P. Buslaev, A.G. Tatashev, On synergy of total connected flows on chainmails, in *The 13th International Conferences of Computational and Mathematical Methods in Science and Engineering, CMMSE 2013. Proceedings*, Cabo de Gata, Almeria, Spain, vol. III, 24–27 June 2013, pp. 861–874. ISBN: 978-84-616-2723-3, http://gsii.usal.es/~CMMSE/images/stories/congreso/volume1-cmmse-20013.pdf
23. A.P. Buslaev, A.G. Tatashev, A system of pendulums on a regular polygon, in *The Fifth International Conference on Advances in System Simulation, 2013, Proceedings*, Venice, p. 36. ISBN:978-1-61208-308-7
24. A.P. Buslaev, A.G. Tatashev, M.V. Yashina, Qualitative properties of dynamical system on toroidal chainmail. AIP Conf. Proc. **1558**, 1144 (2013)

Local Stability Conditions and Calibrating Procedure for New Car-Following Models Used in Driving Simulators

Valentina Kurtc and Igor Anufriev

Abstract The Intelligent Driver Model (IDM) is studied and several drawbacks with respect to driving simulators are defined. We present two modifications of the IDM. The first one gives any predefined distance to the leading vehicle in a steady state. The second modification is a combination of the first one and the optimal velocity model. It takes into account driver's reaction time explicitly and is described by delay differential equation. This model always results in realistic vehicles accelerations what allows simulating real traffic collisions.

Necessary and sufficient conditions are obtained, that guarantee a non-oscillating solution near the equilibrium for the vehicle platoon. We suggest the calibrating framework based on a numerical solution of the constrained optimization problem. Nonlinear constraints are generated by the numerical integration scheme. The suggested procedure incorporates the local stability conditions obtained and takes into account vehicle dynamics, drivers' behavior and weather conditions.

1 Introduction

Driving simulators are certain kind of training systems in a car driving application [1, 12]. Firstly, these were developed for the training in the use of military mechanisms during the Second World War. Later, driving simulators were used to examine drivers' behavior and their interaction with the environment – vehicle controls, other cars, pedestrians and etc. The quality of traffic simulation plays a major role. It is important that the other cars move as naturally as possible, drivers behave in predictable manner and in accordance with traffic rules. This article focuses on appropriate vehicle traffic models for using in driving simulators. The general and necessary features which a model should demonstrate are real vehicle dynamics, adequate driver's behavior and mathematical stability of the solution.

V. Kurtc (✉) • I. Anufriev
St. Petersburg State Polytechnical University, Polytechnicheskaya 29, 195251 St. Petersburg, Russia
e-mail: kurtsvv@gmail.com; igevan@mail.ru

M. Chraibi et al. (eds.), *Traffic and Granular Flow '13*,
DOI 10.1007/978-3-319-10629-8_50

In this paper, we propose two microscopic models. The first one provides any predefined distance in a steady state that allows to take into account road covering and weather conditions. The second modification is the extension of the first one and includes driver's reaction time. Both models are described by continuous acceleration functions and are the car-following type ones.

In Sect. 2 we state some drawbacks of the Intelligent Driver Model (IDM) in application to driving simulators. Then we formulate two modifications based on the IDM in terms of the acceleration function. In Sect. 3 we evaluate linear stability analysis for the case of vehicle platoon for the first proposed model and obtain condition for non-oscillating solution. In Sect. 4 we present calibration framework which is applicable for any microscopic model. It allows considering local stability conditions obtained. In the concluding Sect. 5, we discuss results and further investigations.

2 IDM Drawbacks and Two Modifications

The trainee observes vehicle traffic from their respective cabin so the cars' dynamics and drivers' behavior should be realistic to the highest degree. We considered the Intelligent Driver Model (IDM) [13] as a starting point for using in driving simulators. This model has a set of parameters which can be tuned to achieve desired objectives. After detailed study of this model we discovered several disadvantages in application to driving simulators.

- The IDM admits big deceleration values [6] and, as a result, a collective dynamics is crash-free. However, accidents are probable when people study driving.
- Instant reaction to the leading car. For example, at the signalized intersection cars start simultaneously.
- The steady-state gap does not incorporate the roads covering effect

$$d^*_{IDM}(v) = (s' + Tv)/\sqrt{(1 + (v/v^0)^\delta)} \tag{1}$$

To eliminate these drawbacks two modifications are presented.

2.1 Predefined Distance in a Steady State

Let us formulate the acceleration function for the first proposed model

$$\dot{v} = w(h, d^*, D)a\left(1 - \left(v/v^0\right)^\delta\right) + (1 - w(h, d^*, D))a\left(1 - \left(d^*/h\right)^2\right) \tag{2}$$

Here w is a continuous weight-function, which depends on headway h and parameter D.

$$w(h, d^*, D) = \begin{cases} 0, h \in (-\infty, d^*) \\ -2\left(\frac{h-d^*}{D} - 1\right)^3 - 3\left(\frac{h-d^*}{D} - 1\right)^2 + 1, h \in [d^*, d^* + D] \\ 1, h \in (d^* + D, +\infty) \end{cases} \tag{3}$$

If vehicle is quite far from its leader Eq. (2) has the first term only. If the current gap is less than the steady-state distance set, only the second term works.

This car-following model guarantees any predefined gap between vehicles in the steady-state flow. Equalling the right-hand side of Eq. (2) to zero, it is not difficult to demonstrate that the distance in a steady state is d^*. We chose distance from the Tanaka model [4]. It contains the braking path and the coefficient c that characterizes the roads covering

$$d^*(v) = s' + Tv + cv^2 \,, \tag{4}$$

2.2 Reaction Time

To take into account driver's reaction time we suggest the second modification that is described by the DDEs. It combines the optimal velocity model [2] and the first modification. The acceleration function is as follows

$$\dot{v_i} = w(h_i, d^*, D)a\left(1 - \left(v_i/v^0\right)^\delta\right) + (1 - w(h_i, d^*, D))b\left(V(h_i(t-\tau)) - v_i\right) \,, \tag{5}$$

Here we follow the same logic as in the first model (2) – separate free-road vehicle dynamics and interaction with its leader. Moreover, we suggest to make the parameter s of the optimal velocity function [9] depending from the current distance to the leader h

$$V(h) = \begin{cases} 0, 0 \le h \le s' \\ v^0 \frac{\left(\frac{h-s'}{s(h)}\right)^3}{1+\left(\frac{h-s'}{s(h)}\right)^3}, h > s' \end{cases} \tag{6}$$

This empirical relationship is obtained as follows. We put the vehicle with the velocity v at a distance of the Tanaka model (4) and request it to stop at the distance s' from its fixed leader.

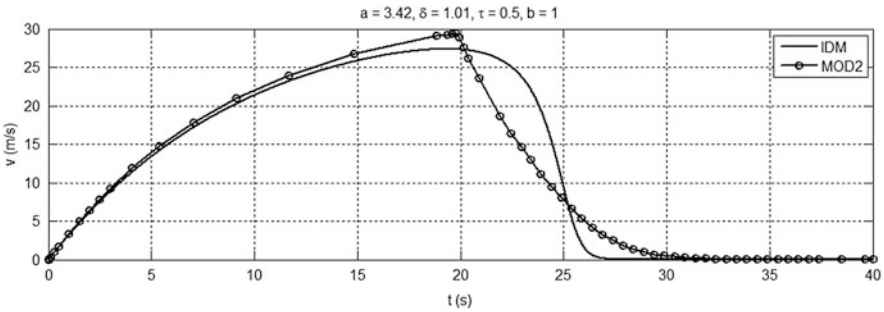

Fig. 1 Comparison of the IDM and model with delay proposed. Fixed leader approaching – velocity time history

Figure 1 compares acceleration dynamics of the IDM and the model (5). According to the model with the delay driver starts deceleration earlier and does it more smoothly with approximately constant rate.

3 Linear Stability Analysis

Here we perform a linear stability analysis for a vehicle platoon. Lets the acceleration of the ith vehicle be set on the basis of its speed v_i, the leaders speed v_{i-1} and the distance between h_i

$$\dot{v_i} = a^{(i)}(v_{i-1}, v_i, h_i) \tag{7}$$

Every vehicle may have its own acceleration function. We have a system of $2n$ ODEs for n vehicles. The Jacobian matrix has the block-like structure, so it is possible to obtain the determinant analytically

$$\chi(\lambda) = \prod_{i=0}^{n} (a_h^{(i)} - \lambda(a_v^{(i)} - \lambda)) \tag{8}$$

Here $a_h^{(i)}$ and $a_v^{(i)}$ are partial derivatives at the steady-state point. Finally we obtain all 2n eigenvalues. The local stability takes place when its real parts of all eigenvalues are negative. If we need no oscillations we require the imaginary parts to be equal to zero:

$$\begin{cases} \text{local stability}, & a_v^{(i)} < 0, \\ \text{no oscillations}, & (a_v^{(i)})^2 - 4a_h^{(i)} > 0. \end{cases} \tag{9}$$

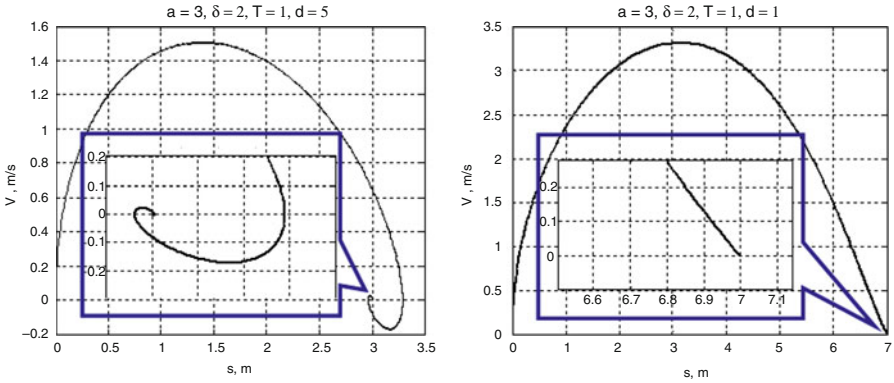

Fig. 2 Phase diagram 'velocity vs. distance'. Oscillations of the velocity and the gap to the fixed leader (*left*), and non-oscillating solution due to conditions obtained (*right*)

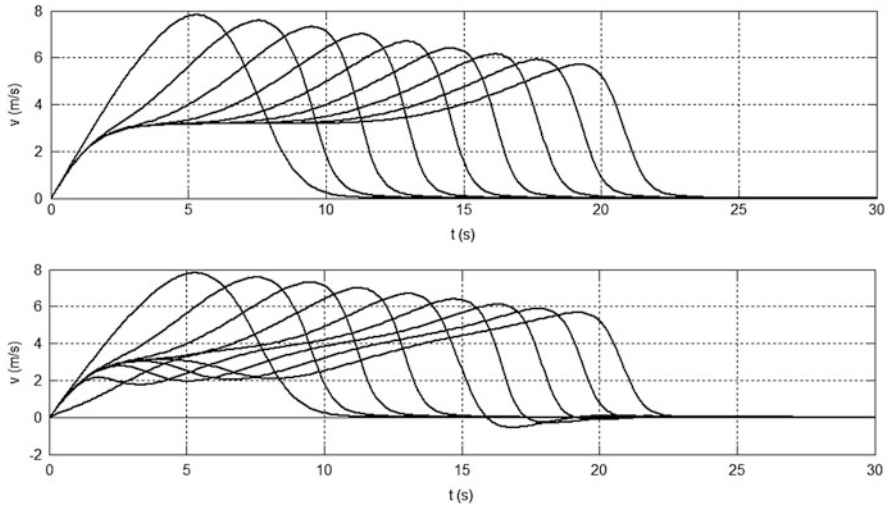

Fig. 3 Platoon stability – 9 vehicles approaching the 10th fixed car. *Top*: model parameters for every vehicle – $a = 2, T = 1.1, s' = 1$. Stability conditions are satisfied for every one – no oscillating solution. *Below*: model parameters for the 5th vehicle – $a = 2, T = 1.1, s' = 4$, for others are the same as in the first case. Stability conditions are broken for the fifth one – oscillations are observed

Now lets apply these conditions to the first model presented. We consider the car approaching its fixed leader. The results are shown at Fig. 2. The horizontal and vertical axes represent the velocity and the distance to the fixed leader respectively. On the left plot the parameters' values do not satisfy inequality obtained and oscillations over the equilibrium take place, whereas the right plot represents their absence. Figure 3 demonstrates the velocity series in case of vehicle platoon. We examine nine vehicles moving one by one in accordance with the model (2). The

10th car is fixed. In the first case the stability condition is fulfilled for all cars and no oscillating solution is observed. Then we break stability condition for the fifth vehicle and observe velocity oscillations of this and all subsequent ones.

4 Model Calibration

The calibration procedure can be carried out on two different levels that are macroscopic and microscopic ones. This former implements calibration with respect to macroscopic traffic data, for example, flow-density data for the specific region, or estimates origin-destination matrices [3]. The latter treats vehicles as an individual entities and uses microscopic trajectory data [5, 11]. The goal is to determine the optimal model parameters that better reproduce vehicle dynamics (acceleration on free-road, deceleration process) and drivers' behavior (distance between vehicles in a steady-state flow). Consequently, the calibration is evaluated on the basis of intra-driver and inter-driver criteria.

Our framework is intended for microlevel calibration and can be used for any parametrical traffic model that is described by ODE or DDE [8]. Let the vehicle's dynamics is defined by the ODE with following initial conditions

$$\begin{aligned} \frac{dh}{dt} &= v_L - v \\ \frac{dv}{dt} &= A(v_L, v, \theta) \\ h(t_0) &= h_0, v(t_0) = v_0 \end{aligned}$$

Here θ contains the set of the model parameters to be determined. In case of the first modification $\theta = (a, \delta, T, c)$. Also the real data – velocity time history $\{\tilde{v_i}\}_{i=1}^{N}$ and trajectory data $\left\{\tilde{h_i}\right\}_{i=1}^{N}$ are provided. We have to determine the model parameters that minimize the objective function with respect to vehicle's speed and its position. The main difficulty is that the second one can not be obtained analytically. Using the Euler method for numerical integration we formulate optimization problem with constraints as below

$$\begin{cases} w_1||v - \tilde{v}||^2 + w_2||h - \tilde{h}||^2 \to min \\ s_{i+1} - s_i = \Delta t \cdot v_i, v_{i+1} - v_i = \Delta t \cdot A(v_i, v_{Li}, h_i, \theta) \\ h(t_0) = h_0, v(t_0) = v_0 \\ + \text{local stability condition (9)} \end{cases} \tag{10}$$

The no oscillation condition obtained for the first modification is here incorporated in the optimization problem as an inequality constraint.

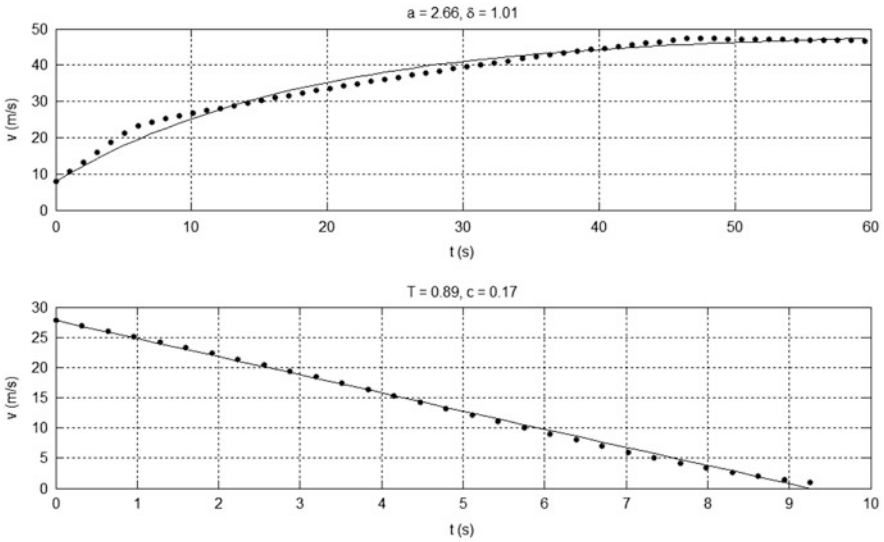

Fig. 4 Solution of the two-step calibrating problem – comparison of simulated and empirical data. The numerical solution and real data are shown as solid and dashed curves respectively. *Top*: free-road acceleration case and values for a and δ. *Below*: emergency deceleration case and values for T and c

We consider two sequent problems for calibrating procedure:

- Free-road acceleration (no leader presents),
- The emergency deceleration to avoid collision.

Solution of the first optimization problem contains values of two parameters – a and δ. Then solving the second one we obtain values for last two parameters T and c (Fig. 4). This calibrating procedure was evaluated for several vehicle models. In summary, this framework provides the parameter space that provides real dynamics of the specific car model and simultaneously ensures solution stability.

5 Discussions

Driving simulator is an effective tool as a training system. It allows to put trainee in real environment with road infrastructure (signs, road surface markings, traffic lights), vehicle traffic and pedestrians. The adequacy of environment reproduction affects on driver's perception and feelings and defines the quality of learning process. The realistic microscopic models are required for vehicle traffic simulation. The training process implies different environment conditions. Moreover, traffic flow should be diverse from two points of view – drivers' behavior and cars' dynamics. In other words, the mathematical models used should reproduce dynamics

of the specific car model, drivers' behavior and take into account weather conditions (e.g. day/night time, fog, snow, surface icing).

In this paper we propose two microscopic models for using with driving simulators. The first one is developed on the basis of the well-known Intelligent Driver Model (IDM). Deriving a continuous weight-function we combine two different modes – free-road acceleration and interaction with the preceding car – in one continuously differentiable acceleration function. This model ensures any predefined distance in a steady state and, thus, allows taking into account weather conditions and consider different physiological types of drivers. This model is investigated with linear stability analysis for the case of vehicle platoon. The stability conditions are obtained in general form and assume that every vehicle in a platoon has its own continuous acceleration function.

To consider human reaction time explicitly we propose the second microscopic model. In accordance with the acceleration function drivers response to their headway via the delay τ. This model combines the first modification and the optimal velocity. When compared to the IDM this model is not crash-free, always results in real acceleration values and allows to simulate collisions. Moreover, to guarantee safe stop before fixed leader with different initial conditions for velocity and position we modified optimal velocity function and calibrated it to fulfill this objective.

The model calibrating procedure is an essential part of model preprocessing. In this work we construct the framework for microlevel calibration. As inputs the velocity and position time history are used. We consider two scenaria – acceleration to the maximum speed with no leader presented and the emergency deceleration with the constant deceleration rate. The minimization of the objective function is evaluated both with respect to the vehicle's velocity and position, each of which has its own weight coefficient. This way, we can indicate what is more important – vehicle's gap or its speed agreement. This framework can be used for any microscopic model with parameters to be determined on the basis of ODEs or DDEs. In this paper, we demonstrate the results for the first microscopic model presented.

For the further work, we are planning to investigate the presented time-delay model with stability analysis. Some articles [9, 10] and approaches [7] have already been studied on this subject. The goal is to find out weather this model admits real human reaction times and simultaneously ensures solution stability. Another issue we are interested in is the effective numerical schemes. The Euler method used now does not work well for such time steps as human reaction time. As a result, we need to use more robust scheme in calculations. Moreover, this scheme should not be numerically consuming in order to simulate city-scale traffic in a real time.

References

1. R.W. Allen, R.H. Klein, K. Ziedman, Automobile research simulators: a review and new approaches. Transp. Res. Board **706**, 9–15 (1979)
2. M. Bando, K. Hasebe, A. Nakayama, A. Shibata, Y. Sugiyama, Phys. Rev. E **51**, 1035 (1995)

3. E. Cascetta, D. Inaudi, G. Marquis, Dynamic estimators of origin-destination matrices using traffic counts. Transp. Sci. **27**, 363–373 (1993)
4. N.H. Gartner, C.J. Messer, A.K. Rathi, *Traffic Flow Theory: A State-of-the-Art Report* (Transportation Research Board, Washington, DC, 2001)
5. A. Kesting, M. Treiber, Calibrating car-following models using trajectory data. J. Transp. Res. Board **2088**, 148–156 (2008)
6. A. Kesting, M. Treiber, D. Helbing, Enhanced intelligent driver model to access the impact of driving strategies on traffic capacity. Philos. Trans. R. Soc. A **368**, 4585–46055 (2010)
7. M. Lakshmanan, D.V. Senthilkumar, *Dynamics of Nonlinear Time-Delay Systems* (Springer, Heidelberg, 2010)
8. Z.F. Li, M.R. Osborne, T. Prvan, Parameter estimation of ordinary differential equations. IMA J. Numer. Anal. **25**, 264–285 (2005)
9. G. Orozs, R.E. Wilson, B. Krauskopf, Global bifurcation investigation of an optimal velocity traffic model with driver reaction time. Phys. Rev. E **70**(2), 026207 (2004)
10. G. Orozs, R.E. Wilson, R. Szalai, G. Stepan, Exciting traffic jams: nonlinear phenomena behind traffic jam formation on highways. Phys. Rev. E **80**, 046205 (2009)
11. S. Ossen, S.P. Hoogendoorn, Car-following behavior analysis from microscopic trajectory data. Transp. Res. Rec.: J. Transp. Res. Board **1934**, 13–21 (2005)
12. K.M. Roberts, The FHWA highway driving simulator. Public Roads **44**(3), 97–102 (1980)
13. M. Treiber, A. Hennecke, D. Helbing, Congested traffic states in empirical observations and microscopic simulations. Phys. Rev. E. **62**, 1805–1824 (2000)

Physically Bounded Solution for a Conserved Higher-Order Traffic Flow Model

Zhi-Yang Lin, Peng Zhang, Li-Yun Dong, S.C. Wong, and Keechoo Choi

Abstract This paper investigates bounded domains of the solution to a higher-order model in the density-velocity phase plane, according to the monotonicity of two characteristic variables. The basic principle is that the evolution of any phase states in a domain can be confined within this domain which is embraced by four isolines of two characteristic variables, if the evolution towards these isolines is impossible or against the monotonicity of the corresponding characteristic variable. The study provides more information than the classical linear analysis regarding the stability of solution to a higher-order model.

1 Introduction

Traffic flow models have been intensively studied (e.g., see [1–12]), among which the higher-order model takes the form of mass and "momentum" conservations, but the solution does not share the total variation diminishing (TVD) property with those for most hyperbolic conservation laws. This is mostly because of a relaxation source term by which the solution to the system is often unstable with oscillations. Thus, physically bounded solutions to higher-order traffic flow models worth investigating.

This paper serves as supplement to the work in Ref. [11] by implementing a systematic study of the physically bounded solution to a conserved higher-order (CHO) model. The discussion is associated with the stability of an initial state by

Z.-Y. Lin • P. Zhang (✉) • L.-Y. Dong
Institute of Applied Mathematics and Mechanics, Shanghai University, Shanghai, China
e-mail: linzy_1990@shu.edu.cn; pzhang@shu.edu.cn; pzhang@mail.shu.edu.cn; dly@shu.edu.cn

S.C. Wong
Department of Civil Engineering, The University of Hong Kong, Pokfulam Road, Hong Kong SAR, China
e-mail: hhecwsc@hkucc.hku.hk

K. Choi
Department of Transportation Engineering, TOD-based Sustainable Urban Transportation Center, Ajou University, Suwon, Korea
e-mail: keechoo@ajou.ac.kr

M. Chraibi et al. (eds.), *Traffic and Granular Flow '13*,
DOI 10.1007/978-3-319-10629-8_51

dividing the velocity-density (or flow-density) phase plane into several regions. A stable region is defined in a way that the evolution of any phase points is confined within this region, but for an unstable region the evolution of a phase point in this region might traverse the boundaries. Here, two phase points are in the link between a stable and an unstable region, which are well known as critical densities for division of equilibrium solution into stable and unstable intervals. Our discussion easily leads to the linear stability conditions; however, it provides more information for stability analysis. Moreover, the solution is indicated to be physically bounded in that all phase points in the largest stable region are physically significant, e.g., the density and velocity are non-negative and are bounded by the desired maximums. Numerical simulation is given to support these findings.

The remainder of the paper is organized as follows. In Sect. 2, the monotonicity of two characteristic variables in the evolution is discussed. In Sect. 3, the isolines of the two characteristic variables are used to find several bounded domains for the evolution of solution in the density-velocity phase plane, and numerical simulation is implemented to support the analytical findings. The paper is concluded by section "Conclusions".

2 Model Equations

In the macroscopic description, traffic flow is modeled as a continuum for which the number of vehicles on a highway road is conserved,

$$\rho_t + (\rho v)_x = 0, \tag{1}$$

where $\rho(x,t)$ and $v(x,t)$ are the average density and velocity in location x at time t. The traffic acceleration is described in higher-order models, among which the "anisotropic" models can be written in the following conservative and transport form:

$$(\rho z)_t + (\rho z v)_x = \beta^{-1}(v - v_e(\rho)), \tag{2}$$

where ρz is analogous to the momentum that must be conserved in a fluid under Newtonian mechanics, and parameter β is associated with relaxation time τ depending on the choice of the relationship: $z = z(\rho, v)$. We note that any two of ρ, v, z and other introduced variables can be chosen as independent solution variables which uniquely determine the others. In this case, it is implied that the Jacobian for the transformation between any two pairs of independent variables is non-singular.

The variable $z(\rho, v)$ usually describes the deviation of a traffic state from some ideal state. In the Aw-Rascle-Zhang (ARZ) or an extended ARZ model [1, 3, 4, 9], z was taken as $z = v - V(\rho)$, and interpreted as a relative speed with respect to

a desired speed $V(\rho)$. In the CHO model [11], z is taken as $z = w\rho^{-1}$, with w being defined by $v = V(w)$ and interpreted as a pseudo-density. Here, the function $V(\cdot)$ is a velocity-density relationship. Accordingly, $\beta = -\tau$ in the ARZ model, and $\beta = -\tau V'(w) \approx \tau V(0)(\rho_{jam})^{-1}$ in the CHO model.

2.1 Characteristic Equations

For a 2×2 system defined by Eqs. (1) and (2), one can always derive two characteristic equations by following a standard procedure. More simply, the operation $((2)–(1) \times z)\rho^{-1}$ directly give the second characteristic equation of the system,

$$z_t + vz_x = (\rho\beta)^{-1}(v - v_e(\rho)), \tag{3}$$

with $\lambda_2 = v$ being the second characteristic speed and z the corresponding characteristic variable. Moreover, the operation $(3)\times(z_v)^{-1}$ gives the first characteristic equation of system (1) and (2):

$$v_t + (v - \rho z_\rho (z_v)^{-1})v_x = (z_v \rho\beta)^{-1}(v - v_e(\rho)),$$

with $\lambda_1 = v - \rho z_\rho (z_v)^{-1}$ being the first characteristic speed and v the corresponding characteristic variable. Thus, the two characteristic fields are defined as follows:

$$1 - field: \quad \frac{dx}{dt} = \lambda_1, \quad \frac{dv}{dt} = (\rho z_v \beta)^{-1}(v - v_e(\rho)), \tag{4}$$

$$2 - field: \quad \frac{dx}{dt} = \lambda_2, \quad \frac{dz}{dt} = (\rho\beta)^{-1}(v - v_e(\rho)), \tag{5}$$

Generally, Eq. (4) or (5) cannot be analytically solved. However, the monotonicity of each characteristic variable with respect to t along the corresponding characteristics can be indicated through the right hand term of (4) or (5), which helps study the boundedness of solution.

2.2 Solution Through Characteristics

Characteristic equations essentially describe the wave propagation in a hyperbolic system. For application problems, only the information that is propagated from initial states through characteristics are physically meaningful, to which the corresponding solution is mostly the "physically relevant" or "entropy" solution. This fact is well known in the literature and is taken as a preliminary in the following discussion.

Assumption 1 *A solution state* $(\rho(x,t), v(x,t))$ *of system (1) and (2) is derived from some two initial states* $(\rho(\xi,0), v(\xi,0))$ *and* $(\rho(\eta,0), v(\eta,0))$*, continuously through propagation of 1-field defined by (4) and 2-field defined by (5), respectively.*

Since $(\rho, v) \to (v, z)$ is assumed to be a reversible transformation, the derivation is through the following three steps. First, $v(\xi,0)$ and $z(\eta,0)$ are determined by $(\rho(\xi,0), v(\xi,0))$ and $(\rho(\eta,0), v(\eta,0))$, respectively. Second, $v(x,t)$ and $z(x,t)$ are determined by $v(\xi,0)$ and $z(\eta,0)$ through propagation of a characteristic defined by (4) and (5), respectively. Third, $(\rho(x,t), v(x,t))$ is obtained through the transformation $(v,z) \to (\rho, v)$. See Fig. 1a for illustration. The argument also implies that each solution state of (ρ, v) in the characteristic connecting $v(\xi,0)$ to $v(x,t)$ is determined through its intersection with a 2-characteristic. Thus, the aforementioned characteristic can be mapped onto ρ-v phase plot, as is the other characteristic that connects $z(\eta,0)$ to $z(x,t)$. Correspondingly, the two mapped curves shown in Fig. 1b are also called a 1- and a 2-characteristic. Since a solution state is derived through intersection between a 1- and a 2-characteristic starting from initial states, it is straightforward to have

Lemma 1 *A phase point in* ρ-v *phase plane can be excluded from the solution domain if it cannot be reached by either a 1- or a 2-characteristic starting from an initial state.*

In a higher-order model, $v_e(\rho)$ is defined as an equilibrium velocity-density relationship with equilibrium solution: $(\rho, v) = (\rho_0, v_e(\rho_0))$. Thus, the evolution of v through a 1-characteristic tends to approach the curve $v = v_e(\rho)$ in ρ-v phase plane, and we have

Lemma 2 *We should reasonably assume that* $z_v\beta < 0$*. Then, we have*

1. *v is increasing/decreasing of t along a 1-characteristic for (ρ, v) below/above the curve $v = v_e(\rho)$;*

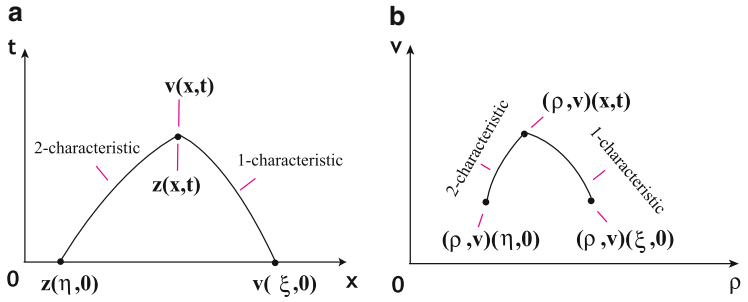

Fig. 1 Derivation of solution through intersection between a 1- and a 2-characteristic. (**a**) In x–t coordinate plane. (**b**) In ρ–v phase plane

2. *z is increasing/decreasing of t along a 2-characteristic for (ρ, v) below/above the curve $v = v_e(\rho)$ in the case where $z_v > 0$, and $\beta < 0$ (applicable to the ARZ model);*
3. *z is decreasing/increasing of t along a 2-characteristic for (ρ, v) below/above the curve $v = v_e(\rho)$ in the case where $z_v < 0$, and $\beta > 0$ (applicable to the CHO model).*

3 Physically Bounded Solution for the CHO Model

Given $v = \tilde{v}$ or $z = \tilde{z}$, the transformation $(v, z) \to (\rho, v)$ defines a curve in ρ-v coordinate plane, which is called the isoline $v = \tilde{v}$ or $z = \tilde{z}$. The isolines of $v = \tilde{v}$ are simply straight lines parallel to ρ axis. The isolines of $z = \tilde{z}$ are a family of parallel curves defined by $w\rho^{-1} = \tilde{z}$ in the CHO model, which are shown in Fig. 2 with a variety of $\tilde{z}$.

3.1 Globally Bounded Solution

Note that in $D \cup \partial D$, the isolines of $v = \tilde{v}$ go increasingly from the boundaries $v = 0$ to $v = v_f$; the isolines of $z = \tilde{z}$ go decreasingly from $z = \infty$ to $z = z_{jam}$, which turn out to be the boundaries $\rho = 0$ and $v = V(\rho)$. Then, starting from initial solution states, a 1-characteristic cannot exceed the boundary $v = 0$ and a 2-characteristic cannot exceed the boundary $\rho = 0$. This is because the characteristic variables v and z propagates increasingly (and continuously) in D^-, according to Lemma 2. Here, we define $D^{\mp} = D \cap \{(\rho, v) |\ v \lesseqgtr v_e(\rho)\}$. It is similarly verified (by considering the domain D^+) that a 1-characteristic cannot exceed the boundary $v = v_f$, and a 2-characteristic cannot exceed the boundary $v = V(\rho)$. These statements imply that any points outside D cannot be solution states, according to Lemma 1. Thus, we have

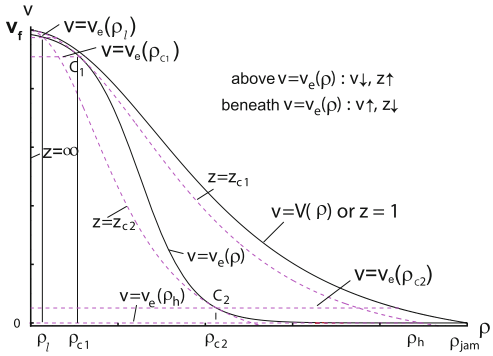

Fig. 2 Physically bounded solutions within the domains D and D_i. Each domain is enclosed by two isolines of $v = \tilde{v}$ and two isolines of $z = \tilde{z}$

Proposition 1 *Assume that the isoline $z = z_{jam}$ ($\equiv 1$) that insects with $(\rho_{jam}, 0)$ is above the curve $v = v_e(\rho)$. Then, the solution of system (1) and (2) is globally bounded by the domain $D = \{(\rho, v)|\ 0 < v < V(\rho),\ \rho > 0\}$, if it is initially in D.*

3.2 Regionally and Locally Bounded Solutions

The isolines of $z = \tilde{z}$ intersect with $v = v_e(\rho)$ at z_{c1} and z_{c2}, which correspond to the two critical densities ρ_{c1} and ρ_{c2} for stability. The occurrence can be associated with most common cases in the literature, but we show more than before in the following.

In Fig. 2, the isoline of $z = z_{ci}$ is tangent to $v = v_e(\rho)$ at $C_i(\rho_{ci}, v_e(\rho_{ci}))$ ($i = 1, 2$). This suggests that (ρ_{ci}, w_{ci}) ($i = 1, 2$) are the roots of the following algebraic equations:

$$wV'(w) = \rho v_e'(\rho), w = V^{-1}(v_e(\rho)), \tag{6}$$

where $w_{ci} = \rho_{ci} z_{ci}$, which helps determine z_{ci}. Equation (6) is exactly the same as that derived from the linear stability analysis [7]. Assume that ρ_h and ρ_l are the densities at the intersections between the isolines $z = z_{ci}$ and $v = v_e(\rho)$. We define the following domains:

$$\begin{aligned}
D_s &= \{(v, z)|\ v_e(\rho_h) < v < v_e(\rho_l),\ z_{c1} < z < z_{c2}\};\\
D_{s1} &= \{(v, z)|\ v_e(\rho_{c1}) < v < v_f,\ z_{c1} < z < z_{c2}\};\\
\tilde{D}_{s1} &= \{(v, z)|\ v_e(\rho_{c1}) < v < v_e(\rho_l),\ z_{c1} < z < z_2\};\\
D_{s2} &= \{(v, z)|\ 0 < v < v_e(\rho_{c2}),\ z_{c1} < z < z_{c2}\};\\
\tilde{D}_{s2} &= \{(v, z)|\ v_e(\rho_h) < v < v_e(\rho_{c2}),\ z_{c1} < z < z_2\};\\
D_u &= \{(v, z)|\ v_e(\rho_{c2}) < v < v_e(\rho_{c1}),\ z_{c1} < z < z_2\}
\end{aligned} \tag{7}$$

Then, by Lemmas 1 and 2 we have

Proposition 2 *Assume that the isoline $z = z_{jam}$ is above the curve $v = v_e(\rho)$. Then, the solution of system (1) and (2) is regionally bounded by each of the following domains: D_s, D_{s1}, $\tilde{D}_{s1}$, D_{s2}, and $\tilde{D}_{s2}$, if it is initially in the referred domain.*

The proof of Proposition 2 is similar to that of Proposition 1. By the subscript "s", Proposition 2 implies that the referred domains are stable. Referring to the stable domains D_{s1} and D_{s2}, we also have

Proposition 3 *The equilibrium solution $(\rho, v) = (\rho_0, v_e(\rho_0))$ of system (1) and (2) is stable for $\rho_0 \in (0, \rho_{c1})$ (or (ρ_{c2}, ρ_{jam})), if this state together with the perturbed state $(\rho_0 + \Delta\rho_0, v_e(\rho_0) + \Delta v)$ is within the domain D_{s1} (or D_{s2}).*

By Proposition 3, we say that the equilibrium solution $(\rho, v) = (\rho_0, v_e(\rho_0))$ is locally bounded for $\rho \in (0, \rho_{c1}) \cup (\rho_{c2}, \rho_{jam})$, because the perturbation can be so sufficiently small that the perturbed state is within D_{s1} or D_{s2}. Propositions 1–3 convey more information for stability of solutions than the linear stability analysis on the equilibrium solution. On the other hand, the equilibrium solution is instable for $\rho_0 \in (\rho_{c1}, \rho_{c2})$, according to the linear stability analysis [7]. More generally, solution states in D_u are not locally bounded. As a consequence, their development would exceed the upper boundary $v = v_e(\rho_{c1})$ or/and the lower boundary $v = v_e(\rho_{c2})$, and fall into the stable region(s) D_{s1} or/and D_{s2}, because v increases for (ρ, v) between $v = v_e(\rho_{c1})$ and $v = v_e(\rho)$, and decreases for (ρ, v) between $v = v_e(\rho_{c2})$ and $v = v_e(\rho)$. If all initial states are in D_u and the total number of vehicles remains unchanged, the stop-and-go wave with low density $\rho < \rho_{c1}$ and high density $\rho > \rho_{c2}$ is expected. This agrees with the illustration in Fig. 2 and the studies in [2–4, 8, 10, 11].

3.3 Numerical Results

Let $v_e(\cdot)$ and $V(\cdot)$ be given by those in [2] and [12], and the Godunov scheme be applied [11, 12]. The simulation time is taken as $t = 3.125$, by using the periodic boundary conditions and the initial data: (i) $(\rho(x, 0), v(x, 0)) = (0.04, 0.975)$, $(0.05, 0.94)$, $(0.1, 0.91)$; and (ii) $(\rho(x, 0), v(x, 0)) = (0.43, 0.05)$, $(0.5, 0.01)$, $(0.85, 0.005)$, for $x \in [0, 0.3125]$, $(0.3125, 0.625]$, $(0.625, 1]$, respectively. We observe that these initial phase states together with their evolution are within $\tilde{D}_{s1}$ and $\tilde{D}_{s2}$ for (i) and (ii), as is shown in Fig. 3a, b, respectively. However, for the following initial data:

$$\rho(x, 0) = 0.22 + 0.2[cosh^{-2}(160x - 60) - \frac{1}{4}cosh^{-2}(40x - \frac{65}{4}))], \; v = v_e(\rho(x, 0)),$$

which are in D_u, the evolution crosses the upper and bottom boundaries of D_u. Nevertheless, the evolution is confined within $D_s \supset D_u$. The simulation results agree with Propositions 1–3 and the analysis in the context.

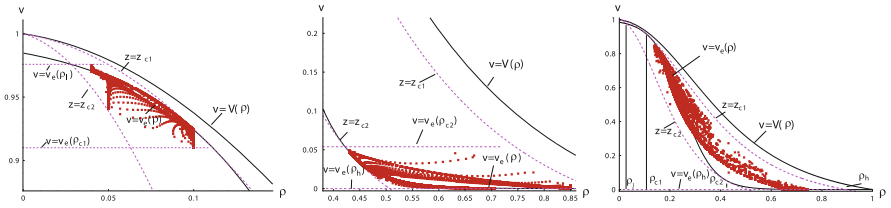

Fig. 3 Evolution of phase states is within stable regions but out of an unstable region. (**a**) Within $\tilde{D}_{s1}$. (**b**) Within $\tilde{D}_{s2}$. (**c**) Out of D_u but within D_s

Conclusions
The study provides a better understanding of the evolution and stability of solutions to the higher-order model of traffic flow. The analytical tool can be helpful for the choice of model parameters or functions to ensure physically bounded solution and improve current formulations in modeling more complex phenomena (e.g., those associated with phase transition and hysteresis in the observation).

Acknowledgements This study was jointly supported by grants from the National Natural Science Foundation of China (11072141,11272199), the National Basic Research Program of China (2012CB725404), the Shanghai Program for Innovative Research Team in Universities, and a National Research Foundation of Korea grant funded by the Korean government (MSIP) (NRF-2010-0029446).

References

1. A. Aw, M. Rascle, Resurrection of "second order" models of traffic flow. SIAM J. Appl. Math. **60**, 916–938 (2000)
2. B.S. Kerner, P. Konhauser, Structure and parameters of clusters in traffic flow. Phys. Rev. E **50**, 54–83 (1994)
3. J.P. Lebacque, S. Mammar, H. Haj-Salem, The Aw-Rascle and Zhang's model: vacuum problems, existence and regularity of the solutions of the Riemann problem. Transp. Res. B **41**, 710–721 (2007)
4. J.P. Lebacque, S. Mammar, H. Haj-Salem, Generic second order traffic flow modelling, in *Transportation and Traffic Theory*, ed. by R.E. Allsop, M.G.H. Bell, B.G. Heydecker (Elsevier, London, 2007), pp. 755–776
5. D. Ngoduy, Platoon-based macroscopic model for intelligent traffic flow. Transportmetrica B: Transp. Dyn. **1**, 153–169 (2013)
6. F. van Wageningen-Kessels, B. van't Hof, S.P. Hoogendoorn, H. van Lint, K. Vuik, Anisotropy in generic multi-class traffic flow models. Transportmetrica A: Transp. Sci. **9**, 451–472 (2013)
7. G.B. Whitham, *Linear and Nonlinear Waves* (Wiley, New York, 1974)
8. R.Y. Xu, P. Zhang, S.Q. Dai, S.C. Wong, Admissiblity of a wide cluster solution in "anisotropic" higher-order traffic flow models. SIAM J. Appl. Math. **68**, 562–573 (2007)
9. H.M. Zhang, A non-equilibrium traffic model devoid of gas-like behavior. Transp. Res. B **36**, 275–290 (2002)
10. P. Zhang, S.C. Wong, Essence of conservation forms in the traveling wave solutions of higher-order traffic flow model. Phys. Rev. E **74**, 026109 (2006)
11. P. Zhang, S.C. Wong, S.Q. Dai, A conserved higher-order anisotropic traffic flow model: description of equilibrium and non-equilibrium flows. Transp. Res. B **43**, 562–574 (2009)
12. P. Zhang, D.L. Qiao, L.Y. Dong, S.Q. Dai, S.C. Wong, A number of Riemann solvers for a conserved higher order traffic flow model, in *Fourth International Joint Conference on Computational Sciences and Optimization (CSO)*, Lijiang (IEEE, 2011), pp. 1049–1053

A Review of Cellular Automata Model for Heterogeneous Traffic Conditions

Gaurav Pandey, K. Ramachandra Rao, and Dinesh Mohan

Abstract Over the years various microscopic traffic models were developed to predict vehicular behaviour from mid-block section of road to the network level. Cellular Automata (CA) was found to be a promising approach to meet this challenge in the recent past. A CA approach to traffic simulation is potentially useful in order to achieve a very high computational rate in microscopic simulation, and to facilitate distributed computing. Because of this CA models are becoming increasingly popular for their potential to simulate large scale road network using macroscopic traffic characteristics like flow and density. Despite an increase in computational power over the past decade, limited efforts have gone in evaluating the model at microscopic level using characteristics like lane keeping and lane change. These characteristics along with traffic composition and density have significant influence on the amount of interaction between different vehicle types. This paper provides a brief review of CA models developed for heterogeneous traffic conditions and provides insights for improvement. Model performance is evaluated at macroscopic and microscopic level using characteristics like speeds and positions obtained from vehicle trajectories. The data was collected on arterial roads in Ludhiana, India for this study.

G. Pandey
Research Scholar, Transportation Research and Injury Prevention Programme and Department of Civil Engineering, Indian Institute of Technology New Delhi, New Delhi, India
e-mail: gauravpandey2006@yahoo.co.in

K.R. Rao (✉)
Associate Professor, Department of Civil Engineering, Indian Institute of Technology New Delhi, New Delhi, India
e-mail: rrkalaga@civil.iitd.ac.in

D. Mohan
Volvo Chair Professor Emeritus, Transportation Research and Injury Prevention Programme, Indian Institute of Technology New Delhi, New Delhi, India
e-mail: dmohan@cbme.iitd.ac.in

M. Chraibi et al. (eds.), *Traffic and Granular Flow '13*,
DOI 10.1007/978-3-319-10629-8_52

1 Introduction

Traffic flow modelling describes the dynamics of different types of vehicles and their interaction. In microscopic simulation model, each vehicle is described by its own equation of motion, hence the computational time and memory required are greater for these models. In this context, Cellular Automata (CA) based models were found to be promising approach to meet this challenge in the recent past. Since the introduction model developed by Nagel and Schreckenberg (NaSch) model, many researchers have developed traffic flow models using CA [8]. Most of the CA based traffic flow models have addressed the homogeneous traffic flow and its behaviour. Due to discreteness of this model, it can simulate large scale real time microscopic phenomena like platoon formation, estimate the capacity drop at transition between free and congested flow. Later many researchers contributed to the development of the model by adding more rule sets to increase its capability and replicate traffic features seen in multilane, heterogeneous traffic [1–3]. Mallikarjuna and Rao further developed the model for Indian conditions. They found that traffic in India is highly heterogeneous with no proper lane discipline hence it was necessary to modify the model to incorporate many types of vehicles and also their lateral movements [5]. Nassab et al. [7] gave symmetric lane changing rules to control vehicle's lateral movement near a partial lane closure. However, the length of transition area was assumed as two cells in their study, which is inconsistent with the real world work zone configuration [7]. Lan et al. developed CA model for cars and two-wheelers to simulate lateral traversing by two-wheelers in stopped traffic [4]. Meng and Weng first calibrated the randomization parameter by using observed work zone data to simulate the homogenous work zone traffic [6]. Vasic and Ruskin developed one dimensional cellular automata model based on Nash model for combined car and bicycle traffic [9]. They found that vehicles have positional discipline based on vehicle types which implies that bicycles keep to the side of the road nearest to the kerb, while cars allow space for any present bicycles by staying as far away from the kerb as possible.

2 Data Collection

Ludhiana city, Punjab, India was selected for the study as it has one of the highest fatality rate and ongoing study aims at understanding accidents from traffic flow point of view. Two road sections were selected for video-graphic traffic survey namely Jagraon bridge to Bharatnagar intersection and Chima intersection to Vishwakarma intersection owing to their higher involvement in fatalities and easy availability of vantage points for mounting camera. Camera was placed along the centreline of one direction on top of foot-over bridge to get required elevation and view needed for image processing software. The focus of camera was adjusted such

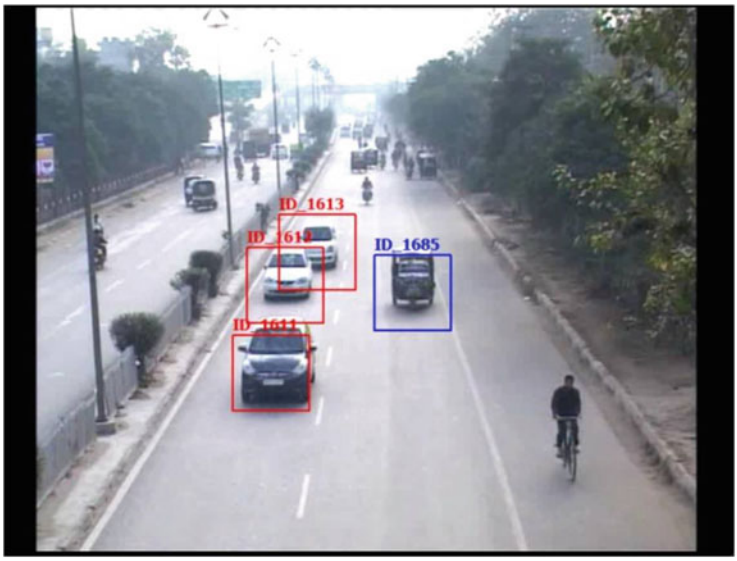

Fig. 1 Location with marked vehicles in ™TRAZER

that it could capture 70 m road stretch. Four points indicating a road trap of 30 m by 7 m were marked on road to facilitate image calibration to ground dimensions. Figure 1 shows one of the location and marked vehicles in ™TRAZER software.

Video data was collected for 2 h on both locations for a total of 4 h covering both morning and evening peaks. These videos were analyzed using ™TRAZER, an image processing software and vehicles trajectories were marked manually to ensure highest accuracy. Each vehicle's position was marked in every 25th frame (approx., 1 s) to generate a total of 2,359 trajectories giving frame-wise x–y coordinates. Out of these 33 % were cars, 3 % were trucks, 17 % were 3 wheelers and 48 % were 2 wheelers. Truck volume was low as the roads being urban arterials. A ™MATLAB program was developed to determine vehicle-wise traffic flow characteristics namely speed, lateral position on the road, lateral and longitudinal gaps from x–y coordinates of vehicles. Speed was calculated using position in first and last frame of trajectory and grouped into 5 classes with an interval of 20 km/h. Gaps were calculated as difference in x–y coordinates of adjacent vehicles in a particular frame after adjusting for vehicle dimensions. These microscopic characteristics were then used to estimate macroscopic characteristics like flow, area occupancy and stream speed. Stream speed is calculated as the arithmetic mean of speeds of all vehicles in a frame and then averaged based on area occupancy. Area occupancy is the ratio of road space occupied by vehicle divided by total area. The mean and maximum area occupancy was found to be 0.03 and 0.08 % respectively. Flow is calculated as a product of stream speed, road width and area occupancy divided by horizontal projection area of standard vehicle (i.e., car).

3 Model

Mallikarjuna and Rao found Knospe's brake light model to be better in reproducing different realistic traffic features. This model is having greater scope to incorporate some heterogeneous traffic features other than variable acceleration/deceleration [5]. For example, in the updating procedure, safe headway and anticipation parameters such as security distance could be useful in representing vehicular interactions observed in the heterogeneous traffic. When the leading vehicle is car, following driver's anticipation is different from the situation where the leading vehicle is a truck. Regarding lateral movement there is no added advantage of BL model compared to the other CA models. Hence a modified brake light model proposed by Mallikarjuna and Rao is further evaluated using microscopic traffic characteristics observed in the field. The longitudinal and lateral update rules of the model are same as those used by Mallikarjuna and Rao. Table 1 below shows the values of different parameters used in the model. In this study maximum speeds of different vehicle types is modified according to field conditions.

A lattice with periodic boundary conditions was used. The lattice consists of 10 × 1,000 cells each cell being 0.7 m wide and 0.5 m long. A total of 1,000 simulation steps were performed at different global area occupancies between 0.06 and 0.15. At each run first 500 time-steps were discarded and second half were considered for analysis. The traffic composition chosen for the simulation is same as that observed in the field data. Each time-step represents 1 s in real world.

Table 1 Parameters used in the model

Parameter	2Wheeler	3Wheeler	Car	Bus	Truck
Length (*cells*)	4	6	7	25	25
Width (*cells*)	1	2	3	4	4
Maximum Speed ($cells/sec$)	26	20	30	28	28
Acceleration ($cells/sec^2$) at speed <5.5 m/s	5	2	4	2	2
Acceleration ($cells/sec^2$) at speed 5.5 and 11 m/s	4	2	3	1	1
Acceleration ($cells/sec^2$) at speed >11 m/s	3	1	2	1	1
p_o	0.3	0.4	0.5	0.6	0.6
p_{dec}	0.1	0.3	0.3	0.1	0.1
Alpha	1.5	2	1.5	1.5	1.5
p_{bl}	0.94	0.94	0.94	0.94	0.94
p_{lc}	0.5	0.5	0.5	0.5	0.5
Security distance (*cells*)	2	5	5	21	21
Interaction headway (*sec*)	6	6	6	6	6

3.1 Local Measurement Using Moving Detectors of Finite Length

Here unlike earlier studies the detectors are not fixed in lattice but each vehicle acts as a moving detector with one end being the headlight and other end being point 50 m ahead of it. Local measurements are not averaged temporally or spatially as values taken over time do not represent same measurement region of lattice. The length of detector is chosen as 50 m because that is the maximum distance a vehicle can travel in one time-step. Also simulated measurement region will be more representative as the field data is collected using camera with trap length of 50 m. In this spatial measurement region, speed and number of cells occupied by each vehicle at particular time-step is observed and then used to calculate space mean speed, local density, area occupancy and flow using fundamental flow equations. Since there are various types of vehicles that occupy different number of cells, each occupied cell is considered as one vehicle and its speed is equal to the speed of vehicle occupying that cell. This means one bus occupying (4×25) cells and speed 20 cells/sec becomes 100 vehicles moving at 20 cells/sec each occupying one cell. Hence we can write from fundamental traffic flow equations

$$k(t) = N(t)/l \times n \tag{1}$$

$$q(t) = \Sigma_{i=1}^{N(t)} V_i(t)/l \times n \tag{2}$$

$$v(t) = q(t)/k(t) = \Sigma_{i=1}^{N(t)} V_i(t)/N(t) \tag{3}$$

Where, $k(t)$, $q(t)$ and $v(t)$ are area occupancy, flow and space mean speed respectively at time-step t, $N(t)$, l and n are number of cells occupied by vehicles, length and width of measurement region in cells respectively, $V_i(t)$ is the speed of vehicle i at time-step t in cells/time-step. Here unlike other studies measurements are not averaged temporally as area occupancy and flow may vary significantly in subsequent time-steps.

4 Results

The flow-occupancy relationship obtained from simulation is shown in Fig. 2. The relationship followed conventional bell-shaped curve but slightly over-estimated the maximum flow. The maximum flow obtained from simulation is around 5,000 vehicles/hr whereas that observed on road is around 3,000 vehicles/hr for two-lane road. Here note that the flow values represent average of all flow values at that occupancy for each simulation run. It was also found that the transition from free flow state to synchronized state occurs around an area occupancy of 0.1.

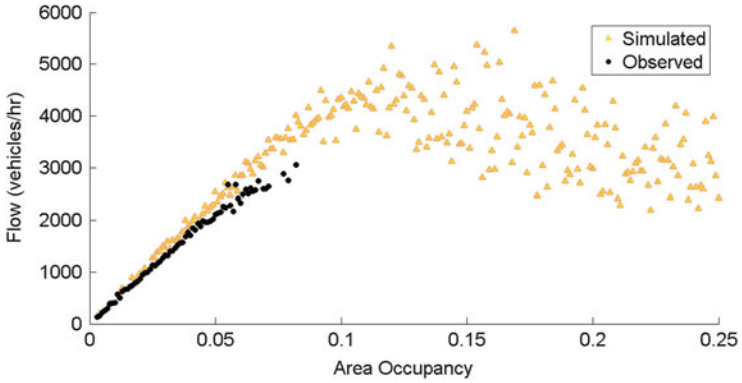

Fig. 2 Flow-occupancy curve

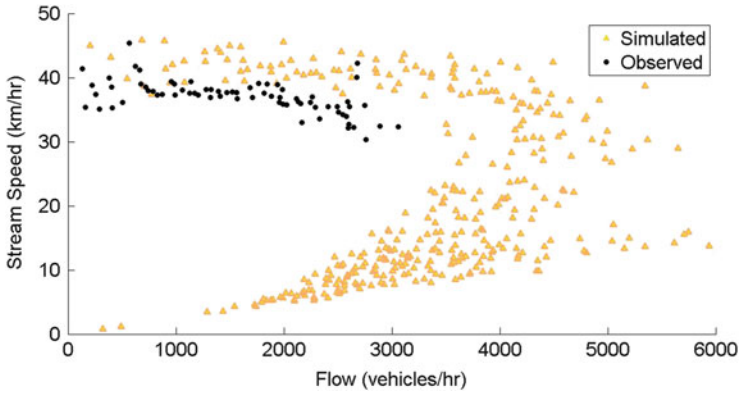

Fig. 3 Speed-flow curve

The $v-q$ and $v-k$ diagrams obtained from simulation are shown in Figs. 3 and 4 respectively. The relationships obtained from model showed conventional traffic flow trends but over-predicted the stream speed by almost 5 km/h. The difference between observed and simulated speeds increased at higher occupancy (i.e., above 0.7). This suggests that vehicles in simulation were able to maintain higher speeds even as the density on road increased. This could possibly explain higher maximum flow for the model. Figure 5 shows lateral position of vehicles on road. It is found that in observed data different vehicle types tend to have position preference so heavy vehicles and cars usually travel closer to median whereas lighter vehicles travel closer to shoulder. Thus if a heavy vehicle coming at higher speed faces a slower moving vehicle in front it would prefer to apply brakes instead of overtaking it from wrong side. Since there are no lateral movement rules in cellular automata

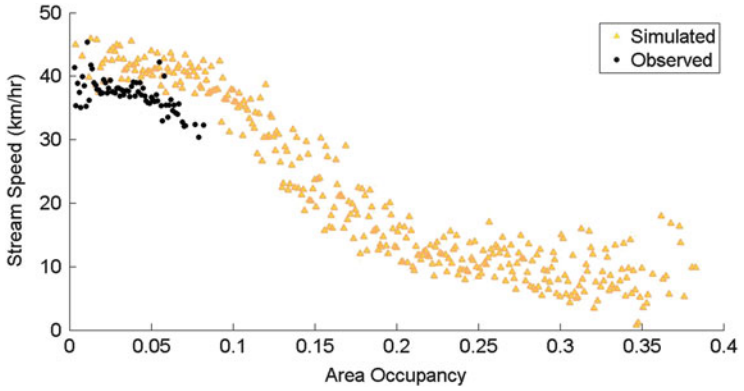

Fig. 4 Speed-occupancy curve

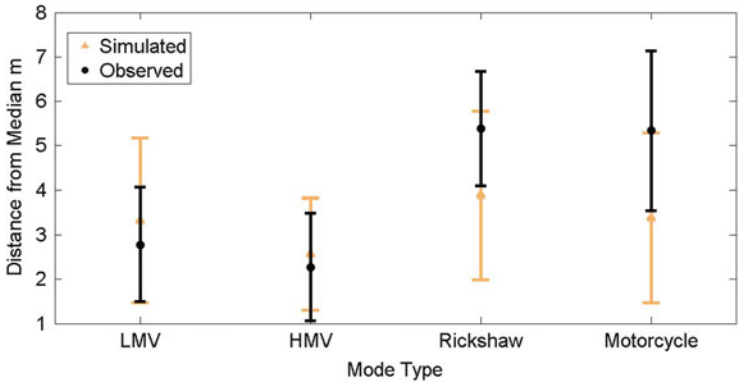

Fig. 5 Modewise lateral position curve

which consider driver preference while making lane change, many heavy vehicles and cars end up travelling on furthermost lane. This is very unrealistic and gives higher stream speeds and flow for given occupancy.

Conclusions

It is clear from the studies that cellular automata models can reproduce fundamental traffic flow diagrams but little work has been done to validate it using microscopic driving characteristics. Lane keeping behaviour of drivers plays important role in determining the amount of interaction that different vehicle types would have at given density and composition. These interactions dictate many traffic phenomenons like accidents and capacity. Hence CA

(continued)

model need to consider position preference for different vehicle types to produce realistic microscopic interactions. This would help in identifying the vehicular interactions in terms of safe and unsafe operations which can further lead to the assessment of risk propensity of their operations.

References

1. D. Helbing, M. Schreckenberg, Cellular automata simulating experimental properties of traffic flow. Phys. Rev. E **59**, R2505–R2508 (1999)
2. B.S. Kerner, S.L. Klenov, D.E. Wolf, Cellular automata approach to three-phase traffic theory. J. Phys. A: Math. Gen. **35**(47), 9971–10013 (2002)
3. W. Knospe, L. Santen, A. Schadschneider, M. Schreckenberg, Towards a realistic microscopic description of highway traffic. J. Phys. A: Math. Gen. **33**(48), L477–L485 (2000)
4. L.W. Lan, Y.C. Chiou, Z.S. Lin, C.C. Hsu, Cellular automaton simulations for mixed traffic with erratic motorcycles' behaviours. Physica A **389**(10), 2077–2089 (2010)
5. C. Mallikarjuna, K.R. Rao, Heterogeneous traffic flow modelling: a complete methodology. Transportmetrica **7**(5), 321–345 (2011)
6. Q. Meng, J. Weng, An improved cellular automata model for heterogeneous work zone traffic. Transp. Res. C: Emerg. Technol. **19**(6), 1263–1275 (2011)
7. K. Nassab, M. Schreckenberg, S. Ouaskit, A. Boulmakoul, Impacts of different types of ramps on the traffic flow. Physica A **352**(2–4), 601–611 (2005)
8. M. Rickert, K. Nagel, M. Schreckenberg, A. Latour, Two lane traffic simulations using cellular automata. Physica A **231**(4), 534–550 (1996)
9. J. Vasic, H.J. Ruskin, Cellular automata simulation of traffic including cars and bicycles. Physica A **391**(8), 2720–2729 (2012)

A Demonstration Experiment of a Theory of Jam-Absorption Driving

Yohei Taniguchi, Ryosuke Nishi, Akiyasu Tomoeda, Kenichiro Shimura, Takahiro Ezaki, and Katsuhiro Nishinari

Abstract We have conducted an experiment to demonstrate "jam-absorption driving", which is a method of driving with a single car to avoid being entangled in a jam by changing its headway and velocity dynamically. We used real cars on a circuit. In the experiment, the car doing jam-absorption driving takes a long headway in advance before a jam comes. We draw a time-space diagram and it is found the jam can be removed by this driving method.

1 Introduction

Many drivers have been troubled in traffic jams on highway. In Japan, the economic losses caused by such traffic jams are about 11 trillion yen in 2005 [10]. Recently, not only engineers but also scientists have studied the traffic flow to clarify the

Y. Taniguchi (✉)
Graduate School of Engineering, Department of Advanced Interdisciplinary Studies (AIS), The University of Tokyo, Meguro-ku, Tokyo 153-8904, Japan
e-mail: taniguchi@jamology.rcast.u-tokyo.ac.jp; ytaniguchi527@gmail.com

R. Nishi
National Institute of Informatics, 2-1-2 Hitotsubashi, Chiyoda-ku, Tokyo 101-8430, Japan

JST, ERATO, Kawarabayashi Large Graph Project, 2-1-2 Hitotsubashi, Chiyoda-ku, Tokyo 101-8430, Japan

A. Tomoeda
Meiji Institute for Advanced Study of Mathematical Sciences, Meiji University 4-21-1 Nakano, Nakano-ku, Tokyo 164-8525, Japan

JST, CREST, 4-21-1 Nakano, Nakano-ku, Tokyo 164-8525, Japan

K. Shimura • K. Nishinari
Research Center for Advanced Science and Technology, The University of Tokyo, Komaba, Meguro-ku, Tokyo 153-8904, Japan

T. Ezaki
School of Engineering, Department of Aeronautics and Astronautics, The University of Tokyo, 7-3-1 Hongo, Bunkyo-ku, Tokyo 113-8656, Japan

Japan Society for the Promotion of Science, 5-3-1 Ichibancho, Kojimachi, Chiyoda-ku, Tokyo 102-0083, Japan

M. Chraibi et al. (eds.), *Traffic and Granular Flow '13*,
DOI 10.1007/978-3-319-10629-8_53

mechanism of traffic congestion [3, 4, 6, 7, 11, 13]. In order to avoid jams, various strategies controlling traffic flow such as the ramp metering [2, 9] and the variable speed limits (VSL) [5, 12, 15] have been proposed and operated. Not only such strategies based on road infrastructures, but also strategies based on focusing each car's behavior such as car-following behaviors have been studied. One of famous study in this scope is utilizing a system of adaptive cruise control (ACC) for improving the efficiency of traffic flow [14]. ACC is an on-board system on a car controlling time-headways as well as velocities according to a headway sensor, and enables the car to drive car-following behaviors more accurately than manual cars.

Relative to these strategy performing such dynamical driving, the effect of a car taking a large headway before being entangled in a jam was discussed by Beaty [1]. He suggested that cars running behind the car performing this action avoid braking if the car forecasts right the timing of approaching a jam. This driving method has a good characteristic that a jam can be removed by just a single car. However, his driving method lacks theoretical supports. Later, a theoretical framework of a car's driving to absorb a jam is constructed with a kinematic-like traffic model and named "jam-absorption driving" [8]. The car performing jam-absorption driving (called "the absorbing car") has a chain of two actions, slow-in and fast-out. Slow-in is to avoid being involved in a jam and remove it by decelerating and enlarging own headway. Fast-out is performed after slow-in, and it is to follow the car in front without any extra time headway by accelerating quickly. The theory indicates the condition to remove a jam and without causing so-called "secondary jam", i.e., the condition on which the perturbation caused from jam-absorption driving does not grow to another jam.

Beyond the theoretical study [8], we aim to verify the jam absorption driving with real cars. To this aim, we conducted an experiment of jam-absorption driving in a closed circuit with human-driving cars. We simplify the experimental scenario such that the absorbing car initially obtains large gaps at the beginning of the experiment.

2 Settings

Five cars run in a column on a circuit. We assume that a jam already occurred far downstream of the five cars and it is coming to them. In the experiment, the absorbing car is in the column and keeps the extra amount of gaps to remove the jam. Under this situation, we introduce the scenario of our experiment. First, as the initial state, all the five cars remain stationary and the cars except for the absorbing car have the same headway h_1. It should be noted that the headway of a car is defined as the sum of the car's inter-vehicular distance and the cars length. The absorbing car is the third car and it has the headway h_a. They start simultaneously and run in a platoon with velocity v_F. Each car keeps its headway at the initial state. After a stable platoon is formed, the first car causes a perturbation by a sequence of actions:

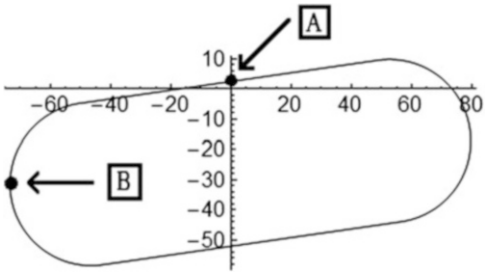

Fig. 1 The circuit for the experiment. The horizontal and vertical axes denote the longitude and latitude, respectively. The unit of length is meter. The *black loop* represents the circuit and is composed of the two chords of the hemispheres and the two *straight lines*. All cars move to the counterclockwise direction. They run several laps and try to make a platoon. After making it, the first car decelerates at the "A" point and accelerates again at the "B" point

decelerating from v_F to v_J, keeping v_J for a period T, and accelerating to v_F. These actions represent that the first car enters the jam, stays inside it for T and goes out of it. The absorbing car tries to remove this perturbation by keeping v_F and consuming its gap.

The circuit is composed of two straight lines and two circular curves as shown in Fig. 1. For the aspect of safety, cars cannot run over 40 km/h. All the five cars traveled in counterclockwise direction. The leader car was ordered to run at $v_F = 35$ km/h. We set the two points A and B on the circuit where the first car took actions. At the point A, it was ordered to decelerate to $v_J = 20$ km/h and keep this velocity. At the point B, it was ordered to accelerate to $v_F = 35$ km/h. We set the period for which the first car keeps the velocity v_J as $T = 15$ s. We put marks to visualize the points A and B thus every driver recognized where the first car decelerated and accelerated. These marks are necessary for the drivers' safety. We chose $h_1 = 13$ m.

3 Results

We pick a trial where jam absorption succeeded. In this trial, h_a is set to 50 m. We show the time-space diagram of all cars in the trial in Fig. 2. The second car's line are clearly bended, that is, the second car brakes on the way of the circuit because of the perturbation caused by the first car. On the other hand, the lines of the third, forth and fifth car are mostly straight, that is, these cars can keep the velocity around v_F. It is because the third car has a longer headway h_a at the beginning of the trial and does not catch up with the second car.

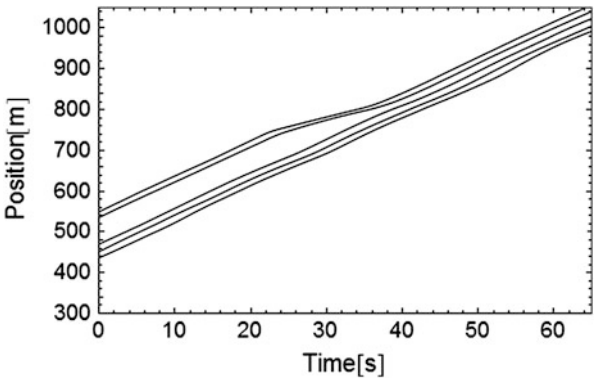

Fig. 2 A time-space diagram with $h_a = 50$ m. The trajectory of each car is depicted as a line

Conclusion

We have conducted an experiment to demonstrate "jam-absorption driving". We succeeded in observing a situation where a jam generated by a preceding car is removed by the absorbing car.

As our future work, it is necessary to perform social experiments of jam-absorption driving in real highway traffic. Our experiment was conducted with low velocities around 35 km/h due to the limitation of the length of the straight track. Hence, we are going to investigate jam-absorption driving with higher velocities such as 100 km/h, which is popular speed limits in Japanese highways.

References

1. W.J. Beaty, Traffic waves: sometimes one driver can vastly improve traffic (1998). http://trafficwaves.org/
2. M. Cassidy, J. Rudjanakanoknad, Increasing the capacity of an isolated merge by metering its on-ramp. Transp. Res. B **39**, 896–913 (2005)
3. D. Chowdhury, L. Santen, A. Schadschneider, Statistical physics of vehicular traffic and some related systems. Phys. Rep. **329**, 199–329 (2000)
4. C.F. Daganzo, *Fundamentals of Transportation and Traffic Operations* (Elsevier Science, New York, 1997)
5. A. Hegyi, B.D. Schutter, J. Hellendoorn, Optimal coordination of variable speed limits to suppress shock waves. IEEE Trans. Intell. Transp. Syst. **6**, 102–112 (2005)
6. D. Helbing, Traffic and related self-driven many-particle systems. Rev. Mod. Phys. **73**, 1067–1141 (2001)
7. B.S. Kerner, *Introduction to Modern Traffic Flow Theory and Control* (Springer, Berlin, 2009)
8. R. Nishi, A. Tomoeda, K. Shimura, K. Nishinari, Theory of jam-absorption driving. Transp. Res. B **50**, 116–129 (2013)
9. M. Papageorgiou, A. Kotsialos, Freeway ramp metering: an overview. IEEE Trans. Intell. Transp. Syst. **3**, 271–281 (2002)

10. Road Bureau, Ministry of Land, Infrastructure, Transport and Tourism, Japan, http://www.mlit.go.jp/road/ir/ir-perform/h18/07.pdf. Accessed 27 Jan 2014, Japanese
11. A. Schadschneider, D. Chowdhury, K. Nishinari, *Stochastic Transport in Complex Systems: From Molecules to Vehicles* (Elsevier Science, Amsterdam, 2010)
12. S. Smulders, Control of freeway traffic flow by variable speed signs. Transp. Res. B **24**, 111–132 (1990)
13. The Committee on Traffic Flow Theory and Characteristics (AHB45), Traffic flow theory monograph a state-of-the-art report revised (2001), http://www.tft.pdx.edu/docs.htm
14. A. Vahidi, A. Eskandarian, Research advances in intelligent collision avoidance and adaptive cruise control. IEEE Trans. Intell. Transp. Syst. **4**, 143–153 (2003)
15. E. van den Hoogen, S. Smulders, Control by variable speed signs: results of the dutch experiment, in *7th International Conference on Road Traffic Monitoring and Control*, London (IEEE Conference Publication, London, 1994), pp. 145–149

Generic First-Order Car-Following Models with Stop-and-Go Waves and Exclusion

Antoine Tordeux, Sylvain Lassarre, Michel Roussignol, and Vincent Aguiléra

Abstract A new Optimal Velocity (OV) car-following model is defined and explored. The model is solely based on an optimal speed function and a reaction time, and, oppositely to classical OV models, is intrinsically collision-free. If the model has uniform solutions, kink-antikink and soliton stop-and-go patterns can be described with a linear bounded optimal velocity function when the reaction time is high enough.

1 Introduction

Observations of congested road traffic flows present stable propagation of stop-and-go waves (see e.g. [1, 2]). Such waves are observed on highways or during experiments [3], where the disturbance due to the infrastructure can not explain their presence. The phenomenon is collective and complex.

Many approaches are developed to understand non linear traffic waves, instability, hysteresis, or more generally non uniform solutions [4,5]. Most of the studies are done with microscopic models. One of the best investigated model is the Optimal Velocity (OV). The first OV models are car-following microscopic ones [6,7]. They are solely based on the optimal (or equilibrium) speed function, and the reaction (or relaxation) time parameter. The OV models are simple, with few parameters that could be estimated from traffic data. Despite of their simplicity, the dynamics obtained are rich and allow to describe many empirical features, and notably stop-and-go waves [8,9].

A. Tordeux (✉) • V. Aguiléra
Paris-Est University LVMT, 19 rue Alfred Nobel, 77455 Marne-la-Vallée, France
e-mail: antoine.tordeux@enpc.fr; vincent.aguilera@enpc.fr

S. Lassarre
IFSTTAR GRETTIA, 19 rue Alfred Nobel, 77455 Marne-la-Vallée, France
e-mail: sylvain.lassarre@ifsttar.fr

M. Roussignol
Paris-Est University LAMA, 5 bvd Descartes, 77454 Marne-la-Vallée, France
e-mail: michel.roussignol@univ-paris-est.fr

M. Chraibi et al. (eds.), *Traffic and Granular Flow '13*,
DOI 10.1007/978-3-319-10629-8_54

The OV models have stationary uniform solutions that can be unstable. Yet, classical OV models locally oscillate, leading to collisions or negative speed when unstable. Only particular sigmoid optimal speed functions give collision-free solutions [7, 10]. This prevents to well describe the space phase of the OV models. These deficiencies are clearly established and debated in the literature [11–13]. Extensions of the OV models are able to solve the problems (see for instance [14–16]), but with the drawback of increasing the numbers of model parameters. At present, there exist no consensus for one or an other extended model and it is unclear whether a higher modeling complexity is necessary or not.

In this paper, we explore a new generic OV model, intrinsically collision-free. The model is from the first order with two predecessors in interaction.

2 Optimal Velocity Models

2.1 Classical Models

The OV models are set by the optimal (or equilibrium) speed function V depending on the spacing (the difference of the central positions of a considered vehicle and the predecessor). The function describes how drivers regulate their speed. It is helpful to describe the dynamic of traffic systems but it is not derived from fundamental physical laws. On one side it contains strong physical constraints like the volume exclusion or finite desired speed. On the other side, it contains factors determined by the perception and behavior of drivers. Classical modelings assume V positive, differentiable and increasing with finite limit value (the desired speed). The function is nil when the spacing is smaller than the length of the vehicle. A simple speed function is the bounded linear

$$V(d) = \min\left\{v_0, \max\left\{0, (d-\ell)/T\right\}\right\} \tag{1}$$

with v_0 the desired speed (in free situation), ℓ the vehicle length (with potentially a marge), and T the time gap (in following situation).

The most basic OV model [17] is from the first order:

$$\dot{x}_n(t) = V(\Delta x_n(t)), \tag{2}$$

where $x_n(t)$ is the position of the considered vehicle and $\Delta x_n(t) = x_{n+1}(t) - x_n(t)$ is the spacing of the vehicle n at time t ($n+1$ is the predecessor).

More realistic dynamics are obtained by introducing a delay time $\tau > 0$ in the model, corresponding to the observed driver and vehicle reaction time [6]

$$\dot{x}_n(t+\tau) = V(\Delta x_n(t)). \tag{3}$$

A Taylor expansion to the delayed quantity in (3) leads to the second-order OV model [7], where the reaction time τ is considered as a relaxation time

$$\ddot{x}_n(t) = \frac{1}{\tau}\big[V(\Delta x_n(t)) - \dot{x}_n(t)\big]. \tag{4}$$

The OV model (2) is solely based on the optimal speed function V, while the models (3) and (4) also incorporate the parameter τ. More complex OV models exist, with more parameters. See for instance the Generalized Force [14] or Full Velocity Difference [16] models incorporating a speed difference term and two relaxation times, or even the multi-anticipative OV model [15], with $K \geq 1$ predecessors in interaction.

For a given mean spacing $d > 0$, all the OV models have uniform solutions

$$\Delta x_n^U(t) = d, \quad x_n^U(t) = x_n^U(0) + tV(d), \qquad \forall n,\ \forall t \geq 0. \tag{5}$$

The uniform solution can be stable, when perturbations vanish, or unstable. The analysis of the stability allows to determine these properties according to the values of the parameters.

The solutions are collision-free if initially $x_n(0) + \ell \leq x_{n+1}(0)$ for all n, with $\ell \geq 0$ the length of the vehicles, and if

$$\forall n, \quad x_n(t) + \ell \leq x_{n+1}(t), \qquad \forall t \geq 0. \tag{6}$$

Using the terminology of discrete models, the property describes the volume exclusion of vehicles. The uniform solutions are trivially collision-free. If non uniform solutions exist, they have to satisfy the exclusion property (6).

Both local and global stability conditions of the OV models are well-know (see for instance [18]). We remind them here. The basic first order model (2) is locally and globally linearly stable and non-oscillating if $V'(d) > 0$. This assumption is natural for a model. With the delayed model (3), the local linear stability holds if $0 < \tau V'(d) < \pi/2$, while it is non-oscillating if $0 < \tau V'(d) < 1/e$ (see for instance [19]). The second order model (4) is locally linearly stable if $V'(d), \tau > 0$, and non-oscillating if $0 < \tau V'(d) < 1/4$. The models (3) and (4) both have the condition for global linear stability $0 < \tau V'(d) < 1/2$ (see for instance [7]).

For high enough reaction time τ, the models (3) and (4) can produce unstable uniform solutions. Yet, they are only collision-free (i.e. locally non-oscillating) under more restrictive conditions (we have $\tau V' < 1/4 < 1/e < 1/2$). This means that instability of uniform solutions for models with two parameter (τ and V') can not be combined with collision-free property. This can be argued using the general second order model with two parameters $\ddot{x}_n(t) = F\big(x_{n+1}(t) - x_n(t), \dot{x}_n(t)\big)$. If we denote $F : (d, v) \mapsto F(d, v)$ and the parameters $\alpha = \partial F/\partial d > 0$ and $\beta = \partial F/\partial v$, the condition $\beta^2 - 4\alpha < 0$ for which the model

is locally non-oscillating is incompatible with the condition for global instability $\beta^2 - 2\alpha > 0$.

Many studies report the presence of collisions with two parameters OV model [7, 10–12, 20]. Extended OV models can be simultaneously locally non-oscillating and globally unstable [14, 16]. Yet, this is done by adding parameters to the dynamics, that may be unnecessary for the modeling of stop-and-go waves.

2.2 *Definition of a New OV Model*

The presence of collision is hard to control with OV model by delayed differential equation, or second order ones. This is due to their tendency to locally oscillate. In contrast, it is easy to control the exclusion with ordinary first order models. With these models, the exclusion property (6) holds if the optimal speed function is positive and nil when the distance spacing is nil. However, first order model always have stable uniform solutions if they do not consider a reaction time. Therefore, our purpose is to develop an ordinary first-order OV model including a reaction time parameter.

The second order OV model (4) can be obtained by applying a Taylor expansion around t to the left part of the delayed first order model (3). We propose here to apply a Taylor expansion to the right part of (3). This leads to an implicit equation on the speed, sometimes related as the generalized optimal velocity model $\dot{x}_n(t) = V\big(\Delta x_n(t) - \tau\big[\dot{x}_{n+1}(t) - \dot{x}_n(t)\big]\big)$.

To approximate the solution of the implicit equation, the speeds in the right part are substituted by the optimal speed function of the spacing:

$$\dot{x}_n(t) = V\big(\Delta x_n(t) - \tau[V(\Delta x_{n+1}(t)) - V(\Delta x_n(t))]\big). \tag{7}$$

This model is from first-order. It is based on an optimal speed function and incorporates a parameter for the reaction time. It takes two predecessors in interaction. For a given spacing d, the speed of a vehicle varies between the borders $b_-(d) = V(d + \tau V(d) - \tau \inf_{d_1} V(d_1))$ and $b_+(d) = V(d + \tau V(d) - \tau \sup_{d_1} V(d_1))$ according to the spacing of the predecessor. With the bounded linear speed function (1), theses borders are

$$\begin{aligned} b_-(d) &= \min\big\{v_0, \max\big\{0, (1+\tau/T)(d-\ell)/T - v_0\tau/T\big\}\big\} \\ b_+(d) &= \min\big\{v_0, \max\big\{0, (1+\tau/T)(d-\ell)/T\big\}\big\} \end{aligned} \tag{8}$$

The generic first order model (7) is trivially collision-free, if V is such that

$$V(d) \geq 0 \quad \forall d, \qquad V(d) = 0, \quad \forall d \leq \ell, \tag{9}$$

since in this case the speed of a vehicle is nil when the spacing is nil. The linear bounded function (1) satisfies this property. The stability analysis of the model (7) (not presented here) shows that the uniform solutions (5) are linearly stable under the same conditions than the classical models (3) and (4), i.e. if

$$0 < \tau V'(d) < 1/2. \tag{10}$$

The condition is $0 < 2\tau < T$ with the bounded linear function (1). Therefore the model is able to have non-uniform collision-free solution with no use of additional parameter. The non uniform solution obtain with V bounded linear are described in the next section by simulation.

3 Simulation Results

3.1 Settings

The solutions of the new model (7) are simulated on a ring of length L. We use the parallel explicit Euler scheme

$$x_n(t+\delta t) = x_n(t) + \delta t\, V\big(\Delta x_n(t) - \tau[V(\Delta x_{n+1}(t)) - V(\Delta x_n(t))]\big) \tag{11}$$

with $\delta t = 10^{-2}\,s$ the time step. The optimal speed function is the bounded linear (1) with $\ell = 5\,\text{m}$, $v_0 = 20\,\text{m/s}$. $T = 1.5\,\text{s}$. We set $\tau = 1\,\text{s}$ for that the stability condition (10) does not hold. The length of the ring is $L = 205\,\text{m}$. We successively simulated the trajectories of $N = 9, 10, 12$ vehicles from random initial condition such that $\min_n \Delta x_n(0) \geq \ell$.

3.2 Results

The trajectories obtained are drawn in the top of Figs. 1–3 during the first 120 s with respectively $N = 9, 10, 12$ vehicles. The sequence of speed and spacing, and the speed function of the spacing, with the optimal speed function (1) and the borders (8) in dotted line, are plotted for $t \in [60, 120\,\text{s}]$ at the bottom of the figures.

For all the experiments, a unique stop-and-go wave emerges and propagates. This phenomenon is realistic. It has been observed in real experiment with 22 vehicles on a ring of length 250 m [3]. The speed and spacing converge to a limit-cycle into the borders (8). The waves are solitons when $N = 9$ and $N = 12$. For $N = 9$ the speed of a vehicle varies from $v > 0$ to v_0, with a plateau in v_0. For $N = 12$ the speed varies from 0 to $v < v_0$, with a plateau in 0. The speed of propagation

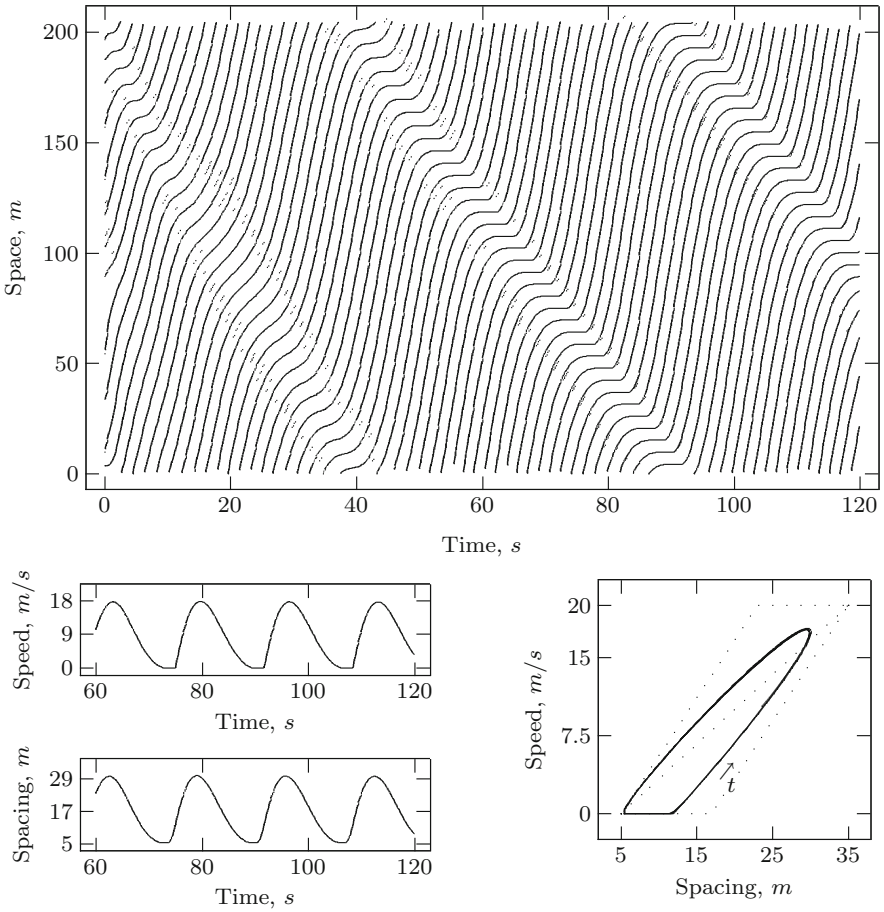

Fig. 1 *Top*, trajectories of 12 vehicles from random initial configuration. *Bottom* the sequence of speed and spacing and the speed function of the spacing of a vehicle

of the waves are approximately -4.27 and -5.54 m/s for respectively $N = 9$ and $N = 12$. The solution is a kink-antikink for $N = 10$, with speed varying from 0 to v_0, and plateau for both values. The speed of the waves is -4.77 m/s. The characteristics of the wave seem to depend on the system size. On large systems, the waves are generally solely kink-antikink ones, with constant characteristic speed.

Here a unique wave is observed. Further experiments not shown here show that several waves can propagate if the system is large enough. This suggests that the waves produced by the model have characteristic length.

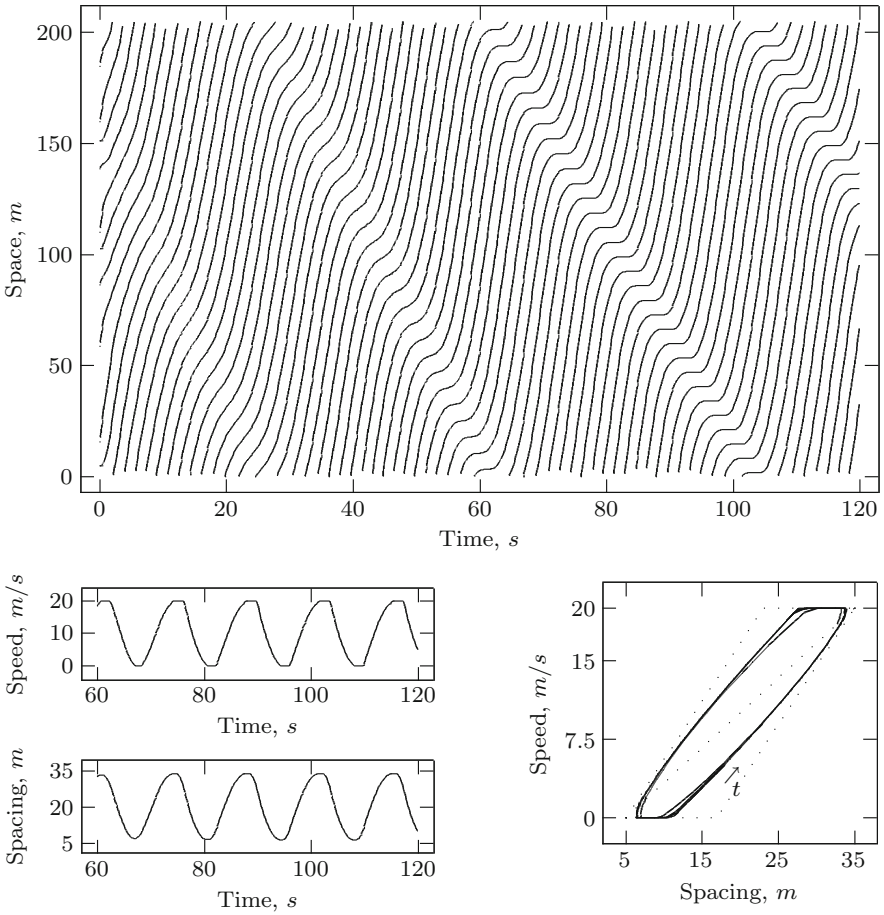

Fig. 2 *Top*, trajectories of 10 vehicles from random initial configuration. *Bottom* the sequence of speed and spacing and the speed function of the spacing of a vehicle

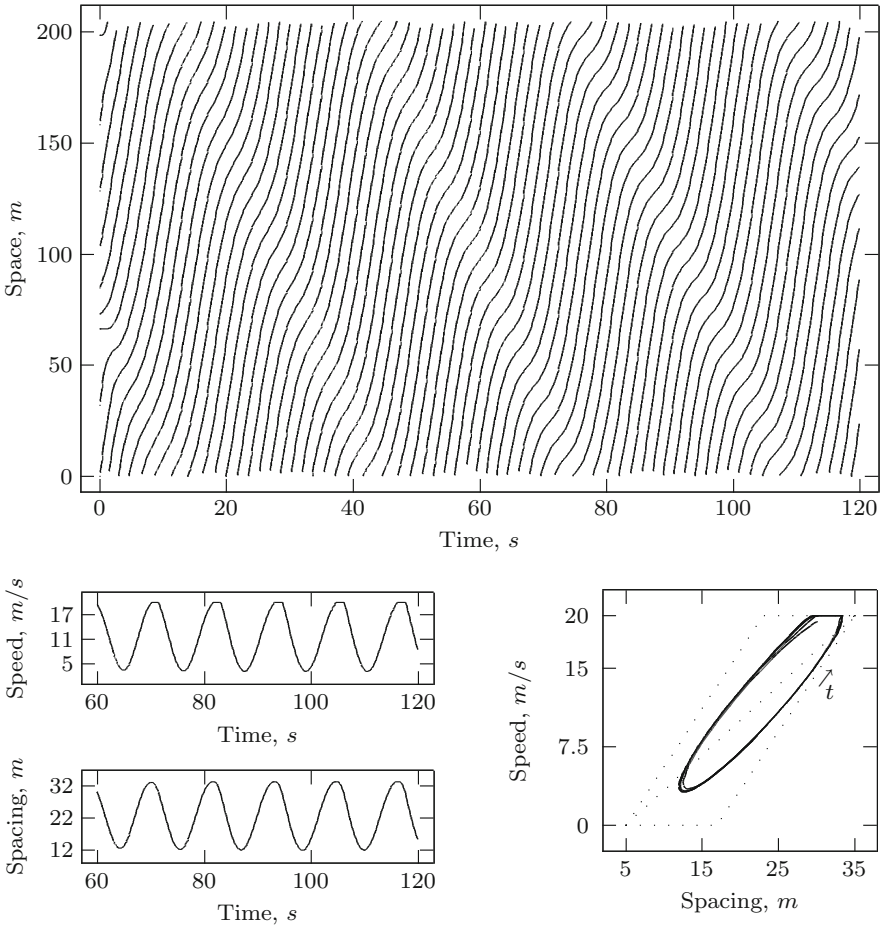

Fig. 3 *Top*, trajectories of 9 vehicles from random initial configuration. *Bottom* the sequence of speed and spacing and the speed function of the spacing of a vehicle

Conclusion

A new continuous OV car-following model is proposed for traffic applications. The model is a generic first order one, based on the optimal speed function and the reaction time parameter. Oppositely to classical OV models, it does not produce local oscillating dynamics and is intrinsically collision-free. The model has the same stability condition of the uniform solution as classical OV models. It is unstable for high enough reaction time.

(continued)

The model is performed with bounded linear optimal speed functions with three parameters. When unstable, the solutions are realistic collision-free stop-and-go, with kink-antikink and soliton implying several vehicles. Further results not shown here show that waves and vehicle's speed modal value can be controled using non-linear optimal speed function.

The modeling framework proposed gives a way to basically describe on continuum stop-and-go waves. It could be useful for the microscopic simulation of traffic or pedestrian flows, as well as for theoretical investigations.

References

1. B.S. Kerner, H. Rehborn, Phys. Rev. E. **53**(2), 1297 (1996)
2. G. Orosz, R.E. Wilson, G. Stepan, Proc. R. Soc. A **368**(1957), 4455 (2010)
3. Y. Sugiyama, M. Fukui, M. Kikushi, K. Hasebe, A. Nakayama, K. Nishinari, S. Tadaki, New J. Phys. **10**(3), 033001 (2008)
4. T. Li, Physica D **207**(1–2), 41 (2005)
5. R.E. Wilson, J.A. Ward, Transp. Plan. Tech. **34**(1), 3 (2011)
6. G.F. Newell, Oper. Res. **9**(2), 209 (1961)
7. M. Bando, K. Hasebe, A. Nakayama, A. Shibata, Y. Sugiyama, Phys. Rev. E **51**(2), 1035 (1995)
8. M. Schönhof, D. Helbing, Transp. Sci. **41**(2), 135 (2007)
9. M. Treiber, A. Kesting, D. Helbing, Transp. Res. **B44**(8–9), 983 (2010)
10. I. Gasser, T. Seidel, G. Sirito, B. Werner, Bull. Inst. Math. **2**(2), 587 (2007)
11. L.C. Davis, Phys. A **319**, 557 (2003)
12. R.E. Wilson, P. Berg, S. Hooper, G. Lunt, Eur. J. Phys. B **39**(3), 397 (2004)
13. D. Helbing, A.F. Johansson, Eur. Phys. J. B **69**(4), 549 (2009)
14. D. Helbing, B. Tilch, Phys. Rev. E **58**(1), 133 (1998)
15. H. Lenz, C.K. Wagner, R. Sollacher, Eur. Phys. J. B **7**(2), 331 (1999)
16. R. Jiang, Q. Wu, Z. Zhu, Phys. Rev. E **64**(1), 017101 (2001)
17. L.A. Pipes, J. Appl. Phys. **24**(3), 274 (1953)
18. M. Treiber, A. Kesting, *Traffic Flow Dynamics* (Springer, Dordrecht, 2006)
19. X. Zhang, D.F. Jarrett, Transp. Res. B **31**(6), 441 (1997)
20. G. Orosz, R. Wilson, R. Szalai, G. Stépán, Phys. Rev. E **80**(4), 046205 (2009)

Influence of Velocity Variance of a Single Particle on Cellular Automaton Models

Daichi Yanagisawa, Takahiro Ezaki, Akiyasu Tomoeda, and Katsuhiro Nishinari

Abstract We have developed a new calibration method to analyze the effect of velocity variance of a single particle (VVSP) on flow in cellular automaton (CA) models. We have verified that the flow in the totally asymmetric simple exclusion process (TASEP) decreases when VVSP increases even if the mean velocity of each particle is same. The effect of VVSP on other CA models, such as a stochastic Fukui-Ishibashi (SFI) model and a simple evacuation (SEV) model, are also investigated. When VVSP increases, the flow decreases in the one dimensional models (TASEP and SFI model), whereas, it increases in SEV model. Furthermore, it is investigated how the effect of VVSP is strengthened or weakened by the characteristic parameter in SFI model.

D. Yanagisawa (✉)
College of Science, Ibaraki University, 2-1-1, Bunkyo, Mito, Ibaraki, 310-8512, Japan
e-mail: tDaichi@mail.ecc.u-tokyo.ac.jp

T. Ezaki
Department of Aeronautics and Astronautics, School of Engineering, The University of Tokyo, 7-3-1, Hongo, Bunkyo-ku, Tokyo, 113-8656, Japan

Japan Society for the Promotion of Science, 5-3-1, Ichibancho, Kojimachi, Chiyoda-ku, Tokyo 102-0083, Japan
e-mail: ezaki@jamology.rcast.u-tokyo.ac.jp

A. Tomoeda
Meiji Institute for Advanced Study of Mathematical Sciences, Meiji University, 4-21-1, Nakano, Nakano-ku, Tokyo, 164-8525, Japan

CREST, Japan Science and Technology Agency, 4-21-1, Nakano, Nakano-ku, Tokyo, 164-8525, Japan
e-mail: atom@isc.meiji.ac.jp

K. Nishinari
Research Center for Advanced Science and Technology, The University of Tokyo, 4-6-1, Komaba, Meguro-ku, Tokyo, 153-8904, Japan

M. Chraibi et al. (eds.), *Traffic and Granular Flow '13*,
DOI 10.1007/978-3-319-10629-8_55

1 Introduction

Cellular automaton (CA) [1] is widely applied to model traffic flow, pedestrian dynamics, and other self-driven particles [2–5].

The research on traffic flow by using CA has been started from the elementary CA Rule 184 [1]. In spite of the very simple updating rule, it has reproduced the fundamental characteristic of traffic flow. Namely, a cluster of vehicles (traffic jam) moves backward. By extending this model, one of the most famous traffic CA model, the Nagel-Schreckenberg (NaSch) model [6], which implements acceleration and random braking rule, has been developed. It has succeeded to reproduce a fundamental diagram in real traffic and become a basic CA model for traffic flow. Following NaSch model, Fukui-Ishibashi (FI) model [7] has been considered. It is a deterministic model and implements the maximum velocity of vehicles as a controllable parameter. The critical density is clearly expressed by simple mathematical formulation. Effects of drivers' anticipation and vehicles' inertia are also studied in Quick-Start model [8] and Slow-to-Start model [9, 10]. Furthermore, an integrated model which includes the parameters of maximum velocity, anticipation, and inertia is also developed [11].

Another major application of CA is pedestrian-dynamics models. The lattice-gas model [12] and the floor-field model [13] are two famous CA models for pedestrian dynamics. They enable us to simulate lane-formation phenomenon in pedestrian counter flow in a corridor. Evacuation is one of the most important topic in pedestrian dynamics, so that it is eagerly studied by both theoretical analysis [14] and computer simulation [15] of CA models. Method for shorten the evacuation time is also considered. In Ref. [16], it is investigated that an obstacle which is put appropriate position in front of an narrow exit shorten the total evacuation time from a room.

As shown in the previous paragraphs, many CA models have been developed to study the dynamics of self-driven particles such as vehicles and pedestrians. One of the many reasons of this success is introduction of stochastic parameters. Movement of self-driven particles is not always exactly constant. Even if one particle moves straightly in vacant space without any interaction with others, its velocity fluctuates. Hopping probability in stochastic CA models well represents this phenomenon. However, the effect of velocity variance of a single particle (VVSP) has been seldom discussed when the models are developed. This is because the hopping probability does not only control the variance but also influences the mean velocity of a particle. By contrast, collective phenomena of pedestrian dynamics related with VVSP are studied in experimental researches. References [17] indicates that rhythm removes the heterogeneity of pedestrians' movement, synchronizes it (decrease VVSP), and contributes to the homogeneous spatial distribution. Moreover, Ref. [18] has reported that movement of pedestrians synchronizes especially in the high density regime. Therefore, theoretical research on VVSP is important for analyzing these phenomena.

In order to investigate the effect of VVSP, we have newly developed a simple calibration method that enables us to control VVSP without changing the mean velocity. By using this method, we have succeeded in analyzing the effect of VVSP on CA models such as the totally asymmetric simple exclusion process (TASEP), a stochastic FI (SFI) model, and a simple evacuation (SEV) model.

2 Calibration Method

In this section, we would like to propose a new calibration method for controlling VVSP independent from mean velocity in CA models. We consider a very simple stochastic CA model where one particle is in one-dimensional space consisted of discrete cells. Time is also discrete in this CA model. If the particle moves one cell with the probability p in one time step, its mean and variance of traveling time for one cell are

$$\begin{aligned} &\text{Mean:} \quad \frac{1}{p} \quad [\text{step}], \\ &\text{Variance:} \quad \frac{1-p}{p^2} \quad [\text{step}], \end{aligned} \tag{1}$$

respectively. As we see from the equations above, both the mean and variance of traveling time dependent on the hopping probability p. Thus, we develop a method for determining the mean and variance independently in the following. Note that a calibration method of the particle density in CA models is developed in [19].

When we apply CA models to the real situation, we have to determine the size of a cell and the length of one time step since both space and time are discrete. Let us denote them as Δl [m/cell] and Δt [sec/step]. If a particle moves one cell with the probability p in one time step, its mean velocity in the real situation is calculated as

$$v(p, \Delta l, \Delta t) = p\frac{\Delta l}{\Delta t}[\text{m/sec}]. \tag{2}$$

In the equation above, the mean velocity v is a function of the parameters p, Δl and Δt. If we transform this equation as follows:

$$\Delta t(v, p, \Delta l) = p\frac{\Delta l}{v} \ [\text{sec/step}], \tag{3}$$

then the length of one time step Δt becomes a function of v, p and Δl. Since the mean velocity is determined by v in this equation. The parameter p no longer affects the mean velocity, and can be utilize for controlling the variance. Thus, when we substitute this equation to other equations which represent a physical quantity, we are able to determine the mean and variance of the velocity independently. Let us

examine the validity of this method by applying to the traveling time for one cell calculated in the beginning of this section. We multiply Eq. (1) by Δt and $(\Delta t)^2$ and substitute Eq. (3), then the mean velocity and VVSP are describe as

$$\begin{aligned} \text{Mean:} \quad & \frac{\Delta t}{p} = \frac{\Delta l}{v} \quad [\text{sec}], \\ \text{Variance:} \quad & \frac{(1-p)(\Delta t)^2}{p} = \frac{(1-p)(\Delta l)^2}{v^2} \quad [\text{sec}^2]. \end{aligned} \tag{4}$$

The parameter p disappears from the equation of the mean, so that we are able to change the mean velocity and VVSP independently. Since p is a probability, its domain is [0,1], thus the variance achieves the maximum $(\Delta l/v)^2$ and the minimum 0 at $p = 0$ and $p = 1$, respectively.

3 Influence of Velocity Variance of a Single Particle on CA Models

In this section, we see how VVSP affects on flow in CA models such as TASEP, SFI model, and SEV model.

3.1 Totally Asymmetric Simple Exclusion Process (TASEP)

First, we apply our calibration method to TASEP [20, 21]. It is one of the basic one-dimensional stochastic CA model. A schematic view of the TASEP with parallel-update rule and periodic boundary condition is depicted in Fig. 1. Particles represented by black circles proceed one cell to the right with the probability p in one time step, only if its right neighboring cell is empty. Since the effect of excluded-volume effect is implemented automatically in TASEP, it can be utilized for considering dynamics of self-driven particles. The expression of flow in TASEP is described as

$$Q(\rho, p) = \frac{1 - \sqrt{1 - 4p\rho(1-\rho)}}{2} \ [\text{step}^{-1}], \tag{5}$$

Fig. 1 Schematic view of TASEP and SFI model ($V_{max} = 3$) with parallel-update rule and periodic-boundary condition. Particles move to their target cells with the probability p in one time step. Solid and dashed arrows represent movements of the particles in TASEP and SFI model ($V_{max} = 3$), respectively

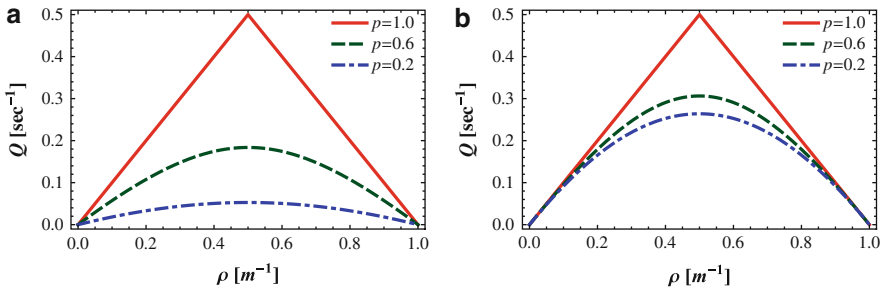

Fig. 2 Flow-density diagram of TASEP. (**a**) (TASEP-a) $Q(\rho, p, \Delta t = 1)$ Before substituting Eq. (3). (**b**) (TASEP-b) $Q(\rho, v = 1, p, \Delta l = 1)$ After substituting Eq. (3)

where ρ is the number density of particles. By dividing the equation above by Δt and substituting (3), the expression of the flow is transformed as

$$\begin{aligned} \text{(TASEP-a)}\ Q(\rho, p, \Delta t) &= \frac{1 - \sqrt{1 - 4p\rho(1-\rho)}}{2\Delta t} \quad [\text{sec}^{-1}], \\ \text{(TASEP-b)}\ Q(\rho, v, p, \Delta l) &= \frac{v}{\Delta l} \frac{1 - \sqrt{1 - 4p\rho(1-\rho)}}{2p} \quad [\text{sec}^{-1}]. \end{aligned} \tag{6}$$

By changing the value of p in Eq. (6) (TASEP-b), we are able to analyze the effect of variance on flow in TASEP. Figure 2a, b show flow-density diagrams (fundamental diagrams) depicted by using Eq. (6) (TASEP-a) with $\Delta t = 1$ and (TASEP-b) with $v = 1$ and $\Delta l = 1$, respectively. The result of Fig. 2a is well known; the flow achieves the maximum at $\rho = 0.5$ and increases as p increases. Since p represents the mean velocity of a single particle, it is obvious that large p attains large flow. Figure 2b is similar to Fig. 2a; however, this result is new and surprising because the values of v and Δl are constant, i.e., mean velocity is same in all the three curves ($p = 0.2, 0.6, 1.0$). Small p implies large VVSP, so that the flow becomes large when VVSP is small even if the mean velocity of single particle is same.

3.2 Stochastic Fukui-Ishibashi (SFI) Model

Next, we apply our calibration method to SFI model [22]. In SFI model, particles can maximally move $V_{max} \in \mathbb{N}$ cells, if there are enough empty cells. A hopping probability p is introduced, so that the particles maximally move V_{max} cells with the probability p or remain their cell with probability $1 - p$. The model is reduced to TASEP in the case $V_{max} = 1$.

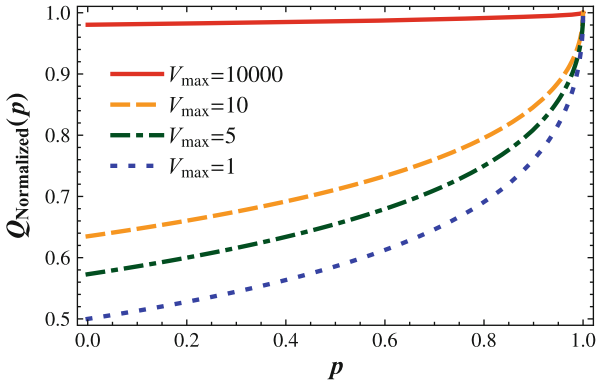

Fig. 3 Normalized maximum flow $Q_{\mathrm{Normalized}}$ against hopping probability p for various $V_{\max}$

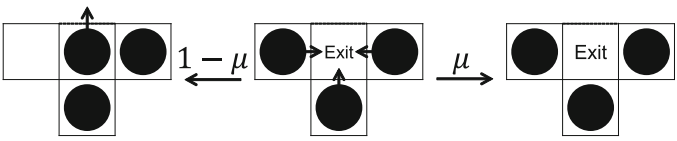

Fig. 4 Schematic view of SEV model in the case $n = 3$

Figure 3 shows the normalized maximum flow with $V_{\max} \geq 1$ against the hopping probability p. Normalized maximum flow is defined as

$$Q_{\mathrm{Normalized}}(p) = \frac{Q_{\max}(p)}{Q_{\max}(p=1)}, \tag{7}$$

$$Q_{\max}(p) = Q(\rho_{\mathrm{cr}}(p, V_{\max}), p), \tag{8}$$

where ρ_{cr} achieves maximum flow for given p and V_{max}. When our method is applied to the model, increase of p corresponds to decrease of VVSP and vice versa. Therefore, we see that the normalized maximum flow increases when VVSP decreases in Fig. 3. It is also observed that when $V_{\max}$ is small, the normalized maximum flow greatly changes against the change of p, whereas, when $V_{\max}$ is large, the change is small. This result implies that $V_{\max}$ weakens the effect of VVSP on the flow.

3.3 Simple Evacuation (SEV) Model

Finally, we would like to apply our calibration method to SEV model as shown in Fig. 4. The model focuses on an exit cell and its neighboring cells, and is updated in parallel. The number of the neighboring cells is given as n. Since we consider

congested situation, we assume that particles enter the n neighboring cells with the probability 1 if they are empty. The particles at the n neighboring cells move to the exit cell with the probability p. When more than one particle move to the exit cell at the same time, a conflict occur. We solve this phenomenon by using friction parameter $\mu \in [0, 1]$. One of them randomly succeeds to move to the exit cell with the probability $1-\mu$, while movements of all of them are denied with the probability μ. The particle at the exit cell get out from the room with the probability 1. Average outflow through the exit cell, i.e., the average number of particles go through the exit cell in one time step, is calculated as follows:

$$Q(n, p) = \left[\frac{1}{r(n)} + \frac{1}{p}\right]^{-1} \ [\text{step}^{-1}], \tag{9}$$

where

$$\begin{cases} b(k) = \binom{n}{k} p^k (1-p)^{n-k}, \\ r(n) = \sum_{k=1}^{n} \left[\{1-\mu\}\, b(k)\right]. \end{cases} \tag{10}$$

By dividing Eq. (9) by Δt and substituting Eq. (3), the expression of the average outflow is transformed as

$$\begin{aligned} \text{(SEV-a)}\ Q(n, p, \Delta t) &= \frac{1}{\Delta t}\left[\frac{1}{r(n)} + \frac{1}{p}\right]^{-1} \ [\text{sec}^{-1}], \\ \text{(SEV-b)}\ Q(n, v, p, \Delta t) &= \frac{v}{\Delta l}\left[1 + \frac{p}{r(n)}\right]^{-1} \ [\text{sec}^{-1}]. \end{aligned} \tag{11}$$

Plots of (SEV-a) with $\Delta t = 1$ and (SEV-b) with $v = 1$ and $\Delta l = 1$ as a function of the parameter n in the case $\mu = 0.2$ are shown in Fig. 5a, b, respectively. In

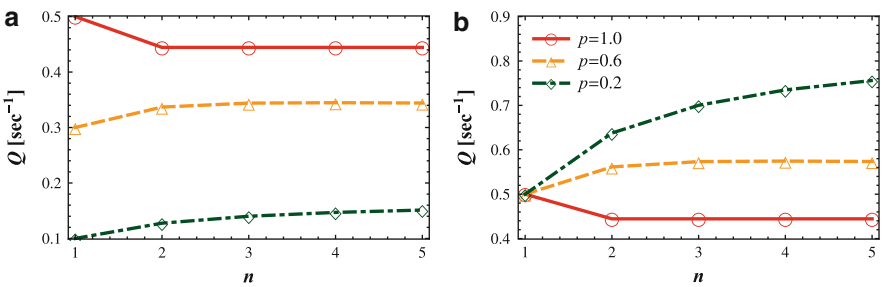

Fig. 5 Average outflow as a function of the number of neighboring cells n in the case $p = 0.2$. (**a**) (SEV-a) Before substituting Eq. (3). (**b**) (SEV-b) After substituting Eq. (3)

Fig. 5a, the outflow in the case $p = 1$ is the largest of the three. Since the parameter p represents the mean velocity before the calibration and the friction parameter is small ($\mu = 0.2$), large average flow achieved by large p. By contrast, in Fig. 5b, the outflow in the case $p = 1$ is the smallest of the three. The small p indicates the movement of pedestrians varies, thus, contrary to TASEP and SFI model cases; unsynchronized movement improves the outflow in SEV. Synchronized movement induces increase of conflicts, so that it is not adequate for situations where many particles gather at one place such as evacuation.

Conclusion

We have developed a new calibration method to analyze the effect of velocity variance of a single particle (VVSP) in cellular automaton (CA) models. The method is applied to the totally asymmetric simple exclusion process, a stochastic Fukui-Ishibashi (SFI) model, and a simple evacuation (SEV) model. It is elucidated that VVSP decreases flow in one-dimensional CA models, while it increase outflow in SEV model that includes merging dynamics. Furthermore, we have investigated that the parameter of the maximum velocity V_{max} in SFI model influences on the effect of VVSP on the flow. When V_{max} is small, flow greatly changes against the change of VVSP, whereas, when V_{max} is large, flow little changes against the change of VVSP.

We would like to analyze the effect of VVSP on other CA models such as quick-start and slow-to-start models in the near future.

Acknowledgements This work is financially supported by the Japan Society for the Promotion of Science.

References

1. S. Wolfram, *Cellular Automata and Complexity: Collected Papers* (Westview Press, Boulder, 1994)
2. D. Chowdhury, Phys. Rep. **329**(4–6), 199–329 (2000)
3. D. Helbing, Rev. Mod. Phys. **73**(4), 1067–1141 (2001)
4. T. Nagatani, Rep. Prog. Phys. **65**(9), 1331–1386 (2002)
5. A. Schadschneider et al., *Stochastic Transport in Complex Systems* (Elsevier, Amsterdam/Oxford, 2010)
6. K. Nagel et al., J. Phys. I **2**(12), 2221–2229 (1992)
7. M. Fukui et al., J. Phys. Soc. Jpn. **65**(6), 1868–1870 (1996)
8. H. Fuks et al., Int. J. Mod. Phys. C **9**(1), 1–12 (1998)
9. M. Takayasu et al., Fractals **1**(4), 860–866 (1993)
10. S.C. Benjamin et al., J. Phys. A. Math. Gen. **29**(12), 3119–3127 (1996)
11. S. Sakai et al., J. Phys. A. Math. Gen. **39**(50), 15327–15339 (2006)
12. M. Muramatsu et al., Phys. A Stat. Mech. . . . **267**, 487–498 (1999)
13. C. Burstedde et al., Phys. A Stat. Mech. Appl. **295**(3–4), 507–525 (2001)

14. D. Yanagisawa et al., Phys. Rev. E **76**(6), 061117 (2007)
15. A. Kirchner et al., Phys. A Stat. Mech. Appl. **324**(3–4), 689–697 (2003)
16. D. Yanagisawa et al., Phys. Rev. E **80**(3), 036110 (2009)
17. D. Yanagisawa et al., Phys. Rev. E **85**(1), 016111 (2012)
18. A. Jelić et al., Phys. Rev. E **86**(4), 046111 (2012)
19. M. Kanai, J. Phys. Soc. Jpn. **79**(7), 075002 (2010)
20. C.T. MacDonald et al., Biopolymers **6**(1), 1–5 (1968)
21. C.T. MacDonald et al., Biopolymers **7**(5), 707–725 (1969)
22. T. Ezaki et al., J. Phys. A Math. Theor. **45**(4), 045101 (2012)

Critical Density of Experimental Traffic Jam

Shin-ichi Tadaki, Macoto Kikuchi, Minoru Fukui, Akihiro Nakayama, Katsuhiro Nishinari, Akihiro Shibata, Yuki Sugiyama, Taturu Yosida, and Satoshi Yukawa

Abstract In a previous experiment, we have demonstrated that a traffic jam emerges without any bottleneck at a certain high density. In the present work, we performed an indoor circuit experiment in Nagoya Dome and estimated the critical density. The circuit is large (314 m in circumference) compared to the previous experiment. Positions of cars were observed in 0.16 m resolution. We performed 19 sessions by changing the number of cars from 10 to 40. We found that jammed flow was realized in high density while free flow in low density. We also found the indication of metastability at an intermediate density. The critical density is estimated by analyzing the density-flow relation. The critical density locates between 0.08 and 0.09 m^{-1}. It is consistent with that observed in real expressways.

S. Tadaki (✉)
Department of Information Science, Saga University, Saga 840-8502, Japan
e-mail: tadaki@cc.saga-u.ac.jp

M. Kikuchi
Cybermedia Center, Osaka University, Toyonaka 560-0043, Japan

M. Fukui • T. Yosida
Nakanihon Automotive College, Sakahogi 505-0077, Japan

A. Nakayama
Faculty of Science and Technology, Meijo University, Nagoya 468-850, Japan

K. Nishinari
Research Center for Advanced Science & Technology, The University of Tokyo, Meguro 153-8904, Japan

A. Shibata
Computing Research Center, High Energy Accelerator Research Organization (KEK) & Graduate University for Advanced Studies (Sokendai), Tsukuba 305-0801, Japan

Y. Sugiyama
Department of Complex Systems Science, Nagoya University, Nagoya 464-8601, Japan

S. Yukawa
Department of Earth and Space Science, Osaka University, Toyonaka 560-0043, Japan

M. Chraibi et al. (eds.), *Traffic and Granular Flow '13*,
DOI 10.1007/978-3-319-10629-8_56

1 Introduction

Traffic jams are familiar daily phenomena observed on expressways and city streets. Even from naive observations, traffic flow can be divided into two types: smooth flow, which occurs under light traffic and in which cars run almost at the allowed maximum speed; and jammed flow, which occurs under heavy traffic. In jammed flow, jam clusters, in which cars stop or move slowly, emerge and propagate upstream.

Fundamental diagrams describing the density-flow relation are widely used for analyzing traffic flow. Observations of real expressway traffic show that fundamental diagrams (e.g. Fig. 1) have two regions divided by a certain density value: free (smooth) flow with low density, and jammed flow with high density. In low density traffic, cars run at an almost constant speed, and therefore the flow increases in proportion to the density. The flow and the average speed for high density traffic, on the other hand, decrease with the density. The data points from high density traffic are broadly scattered; i.e. the speed and density fluctuate widely in jammed flow due to the existence of jam clusters.

Since the 1990s, many researchers have studied traffic flow from a physics point of view and various theoretical models for traffic flow have been proposed and studied extensively [1–6]. Those approaches have clarified that a homogeneous flow becomes unstable, leading to a traffic jam, if the density exceeds a critical value. Therefore the emergence of traffic jams is understood as a dynamical phase transition controlled by the density of cars.

In a previous study, we performed a traffic jam experiment using real cars on an outdoor circuit of 230 circumference in order to verify the theoretical understanding of traffic jams as a dynamical phase transition [7, 8]. In the study, we demonstrated

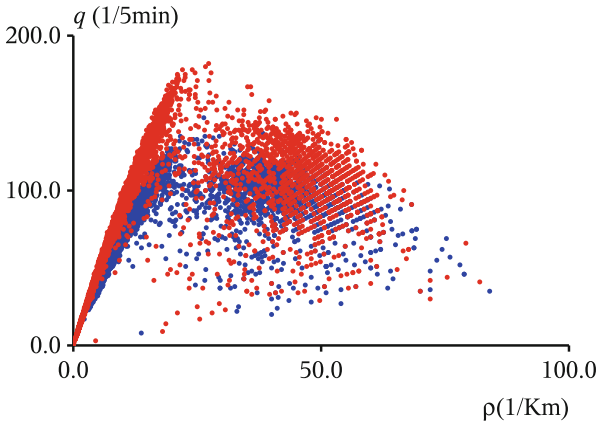

Fig. 1 Fundamental diagram observed on a Japanese highway. *Red* points are taken from the fast lane and *blue* ones from the slow lane

that traffic jams emerge at a certain high density without bottlenecks. And we observed the metastable homogeneous flow that appears as a precursor to traffic jams.

An experimental investigation of the density dependence of flow is required for confirming that the emergence of traffic jams is a really dynamical phase transition. For this purpose, we performed an extended experiment with varying number of cars under an improved environment [9]. The experiment was conducted on a circuit set in the Nagoya Dome, an indoor baseball field [10]. The new circuit was larger (314 m in circumference) than that used in the previous experiment. And we employed a laser scanner for higher-resolution positioning of the cars. We intend to estimate the critical density by comparing observations in real highways. To this end, we study the fundamental diagrams from the experimental data.

2 The Experiment

In order to study the effects of car density on traffic flow, inhomogeneity in the circuit should be reduced as low as possible, as it may act as bottlenecks. Therefore we needed to use a circular road on flat ground with homogeneous conditions. For accessing a flat, concrete floor of the Nagoya Dome, the pitching mound and artificial turf were removed and areas around the bases were covered with gray sheets in order to reduce visual inhomogeneity (Fig. 2). On a circuit of 314 m circumference, we were able to vary the density of cars by $10^{-2}\,\mathrm{m}^{-1}$.

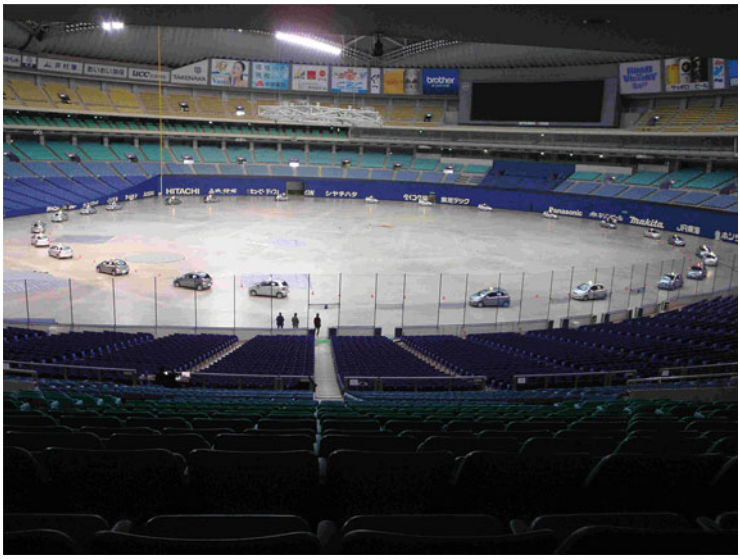

Fig. 2 Bird's-eye view of 50 m radius (314 m circumference) circuit in the Nagoya Dome. The field is flattened by removing the pitching mound and artificial turf

In the previous experiment, we read car positions manually from video data captured by a 360° camera; the positioning error in this case was roughly ±0.5 m. In this experiment, we employed a laser scanner (Sick LD-LRS 1000) located at the center of the circuit to measure car positions with an improved resolution. The scanner rotated at a frequency of 5 Hz, detecting the distance to objects every 360°/1,920°; the resulting time resolution was 10^{-4} s, and the spatial resolution was 0.16 m at a distance of 50 m. The stream of data was stored in a computer connected to the scanner, allowing sequences of position and speed for each car to be reconstructed. The details of the data acquisition and the spacetime diagrams are given in Ref. [9].

We conducted 19 sessions. For each session, the number of cars are varied from 10 to 40. All of cars were of the same model and specifications (Toyota Vitz: 1.3L, 3885m long, automatic transmission). We use data from 14 sessions for analyses.

3 Fundamental Diagrams and Estimating the Critical Density

We examined the fundamental diagrams which represent the density-flow relation. On real expressways, induction-loop coils are buried beneath observational points on a road and count the cars passing by the point and measure their speed. The number of cars q and their average speed v are recorded, for example, every 5 min. Then the density ρ at a given point and time is calculated from the relation $q = \rho v$.

To obtain a fundamental diagram from the experimental data, we place three virtual observational points, which are spaced at intervals of 120° for collecting a sufficient number of data. At each observational point, we count the number of cars passing and average their speed by intervals of 45 s, the duration determined based on the time needed for a jam cluster to move around the circuit.

Figure 3 shows the fundamental diagram for all sessions except two sessions which exhibited stop-and-go motions. This fundamental diagram is similar to that

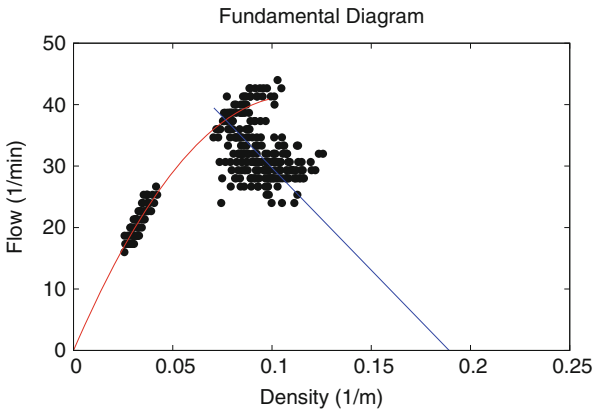

Fig. 3 Fundamental diagram for the selected sessions excluding two sessions with stop-and-go traffic. The *red curve* and the *blue line* are drawn as references to show the typical behavior of free and jammed flows

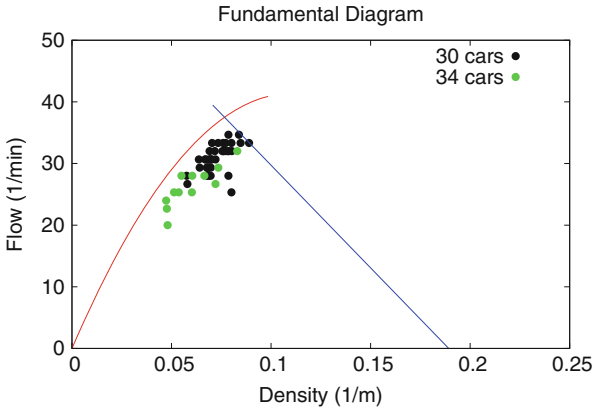

Fig. 4 Fundamental diagram for the selected sessions with stop-and-go traffic

extracted from traffic on real expressways. In Fig. 3 we find three typical features: free flow, jammed flow and metastable states. The red curve and the blue line in Fig. 3 are drawn as references to show the typical behavior of free and jammed flows, respectively.

Data points from the sessions with small numbers of cars, $10 \leq N \leq 25$, locate in the vicinity of the red curve. Here, the flow is an increasing function of the density, which is a typical feature of free flow. For the sessions with large numbers of cars, $N \geq 32$, data points are scattered broadly near the blue line. The flow shows the typical feature of jammed flow. Data points from the sessions with intermediate number of cars, $N = 28$ and 30, distribute around both the red curve and the blue line. This shows the typical feature of metastable states. Thus, we can conclude that critical density locates between $0.08\,\mathrm{m}^{-1}$ ($N = 25$) and $0.09\,\mathrm{m}^{-1}$ ($N = 28$).

The fundamental diagram for the two sessions that exhibited stop-and-go traffic, in which cars stop or nearly stop in jam clusters, is shown in Fig. 4. Because cars are detected only when they pass by the observation point, stopped cars are not taken into account in the flow measurement and in the average speed. In other word, the fundamental diagram consists mainly of data from cars moving smoothly outside of jam clusters. Because the speeds of cars outside the jam cluster are nearly the same as those in free flow, the diagram resembles that for a free flow. It can be seen that the average speed is a bit smaller and the amplitude of fluctuation is larger than those in a 'true' free flow because the motions of cars catching up with and escaping from the jam clusters are also included in the data. The resemblance between stop-and-go traffic and free flow has been reported also for the fundamental diagram of a real expressway traffic [11].

4 Summary and Discussions

We conducted the experiment to confirm that the emergence of a traffic jam is a dynamical phase transition controlled by the density of cars. And we estimated the critical density based on the experimental data. In our previous study [7, 8], which

was conducted on an outdoor field, we demonstrated that a traffic jam occurs at a certain high density without bottlenecks. The current experiment was carried out on an indoor circuit of 314 m circumference with high resolution measurements (i.e. 0.2 s in time and 0.16 m in space). For estimating the critical density, the number of cars was varied from 10 to 40 [9]. Based on our analysis of fundamental diagrams, we confirmed that a dynamical phase transition between free and jammed flow occurs at a critical density. We also observed that metastable states occur at intermediate densities between free and jammed flows. The critical density was estimated to locate between 0.08 and 0.09 m^{-1}.

We can compare the critical density obtained in this study with that measured on a real expressway. The critical density of an expressway in which the observed average speed is 120 $\mathrm{km\,h}^{-1}$ in free flow is known to be 0.025 m^{-1} (25 cars km^{-1}) [7]. In our present experiment, on the contrary, the average speed in free flow was about 40 $\mathrm{km\,h}^{-1}$. Suppose a car requires a headway that is three times larger when driving three times faster, our measured experimental critical density is consistent with values observed on the expressway.

In this paper, we discussed the phase transition based on conventional observables, such as fundamental diagrams, measured in real expressways. And we did not mention any models, because we intended to estimate the critical density by comparing with observations in real expressways without depending on any models.

We showed that the transition between free and jammed flow occurs at a critical density and metastable states appear around the critical density. In this sense, the transition seems to be first order. However, it is different from phase transitions of ordinary equilibrium systems. In a traffic flow, particles (cars) in the system are moving, and emerged patterns (jam clusters) also move. Therefore the transition is essentially dynamical.

Acknowledgements We thank Nagoya Dome Ltd, where the experiment was performed. We also thank SICK KK for their technical support with the laser scanner. And finally we thank H Oikawa and the students of Nakanihon Automotive College for assisting with this experiment. This work was partly supported by The Mitsubishi Foundation and a Grant-in-Aid for Scientific Research (B) (no. 20360045) of the Japanese Ministry of Education, Science, Sports and Culture.

References

1. D.E. Wolf, M. Schreckenberg, A. Bachem (eds.), *Workshop on Traffic and Granular Flow* (World Scientific, Singapore, 1996)
2. M. Fukui, Y. Sugiyama, M. Schreckenberg, D.E. Wolf (eds.), *Traffic and Granular Flow'01* (Springer, Berlin, 2003)
3. D. Chowdhury, L. Santen, A. Schadschneider, Phys. Rep. **329**(4–6), 199 (2000)
4. D. Helbing, Rev. Mod. Phys. **73**(4), 1067 (2001)
5. T. Nagatani, Rep. Prog. Phys. **65**(9), 1331 (2002)
6. B.S. Kerner, *The Physics of Traffic* (Springer, Berlin, 2004)
7. Y. Sugiyama, M. Fukui, M. Kikuchi, K. Hasebe, A. Nakayama, K. Nishinari, S. Tadaki, S. Yukawa, New J. Phys. **10**(3), 033001 (2008)

8. A. Nakayama, M. Fukui, M. Kikuchi, K. Hasebe, K. Nishinari, Y. Sugiyama, S. Tadaki, S. Yukawa, New J. Phys. **11**(8), 083025 (2009)
9. S. Tadaki, M. Kikuchi, M. Fukui, A. Nakayama, K. Nishinari, A. Shibata, Y. Sugiyama, T. Yosida, S. Yukawa, New J. Phys. **15**(10), 103034 (2013)
10. Nagoya Dome Ltd., http://www.nagoya-dome.co.jp/
11. L. Neubert, L. Santen, A. Schadschneider, M. Schreckenberg, Phys. Rev. E **60**, 6480 (1999)

Weather and Road Geometry Impact on Acceleration Behavior: Experimental Set-Up and Data Collection Using a Driving Simulator

Lingqiao Qin and Samer H. Hamdar

Abstract Transportation researchers tried for decades to investigate the dynamics of traffic flow in order to "optimize" the movement of goods and people under different surrounding conditions while reducing the negative environmental impacts and the economic losses due to congestion and traffic incidents. An important aspect missing from some previous studies relates to the activities through which drivers process the information representing a given surrounding. Such activities include: perception, evaluation, judgment and execution. Recognizing such limitation, the objective of this paper is utilize a 3-D driving simulator to advance the state of knowledge related to driving behavior while considering the surrounding environment's impact (weather and road geometry) on drivers' decision-making logic.

Through a thorough literature review, the authors looked at the external factors that may impact longitudinal driving behavior. The major factors considered include visibility level, road friction, curvature, gradient, median existence, lane width and shoulder width. The literature review is then translated to an experimental set-up with variables that "parameterize" the external environment's characteristics. A total of 36 students and staff from the George Washington University, 26 male and 10 female, with varying driving experience participated in the experiments. The participants drove behind a yellow cab which speed patterns are dictated by real-word trajectories taken from the NGSIM trajectory data. The collected performance measures include accelerations, speeds, longitudinal and lateral coordinates of the subject vehicle and the lead vehicle.

L. Qin
Traffic and Networks Research Laboratory, The George Washington University, Exploration Hall, Room 301, 20101 Academic Way, Ashburn, VA 20147, USA
e-mail: lingqiao.qin@gmail.com

S.H. Hamdar (✉)
Department of Civil and Environmental Engineering Academic Center, School of Engineering and Applied Science, The George Washington University, Phillips Hall, Room 631, 801 22nd Street NW, Washington, DC 20052, USA
e-mail: hamdar@gwu.edu

M. Chraibi et al. (eds.), *Traffic and Granular Flow '13*,
DOI 10.1007/978-3-319-10629-8_57

1 Introduction and Motivation

Different environmental conditions have been identified to have an impact on individuals' driving behaviors. Examples of different environmental conditions are weather-related factors and road geometry-related factors. For instance, it has been shown that reduced visibility has a substantial impact on traffic flow dynamics [14] while the geometry of the road layouts leads to changes in driving behavior [23]. Weather condition and road geometry are the two congestion and crash triggering factors which are still insufficiently understood. A large quantity of evidence exists about the likelihood of rear-end crashes during abnormal weather or at accident prone sections [3, 18, 19, 26, 33], but little effort has been devoted to quantify their effects on driving behavior (in the micro scale) and congestion and safety (in the macro scale) in the literature. Therefore, more detail behavioral bases studies are required to describe the driving behavior of pre-crash in such situations.

Driving behavior is subject to change according to the surrounding environment. While it is expected that different driving environments impose different changes to the driving behavior of an individual, the magnitude of deviation from normal driving behavior varies among drivers. Comprehensive study of the effect of certain driving environments on driving behavior has been presented in the literature [3], however, little effort has been presented to quantify the effects of different weather conditions and road geometrical configuration on driving behavior. The main objective of this paper is to use a driving simulator to test individual driving behavior in different environmental situations and then use the data obtained to understand how a driver perceives the dynamic changing driving surroundings (i.e. different weather conditions and road geometrical configurations) and executes acceleration maneuvers accordingly.

The structure of the remainder of this paper is as follows. First a background review on the effects of weather and road geometry on the driving behavior is presented. This section is followed by the experimental setup. The data collection procedure is presented which is followed by a thorough numerical analysis. The concluding remarks and future research directions are presented next.

2 Background Review

2.1 Weather

Multiple studies have focused on the statistical relationships between different traffic measures and different surrounding weather conditions. The overall findings of these macro level studies denote that visibility impairment, precipitation, and temperature extremes may affect driver behavior and vehicle maneuverability. Chen et al. [4] found that weather and road surface conditions bring about some differences in car-following behavior. Based on recorded traffic data, Ibrahim and

Hall [16] found that free-flow speed reduces 1.9 mph in light snow, 3.1–6.2 mph in heavy rain, and 23.6–31 mph during heavy snow. Liang et al. [21] conducted a study to investigate the impact of visibility on speed. Through data collection, they found that average speed reduces 11.9 mph during snow events, and that the overall variability in average speed during snow events was nearly three times larger than normal weather conditions.

Another group of studies have focused on the concepts and theories of car following to understand drivers' car following behavior, their headway maintenance and how the choice of headway affects safety [3, 33]. It was suggested that drivers' car following behavior can be affected in dense fog resulting from obscure scenery [7]. Evans also observed that drivers tended to follow the lead vehicles much closer from the fear of losing a reference when driving in foggy weather. Hawkins [13] reported a significant increase in distance headways when visibility distance was 150 m. Van Der Hulst et al. [31] studied driving behavior in fog with a visibility distance of 150 m. They noted that due to the difficulty in anticipation that the visibility reduction causes, drivers increase time headway under low visibility conditions. They also found that drivers' reactions to decelerations of the leader were very accurate even when visibility was reduced.

The friction coefficient of the road surface, which influences vehicle's maneuverability, has been widely studied. Perrin and Martin [25] analyzed traffic flow in Salt Lake Valley, Utah during winter. The results indicated that start-up delays on snowy pavement and wet pavement was 23 and 5 % higher, respectively, than the delays observed on dry pavement. As friction and precipitation types are highly correlated, Wu et al. [34] presented a novel car-following model according to the relationship between vehicle deceleration and passenger comfort levels. In this model, the friction coefficient between vehicles and road surface is considered and experiments with this model showed high compatibility with real-life observations. Wallman et al. [32] found that average speed reduces by 10–30 % in icy and snowy weather conditions respectively. Tanaka et al. [30] studied the influence of different road surfaces through car-following platoon experiments and they discovered a significant difference in driving behavior between icy and dry roadway surfaces.

2.2 Road Geometry

Roadway layouts, including lane and shoulder width, median existence, horizontal and vertical alignment, also have considerable impact on driving behavior. Roadway geometry affects drivers' perception of driving environment and therefore influences their driving behavior [17]. Several studies showed that crash rate were associated with roadway design [18, 19, 26]. However, only few studies directly investigated the effects of a specific roadway design elements on driving behavior through controlled manipulations [22]. In this paper and based on the above studies, horizontal and vertical alignments, lane width, shoulder width, and median existence are considered as the geometric features of interest.

Different road characteristics such as road curvature and gradient affect driving behavior differently, as suggested by Rockwell [27]. Andueza [2] developed a model to estimate vehicular speed on curves and tangents of roads. The study found that drivers' choice of speed within horizontal curves highly depended on the roadway features before the start point of the curve. McLean [23] studied the influences of rural road alignment on drivers' speed selection behavior by collecting free-flow speed data at 120 curves with approach tangent sites on two-lane rural highways. Their analysis suggested that the observed 85th percentile car speeds were dominantly influenced by the desired speed.

Yang and Peng [36] identified the road gradient as an exogenous disturbance of longitudinal driving behaviors in an error-able car-following model. Mullins and Keese [24] also suggested that rear-end accidents were common at vertical curve locations where unfavorable sight conditions existed. Lefeve [20] investigated driver behavior on two lane rural highways with vertical curves, where the minimum sight distances ranged between 150 and 500 ft. It was well observed that drivers invariably reduced the speeds as they approached vertical curves with short sight distances. It was also found that speeds at the vertical curves (regardless of the sight distance) appeared to be determined by present operating speeds. According to this study, roadway crash rate was much higher on sag curves than on crest curves. Glennon [10] noted that crash rate at grade sections were much higher than crash rate at level sections. Their findings showed that crash rate is higher at steep gradients and down-hill sections.

The effect of lane width on traffic flow efficiency as well as safety implications has been investigated for many years. Harwood et al. [12] suggested that the roadway capacity would drop when the width of traffic lanes is below 12 ft. Specifically, 11 ft lanes have 3 % less capacity than 12 ft lanes; 10 ft lanes have 7 % less capacity than 12 ft lanes; 9 ft lanes streets have 10 % less capacity than 12 ft lanes. Narrower lanes are perceived as less tolerant and less secure. This led drivers to adopt speed control to avoid dangerous or risky situations [29]. De Waard [6] noted that driving on a narrow lane requires greater mental effort than driving on a wide lane, because drivers need to keep vehicles within the lane. Yagar and Van [35] reported 1.1 mph reduction in average speed for every 1 foot reduction in lane width. Likewise, Heimbach et al. [15] found that during off-peak hours, if lanes narrowed by 1 ft, speed would tend to reduce 0.6 mph, when other factors are held constant. They showed that during peak hours, speed decreases by 1 mph per foot of lane width. Besides the impact of lane width on driving behavior and speed selection, lane width has an effect on roadway safety. It has been demonstrated that the use of narrower lanes would lead to more crashes if other roadway characteristics remain unchanged [11]. Heimbach et al. [15] showed that crash rate increases as lane width decreases, but the relationship is not linear. Karlaftis and Golias [18] quantitatively assessed the effects of various highway characteristics on crash rate using a crash database. They identified lane width as one of the most important factors affecting crash rate on two-lane roadways.

Shoulder width has also an impact on driving behavior. Yagar and Van [35] found a small increase in driving speed on 2-lane rural roads if an emergency lane/hard

shoulder was added. Stamatiadis, et al. [28] suggested that wider shoulders give drivers a sense of security and much space to correct their driving errors. However, narrow lanes demand more mental concentration and could decrease the positive effects of wide shoulders on safety. In a study on safety relationships between geometric characteristics and crashes, Zegeer and Deacon [37] concluded that crash rate decreased with increasing lane width and shoulder width. It was also observed that lane width had a greater impact on crash rate compare to shoulder-width.

Finally, it has been confirmed that the existence of median on highways have substantial influence on traffic flow operations and traffic safety. For example, Council and Stewart [5] examined the safety differences between divided two-lane and undivided four-lane rural roadways. It was concluded that the existence of median barriers had positive effect on crash rate. Fitzpatrick et al. [9] pointed out that the presence of medians results in higher speeds than where no median existed. The speed on streets without medians was about 38 mph, and the speed was 42 mph with a raised median in urban areas.

3 Experimental Set-Up

By reviewing the external factors of weather and road geometry, the objective is to investigate drivers' responses (in terms of basic traffic measures of effectiveness) to reduced visibility, different road surface conditions, different horizontal and vertical curves, and different lane and shoulder widths in real-world conditions. This investigation is performed using a driving simulator. Using a driving simulator is an alternative for on-road tests when researchers wish to use more controlled circumstances, or manipulate specific test conditions such as weather conditions and road geometric configurations. Since the hazard normally faced on a roadway due to inclement weather conditions or to challenging geometric conditions may be minimized, driving simulators are useful tools for the studies of driving behavior and traffic safety. A total of 36 students and staff from the George Washington University, 26 male and 10 female, with different driving experience participated in the experiments. The participants' average age was 24.8 years (std 4.02 years), ranging from 20 to 35 year. Every participant had a valid US driving license with 6 years of driving experience in average (std 4.50 years). None of the participants had previous experience with the driving simulator or reported any history of visual problems. Among 36 participants, 6 (1 female, 5 males) had road crashes in the past 5 years and 1 (male) refused to answer this question. The 26 males and 10 females were randomly assigned to 2 or 3 of the 15 experimental scenarios (5.5 min each). Details about these experiments are presented later. With this assignment, each experiment had at least three participants (one female participant and two male participants).

The simulation scenarios in our study consist of different weather conditions and road geometric configurations. In standard scenario, the test route is an 8,000 ft stretch of two-way, two-lane roadway through a rural landscape. A series of metal median barriers with the dimensions of 10 ft long, 1.5 ft wide and 1.5 ft high are

displayed in the middle of the roadway. The lane width and the shoulder width of the roadway in both directions in the standard scenario are 12 and 6 ft, respectively. Speed limit signs of 65 mph, white dashed lines as the lane markings and white solid line at edge were posted throughout the scenario. The weather condition for the standard scenario is set as clear day with blue skies with no wind that may influence vehicle maneuverability. In terms of traffic condition, multiple vehicles traveling on both directions of the road are inserted. Steady streams of oncoming vehicles were created throughout each simulation. There was also steady traffic traveling in the same direction as the driver in both the center lane and side lane. In addition, one lead vehicle was programmed to travel on the side lane throughout the simulation of the standard scenario (a yellow cab). In order to make the movement of the lead vehicle as generic as possible, the traffic data collected in the Federal Highway Administration's Next Generation Simulation project [8] were adopted to define the speed profile of the lead vehicle in this study.

Two different median types: metal median barrier and concrete median barrier were used in the experiment. Undivided road was also tested in the studies. The lane width of a roadway also greatly affects the safety and comfort of drivers as reviewed in the previous sections. Although 12 ft lane width is desirable on both rural and urban roadways, lane width of 9, 10 and 11 ft are all in use in real word [1] and thus were tested in the simulator experiment. In terms of the horizontal and vertical curves, the spiral curve design standards were adopted (per AASHTO [1]). When designing the roadway layouts in mountainous area, six different horizontal curves were adopted. Three smooth horizontal curves were also used in the case of rolling terrain scenario.

On the other hand, it was confirmed in the literature that reduced visibility conditions have huge impact on rear-end crash rate. In order to see the weather influence on longitudinal driving behavior, the current study utilizes the driving simulator-based method where fog is simulated as a distance dependent contrast reduction while having participants follow a lead vehicle in front of them. Fog density is considered uniform throughout each driving test and is adjusted to present four different sight distances (65.62, 164, 328 and 656.2 ft) for each of the four fog-related experimental scenarios. Road surface condition also affects vehicle stability of driving behavior. The Road Surface Attribute event in STISIM Drive (Software operating the simulator) is used to define different road surface conditions. In this driving experiment, two different road surface conditions were created to simulate wet and icy roadway surfaces. When driving on normal roadway surfaces, the vehicle tires will have enough traction, which is sufficient to respond to steering input. However, when the friction coefficient reduced to 0.2 (icy condition) and 0.4 (wet condition), drivers will find that the vehicle is harder to control and less responsive.

Table 1 presents the summery of all 15 scenarios that resulted from the change of the surrounding parameters presented above. Note that in all of the 14 scenarios (excluding the standard scenario), only one external factor was changed while the other conditions remained as in standard scenario. The standard scenario consists of two-lane rural road marked with single white edge lines and separated by metal median barrier.

Table 1 Test variables in each driving scenario (HC: horizontal curve length; VC: vertical curve length)

External factors	Items	Specification	
Road geometry	Median	10 ft long, 2 ft wide, 3 ft high concrete barrier	
		10 ft long, 1.5 ft wide and 1.5 ft metal barrier	
		Undivided Road (Double Solid Yellow Line)	
	Lane width (LW)	LW = 9 ft	
		LW = 10 ft	
	Shoulder width (SW)	SW = 0 ft	
		SW = 3 ft	
	Mountainous area	HC = 172 ft	VC = 134 ft
		HC = 344 ft	VC = 200 ft
		HC = 515 ft	VC = 300 ft
		HC = 345 ft	VC = 500 ft
		HC = 687 ft	
		HC = 1,716 ft	
	Rolling terrain	HC = 572 ft	VC = 500 ft
		HC = 1,030 ft	VC = 963 ft
		HC = 1,145 ft	VC = 843 ft
Weather	Visibility distance (VD)	VD = 65.62 ft	
		VD = 164 ft	
		VD = 328 ft	
		VD = 656.2 ft	
	Friction coefficient (FC)	FC = 0.2 (ice condition)	
		FC = 0.4 (wet condition)	

4 Exploratory Numerical Analysis: Speeds and Headways

In this section, the results of driving simulator experiments are presented and the impacts of the external factors on longitudinal driving behavior are discussed in detail. The average speed is calculated for each group in the 15 experiments. The average choice of time headway and its standard deviation is also calculated for each experiment. The results reveal that participants tend to choose lower speed when traveling on narrower lanes or narrow shoulders. Likewise, the average speed under wet and icy road surface conditions are also slightly lower than under other conditions, which were 23.94 and 23.82 ft/s. The results show that fog density has little to no effect on the drivers' choice of speed (average speeds in four different foggy conditions were all about 24 ft/s). However, the standard deviations of speed in foggy conditions were greater than under standard condition, except for the third case (VD = 328 ft), which indicates that poor visibility to some extent does not always confine drivers' traveling speed but it does cause much more uncertainties and therefore leads to much more changes in drivers' speed choices when following a leader.

When looking at the longitudinal driving behavior, the distance to a vehicle ahead is one of the important safety margins that drivers have to maintain properly.

Generally, the distance to a vehicle ahead is expressed in terms of time headway that is defined as the distance gap between the preceding and the following vehicles divided by the following vehicle's speed. Choice of time headway is also affected by different weather and roadway conditions. When traveling on the undivided roadway, the participants had the smallest time headway (4.71 s). This means that, without additional objects/separations on the roadway, drivers feel much more freedom and less constraint to keep a short gap following a leader. It is well established that undivided roadways are less safe than divided ones. Therefore short time headways on undivided roadways may appear to explain why crash history on undivided roadways is relatively higher. Drivers' behavior in dealing with foggy condition is however different depending on the fog density. In very low and low visibilities, driver tends to keep their distance from the leader, therefore, very high time headways are observed. As the visibility distance increases, the drivers tend to consider the leader in their decision making process; therefore, a decrease in time headways is observed (comparing to the cases on very low and low visibilities). Note that, the average time headway when visibility is 656.2 ft is less than most of other scenarios. This finding is consistent with the previous research's conclusions that drivers tend to follow a lead vehicle much closer for visible cues under poor visibility condition [7]. In addition, the time headway in rolling terrain is 10.14 s that is the greatest in all experiment. This result suggests that following a lead vehicle on a stretch of road with a number of uphill and downhill requires much more effort dealing with the vertical alignment changes and drivers tend to "lose" the leader which results in an increased in average time headway.

Conclusions and Future Research Needs

It is known that road traffic efficiency and safety result from a series of factors including road-geometry factors, weather factors, vehicles, and traffic dynamics. This study investigates the longitudinal driving behavior under different road-geometry and weather conditions. Based on an extensive literature review, 15 driving experiments are designed using the STISIM Drive simulator. Throughout the test, 66 effective results are collected.

Testing the roadway-related factors (lane width, shoulder width, median existence, median type, horizontal curves and vertical curves) and weather related factors (foggy weather and icy and wet road surface conditions) in 15 driving scenarios, it is found that overall drivers' average speed, time headway, and distance headway are affected by these factors. It has been confirmed repeatedly that undivided road will cause drivers to adopt an aggressive driving strategy (less safety margins reflected by smaller time headways). Conversely, traveling on the divided road, drivers adopt less

(continued)

aggressive behavior since they try to avoid the barrier. The narrower lanes are also found to be one of the influential factors that impact drivers driving style when following a leader. The most extreme case of 9 ft traveling lane would increase their distance with the leader compare to the normal case. Drivers driving on a road without hard shoulders would less likely follow the leader at a dangerously close distance. Inadequate visibility distance is also found to influence driving behavior. Low visibility cause drivers to increase their distance with the leader, while in higher visibility drivers tend to follow the leader more closely.

Given the meticulous design of the experiments and the extensive data collection efforts made, extending the findings of this study to calibrate existing microscopic acceleration models while analyzing further the resulting acceleration and deceleration patterns may constitute the future direction of this research.

References

1. American Association of State Highway and Transportation Officials (AASHTO), *A Policy on Geometric Design of Highways and Streets*, 4th edn. (American Association of State Highway and Transportation Officials, Washington, D.C., 2001)
2. P.J. Andueza, Mathematical Models of Vehicular speed on mountain roads. Transp. Res. Rec. **1701**, 104–110 (2000). Transportation Research Board, Washington, D.C.
3. M. Brackstone, B. Waterson, M. McDonald, Determinants of following headway in congested traffic. Transp. Res. Part F **12**, 131–142 (2009)
4. S. Chen, T. Sheridan, S. Ahn, M. Mathew, M. Kambourides, H. Kusunoki, N. Komoda, Car-following behavior: effect of environment, in *Proceedings of the 1995 Annual Meeting of ITS America*, Washington, D.C., 1995, pp. 993–999
5. F.M. Council, J.R. Stewart, Safety effects of the conversion of rural two-lane to four-lane roadways based on cross-sectional models. Paper presented at the 78th annual meeting of the transportation research board, Washington, D.C., 1999
6. D. De Waard, M. Jessurun, F.J. Steyvers, P.T. Raggatt, K.A. Brookhuis, Effect of road layout and road environment on driving performance, drivers' physiology and road appreciation. Ergonomics **38**(7), 1395–1407 (1995)
7. L. Evans, *Traffic Safety* (Science Serving Society, Bloomfield Hills, 2004)
8. FHWA, NGSIM Task E.1-1: core algorithms assessment, final report, Cambridge Systematic, 2005
9. K. Fitzpatrick, P.J. Carlson, M.D. Wooldridge, M.A. Brewer, Design factors that affect driver speed on suburban arterials. Project summary report 1769-S. Texas Transportation Institute, Austin, 2000
10. J. Glennon, Effect of alignment on highway safety, in *Relationship Between Safety and Key Highway Features*. SAR 6 (Transportation Research Board, Washington, D.C., 1985), pp. 48–63
11. D.W. Harwood, Effective utilization of street width on urban arterials, National Cooperative Highway Research Program Report 330, Transportation Research Board 1990

12. D.W. Harwood, F.M. Council, E. Hauer, W.E. Hughes, A. Vogt, Prediction of the expected safety performance of rural two-lane highways, Report FHWA-RD-99-207, Federal Highway Administration, 2000
13. R.K. Hawkins, Motorway traffic behaviour in reduced visibility conditions, in *Proceedings of the Second International Conference in Vision in Vehicles*, Amsterdam, 1988, ed. by A.G. Gale, pp. 9–18
14. R.G. Hoogendoorn, S.P. Hoogendoorn, K.A. Brookhuis, W. Daamen, Simple and multi-anticipative car-following models: performance and parameter value effects in case of fog, in *Proceedings of the Transportation Research Board (TRB) Traffic Flow Theory and Characteristics Committee (AHB45) Summer Meeting*, Annecy, France, July, 2010, pp. 2–16
15. C.L. Heimbach, P.A. Cribbins, M.S. Chang, Some partial consequences of reduced traffic lane widths on urban arterials. Transp. Res. Rec. **923**, 69–72 (1983)
16. A.T. Ibrahim, F.L. Hall, Effect of adverse weather conditions on speed-flow-occupancy relationships. Transp. Res. Rec. **1457**, 184–191 (1994)
17. W.H. Janssen, S.N. de Ridder, R.F.T. Brouwer, The RISER consortium, roadside Infrastructure for safer European roads: D02-summary of driver Behaviour and driver interactions with roadside Infrastructure, Project RISER, European Community under the Competitive and Sustainable Growth Program, 2006
18. M.G. Karlaftis, I. Golias, Effects of road geometry and traffic volumes on rural roadway accident rates. Accid. Anal. Prev. **34**, 357–365 (2002)
19. M.W. Knuiman, F.M. Council, D.W. Reinfurt, Association of median width and highway accident rates. Transp. Res. Rec. **1401**, 70–82 (1993)
20. B.A. Lefeve, Speed characteristics on vertical curves. Highw. Res. Board Proc. **32**,395–413 (1953)
21. W.L. Liang, M. Kyte, F. Kitchener, P. Shannon, The effect of environmental factors on driver speed: a case study, Transportation Research Record 1635, Transportation Research Board, National Research Council, Washington, D.C., 1998, pp. 155–161
22. M. Martens, S. Comte, N. Kaptein,. The effects of road design on speed behaviour: a literature review. Deliverable D1 (Report 2.3.1), MASTER (1997)
23. J. McLean, Driver speed behavior and rural road alignment design. Traffic Eng. Control **22**(4), 208–211 (1981)
24. B.F.K. Mullins, J.F. Keese, Freeway traffic accident analysis and safety study. Highw. Res. Board Bull. **2915** (1961). Highway Research Board
25. J. Perrin, P. Martin, Modifying signal timing during inclement weather. Presented at the 2002 Institute of Transportation Engineers annual meeting, University of Utah Traffic Lab, 2002
26. A. Polus, M. Pollatschek, H. Farah, Impact of infrastructure characteristics on road crashes on two-lane highways. Traffic Inj. Prev. **6**(3), 240–247 (2005)
27. T.R. Rockwell, *Skills, Judgment, and Information Acquisition in Driving, Human Factors in Highway Traffic Safety Research* (Wiley, New York, 1972)
28. N. Stamatiadis, J. Pigman, J. Sacksteder, W. Ruff, D. Lord, Impact of shoulder width and median width on safety, National Cooperative Highway Research Program (NCHRP), Report No. 633, Transportation Research Board, 2009
29. H. Summala, Accident risk and driver behavior. Saf. Sci. **22**(1–3), 103–117 (1996)
30. M. Tanaka, P. Ranjikar, T. Nakatsuji, Comparison of driving behavior and safety in car-following platoons under icy and dry surface conditions, in *Transportation Research Board 89th Annual Meeting*, Washington, D.C., 2010. Compendium of Papers DVD, 10-0504, Monograph Accession, 01147878
31. M. Van Der Hulst, T. Rothengatter, T. Meijman, Strategic adaptations to lack of preview in driving. Transp. Res. Part F **1**(1), 59–75 (1998)
32. C.G. Wallman, P. Wretling, G. Oeberg, Effects of winter road maintenance: state of the art. Swedish Road and Traffic Research Institute (VTI) Sartryck, report no. 423, 1997
33. W.V. Winsum, The human element in car following models. Transp. Res. Part F **2**, 207–211 (1999)

34. Y. Wu, G. Pan, A smart car control model for brake comfortable based on car following. IEEE Trans. Intell. Transp. Syst. **10**(1), 42–46 (2009)
35. S. Yagar, M.A. Van. Geometric and environmental effects on speeds on 2-lane rural roads. Transp. Res. Rec. **17A**(4), 315 (1983)
36. H.H. Yang, H. Peng, Development and evaluation of collision warning/collision avoidance algorithms using an errable driver model. Veh. Syst. Dyn. **48**(Supplement 1), 525–535 (2010)
37. C.V. Zegeer, J.A. Deacon, Effect of lane width, shoulder width and shoulder type on highway safety, in *State of the Art Report Number 6: Relationship Between Safety and Key Highway Features* (Transportation Research Board, Washington, D.C., 1987), pp. 1–21

The Stability Analysis of a Macroscopic Traffic Flow Model with Two-Classes of Drivers

Alma R. Méndez and R.M. Velasco

Abstract One of the most important objectives in the development of traffic theories is the improvement of traffic conditions. To achieve this goal, it is important a good understanding of multistyle and/or multilane traffic. In this work, we summarize the traffic model presented in Mendez and Velasco (FTC J Phys A Math Theor 46(46):462001, 2013) and additionally include the stability analysis of the same. The presented traffic model considers different driving styles, different vehicle types or both, for a two-classes of vehicles in which a model for the average desired speed is introduced (the aggressive drivers model) (Mendez and Velasco, Transp Res Part B 42:782–797, 2008; Velasco and Marques, Phys Rev E 72:046102, 2005). The kinetic model was solved for the steady and homogeneous state and also we obtained the local distribution function from an information entropy maximization procedure. The macroscopic traffic model is constructed by the usual methods in kinetic theory and a method akin with the Maxwellian iterative procedure is accomplished in order to close the macroscopic model for the mixture, where only the densities are present as relevant quantities. The linear stability analysis is carried out in order to have an insight of the unstable traffic regions of the model, which is very helpful in the numerical solution.

1 Introduction

Kinetic theory methods have been largely used in the study of the traffic flow phenomena [1–3, 5, 10, 12]. This kind of methods links the microscopic and macroscopic modeling giving a theoretical support to phenomenological models.

A.R. Méndez (✉)
Department of Applied Mathematics and Systems, Universidad Autónoma Metropolitana (Cuajimalpa), Av. Vasco de Quiroga 4871, Col. Santa Fe Cuajimalpa, Cuajimalpa de Morelos, 05300, México
e-mail: amendez@correo.cua.uam.mx; armendezr@gmail.com

R.M. Velasco
Department of Physics, Universidad Autónoma Metropolitana (Iztapalapa), San Rafael Atlixco 186, Col. Vicentina, Iztapalapa, 09340, México
e-mail: rmvb@xanum.uam.mx

M. Chraibi et al. (eds.), *Traffic and Granular Flow '13*,
DOI 10.1007/978-3-319-10629-8_58

Empirical observations have highlighted the wide variety of phenomena observed in traffic flow [6–9,14,15], and recently there have merged many efforts to describe and explain the wealth of traffic flow phenomena. In this work we present the stability analysis of a model that considers different driving styles, different vehicle types or both. The point of view we will follow to study such a problem is based on the kinetic theory of traffic flow. In Sect. 2 we summarize (see [12]) some details of the kinetic equation describing the evolution of each class of vehicles for aggressive drivers which has been also addressed before for a single class of driver [11, 16]. The kinetic model is solved for the steady and homogeneous state and also we have obtained a local distribution function from an information entropy maximization procedure. In Sect. 3 the macroscopic traffic model is constructed by means of a general transport equation obtained by the usual methods in kinetic theory. Then, a method akin with the Maxwellian iterative procedure is achieved in order to close the macroscopic model for the mixture where only the species densities are considered as relevant quantities. The linear stability analysis is presented and discussed in Sect. 4.

2 The Kinetic Model with Two-Classes of Vehicles

For a two-classes of drivers with punctual vehicles and diluted traffic, the equations describing the evolution of the distribution function $f_i = f_i(x, v_i, t)$ for individual vehicles of class $i = a, b$ is

$$\frac{\partial f_i}{\partial t} + v_i \frac{\partial f_i}{\partial x} + \frac{\partial}{\partial v_i}\left[\frac{W_i(x, v_i, t) - v_i}{\tau_i} f_i\right] = \sum_{j=a,b} Q(f_i f_j), \tag{1}$$

where

$$Q(f_i f_j) = (1-p)\left[\int_v^\infty dw_j\, f_i(v_i) f_j(w_j)(w_j - v_i) - \int_0^v dw_j\, f_i(v_i) f_j(w_j)(v_i - w_j)\right]. \tag{2}$$

for self-interaction we have terms $i = j$ and cross-interaction are represented by $i \neq j$.

In Eqs. (1) and (2) p is the overtaking probability and W_i is the mean desired velocity. We propose the following prescription for the former velocity

$$W_i(x, v_i, t) = \omega_i v_i, \tag{3}$$

where $\omega_i \gtrsim 1$ is a constant called the aggressivity parameter of $i-$class vehicles. Relation (3) indicates that drivers desired velocity increases as their actual velocity increases, i.e., drivers want to drive faster than they do [11, 16].

As usual in kinetic theory, the local variables such as the traffic density and the mean velocity of each vehicle class i are defined through the first two moments of the distribution function as follows

$$\int f_i dv_i = \rho_i \qquad \int f_i v_i dv_i = \rho_i V_i, \qquad \sum_i \int f_i v_i dv_i = \rho V. \tag{4}$$

2.1 Equilibrium Solution and the Information Entropy

For the homogeneous and steady state, Eq. (1) can be solved analytically assuming relation (3) for the mean desired velocity. The details of this calculation are analogous to the single class case and can be consulted in [16], the result is

$$f_{ie}(v_i) = \frac{\rho_{ie}\alpha_i}{\Gamma(\alpha_i) V_e} \left(\frac{\alpha_i v_i}{V_e}\right)^{\alpha_i - 1} \exp\left[-\frac{\alpha_i v_i}{V_e}\right], \qquad \alpha_i = \frac{\tau_i}{\omega_i - 1}(1-p)\rho_e V_e. \tag{5}$$

α_i is a constant that contains information on the equilibrium state and the model parameters τ_i, ω_i and p and $\Gamma(\alpha_i)$ is the gamma function with argument α_i. In this case the e-subindex means that the quantity corresponds to the steady and homogeneous case, usually called as the equilibrium state.

The local zeroth-order approximation for the one-vehicle distribution function follows through a maximization procedure of the information entropy referred to the equilibrium state. First we write the information entropy as

$$S[f_i(x, v_i, t)] = \sum_{i=a,b} \int_0^\infty f_i^{(0)}(x, v_i, t) \ln\left(\frac{f_i^{(0)}(x, v_i, t)}{f_{ie}(v_i)}\right) dv_i, \tag{6}$$

and consider relations (4) as restrictions for the optimization procedure. With this information the corresponding Lagrangian function, $\mathscr{F}$, is constructed and the distribution function which satisfies the optimality condition $\delta\mathscr{F}/\delta f_i^{(0)} = 0$ is given by

$$f_i(x, v_i, t) = \frac{\rho_i(x,t)\alpha_i}{\Gamma[\alpha_i] V(x,t)} \left(\frac{\alpha_i v_i}{V(x,t)}\right)^{\alpha_i - 1} \exp\left[-\frac{\alpha_i v_i}{V(x,t)}\right]. \tag{7}$$

At this point it seems important to emphasize that the distribution function (7) has the same functional structures that (5), both the equilibrium values are replaced by the local variables.

2.2 Model Equation

The mathematical complexity of the non-linear interaction operator Q_{ij} can be avoided if we replace the right hand side of Eq. (1) by a simple relaxation-time term of the form [4]:

$$\frac{\partial f_i}{\partial t} + v_i \frac{\partial f_i}{\partial x} + \frac{\partial}{\partial v_i}\left[\left(\frac{W_i(x, v_i, t) - v_i}{\tau_i}\right) f_i\right] = -\sum_{j=a,b} \sigma_{ij}\left(f_i - f_{ij}\right), \qquad (8)$$

where f_{ij} is a reference distribution function to be determined. Our aim is to derive a model equation for a two-classes of vehicles characterized by the ρ_i, V_i. We propose the following form for the reference distribution function f_{ij}:

$$f_{ij} = f_i^{(0)}\left(1 + A^{ij} + B^{ij} C_i\right) \quad \text{where} \quad C_i = (v_i - V) \qquad (9)$$

$f_i^{(0)}$ given by (7) and A^{ij} and B^{ij} are undetermined coefficients. To specify these coefficients we assume

$$f_i = f_i^{(0)}(1 + \phi_i) \qquad (10)$$

where the deviation ϕ_i is a linear function of the spatial gradients and must satisfy compatibility conditions. Inserting (9) and (10) in (8)

$$\phi_i = \frac{1}{\sigma_i}\left[1 + \frac{2}{V_i}(v_i - V_i) - \frac{\alpha_i}{V_i^2}(v_i - V_i)^2\right]\left(\frac{\partial V_i}{\partial x}\right). \qquad (11)$$

where restrictions (4) have been used. It is worth noticing that the deviation ϕ to the distribution function depends on the velocity gradients.

3 The Macroscopic Equations and the Iterative Procedure

Once we have the distribution function f_i, through (10) and (11), it is possible to obtain the macroscopic equations and close them. The procedure is the standard in kinetic theory, the resulting balance equations are

$$\frac{\partial \rho_i}{\partial t} + \frac{\partial \rho_i V_i}{\partial x} = (1 - p)\rho\rho_i(V - V_i), \qquad (12)$$

$$\frac{\partial V_i}{\partial t} - \frac{V_i}{\rho_i}\frac{\partial \rho_i V_i}{\partial x} + \frac{1}{\rho_i}\frac{\partial p_i}{\partial x} - \gamma_i V_i = -(1 - p)\rho\theta_i. \qquad (13)$$

where $\rho_i \theta_i = \int f(x, v_i, t)(v_i - V_i)^2 dv_i$, $i = a, b$ are the speed variances. To be practical, we now apply a method akin to the Maxwell iterative procedure [13], to obtain a first order model for each different class of vehicle. We assume that $V_i(x,t) = V_{ie}^{(0)}(\rho_i(x,t)) + \hat{V}_i(x,t)$. In this case we obtain the closure relation

$$\hat{V}_i = -\frac{\rho[V_{ie}^{(0)}]^2 \Gamma_i}{\rho_e V_e \left[1 - 2\frac{\rho V_{ie}^{(0)}}{\rho_e V_e}\right]} \frac{\partial V_{ie}^{(0)}}{\partial x}, \quad \text{with} \quad \Gamma_i = \frac{2(\alpha_i + 1)}{\sigma_i \alpha_i}. \tag{14}$$

By introducing (14) in (12) we get the model

$$\frac{\partial \rho_i}{\partial t} + b(\rho_i, \rho_j)\rho_i \frac{\partial \rho_i}{\partial x} - D(\rho_i, \rho_j)\frac{\partial^2 \rho_i}{\partial x^2} = 0 \qquad i, j = a, b \quad j \neq i \tag{15}$$

where $D(\rho_i, \rho_j) = \left[\left(\Gamma_i \rho V_{ie}^2 V_e'\right) / \left(\rho_e V_e - 2\rho V_{ie}\right)\right]\rho_i$, we have considered $V_e(\rho_e) = V_e$, $V_i^{(0)} = V_e(\rho_i) = V_{ie}$ and

$$b(\rho_i, \rho_j) = \frac{V_i}{\rho_i} - V_e' + (V_i - V_{ei})\left[\frac{1}{\rho} + 2\frac{V_{ei}'}{V_{ei}} + \frac{V_{ei}''}{V_{ei}'} + 2\frac{\left(V_{ei} + \rho V_{ei}'\right)}{\left(\rho_e V_e - 2\rho V_{ei}\right)}\right].$$

4 Linear Stability Analysis and Concluding Remarks

In order to determine if our model equation produces unstable traffic regions, a linear stability analysis of Eqs. (15) will be carried out. We write the perturbed densities as

$$\rho_i(x,t) = \rho_{ie} + \overline{\rho}_i \exp(-\gamma t + ikx) = \rho_{ie} + \tilde{\rho}_i(x,t) \tag{16}$$

for $i = a, b$ where k is the wave number and γ is the growth parameter. The procedure consists in inserting perturbations (16) into Eqs. (15) and neglect nonlinear contributions. The following linear system is obtained

$$\begin{pmatrix} \mathscr{A}(k,\gamma) & (1-p)\rho_{ae}\rho_{be}V_e'(\beta_{be}ik - 1) \\ (1-p)\rho_{ae}\rho_{be}V_e'(\beta_{ae}ik - 1) & \mathscr{B}(k,\gamma) \end{pmatrix} \begin{pmatrix} \tilde{\rho}_a \\ \tilde{\rho}_b \end{pmatrix} = \begin{pmatrix} 0 \\ 0 \end{pmatrix} \tag{17}$$

where

$$\mathscr{A}(k,\gamma) = \left[-\gamma + ikc_{ae} + \beta_{ae}k^2 V_e'\rho_{ae} + (1-p)\rho_{ae}\rho_{be}V_e'(1 - \beta_{ae}ik)\right],$$
$$\mathscr{B}(k,\gamma) = \left[-\gamma + ikc_{be} + \beta_{be}k^2 V_e'\rho_{be} + (1-p)\rho_{be}\rho_{ae}V_e'(1 - \beta_{be}ik)\right],$$
$$\beta_{ae} = \frac{\alpha_a V_{ae}^2 \Gamma_a}{[V_e - 2V_{ae}]} \qquad \text{and} \qquad c_{ae} = \left(V_{ea} + V_e'\rho_{ae}\right).$$

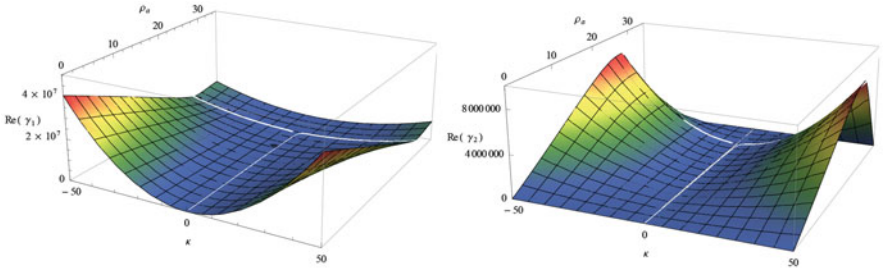

Fig. 1 The stable region for $\rho_e = 35$ veh/km

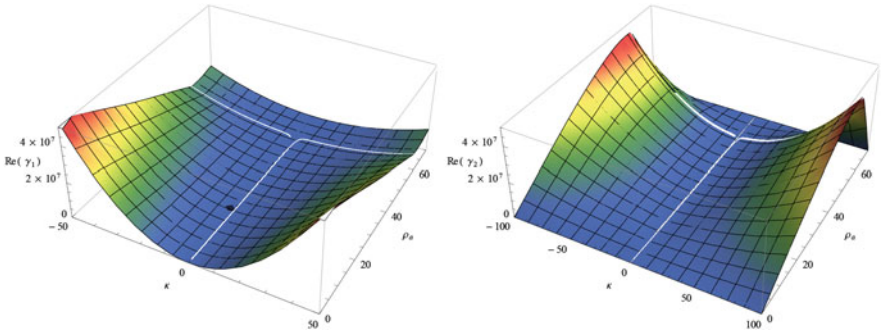

Fig. 2 The stable region for $\rho_e = 70$ veh/km

Table 1 Parameters for the graphics

Vehicle class		
Class a	$\alpha_a = 120$	$\Gamma_a = 0.012$
Class b	$\alpha_b = 100$	$\Gamma_b = 0.06$

The nontrivial solutions of system (17) are obtained when the determinant of the coefficient matrix vanishes, leading to a dispersion relation of the form $\gamma^2 + \gamma b(k) + c(k) = 0$.

This relation is very complex and is solved in Mathematica for some specific values. The results in Figs. 1 and 2 show the stable regions, corresponding to $\mathbb{R}[\gamma_{1,2}] > 0$, that is, when both γ_1 and γ_2 are positive. The parameters used in these figures are in Table 1 and we have used also the relations $V_e(\rho) = V_{max}(1 - \rho/\rho_{max})$ and $(1 - p) = \rho/\rho_{max}$ with $\rho_{max} = 140$ veh/km and $V_{max} = 120$ km/h.

Figures 1 and 2 show that we have stable regions. Worth be mentioned that a linear stability give us just a guide of the real stability regions, in order to have a better understanding a non-liner stability analysis should be done.

References

1. N. Bellomo, A. Bellouquid, On the derivation of macroscopi equations in the mathematical kinetic theory of actives particles with discrete states. Math. Comput. Model. **44**, 397–404 (2006)
2. A. Bellouquid, E. De Angelis, L. Fermo, Towards the modeling of vehicular traffic as complex system: a kinetic theory approach. Math. Models Methods Appl. Sci. **22**(Suppl.), 1140003 (2012)
3. L. Fermo, A. Tosin, A fully-discrete-state kinetic theory approach to modeling vehicular traffic. SIAM J. Appl. Math. **73**(4), 1533–1556 (2013)
4. A.S. Fernandes, W. Marques Jr., Sound propagation in binary gas mixtures from a kinetic model of the Boltzmann equation. Physica A **332**, 29–46 (2004)
5. D. Helbing, Traffic and related self-driven many-particle systems. Rev. Mod. Phys. **73**(4), 1067–1141 (2001)
6. D. Helbing, A.F. Johanson, Johanson, On the controversy around Daganzo's requiem for the Aw-Rascle's resurrection of second-order traffic flow models. Eur. Phys. J. B **69**, 549–562 (2009)
7. B.S. Kerner, *The Physics of Traffic* (Springer, Berlin New York, 2004)
8. B.S. Kerner, *Introduction to Modern Traffic Flow Theory and Control* (Springer, Heidelberg Dordrecht London New York, 2009)
9. B.S. Kerner, Criticism of generally accepted fundamentals and methodologies of traffic and transportation theory: A brief review. Physica A **392**, 5261–5282 (2013)
10. W. Marques Jr., A.R. Mendez, On the kinetic theory of vehicular traffic flow: Chapman-Enskog expansion versus Grad's moment method. Physica A **392**, 3430–3440 (2013)
11. A.R. Mendez, R.M. Velasco, An alternative model in traffic flow equations. Transp. Res. Part B **42**, 782–797 (2008)
12. A.R. Mendez, R.M. Velasco, Kerner's free-synchronized phase transition in a macroscopic traffic flow model with two classes of drivers. FTC: J. Phys. A: Math. Theor. **46**(46), 462001 (2013)
13. H. Struchtrup, *Macroscopic Transport Equations for Rarefied Gas Flows* (Springer-Verlag, Berlin Heidelberg, 2005)
14. M. Treiber, A. Kesting, Evidence of convective instability in congested traffic flow: a systematic empirical and theoretical investigation. Transp. Res. B **45**, 1362–1377 (2011)
15. M. Treiber, A. Kesting, D. Helbing, Three-phase traffic theory and two-phase models with a fundamental diagram in the light of empirical stylized facts. Transp. Res. B **44**, 983–1000 (2010)
16. R.M. Velasco, W. Marques Jr., Navier-Stokes-like equations for traffic flow. Phys. Rev. E **72**, 046102 (2005)

Driver Heterogeneity in Rubbernecking Behaviour at an Incident Site

Shahreena Rhasbudin Shah, Victor L. Knoop, and Serge P. Hoogendoorn

Abstract Incidents can reduce roadway capacity due to lanes blockages, and in some cases, also affect the flow in non-incident direction. This paper provides insights into change of driving behaviour while passing an incident site in attempt to assess rubbernecking activity. We use empirical trajectory data obtained from a helicopter-mounted video camera. By assessing the points where acceleration changes on speeds profiles over distance of individual vehicle, the behavioural changes of driver passing in the opposite direction of the freeway incident can be determined. Results show that the variations in speed in the upstream of incident location are substantially higher within passenger car drivers then within the truck drivers. The passenger cars in the median lane reduce the speed further upstream, mostly with sharp deceleration while passenger cars in the shoulder lane reduce the speed closer to the incident scene. Truck drivers, on the other hand, tend to decelerate earlier and farther upstream, more than 125 m from the incident site. Some drivers did not exhibit rubbernecking behavior, passing the incident with a steady speed. This study emphasizes the difference between passenger car and truck driving behaviour while passing an incident location. The results provide a better understanding of rubbernecking behaviour and useful for modeling driver behaviour under incident conditions.

1 Introduction

Most of traffic incidents such as crashes, spilled load, or temporary road maintenance that happens on a roadway can affects traffic due to physical reductions (lane blockages). However, traffic incidents also can cause a phenomenon, which significantly affects the traffic flow referred to as rubbernecking. Rubbernecking term is widely used in incident study to describe the breakdown of traffic in the opposite direction of the incident resulted by non-physical bottlenecks. It is caused by change in driver behaviour when passing an incident. Knoop et al. [1, 2] have

S.R. Shah • V.L. Knoop (✉) • S.P. Hoogendoorn
Faculty of Civil Engineering and Geosciences, Delft University of Technology,
Stevinweg 1, 2628 CN Delft, The Netherlands
e-mail: v.l.knoop@tudelft.nl; s.p.hoogendoorn@tudelft.nl

M. Chraibi et al. (eds.), *Traffic and Granular Flow '13*,
DOI 10.1007/978-3-319-10629-8_59

shown that rubbernecking may reduce the capacity per available lane by about 50 %. According to that study, the behavioural changes of drivers (lower speed, increase in time headway and increase in reaction time) during incident conditions lead to a 25–40 % reduction of normal queue discharge rates [3]. It has been reported in [4] that about 10 % of accidents caused rubbernecking in the opposite direction.

To the best of our knowledge, only average rubbernecking effects have been analyzed but in depth the heterogeneity in the behavioural change has never been look into. In this paper, heterogeneity not only focuses on the behavioural difference between passenger cars and trucks but defined as difference in individual driver behaviour when passing an incident. In this study, acceleration changes while approaching the incident scene are attributed to a rubbernecking behaviour, due to driver attention shift to the incident. The main goal of this paper is to improve understanding on the heterogeneity in rubbernecking behaviour. Therefore, the main question addressed in this paper is: is there a variation on driver behaviour between vehicle groups and within vehicle groups when passing an incident? We do so by identifying differences in speed changes between passenger cars and trucks while passing an incident site. The findings of this paper will be useful in considering the heterogeneity in modeling microscopic driver behaviour under incident conditions.

2 Data Extraction and Handling

2.1 Incident Description

The incident site is located on Motorway A1, near the city of Apeldoorn, The Netherlands. The incident type is a rolled over van, ended in the median (unpaved area which separates opposing lanes of the motorway), and happened around 9:15 a.m. on 6 June 2007, at the eastbound direction. There are two main lanes and one shoulder lane in each direction of the motorway, and no gradient. The speed limit on the motorway is 120 km/h. The weather condition during the incident was clear. Emergency vehicles were presence during the collection of data and blocked one lane in the incident direction.

2.2 Data Collection and Description

The empirical trajectory data in the opposite direction of the incident location have been collected using a digital camera mounted under a helicopter. Microscopic data was obtained over a length of 230 m, starting approximately 125 m upstream of the incident site. A total of 199 vehicle trajectories were observed and collected on both lanes, consisting of 123 passenger cars in the median (left/fast) lane, 35 trucks and 41 passenger cars in the shoulder (right/slow) lane. The trajectories have undergone

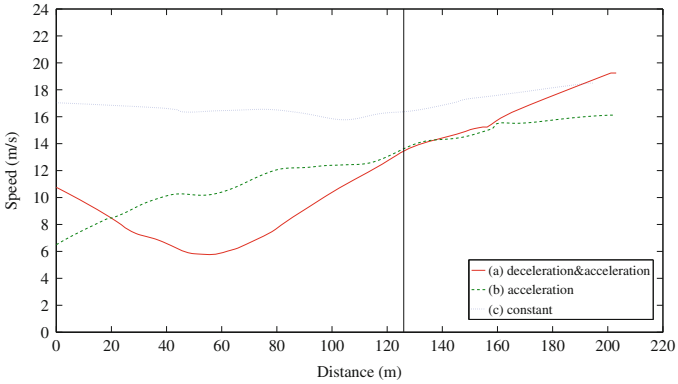

Fig. 1 The examples of speed patterns of individual vehicles

several processes before proceeding with the analysis. For further explanation, we refer to [5].

2.3 Overview of the Collected Data

The speed data were separated into three vehicle groups: passenger cars in the median lane, trucks, and passenger cars in the shoulder lane. In order to determine the changes in speed due to rubbernecking behaviour, we plot the speed (calculated with 0.1 s intervals) over incremental distances for each individual vehicle. Analysis of the individual vehicle speed profiles show that there are three distinct speed patterns as shown in Fig. 1. The black vertical line on the graph represents the location of the incident.

3 Data Analysis and Results

3.1 Analysis on Difference in Speed at a Location

We analyzed the speed data for different parts along the road. We focus on the variation in vehicle speeds and the statistical difference in speed between each vehicle class and within vehicle class, spatially split the roadway in segments of 10 m. In each segment, there are speeds for vehicles in all groups. Using a t-test, we test whether differences in mean speed between the vehicle groups are significant. In the remainder of the paper, the distance along the roadway is denoted by x.

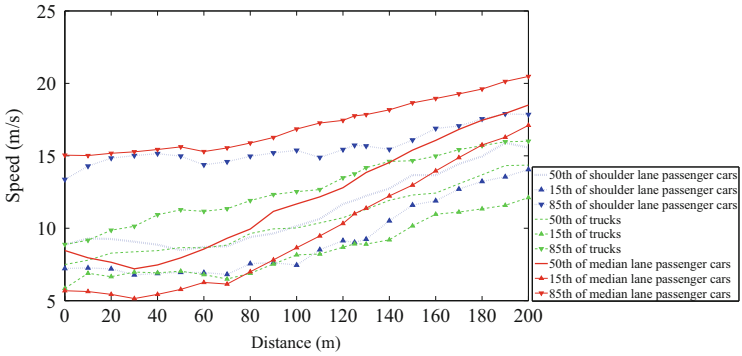

Fig. 2 Speed distributions (15th percentile, median and 85th percentile)

3.2 Statistical Analysis on Speed Data

This section presents the statistical analysis on driver speed passing the incident site. Figure 2 shows the spread in speed for each vehicle group. We can observe that there are wide variations of speed of passenger car drivers at the beginning of study section, especially the one in the median lane. From the observation of individual speed profiles, all of the passenger cars show the three reaction patterns. Measurement of central tendency suggest that most of the passenger cars in the median lane reduce the speed between $x = 20$ and 40 m, while in the right lane they reduce speed between $x = 50$ and 70 m. Since this is the point where the average speed drops, it can be assumed that the points are the rubbernecking zone, where most of the drivers reduce their speed. However, there is no speed drop for truck drivers, suggesting that most of the truck drivers continue to accelerate when passing the incident location, as conform to the speed profiles of truck drivers where majority show acceleration pattern within the study area.

Figure 3 shows the difference of mean speed between each vehicle group and the results of independent t-test. There are three sets of pairs in this test: (1) Trucks in the shoulder lane and passenger cars in the shoulder lane, (2) Trucks in the shoulder lane and passenger cars in the median lane and (3) Passenger cars in the median and passenger cars in the shoulder lane. The plots show large differences in speed between the first pair, even though both vehicle groups are in the same lane. The passenger car drivers start with a higher speed than truck drivers, but the wide difference in speed between them is closer towards the incident site, hence there is no statistical difference in speed between the two groups between $x = 90$ and 120 m. After passing the incident, the difference continues to increase with a slow rate, due to trucks capability to accelerate.

As for the second pair, the approaching mean speed of passenger cars in the median lane is higher than trucks drivers but the difference decreased until there is no significant difference between $x = 30$ and 40 m. This is believed to be where the

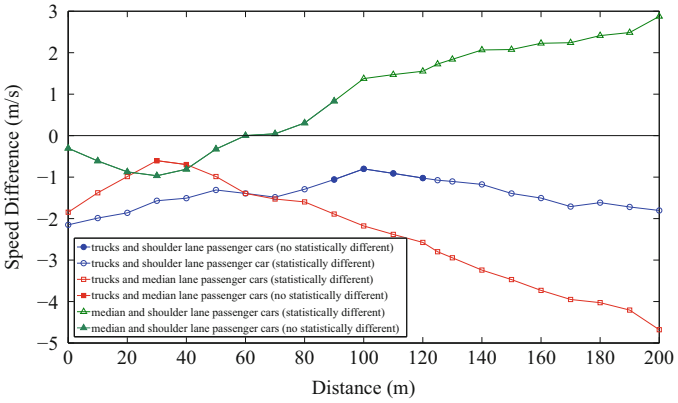

Fig. 3 Mean speed difference and independent t-test

drivers drive at the lowest speed to look on the incident. After passing this point, the passenger cars continue to speed up and resulting a large difference in mean speed.

Between the passenger cars, shoulder lane drivers approaching the incident location with a slightly higher speed than median lane drivers, but there is no significant difference in speed. At $x = 60$–80 m, the difference in mean speed between this vehicle groups is nil. After this point, the median lane passenger cars accelerate and increase the difference between these two vehicles.

4 Discussion

This study provides the insight into heterogeneity of vehicle speed in rubbernecking behaviour. The analysis shows that there is a high variation in speed profiles between individual vehicles. The variation in speed of passenger cars are higher upstream of incident site and lower downstream of the incident site. It was found that the lowest speed of median lane vehicles is further upstream than shoulder lane passenger cars, within $x = 25$–70 m. On the other hand, the shoulder lane passenger cars reduce the speed when closer to the incident scene. This can be described by the location of the incident itself. Since the passenger cars in the median lane is close to median (where the incident happened), the drivers are aware of the incident earlier than drivers in the shoulder lane. In contrast, variation in speed of trucks is low and constant through out the incident area. They mainly accelerate through the section, indicating that they had to slow down for the congestion caused by the other drivers, but they anticipated and started accelerating earlier, thus the rubbernecking zone of trucks is nowhere to be found in the study section.

There is significance difference in mean speed between vehicles in median and shoulder lanes. However, the mean speed difference in the upstream of incident is

lower compared to downstream, and at certain points the results show no statistical difference in mean speed between these vehicle groups. Further examination on individual speed profiles shows that passenger cars in the median lane are significantly affected by the incident, and demonstrate a sharp deceleration when approaching the incident scene. On the other hand passenger cars in the shoulder lane approach the incident with a higher speed than those in the median lane. Some drivers, however, were not affected by the existence of incident and maintain a steady speed, suggesting that not all vehicles choose to slow down the vehicles while passing an incident site.

Conclusions and Future Work

This study analyzed the rubbernecking behaviour in the opposite direction of the freeway accident, and shows that there is high variation in driver behaviour under incident conditions due to different driver reaction. Passenger cars in the median lane show a much higher variation in speed. Truck drivers, all in the shoulder lane, showed a completely different type of behaviour. Drivers of passenger car in the shoulder lane showed a more dynamic behaviour than the truck drivers, but speed variations were less than the passenger cars in the median lane. The findings show that the speed of individual vehicle varies between vehicle class, occupying lane and visibility of the incident. Vehicles in either the same or different groups react differently while passing an incident.

This study gives an insight into underlying processes that leads to a speed reduction and variation in non-incident direction. The results provide a better understanding of underlying activity in rubbernecking and can be used to establish a framework in quantifying the rubbernecking effects. In this study, we did not differentiate between speed reductions due to car-following behaviour and speed reductions due to rubbernecking. And also the variation of other parameter such as headway and reaction time, as well as lane changing behaviour. This will get more attention in future work.

References

1. V.L. Knoop, S. Hoogendoorn, H. van Zuylen, Capacity reduction at incidents: empirical data collected from a helicopter. Trans. Res. Rec.: J. Transp. Res. Board **2071**, 19–25 (2008)
2. V.L. Knoop, S. Hoogendoorn, K. Adams, Capacity reductions at incidents sites on motorways. Eur. J. Transp. Infrastruct. Res. **9**, 363–379 (2009)
3. V.L. Knoop, H.J. van Zuylen, S.P. Hoogendoorn microscopic traffic behaviour near incidents, in *Transportation and Traffic Theory 2009: Golden Jubilee*, ed. by W.H.K. Lam, S. C. Wong, H.K. Lo (Springer, New York, 2009), pp. 75–97

4. J.P. Masinick, B.L. Smith, An analysis on the impact of rubbernecking on urban freeway traffic, no. UVACTS-15-0-, University of Virginia, Charlottesville, 2004
5. V.L. Knoop, S.P. Hoogendoorn, H.J. van Zuylen, Processing traffic data collected by remote sensing. Transp. Res. Rec.: J. Transp. Res. Board **2129**, 55–61 (2009). Transportation Research Board of the National Academies, Washington, D.C.

Why Does Traffic Jam Acts Universally?

Tsumugi Ishida and Yūki Sugiyama

Abstract The theoretical reason for the existence of universal features of traffic jams forming in various places and with different number of cars on highways is provided using exact solutions of a mathematical model for traffic flow, the Optimal Velocity (OV) model. The OV model well reproduces real traffic data of jams in several aspects, such as the critical density of jam formation, the velocity of a jam cluster, etc. where each value is almost universal. The OV model with Heaviside step function as OV-function has essentially the same properties as a realistic OV model. Recently, we have obtained exact solutions of jam flow in the model for an arbitrary number of cars $N > 3$ and car-density. In the solutions, the dependence on N and the density are exponentially reduced for $N \to \infty$. This means that the properties of jams with more than about ten cars are almost the same as that of an infinite jam. This result is originated in the fact that the model is built mathematically based on the concept that traffic flow is a non-equilibrium dissipative system. This explains the universality of jam flow.

1 Introduction and OV Model

Traffic jams appear on a highway in several places, with different numbers of cars and under different conditions of the road. However, the properties of traffic jams, such as the critical car-density of emergence of a jam, the fundamental diagram (the relation between car-density and flow), the velocity of a cluster of jam, etc. These properties are very common independent of such conditions. We naturally wonder why traffic jams act highly universal. The question seems naive, but the answer is not trivial at all. In this paper we provide a physical and mathematical answer using the exact solution of a traffic flow model, the Optimal Velocity model.

T. Ishida • Y. Sugiyama (✉)
Department of Complex Systems Science, Nagoya University, 464-8601 Nagoya, Japan
e-mail: sugiyama@phys.cs.is.nagoya-u.ac.jp; sugiyama@is.nagoya-u.ac.jp

M. Chraibi et al. (eds.), *Traffic and Granular Flow '13*,
DOI 10.1007/978-3-319-10629-8_60

The OV model is a minimal 1-dimensional system of particles with nonlinear asymmetric interactions and a dissipative (viscous) term, which was first introduced as a traffic flow model in [1, 2]. The equation of motion is formulated as

$$\frac{d^2x_n}{dt^2} = a\left(V(\Delta x_n) - \frac{dx_n}{dt}\right), \tag{1}$$

where x_n is the position of the nth car, and $\Delta x_n = x_{n+1} - x_n$ is the headway distance. a is a control parameter, which dimension is the inverse of time. The OV-function $V(\Delta x_n)$ determines the interaction with a car moving ahead. $V(\Delta x_n)$ should be a sigmoidal function. The model well describes the emergence of a jam in traffic flow and clearly explains its physical mechanism.

As for the simple case choosing the Heaviside step-function as OV-function, such that $V(\Delta x) = 0$ for $\Delta x < d$, and $V(\Delta x) = v_{max}$ for $\Delta x \geq d$, the emergence of a traffic jam is observed as in Fig. 1.

The jam flow solution in this model can be obtained analytically based on some hypothesis, which is justified for the case of large N [3]. Moreover, the N-body problem for the jam flow solution is exactly solved for $N = 2, 3, 4, \cdots$, in the special case of car-density $L/N = d$ [4]. Recently, we have obtained the most general jam flow solution for arbitrary N and L.

The profile of a jam flow is described by a limit cycle solution in the phase space $(\Delta x_n, \frac{dx_n}{dt})$, which expresses the two regions in a jam cluster and that cars move smoothly [2]. Profiles of jam flow solutions for several N, L, and car-densities are presented in Fig. 2.

We notice that solutions with the same density L/N but with different number of cars N, are different. However, these differences seem to be reduced for large N.

In this paper, using the exact solution for an arbitrary number of cars N and length of circuit L, we discuss the universality of traffic jams.

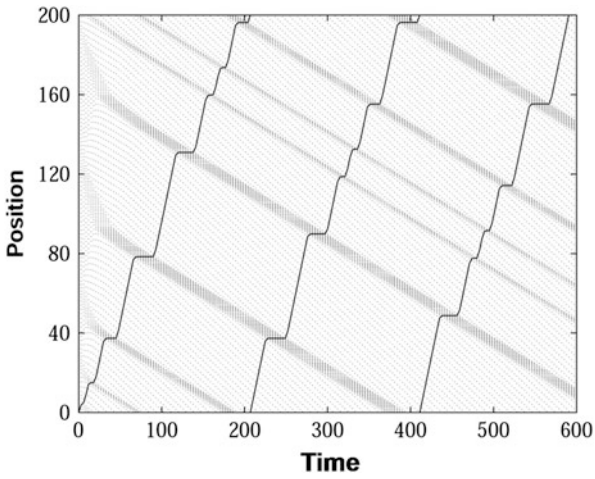

Fig. 1 Plot of all cars, $N = 100$, for the process of jam formation on a circuit in the OV model with Heaviside step function as OV-function. The initial condition is set as homogeneous flow. The orbit for a car is represented as an example

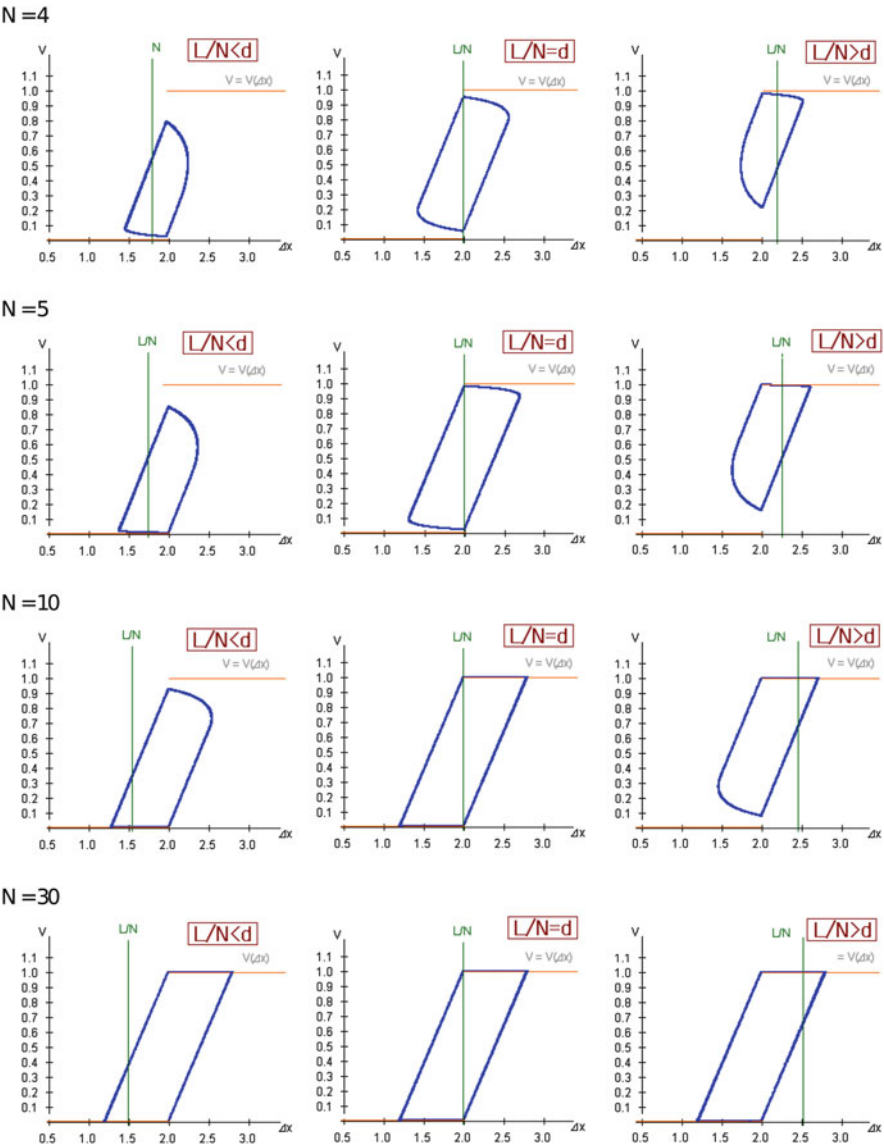

Fig. 2 Profiles of jam flow solutions (limit cycles) for $N = 4, 5, 10, 30$ with several densities, $L/N = d \pm \epsilon$. The horizontal axis is the headway distance Δx, and the vertical axis is the velocity $\frac{dx}{dt}$

2 Procedure of Solving the OV Model

The equation of motion Eq. (1) consists of two parts according to $\Delta x < d$ or $\Delta x \geq d$. Each case is easily solved as follows. At the initial condition, $x_n(t_0)$, $\dot{x}_n(t_0)$ for $t = t_0$, in the case $\Delta x < d$,

$$x_n(t) = x_n(t_0) + \frac{\dot{x}_n(t_0)}{a}(1 - e^{-a(t-t_0)}), \tag{2}$$

and in the other case $\Delta x \geq d$,

$$x_n(t) = x_n(t_0) + v_{max}(t - t_0) - \frac{v_{max} - \dot{x}_n(t_0)}{a}(1 - e^{-a(t-t_0)}) \tag{3}$$

The motion of each particle is constructed by changing these two solutions depending on its headway distance Δx. The important point for obtaining a jam flow solution is how to connect the above two solutions in the appropriate condition.

If we obtain five unknown variables, we can determine the connection condition to build up a jam flow solution for N and L. They are the following: The velocity v_{RB} of a particle at the time when $\Delta x = d$ where the solution changes from Eqs. (2) to (3), and the velocity v_{BR} when the solution changes from Eqs. (3) to (2); the time delay τ; the period of the same relative position shifting one number of particle, satisfying $x_n(t + \tau) = x_{n+1} - v_c\tau$; the shift of time beyond τ, denoted by Δt, that is the difference between the period in $\Delta x < d$ and that in $\Delta x > d$; and v_c, the velocity of a cluster moving in the opposite direction of the car motion. We can write down five independent equations including the above five unknown variables and derive these variables from the solution.

3 Exact Solution of a Jam Flow

A cluster flow solution for a given arbitrary number of cars, N and circuit length, L, with a density $L/N = d + \epsilon$, $(\epsilon \geq 0)$ is expressed by using five unknown variables; v_{RB}, v_{BR}, v_c, τ, Δt.[1] They are obtained as

$$v_{RB} = \frac{v_{max}(1 - e^{\frac{N}{2}a(\tau - \Delta t)})}{(1 + e^{\frac{N}{2}a\tau})(1 - e^{\frac{N}{2}a\tau})}, \tag{4}$$

$$v_{BR} = \frac{v_{max}(1 - e^{-\frac{N}{2}a(\tau - \Delta t)})}{(1 + e^{-\frac{N}{2}a\tau})(1 - e^{-\frac{N}{2}a\tau}),} \tag{5}$$

[1] The solution with a density $L/N = d - \epsilon$ is also obtained, which has the symmetry of duality.

$$v_c = \frac{d - \frac{1}{2}v_{max}\tau}{\tau} + f(\Delta t; N), \tag{6}$$

$$\frac{a\tau(1 + e^{-\frac{N}{2}a\tau})(1 - e^{-\frac{N}{2}a\tau})}{1 - \frac{e^{-\frac{N}{2}a\tau}(e^{-\frac{N}{2}a\Delta t} + e^{\frac{N}{2}a\Delta t})}{2}} = 2(1 - e^{-a\tau}), \tag{7}$$

where $f(\Delta t; N)$ is given as

$$f(\Delta t; N) = \frac{v_{max}}{2a\tau} \frac{e^{\frac{N}{2}a\Delta t} - e^{-\frac{N}{2}a\Delta t}}{e^{\frac{N}{2}a\tau} - e^{-\frac{N}{2}a\tau}}(1 - e^{-a\tau}). \tag{8}$$

The difference of density from the self-dual case $d = L/N$, denoted by ϵ, is expressed with Δt as

$$\epsilon = \frac{v_{max}\Delta t}{2} - f(\Delta t; N)\tau \tag{9}$$

4 Rapid Convergence to the Universal Solution for Large N

The property of convergence for large N in the formula of the obtained solution is determined by the largest of the two values $a\tau$ and $a\Delta t$. Figure 3 shows the relation

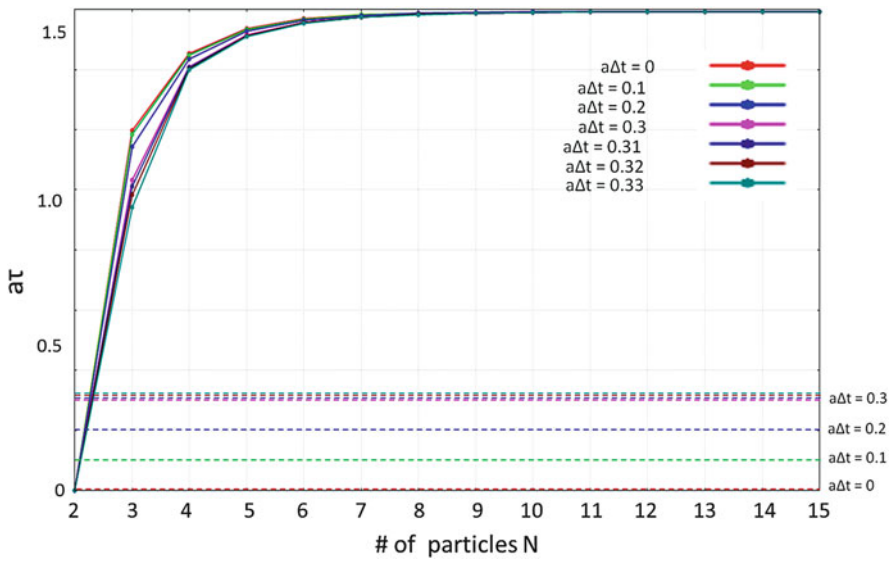

Fig. 3 N-dependence of $a\tau$ and $a\Delta t$

obtained by solving Eq. (7) numerically for given N, which indicates

$$a\tau > a\Delta t, \tag{10}$$

for $N \geq 3$. Thus, $f(\Delta t; N) \to 0$ for $N \to \infty$ in Eq. (8), and Eqs. (4)–(7) are reduced to

$$v_{RB} = 0, \tag{11}$$

$$v_{BR} = v_{max}, \tag{12}$$

$$v_c = \frac{d - \frac{1}{2}v_{max}\tau}{\tau}, \tag{13}$$

$$a\tau = 2(1 - e^{-a\tau}), \tag{14}$$

independent of Δt or ϵ, which means independent of the density L/N. The jam flow solution for $N \to \infty$ is already known 10 years before [3]. In addition, as for Eq. (9),

$$\epsilon = \frac{v_{max}\Delta t}{2}. \tag{15}$$

Jam flow solutions depending on N and L converge exponentially, as $e^{-\frac{N}{2}a\tau}$ and $e^{-\frac{N}{2}a\Delta t} \to 0$, for large N to the universal self-dual solution. They are independent of the car density $L/N = d \pm \epsilon$ and the number of cars N. Based on these results, we can explain analytically that the motion of every car in a jam flow built with more than several 10 cars shows the same universal profile of the limit cycle as in Fig. 2.

5 Answer of the Question

The property of the rapid convergence to the universal profile of the limit cycle solution for jam flow explains that any jam flow shows the same behavior with the common features independent of the condition and situation on real highways.

The characteristic factor of convergence as $e^{-\frac{N}{2}a\tau}$ is originated in the dissipative (viscous) term in the basic equation of motion in OV model. This is evidence that phenomena of traffic flow, such as jam flow, follow from the dissipative features in physics.

References

1. M. Bando, K. Hasebe, A. Nakayama, A. Shibata, Y. Sugiyama, Phys. Rev. E **51** 1035 (1995); Jpn. J. Ind. Appl. Math. **11** 203 (1994)
2. Y. Sugiyama, in *Traffic and Granular Flow*, ed. by D.E. Wolf, M. Schreckenberg, A. Bachem (World Scientific, Singapore/River Edge, 1996), p. 137
3. Yūki Sugiyama and Hiroyasu Yamada: Phys. Rev. E **55**, 7749 (1997)
4. Y. Sugiyama, K. Masuoka, T. Ishida, *Traffic and Granular Flow '07* (Springer, Berlin, 2009), p. 555

Stability and Homogenization of the Optimal Velocity Model

Antoine Tordeux

Abstract Local and collective stability analysis give the conditions for that the stationary solutions of car-following models are uniform. Recent homogenization methods allow to obtain sufficient conditions for that the system converges with no collision to the uniform solution. These conditions are calculated and illustrated by numerical experiments with the linear optimal velocity model. As expected, the homogenization condition is more restrictive than the condition for the collective stability. More precisely, the homogenization condition corresponds to the over-damped case of the local stability.

1 Introduction

The paper is devoted to the "Optimal Velocity" (OV) car-following model for traffic developed by Bando et al. [1]. This model assumes a relaxation of the vehicle speed towards an optimal speed that is a function of the distance gap.

Let denote $x_n(t) \in \mathbb{R}$ the position of the vehicle $n \in \mathbb{N}$ at time $t \geq 0$. The dynamics of the model are the differential system

$$\begin{cases} \dot{x}_n(t) = v_n(t), \\ \dot{v}_n(t) = \dfrac{x_{n+1}(t) - x_n(t)}{\tau\, T} - \dfrac{v_n(t)}{\tau}, \end{cases} \tag{1}$$

with the parameters $\tau, T > 0$, and $n+1$ the predecessor (or leading) vehicle. Here the length of the vehicle is neglected. The parameter τ calibrates the sensitivity (or reactivity) of the driver, while T is the targeted time gap. The optimal velocity implicitly used here is the linear function $V : d \mapsto d/T$.

Due to its simple form, the model is frequently mathematically investigated in the literature. The stability conditions of the uniform solutions are well-known with the OV model. Local analysis, when the dynamics of a single vehicle is described, as well as collective (or string) stability of a line of vehicles, have been explored

A. Tordeux (✉)
Paris-Est University, 19 rue Alfred Nobel, cité Descartes, 77455 Marne-la-Vallée, France
e-mail: antoine.tordeux@enpc.fr

M. Chraibi et al. (eds.), *Traffic and Granular Flow '13*,
DOI 10.1007/978-3-319-10629-8_61

since the 1990s. See for instance [2, 3] for string analysis performed on a ring, or [1, 4] for the case of an infinite line.

In the same spirit but with more rigorous constraints, invariance and homogenization methods have been developed with more general models, see [5]. The approach, coming from the deterministic theory of infinite particles systems, is based on viability techniques. It has been recently applied to the adaptive time gap car-following model [6].

Both methods give the condition for that 1D systems of vehicles converge to uniform solutions. We propose here to bring back the stability conditions, and to calculate the homogenization conditions of the linear OV model (1). The simple form of the results allows an explicite comparison. The paper is organized as follows. Section 2 is devoted to the stability conditions, while Sect. 3 concerns the homogenization properties. The results are illustrated through simulations in Sect. 4, and discussed and resumed in the conclusion section

2 Stability Condition

We remind here successively the conditions for the local and for the collective stability of the OV model (1). The results presented are well-known, see [7].

2.1 Local Stability

Within the local stability we describe the motion of a vehicle following a leader moving at a constant speed $v_1 \geq 0$. We denote $x(t)$ the position of the consider vehicle at time $t \geq 0$ and $x_1(t) = x_1(0) + v_1 t$ the position of the leader. The dynamics are

$$\begin{cases} \dot{x}(t) = v(t), \\ \dot{v}(t) = \dfrac{x_1(t) - x(t)}{\tau T} - \dfrac{v(t)}{\tau}. \end{cases} \tag{2}$$

Let introduce $y(t) = x_1(t) - x(t) - v_1 T$. The spacing $x_1(t) - x(t)$ of the consider vehicle converges to the equilibrium spacing $v_1 T$ if $\lim_t y(t) = \lim_t \dot{y}(t) = 0$.

We have by construction $-\ddot{y}(t) = y(t)/(\tau T) + \dot{y}(t)/\tau$. The equation corresponds to the damped harmonic oscillator with angular frequency $\omega_0 = 1/\sqrt{\tau T}$ and damping ratio $\xi = (2T\omega_0)^{-1}$. The characteristic equation of this linear differential equation is $\lambda^2 + \lambda/\tau + 1/\tau T = 0$, with $\lambda \in \mathbb{C}$. All the solutions $y(t)$ are linear combinations of $e^{\lambda t}$ and $\lambda e^{\lambda t}$ terms. Hence, the spacing converges to $v_1 T$ if the real part $\Re(\lambda) < 0$. More precisely, this convergence is strictly monotone (i.e. with no oscillation, this is called over-damped for the oscillator) if the imaginary

part $\Im(\lambda) = 0$. We have here $\lambda = -\frac{1}{2T}\left(1 \pm (1 - 4\tau/T)^{1/2}\right)$, and $\Re(\lambda) < 0$ since

$$T, \tau > 0 \tag{3}$$

(except for the special case $4\tau/T \ /= 1$ where $\lambda = 0$). The spacing $v_1 T$ is then (almost) always stable. Moreover, $\Im(\lambda) = 0$ if $1 - 4\tau/T \geq 0$, i.e. the convergence is strictly monotone (or over-damped) if

$$4\tau \leq T. \tag{4}$$

An oscillating convergence to the spacing $v_1 T$ can lead to collision. This is trivially the case if $v_1 = 0$. Thus, the condition (4) locally ensures no collision.

2.2 *Collective Stability*

We consider here an infinite line of vehicles. One denotes the density level $\rho > 0$. The uniform (or homogeneous) solution H is such that $x_{n+1}^H(t) - x_n^H(t) = 1/\rho$ and $x_n(t) = x_n(0) + v_\rho t$, for all n and all $t \geq 0$, with $v_\rho = \frac{1}{T\rho}$. The homogeneous configuration is an equilibrium solution.

If $y_n(t) = x_n(t) - x_n^H(t)$, the solution H is said to be stable if $\lim_t y_n(t) = \lim_t \dot{y}_n(t) = 0$ for all n. It is easy to check using (1) that $\ddot{y}_n(t) = \alpha(y_{n+1}(t) - y_n(t)) + \beta \dot{y}_n(t)$, with $\alpha = 1/(\tau T) > 0$ and $\beta = -1/\tau < 0$. The characteristic equation of the system is $\lambda_\theta^2 - \beta\lambda_\theta + \alpha\left(1 - e^{i\theta}\right) = 0$, with $\lambda_\theta \in \mathbb{C}$ and $\theta \in \mathbb{R}$. All the solutions $y(t)$ are linear combinations of $e^{\lambda_\theta t}$ and $\lambda_\theta e^{\lambda_\theta t}$, and the homogeneous configuration is stable if $\Re(\lambda_\theta) < 0$ for all $\theta \in (0, 2\pi)$.

Solving the characteristic equation, it is well-know that stability holds if $\alpha(1 + \cos\theta) < \beta^2 \Leftarrow 2\alpha < \beta^2$ (see for instance [1]), that is, using the initial parameter,

$$2\tau < T. \tag{5}$$

Note that for a general optimal speed function $V \in C^1$, the condition, corresponding to the *linear* stability condition, is $0 < V'(1/\rho) < 1/(2\tau)$, and that the strict inequality is a simple one for the case of a finite system (ring).

The condition obtained for the collective stability is stronger than the condition for local stability (3), but weaker than that of the over-damped local stability (4).

3 Homogenization Condition

The homogenization condition of the optimal velocity model are calculated as in [6] with the adaptive time gap model. The method is extracted from deterministic theory of infinite particles systems. It consists to use an equivalent system of spatial variables, and to determine sufficient conditions for that it exists invariant

(viable) sets for successive difference (or spacing) variables. This enables to obtain a comparison principle, ergodic property and, after rescaling, homogenization to the macroscopic LWR model [8, 9].

The approach is close to the one use by Aw et al. [10], who used Euler/Lagrange changing of variables instead of viability techniques with invariant sets and comparison principle. Note that invariant set for spacing variables (and collision presence) is also investigated by Greenberg et al. [11] but in a different way, using discrete estimates and monotonic properties.

We propose here a brief analysis allowing to obtain the invariant sets (and refer to [6] for a complete approach). Let first introduce the variable

$$\xi_n(t) =: x_n(t) + \tau\gamma v_n(t), \qquad \gamma > 0. \tag{6}$$

Then, $(x_n, v_n)_n$ solves (1) if and only if $(x_n, \xi_n)_n$ solves

$$\begin{cases} \dot{x}_n(t) = \dfrac{1}{\tau\gamma}\big(\xi_n(t) - x_n(t)\big), \\ \dot{\xi}_n(t) = F(x_n(t), x_{n+1}(t), \xi_n(t)), \end{cases}$$
$$\text{with} \quad F(x_n(t), x_{n+1}(t), \xi_n(t)) = \tfrac{1-\gamma}{\tau\gamma}\big(\xi_n(t) - x_n(t)\big) + \tfrac{\gamma}{T}\big(x_{n+1}(t) - x_n(t)\big). \tag{7}$$

The two systems $(x_n, v_n)_n$ with (1) and $(x_n, \xi_n)_n$ with (7) are equivalent. We henceforth work with the second system, that is linear. Given any initial condition $(x_n(0), \xi_n(0))_n$, classical Cauchy-Lipschitz theorem ensures that there exists a unique solution $(x_n(t), \xi_n(t))_n$ of (7) defined for all times $t \geq 0$. Oppositely to [6], there is no requirement of using a truncated system.

Consider $0 < a < b$ and an initial configuration such that at $t = 0$

$$\begin{cases} a \leq x_{n+1}(t) - x_n(t) \leq b, \\ a \leq \xi_{n+1}(t) - \xi_n(t) \leq b, \end{cases} \qquad \forall n. \tag{8}$$

We show sufficient conditions for that (8) holds for all $t > 0$. Note that since $a > 0$, the assumption ensures that no collision appears at any time.

Let define

$$\begin{aligned} z_n^1(t) &= x_{n+1}(t) - x_n(t) - b, & z_n^3(t) &= \xi_{n+1}(t) - \xi_n(t) - b, \\ z_n^2(t) &= a - (x_{n+1}(t) - x_n(t)), & z_n^4(t) &= a - (\xi_{n+1}(t) - \xi_n(t)). \end{aligned} \tag{9}$$

We set $M(t) = \sup_{n\in\mathbb{Z}} \max_{j=1,2,3,4} z_n^j(t)$. Notice that $M(t) \leq 0$ is equivalent to (8). Let $t_* \geq 0$ such that $M(t_*) = z_{n_*}^j(t_*)$, for some $n_* \in \mathbb{Z}$ and $j \in \{1, 2, 3, 4\}$.

Suppose $j = 1$ or $j = 2$. We have using the dynamics (7)

$$\dot{z}_{n_*}^1 = \frac{1}{\tau\gamma}\left(z_{n_*}^3 - z_{n_*}^1\right) \leq 0 \quad \text{and} \quad \dot{z}_{n_*}^2 = \frac{1}{\tau\gamma}\left(z_{n_*}^4 - z_{n_*}^2\right) \leq 0, \tag{10}$$

since for both cases $z^j_{n_*}$ is maximal for, respectively, $j = 1$ and $j = 2$. Note that this step does not hold if we have used the initial speed/position variables because the signs of speed differences are not constant. For $j = 3$, we set $Y_{n_*} = ((Y_{n_*})_1, (Y_{n_*})_2, (Y_{n_*})_3) = (x_{n_*}, x_{n_*+1}, \xi_{n_*})$. We have with $B = (b, b, b)$

$$\begin{aligned}\dot{z}^3_{n_*} &= F(Y_{n_*+1} - B) - F(Y_{n_*}) = \textstyle\sum_{i=1,2,3}((Y_{n_*+1})_i - (Y_{n_*})_i - b)F_i'(Z) \\ &= z^1_{n_*} F_1'(Z) + z^1_{n_*+1} F_2'(Z) + z^3_{n_*} F_3'(Z) \le z^3_{n_*} \textstyle\sum_{i=1,2,3} F_i'(Z) = 0.\end{aligned} \tag{11}$$

using successively the fact that $F(Y + (z, z, z)) = F(Y)$ for all z, the Taylor-Lagrange development $Z = \theta(Y_{n_*+1} - B) + (1 - \theta)Y_{n_*}$ with $\theta \in [0, 1]$, the monotonicity $F_1', F_2' \ge 0$ (that remains to be proved), the fact that $z^1_{n_*} \le z^3_{n_*}$ and $\sum_{i=1,2,3} F_i' = 0$. Similarly, we get $\dot{z}^4_{n_*} \le 0$ for $j = 4$.

This formally shows that $\dot{M}(t) \le 0$. We have $M(0) \le 0$ because the initial data satisfies (8). Then a Gronwall type argument implies $M(t) \le 0$, for all $t \ge 0$.

The monotonicity assumptions used here to obtain the invariant property (8) for all t are $F_2' = \gamma/T \ge 0$, this is always true since $\gamma, T > 0$, and $F_1' = -(1 - \gamma)/(\tau\gamma) - \gamma/T \ge 0$. As $\gamma, \tau > 0$, the sign of F_1' is the sign of $g(\gamma) = -\gamma^2 \frac{\tau}{T} + \gamma - 1$. It is positive if $4\tau \le T$ and $\gamma \in \left[T\left(1 \pm (1 - 4\tau/T)^{1/2}\right)(2\tau)^{-1}\right]$.

The results show that if $4\tau \le T$, there exists $\gamma > 0$ for that (8) holds for all $t \ge 0$. Using the equivalence of the systems, the homogenization condition of the model (1) is then simply

$$4\tau \le T. \tag{12}$$

For a general optimal speed function $V \in C^1$, the homogenization condition is $0 < V'(d) < 1/(4\tau)$ for all $d \in [a, b]$. Note that bounds on vehicle speed $V(a) \le v_n(t) \le V(b)$ for all n and all $t \ge 0$ can be obtain with no more assumption on $V(.)$ and τ (only more constraint initial data and γ parameter).

As expected, the homogenization condition (12) implies the stability condition (5). Yet, it is surprising to see that the homogenization condition, that is only a sufficient condition, directly coincides with the local over-damped one (4).

4 Simulation Experiments

Some simulations are presented to illustrate the results. One considers a 20-long ring, with 10 vehicles and initial jam condition ($\min_n x_{n+1}(0) - x_n(0) = a = 0.1$).

Two experiments are realized: One with $T/\tau = 2$, corresponding to solely stable conditions, see Fig. 1; The second with $T/\tau = 4$, corresponding to stable and homogenization conditions, see Fig. 2.

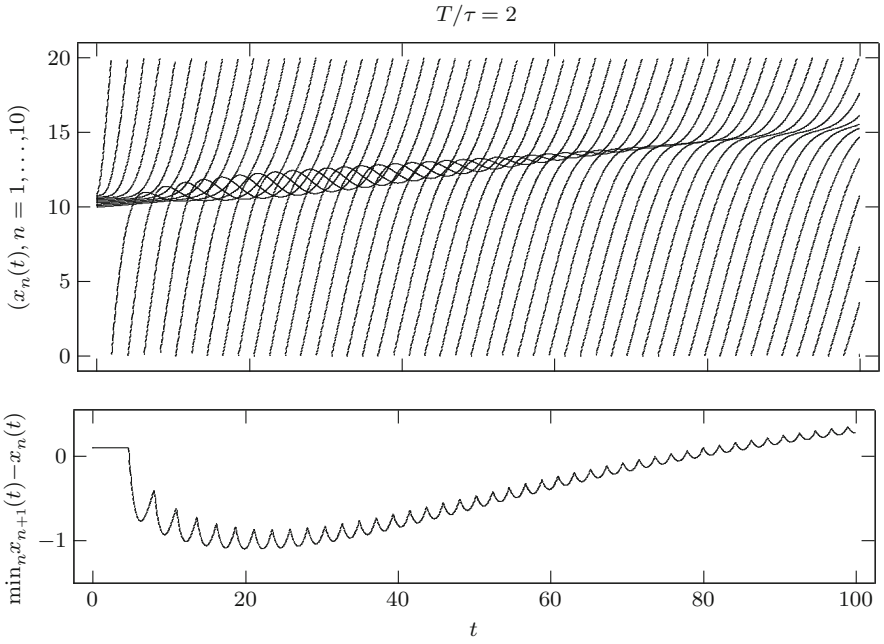

Fig. 1 *Top*: trajectories of 10 vehicles. *Bottom*: minimum spacing over the time

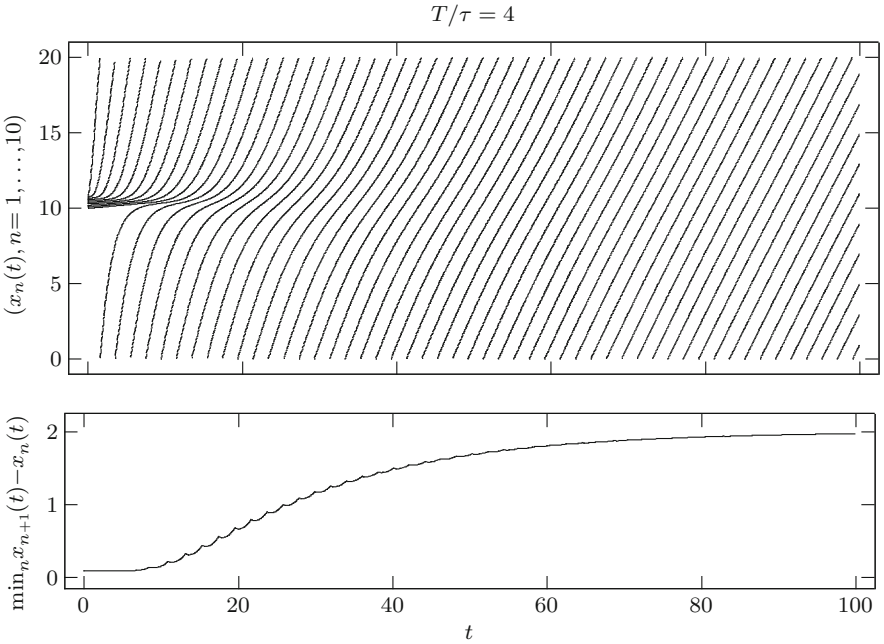

Fig. 2 *Top*: trajectories of 10 vehicles. *Bottom*: minimum spacing over the time

One observes that, as expected, the two systems convergence to an uniform solution. Yet, the set for spacing variables (8) is invariant only for the second experiment, where the homogenization condition (12) holds. For the first experiment where solely the stability condition (5) holds, one has $t > 0$, $\min_n x_{n+1}(t) - x_n(t) < a$, with collisions and unphysical behaviors.

Conclusion

Stable and homogenization conditions are investigated within the linear OV model. The results show that the condition for stability is not enough to ensure that spacing variables keep in bounded sets. This means that a system can lead to unphysical behaviors during the convergence to an uniform solution, even if the conditions are stable. No collision occurs for any initial condition when the homogenization (or local over-damped) condition holds. A space parameter can hence been suggested : Unstable (with potentially collisions in transient and stationary states), stable (with potentially collisions in transient state) and stable with no collision.

The spacings keep in invariant sets for stronger conditions than the ones for the stability, related here as the homogenization condition. For the basic linear OV model we used, the homogenization condition coincides with the condition for over-damped local stability. Since the homogeneous condition is a sufficient one, it was expected stronger than local over-damping one. This is notably the case for the adaptive time gap model, which is always locally over-damped stable while the homogenization condition is more restrictive.

References

1. M. Bando, K. Hasebe, A. Nakayama, A. Shibata, Y. Sugiyama Y, Phys. Rev. E **51**, 1035 (1995)
2. G. Orosz, G. Stépán, Proc. R. Soc. A **462**(2073), 2643–2670 (2006)
3. S. Lassarre, M. Roussignol, A. Tordeux, Phys. Rev. E **86**(3), 036207 (2012)
4. E. Wilson, Philos. Trans. R. Soc. A **366**(1872), 2017–2032 (2008)
5. N. Forcadel, C. Imbert, R. Monneau, J. Differ. Equ. **246**(3), 1057–1097 (2009)
6. R. Monneau, M. Roussignol, A. Tordeux, Invariance and homogenization of an adaptive time gap car-following model. Nonlinear Differ. Equ. Appl. NoDEA **21**(4), 491–517 (2014)
7. M. Treiber, A. Kesting, *Traffic Flow Dynamics* (Springer, Berlin, 2006)
8. M.H. Lighthill, G.B. Whitham, Proc. R. Soc. A **229**, 317–345 (1955)
9. P.I. Richards, Oper. Res. **4**(1), 42–51 (1956)
10. A. Aw, A. Klar, T. Materne, M. Rascle, SIAM. J. Appl. Math. **63**(1), 259–278 (2002)
11. J.M. Greenberg, A. Klar, M. Rascle, SIAM J. Appl. Math. **63**(3), 818–833 (2003)

Statistical Analysis of High-Flow Traffic States

Florian Knorr, Thomas Zaksek, Johannes Brügmann, and Michael Schreckenberg

Abstract We present an analysis on the characteristics of so-called high-flow states of traffic, i.e. traffic states where the flow rate exceeds 50 vehicles per minute and lane. We investigate the duration, frequency and other statistics of such states. Moreover, we study the conditions under which they occur. The factors that influence the existence and occurrence of high-flow states in traffic are, for instance, the fraction of slow vehicles, the motorways' general topology (e.g. number of lanes, slope, interchanges, ramps and exits), the flow rate on neighboring lanes, the hour of the day and day of the week.

1 Introduction

It is well known that traffic exhibits metastable states and hysteresis behavior [1]: At high vehicle flow rates, a transition from free to congested flow is likely to occur—resulting in a considerable decrease of the flow rate and significant changes of other traffic characteristics such as the average velocity. To restore high traffic flows after such a transition, it is necessary that the flow rate drops below a threshold value first.

But states of high traffic flow are not only interesting from a physical point of view. At high flow rates, the road is operating close to its optimum. Therefore, it is also of practical importance to investigate under what conditions these so-called high-flow states occur.

We will present an analysis of detector data collected from the motorway network of the German state of North Rhine-Westphalia (e.g., see [2, 3]). This analysis focuses on the characteristics of so-called high-flow states (e.g., when and how often do they occur, on which lane can they usually be observed). In the following, we refer to a flow rate as high, if it exceeds 50 vehicles per minute and lane (i.e., 3,000 veh/h/lane).

F. Knorr (✉) • T. Zaksek • J. Brügmann • M. Schreckenberg
Fakultät für Physik, Universität Duisburg-Essen, 47048 Duisburg, Germany
e-mail: florian.knorr@uni-due.de; thomas.zaksek@uni-due.de;
johannes.bruegmann@uni-due.de; michael.schreckenberg@uni-due.de

M. Chraibi et al. (eds.), *Traffic and Granular Flow '13*,
DOI 10.1007/978-3-319-10629-8_62

2 Analyzed Data

Our analysis is based on detector data provided by more than 3,000 loop detectors during December 19, 2011 and May 31, 2013 on the motorway network of the state of North Rhine-Westphalia. Inductive loop detectors still are the most common source of traffic data: for each (1 min)-interval, loop detectors count the number of passing vehicles, they measure the vehicles' velocity distinguished by vehicle type (passenger cars and trucks), and they determine the fraction of time within they are covered by passing vehicles.

We restricted our analysis to 178,800 measurements exhibiting high flow characteristics (flow >50 veh/min) and to valid values only for each of the just mentioned observables. Figure 1 shows the frequencies of high-flow states depending on the corresponding flow rate (Fig. 1a). It turns out that, up to flow rates of about 73 veh/min, the frequencies of high-flow states of a given flow rate J follow the power law

$$\text{frequency} = A \times \exp(-\alpha \times J)$$

with $A \approx 3.11 \times 10^{14}$ and $\alpha \approx 0.44$.

For the small number of data sets with a higher flow rate (less than 0.03 %, 47 total) it is not clear whether they actually deviate from the power law or whether these data sets indicate erroneous measurements: As we will see, the average velocity of high-flow states varies between 60 and 120 km/h. Therefore, high flow rates with an average time headway of 1 s and less pose an actual risk for drivers. Even though such time headways have already been observed at similar velocities for single vehicles [4], it may be doubted whether this behavior can be observed for a sequence of 70 (and more) vehicles.

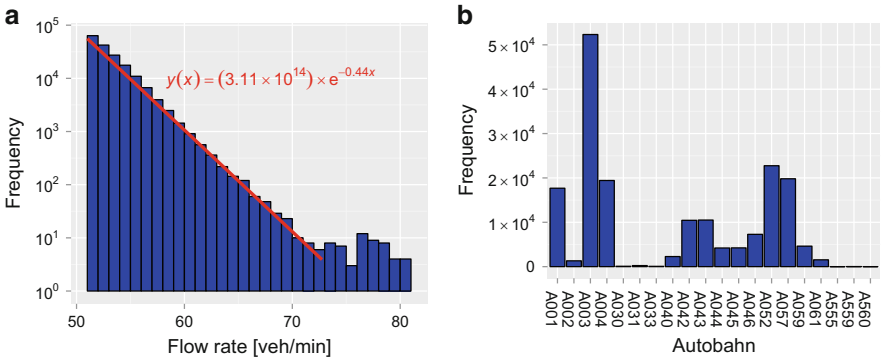

Fig. 1 (**a**) Frequency of high-flow states and (**b**) the number of the Autobahn

3 Share of Trucks and Lane Usage

As the detectors used for this analysis classify the detected vehicles into two groups [5], namely 'trucks' and 'passenger cars', we can also investigate the influence of heterogeneous traffic flow on the occurrence of high-flow states. From Fig. 2a it becomes obvious that the likelihood of high traffic flows decreases with an increasing share of trucks contributing to the total flow rate. This phenomenon is caused by trucks that generally are restricted to a velocity of 80 km/h in Germany. Therefore, trucks lower the maximum achievable average velocity in traffic flow and, due to their length, they block detectors for a longer period. On the other hand, high traffic flows require high average velocities (60–120 km/h). Consequently, high-flow traffic states are expected to favor an almost homogeneous flow of the faster passenger cars.

At least some high-flow traffic measurements including trucks may be explained by the classification of the detector loops: light trucks (e.g., SUVs and small buses/vans) are classified as trucks, but the general speed limit for trucks does not apply to them and they exhibit driving characteristics similar to passenger cars.

For a similar reason the occurrence of high traffic flows is practically limited to the leftmost lane (see Fig. 2b). In Germany, the leftmost lane is reserved for fast-traveling vehicles to overtake, whereas the right lane is reserved for slow vehicles (i.e., usually trucks). Therefore, traffic flow on the left and middle lanes is characterized by a relatively low share of trucks and high average velocities, which facilitates the formation of high flow rates.

These results also confirm an observation first made by Sparmann [6] and Leutzbach and Busch [7] that is known as *lane inversion*: They found that, close to the optimal flow rate, the vehicle density in the left lane surmounts the density in the right lane. This observation surprises as by German law drivers are required to use the right (and middle) lane whenever possible.

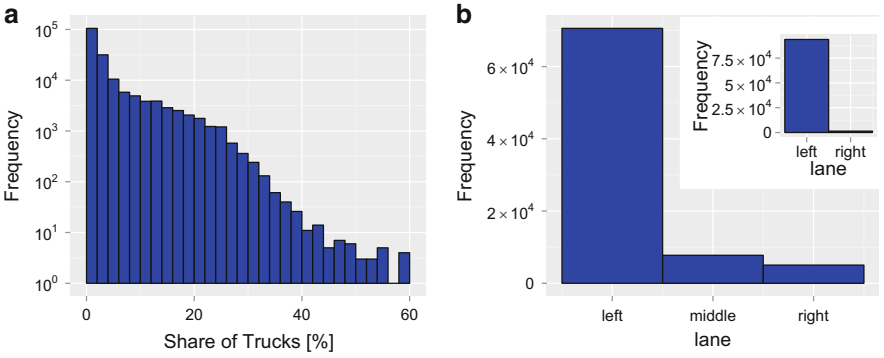

Fig. 2 Frequencies of high-flow traffic states (**a**) for a given share of trucks and (**b**) resolved by the lane, on which they were observed for three-lane and two-lane (*inset*) motorways

4 Average Velocities of High-Flow Traffic States

As already stated in the previous section, the average velocities of high-flow states range from approximately 60–120 km/h. In Fig. 3a, one can see the distribution of the average velocities. For better analysis, these measurements were subdivided into two classes: (i) measurements without trucks (in this case the depicted average velocity is identical to the average velocity of all cars on the road) and (ii) measurements in which at least one vehicle was identified as a truck.

From these histograms we see that the average velocity in homogeneous traffic, consisting of passenger cars only, is considerably higher than in mixed traffic of passenger cars and trucks with a single peak at approximately 100 km/h. In mixed traffic, we observe two peaks: one at 100 km/h and another one at approximately at 60 km/h. The first one (at 100 km/h) corresponds to a very low number of trucks contributing to the total flow. The second one results from measurements with roughly four or more trucks. This could be verified by varying the threshold (i.e., the number of trucks) which separate the two curves (not depicted). It should also be noted that the classification of vehicle types, which is mostly based on the estimated vehicle length [5], is not free of fault. Therefore, it is safe to assume that a certain amount of the measurements which contributed especially to the first peak consisted of passenger cars only.

Figure 3b shows the difference in the average velocities of trucks and passenger cars for the observed high flow states. This histogram illustrates very well the synchronization of average velocities in high traffic flow: the distribution's mean is at 0 km/h (0.52 km/h) with a variance of $\sigma^2 \approx 35\,\mathrm{km/h}^2$. Moreover, the resulting distribution is strongly peaked around its mean (leptokuric with a sample excess kurtosis of 3.89).

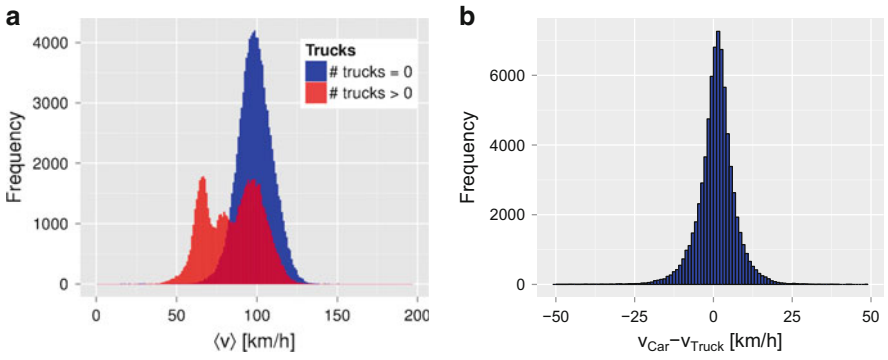

Fig. 3 Average velocities $\langle v \rangle$ of high-flow states and the difference in the average velocities of trucks (v_{Truck}) and cars (v_{Car})

5 Temporal Occurrences and Lifetimes of High-Flow Traffic States

The histograms given in Fig. 4 show the temporal occurrence and the duration (i.e., lifetime) of high-flow states. If one considers that a high flow rate indicates a high traffic volume, the results of Fig. 4b, c are easy to understand. High-flow states occur on work days during peak-hours. At these times, there is a huge demand of commuters (i.e., many passenger cars) traveling to or from work.

As the lifetime of a high-flow state we defined the number successive (1 min)-intervals that were classified as "high-flow state". The resulting distribution of lifetimes is given in Fig. 4d. One can easily see that such states hardly last longer than a few minutes. This observation only confirms the long-known metastable character of traffic flow: An increased flow rate also increases the probability of a traffic breakdown [1, 8]. Especially at flow rates such as the ones considered in

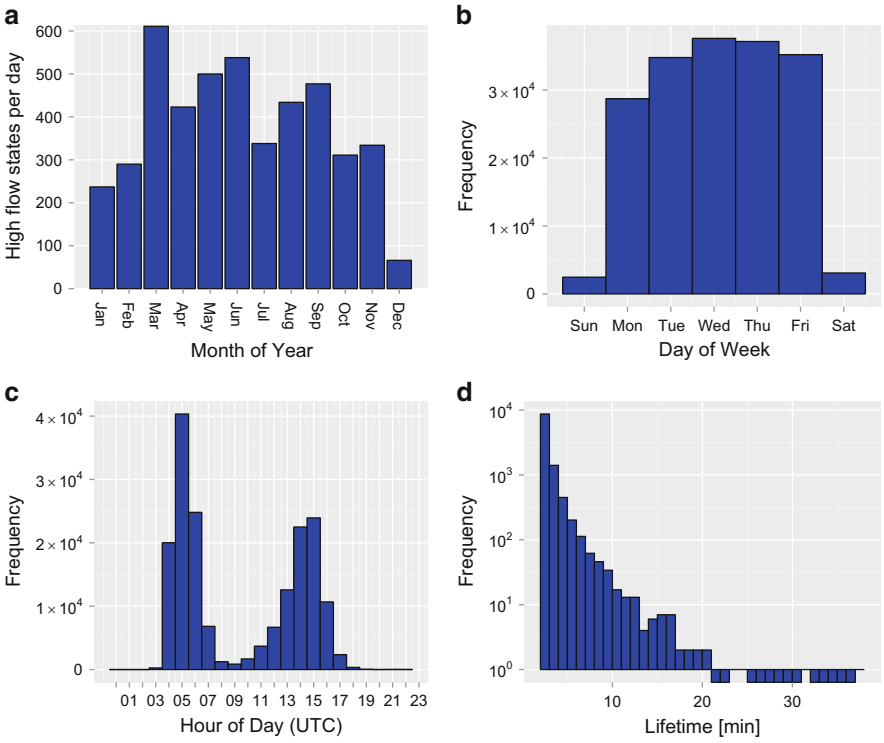

Fig. 4 Temporal distribution of high-flow states depending on (**a**) the month, (**b**) the weekday, and (**c**) the hour of day. (The hour of day is given as UTC. The actual hour of day follows by adding 1 or 2 h—depending on daylight saving time.) (**d**) The frequency of successive measurements classifying as high-flow

this article traffic flow is very unstable and long-lasting high-flow states could not be expected.

Conclusions
The findings of our analysis can be summarized as follows: high-flow states make high demands on the traffic conditions.

- As a large number of vehicles is required for high-flow states, such states are usually observed during the morning and evening peak hour on workdays (from Monday to Friday).
- The requirement of good road conditions is reflected by the fact that high-flow states are more likely to be observed in the summer.
- The share of trucks must be close to zero for high flows to occur as high average velocities are required. The lower the share of trucks, the higher is the average velocity.
- The lifetime of high-flow states is typically limited to intervals of a few minutes length because traffic flow tends to be very unstable on this regime.

Acknowledgements JB and FK thank the German Research Foundation (DFG) for funding under grant no. SCHR 527/5-1.

References

1. A. Schadschneider, D. Chowdhury, K. Nishinari, *Stochastic Transport in Complex Systems: From Molecules to Vehicles* (Elsevier Science, Oxford, 2010)
2. S. Hafstein, R. Chrobok, A. Pottmeier, M. Schreckenberg, F. Mazur, Comput.-Aided Civ. Infrastruct. Eng. **19**, 338–350 (2004)
3. J. Brügmann, M. Schreckenberg, W. Luther Real-time traffic information system using microscopic traffic simulation, in *Proceedings of the 8th EUROSIM Congress on Modelling and Simulation*, Cardiff, 2013, pp. 448–453
4. C. Appert-Rolland, Phys. Rev. E, **80**(3), 036102 (2009)
5. Bundesministerium für Verkehr, Bau und Stadtentwicklung, *Technische Lieferbedingungen für Streckenstationen: TLS 2002* (Wirtschaftsverl. NW, Verlag für Neue Wiss, Bremerhaven, 2002)
6. U. Sparmann, *Spurwechselvorgänge auf zweispurigen BAB-Richtungsfahrbahnen*. Forschung Straßenbau und Straßenverkehrstechnik (Bundesministerium für Verkehr, Bonn, 1978)
7. W. Leutzbach, F. Busch F, *Spurwechselvorgänge auf dreispurigen BAB-Richtungsfahrbahnen* (Universität Karlsruhe, Karlsruhe, 1984)
8. B. Persaud, S. Yagar, R. Brownlee, Transp. Res. Rec. **1634**, 64–69 (1998)

Simulations of Synchronized Flow in TomTom Vehicle Data in Urban Traffic with the Kerner-Klenov Model in the Framework of the Three-Phase Traffic Theory

Gerhard Hermanns, Igor N. Kulkov, Peter Hemmerle, Hubert Rehborn, Micha Koller, Boris S. Kerner, and Michael Schreckenberg

Abstract In this article, we describe our simulations of TomTom probe vehicle data measured in city traffic. An analysis of the vehicle trajectories in the TomTom data reveals the typical features of the traffic phases as defined in Kerner's three-phase traffic theory: free flow, synchronized flow and wide moving jam (moving queues). The existence of the synchronized flow phase has previously been found within traffic data from highways, but not within data from urban road networks. We will show that the microscopic simulation of vehicular traffic with the stochastic Kerner-Klenov model on a multi-lane urban road stretch reproduces the synchronized flow found in the TomTom data.

1 Introduction

In three-phase traffic theory in addition to the free flow traffic phase there are two phases in congested traffic: the synchronized flow phase and the wide moving jam phase. Up to now synchronized flow has been studied empirically and theoretically in highway traffic only. As we have found recently by empirical studies of TomTom vehicle probe data in oversaturated traffic measured in Düsseldorf (Germany), synchronized flow can also be observed in city traffic [6, 7]. A theory that gives a physical mechanism as explanation of such a synchronized flow in oversaturated city traffic has recently been developed [2, 5]. In this article that is based on the aforementioned theory we present more detailed simulation results of synchronized flow in oversaturated city traffic. The article is organized as follows: In Sect. 2 we

G. Hermanns (✉) • I.N. Kulkov • B.S. Kerner • M. Schreckenberg
University of Duisburg-Essen, Lotharstr. 1, 47057 Duisburg, Germany
e-mail: gerhard.hermanns@uni-due.de

P. Hemmerle • H. Rehborn
Daimler AG, HPC: 059-X832, 71063 Sindelfingen, Germany

M. Koller
IT-Designers GmbH, Entennest 2, 73730 Esslingen, Germany

M. Chraibi et al. (eds.), *Traffic and Granular Flow '13*,
DOI 10.1007/978-3-319-10629-8_63

formulate the Kerner-Klenov model used for all simulations. In Sect. 3 we consider simulations of synchronized flow on one of the roads in the city of Düsseldorf and compare them with empirical findings of synchronized flow in oversaturated city traffic of [6,7].

2 Kerner-Klenov Stochastic Microscopic Three-Phase Traffic Flow Model

We use a discrete version of a stochastic three-phase microscopic model of Kerner and Klenov [4]. The physics of the model variables have been explained in [1] and more detailed in [8]. In the model whose parameters have been adapted for city traffic in [3], the vehicle speed v_{n+1}, the coordinate x_{n+1}, and the acceleration A_{n+1} at time step $n+1$ are found from the following equations:

$$v_{n+1} = \max(0, \min(v_{\text{free}}, \tilde{v}_{n+1} + \xi_n, v_n + a_{\max}\tau, v_{\text{s},n})), \tag{1}$$

$$x_{n+1} = x_n + v_{n+1}\tau, \tag{2}$$

$$A_{n+1} = (v_{n+1} - v_n)/\tau, \tag{3}$$

$$\tilde{v}_{n+1} = \min(v_{\text{free}}, v_{\text{s},n}, v_{\text{c},n}), \tag{4}$$

$$v_{\text{c},n} = \begin{cases} v_{\text{c},n}^{(1)} \text{ at } \Delta v_n + A_{\ell,n}\tau < \Delta v_{\text{a}}, \\ v_{\text{c},n}^{(2)} \text{ at } \Delta v_n + A_{\ell,n}\tau \geq \Delta v_{\text{a}}, \end{cases} \tag{5}$$

Δv_{a} is constant.

$$v_{\text{c},n}^{(1)} = \begin{cases} v_n + \Delta_n^{(1)} \text{ at } g_n \leq G_n, \\ v_n + a_n\tau \text{ at } g_n > G_n, \end{cases} \tag{6}$$

$$\Delta_n^{(1)} = \max(-b_n\tau, \min(a_n\tau,\ v_{\ell,n} - v_n)), \tag{7}$$

$$v_{\text{c},n}^{(2)} = v_n + \Delta_n^{(2)}, \tag{8}$$

$$\Delta_n^{(2)} = k_{\text{a}} a_n \tau \max(0, \min(1,\ \gamma(g_n - v_n\tau))), \tag{9}$$

$$a_{\max} = \begin{cases} a \quad \text{at } \Delta v_n + A_{\ell,n}\tau < \Delta v_{\text{a}}, \\ k_{\text{a}} a \text{ at } \Delta v_n + A_{\ell,n}\tau \geq \Delta v_{\text{a}}, \end{cases} \tag{10}$$

$$a_n = a\Theta(P_0 - r_1),\ b_n = a\Theta(P_1 - r_1), \tag{11}$$

$$P_0 = \begin{cases} p_0 \text{ if } S_n \neq 1, \\ 1 \quad \text{if } S_n = 1, \end{cases} \qquad P_1 = \begin{cases} p_1 \text{ if } S_n \neq -1, \\ p_2 \text{ if } S_n = -1, \end{cases} \tag{12}$$

$$S_{n+1} = \begin{cases} -1 \text{ if } \tilde{v}_{n+1} < v_n, \\ 1 \quad \text{if } \tilde{v}_{n+1} > v_n, \\ 0 \quad \text{if } \tilde{v}_{n+1} = v_n, \end{cases} \tag{13}$$

$r_1 = \text{rand}(0,1)$, $\Theta(z) = 0$ at $z < 0$ and $\Theta(z) = 1$ at $z \geq 0$, $p_0 = p_0(v_n)$, $p_2 = p_2(v_n)$, p_1 is constant.

$$\xi_n = \begin{cases} \xi_\text{a} \quad \text{if } S_{n+1} = 1, \\ -\xi_\text{b} \text{ if } S_{n+1} = -1, \\ \xi^{(0)} \text{ if } S_{n+1} = 0, \end{cases} \tag{14}$$

$$\xi_\text{a} = a^{(\text{a})}\tau\Theta(p_\text{a} - r), \ \xi_\text{b} = a^{(\text{b})}\tau\Theta(p_\text{b} - r), \tag{15}$$

$$\xi^{(0)} = a^{(0)}\tau \begin{cases} -1 \text{ if } r \leq p^{(0)}, \\ 1 \quad \text{if } p^{(0)} < r \leq 2p^{(0)} \text{ and } v_n > 0, \\ 0 \quad \text{otherwise}, \end{cases} \tag{16}$$

$r = \text{rand}(0,1)$; $a^{(\text{b})} = a^{(\text{b})}(v_n)$; p_a, p_b, $p^{(0)}$, $a^{(\text{a})}$, $a^{(0)}$ are constants; synchronization gap G_n and safe speed $v_{\text{s},n}$ are

$$G_n = G(v_n, v_{\ell,n}), \tag{17}$$

$$G(u,w) = \max(0, \lfloor k\tau u + a^{-1}\phi_0 u(u-w) \rfloor), \tag{18}$$

$$v_{\text{s},n} = \min\left(v_n^{(\text{safe})}, g_n/\tau + v_\ell^{(\text{a})}\right), \tag{19}$$

$$v_n^{(\text{safe})} = \lfloor v^{(\text{safe})}(g_n, \ v_{\ell,n}) \rfloor, \tag{20}$$

$v^{(\text{safe})}\tau_\text{safe} + X_\text{d}(v^{(\text{safe})}) = g_n + X_\text{d}(v_{\ell,n})$, $X_\text{d}(u) = b\tau^2\left(\alpha\beta + \frac{\alpha(\alpha-1)}{2}\right)$, $\alpha = \lfloor u/b\tau \rfloor$, $\beta = u/b\tau - \alpha$, $v_\ell^{(\text{a})} = \max(0, \min(v_{\ell,n}^{(\text{safe})}, v_{\ell,n}, g_{\ell,n}/\tau) - a\tau)$, τ_safe is a safe time gap; b, $k > 1$, a, k_a, and ϕ_0 are constants; $\lfloor z \rfloor$ denotes the integer part of a real number z. In (1)–(20), $n = 0, 1, 2, \ldots$ is the number of time steps, $\tau = 1\,\text{s}$ is a time step, a_max is a maximum acceleration, v_free is a maximum speed in free flow, $\tilde{v}_n$ is the vehicle speed without speed fluctuations ξ_n, ℓ marks the preceding vehicle, $g_n = x_{\ell,n} - x_n - d$ is the space gap between vehicles, d is the vehicle length, $\Delta v_n = v_{\ell,n} - v_n$; x_n and v_n are measured in units $\delta x = 0.01\,\text{m}$ and $\delta v = 0.01\,\text{m/s}$, respectively.

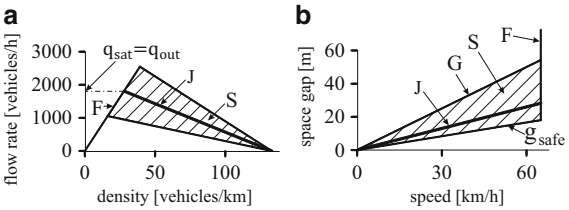

Fig. 1 2D-regions for steady states of synchronized flow in the flow–density (**a**) and the space-gap–speed planes (**b**) [3,4]. *F* – free flow, *S* – synchronized flow, *J* – line *J* [1]

In the model, vehicles decelerate at the upstream front of a moving queue at a signal as they do at the upstream front of a wide moving jam propagating on a road without traffic signals [1]. During the green phase, vehicles accelerate at the downstream front of the moving queue (queue discharge) with a random time delay as they do at the downstream jam front. In other words, the well-known saturation flow rate of moving queue discharge is equal to the jam outflow q_{out} under the condition that vehicles accelerate to the maximum speed v_{free}, i.e., in this case $q_{\text{sat}} = q_{\text{out}}$ (Fig. 1a). During the yellow phase a vehicle passes the signal location, if the vehicle can do it until the end of the yellow phase; otherwise, the vehicle comes to a stop at the signal. It is sufficient to consider traffic at a *single* city intersection. Open boundary conditions have been used in all simulations.

We use a stochastic description of the driver's speed adaptation through probabilities p_2 and p_1 in (12). Introducing a coefficient of speed adaptation ε, we write these probabilities as follows:

$$p_1 = \min(1, (1+\varepsilon)p_1^{(0)}), \quad p_2 = \min(1, (1+\varepsilon)p_2^{(0)}(v_n)), \tag{21}$$

where $p_1^{(0)} = 0.3$, $p_2^{(0)}(v_n) = 0.48 + 0.32\Theta(v_n - v_{21})$. We have found that the larger ε, the stronger the speed adaptation and, therefore, the larger the mean space gap (the longer the mean time headway) between vehicles in synchronized flow.

In accordance with the classical theory [9], well-developed oversaturated traffic consists of a sequence of moving queues with stopped vehicles separated by regions in which vehicles move from one moving queue to the adjacent downstream moving queue. The mean duration of the vehicle stop within a moving queue usually does not change while the moving queue propagates upstream of the signal (Fig. 2). Rather than such a well-known stop-and-go pattern (Fig. 2b, c), it has recently been found [6,7], that synchronized flow is very often observed in TomTom vehicle probe data in real oversaturation city traffic. Below we briefly consider this empirical data and show simulation results of synchronized flow.

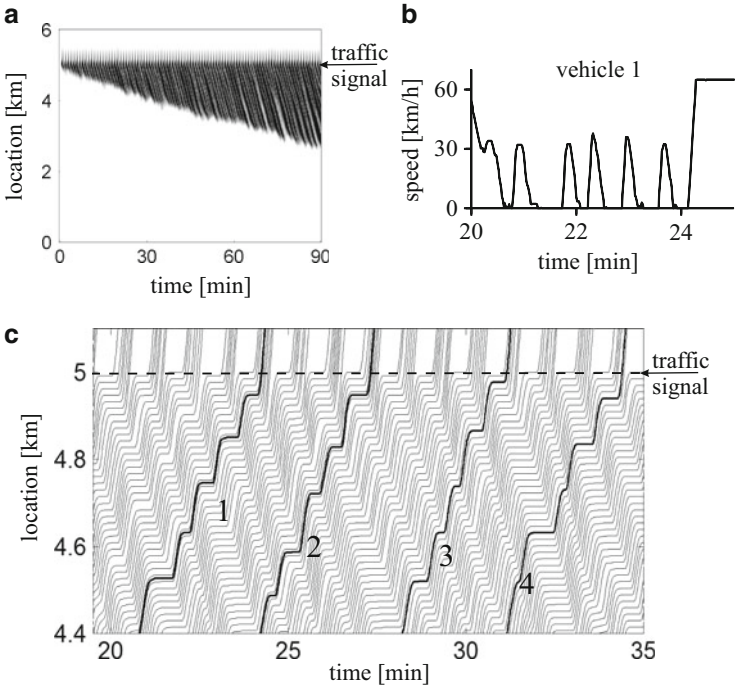

Fig. 2 Spatiotemporal structure of oversaturated traffic at a traffic signal of the classical theory of city traffic [9] simulated with model (1)–(21). In all simulations we use the following model parameters: $\tau_{\text{safe}} = \tau = 1$, $d = 7.5\,\text{m}$, $v_{\text{free}} = 18.0558\,\text{m}\,\text{s}^{-1}$ (65 km/h), $b = 1\,\text{m}\,\text{s}^{-2}$, $a = 0.5\,\text{m}\,\text{s}^{-2}$, $k = 3$, $\phi_0 = 1$, $\Delta v_a = 2\,\text{m}\,\text{s}^{-1}$, $k_a = 4$, $\gamma = 1$, $p_b = 0.1$, $p_a = 0.03$, $\varepsilon = 0$, $p^{(0)} = 0.005$, $p_0(v_n) = 0.667 + 0.083 \min(1, v_n/v_{01})$, $v_{01} = 6\,\text{m}\,\text{s}^{-1}$, $v_{21} = 7\,\text{m}\,\text{s}^{-1}$, $a^{(a)} = a$, $a^{(0)} = 0.2a$, $a^{(b)}(v_n) = 0.2a + 0.8a \max(0, \min(1, (v_{22} - v_n)/\Delta v_{22}))$, $v_{22} = 7\,\text{m}\,\text{s}^{-1}$, $\Delta v_{22} = 2\,\text{m}\,\text{s}^{-1}$

3 Synchronized Flow in Oversaturated City Traffic

In Fig. 3 we show a part of the road Völklinger Straße in Düsseldorf at which oversaturated traffic has been measured. At the beginning of the road there is a road detector that measures speed and flow rate at 1 min intervals, at the end of the road stretch there is a traffic signal.

Typical distribution of vehicle speed along TomTom probe vehicles moving through this road is shown in Fig. 4a. We can see that vehicles move almost without a stop up to the queue at the signal. In accordance with the microscopic criterion for traffic phases in congested traffic the observed oversaturated traffic is associated with the synchronized traffic flow phase. To simulate the synchronized flow we increase the parameter of drivers speed adaptation ε (21). This means that a driver on average chooses a larger space gap (time headway) to the preceding vehicle. The simulations show that due to the increase in space gaps instead of a stop-and-go

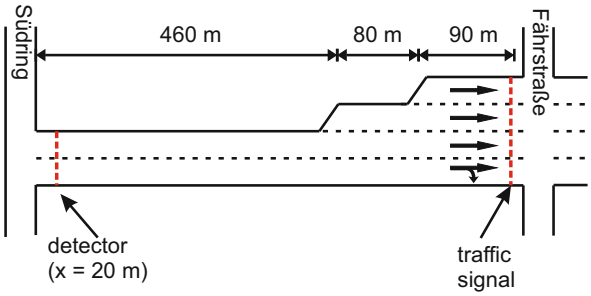

Fig. 3 Layout of test track Völklinger Straße from Südring to Fährstraße. Video detector at $x = 20$ m, traffic light at $x = 630$ m (cycle time $\vartheta = 70$ s, red phase duration $T_R = 35$ s, yellow phase duration $T_Y = 4$ s), speed limit $v_{max} = 60$ km/h

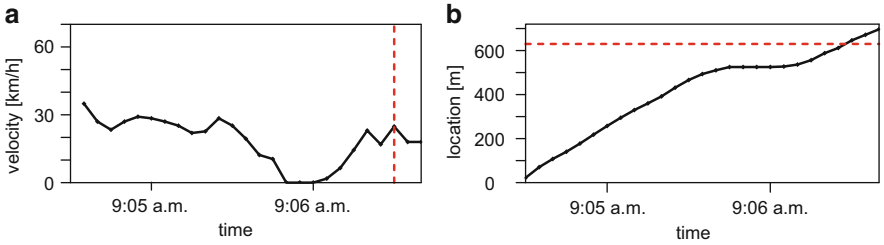

Fig. 4 Empirical synchronized flow measured with TomTom vehicle traces: time-dependence of microscopic (single) vehicle speed (**a**), along vehicle trajectory shown in time-space diagram (**b**). Measured by TomTom navigation devices on Völklinger Straße in Düsseldorf, Germany (see Fig. 3)

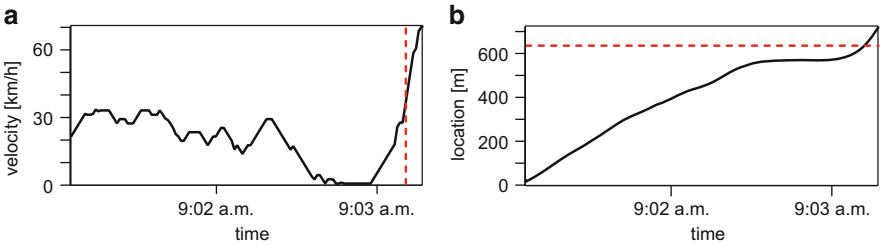

Fig. 5 Simulated synchronized flow: time-dependence of microscopic (single) vehicle speed (**a**) related to vehicle trajectory shown in time-space diagram (**b**). Simulations made on infrastructure of Völklinger Straße in Düsseldorf, Germany (see Fig. 3). Model parameters are the same as those in Fig. 2 with the exception of the value of ε, that is taken as $\varepsilon = 1.333$

pattern of oversaturated traffic we find a synchronized flow pattern (Fig. 5) that is very similar to the one observed in TomTom empirical data (Fig. 4).

The physics of synchronized flow patterns in oversaturated city traffic is as follows. For strong enough driver's speed adaptation, the mean space gap between vehicles is large. Therefore, space gaps (time headways) between vehicles increase

considerably upstream of moving queues. As a result, the absolute value of the upstream front velocity of a moving queue becomes smaller than that of the downstream front of the moving queue, resulting in moving queue dissolution and leading to synchronized flow.

Conclusions
Traffic data measured by TomTom navigation devices shows synchronized flow in oversaturated city traffic [6, 7]. We have simulated empirical data in oversaturated city traffic with the Kerner-Klenov three-phase traffic flow model. The simulations show that under strong speed adaptation synchronized flow patterns which are very close to empirical data can be reproduced with this model. Strong speed adaptation is associated with an average increase of space gaps (time headways) which drivers choose moving in very dense city traffic.

Acknowledgements We thank our partners for their support in the project "UR:BAN - Urban Space: User oriented assistance systems and network management", funded by the German Federal Ministry of Economics and Technology by resolution of the German Federal Parliament.

References

1. B.S. Kerner, *The Physics of Traffic* (Springer, Berlin/New York 2004); *Introduction to Modern Traffic Flow Theory and Control* (Springer, Berlin/New York, 2009)
2. B.S. Kerner, Phys. Rev. E **85**, 036110 (2012)
3. B.S. Kerner, E-Print: arXiv:1211.2535v1 (2012); Europhys. Lett. **102**, 28010 (2013)
4. B.S. Kerner, S.L. Klenov, J. Phys. A: Math. Gen. **35**, L31–L43 (2002); Phys. Rev. E **68**, 036130 (2003); **80**, 056101 (2009)
5. B.S. Kerner, S.L. Klenov, G. Hermanns, P. Hemmerle, H. Rehborn, M. Schreckenberg, Phys. Rev. E **88**, 054801 (2013)
6. P. Hemmerle, M. Koller, H. Rehborn, G. Hermanns, B.S. Kerner, M. Schreckenberg, Increased consumption in oversaturated city traffic based on empirical vehicle data, in *Advanced Microsystems for Automotive Applications 2014*. Smart Systems for Safe, Clean and Automated Vehicles (Springer, Cham/Heidelberg/New York/Dordrecht/London, 2014), pp. 71–79
7. H. Rehborn, M. Schreckenberg, B.S. Kerner, G. Hermanns, P. Hemmerle, I.N. Kulkov, O. Kannenberg, S. Lorkowski, N. Witte, H. Böhme, T. Finke, P. Maier, Straßenverkehrstechnik **3**, 151–157 (2014)
8. See Supplemental Material at http://pre.aps.org/supplemental/PRE/v88/i5/e054801 for model details
9. F.V. Webster, Road research technical paper no. 39, Road Research Laboratory, London (1958); G.F. Newell, SIAM Rev. **575**, 223–240 (1965); J.D.C. Little, Oper. Res. **14**, 568–594 (1966); D.I. Robertson, TRRL report no. LR 253, Transp. and Road Res. Lab., Crow Thorne, UK (1969); N.H. Gartner, Ch. Stamatiadis, in *Encyclopedia of Complexity and System Science*, ed. by R.A. Meyers (Springer, Berlin, 2009), pp. 9470–9500; F. Dion, H. Rakha Y.S. Kang, Transp. Rec. B **38** 99–122 (2004)

Relation Between Longitudinal and Lateral Action Points

Victor L. Knoop and Serge P. Hoogendoorn

Abstract Delay on the motorways can be reduced by traffic management measures changing driving behaviour, which need to be tested before implementation. Microscopic traffic simulation is well suited for this, if sufficiently accurate. Recent studies show that drivers do not continuously change their acceleration, but rather at specific moments in time. These moments are called longitudinal action points. Also for lane changing, moments in time can be identified when drivers start and end changing lanes, so called lateral action points. This paper develops a methodology to find these action points. Data of individual driving behavior, collected from a helicopter, show that the approach with action points is plausible. Moreover, the longitudinal and lateral action points are correlated. Current models not incorporating this discontinuous behaviour correctly, might produce incorrect predictions.

1 Introduction

Delay on the motorways can be reduced by traffic management measures changing driving behaviour, which need to be tested before implementation. Microscopic traffic simulation is well suited for this, if sufficiently accurate.

Recent studies show that drivers do not continuously change their acceleration, but rather at specific moments in time [2]. These moments are called longitudinal action points. Also for lane changing, moments in time can be identified when drivers start and end changing lanes, so called lateral action points. Up to now, most traffic simulation models consider longitudinal behaviour separately from lane change behaviour, where in fact, the two are closely coupled. A lateral action (lane change), is generally is triggered by a lack of longitudinal space. But also a longitudinal action can be triggered by a (planned) lane change. This raises the idea that these two processes might hence be intertwined. In particular, in this paper we test whether the action points on the longitudinal an lateral processes perhaps are the same.

V.L. Knoop (✉) • S.P. Hoogendoorn
Department of Transport and Planning, Delft University of Technology, Stevinweg 1, 2628 CN Delft, The Netherlands
e-mail: v.l.knoop@tudelft.nl; s.p.hoogendoorn@tudelft.nl

M. Chraibi et al. (eds.), *Traffic and Granular Flow '13*,
DOI 10.1007/978-3-319-10629-8_64

The idea that the two are related is not new. For instance, the Mobil lane change model [3] makes a lane change decision based on the possible accelerations, which are calculated using a longitudinal model. The integrated model [7] chooses a path over different lanes, and hence makes the decision to accelerate dependent on the lane change model. It also is useful to mention an earlier approach, the LMRS (lane change model with relaxation and synchronisation [6]) which accounts for accelerations related to a lane change, both for the lane changer as for the putative follower. However, none of these models consider joint action points which are the only points at which acceleration changes.

If accelerations indeed only change at action points, and these are related to the action points of lane changing, this changes the way we should consider microscopic traffic simulators. The idea of not continuously changing acceleration might seriously impact the traffic streams.

2 Methodology

It can be hypothesised that drivers accelerate or decelerate in order to perform a lane change. In fact, we developed a methodology to fit piecewise linear functions in speed-time and lateral position as function of time, revealing the longitudinal and lateral action points. We calculated these best fits for longitudinal and lateral behaviour separately first, and then do the same if we require the action points to be the same.

2.1 Fitting Action Points Separately

Fitting the action points separately means that we find the longitudinal and the lateral action points jointly. For the longitudinal action points we follow [2]. In summary, we do as follows. We fit a piecewise linear function on the speed-time $(\dot{x},t)$. The quality of the fit is expressed as root mean squared error between the fitted speed and the observed speed. Obviously, the higher the number of intermittent points, the better the fit becomes. For each intermediate point a cost of 2 m/s is added, so any new point should improve the RMSE of the fit by 2 m/s.

For the lateral positions as function of time also a piecewise linear fit is made. There are, however, more restrictions than in the speed profile. We consider that the vehicle needs to drive in a lane unless it is changing lanes, so at a constant y value. For one lane change, we consider two action points: one for the start and one for the end of a lane change. Further constrains are that a lane change cannot start within 2 s of the end of the previous lane change, and all lane changes should have a duration of at least 2 s. Opposed to the piecewise linear fit, adding extra intermediate points cannot improve the fit since it is required that the lane change is finished. However, at the beginning and the end of the trajectory a slight offset of the middle of the lane

can be "corrected" by the model by initiating a lane change just before the beginning or the end of the trajectory. Therefore, it is also required that more than half of the lane change is within the observed trajectory.

2.2 Fitting Action Points Jointly

If we consider joint action points, we restrict action points of the start of the lane change is coupled with the longitudinal action point. The error is combined where 1 m/s error has an equal weight as begin a lane off in the lateral direction. Using *Matlab*'s build in function *fmincon* we search the action points which minimize the error. Moreover, the number of longitudinal action points is fixed at the same number as found in the separate fit method. Also the speed at the start and the end of the trajectory is fixed at the values found for the separate fit of speed over time. Similarly, the number of lane changes, as well as the lanes, are the same as found for the separate fits.

3 Data Collection

The ideas have been applied on trajectory data collected at a Dutch motorway. We used a high resolution video camera attached to a helicopter to collect images of the traffic stream. Later, the trajectories of the vehicles were extracted from the video footage using the procedure described in [1].

We collected data at a freeway in the Netherlands, near Everdingen. The data is the same as used by Ossen [5]. It is a three lane freeway with no gradient. Traffic conditions were changing, with speeds from complete standstill up to freeway speeds 32 m/s. The video recorded a road stretch of approximately 300 m. Due to unavoidable movement of the helicopter the exact location of the road which was in sight moves forward and backward by approximately 100 m. For this paper, we use video footage of a little over 5.5 min, in which time 301 are in view for a sufficiently long time to have a useful trajectory. Twenty-three of these vehicles change lane in the captured scene.

4 Results

Figure 1 shows the trajectories and the fits for different vehicles. It shows that if fitted separately both the longitudinal fit as well as the lateral fit follow the real data quite closely. On average, the mean of the root mean square error in the speed over all vehicles is 0.6 m/s (standard deviation: 0.27 m/s), see Table 1. This supports the

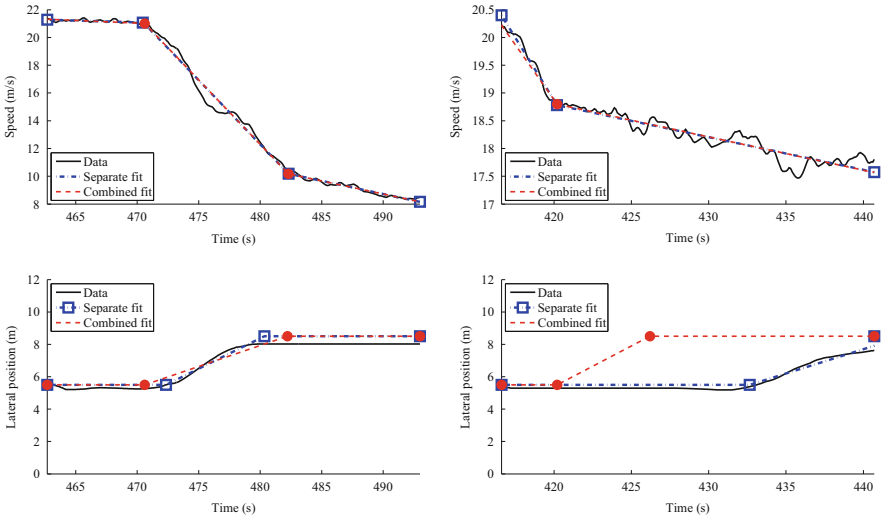

Fig. 1 Examples of the speed and lateral position over time for two vehicles. *Left*: good fit. *Right*: bad fit

Table 1 Overview of the typical errors for the fits of 25 vehicles performing a lane change

	RMSE speed (m/s)		RMSE lateral position (m)		Weighted error (−)	
Fit	Mean	Stdev	Mean	Stdev	Mean	Stdev
Separate	0.40	0.13	0.56	0.22	0.51	0.13
Joint	0.51	0.26	1.42	0.99	0.75	0.26

idea that drivers do not change their speed continuously, but instead have lateral and longitudinal action points.

The effect of combining fits is only relevant for the 23 vehicles which make a lane change during the observation period. These vehicles have an average error of 0.52 m/s in the fitted speed (standard deviation 0.22 m/s). The distribution of the errors (combining error in lateral and longitudinal direction) is shown in Fig. 2a. This shows that indeed the separate fits do better than the combined fit. In fact, this is theoretically required since for each vehicle we impose a restriction during the fitting process. Therefore, the joint fit can never get a lower error than the separate fits. For each vehicle we can calculate how much larger the error in the fit is for the joint fit. The distribution of these ratios can be found in Fig. 2b. The line shows for instance that for approximately 85 % of the vehicles the error in the joint fit is less than 80 % more than in case of the separate fit. The tendency is for a large part of the vehicles the increase in the error is limited. However, for some vehicles the restriction cause a considerably worse fit. An example of a particularly bad fit is given in Fig. 1b. The description of joint behaviour does not match the behaviour of drivers of these vehicles. In fact, that might imply that some drivers do drive according to a different driving scheme than others, which is in line with [4].

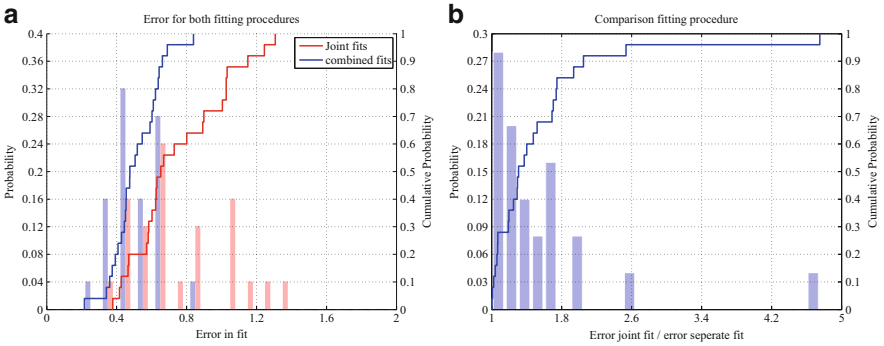

Fig. 2 The resulting errors. (**a**) The errors for the joint and for the separate fitting procedure. (**b**) Comparison of the errors for the joint and for the separate fitting procedure

Conclusions

This paper shows that longitudinally and laterally the movement of vehicles is well captured in a description of action points. Longitudinal action points are moments drivers change their speed, and lateral action points are moment drivers start or end changing lanes.

For many drivers, it is reasonable to assume that the start of a lane change manoeuvre was at the same moment as a change in acceleration. That might imply that for these drivers, performing the lane change might be linked to changing the acceleration. It should also be noted that some other drivers show a completely different behaviour.

This is an important behavioural finding for microscopic traffic flow models. Usually a car-following model is implemented separately from a lane change model, whereas this research suggest drivers might make the decision jointly. Considering these actions jointly can fundamentally change the dynamics of traffic flow. The differences become especially relevant when active traffic management measures are being tested in a traffic simulator.

Acknowledgements This work is supported by the Netherlands Organisation for Scientific Research (NWO) in grant “There is plenty of room in the other lane”.

References

1. S. Hoogendoorn, S. Ossen, M. Schreuder, Properties of microscopic heterogeneous muti-anticipative traffic flow model, in *Proceedings of International Symposium on Traffic and Transport Theory*, ed. by M. Bell, B. Heydecker, R. Allsop (Elsevier, London, 2007)

2. S.P. Hoogendoorn, R.G. Hoogendoorn, W. Daamen, Wiedemann revisited. Transp. Res. Rec.: J. Transp. Res. Board **2260**(1), 152–162 (2011)
3. A. Kesting, M. Treiber, D. Helbing, General lane-changing model mobil for car-following models. Transp. Res. Record: J. Transp. Res. Board **1999**, 86–94 (2007)
4. S. Ossen, S. Hoogendoorn, B.G.H. Gorte, Interdriver differences in car-following: a vehicle trajectory-based study. Transp. Res. Rec.: J. Transp. Res. Board **1965**, 121–129 (2006)
5. S.J.L. Ossen, Longitudinal driving behavior: theory and empirics. Trail thesis series, Delft University of Technology, 2008
6. W.J. Schakel, V.L. Knoop, B. Van Arem, LMRS: integrated lane change model with relaxation and synchronization. Transp. Res. Rec. **2316**, 47–57 (2012)
7. T. Toledo, H.N. Koutsopoulos, M. Ben-Akiva, Integrated driving behavior modeling. Transp. Res. Part C: Emerg. Technol. **15**(2), 96–112 (2007)

Applications of the Generalized Macroscopic Fundamental Diagram

Serge P. Hoogendoorn, Victor L. Knoop, Hans van Lint, and Hai L. Vu

Abstract The generalised Macroscopic Fundamental Diagram (g-MFD) relates the network traffic density and the spatial variation of this density. Recent work of the authors show that by using both the average and the standard deviation in the density, a very crisp relation can be found, also in case the network conditions are inhomogeneous. This paper presents results for the g-MFD using empirical data collected for the freeway network around Amsterdam. Next to presenting the g-MFD, we will show how the dynamics in the network relate to the evolution of the network state in terms of average density and spatial density variation. The paper discusses regular dynamics, as well as the dynamics in case of incidents occurring in the network. The presented results justify using the g-MFD for a number of applications that will be detailed in the rest of the paper. First of all, the g-MFD can be used to determine the network-wide service-level, both for recurrent and non-recurrent situations. The results for incident situations motivate the second application, namely the analysis of the resilience of the network by studying the changes in the service level for specific network states. We will illustrate these applications using the aforementioned Amsterdam test case.

1 Generalised Macroscopic Fundamental Diagrams

The concept of the generalised Macroscopic Fundamental Diagram was first introduced by [1]. The g-MFD generalises the Macroscopic Fundamental Diagram (MFD) by introducing another independent variable next to the average density k, namely the spatial variation in the density. In this manuscript, we will use $\sigma = \sigma(t)$ to denote the standard deviation of the density at time instant t, i.e.:

$$\sigma(t) = \sqrt{\frac{1}{n}\sum_{i=1}^{n}(k_i(t) - k(t))^2} \tag{1}$$

S.P. Hoogendoorn (✉) • V.L. Knoop • H. van Lint • H.L. Vu
Delft University of Technology, Delft, The Netherlands,
e-mail: s.p.hoogendoorn@tudelft.nl

M. Chraibi et al. (eds.), *Traffic and Granular Flow '13*,
DOI 10.1007/978-3-319-10629-8_65

where $k_i(t)$ is the traffic density at segment i of a network consisting of n segments (or links) at time instant t and $k(t)$ denotes the average density at time instant t:

$$k(t) = \frac{1}{n}\sum_{i=1}^{n} k_i(t) \tag{2}$$

The general idea of the g-MFD is that the average network flow Q, and thus the average network speed V are functions of both the average density and spatial standard deviation of the density, that is $Q = Q(k, \sigma)$, and $V = V(k, \sigma)$.

Based on the estimation results in [1], it is shown that this generalisation provides a much better fit to traffic network data than the original MFD. In fact, the g-MFD relaxes the rather restrictive requirement to the applicability of the MFD of network traffic conditions needing to be homogeneous.

In the remainder of this section, we will present a novel intuitive functional form for the g-MFD that will be fitted on motorway traffic data.

2 Example g-MFD for a Freeway Ring Road

This section presents empirical results for the g-MFD using empirical data collected for the freeway network around Amsterdam (so-called A10 ring road, clockwise direction). The 33 km ring road has a general speed limit of 100 km/h, apart for a stretch of about 11 km for which the speed limit is 80 km/h.

Figure 1 shows average results for 2 months of data (November and December 2011), as well as the (k, σ) path of a single day (8th of November 2011). The figure

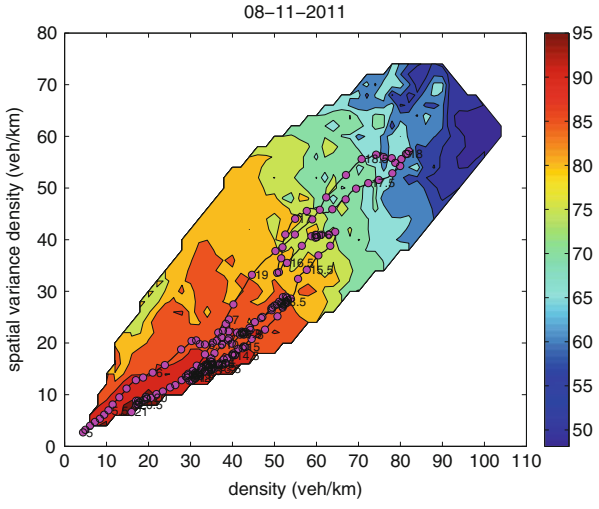

Fig. 1 Network state path $(k(t), \sigma(t))$ in relation to the g-MFD for a regular day

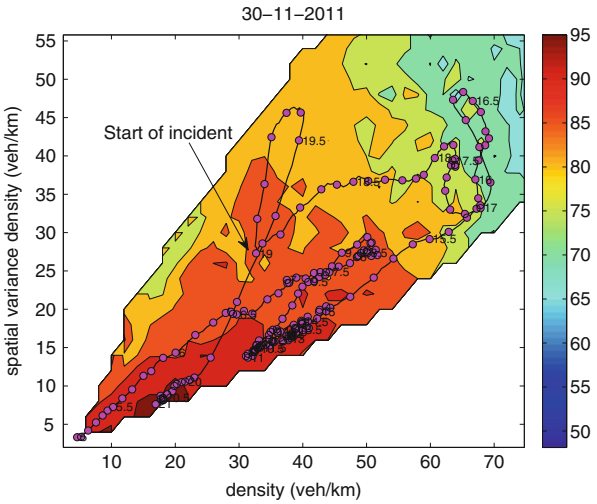

Fig. 2 Network state path $(k(t), \sigma(t))$ in relation to the g-MFD. The *arrow* indicates the starting time of the incident

shows how the morning peak is less congested than the evening peak, maintaining average speeds well above 85 km/h. In the evening however, more severe congestion brings the network speed to around 60 km/h. Note that the path approximately follows a straight line described by $\sigma = 2k/3$. This turns out to be the case for all regular days where no incidents occur. In all of these days, we see slight counterclockwise hysteresis showing that in general, the spatial variation is less when the density is increasing and higher when it is decreasing. Note that the hysteresis phenomena is discussed in detail by [2]

An example is given by Fig. 2, showing the network state path for an incident case. We see how the dynamics of the path are influenced by the incident: when the incident occurs at 19:00, the path breaks away from the congestion recuperation path it was moving along. From this point onwards, the path moves in the vertical direction showing that the average density stays about the same, while the spatial variation increases considerable. The reasons for this are clear: the incident causes an increase in the spatial variation, while the overall density is not necessarily increasing.

3 Functional Relation

A functional form for the g-MFD can be found by fitting a multivariate function to the data. For this function to be realistic, it needs to satisfy some requirements. First of all $V(k, \sigma)$ is a decreasing function of both k and σ, i.e.:

$$\frac{\partial V}{\partial k} < 0 \quad \text{and} \quad \frac{\partial V}{\partial \sigma} < 0 \tag{3}$$

Furthermore, we hypothesise the existence of a maximum density, possibly dependent on the spatial variation, for which the network speed is zero (full gridlock):

$$V(k_{jam}(\sigma), \sigma) = 0 \tag{4}$$

That is, we assume that for each σ we can find a density value for which the speed equals zero. Note that $k_{jam}(0)$ denotes the jam density for fully homogeneous conditions, i.e. when each network link has jam density. We expect:

$$\frac{\partial k_{jam}(\sigma)}{\partial \sigma} < 0 \tag{5}$$

The following function satisfies these conditions. Furthermore, we found that it provided a very reasonable fit to the data on the A10:

$$V(k, \sigma) = \min\left(v_0, \beta \cdot \left(\frac{1}{k} - \frac{1}{k_{jam}}\right)\right) \cdot \left(1 - \frac{\sigma}{\sigma_0}\right) \tag{6}$$

with $v_0 = 100.6$ km/h, $k_j = 166.6$ veh/km/lane, $\sigma_0 = 113.5$ veh/km/lane, and $\beta = 2{,}382$ veh/h; the resulting fit yields an adjusted rho-square of 0.9894. All parameters are statistically significant at 95 %. This function was chosen since the density-dependent part of the function is a often used model form for the (normal) fundamental diagram (i.e. congested branch stemming from a simple car-following model).

Most of the parameters in this equation have a nice interpretation: v_0 can be interpreted as the average free network speed, which for this situation in 100.6 km/h. The parameter k_{jam} can be seen as the average jam density in the network; the estimated value of 166.6 veh/km/lane seems very plausible. The parameter σ_0 denotes a scaling parameter for the spatial variation; note that when $\sigma = \sigma_0 = 113.5$, the speed is zero. The scale parameters β denotes the reduction in the average distances s between vehicles with decreasing speed. This can be seen by noticing that in the congested branch of the (g-) MFD, we have $V/\beta = 1/k - 1/k_{jam} = s - 1/k_{jam}$.

4 Application to Network Resilience Analysis

The g-MFD has many applications, including modelling and control. In [3], the g-MFD is used as a real-time of to determine the network service level (e.g. the average quality of the network operations in the network). In this case, both speed and flow are used to determine the level-of-service, which for example can be defined as an average speed of the network or the production of average speed and density. For more details, we refer to [3].

In this section, we propose a new approach to test the network resilience which uses the concept of using the g-MFD as a network service level indicator. The idea is that the *change in the level-of-service* due changes in the spatial variation is an indicator of resilience. In other words, if the spatial variation in the density increases, the extent in which this yields a change in the level of service (e.g. speed) provides information on how well the network can deal with such disturbances. In Sect. 2 we have illustrated the state dynamics in case of incident conditions. Here it was shown that as an incident occurs, the spatial density variation increases. If this yields only a limited reduction in the level-of-service, then the network is robust since it can deal with such disturbances.

4.1 Network Resilience Definition

The *resilience* of the network is defined by "the ability to provide and maintain an acceptable level of service in the face of faults and challenges to normal operation". For traffic networks, these "faults" could be interpreted as incidents or other events that (temporarily) reduce the capacity of a roadway segment.

Given the path dynamics discussed in Sect. 2, we know that in case of a (possibly temporary or partial) blockade, the (k, σ) path moves in the upward direction: the density remains constant, while the spatial variation in the density increases. The impact on the level-of-service λ – as shown in examples later on – can thus be defined logically by taking the partial derivative of the level-of-service to the spatial density variation, i.e.:

$$\xi = \xi(k, \sigma) = \frac{\partial}{\partial \sigma} \lambda(k, \sigma) \tag{7}$$

From this definition, we see that resilience is defined by *the rate in which the level-of-service drops when the spatial variation in the density increases*. If this rate ξ is high, then a small increase in the standard deviation of the density σ causes a large reduction in the level-of-service λ. On the contrary, when the rate ξ is small, the level-of-service in relatively insensitive to an increase in σ. Note that the resilience is determined by a number of factors, such as the availability of alternative routes in the network, but also the level of information provided to the road users allowing them to reroute in case of an incident.

In the remainder, we will take the average speed $\lambda = V(k, \sigma)$ as a proxy for the level-of-service λ, although other (continuous) definitions can be used as well, for instance the production (which may yield completely different results); see [3] for more information.

4.2 Functional Expression for Network Resilience of the A10 Ring Road

In illustration, let us revisit the A10 ring road example and take a look at the resilience definition. Recall that we used the formal expression Eq. (6). Using this functional form, we get:

$$\xi(k,\sigma) = -\frac{1}{\sigma_0}\min\left(v_0, \beta\cdot\left(\frac{1}{k}-\frac{1}{k_j}\right)\right) \tag{8}$$

This expression shows that ξ becomes smaller when the density becomes larger. That is, when the speed is already low, the extra speed reduction due to for instance an incident is less pronounced. Note that when taking the production as a measure for the level-of-service γ, this conclusion does not hold. In that case, we get:

$$\xi(k,\sigma) = -\frac{1}{\sigma_0}\min\left(v_0\cdot k, \beta\cdot\left(1-\frac{k}{k_j}\right)\right) \tag{9}$$

meaning that the maximum reduction rate in level-of-service occurs at some critical density value k_c.

5 Discussion

This paper has presented the generalised Macroscopic Fundamental Diagram (g-MFD) as a means to analyse the dynamics in a network (for recurrent and non-recurrent conditions) and to assess the level-of-service and network resilience. Using data from a Dutch freeway ring road, we showed that a good fit could be obtained using a pre-specified functional form of the g-MFD that satisfied key functional criteria. Using this fitted functional form, conclusions can be drawn about the network resilience, depending on the used level-of-service indicator (e.g. average speed or production).

Future research focuses on cross-comparing different network structures with different types on traffic information and management strategies. In doing so, insight will be gained into the applicability of the approach presented here to quantify network resilience.

References

1. V.L. Knoop, S.P. Hoogendoorn, Empirics of a generalised macroscopic fundamental diagram for urban freeways. Transp. Res. Rec. (2391), 133–141 (2013)
2. H.S. Mahmassani, M. Saberi, A. Zockaie, Urban network gridlock: theory, characteristics, and dynamics. Transp. Res. C **36**, 480–497 (2013)

3. S.P. Hoogendoorn, R.L. Landman, J. van Kooten, H. Taale, M. Schreuder, Integrated Network Management Amsterdam: Towards a Field Operational Test. Compendium of Papers of the 2014 Transportation Research Board Annual Meeting, Washington D.C., 2014

Network Fundamental Diagrams and Their Dependence on Network Topology

Victor L. Knoop, David de Jong, and Serge P. Hoogendoorn

Abstract Recent studies have shown that aggregated over a whole network a rather crisp relation between average density (accumulation) and average flow (production) exists. This relationship is called the Network Fundamental Diagram (NFD). We developed a tool to automatically design networks. Using this tool, different networks are created for which the following general properties are the same: (1) the number of intersections, (2) length of signalised multi-lane arterial roads, (3) length of single-lane urban roads. The main contribution of this paper is that it shows that NFDs are not only dependent on these properties, but also on the exact network layout (e.g., which link connects to which link) and/or origin-destination pattern. As a consequence, the NFD needs to be determined for each network separately and cannot be derived from these general properties.

1 Introduction

The Network Fundamental Diagram (NFD) is the relationship between the number of vehicles and the average flow in an area. After [2] it gained attention. Recently developed control concepts as for instance perimeter control [6] or routing [8] require the shape of the NFD to be known. This shape can of course be measured in real life. For networks which are not yet implemented in real life, determining this curve empirically is impossible. Therefore it is useful to have techniques to determine this curve based on other principles.

An analytical method has been proposed [4], but this holds only for arterial roads with traffic lights. The network specific effects or influence of road types cannot be captured by this methodology. The question addressed in this paper is there: is the NFD dependent on road types and the specific network layout?

In this paper we will show that the network design can change the shape of NFD, even though the main statistics as roadway length and road types are the same. Mixing road types also has an effect. Methodologically the approach taken in this study is that random networks are being designed with similar properties. This could

V.L. Knoop (✉) • D. de Jong • S.P. Hoogendoorn
Delft University of Technology, Stevinweg 1, 2628 CN Delft, The Netherlands
e-mail: v.l.knoop@tudelft.nl

M. Chraibi et al. (eds.), *Traffic and Granular Flow '13*,
DOI 10.1007/978-3-319-10629-8_66

be networks with and without hierarchical structure (e.g., a ring road and minor roads inside).

The methodology to test different networks with all the same properties raised an issue, namely to create networks with all the same properties. This paper develops a method and a tool to do so, which is described in Sect. 4. This tool is used in the study to create similar networks. The goal of this paper is to test the influence of the road layout. All active traffic management measures are hence not incorporated in this paper and for the traffic lights, a fixed timing is adopted.

The remainder of the paper is set-up as follows. The next section gives an overview of the ways to estimate the NFD. Then, Sect. 3 gives the research set-up and methodology. Section 4 describes the tool which has been developed to create networks. Section 5 presents the resulting NFDs, and finally the last section presents the conclusions.

2 Network Fundamental Diagrams

The field of research into the NFD is rapidly developing. The number of papers on the NFD which appeared recently is too large to discuss all, so we restrict ourselves to the shape of the NFD. For estimating the NFD, an analytical method has been developed [4]. The authors apply variational theory to traffic operations. Integrating the effect of traffic lights into the variational formulation, they are able to present an analytical approximation of the NFD. This is extended by [9] where the effect of route choice is included. Both papers use routes in one dimension, so effects of crossing flows cannot be studied with either of these methods. Effects of signal timing in a regular lattice network are shown by [11].

The dynamics of traffic play an important role in the shape of the NFD. This has been studied for instance for simple insightful networks [3] or grid networks [7]. They show that traffic networks tend to get more congested once traffic congestion sets in and that production decreases with decreasing traffic homogeneity. This feature is explained and seems to be independent of the network layout.

The design of a network itself is also of importance. With design we mean what the exact connections of the links are. The link length and the number of connections can be similar, but how these links are connected by intersections or T-junctions. The influence of these effects is – as far as the authors are aware – not been studied in depth yet, and this will be studied further in this paper.

3 Methodology

The goal of this paper is to study the effect of specific network design on the NFD. We do so by creating different networks which share the same basic properties. This means that the main road (arterials) are the same, as well as the locations of

the connections between the main roads and the underlying road network. For the underlying road network, the roadway length is similar. However, the exact layout of this underlying road network is different. For instance, the underlying network may consist of several housing blocks, and a block of sport facilities. These can be arranged in a different order, changing the network connections. We say that the basic properties of these networks are the same, but the exact network is different.

The NFD represents traffic operations at the network level. It can therefore be conceived that the exact layout is an issue. On these changing underlying road networks, there are no traffic signals, so they cannot play a role. The main question addressed in this paper is: "Can the NFD been constructed from the roadway length, speed limit and capacity?"

Creating similar networks is challenge on its own, which will be tackled by a tool which will be described in Sect. 4. The tool will be used to create three different networks, all 3×3 km with an arterial ring road. However, they differ in the unsignalised roads.

The networks are in the end compared on the relationship between production and accumulation. These are calculated as follows. The production is the average flow, here calculated by the distance that all vehicles cover in a aggregation time divided by the aggregation time and the road length in the network (units: veh/h/lane). The accumulation is the average density, calculated here as the total number of vehicles divided by the road length in the network (units: veh/km/lane). The capacity of the network is the highest production.

4 Designing Random Networks

The networks are created using a tool which takes an input. For a microscopic network simulation program – in this paper, we use *Vissim* – an exact intersection design and signal timing are required as well. The steps to come to a detailed network design are described here. Due to limitation of space, the paper does not describe all steps of the algorithm in detail – for this, we refer to [5] – but describes the main principles.

We want to have three different networks of 3×3 km with an arterial at the outer edge and local roads within. Every 500 m there is an entry point to the local road network, which also acts as OD-zone. Following the Dutch guidelines [1] the intersections are created. A demand of 100 veh/h is set to each directions of the intersections and than the signal scheme for each intersections is determined [10]. The length of auxiliary lanes is set to the minimum for which there is no blocking of the main traffic.

For each OD pair a uniform number between 0 and 1 is drawn, and there are no trips within the same zone. The demand is then scaled to a predefined total number of trips. To compare the shape of the NFD there need to be congested and uncongested conditions. Therefore, simulations are repeated with different demands, proportionally scaled for all OD pairs.

With the obtained flows, first the number of lanes for each link is determined and the layout of each intersection is updated. Within this update, the flow of each link is assigned to the corresponding turn and a new intersection layout with corresponding signal scheme is calculated. If the cycle time is too long (>120 s), an additional lane is added to the turn with the highest flow per lane after which the layout and signal scheme are recalculated. This process is repeated until the cycle time is within the limits.

After the general network layout is created, the areas between the major roads are converted to subnetworks. Along the border of each subnetwork a safety zone is added, in order to accommodate the roads of the main network. Also inserts are made, which are used to accommodate the connection to the main network, using the temporary subnetwork nodes created earlier.

For each of these areas a street pattern, consisting of local, bi-directional, single lane roads is created. This is based on the size of the blocks. Using Google maps, the typical sizes of blocks with different land use houses are determined; we differentiate between high rise buildings, parks and sport facilities. Also, it is determined which fraction of the blocks is used for what purpose. Using these values, a block type and its dimensions are drawn at random, after which the block is inserted at the first possible bottom-left position. Then a local road is added around that block. This process is repeated until the block is filled for a certain percentage, or no more blocks can be added. The remaining areas which are too small to fit any other purpose are filled with parks.

Next the subnetwork is divided in smaller sections. The demand is assigned to the original temporary subnetwork nodes, are now originating at different locations within the subnetwork, inversely proportional to the relative distance to each of the intersections. This avoids demands originating from the eastern intersection to be assigned to a feeder at the west of the subnetwork, resulting in a mismatch of the demand at each intersection. The three resulting networks are shown in Fig. 1.

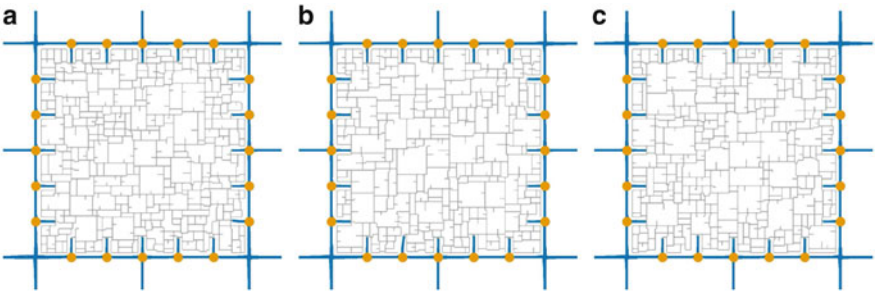

Fig. 1 The networks. (**a**) Network 1. (**b**) Network 2. (**c**) Network 3

5 Traffic Operations

Figure 2 shows the NFDs for the different networks. It shows that although the general pattern is the same (going up and down, quite sharp peak), the differences in the fundamental diagram are – measured by traditional traffic management standards – considerable. The capacity of network 1 is lower by approximately 15 % compared to network 2. There is also quite some spread in the first part of the congested branch of network 1. The free speeds are similar, as well as the expected accumulation for which the speed approaches zero.

After the top, all NFDs decrease to the congested branch. This transition is much sharper than the analytical method with cuts for a ring road with traffic lights [4] suggests. Moreover, the congested branch shows a convex part, which cannot be found using the above mentioned method. Possibly network effects with spillbacks to other links cause this shape. The NFDs, created by averaging all traffic operations on the arterial and the inner network, are quite crisp.

It is remarkable that network 3 the increased demand has a lower effect on the speeds, i.e., the speeds do not decrease as much as for the other two networks (i.e., the congested branch does not reach gridlock accumulation), although the demands are the same. That means that not only the shape of the NFD is different, but also the position of the traffic state on the NFD given a specific demand.

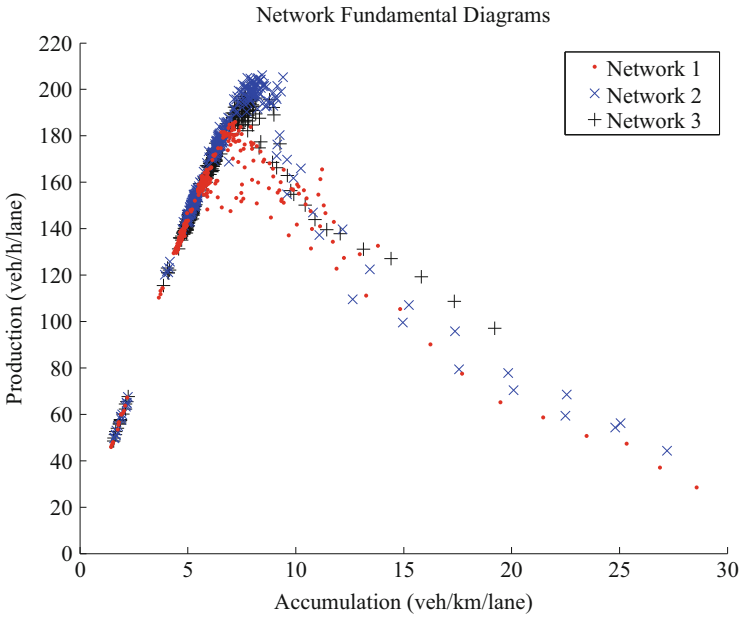

Fig. 2 The fundamental diagrams for all networks

Conclusions
This paper studied NFDs of various road networks. It presented a tool to create random networks based on required properties of the network. This tool has been used to analyse the effect of the network layout on the NFD.

It has been known that signal timing plays an important role in the NFD. However, also Changes in the underlying road network in which no traffic signals are present, result in differently shaped NFDs. That implies that the network structure also has an important role. Traffic control schemes based on the NFD are currently being developed. The findings in this paper show that it is required to determine the NFD for each network layout specifically, and it cannot be based on the general characteristics as network length or road type.

Acknowledgements This work is supported by the ITS Edulab and the Netherlands Organisation for Scientific Research (NWO) in grant "There is plenty of room in the other lane".

References

1. CROW, Handboek wegontwerp wegen buiten de bebouwde kom: Gebiedsontsluitingswegen. Technical Report 164c (2002). In Dutch
2. C.F. Daganzo, Urban gridlock: Macroscopic modeling and mitigation approaches. Transp. Res. Pt. B: Methodol. **41**(1), 49–62 (2007)
3. C.F. Daganzo, V.V. Gayah, E.J. Gonzales, Macroscopic relations of urban traffic variables: bifurcations, multivaluedness and instability. Transp. Res. Pt. B: Methodol. **45**(1), 278–288 (2011)
4. C.F. Daganzo, N. Geroliminis, An analytical approximation for the macroscopic fundamental diagram of urban traffic. Transp. Res. Pt. B: Methodol. **42**(9), 771–781 (2008)
5. D. De Jong, The effect of network structure and signal settings on the macroscopic fundamental diagram. Master's thesis, 2012
6. M. Keyvan-Ekbatani, A. Kouvelas, I. Papamichail, M. Papageorgiou, Exploiting the fundamental diagram of urban networks for feedback-based gating. Transp. Res. Pt. B: Methodol, **46**(10), 1393–1403 (2012)
7. V.L. Knoop, S.P. Hoogendoorn, J.W.C. van Lint, The impact of traffic dynamics on the macroscopic fundamental diagram, in *Proceedings of the 92nd Annual Meeting of the Transportation Research Board* (Washington D.C., 2013)
8. V.L. Knoop, J.W.C. Van Lint, S.P. Hoogendoorn, Route advice and its effect on the marcoscopic fundamental diagram. Transp. Res. Rec. **2315**, 1–10 (2012)
9. L. Leclercq, N. Geroliminis, Estimating mfds in simple networks with route choice, in *Proceedings of the 20th International Symposium on Transportation and Traffic Theory* (Noordwijk, the Netherlands, 2013)
10. T.H.J. Muller, M. de Leeuw, New method to design traffic control programs. Transp. Res. Rec.: J. Transp. Res. Board **1975**, 68–75 (2006)
11. L. Zhang, T.M. Garoni, J. De Gier, A comparative study of macroscopic fundamental diagrams of arterial road networks governed by adaptive traffic signal systems. Transp. Res. Pt. B: Methodol. **49**, 1–23 (2013)

A Simple Cellular Automaton Model with Limited Braking Rule

Thorsten Chmura, Benedikt Herz, Florian Knorr, Thomas Pitz, and Michael Schreckenberg

Abstract Despite its simplicity, the Nagel-Schreckenberg (NaSch) traffic cellular automaton is able to reproduce empirically observed traffic phenomena such as spontaneous traffic jam formation. Most traffic cellular automata models achieve collision-free driving by explicitly allowing for unlimited braking capabilities. However, it is rather natural to view the collision-free traffic flow as a consequence of moderate driving instead of infinite braking capabilities. Lee et al. (Phys Rev Lett 23:238702, 2004) introduced a traffic model that limits the vehicles' acceleration and deceleration rates to realistic values. The underlying rules of motion in this model are, however, quite complicated. In this article, we introduce and analyse a modified version of the NaSch traffic model with simple rules of motion and limited braking capabilities. We achieve collision-free driving with realistic deceleration rates by the introduction of the function $\mu(v_t^{i+1}, \delta_t^i)$ which determines a vehicle's new speed depending on the preceding vehicle's speed v_t^{i+1} and the distance δ_t^i to its predecessor. After proving that this function limits the maximum deceleration rate to realistic values and guarantees the collision-freeness at the same time, we investigate the resulting traffic dynamics.

T. Chmura
Nottingham University, Nottingham, UK

B. Herz
Universitat Pompeu Fabra, Barcelona, Spain

F. Knorr (✉) • M. Schreckenberg
Universität Duisburg-Essen, Essen, Germany
e-mail: florian.knorr@uni-due.de

T. Pitz
Rhine-Waal University of Applied Sciences, Kleve, Germany

M. Chraibi et al. (eds.), *Traffic and Granular Flow '13*,
DOI 10.1007/978-3-319-10629-8_67

1 Introduction

In 1992, Nagel and Schreckenberg [2] proposed one of the first stochastic cellular automaton (CA) models for analyzing traffic on a one-lane road. Various modifications and extensions such as for the analysis of city traffic or the application to complex road networks have been proposed since then (for reviews see, e.g., [3, 4]). The primary criterion to assess these models is their ability to reproduce empirically observed features of traffic flow [5, 6], which follows from the vehicles' rules of motion.

In the Nagel-Schreckenberg model (NaSch), the road is modeled as a one-dimensional array of sites, and each site is occupied by at most one vehicle. The position of the ith car at time t is denoted by x_t^i and the position of its immediate predecessor by x_t^{i+1}. The vehicle's dynamics (i.e., its acceleration and its deceleration) depends on its predecessor on the road. This behaviour is implemented by an update scheme in which the following simple rules are applied to each vehicle in parallel:

1. A car i with speed v_t^i at time t accelerates if the distance to its predecessor $\delta_t^i = x_t^{i+1} - x_t^i$ is large enough. That means if δ_t^i is larger than $v_t^i + 1$ then the speed is advanced by one until the car's maximum speed $v_{\max}$ is reached: $v_{t+1}^i = \min(v_t^i + 1, v_{\max})$.
2. If the distance δ_t^i is too small (i.e., $\delta_t^i \leq v_{t+1}^i$), the car reduces its speed to avoid a collision: $v_{t+1}^i = \min(\delta_t^i - 1, v_{t+1}^i)$.
3. The car's speed is decreased by one at random: $v_{t+1} = \max(0, v_{t+1}^i - 1)$ with probability $1 - p_{\text{acc}}$.
4. Finally, the vehicle moves from its current position x_t^i to its new position $x_{t+1}^i = x_t^i + v_{t+1}^i$.

Note that a car accelerates by one at maximum (step 1), but it can slow down by more than one (step 2). Step 3 mimics speed fluctuations due to human behaviour. It is essential for traffic jams to occur. Nagel and Schreckenberg focused their analysis on the relationship between the density ρ (the number of cars N divided by the length of the road L) and the traffic flow J (the average number of cars which pass a site per time step). They conclude that the traffic flow increases rapidly up to a certain density above which the average traffic flow decreases as the probability of traffic jams increases rapidly. Despite its simplicity, the model is able to reproduce empirically observed traffic phenomena such as the spontaneous formation of traffic jams. A major drawback of the model is that it allows for unrealistically high deceleration rates (step 2).

With our modification of the NaSch we will present a minimalistic discrete CA model with limited braking capabilities for simulating traffic flow on a single lane. We will also show that this modified model (in the following: mNaSch), unlike the Nagel-Schreckenberg model, tends to converge to steady states. First, let us introduce the modified model.

2 Modified Version of the NaSch

Let $L \in \mathbb{N}$ be the number of sites representing the one-lane road. At time t, the car labeled i moves with speed v_t^i which is bounded from above by $\mu(v_{t-1}^{i+1}, \delta_{t-1}^i)$. This upper boundary, whose value depends both on the speed of the leading vehicle and the distance gap, ensures that there are no collisions of two cars as we will show below. In our modified model, a car changes its speed according to the following rule:

$$v_t^i = \begin{cases} v_{t-1}^i + 1 & \text{if } v_{t-1}^i + 1 \le \mu(v_{t-1}^{i+1}, \delta_{t-1}^i) \text{ and } \xi \le p_{\text{acc}}, \\ v_{t-1}^i & \text{if } v_{t-1}^i + 1 \le \mu(v_{t-1}^{i+1}, \delta_{t-1}^i) \text{ and } \xi > p_{\text{acc}}, \\ \mu(v_{t-1}^{i+1}, \delta_{t-1}^i) & \text{otherwise.} \end{cases} \tag{1}$$

The variable ξ denotes a random number uniformly generated in $[0, 1]$. Note that it holds $v_{t-1}^i - 1 \le \mu(v_{t-1}^{i+1}, \delta_{t-1}^i) \le v_t^i \le v_{t-1}^i + 1$. Hence, acceleration and braking capabilities are limited, and a car changes its speed by at most ± 1.

2.1 Collision Free Driving

We will now determine the values of $\mu(v_t^{i+1}, \delta_t^i)$ for the mNaSch which ensure that there are no collisions between any two cars. (Valid initial configurations for open and periodic boundaries are given in the Appendix.) We need to distinguish between two cases:

1. The vehicle i does not have a predecessor. This is only possible in an open system. In this case, the car's speed is only limited by $v_{\max}$, the maximum technical speed of the car. (We assume here $v_{\max} = 6$.)
2. The vehicle i does have a predecessor. That means that there is another car driving ahead of vehicle i. This is always the case in a closed system. The maximum possible speed of car i at time t depends on (i) the speed of its predecessor and (ii) the distance to its predecessor at time $t - 1$.

   This is captured by the function $\mu(v_t^{i+1}, \delta_t^i)$ defined as follows:

$$\mu(v_t^{i+1}, \delta_t^i) = \min \left\{ \left\lfloor \frac{1}{2} \sqrt{8\delta_t^i - 7 + 4v_t^{i+1} \left(v_t^{i+1} - 1\right)} - \frac{1}{2} \right\rfloor ;\ v_{\max} \right\}, \tag{2}$$

   where $\lfloor \cdot \rfloor$ denotes the floor function and δ_t^i the distance between car i and its predecessor $i + 1$ at time t.

   The values resulting from Eq. (2) are given in Table 1 for various combinations of a vehicle's headway and speed.

Table 1 The values of the function $\mu(v_t^{i+1}, \delta_t^i)$ for $v_{\max} = 6$

v_t^{i+1} / δ_t^i	1	2	3	4	5	6	7	8	9	10	11	12	13	14	15	16	17	18	18	20	21	≥ 22
0	0	1	1	2	2	2	3	3	3	3	4	4	4	4	4	5	5	5	5	5	5	6
1	0	1	1	2	2	2	3	3	3	3	4	4	4	4	4	5	5	5	5	5	5	6
2	1	1	2	2	2	3	3	3	3	4	4	4	4	4	5	5	5	5	5	5	6	6
3	2	2	2	3	3	3	3	4	4	4	4	4	5	5	5	5	5	5	6	6	6	6
4	3	3	3	3	4	4	4	4	4	5	5	5	5	5	5	6	6	6	6	6	6	6
5	4	4	4	4	4	5	5	5	5	5	5	6	6	6	6	6	6	6	6	6	6	6
6	5	5	5	5	5	5	6	6	6	6	6	6	6	6	6	6	6	6	6	6	6	6

(To some extent this approach is comparable to the work of Emmerich and Rank [7], who investigated an update mechanism which takes into account both a vehicle's space gap and its speed as well. By ignoring the leading vehicle's speed this mechanism could not avoid collisions.)

Theorem 1 *It holds for all times ($\forall t \in \mathbb{N}$) that for any two cars i, j with $i < j$: $x_t^i < x_t^j$. This means that there are no collisions at any time.*

Proof From Table 1 we see that it holds

$$\mu(v_{t-1}^{i+1}, \delta_{t-1}^i) < \delta_{t-1}^i + \max\{v_{t-1}^{i+1} - 1, 0\} \tag{3}$$

and therefore (using $\delta_{t-1}^i = x_{t-1}^{i+1} - x_{t-1}^i$)

$$x_t^i \leq x_{t-1}^i + \mu(v_{t-1}^{i+1}, \delta_{t-1}^i) < x_{t-1}^{i+1} + \max\{v_{t-1}^{i+1} - 1, 0\} \leq x_t^{i+1}, \tag{4}$$

where we assume without loss of generality that $x_t^i < x_t^{i+1} \forall t \in \mathbb{N}$. Therefore, there are no collisions of any two cars for all times t.

Theorem 2 *By the definition of the function $\mu(v, \delta)$, the braking capabilities of the cars are limited. This means that the following inequality holds:*

$$\mu(v_t^{i+1}, \delta_t^i) \geq \mu(v_{t-1}^{i+1}, \delta_{t-1}^i) - 1 \ \forall t \in \mathbb{N}. \tag{5}$$

Proof The theorem follows directly from the definition of $\mu(v_t^{i+1}, \delta_t^i)$ as shown in Table 1.

3 Results

To begin our analysis we will present fundamental diagrams for different values of p_{acc}. For the simulation we used a road length of $L = 10^4$ sites and averages over $T = L$ time steps after a relaxation time of $10T$. Densities $0.01 \leq \rho \leq 1$ were

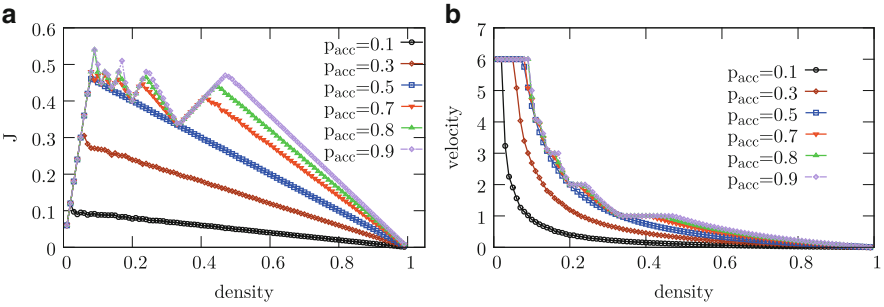

Fig. 1 For periodic boundaries: (**a**) Fundamental diagram for different values of p_{acc}. (**b**) Corresponding average speeds

simulated in steps of 0.01 for several values of p_{acc}. The fundamental diagrams are shown in Fig. 1a and the corresponding average speeds in Fig. 1b.

Similar to the NaSch, the traffic flow increases rapidly up to a critical density. The reason is that for smaller densities all vehicles can accelerate to the maximal speed $v_{\max}$. Therefore, the flow rate J is given by $J = \rho \cdot v_{\max}$.

Unlike in the NaSch, traffic flow is not strictly monotonically decreasing for larger densities. The reason is the major difference between the NaSch and the mNaSch: as opposed to the NaSch, the mNaSch converges to stable states where all vehicles move with the same speed v or with two different speeds v and $v-1$. We will refer to the first case as "speed-synchronized flow". When varying the system's density, the latter case can be regarded as a transition state between two speed-synchronized flows with speeds v and $v-1$.

We use the term "speed-synchronized flow" to make clear that these phases are not necessarily identical with Kerner's three-phase traffic theory: In early investigations (e.g., [8]) the synchronized phase was identified as a phase where vehicles travel with nearly identical speeds (even in different lanes) considerably below their maximum speed. In this sense, our speed-synchronized flow could be identified as Kerner's synchronized flow. Yet, more recent studies (summarized in [9]) have revealed a more complicated structure of synchronized flow.

As an example, Fig. 2a, b show the synchronization in a randomly initialized system with $\rho = 0.22$, $p_{\text{acc}} = 0.9$ and $L = 10^4$. Here the system converges to a stable state of speed-synchronized traffic flow where all cars have a speed of $v = 2$. Thereupon, $v^{\text{sf}}_{\rho,p_{\text{acc}}}$ refers to the speed of a stable state of speed-synchronized flow with given ρ and p_{acc}.

We will now examine the relationship between ρ and $v^{\text{sf}}_{\rho,p_{\text{acc}}}$. We chose $p_{\text{acc}} = 0.9$ for our analysis because, with this value, the non-monotonical decrease for densities $\rho > \rho_{p_{\text{acc}}}$ can be seen particularly well in Fig. 1a.

Figure 2c shows the share of vehicles with a given speed after 10^4 time steps for densities $\rho \in [0.01, 1]$ in steps of 0.01. Note that stable states of speed-synchronized flow with the same $v^{\text{sf}}_{\rho,0.9}$ are connected. We can therefore refer to a region of

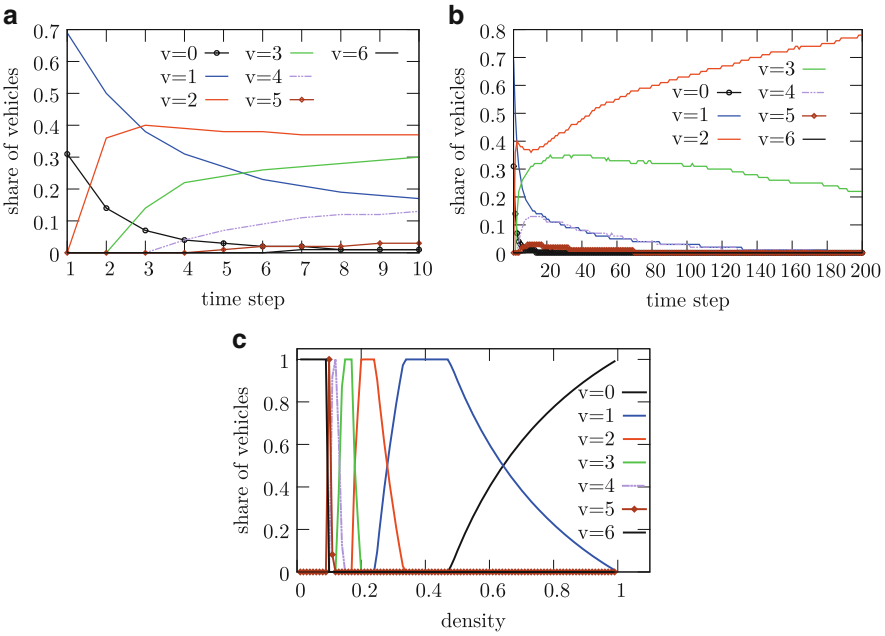

Fig. 2 For periodic boundary conditions one can see (**a**) the convergence to a stable state with speed-synchronized flow; time steps 1 to 10; $\rho = 0.22$, $p_{\text{acc}} = 0.9$ and $L = 10^4$. Each curve shows the percentage of cars with a certain speed. During the first few time steps cars frequently change their speeds. (**b**) After 200 time steps nearly all vehicles travel at a speed of $v = 2$ or $v = 3$. (**c**) The share of vehicles traveling at a given speed after a sufficient relaxation time (10^5 timesteps) for all densities with $p_{\text{acc}} = 0.9$

speed-synchronized flow when we mean a subset of [0.01,1] for which $v^{\text{sf}}_{\rho,0.9}$ is identical. Furthermore, $v^{\text{sf}}_{\rho,0.9}$ is monotonically decreasing with ρ. This is evident, for a higher density implies smaller distances between the cars in a stable state. Obviously traffic flow in a region of speed-synchronized flow is increasing with ρ. This is an important finding as it explains why the fundamental diagram is, in contrast to the fundamental diagram for the NaSch, not monotonically decreasing for $\rho > \rho_{p_{\text{acc}}}$.

Conclusion and Perspectives

The focus of this work was laid on a comparison of the Nagel Schreckenberg model and our modified version (mNaSch). We showed by means of simulations that the mNaSch converges to either a steady state of speed-synchronized flow or a steady state with only two different speeds. We regard the latter case as a transition state between two states of speed-synchronized

(continued)

flow. We found differences between the fundamental diagrams of the two models. The fundamental diagrams of the mNaSch model have been shown to be more complex than those of the NaSch. Traffic flow is not simply increasing until a certain density is reached and decreases then, but it is moving in waves with the peak-values decreasing in density. The two principal differences between the NaSch and the mNaSch are that (i) in the mNaSch braking capabilities are limited and (ii) vehicles accelerate with a certain probability whereas in the NaSch vehicles decelerate at random.

Acknowledgements TC and FK thank the German Research Foundation (DFG) for funding under grant no. SCHR 527/5-1.

Appendix: A Initial Conditions Guaranteeing Collision Free Driving

The proof of collision free driving (Sect. 2.1) requires that the road's previous configuration was free of collisions as well. Therefore, we present valid initial configurations for both open and periodic boundaries. First, the case of periodic boundaries: initially, N vehicles are randomly set on the road, and the initial speed of each vehicle is 0. Consequently, it holds that $x^i \neq x^j$ for $i \neq j$ and $\min(\delta^i) \geq 1 \ \forall i$. For all later times t, it follows $x_t^i = (x_{t-1}^i + v_t^i) \mod L$.

An open system represents a bottleneck situation where each car passes through the road only once. New cars enter the road via the left boundary, which requires that the leftmost site ($x = 1$) is empty. In this case a new car labeled k can be inserted with speed $v_t^k = \min\{v_{\text{in}}, \mu(v_{t-1}^{k+1}, x_{t-1}^{k+1} - 1)\}$ at position $x_t^k = 1 + v_t^k$, where $v_{\text{in}} = 2$ denotes the maximum speed of inserted cars. Afterwards, we apply the rules of motion to the remaining cars (i.e., all but the newly inserted one) and obtain the road's configuration at time t.

References

1. H.K. Lee , R. Barlovic, M. Schreckenberg, D. Kim, Phys. Rev. Lett. **23**, 238702 (2004)
2. K. Nagel, M. Schreckenberg, J. Phys. France I **2**, 2221–2229 (1992)
3. S. Maerivoet, B. De Moor Phys. Rep. **419**, 1–64 (2005)
4. A. Schadschneider, D. Chowdhury, K. Nishinari, *Stochastic Transport in Complex Systems: From Molecules to Vehicles* (Elsevier Science, Amsterdam, 2010)
5. E. Brockfeld, R. Kühne, A. Skabardonis, P. Wagner, Transp. Res. Rec. **1852**, 124–129 (2003)
6. F. Knorr, M. Schreckenberg, J. Stat. Mech. **2012**, P10018 (2012)
7. H. Emmerich, E. Rank, Physica A **234**, 676–686 (1997)
8. B.S. Kerner, H. Rehborn, Phys. Rev. E **53**(2), R1297–R1300 (1996)
9. B.S. Kerner, *Introduction to Modern Traffic Flow Theory and Control: The Long Road to Three-Phase Traffic Theory* (Springer, Berlin, 2009)

Part III
Biological Systems and Granular Flow

Diffusive Transport on Directed Random Networks

M. Reza Shaebani, Zeinab Sadjadi, and Ludger Santen

Abstract We study diffusive motion of non-interacting particles on directed random networks, motivated by the structural polarity of cytoskeletal filamentous structures in biological systems. We consider a complex network consisting of directed intersecting filaments. The network structure can be characterized by the distribution of the segment length between two neighboring intersections and the distribution of the angle between two intersecting filaments. The transport problem is studied by introducing a master equation for the probability of arriving at the vicinity of a given position along a certain direction. Using an analytical Fourier–Z-transform technique, we present expressions for the mean square displacement and the diffusion coefficient in terms of the microscopic geometrical properties of the structure and the persistency of the walker. The method enables us to investigate the influence of structural inhomogeneity and anisotropy of the network on the transport properties.

1 Introduction

Motor proteins are self-propelled particles that are powered by the hydrolysis of ATP and move along the cytoskeletal filaments by converting the chemical energy into mechanical work [1]. More generally, self-propelled particles consume energy, obtained either from external or internal sources, and dissipate it by undergoing active Brownian motion. Several examples exist, ranging from biologically relevant systems to nonliving realizations such as vibrated granular gases and self-motile colloidal particles that use a chemical reaction catalyzed on their surface to swim. Understanding the physical origin of the frequently observed anomalous transport of self-propelled particles in complex systems, specially in biological environments, has attracted much attention [2–7]. Here, by developing a general analytical framework, we study how the structural properties of the underlying network lead to a wide range of different types of anomalous transport on different timescales. We clarify and disentangle the combined effects of motor processivity and the

M.R. Shaebani (✉) • Z. Sadjadi • L. Santen
Department of Theoretical Physics, Saarland University, D-66041 Saarbrücken, Germany
e-mail: shaebani@lusi.uni-sb.de

M. Chraibi et al. (eds.), *Traffic and Granular Flow '13*,
DOI 10.1007/978-3-319-10629-8_68

heterogeneity and anisotropy of the underlying network on transport properties, and show how the competition between these key parameters leads to a rich phase diagram of motion. The method is also applicable to the problem of motion in continuous space, where the stepping strategy of the walker determines the transport properties.

2 Model

The motion of self-propelled particles can be considered as a random walk consisting of consecutive steps of different length and direction. We assume that the motion of the walker on the filamentous structure is characterized by the normalized probability distributions $R(\phi)$ and $F(\ell)$ for the intersection angle ϕ and the segment size ℓ, respectively. Note that a motor protein has an effective processivity, i.e. the tendency to move along the same filament [8, 9]. This effect is taken into account in our formalism by introducing a persistency probability p to stay on the same filament when crossing an intersection. We describe the motion of the particle by a Markovian stochastic process in discrete time and introduce $P_n(x, y|\theta)$ as the probability density for a particle to arrive at the position (x, y) with a direction of motion θ at time step n. The dynamical evolution of $P_n(x, y|\theta)$ is then expressed by the following master equation

$$\begin{aligned} P_{n+1}(x, y|\theta) &= p \int d\ell\, F(\ell)\, P_n\big(x-\ell\cos(\theta), y-\ell\sin(\theta)\big|\theta\big) \\ &+ s \int d\ell\, F(\ell) \int_{-\pi}^{\pi} d\gamma\, R(\theta-\gamma)\, P_n\big(x-\ell\cos(\theta), y-\ell\sin(\theta)\big|\gamma\big), \end{aligned} \tag{1}$$

where the first term on the right hand side describes the motion in the same direction as the previous step with probability p, representing the persistency of the walker. The second term corresponds to changing the direction with probability $s=1-p$ (see Fig. 1). It is quite hard to obtain an exact solution for the master equation

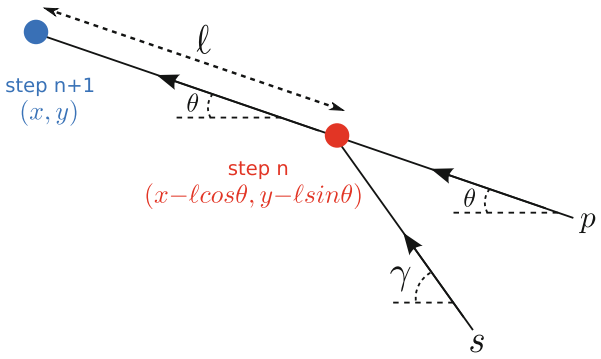

Fig. 1 Trajectory of the walker during two successive steps

(1), however, the explicit analytical expression for $P_n(x, y|\theta)$ is not necessarily required. Here, we use an analytical Fourier–Z-transform technique to evaluate the moments of the displacement without having the exact form of $P_n(x, y|\theta)$. See also Ref.[10] for a simplified version of the formalism applied for studying diffusive transport of light in wet foams.

We first introduce the characteristic function $P_n(\boldsymbol{\omega}|m)$ associated with $P_n(x, y|\theta)$, where $\boldsymbol{\omega}$ is the transform variable with components (ω_x, ω_y), or (ω, α) in polar representation. We define $P_n(\boldsymbol{\omega}|m)$ as a Fourier transform of the form

$$P_n(\boldsymbol{\omega}|m) \equiv \int_{-\pi}^{\pi} d\theta\, e^{im\theta} \int dy \int dx\, e^{i\boldsymbol{\omega}\cdot\boldsymbol{r}}\, P_n(x, y|\theta), \tag{2}$$

thus, the moment $\langle x^{k_1} y^{k_2}\rangle$ can be obtained as

$$\begin{aligned} \langle x^{k_1} y^{k_2}\rangle_n &\equiv \int d\theta \int dy \int dx\, x^{k_1} y^{k_2} P_n(x, y|\theta) \\ &= (-i)^{k_1+k_2} \frac{\partial^{k_1+k_2} P_n(\omega_x, \omega_y|m=0)}{\partial\omega_x^{k_1}\partial\omega_y^{k_2}}\bigg|_{(\omega_x,\omega_y)=(0,0)} . \end{aligned} \tag{3}$$

We are interested in the first and second moments of $P_n(x, y|\theta)$, namely, $\langle x\rangle_n$, $\langle y\rangle_n$, $\langle x^2\rangle_n$, and $\langle y^2\rangle_n$. Therefore, it is sufficient to evaluate the terms up to second order in ω in the Taylor series of $P_n(\boldsymbol{\omega}|m)$, given in the polar representation as

$$\begin{aligned} P_n(\omega, \alpha|m) &= Q_{0,n}(\alpha|m) + i\omega \int d\ell\, F(\ell)\, \ell\; Q_{1,n}(\alpha|m) \\ &\quad - \frac{1}{2}\omega^2 \int d\ell\, F(\ell)\, \ell^2\; Q_{2,n}(\alpha|m) + \cdots \\ &= Q_{0,n}(\alpha|m) + i\omega\, \langle\ell\rangle\, Q_{1,n}(\alpha|m) \\ &\quad - \frac{1}{2}\omega^2\, \langle\ell^2\rangle\, Q_{2,n}(\alpha|m) + \cdots . \end{aligned} \tag{4}$$

Then, from Eqs. (3) and (4) it follows that

$$\begin{aligned} \langle x\rangle_n &= \int d\ell\, F(\ell)\, \ell\; Q_{1,n}(0|0) &&= \langle\ell\rangle\, Q_{1,n}(0|0), \\ \langle y\rangle_n &= \int d\ell\, F(\ell)\, \ell\; Q_{1,n}\big(\frac{\pi}{2}|0\big) &&= \langle\ell\rangle\, Q_{1,n}\big(\frac{\pi}{2}|0\big), \\ \langle x^2\rangle_n &= \int d\ell\, F(\ell)\, \ell^2\; Q_{2,n}(0|0) &&= \langle\ell^2\rangle\, Q_{2,n}(0|0), \\ \langle y^2\rangle_n &= \int d\ell\, F(\ell)\, \ell^2\; Q_{2,n}\big(\frac{\pi}{2}|0\big) &&= \langle\ell^2\rangle\, Q_{2,n}\big(\frac{\pi}{2}|0\big). \end{aligned} \tag{5}$$

Fourier transforming Eq. (1), one can obtain

$$P_{n+1}(\omega,\alpha|m) = \sum_{k=-\infty}^{\infty} \Big[i^k e^{-ik\alpha} \times P_n(\omega,\alpha|m+k)\big(p + s\,\mathscr{R}(m+k)\big) \int d\ell\, F(\ell) J_k(\omega\ell) \Big], \tag{6}$$

where $\mathscr{R}(m) = \int_{-\pi}^{\pi} d\phi\; e^{im\phi} R(\phi)$ is the Fourier transform of the intersection angle distribution $R(\phi)$ and $J_k(z) = \frac{1}{2\pi i^k} \int_{-\pi}^{\pi} d\theta\; e^{iz\cos\theta} e^{-ik\theta}$ is the kth order Bessel function. As we are interested only in the Taylor coefficients $Q_{1,n}(\alpha|m)$ and $Q_{2,n}(\alpha|m)$, we insert Eq. (4) into Eq. (6). Using the Taylor expansion of the relevant Bessel functions $J_k(z)(|k| \le 2)$ and collecting all terms with the same power in ω, we get the following recursion relations for the Taylor coefficients $Q_{i,n}(\alpha|m)$:

$$Q_{0,n+1}(\alpha|m) = Q_{0,n}(\alpha|m)\big(p + s\,\mathscr{R}(m)\big),$$

$$Q_{1,n+1}(\alpha|m) = Q_{1,n}(\alpha|m)\big(p + s\,\mathscr{R}(m)\big) + \frac{1}{2}\Big[e^{i\alpha} Q_{0,n}(\alpha|m-1)\big(p + s\,\mathscr{R}(m-1)\big) + e^{-i\alpha} Q_{0,n}(\alpha|m+1)\big(p + s\,\mathscr{R}(m+1)\big) \Big],$$

$$Q_{2,n+1}(\alpha|m) = \Big[\frac{1}{2} Q_{0,n}(\alpha|m) + Q_{2,n}(\alpha|m) \Big]\big(p + s\,\mathscr{R}(m)\big) + \frac{\langle\ell\rangle^2}{\langle\ell^2\rangle} \Big[e^{i\alpha} Q_{1,n}(\alpha|m-1)\big(p + s\,\mathscr{R}(m-1)\big) + e^{-i\alpha} Q_{1,n}(\alpha|m+1)\big(p + s\,\mathscr{R}(m+1)\big) \Big] + \frac{1}{4} e^{2i\alpha} Q_{0,n}(\alpha|m-2)\big(p + s\,\mathscr{R}(m-2)\big) + \frac{1}{4} e^{-2i\alpha} Q_{0,n}(\alpha|m+2)\big(p + s\,\mathscr{R}(m+2)\big).$$

In order to solve these set of coupled equations we use the z-transform method. The z-transform $Q(z)$ of a function Q_n of a discrete variable $n = 0, 1, 2, \cdots$ is defined by

$$Q(z) = \sum_{n=0}^{\infty} Q_n z^{-n}. \tag{7}$$

By using z-transform we are able to solve the above set of coupled linear equations in z-space. We obtain a set of algebraic equations, whose z-transforms are accessible. Thus, we can obtain the first and second moments of x and y in n-space by means of inverse z-transform. Since the general expression for the mean square displacement

is lengthy in form, here we present the final result in a simple case of motion with left-right symmetry, and no processivity (p=0):

$$\langle r^2\rangle_n = n\langle\ell\rangle^2\left[\lambda + \frac{2\mathscr{R}}{1-\mathscr{R}}\right] + \langle\ell\rangle^2 \frac{2\mathscr{R}}{\left(1-\mathscr{R}\right)^2}\left(\mathscr{R}^n - 1\right), \tag{8}$$

where $\lambda = \langle\ell^2\rangle/\langle\ell\rangle^2$ is the relative variance of the segment-size distribution.

3 Results

In this section we briefly introduce the possible scenarios of anomalous diffusion which directly originate from the microscopic details of the stepping strategy of the walker. The time evolution of the mean square displacement $\langle r^2\rangle$ is shown in Fig. 2 for different values of the parameters p, $\mathscr{R}$, and λ. Interestingly, it turns out that the behavior at small time scales can vary from super to normal diffusion and even to subdiffusion and oscillatory behavior (not shown). Indeed, positive values of $\mathscr{R}$ facilitate the forward motion of the particle and lead to superdiffusion, while a negative $\mathscr{R}$ competes against the processivity, leading to a variety of anomalous behavior depending on the relative importance of p and $\mathscr{R}$. Another point is that increasing the heterogeneity of the structure pushes the initial slope of $\langle r^2\rangle$ towards normal diffusion. The heterogeneity λ appears only in the linear term with n in Eq. (8), therefore, increasing λ increases the contribution of the linear term which changes the initial slope of the curve towards normal diffusion. To conclude, one may observe up to three different regimes of motion at short, intermediate, and large time scales (see Fig. 2(right)).

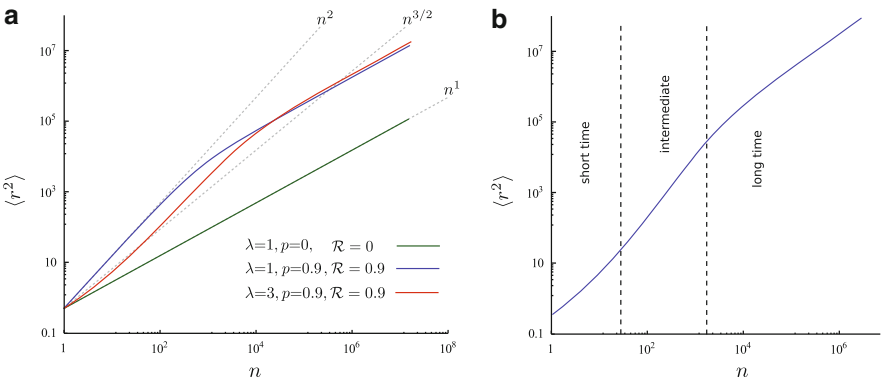

Fig. 2 (**a**) A few examples of different types of motion. The mean square displacement $\langle r^2\rangle$ versus the number of time steps n for different values of p, $\mathscr{R}$, and λ. (**b**) Schematic diagram of the three possible regimes of motion

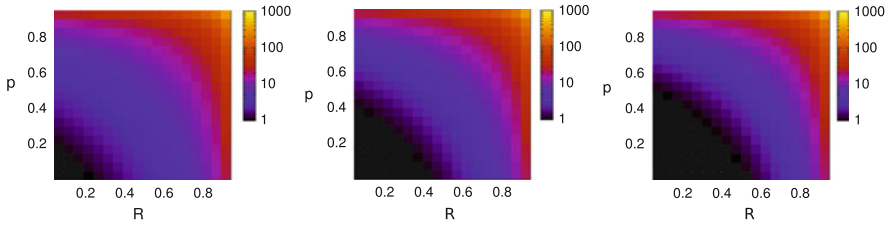

Fig. 3 The crossover time to the asymptotic diffusion in $p - \mathscr{R}$ plane for (*left*) $\lambda=1$, (*middle*) $\lambda=5$, and (*right*) $\lambda=10$. The color intensity reflects the number of time steps at which the crossover occurs

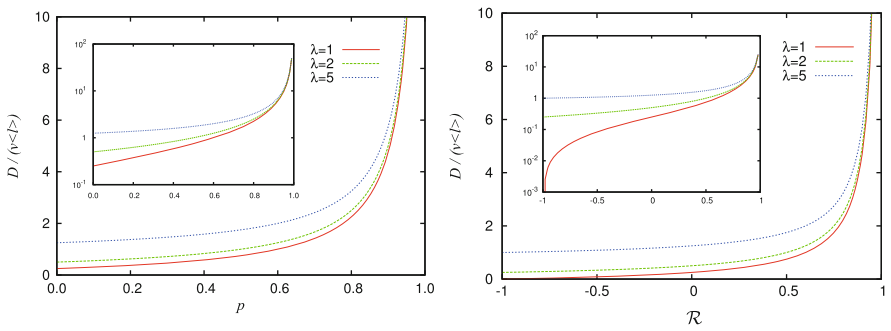

Fig. 4 The long-term diffusion coefficient D in terms of (*left*) p (at $\mathscr{R}=0$) and (right) $\mathscr{R}$ (at $p=0$) for different values of λ. *Insets*: The same plots in log-lin scales

The correlation between consecutive turning angels has a finite length scale, i.e. the particle eventually (on large time scales) forgets its local direction and gets completely randomized. The crossover time to reach the asymptotic diffusive regime is shown in Fig. 3. The time scale varies several orders of magnitude depending on the choice of the parameter values. This indicates that the time window in experiments should be chosen wide enough to capture all possible regimes of motion. Finally, we investigate how the asymptotic diffusion coefficient D varies with the control parameters of the problem. As shown in Fig. 4, D increases several orders of magnitude with increasing p, $\mathscr{R}$, or λ.

In summary, we disentangled the combined effects of the structural properties and motor processivity, and related the details of the transport on the level of individual steps to the macroscopically observable transport coefficients.

Acknowledgements This work was funded by the Deutsche Forschungsgemeinschaft (DFG) through Collaborative Research Centers SFB 1027 (Projects A7 and A3).

References

1. M. Schliwa, G. Woehlke, Nature **422**, 759 (2003)
2. P.C. Bressloff, J.M. Newby, Rev. Mod. Phys. **85**, 135 (2013)
3. F. Höfling, T. Franosch, Rep. Prog. Phys. **76**, 046602 (2013)
4. T. Neusius, I.M. Sokolov, J.C. Smith, Phys. Rev. E **80**, 011109 (2009)
5. M. Magdziarz, A. Weron, K. Burnecki, J. Klafter, Phys. Rev. Lett. **103**, 180602 (2009)
6. S. Klumpp, R. Lipowsky, Phys. Rev. Lett. **95**, 268102 (2005)
7. A. Caspi, R. Granek, M. Elbaum, Phys. Rev. Lett. **85**, 5655 (2000)
8. M.Y. Ali et al., Proc. Natl. Acad. Sci. **104**, 4332 (2007)
9. K. Shiroguchi, K. Kinosita, Science **316**, 1208 (2007)
10. Z. Sadjadi, M.F. Miri, M.R. Shaebani, S. Nakhaee, Phys. Rev. E **78**, 031121 (2008)

Stochastic Modeling of Cargo Transport by Teams of Molecular Motors

Sarah Klein, Cécile Appert-Rolland, and Ludger Santen

Abstract Many different types of cellular cargos are transported bidirectionally along microtubules by teams of molecular motors. The motion of this cargo-motors system has been experimentally characterized *in vivo* as processive with rather persistent directionality. Different theoretical approaches have been suggested in order to explore the origin of this kind of motion. An effective theoretical approach, introduced by Müller et al. [9], describes the cargo dynamics as a tug-of-war between different kinds of motors. An alternative approach has been suggested recently by Kunwar et al. [7], who considered the coupling between motor and cargo in more detail.

Based on this framework we introduce a model considering single motor positions which we propagate in continuous time. Furthermore, we analyze the possible influence of the discrete time update schemes used in previous publications on the system's dynamic.

1 Introduction

In the last years bidirectional motion along microtubules was observed in many different cell types [10, 12]. In most of these cells it is still not clear how this bidirectional motion is realized.

S. Klein (✉)
Theoretical Physics, Universität des Saarlandes, Postfach 151150 - Gebäude E2.6, 66041 Saarbrücken, Germany

Laboratory of Theoretical Physics, Batiment 210, University Paris-Sud, F-91405 Orsay Cedex, France
e-mail: sarah.klein@th.u-psud.fr

C. Appert-Rolland
Laboratory of Theoretical Physics, Batiment 210, University Paris-Sud, F-91405 Orsay Cedex, France

L. Santen
Theoretical Physics, Universität des Saarlandes, Postfach 151150 - Gebäude E2.6, 66041 Saarbrücken, Germany

M. Chraibi et al. (eds.), *Traffic and Granular Flow '13*,
DOI 10.1007/978-3-319-10629-8_69

Similar to a human road network connecting different places, the cell provides several filaments which can be used for directed transport. Besides the transport utility, the filaments give the cell its characteristic shape. To achieve this double goal the cell produces a cortex of filaments close to the membrane and radial growing filaments from the nucleus to the periphery. The set of these filaments constitutes the cytoskeleton. Intracellular transport along microtubules, which is a radial growing filament, is managed by mainly two kinds of transporters, the so-called molecular motors which are identified as kinesin and dynein [6]. The principal difference between the two kinds of motors is their preferred walking direction. The microtubules are polarized, i.e. they have well-defined directions which are called plus- and minus-direction, respectively. Kinesin's preferred orientation is to the plus-end of the microtubule, while dynein's orientation is opposed. Assuming that microtubules mainly grow with their plus end to the cell periphery cellular cargos can be moved to the nucleus and to the membrane by dynein and kinesin, respectively. However, secretory cargos which could be thought to leave the cell as fast and straight as possible, actually show a saltatory motion in vivo [11]. This behavior suggests that a number of cellular cargos exists, on which kinesins as well as dyneins are bound at the same time. One possible reason for this motion is to pass obstacles by a second try [2]. The detailed mechanisms, which are leading to this unconventional bidirectional motion are for most of the motor-cargo systems still unknown.

To describe this bidirectional motion theoretically two mechanisms have been suggested: The first one assumes that N_+ kinesins and N_- dyneins are involved in a mechanical tug-of-war and fight for the direction the cargo effectively moves, while the second one requires a control mechanism to achieve coordinated in vivo-behavior [5, 13]. The *pure* tug-of-war model was introduced by Müller et al. [9] to describe lipid droplet movement in evolving *Drosophila* embryo cells. They use a mean-field model, meaning that the motors of one team share the load equally. As a consequence, all kinetic quantities are determined by the number of attached motors to the filament. Indeed, since the motors can bind to and unbind from the filament, the number of motors of each kind attached to the filament fluctuates between zero and $N_\pm$ with time. Between two attachment/detachment events, the cargo's velocity is constant and determined by the strength of the two teams (which depends on the number of attached motors). The number of attached motors also determines the load force felt by each team of motors, and exerted by the opposite team via the cargo. Once one motor detaches one observes a cascade of detachments of motors of this kind and therewith it is possible, in the framework of this model, to generate motility states with high velocity, where one team *wins* over the other.

This model is quite elegant since experimental observables like the cargo's velocity can be calculated analytically. However, since this walking in concert was not yet observed in vitro, Kunwar et al. had a closer look at different observables, like the pausing time and run length of single trajectories but did not find matching results in experiments. Therefore they introduced a model taking explicitly the motor positions into account and models the motor-cargo coupling as a linear spring.

In this contribution, we introduce a general model with simple reaction rates which propagates the cargo along its equation of motion in *continuous* time.

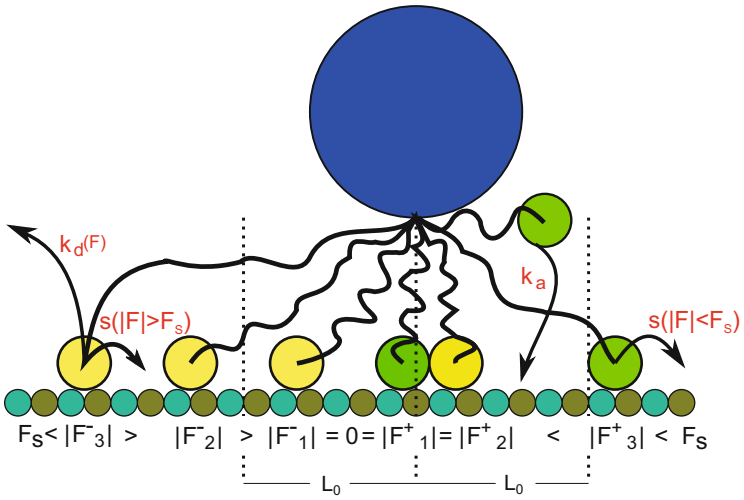

Fig. 1 Sketch of the model dynamics. Two kind of motors: one team prefers to walk to the plus-end (*green*) while the other prefers walking to the minus-end (*yellow*) of a microtubule. Within the region L_0 around the cargo's center of mass the motors apply no force on the cargo (*blue*)

Furthermore, we compare and discuss the consequences of using different update schemes.

2 Model

Inspired by the bidirectional cargo transport models of [7, 9] we define a stochastic model to move a cargo by teams of molecular motors along a microtubule. N_+ and N_- motors are tightly bound to the cargo and pull it in plus- and minus-direction, respectively, as shown in Fig. 1. In contrast to [9] and in agreement with [7] we take every single motor position x_i into account and calculate the thereby generated force F_i on the cargo. We model the motor tail, which permanently connects the motor head to the cargo, as linear spring with an untensioned length L_0 and a spring constant α. In contrast to Müller's model [9] where the motors can attach (with rate k_a) to and detach from the filament (with force-dependent rate $k_d(F_i)$) only, in our model the motors can once bound to the filament, a one-dimensional infinite lattice, can make a step of size d with a force-dependent rate $s(F_i)$. Since it seems to be biological relevant that the motors feel no force when they attach to the filament we reduce the allowed attachment region to $\pm L_0$ around the center of mass of the cargo.

Due to the de-/attaching events the number $n_\pm$ of plus (minus) motors bound to the filament is in the range $0 \leq n_+ \leq N_+$ ($0 \leq n_- \leq N_-$). The resulting force on the cargo at position $x_C(t)$ at time t is then given by the sum of all single forces

$$F\ (x_C(t), \{x_i\}) = \sum_{i=1}^{n_+ + n_-} F_i(x_C(t), \{x_i\}) \tag{1}$$

$$= \sum_{i=1}^{n_+ + n_-} \alpha \Big[\Big((x_i - x_C(t)) - L_0 \operatorname{sgn}(x_i - x_C(t)) \Big) \cdot \Theta\big(|x_C(t) - x_i| - L_0\big) \Big],$$

with the Heaviside step function $\Theta(.)$. In this paper we illustrate how we extend the model of Kunwar et al. for a continuous time propagation of the cargo in the case of the simple relations for the stepping and detachment rates introduced in [9] and given below.

The motors cannot stand arbitrarily high forces. Thus the so-called stall force F_S gives the maximal force under which a motor can walk in its preferred direction. We split the stepping rate $s(F_i)$ in two regimes: (I) forces smaller in absolute value than the stall force ($|F_i| < F_S$) where the motors walk in their preferred direction and (II) forces bigger in absolute value than the stall force ($|F_i| \geq F_S$) where the motors walk opposed to their preferred direction and use

$$s(|F_i|) = \begin{cases} \frac{v_f}{d}\left(1 - \frac{|F_i|}{F_S}\right) & |F_i| < F_S \\ \\ \frac{v_b}{d}\left(1 - \frac{|F_i|}{F_S}\right) & |F_i| < F_S \end{cases} \tag{2}$$

with $v_b \ll v_f$ [1, 8].

Assuming that the motors can walk on several close microtubules in a crowded environment and that their attachment point to the cargo is not necessarily the same, a sterical exclusion of the motor heads on the lattice is not regarded in the model.

For the detachment rate we use [9]

$$k_d(|F_i|) = k_d^0 \exp\left(\frac{|F_i|}{F_D}\right), \tag{3}$$

with the force-free detachment rate k_d^0 and the detachment force F_D, which determines the force scale.

Update Mechanisms

In the mean-field model [9] the cargo moves with a constant velocity during two motor events, calculated by the number of attached motors of each team. The time

at which the next event occurs, is calculated by means of Gillespie's algorithm [3]. Within this framework the cargo's velocity is piecewise linear.

Kunwar et al. [7] use a parallel, thus discrete time update scheme to propagate the system. At every fixed time step Δt they calculate the probability that a motor event occurs within this time step. An event should be rare within Δt to get a good approximation of the exact solution in continuous time. In their simulations they use $\Delta t = 10^{-6}$ s.

Once the motor dynamic is determined, one has to decide how the cargo reacts to each change in the motor configuration. In [7] two different cargo dynamics are introduced: either the cargo moves instantaneously to the position with balanced forces, or it undergoes a viscous force from the environment. The mean-field model of [9] was treated in the case of an instantaneously reacting cargo.

In [7] a viscous environment was taken into account by calculating the position of a cargo with radius R after Δt according to

$$x_C(t + \Delta t) = x_C(t) + \sum_{i=1}^{n_+ + n_-} \frac{F_i}{6\pi\eta R}, \tag{4}$$

where η is the fluid's viscosity.

To get a more general approach we rather use the cargo's equation of motion

$$m\frac{\partial^2 x_C(t)}{\partial t^2} = -\beta\frac{\partial x_C(t)}{\partial t} + \sum_{i=1}^{n_+ + n_-} F_i(x_C(t), \{x_i\}), \tag{5}$$

with $\beta = 6\pi\eta R$ and the cargo's mass m, to determine the time-dependent position of the cargo.

By determining the force applied on each motor by the distance between motor head position and the center of mass of the cargo, the force F_i depends on time, too. Hence, the motor rates for stepping and detaching are time-dependent. Thus the cargo moves in a viscous medium in a harmonic potential of the sum of the springs. Note that the number of engaged springs changes, if the distance between a motor and the cargo falls below or exceeds L_0. Therefore we have to solve Eq. (5) piecewise on segments with a constant number of motors which pull the cargo. On every single segment we solve the equation

$$m\frac{\partial^2 x_C(t)}{\partial t^2} = -\beta\frac{\partial x_C(t)}{\partial t} - \epsilon x_C(t) + \epsilon\zeta, \tag{6}$$

with

$$\epsilon = \sum_{i=1}^{n_+ + n_-} \alpha \cdot \Theta\big(|x_C(t) - x_i| - L_0\big) \tag{7}$$

which determines the effective spring constant and

$$\zeta = \sum_{i=1}^{n_+ + n_-} \big(x_i - \mathrm{sgn}(x_C(t) - x_i) L_0\big) \cdot \Theta\big(|x_C(t) - x_i| - L_0\big), \tag{8}$$

the effective potential generated by the given motor configuration. We then get the cargo position $x_C(t)$ at time t on the segments with constant number of pulling motors

$$x_C(t) = \frac{\lambda_1 \zeta + \lambda_1 x_0 - v_0}{\lambda_1 - \lambda_2} \exp(\lambda_2 t) + \frac{v_0 - \lambda_2 \zeta - \lambda_2 x_0}{\lambda_1 - \lambda_2} \exp(\lambda_1 t) - \zeta \tag{9}$$

with

$$\lambda_1 = -\frac{\beta}{2m} + \sqrt{\left(\frac{\beta}{2m}\right)^2 - \frac{\epsilon}{m}} \quad \text{and} \quad \lambda_2 = -\frac{\beta}{2m} - \sqrt{\left(\frac{\beta}{2m}\right)^2 - \frac{\epsilon}{m}}. \tag{10}$$

Now knowing the cargo position at an arbitrary time t we can use Gillespie's algorithm for time-dependent rates [4] to calculate the next event time.

3 Results

At first we analyze the distribution of times between two motor updates which we generate with the exact algorithm and the parameter set given in Table 1.

In Fig. 2 the normalized count of times between events is shown in a double logarithmic plot. Obviously, times smaller than $\Delta t = 10^{-6}$ s occur if we propagate the system with the exact algorithm. By analyzing 10^5 events we calculated the mean time between events $\langle t \rangle$ for the two stall forces as well as the smallest t_s and the longest time t_l between two events and get

$$\underline{F_S = 2\,\mathrm{pN}} \quad \langle t \rangle = 3.5 \cdot 10^{-3}\,\mathrm{s} \quad t_s = 3.1 \cdot 10^{-8}\,\mathrm{s} \quad t_l = 1.8 \cdot 10^{-1}\,\mathrm{s}$$

$$\underline{F_S = 6\,\mathrm{pN}} \quad \langle t \rangle = 1.8 \cdot 10^{-3}\,\mathrm{s} \quad t_s = 1.6 \cdot 10^{-8}\,\mathrm{s} \quad t_l = 8.1 \cdot 10^{-2}\,\mathrm{s}.$$

Table 1 Simulation parameter for the results below

$N_\pm$	5
v_f	1,000 nm/s
v_b	6 nm/s
D	0.32 pN/nm
F_D	3 pN
k_a	$5.0\,\mathrm{s}^{-1}$
k_d^0	$1\,\mathrm{s}^{-1}$
F_S	6 / 2 pN
R	250 nm

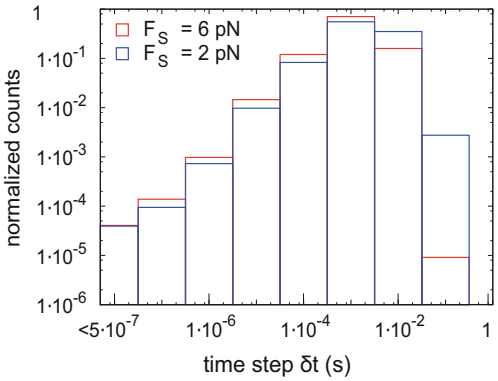

Fig. 2 Log-log plot of the normalized count of times between two occurring events calculated by the exact algorithm [4] for $F_S = 2$ pN (*blue*) and $F_S = 6$ pN (*red*). Obviously, times between events smaller than 10^{-6} s occur for both stall forces

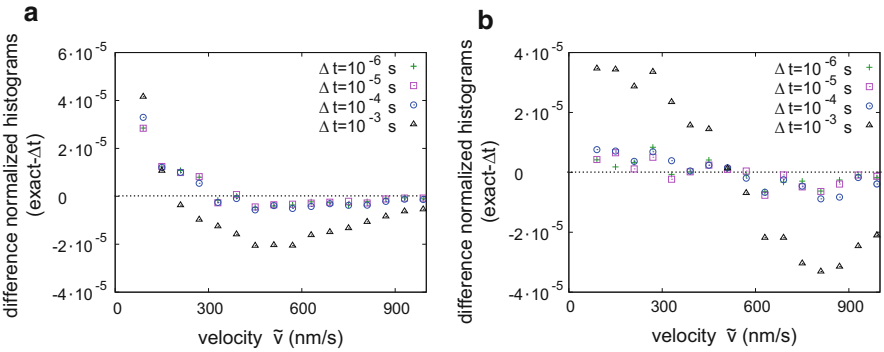

Fig. 3 Difference between the exact velocity histogram generated with Gillespie's algorithm [4] and the parallel update scheme suggested in [7] with different Δt for **(a)** $F_S = 2$ pN and **(b)** $F_S = 6$ pN. Sample size per histogram: $5 \cdot 10^6$

It remains the question how this influences the system's observables. In [7] the focus is on the run length and pause duration of the single walks. However, as the motion is stepwise, these observables are defined from quite arbitrary time/distance thresholds. That is why we preferred to concentrate on another quantity to compare our data to the parallel update scheme, namely the discrete velocity

$$\tilde{v} = \frac{|x(t + \mathrm{D}t) - x(t)|}{\mathrm{D}t}, \tag{11}$$

where we use $\mathrm{D}t = 0.16$ s as it was suggested in [9].

In Fig. 3 we show the difference between the normalized velocity histogram generated by Gillespie's algorithm [4] and those generated by the parallel update

Table 2 Mean discrete velocity $\langle \tilde{v} \rangle$ in nm/s for the exact and the parallel update

		Δt			
F_S	Exact	10^{-6} s	10^{-5} s	10^{-4} s	10^{-3} s
2 pN	149.0	149.8	149.7	150.3	155.4
	±0.10	±0.05	±0.05	±0.08	±0.08
6 pN	449.4	450.2	450.4	451.1	458.5
	±0.18	±0.09	±0.13	±0.13	±0.13

scheme for different Δt and for two different stall forces F_S. In both cases an increase in Δt increases the cargo's velocity as shown in Table 2.

4 Discussion

We have introduced in this contribution an exact algorithm to propagate the motors-cargo system in continuous time.

An analysis of the times between two events reveals that very different time scales are involved: while most times between two events are greater than 10^{-3} s, a fraction of events are separated by less than 10^{-7} s.

From our results, a first conclusion is that if one uses parallel update, the time step Δt should at least be less than 10^{-5} s to expect results in good agreement with the continuous time dynamics. However, the continuous time dynamics reveals that much shorter time scales are involved, as a signature of cascades of events. These cascades are overlooked in the discrete updates even for time steps as small as $\Delta t = 10^{-6}$ s. While we have found that this approximation does not alter the quality of measurements of most quantities when such a small time step is used (as it is the case in [7]), one cannot exclude that for some other sets of parameters, and/or for more sensitive observables, these cascades could have a stronger effect. Actually, though further numerical support should be provided to conclude, our results seem to indicate that discrete updates systematically slightly underestimate the probability to have weak cargo velocities (unless prohibitively small time steps would be used). This can be understood as an effect of the synchronization of the motors induced by the time discretization, similarly to what happens with the mean-field assumption used in [9] (which can also be seen as a synchronization mechanism) which overemphasizes large velocity states. As a conclusion, in such a system involving very different time scales, an exact algorithm in continuous time provides an efficient numerical scheme: it allows to avoid any possible artefact that would come from the discretization, without any extra numerical cost.

In further work we will extend this model to more realistic motor rates and show for biologically relevant parameter sets how some external quantity like the ATP concentration or the viscosity of the surrounded fluid can control the drift of the cargo [14].

Acknowledgements This work was supported by the Deutsche Forschungsgemeinschaft (DFG) within the collaborative research center SFB 1027 and the research training group GRK 1276.

References

1. N. J. Carter et al., Nature **435**(7040), 308–312 (2005)
2. K. Döhner et al., Trends Microbiol. **13**(7), 320–327 (2005)
3. D.T. Gillespie, J. Comput. Phys. **22**(4), 403–434 (1976)
4. D.T. Gillespie, J. Comput. Phys. **28**(3), 395–407 (1978)
5. S.P. Gross et al., J. Cell Biol. **156**(4), 715–724 (2002)
6. N. Hirokawa et al., Curr. Opin. Cell Biol. **10**(1), 60–73 (1998)
7. A. Kunwar et al., Proc. Nat. Acad. Sci. **108**(47), 18960–18965 (2011)
8. R. Mallik et al., Curr. Biol. **15**(23), 2075–2085 (2005)
9. M.J.I. Müller et al., Proc. Nat. Acad. Sci. **105**(12), 4609–4614 (2008)
10. G. Steinberg et al., J. Microsc. **214**(2), 114–123 (2004)
11. B. Trinczek et al., J. Cell Sci. **112**(Pt 14), 2355–2367 (1999)
12. M.A. Welte, Curr. Biol. **14**(13), R525–R537 (2004)
13. M.A. Welte et al., Cell **92**(4), 547–557 (1998)
14. S. Klein, C. Appert-Rolland, L. Santen, EPL **107**(1), 18004 (2004)

Molecular Motors with a Stepping Cycle: From Theory to Experiments

Luca Ciandrini

Abstract The traffic of molecular motors is often represented by means of Poissonian particles moving on a unidimensional track. However, biological 'particles' generally advance with complicated stepping cycles, passing through different biochemical and conformational states. In this contribution we review an extension of the typical exclusion process, the archetypical model of unidimensional transport; we explore it first from a theoretical point of view, and then we show how it has been possible to provide quantitative comparisons to experiments in the context of mRNA translation.

1 Introduction

Many macromolecules perform active directed motion on different biological tracks inside the cell. Often called molecular motors, all those molecules share the same general feature: they convert energy from a biochemical source into mechanical motion. Among the several types of self-propelled molecules involved in sub-cellular processes, some move on linear substrates in order to efficiently transport matter and organise large-scale structures inside the cell (such as kinesins or myosins on microtubules or dyneins on actin filaments). In addition to those, other linear motors are implicated in biopolymerisation processes. For instance, RNA polymerases are complexes that 'walk' on a strand of DNA to produce a messenger RNA (mRNA), and ribosomes are molecular motors that are able to read and translate the genetic information encoded in the mRNAs, and assemble the corresponding proteins [1]. Interestingly, many motors can bind their corresponding unidimensional tracks (e.g. microtubules, mRNA, ...) concurrently; since they cannot overtake each other, this causes traffic effects and collective phenomena of molecular motors.

Although the model reviewed in this contribution is rather general and its different aspects can be adapted to different types of motors, here we will deal in particular on the traffic of ribosomes moving on mRNAs and translating their

L. Ciandrini (✉)
DIMNP UMR 5235 CNRS, and Laboratoire Charles Coulomb UMR 5221 CNRS, Université Montpellier II, Montpellier Cedex, France
e-mail: luca.ciandrini@univ-montp2.fr

M. Chraibi et al. (eds.), *Traffic and Granular Flow '13*,
DOI 10.1007/978-3-319-10629-8_70

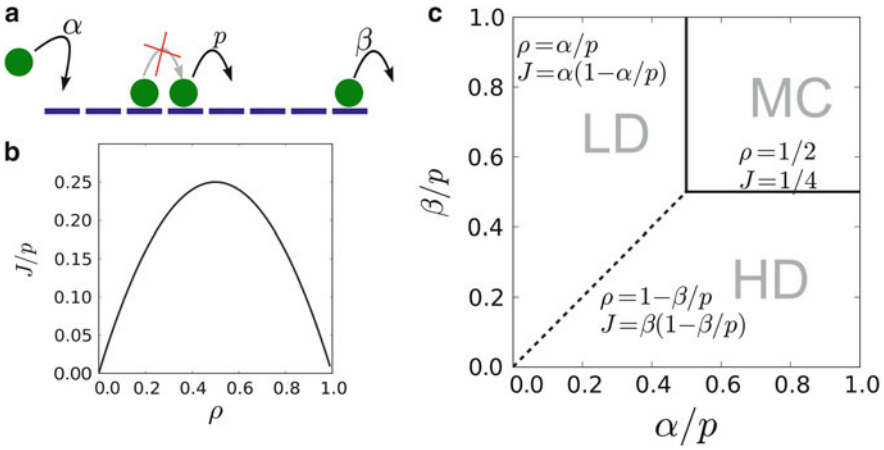

Fig. 1 A standard exclusion process is represented in panel (**a**), with the particle dynamics explained in the main text. Panel (**b**) shows the typical density-current relation $J = p\rho(1-\rho)$, while in (**c**) we have drawn the phase diagram of the system, highlighting the three phases the system shows: low density (*LD*), high density (*HD*) and maximal current (*MC*). The *dashed line* represents a first order transition (where LD and HD coexist) and the *continuous line* represents the second order transition towards the MC

encoded message. It was precisely for this problem that a prototypic model of traffic in one dimension has been introduced in the literature by MacDonald and coworkers in 1968 [2]: the totally asymmetric simple exclusion process (TASEP). In this model, particles (ribosomes) are injected from one side of a discrete unidimensional lattice composed of L sites (an mRNA with L codons, i.e. triplets of nucleotides) with a rate α, then they move from one site to the following one with a hopping rate p (provided that it is not occupied by another particle), and at the end of the chain they are depleted with a rate β (see Fig. 1a). This apparently simple model has however a very rich phenomenology, and for this reason it has been deeply studied in the mathematical and physical literature since the 1970s. In the following we will give a brief and not exhaustive summary of some known results of the TASEP.

1.1 The TASEP: Survival Guide

The exclusion process, being one of the few out of equilibrium models that can be exactly solved, has become a paradigmatic subject of study in nonequilibrium statistical mechanics. More in particular, for each couple of parameters α and β, the particle density ρ (average amount of particles on a lattice divided by L) and the particle current J (particles passing through a site per unit of time) are known [3]. The system shows boundary-induced transitions, where the current J plays a role analogous to the free energy of an equilibrium system. Intuitively, if the particles

are slowly injected in the system, i.e. if the entry rate α is smaller than the other rates, the lattice is found in a low density (LD) phase, with just a few particles on it; on the contrary, if the exit rate β is limiting, the lattice will be in a high density (HD) phase, with particles start jamming from the end of the lattice. However, if none of the boundaries is limiting, the system enters a so called maximal current (MC) phase, where the density and the current no longer depends on α and β.

A mean-field (MF) theory is proved to be correct in the limit of large systems ($L \to \infty$) and it provides the correct fundamental diagram (Fig. 1b), and phase diagram of the system (Fig. 1c). For instance, the fundamental diagram shows the dependency of the current over the density: in MF, interpreting ρ as the probability of finding a particle on a given site and $1 - \rho$ as the probability of finding a hole, the current can be expressed as $J = p\rho(1 - \rho)$ (Fig. 1b). The MF values of density and current in the different phases can be found in (Fig. 1c); a refined examination of the features of the exclusion process is beyond the scope of this work, but it can be found in other publications (see, e.g., [3]).

Different 'flavours' or variants of the TASEP have been developed during the years to describe several traffic problems, often related to biological systems. Among the many variants to the standard homogeneous exclusion process described above, we remind here the works on lattices with inhomogeneities (e.g. [4, 5]), static defects [6–8] or dynamical ones [9], once again inspired by the translation of the mRNA by ribosomes; the TASEP-LK [10] (TASEP with Langmuir Kinetics) where particles can attach and detach anywhere in the lattice like motor proteins do; TASEP with finite resources of particles [11–14], or in which particles occupy more than one site at a time [15, 16], or where they have to undergo a stepping cycle to advance [17]. The following part of this contribution is indeed focused on particles having a stepping cycle, and we show that the presence of even the simplest stepping kinetics can induced large changes in the phenomenology of the transport process.

2 A Simple Stepping Cycle: Theory

In contrast to a standard TASEP, where particles attempt to translocate to the next site as Poissonian steppers, here we study a model with particles having an extra degree of freedom, or stepping cycle. Biological 'particles' are in fact much more complicated objects than Poissonian walkers and, to advance, they need to undergo several biochemical and mechanical stages. Here we consider a lattice gas with particles having the simplest stepping kinetics, where they need to be excited before translocating, and only excited particles can move (if the following site is empty), see Fig. 2. All other features (such as exclusion and boundaries) remain the ones introduced above for the TASEP.

From a more mathematical point of view, the occupation number $n_i = 0, 1, 2$ of a site i of the lattice describes the different states in which it can be found: if a site is empty its occupation number is 0, while a site i occupied by a particle in the ground or excited state is respectively described by $n_i = 1$ or $n_i = 2$. Then the only

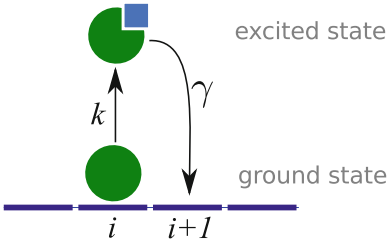

Fig. 2 A schematic representation of the simplest stepping cycle: a particle in the ground state becomes excited (in the figure an excited particle is marked with a *square* on the top-right), and only after the excitation it can move to the following site

transitions allowed by the stepping cycle described above are the following:

$$1 \rightarrow 2 \quad \text{with rate } k \tag{1}$$

$$20 \rightarrow 01 \quad \text{with rate } \gamma, \tag{2}$$

where the first line means that a particle in the ground state becomes excited with rate k, and the second line is a schematic representation of the translocation of an excited particle to the empty next site. This dynamics has been first introduced in the literature by Klumpp and coworkers in [18] to model the traffic of molecular motors on a filament, and then investigated in [19] in the perspective of mRNA translation and having in mind the properties of the ribosomal bio- and mechano-chemical cycle. The formalism is adapt to describe molecular motors whose movement is controlled by a biological substrate that provides the energy necessary to some conformational changes, then followed by the translocation of the motor.

The values of the occupation numbers n_i's change with time according to these dynamical rules:

$$\frac{d\langle n_i\rangle}{dt} = \gamma\langle\delta_{n_{i-1},2}\delta_{n_i,0}\rangle + k\langle\delta_{n_i,1}\rangle - 2\gamma\langle\delta_{n_i,2}\delta_{n_{i+1},0}\rangle \ , \tag{3}$$

where, with the presence of the Kronecker δ, the first two terms represent an increase of n_i by one due to an incoming particle ($n_i = 0 \rightarrow 1$) or a particle undergoing a transition ($n_i = 1 \rightarrow 2$), while the last term represents an excited particle leaving the site ($n_i = 2 \rightarrow 0$). The brackets indicate the average of the quantities over time, which are equivalent to ensemble averages. By defining $\lambda_i \equiv \langle\delta_{n_i,1}\rangle$, $\sigma_i \equiv \langle\delta_{n_i,2}\rangle$ as the average occupancy of respectively ground and excited particles on the site i, and $\rho_i \equiv \langle\delta_{n_i,1} + \delta_{n_i,2}\rangle$ as the total occupancy of the site i, it is possible to establish a MF theory. In this framework, we will approximate $\langle\delta_{n_i,2}\delta_{n_j,1}\rangle \sim \sigma_i\rho_j$ and the

mean-field equations describing the evolution of the densities at site i can be written as [19]:

$$\frac{d\lambda_i}{dt} = \sigma_{i-1}(1-\lambda_i-\sigma_i)\gamma - k_i\lambda_i \tag{4}$$

$$\frac{d\sigma_i}{dt} = k_i\lambda_i - \sigma_i(1-\lambda_{i+1}-\sigma_{i+1})\gamma \ . \tag{5}$$

We will first review the periodic boundary case (a circular lattice with a fixed total density of particle ρ) to study the fundamental diagram of this model, and then move our attention to the open boundary case.

2.1 The Periodic Boundary Case: Fundamental Diagram

Considering the steady-state, from Eqs. (4) and (5) one can find the MF value of the current of particles J as a function of the total density ρ (see [19]):

$$J = k\frac{\rho(1-\rho)}{w+(1-\rho)} \ , \tag{6}$$

where $w \equiv k/\gamma$ is the ratio between the excitation and translocation rate. The values of the densities only depend on w and ρ, while the current timescale also depends on their absolute values (presence of k in Eq. (6)). In the large w limit we recover the TASEP results, while new properties emerge when the internal transition becomes limiting.

We make use of a standard TASEP with hopping rate $p = k\gamma/(k+\gamma)$ to compare the two models (the TASEP and the model with two internal states, the *two-state model*): an isolated particle that moves with rate p has the same (mean) hopping time of an isolated two-state particle. Hence, the two models should behave similarly in the low density regime, and the differences arise only as a consequence of the internal transition.

Figure 3 shows the comparison between the density-current relation of two-state model (MF, and simulations carried out with a Gillespie-like algorithm) and the TASEP. We immediately notice that (i) the two-state model carries higher currents compared to the TASEP, and (ii) that it reaches its maximum for higher densities (larger than 0.5), indicating that the particle-hole symmetry no longer holds in the two-state model. Moreover, (iii) for small values of w the MF breaks down and does not provide a good approximation anymore. This in sharp contrast to the TASEP, for which the MF works well: here, instead, for small w's we observe a large deviation between theory and simulations.

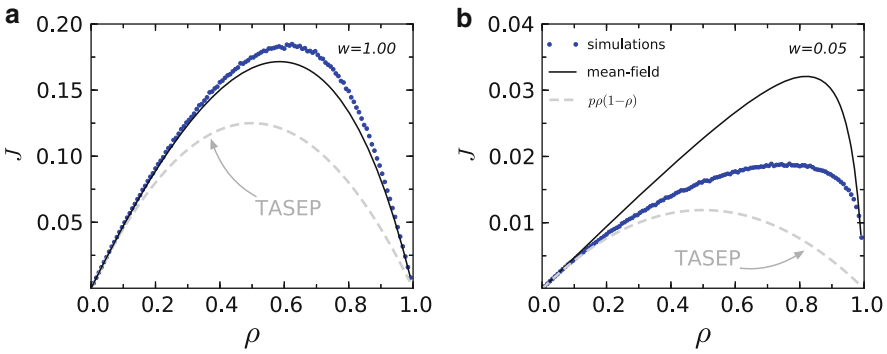

Fig. 3 Comparison between the fundamental diagram of the TASEP and of the two-state model (mean-field and simulations) for different values of w

An explication for these behaviours can be found in [20], where It has been shown that this simple stepping cycle can induce moving clusters of particles, causing correlations between sites neglected by the MF theory. A particle blocked in the queue can use the time spent there to make the transition towards the excited state, and then jump with a rate γ when the next site becomes empty. When w is small, this effectively changes the hopping rate of particles when the traffic effects are relevant. For this reason, the two-state model cannot be mapped onto a TASEP with hopping rates that are independent from the density; this is also clear from Fig. 3.

2.2 *The open Boundary Case: Phase Diagram*

If we now focus on a system with open boundaries, the density ρ is not fixed but its mean is controlled by the boundaries α and β. Although it is out of the scope of this work to provide a detailed illustration of the model with open boundaries, the MF phase diagram is known, and it is compared to the standard TASEP one in Fig. 4a.

The structure of the MF phase diagram remains the same of the TASEP one, oppositely to what other MF theories predicts for various models with particles having internal states, e.g. [21, 22]. However, numerical simulations (Fig. 4b, c) seem to confirm qualitatively the MF form of the phase diagram. One should however notice that, as in the periodic boundary case, important deviations between MF and simulations are present [19], and the development of refined theories to obtain a more quantitative phase diagram will be the subject of future investigations.

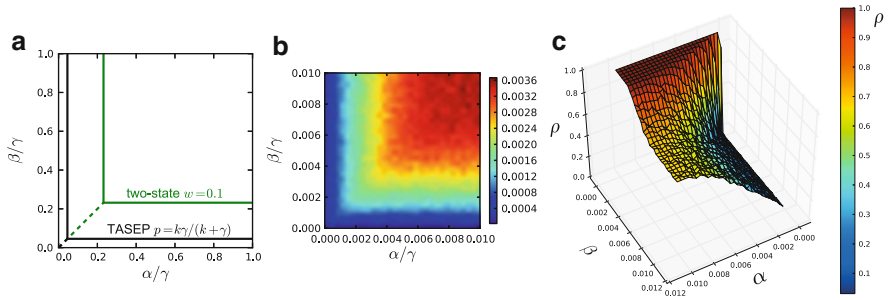

Fig. 4 (**a**) Comparison between the phase diagram of a TASEP with rate p and of the two-state model (mean-field). In (**b**) and (**c**) we show the numerical phase diagram for the two-state model with $k = 10^{-2}$ and $\gamma = 1$. Panel (**b**) is the colormap of the current J while in (**c**) one can observe the 3D plot of the density ρ for different values of α and β

3 Experiments

In this section we use the two-state model previously discussed, and apply it to the study of mRNA translation. In this process ribosomes enter the mRNA from one end ($5'$), then move codon by codon (one codon is a triplet of nucleotides) towards the other end ($3'$), from which they then detach. The translocation by one codon is only possible if a transfer RNA (tRNA) carrying an amino acid is captured by the ribosomes; a complex formed by the ribosome and the correct tRNA can then move to the following codon.

Because of the presence of a biochemical stepping cycle (capture of the correct tRNA and several biochemical intermediate conformations), a quantitative more reliable study of mRNA translation is possible with a model explicitly considering the transition to an excited state, followed by the translocation. Instead, mapping the biological process to a standard lattice gas model with Poissonian particles becomes cumbersome: the choice of the effective hopping rates would in fact depend on the density. As a result of the inhomogeneity of the lattice (there are different tRNAs associated to different codons, and therefore the hopping rate can change from site to site), mapping the biological process to the standard TASEP is even more complicated in the case of mRNA translation. The problem of the choice of rates can be overcome with introducing a stepping cycle of the type discussed in the previous section, where the transitions correspond to known biochemical processes. More in particular, in this case we will interpret k as the rate at which the ribosome is able to get a correct tRNA, and γ as the translocation rate of "excited" ribosomes. Different genes, i.e. codon sequences, are then represented by different lattices with characteristic sequences of k rates. It turns out that most of the codon have a ratio $w < 1$, meaning that the inclusion of the ribosomal stepping cycle is biologically relevant. More details about the rates and the biological process can be found in [19, 23], and references therein.

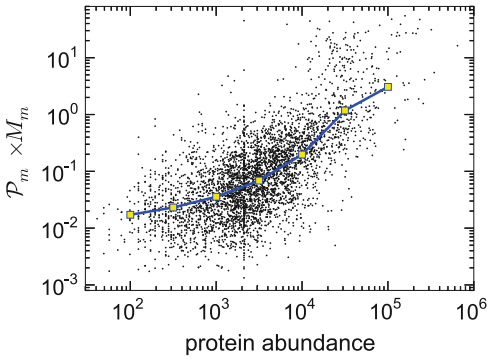

Fig. 5 Scatter plot of the predicted protein production rate versus the measured protein abundances. These two quantities, although they are not the same, should correlate. In the figure, each *black point* represents a gene m, while the *yellow square* are their average made with a logarithmic binning

Knowing the set of parameters for all mRNAs, it is then possible to simulate the translation of the entire genome of an organism as done in [23] for yeast, *S.cerevisiae*. With this model it has been possible to deduce biologically important outcomes, such as the classification of the mRNAs according to their translation properties based on the phase diagram of the individual mRNA, or the evaluation of the ribosomal entry rates (the rate α of each mRNA). Moreover, by calculating the current J at the estimated value of α for each gene m (α_m), it has been possible to provide an estimate of the protein production rate $\mathcal{P}_m \equiv J_m(\alpha_m)$. This quantity, multiplied by the amount of the corresponding mRNA M_m, well correlates (and better than other quantities currently used, see [23]) with the protein abundance as shown in Fig. 5.

Furthermore, the two-state model provides good predictions for single-gene *in vivo* experiments [24]. These, at our knowledge, are the first attempts to use TASEP-based models to quantitatively describe *in vivo* experiments.

4 Summary

We have presented features of a driven lattice gas model with internal states mimicking a stepping cycle. The model is presented in the perspective of mRNA translation, for which we have compared the results to experiments, but the formalism introduced could in principle be applied to different types of molecular motors whose biochemical stepping cycle is composed of two main stages. For example, this could be an approximation of other motors whose stepping is limited by the concentration of a substrate (e.g. ATP).

The simplest stepping cycle (two-state model) already presents remarkable differences to the standard TASEP, which indicates the importance of considering the stepping cycle to compare the model to experiments.

Acknowledgements I would like to thank I. Stansfield, M.C. Romano and A. Parmeggiani. A special thanks also goes to I. Neri and D. Levis.

References

1. B. Alberts, J.H. Wilson, T. Hunt, *Molecular Biology of the Cell*, 5th edn. (Garland Science, New York, 2008)
2. C.T. MacDonald, J.H. Gibbs, A.C. Pipkin, Biopolymers **6**(1), 1–5 (1968)
3. T. Chou, K. Mallick, R.K.P. Zia, Rep. Prog. Phy. **74**, 116601 (2011)
4. R.J. Harris, R.B. Stinchombe, Phys. Rev. E **70**, 016108 (2004)
5. L.B. Shaw, J.P. Sethna, K.H. Lee, Phys. Rev. E **70**, 021901 (2004)
6. S.A. Janowsky, J.L. Lebowitz, J. Stat. Phys. **77**, 35 (1994)
7. T. Chou, G. Lakatos, Phys. Rev. Lett. **93**(19) (2004)
8. J.J. Dong, B. Schmittmann, R.K.P. Zia, Phys. Rev. E **76**(5 Pt 1), 051113 (2007)
9. F. Turci, A. Parmeggiani, E. Pitard, M.C. Romano, L. Ciandrini, Phys. Rev. E **87**(1), 012705 (2013)
10. A. Parmeggiani, T. Franosch, E. Frey, Phys. Rev. Lett. **90**(8), 086601 (2003)
11. D.A. Adams, B. Schmittmann, R.K.P. Zia, J. Stat. Mech. p. P06009 (2008)
12. P. Greulich, L. Ciandrini, R.J. Allen, M.C. Romano, Phys. Rev. E **85**(1), 011142 (2012)
13. C.A. Brackley, L. Ciandrini, M.C. Romano, J. Stat. Mech. **2012**(03), P03002 (2012)
14. L.J. Cook, R.K.P. Zia, J. Stat. Mech. **2012**(05), P05008 (2012)
15. G. Lakatos, T. Chou, J. Phys. A **36**(8), 2027 (2003)
16. J.J. Dong, R.K.P. Zia, B. Schmittman, J. Phys. A **42**, 015002 (2009)
17. D. Chowdhury, Phys. Rep. **529**(1), 1 (2013)
18. S. Klumpp, Y. Chai, R. Lipowsky, Phys. Rev. E **78**, 041909 (2008)
19. L. Ciandrini, I. Stansfield, M.C. Romano, Phys. Rev. E **81**(5), 051904 (2010)
20. L. Ciandrini, M.C. Romano, A. Parmeggiani, Biophys. J. **107**(5), 1176–1184 (2014)
21. A. Garai, D. Chowdhury, D. Chowdhury, T.V. Ramakrishnan, Phys. Rev. E **80**, 011908 (2009)
22. T. Tripathi, G.M. Schutz, D. Chowdhury, J. Stat. Mech. p. P08018 (2009)
23. L. Ciandrini, I. Stansfield, M.C. Romano, PLoS Comput. Biol. **9**(1), e1002866 (2013)
24. A.J. Kemp, R. Betney, L. Ciandrini, A.C.M. Schwenger, M.C. Romano, I. Stansfield, Mol. Microbiol. **87**(2), 284 (2013). PMID: 23146061

Correlation Functions and Finite–Size Effects in Granular Media

Jevgenijs Kaupužs

Abstract A model is considered, where the local order parameter is an n–component vector. This model allows us to calculate correlation functions, describing the correlations between local order parameter at different spatial coordinates. The longitudinal and transverse Fourier–transformed two–point correlation functions $G_{\parallel}(\mathbf{k})$ and $G_{\perp}(\mathbf{k})$ in presence of an external field h are considered in some detail. In the thermodynamic limit, these correlation functions exhibit the so-called Goldstone mode singularities below certain critical temperature at an infinitesimal external field $h = +0$. The actual model can be applied to granular media, in which case it describes a small particle and, therefore, the finite–size effects have to be taken into account. Based on Monte Carlo simulation data for different system (lattice) sizes, we have found that the correlation functions are reasonably well described by certain analytic approximation formulas.

1 Introduction

We consider here the n–component vector–spin models, called also n–vector models or $O(n)$ models. These models describe the magnetism phenomena and can be applied also to small systems like granules. Description of a system of interacting magnetic particles is a challenging problem, which can be tackled with this approach. Historically, the n–vector models have attracted significant interest during the last decades owing to the critical phenomena (see, e.g., [1–9] and references therein) and also the so–called Goldstone mode singularities observed here (see, e. g., [6, 9–21] and references therein). We will briefly review this subject in the following section, discussing the application to a small granule later on.

J. Kaupužs (✉)
Institute of Mathematical Sciences and Information Technologies, University of Liepaja, Liepaja LV–3401, Latvia

Institute of Mathematics and Computer Science, University of Latvia, LV–1459 Riga, Latvia
e-mail: kaupuzs@latnet.lv

M. Chraibi et al. (eds.), *Traffic and Granular Flow '13*,
DOI 10.1007/978-3-319-10629-8_71

2 The *n*–Vector Model and Its Relation to Critical Phenomena and Goldstone–Mode Singularities

The n–vector model describes a Hamiltonian system of interacting spins. The Hamiltonian $\mathscr{H}$ is

$$\frac{\mathscr{H}}{T} = -\beta \left(\sum_{\langle ij \rangle} \mathbf{s}_i \mathbf{s}_j + \sum_i \mathbf{h}\mathbf{s}_\mathbf{i} \right) , \tag{1}$$

where T is temperature, measured in energy units, $\mathbf{s}_i$ is the spin variable (n–component vector of unit length) of the i-th lattice site, β is the coupling constant, and $\mathbf{h}$ is the external field with magnitude $| \mathbf{h} | = h$. The summation in (1) runs over all nearest neighbors $\langle ij \rangle$ in the lattice. Each spin configuration has an equilibrium statistical weight $\propto \exp(-H/T)$ consistent with the Boltzmann distribution. The model with $\beta > 0$ describes the ferromagnetism, whereas that with $\beta < 0$ – the anti-ferromagnetism. Note that in a special case of $n = 1$, the considered here n–vector model is the well known Ising or Lenz–Ising model.

A quantity of particular interest here is the two–point correlation function

$$\grave{G}_i(\mathbf{x}) = \langle s_i(\mathbf{0}) s_i(\mathbf{x}) \rangle , \tag{2}$$

where $s_i(\mathbf{x})$ is the i-th component of the spin ($i = 1, 2, \ldots, n$) at the lattice site with coordinate $\mathbf{x}$. In the following, we assume that the external field is oriented along the axis labeled by $i = 1$. At $h \neq 0$, the longitudinal ($i = 1$) and transverse ($i \geq 2$) correlation functions have to be distinguished for models with $n \geq 2$. The Fourier–transformed two–point correlation function is

$$G_i(\mathbf{k}) = \sum_{\mathbf{x}} \grave{G}_i(\mathbf{x})\, e^{-i\mathbf{k}\mathbf{x}} . \tag{3}$$

Further on, the longitudinal correlation function ($i = 1$) is denoted by $G_\parallel(\mathbf{k})$, and the transverse one ($i \geq 2$) – by $G_\perp(\mathbf{k})$.

Consider the lattice with spatial dimensionality d. In the thermodynamic limit at zero external field, the n–vector model with $d > 2$ for $n \geq 2$ or with $d \geq 2$ for $n = 1$ undergoes the phase transition from a disordered state to a state with long–range order at a certain critical coupling $\beta = \beta_c$. We will focus only on the ferromagnetic case $\beta > 0$, where the disordered state at $\beta < \beta_c$ is characterized by zero spontaneous magnetization $M = 0$, whereas the ordered state at $\beta > \beta_c$ – by $M > 0$. The spontaneous magnetization is equal to the average longitudinal spin component $\langle s_1 \rangle$ at a vanishingly small external field $h = +0$ in the thermodynamic limit.

From the exact solution found by Onsager [1] we know that the phase transition in the 2D Ising model on a square lattice takes place at $\beta_c = \frac{1}{2} \ln(1+\sqrt{2})$. This is the

second–order phase transition, which is characterized by power–law singularities. In particular, the spontaneous magnetization behaves as $M \sim (\beta - \beta_c)^{1/8}$ at $\beta \to \beta_c$ for $\beta > \beta_c$, the correlation length diverges as $\xi \sim \mid \beta - \beta_c \mid^{-\nu}$ with $\nu = 1$ at $\beta \to \beta_c$, whereas $G(\mathbf{k})$ (here index $i \equiv 1$ is omitted) behaves as $G(\mathbf{k}) \sim k^{-2+\eta}$ with $\eta = 1/4$ for small wave vectors $\mid \mathbf{k} \mid = k \to 0$ at the critical point $\beta = \beta_c$ [1–3]. The exponents in these expressions are called the critical exponents. According to the universality hypothesis, these are universal in the sense that the same exponents correspond to certain class of models with given d and n.

Exact and rigorous results in critical phenomena are mainly restricted to two–dimensional models [3]. In three–dimensional cases, perturbative renormalization group (RG) methods, high temperature series expansion, as well as numerical simulations are commonly used – see [6] for a review. A controversy between the perturbative RG method [5,6] and an alternative analytical approach, called the GFD (grouping of Feynman diagrams) theory [7, 18], has been recently discussed in [9].

In the models with $n \geq 2$, certain singularities appear not only near and at the critical point, but also below the critical temperature, i.e., at any $\beta > \beta_c$. These are the Goldstone mode singularities, which are related to the global rotational $O(n)$ symmetry of the model at $h = 0$. At $h \to 0$ and $\beta > \beta_c$, the ordering direction of an infinitely large spin system with the linear lattice size $L \to \infty$ is fixed – parallel to $\mathbf{h}$. At the same time, an infinitesimal variation δh of the external field in the transverse (perpendicular to $\mathbf{h}$) direction leads to the rotation of the total magnetization vector by an angle $\delta h / h$. It results into the divergence of the transverse magnetic susceptibility $\chi_\perp = G_\perp(\mathbf{0})$ at $h \to 0$. Other singularities are induced by this effect, as well. In the thermodynamic limit $L \to \infty$ at $\beta > \beta_c$, we have the following Goldstone mode power–law singularities:

$$M(h) - M(+0) \propto h^{\rho} \quad \text{at} \quad h \to 0 \,, \tag{4}$$

$$G_\perp(\mathbf{k}) \propto k^{-\lambda_\perp} \,, \; G_\parallel(\mathbf{k}) \propto k^{-\lambda_\parallel} \quad \text{at} \quad h = +0 \,, \, k \to 0 \,. \tag{5}$$

Here $M(h)$ is the magnetization depending on h, and $M(+0)$ is the spontaneous magnetization. According to the standard theory [10–14], $\lambda_\perp = 2$ and $\lambda_\parallel = 4 - d$ hold for $2 < d < 4$. This approach gives $\lambda_\perp = 2$, $\lambda_\parallel = 1$ and $\rho = 1/2$ in three dimensions $d = 3$. Predictions of the GFD theory [18] are somewhat different:

$$d/2 < \lambda_\perp < 2 \,, \qquad \lambda_\parallel = 2\lambda_\perp - d \,, \qquad \rho = (d/\lambda_\perp) - 1 \,. \tag{6}$$

Several Monte Carlo simulations have been performed earlier [15–17] to verify the compatibility with standard–theoretical expressions, where the exponents are fixed. In recent years, a series of accurate Monte Carlo simulations [9, 19–21] have been performed for remarkably larger lattices than previously were available, with an aim to evaluate the exponents in (4)–(5). The results point to some deviations from the standard–theoretical values, in agreement with (6).

3 Relation to Granular Media

Here we would like to emphasize several aspects, which might be important in various applications of the n–vector model to magnetism phenomena in granular media:

- A separate small particle (granule) has a finite size.
- Boundary spins have different conditions than the bulk spins.
- Interaction between magnetic particles (granules) can be important.

In the current study only the first aspect is taken into account, considering this as a first step towards a more realistic description. Here we assume periodic boundary conditions for a finite–size system. One has no notice that the n–vector model is suited to describe the magnetism of granular media. In this case, dissipative forces and friction between granules might be neglected.

4 Analytic Approximations for the Two–Point Correlation Functions

We have evaluated the Fourier–transformed transverse and longitudinal two–point correlation functions of the $O(4)$ (i.e., $n = 4$) model in the $\langle 100 \rangle$ crystallographic direction of the simple cubic lattice. These are denoted as $G_\perp(k)$ and $G_\parallel(k)$, respectively. We have used the Monte Carlo techniques of [20]. The results for relatively large system sizes, up to $L = 350$, have been analyzed in [20] with an aim to evaluate the thermodynamic limit. Here we will show the simulation results for much smaller sizes in order to examine the finite–size effects.

In addition, here we propose and test certain analytic approximations

$$G_\perp(k) \approx \chi_\perp \left(\frac{\tilde{a}(h)}{\tilde{a}(h) + \tilde{k}^2} \right)^{\lambda_\perp/2} , \tag{7}$$

$$G_\parallel(k) \approx \chi_\parallel \left(\frac{\tilde{b}(h)}{\tilde{b}(h) + \tilde{k}^2} \right)^{\lambda_\parallel/2} , \tag{8}$$

where $\chi_\perp$ and $\chi_\parallel$ are the transverse and longitudinal susceptibilities, respectively, and $\tilde{k}^2 = (2\sin(k/2))^2$. These approximations have a set of expected properties under appropriate choice of parameters $\tilde{a} = \tilde{a}(h)$ and $\tilde{b} = \tilde{b}(h)$. The actual choice of $\tilde{k}^2$ ensures the periodicity $G_\perp(k + 2\pi) = G_\perp(k)$ and $G_\parallel(k + 2\pi) = G_\parallel(k)$ and, at the same time, $\tilde{k}^2 \to k^2$ at $k \to 0$. The formulas (7) and (8) ensure that the correlation functions can be expanded in powers of k^2 in vicinity of $k = 0$ for any nonzero h. At the same time they ensure the power–law asymptotic $G_\perp(k) = a\, k^{-\lambda_\perp}$ and $G_\parallel(k) = b\, k^{-\lambda_\parallel}$ in the thermodynamic limit at $h \to 0$

provided that $\tilde{a}(h) \sim \tilde{b}(h) \sim h^{2/\lambda_\perp}$ holds at $h \to 0$, taking into account the relations $\chi_\perp = M(h)/(\beta h)$ and $\chi_\parallel \sim h^{-\lambda_\parallel/\lambda_\perp}$. The latter one is true at $h \to 0$ according to Eq. (9.25) in [18]. This behavior of $\tilde{a}(h)$ and $\tilde{b}(h)$ implies that $\xi_\perp(h) \sim \xi_\parallel(h) \sim h^{-1/\lambda_\perp}$ holds for small h, where $\xi_\perp$ and $\xi_\parallel$ are the transverse and the longitudinal correlation lengths. Note also that (7) is the well–known Gaussian approximation at $\lambda_\perp = 2$, although our fits give $\lambda_\perp < 2$.

Equations (7) and (8), apparently, represent the simplest analytic formulas having all the discussed here expected properties. Therefore, they might be very meaningful approximations. We have tested them in the $O(4)$ model at $\beta = 1.1 > \beta_c \approx 0.936$ (an estimate given in [15]) and a small value of the external field $h = 0.0003125$. In the following, we discuss Monte Carlo data for three relatively small lattice sizes – $L = 16$, $L = 32$ and $L = 64$. The fit results for $G_\perp(k)$ and $G_\parallel(k)$ are shown in Figs. 1 and 2, respectively. The corresponding fit parameters are collected in Table 1. Note that the values of susceptibilities have been determined directly from the simulation data as $\chi_\perp = M(h)/(\beta h)$ and $\chi_\parallel = G_\parallel(\mathbf{0})$.

It turns out that the transverse correlation function $G_\perp(k)$ can be quite well fit to (7) within the whole range of the wave vector values $k \leq \pi$. The longitudinal correlation function $G_\parallel(k)$ is quite similar to the transverse one for $L = 16$, and also can be fit over the whole k range to the corresponding formula (8). For $L = 32$ such a fit is still good, but for a larger system size $L = 64$ the fit is acceptable only

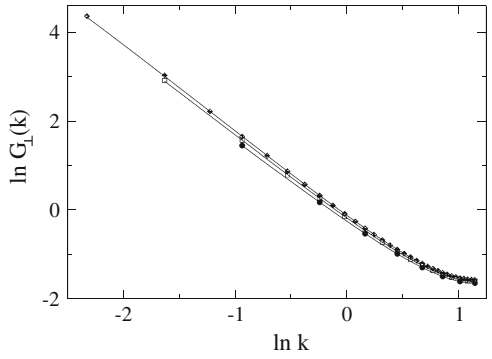

Fig. 1 The $\ln G_\perp(k)$ vs $\ln k$ plots for the $O(4)$ model at $\beta = 1.1$ and $h = 0.0003125$. The Monte Carlo results for lattice sizes $L = 16$ (*circles*), $L = 32$ (*squares*) and $L = 64$ (*diamonds*) are shown

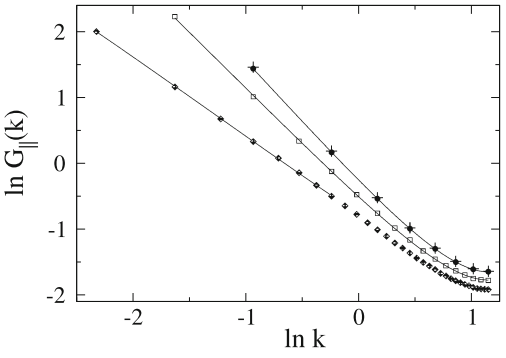

Fig. 2 The $\ln G_\parallel(k)$ vs $\ln k$ plots for the $O(4)$ model at $\beta = 1.1$ and $h = 0.0003125$. The Monte Carlo results for lattice sizes $L = 16$ (*circles*), $L = 32$ (*squares*) and $L = 64$ (*diamonds*) are presented. For comparison, the values of $\ln G_\perp(k)$ at $L = 16$ are shown by pluses

Table 1 Parameters in (7) and (8) depending on the linear lattice size L for the $O(4)$ model at $\beta = 1.1$ and $h = 0.0003125$, evaluated from Monte Carlo simulations

L	$\chi_\perp$	$\tilde{a}(h)$	$\lambda_\perp$	$\chi_\parallel$	$\tilde{b}(h)$	$\lambda_\parallel$
16	270.7(1.0)	0.001932(11)	1.8961(12)	259.70(29)	0.001932(12)	1.8877(17)
32	1095.2(1.1)	0.0005694(26)	1.9410(11)	340.3(2.1)	0.0005578(51)	1.7124(18)
64	1389.21(58)	0.0005376(24)	1.9744(11)	50.1(1.3)	0.000426(18)	1.2198(49)
350	1422.831(40)	0.0005354(26)	1.9776(11)	7.41(20)	0.00277(36)	0.872(22)

within a narrower k interval. Therefore, the fit over the range $k \leq \pi/4$ is shown in this case.

As we can see from Figs. 1, 2 and Table 1, the finite–size effects are remarkably larger for the longitudinal correlation function as compared to the transverse one within $16 \leq L \leq 64$. We have considered also a much larger lattice size $L = 350$. The transverse correlation function, again, is well fit within $k \leq \pi$, whereas the longitudinal one – within $k < 0.28$. The values of parameters are given in Table 1. Comparing the results in Tab. 1, we conclude that the size $L = 64$ is already quite close to the thermodynamic limit for $G_\perp(k)$, but not for $G_\parallel(k)$ at the actual parameters $\beta = 1.1$ and $h = 0.0003125$. One has to note that the smaller is h, the larger are transverse and longitudinal correlation lengths and, therefore, the larger are lattice sizes L at which the thermodynamic limit is reached with certain accuracy.

Interestingly, the transverse and longitudinal correlation functions in our example are practically the same for the smallest lattice size $L = 16$. It can be seen in Fig. 2, where $\ln G_\parallel(k)$ and $\ln G_\perp(k)$ for $L = 16$ are shown by solid circles and pluses, respectively. The reason of this is the smallness of the term $\sum_i \mathbf{h} \cdot \mathbf{s_i}$, which contains the sum over L^3 lattice sites and represents the interaction of spins with the external field in Hamiltonian (1). Indeed, this term is responsible for the breaking of rotational symmetry and the related differences between $G_\parallel(k)$ and $G_\perp(k)$.

Summary and Conclusions

In the actual work, the n–component vector spin model (n–vector model or $O(n)$ model) has been considered. We have briefly reviewed its relation to critical phenomena and Goldstone mode singularities and have considered also its application to magnetic phenomena in a granular media. In particular, two–point correlation functions and finite–size effects have been discussed in some detail based on Monte Carlo simulation data and certain analytical approximations.

Acknowledgements This research is supported by the Baltic–German University Liaison Office through German Academic Exchange Service (DAAD) with funds from the Foreign Office of the Federal Republic of Germany.

References

1. L. Onsager, Phys. Rev. **65**, 117 (1944)
2. B. McCoy, T. T. Wu, *The Two–Dimensional Ising Model* (Harvard University Press, 1973)
3. R.J. Baxter, *Exactly Solved Models in Statistical Mechanics* (Academic, London, 1989)
4. D.J. Amit, *Field Theory, the Renormalization Group, and Critical Phenomena* (World Scientific, Singapore, 1984)
5. J. Zinn–Justin, *Quantum Field Theory and Critical Phenomena* (Clarendon Press, Oxford, 1996)
6. A. Pelissetto, E. Vicari, Phys. Rep. **368**, 549 (2002)
7. J. Kaupužs, Ann. Phys. (Berlin) **10**, 299 (2001)
8. J. Kaupužs, Int. J. Mod. Phys. A 27, 1250114 (2012)
9. J. Kaupužs, Can. J. Phys. **9**, 373 (2012)
10. L. Schäfer, H. Horner, Z. Phys. B **29**, 251 (1978)
11. I. D. Lawrie, J. Phys. A **14**, 2489 (1981)
12. U. C. Täuber, F. Schwabl, Phys. Rev. B **46**, 3337 (1992)
13. R. Anishetty, R. Basu, N. D. Hari Dass, H. S. Sharatchandra, Int. J. Mod. Phys. A **14**, 3467 (1999)
14. N. Dupuis, Phys. Rev. E **83**, 031120 (2011)
15. J. Engels, T. Mendes, Nucl. Phys. B **572**, 289 (2000)
16. J. Engels, S. Holtman, T. Mendes, T. Schulze, Phys. Lett. B **492**, 492 (2000)
17. J. Engels, O. Vogt, Nucl. Phys. B **832**, 538 (2010)
18. J. Kaupužs, Progress of Theoretical Physics **124**, 613 (2010)
19. J. Kaupužs, R. V. N. Melnik, J. Rimšāns, Commun. Comput. Phys. **4**, 124 (2008)
20. J. Kaupužs, R. V. N. Melnik, J. Rimšāns, Phys. Lett. A **374**, 1943 (2010)
21. J. Kaupužs, R. V. N. Melnik, J. Rimšāns, Condens. Matter Phys. **15**, 43005 (2012)